

平成 26 年度～平成 30 年度 「私立大学戦略的研究基盤形成支援事業」

豊田工業大学

「グリーン電子素子・材料研究センター」

研究成果報告書

2019 年 5 月

目 次

平成 26 年度～平成 30 年度 「私立大学戦略的研究基盤形成支援事業」

I. 豊田工業大学 「グリーン電子素子・材料研究センター」 研究成果報告書概要

II. 研究報告

1. 「先進エネルギー変換素子・材料 — 熱電材料、熱ダイオード、熱スイッチ」
2. 「界面・電極制御による電力損失の低減 — 界面制御磁性メモリ」
3. 「界面・電極制御による電力損失の低減 — 光電・電光変換素子」
4. 「界面・電極制御による電力損失の低減 — 有機電子素子」
5. 「界面・電極制御による電力損失の低減 — 界面改質プロセス」

法人番号	231023
プロジェクト番号	S1411027

**平成 26 年度～平成 30 年度「私立大学戦略的研究基盤形成支援事業」
研究成果報告書概要**

- 1 学校法人名 トヨタ学園 2 大学名 豊田工業大学
- 3 研究組織名 豊田工業大学大学院工学研究科
グリーン電子素子・材料研究センター
- 4 プロジェクト所在地 名古屋市天白区久方 2-12-1
- 5 研究プロジェクト名 マイクロ・メソ構造制御による革新的グリーン電子素子・材料技術の
基盤形成
- 6 研究観点 研究拠点を形成する研究

7 研究代表者

研究代表者名	所属部局名	職名
神谷 格	大学院工学研究科	教授

- 8 プロジェクト参加研究者数
- 11
- 名

- 9 該当審査区分
- 理工・情報
- 生物・医歯
- 人文・社会

10 研究プロジェクトに参加する主な研究者

研究者名	所属・職名	プロジェクトでの研究課題	プロジェクトでの役割
神谷 格	大学院 工学研究科 ・教授	・先進的電極界面構造の開発・ 制御 ・歪制御半導体の光電変換素子 応用	・統括 ・電極の革新・低損失化 ・歪制御・光電素子開拓
竹内 恒博	大学院 工学研究科 ・教授	・熱電材料、熱ダイオード	・革新的熱電素子の開拓 ・電子機構の解明
松波 雅治	大学院 工学研究科 ・准教授	・熱電材料、熱ダイオード	・革新的熱電素子の開拓 ・熱電特性と電子間相互作用 の関係の解明
栗野 博之	大学院 工学研究科 ・教授	・低消費電力磁性記録素子	・超低消費電力メモリの開 拓
吉村 雅満	大学院 工学研究科 ・教授	・先進的電極界面構造の開発・ 制御	・ナノカーボン利用素子技術 の確立
原 正則	大学院 工学研究科 ・准教授	・先進的電極界面構造の開発・ 制御	・界面評価 ・新規電極開発
荒川 修一	大学院 工学研究科 ・助教	・界面構造制御と応用	・新規プロセスによる素子作 製法開拓

法人番号	231023
プロジェクト番号	S1411027

岩田 直高	大学院 工学研究科 ・教授	・ワイドギャップ素子の電極、物性 性と低損失化 ・紫外線受光素子	・ワイドギャップ素子の低損失化 と機能拡大 ・電極の革新と低損失化
大下 祥雄	大学院 工学研究科 ・教授	・先進的電極界面構造の制御 ・歪制御半導体の光電変換素子 応用	・電極の革新と低損失化 ・歪制御・光電素子開拓
小島 伸晃	大学院 工学研究科 ・助教	・先進的電極界面構造の制御 ・歪制御半導体の光電変換素子 応用	・電極の革新と低損失化 ・歪制御・光電素子開拓
榊 裕之	大学院 工学研究科 ・学長	・量子構造光電素子	新規量子構造を用いた受光素子の 実現
(共同研究機関等)			

<研究者の変更状況(研究代表者を含む)>

新

変更前の所属・職名	変更(就任)後の所属・職名	研究者氏名	プロジェクトでの役割
分子研・研究員	大学院工学研究科 ・准教授	松波 雅治	・革新的熱電素子の開拓 ・熱電特性と電子間相互作用の 関係の解明

(変更の時期:平成27年 6月 1日)

新

変更前の所属・職名	変更(就任)後の所属・職名	研究者氏名	プロジェクトでの役割
山梨大学・特任助教	大学院工学研究科 ・准教授	原 正則	・界面評価 ・新規電極開発

(変更の時期:平成28年 4月 1日)

11 研究の概要(※ 項目全体を10枚以内で作成)

(1)研究プロジェクトの目的・意義及び計画の概要

<p>【目的】 熱電素子などエネルギー変換素子・材料を軸に、新構造の可能性を示すとともに、界面や電極構造の制御を通じ、電子流をより良く制御し、電力損失の低減法の向上と新機能の実現を目的としている。</p> <p>【意義】 世界的に資源とエネルギーの確保は厳しさを増しており、我国を始め、先進国にはエネルギー消費の低減と利用効率の向上のための革新技術の開発が喫緊の課題となっている。特に、エネルギー変換機器や素子の効率向上、未利用エネルギーの活用、大量に使われるIT機器などの電力消費の大幅低減などが不可欠である。これらの機器・素子・材料の多くでは、動作原理や損失要因が、それらの材料や素子のマイクロおよびメソスケールでの構造によって決定されており、そうした構造を刷新すれば、電子物性、光学物性、熱的物性なども変わり、より優れた特性や機能を持つ材料や素子を実現できる可能性があり、この研究により新たな展望を開く。</p>

法人番号	231023
プロジェクト番号	S1411027

【計画の概要】 基盤技術としての構造制御、そして具体的なテーマとしてエネルギー変換素子・材料の開発と界面・電極構造制御による素子の電力損失の低減を目指している。これらを組み合わせ、スパイラルアップで取り進めている。

I. エネルギー関連素子・材料の性能向上のためのマイクロ・メソ構造制御技術の確立

本研究で取組む熱電素子では、Siを基体にMnやAlを加えた合金相の構造を、原子スケールでマイクロに制御する必要がある。また、ナノ構造中の量子準位を用いた光電材料では、10nm オーダで組成と形状の制御を必要とする。このように、所望の機能や性能の実現のために、マイクロおよびメソスケールでの構造制御技術の確立を図る。

II A. 先進エネルギー変換素子・材料の開発

熱電素子は長い歴史を持つが、実用面では BiTe 系に限られている。本チームの竹内は、SiMnAl 系合金が BiTe に迫る特性を持つことを発見しており、特性の改良次第で本命となる可能性も持つ。本研究では、熱流の制御も含め、特性向上を目指す。また、ナノ細線やナノアイランド構造など量子構造の持つ特異な光物性を活かした光電変換素子の研究を進め、変換効率や検出効率の向上可能性を示す。

II B. 界面・電極構造制御による素子の電力損失の低減

多くの素子では、電極部の抵抗が、電力損失を増大させ、信頼性を低下させる。そこで界面・電極構造を制御し、界面を通過する電子流による損失の低減を図る。特に、大電流を流す GaN 系パワー素子への電極技術や電極形成が容易でないグラフェンに対する電極技術などの確立を図る。

[年次計画概要]

- 1 年目: 従来の熱電変換素子や光電変換素子の研究と界面・電極構造に関する取組みを再整理し、開発すべき新素子の設計、関連の基礎実験を行う。また、電子状態計測用 XPS 装置などの新規設備の設置・稼働を図る。
- 2 年目: 開発すべき素子の設計に基づき、素子・材料中のマイクロ・メソ構造制御の実験を進め、評価する。
- 3 年目: 新規の熱電変換素子や光電素子、制御された界面・電極構造等の試作を進め、初期的評価を行う。
- 4 年目: 前年度の試作・評価結果を基に、素子や構造の再設計・再試作を行い、性能・機能の改良を行う。
- 5 年目: 試作した熱電素子・光電変換素子・新規界面・電極構造などの総合評価を行い、変換効率の向上や損失の低減の達成度を明らかにする。得られた知見に基づき、さらなる機能・性能向上の方向性を示す。

(2) 研究組織

物質・材料科学分野の6名と電子・情報工学分野の5名(当初4名)の教員が「グリーン電子素子・材料研究センター」を形成し、これらに加え、学内外の関連する他の教員から適宜協力を得ている。各テーマ担当教員指導の下、延べ50名程度の博士研究員(PD)や学生・院生が研究に参加。研究センター全体としてのシナジーを持たせるべく、年に数回、若手研究員による研究紹介等を行っている。施設は、参加教員の保有施設の相互利用の他、本学の「共同利用クリーンルーム」を積極利用している。

外部評価委員としては、企業からは豊田中研の竹田康彦氏、また、アカデミアからは NIMS (MANA)の青野正和氏にお願いし、適宜ご助言頂いている。

(3) 研究施設・設備等

X線光電子分光装置 アルバックファイ社 PHI5000 VersaProbeTI
原子層堆積装置: Fiji F200

法人番号	231023
プロジェクト番号	S1411027

半導体エッチング装置: RIE-101iPH
 全自動多目的X線回折装置 ブルカー・エイエックエス社: D8 Advance TKT
 熱拡散率測定装置 NETZSCH 社: LFA 457 MicroFlash
 熱電物性測定装置用ヘリウム再凝縮デューワー カンタム・デザイン社: P935(A)SR
 磁化率測定装置: カンタム・デザイン社: P525SR
 フローティング型アルゴンイオン銃: 04-370Z
 エキシマーレーザー: ExciStarXS-500-ArF
 PL マッピング装置: PL-SMAP-RT100

(4) 研究成果の概要 ※下記、13及び14に対応する成果には下線及び*を付すこと。

【先進エネルギー変換素子・材料 - 熱電材料、熱ダイオード, 熱スイッチ】

<優れた成果が上がった点>

熱電物性を電子構造とフォノン分散の観点から定量的に解析し、高性能熱電材料を得る条件を検討し、容易に利用可能な材料設計指針を構築し^{*T1}、論文等で発表した。提案した指針と電子構造解析(理論計算と先端計測実験)の併用で、様々な高性能熱電材料を開発した^{*T2}。実用化されている材料の性能を遥かに凌駕する $ZT > 1.8$ (n型)^{*T3}, $ZT > 1.6$ (p型)を示す材料を創製した。さらに、狭い温度領域ではあるものの、 $ZT = 470$ を示す材料を発見するに至った。この性能指数は、既存材料の180倍にも達している^{*4}。

固体熱ダイオードでは、300Kと900Kの熱浴で挟んだ際、世界最高の熱整流比 $TRR = J_1/J_2 > 2.2$ を示す材料を開発した^{*T4}。さらに110°C付近で熱浴間の温度差が僅か50Kで、 $TRR > 2$ を示す熱ダイオードの開発にも成功した。また、 $TRR > 3.0$ を示す素子の構成材料を特定した。

熱スイッチ材料では、新しい機構を提案し、機械的な要素なしに熱流を変化させる事に成功した。現状熱流の変化率は50%を超えており、素子構造を作り込むことで、600%を超える熱流の変化をもたらす素子を作りだせると見積もった。

<課題となった点>

熱電材料の開発において $ZT = 470$ (既存材料の180倍)を示す材料を発見するに至ったが、その性能が得られる温度領域が狭く、かつ、特殊な温度勾配を必要とする。この性能を実用化に結びつけるためには、性能を導く機構の正確な理解に基づき、利用可能温度を広範囲にし、かつ、一般的な温度勾配で動作するように材料を改質する必要がある。

熱ダイオードおよび熱スイッチに関しては、5年間のプロジェクトにより確実に性能が向上しつつあるものの、実用化を促すだけの性能が得られたとは言い難い。

<自己評価の実施結果と対応状況>

中間報告の段階で既にMnとSiから成り安価で無害^{*2}な熱電材料を作製。また、熱電材料利用には同程度の熱膨張計係数を有するn型とp型が必要だが本研究で同じ合金系においてキャリア濃度を調整し、 $ZT > 1$ のp型材料^{*3}と、 $ZT > 0.8$ のn型材料^{*4}の創製に成功し、世界最高性能を有する熱ダイオードの試作、そしてその動作温度調整にも成功していた。しかし、実用化のためにはさらなる動作温度の低下が必要であったが、110°C付近で熱浴間の温度差が僅か50Kで、 $TRR > 2$ を示す熱ダイオードも実現した。

また、熱スイッチについても中間報告で10%以下だった熱流変化率を50%以上まで向上させるなどの対応を行った。

<研究期間終了後の展望>

2014年より実施してきた熱電材料に関する研究において、材料設計指針の構築の高度化と、提案する材料設計指針が正しいことを証明する取り組みを行ってきた。その結果として、熱電材料の性能を向上させる指針を高度化できた。この成果を活用することで、様々な温

法人番号	231023
プロジェクト番号	S1411027

度領域で利用される新規熱電材料が創製できるはずである。今後、特に重要となるのは莫大な熱量が存在する 100℃以下の低温熱電である。この温度領域で電力を有効に創製できる材料を開発できれば、その波及効果は極めて大きいと考えている。100℃以下の低温領域で $ZT > 2.0$ を示し、かつ、環境に負荷をかけない材料の開発を目指す。

熱ダイオードについては、現在、 $Ag_2(S, Se, Te)$ 化合物で観測される異常な熱伝導度の起源解明、制御指針の構築、および、それらを使った高性能熱整流素子の開発を現在も続けている。特に、3 倍を超える整流効果を示す可能性が高い素子を試作、および、その性能評価が急務である。

熱スイッチについては、今後、 $Ag_2(S, Se)$ を用いた薄膜素子の作製と評価を行う。また、リーク電流の熱流に及ぼす寄与を精密に測定し、制御する指針を構築する計画である。最終的には、バイアス電圧により 1000% の熱流変化を実現する素子の開発を目指す。

<研究成果の副次的効果>

熱電材料の研究は、複数企業との共同研究に発展。特許は 8 件申請した。これら企業と実用的素子の作製を検討している。熱ダイオード・スイッチ材料についても、企業との共同研究に繋がった。さらに、本研究の独創性を生かすことで、2018 年に JST CREST への応募し、採択された。

【界面・電極制御による電力損失の低減 - 界面制御磁性メモリ】

<優れた成果が上がった点>

磁性層と重金属層からなるヘテロ構造を有する磁性細線に電流を注入すると、このヘテロ界面を通過する伝導電子がスピンホール効果によりスピン分極して磁性層内に侵入し大きな磁気トルクを与える。これをスピン軌道トルクと呼ぶ。このスピン軌道トルクは磁性細線中の磁壁の駆動力となりメモリやセンサーへの応用が期待されている。しかし、磁性層がフェロ磁性体の場合、スピン軌道トルクは界面から 2nm くらいまでの磁性層にしか及ばないため素子応用を考える時、問題となっていた。これは磁気熱揺らぎ問題と呼ばれ、メモリ最小単位の 1 ビットの磁気ボリュームが少ないと磁気エネルギーが室温の熱エネルギーの影響で磁化状態を維持することができない問題である。しかし、磁性層をフェロ磁性体から希土類金属と遷移金属からなるフェリ磁性体に変えるとスピン軌道トルクの及ぶ範囲を数 100nm にまで拡張することができ、この磁気ボリューム問題を解決することが出来た^{*M1}。

このメカニズムとして、希土類金属の磁気モーメントと 3d 遷移金属の磁気モーメントが互いに逆向きであるフェリ磁性体特有のものと考えられる。磁性層が 3d 遷移金属だけで構成されている一般的な磁性細線においては、スピン偏極電流のスピンは磁性層内を進むうちにすぐに 3d 遷移金属と同じ向きに揃う。すなわち、スピンコヒーレンス長が短い。しかし、希土類・遷移金属合金の場合には、伝導電子のスピンは互いに逆向きである希土類金属と 3d 遷移金属のスピンのもつ向きにも向きに揃えようとするため、磁性層の奥深くまで進んでも初めのスピンの向きを維持することになり、スピンコヒーレンス長が極めて長くなる^{*M1}。そのため、磁性層厚が厚くてもスピン軌道トルクが働き続けることになる。このように、フェリ磁性細線は、磁性層を厚くできるのでメモリやセンサーに適した材料であることを見出した^{*M2}。

<課題となった点>

上述したように、希土類金属と遷移金属の磁気モーメントが互いに逆向きに磁気結合しているフェリ磁性体を磁性細線材料として利用することで、スピン軌道トルクの磁性層厚制限を克服して厚膜利用することが出来る。

<自己評価の実施結果と対応状況>

法人番号	231023
プロジェクト番号	S1411027

中間報告の段階では、希土類・遷移金属磁性膜/Pt ヘテロ構造からなる磁性細線に電流を注入し、従来はヘテロ界面のみに生じるスピホール効果が希土類・遷移金属磁性膜の奥深くまで作用することを示していたが、このメカニズムは推察に留まっていた。今回、これをきちんと示すに至り、その結果フェリ磁性細線は、磁性層を厚くすることでメモリやセンサーに適した材料であることを示した。

<研究期間終了後の展望>

希土類金属のスピン構造は通常スペリ構造となるため、希土類金属とスピンと3d遷移金属のスピンは完全に反平行にはならない。したがって、上述のスピンコヒーレンス長の長さは、希土類金属の種類によって異なるはずである。そこで、今後は希土類金属の種類とスピンコヒーレンス長の関係を明らかにしたい。

<研究成果の副次的効果>

副次効果として角運動量補償温度と磁化補償温度に差異が生ずることが分かった。これをうまく使いこなすことで、フェリ磁性細線を用いた磁性細線メモリやセンサーの性能向上を実現し、これらへの応用展開を目指す。

【界面・電極制御による電力損失の低減 -光電・電光変換素子】

<優れた成果が上がった点>

1)トンネル接合による光素子の高効率化

結晶 Si 太陽電池高効率化へ向け、電極材料間に数 nm の薄い Si 酸化膜を挿入したトンネル電極構造を検討。Si 結晶/Si 酸化膜界面では光生成少数キャリアの再結合準位数が少なく、低再結合速度・高い開放電圧、また電極材料の仕事関数制御で、pn 接合なしの太陽電池動作が期待されるが実際の素子の効率は低く、欠陥形成や膜界面近傍での電極材料の仕事関数がバルク値と異なるためと考えられる。そこで、Si/Si 酸化膜界面の欠陥と界面近傍での電極材料の仕事関数を、MOS 型評価素子の電気容量-電圧測定を行い、熱処理条件依存性を考察した。また界面近傍の電極の仕事関数がバルク値と違う事を明らかにした^{*P1}。電極材料の界面近傍の仕事関数とプロセス誘起欠陥の情報を得た^{*P1}。

2)層状化合物半導体を中間層に用いた GaAs/Si 光素子の高効率化

高効率 III-V 族半導体光素子のための GaAs/Si モノリシック素子では、GaAs/Si 間の大きな格子不整合・熱膨張係数差により、GaAs 層に $>10^{10}\text{cm}^{-2}$ の密度で転位が発生し、キャリア再結合により電力損失が生じる。本研究では In_2Se_3 層状半導体を GaAs/Si 間に中間層として挟み、vdW 界面により生じる歪を緩和させ GaAs 層の転位密度低減を目指した。特に微傾斜基板の影響を検討し、GaAs(111)、Si(111)の微傾斜基板に $\alpha\text{-In}_2\text{Se}_3$ の単一相 (In_2Se_3 は多形構造)でのエピ成膜、更にこの $\alpha\text{-In}_2\text{Se}_3$ 上への GaAs エピ成膜にも成功した。^{*P2}

3)光センサーの開発

NIR(1~2 μm)領域での高感度光センサー実現のため、InGaAs TBP 光増倍型素子を MBE とフォトリソを用い試作し、波長 1.7 μm 迄感度を持つ素子で受光感度~4A/W を達成^{*P3}。また TBP と CMOS 回路兼備のアレーセンサを試作し、128 画素のリニアアレーを用いイメージスキャンも実現した。

4)GaN デバイスの開発

Si基板上のAlGaN/GaN HEMTの作製プロセスの研究では、低い接触抵抗を示すオーミック電極を開発すると共に、ALDによる表面安定化保護膜技術を実現し、高電流と高耐圧特性を同時に達成した。特に、SiN膜を原子層堆積法で形成する前に、HEMT表面のHCl処理により、良好な素子特性を得た^{*P4}。さらに、低オン抵抗とノーマリオフ動作を示すp型GaNゲート

法人番号	231023
プロジェクト番号	S1411027

を用いたAlGaIn/GaN HEMTを実現した^{*P4}。これの実現に向けては、選択ドライエッチング技術を開発するとともに、そのゲート構造やエッチングプロセスが素子特性に及ぼす影響を調べた^{*P4}。

一方、縦型のGaInトランジスタの実現に向けて、p型GaIn層を局所的に形成する技術を開発した^{*P5}。これは、MgドープGaInに対してArFエキシマレーザーを局所的に照射することにより、その照射部分の局所的なp型化を実現する技術である。また、ワイドバンドギャップのAlGaInのpn接合をSi上に縦方向に形成し、素子応用の研究を進めた。このpn接合でフォトダイオードを試作し、深紫外での光応答特性を測定評価した^{*P5}。

5) InAs系量子構造の構造制御と界面

既にQWIと呼ばれる構造で光の短波長変換(アップコンバージョン)^{*P6}を実現させたが、低効率と構造作製の難しさが課題。そこで、MBEによるsubmonolayer (SML) 成長法と呼ばれる結晶成長法を新たに導入し検討した。この手法により、従来と異なるQWIの形状が得られることが判明すると共に、これを介した光アップコンバージョンを実証した^{*P6}。

下層にシードと呼ばれる小さいドットを埋め込むことで歪制御された上層に成長したInAs量子ドットにより1.7 μ m超えの長波長発光を実現させた^{*P7}。更に素子改善を試み、シード層と発光層のドットの間の中間層に工夫を加え、更に、1.9 μ m程度までの長波長発光も実現させた^{*P7}。

表面InAsドットのKFM計測でドット周辺のポテンシャルの凹みを見出し、リング状の電子の蓄積域形成の可能性を指摘した^{*P8}。

<課題となった点>

- 1) 電極材料の基礎的な物性や、堆積方法の検討は進めたが、今後は実装へ向けた検討、そしてこれを用いた高効率結晶 Si 太陽電池の実現が必要である。
- 2) 層状半導体層の成膜の検討は進んだ。今後、この積層構造を基に GaAs/Si 光素子の作製と、それによる光電変換の高効率化を目指す必要がある。
- 3) 近赤外域用の三角障壁フォトリソトランジスタの実証はしたが、その感度がまだ十分とは言えないため、素子設計の改善が必要である。
- 4) Si 基板上 AlGaIn/GaN HEMT の研究では、低オン抵抗とノーマリオフ動作を示す p 型 GaIn ゲートを用いた AlGaIn/GaN HEMT を実現したが、その選択エッチングプロセスが素子特性に及ぼした影響の起源までは明らかにできなかった。欠陥と散乱体の形成などの評価を進める。レーザー照射による p 型 GaIn 層を局所的に形成する技術では、その有効性は示したが、高いアクセプタ活性化率の実現と実際のデバイス適用が課題である。また、Si 上に pn 接合素子を縦方向に形成する研究では、各種のダイオード素子を実現できたものの、トランジスタの試作が行えなかった。
- 5) 新規手法で作製した InAs QWI を介しての光アップコンバージョンは実証したが、まだその効率は低く、また、形状の最適化には至らなかった。

InAs 量子ドットの発光長波長化については、発光強度制御まで至らなかった。また、実験室では歪の詳細の検討ができないため、引き続き検討が必要である。

<自己評価の実施結果と対応状況>

- 1) 高効率結晶 Si 太陽電池の実現のため、トンネル電極の材料、その膜堆積方法と界面欠陥、仕事関数との関係の系統的検討が必要としていた。今回、界面近傍の電極の仕事関数がバルク値と違う事を明らかにした。また電極材料の界面近傍の仕事関数とプロセス誘起欠陥の情報を得た。

法人番号	231023
プロジェクト番号	S1411027

2) $\text{In}_2\text{Se}_3/\text{GaAs}$ 積層について、歪と界面での固相拡散の抑制が課題であったが、ここでは歪制御に注力した。GaAs/Si 間に In_2Se_3 層状半導体を中間層として挟み、vdW 界面により生じる歪を緩和させることで GaAs 層の転位密度低減を特に微傾斜基板の影響に絡めて検討し、GaAs(111)、Si(111)の微傾斜基板に $\alpha\text{-In}_2\text{Se}_3$ の単一相 (In_2Se_3 は多形構造)でのエピ成膜、この上への GaAs エピ成膜に成功した。

4) 検討を始めていたレーザー照射による p 型 GaN 層を局所的に形成する技術を確立する必要があったが、これを実現し、選択励起なども可能にした。これにより、縦型デバイス含め素子構造作製技術が大幅に向上した。

5) InAs QWI を介した UC について、AlGaAs を含むと難しい事が判明したため、この回避法を検討することとした。AlGaAs の回避に加え、SML 成長法の導入で QWI の形状制御を進めることができた UC も実証したが、まだこの努力は途上である。

InAs 量子ドットの $1.55\mu\text{m}$ での発光強度増大と EL 素子を構造改善を課題として研究を進めていたが、EL 化を目指して改良した構造が発光のさらなる長波長化をもたらしたため、これに注力した。

表面 InAs ドットの導電性制御については歪制御やドーピング制御を試みたが、未完成である。

<研究期間終了後の展望>

1) 電極材料、その膜堆積方法と界面欠陥、仕事関数との関係を系統的に調べ、本構造による高効率結晶 Si 太陽電池の実現を目指す。

2) 層状半導体層の成膜条件・構造最適化により GaAs 層の欠陥密度低減をはかる。GaAs/Si 光素子に本手法を適用し、光電変換の高効率化を目指す。

3) 近赤外域用の三角障壁フォトトランジスタの素子設計の改善による高感度化。

4) 縦型構造の GaN トランジスタの実現に向け、結晶成長とデバイス作製プロセスの研究、特にレーザー照射による p 型 GaN 層を局所的に形成する技術を用いて、p 型領域と n 型領域を交互に並べた構造の実現に注力する。

5) InAs 量子ドットの発光は、想定した以上の長波長化が実現されたが、その機構が歪緩和以外の要因も寄与している可能性もあり、詳細な検討を続ける。また、EL 素子の作製には至らなかったため、この実現が必要である。表面 InAs ドットのポテンシャルの凹みの機構解明を素子応用と合わせて行う必要がある。

InAs QWI は新規作製手法を開拓したが、引き続き形状制御と UC 高効率化が必要。

<研究成果の副次的効果>

1) 上述の太陽電池特性の界面近傍の新規評価法を利用し、新たな材料の探索やプロセス技術の向上が期待される。

2) GaAs/Si 系のヘテロエピ成長に層状化合物を中間層に用い、vdW 界面で劈開し、GaAs エピ層の剥離も可能。より安価な支持基板上への GaAs 薄膜の移載や、flexible GaAs 薄膜素子への応用展開が期待される。

4) レーザー照射による p 型 GaN 層を局所的に形成する技術は、原子層レベルで照射領域を加工する技術に繋がる。この副次的な効果は、微細な半導体デバイスを精密に作製する技術への発展である。

5) InAs 量子ドットの発光は、想定した以上の長波長化が実現された。他の量子構造への展開が期待できる。また、表面 InAs ドットのポテンシャルの凹みの新規電極作製への転用の可能性の浮上。

法人番号	231023
プロジェクト番号	S1411027

【界面・電極制御による電力損失の低減 -有機電子素子】

<優れた成果が上がった点>

1) グラフェンの大面積合成及び電子・光学素子への応用^{*01}

大気圧 CVD を用い銅基板上へ mm スケールのグラフェン合成技術を確立した。大面積成長には、基板表面の精密構造制御による核生成の抑制が必要だが、成長直前に基板表面に極薄酸化膜を形成することで核密度が制御可能であることを見いだした。また、電子素子応用にはグラフェンの転写が必要であるが、転写基板をあらかじめ酸素プラズマ処理することが、動作が安定した電子素子作製に必須であることがわかった。一方、光学素子への応用として、銀微粒子表面を大面積グラフェンで被覆することにより、高温大気中や塩基溶液中でも安定に使用できる新たな表面増強ラマン用基板を開発することに成功した。

2) 探針増強ラマン、電気化学測定によるナノカーボン(NC)材料の評価^{*02}

NC 材料は次世代センサーや二次電池に期待されているが、表面の欠陥などの局所構造が特性に大きく影響する。水素プラズマを用いてグラフェンに欠陥を導入することにより、触媒特性が向上することを見いだした。また、自作探針を用い、探針先端に誘起されたプラズモン電場を利用した探針増強ラマン散乱分光法で、酸化グラフェンの構造評価を行い、単層及び二層グラフェンのナノスケールでの構造観察に成功し、ラマン強度の層数依存性を明らかにした。

<課題となった点>

グラフェンの転写では、Cu 基板上のグラフェンを PMMA で支持し、最終的にこれを薬品で取り除くが、十分には除去されない。電子素子のサイズを小さくしたときに、これらの不純物は問題になるので、ドライ法も含めた新規除去法の開発が必須となる。一方、探針増強ラマンは、ナノレベルで光学特性を調べることができる魅力的な装置であるが、プローブとなる金属探針の歩留まりが 50%にとどまっている(市販探針はあるが同程度)。

<自己評価の実施結果と対応状況>

素子作製において歩留まりが約 30%に留まっていたものを向上することが1つの課題であったが、酸素プラズマ処理の条件の適正化の検討で 50%程度にまで改善した。但し、引き続きの改善が必要である。

<研究期間終了後の展望>

大面積グラフェンについては、異種材料を基板に配置することによりさらにドメインサイズが拡大することを本グループが最近見だし、そのメカニズム解明も含めた研究を継続する。一方、探針増強ラマン分光法は多くの分野で期待されており、今後探針の開発及び標準化が必須となる。また現在は大気中で測定をおこなっているが、例えば電池材料などの開発においては、液中での測定が望まれており、その開発を進めていく予定である。

<研究成果の副次的効果>

探針増強ラマン分光技術に関して、企業との共同研究などに繋がった。今後標準探針販売の事業化なども検討していく予定である。

【界面・電極制御による電力損失の低減 -界面改質プロセス:配向セラミックス薄膜の作製】

<優れた成果が上がった点>

1) YAG 結晶配向薄膜の作製と結晶配向性評価^{*C1}

固体レーザーの性能低下抑制には、励起時の熱誘起複屈折による脱分極の低減が必要

法人番号	231023
プロジェクト番号	S1411027

である。典型的な母材 YAG 単結晶では、脱分極がロッドの軸方位に依存し、方位によっては(111)カットのロッドより小さい。しかし既存の YAG 多結晶セラミックスは粒子の結晶方位はランダムである。そこで、本研究では Reactive Templated Grain Growth (RTGG)法による結晶配向性制御で異方性 YAG セラミックスの実現を目指し、サファイア(0001) 面基板上に化学溶液法で成膜した[111]配向 Y_2O_3 薄膜を加熱処理し[211]優先配向 YAG 薄膜を作製し^{*C1}、基板/薄膜界面を起点とする結晶相遷移・方位継承、結晶配向性発現の原因を解明した^{*C1}。具体的には、 Y_2O_3 から YAG への相変化は主に準安定六方晶 $YAIO_3$ (YAH) 相を経由し、この準安定 YAH 相が Y_2O_3 の[111]自己配向を継承して強く優先配向する事を発見した。さらに、X 線極点測定を用い、YAG の[211]優先配向はエピタキシャル成長による事を明らかにした。RTGG 法の適用で最重要課題である異方性粒子の選択に目途が立った。

2) LSO 結晶配向薄膜の作製と結晶配向性評価

SOFC 用素子の固体電解質としてのアパタイト型ランタンシリケート ($La_{0.33}Si_6O_{27}$, LSO) の活用には c 軸配向化が不可欠である。石英ガラス基板上に化学溶液法で成膜した La_2O_3 薄膜の熱処理により、膜厚方向の組成分布が一般的な c 軸高配向 LSO 薄膜が得られることを発見し、そして LSO 結晶自身の表面エネルギー最小が形成要因となる自己配向によるものであることを解明した。

<課題となった点>

- 1) C 面が露出したアルミナの板状粒子が異方性原料粒子として適切であることが明らかになったが、RTGG 法による異方性 YAG セラミックスの合成には、さらに多くのプロセスパラメータの最適化が必要である。また、YAG の[211]優先配向薄膜は得られたが、単結晶化を含めさらなる結晶配向性向上が必要。
- 2) 結晶配向度が現状で最高 0.7 程度であり、さらに向上させる必要がある。

<自己評価の実施結果と対応状況>

RTGG 法による異方性 YAG セラミックスの合成には、多くのプロセスパラメータの最適化が必要。他のパラメータの考慮を排除すべく、異方性粒子を単結晶性基板とみなし、その上に薄膜を形成して配向結晶の形成を確認する事で、最重要課題の異方性粒子の選択に目途が立った。C 面が露出したアルミナの板状粒子が適切と考えられ、今後実施していく。

<研究期間終了後の展望>

- 1) Y_2O_3 自己配向膜の単結晶化により、YAG の[211]優先配向薄膜の単結晶化が期待できる。また、プロセスパラメータの最適化をさらに進めることで RTGG 法による異方性 YAG セラミックス作製の実現とマイクロチップレーザー等への適用が期待できる。
- 2) 溶液濃度、焼成雰囲気制御により、LSO 薄膜の結晶配向性向上が期待できる。また、Si を基板とした MEMS センサーへの展開も考えられる。さらに、プロセスパラメータの最適化を進めることで RTGG 法による異方性 LSO セラミックス作製の実現も期待できる。

<研究成果の副次的効果>

- 1) 2) 異方性原料粒子と補完粒子をそれぞれ単結晶またはガラス基板 ("Reactive substrate" と命名) と薄膜に見立て検討を進めた本手法は、RTGG 法による異方性セラミックスの合成を新規な系に展開する際にも適用可能である。

<外部(第三者)評価の実施結果と対応状況>

中間報告時、外部評価委員からプロジェクト全体の評価を頂いた。この際、全般に良好な評価を頂き、個々の研究内容について、具体的に対応を要求されたものはなかった。が、

法人番号	231023
プロジェクト番号	S1411027

一名の評価委員からは「本プロジェクトでの成果の世の中への普及」がなされれば、というご指摘を頂いた。元々、次期のグリーン素子・材料の開発を念頭にした本プロジェクトではあるが、この点に留意して研究を進め、熱電・GaN系・磁性メモリ、などでデバイスのプロトタイプングを行った。

12 キーワード(当該研究内容をよく表していると思われるものを8項目以内で記載してください。)

- (1)熱電材料, 熱電発電 (2)電子構造・電子物性 (3)フォノン分散・熱伝導評価
 (4)電極・金属界面 (5)スピン軌道トルク (6)希土類・遷移金属磁性細線
 (7)光電・電光変換 (8)結晶成長

13 研究発表の状況(研究論文等公表状況。印刷中も含む。)

上記、11(4)に記載した研究成果に対応するものには*を付すこと。

<雑誌論文>

【先進エネルギー変換素子・材料 - 熱電材料、熱ダイオード, 熱スイッチ】

- T1. “Thermoelectric properties of Al-(Mn,X)-Si C54-phase (X = Ru and Re),” A. Yamamoto, H. Miyazaki, and T. Takeuchi, J. Appl. Phys. **115**, 023708 (2014).
- T2. “Evaluation of the Thermoelectric Module Consisting of W-Doped Heusler Fe₂VAl Alloy,” M. Mikami, M. Mizoshiri, K. Ozaki, H. Takazawa, A. Yamamoto, Y. Terazawa, and T. Takeuchi, J. Elec. Mater. **43**, 1922-1926 (2014).
- T3. “Fe₂VAl-Based Thermoelectric Thin Films Prepared by a Sputtering Technique,” Y. Furuta, K. Kato, T. Miyawaki, H. Asano, and T. Takeuchi, J. Elec. Mater. **43**, 2157-2164 (2014).
- T4. “Very large thermal rectification in bulk composites consisting partly of icosahedral quasicrystals,” T. Takeuchi, Sci. Technol. Adv. Mater. **15**, 064801 (2014). (*T5)
- T5. “Thermal Rectification in Bulk Material Through Unusual Behavior of Electron Thermal Conductivity of Al-Cu-Fe Icosahedral Quasicrystal,” R. Nakayama and T. Takeuchi, J. Elec. Mater. **44**, 356-361 (2014).
- T6. 「C40相を微量に含有するAl-Mn-Si基C54相の熱電特性」山本晃生、宮崎秀俊、西野洋一、竹内恒博、日本金属学会誌 特集「熱電材料研究の新展開~新しい物性解析技術と新材料~」 **79**, 577-580 (2015).
- T7. “Thermoelectric properties of Al-Mn-Si C40 phase containing small amount of W or Ta,” A. Yamamoto, H. Miyazaki, M. Inukai, Y. Nishino, and T. Takeuchi, Jpn. J. Appl. Phys. **54**, 071801 (2015).
- T8. “Thermoelectric properties of β-Indium sulfide with sulphur deficiencies,” Y.-X. Chen, K. Kitahara, and T. Takeuchi, J. Appl. Phys. **118**, 245103 (2015).

法人番号	231023
プロジェクト番号	S1411027

- T9. 「準結晶の異常電子熱伝導度が生み出す巨大な熱整流効果」 竹内恒博、固体物理 **50**, 33-41 (2015). (解説論文) (*T5)
- T10. “Thermoelectric properties of super-saturated Re solid solution of higher manganese silicides,” A. Yamamoto, S. Ghodke, H. Miyazaki, M. Inukai, Y. Nishino, M. Matsunami, and T. Takeuchi, Jpn. J. Appl. Phys. **55**, 020301 (2016). (*T2)
- T11. “Thermal Conductivity Measurement of Liquid-Quenched Higher Manganese Silicides,” S. Nishino, M. Miyata, K. Ohdaira, M. Koyano, and T. Takeuchi, J. Elec. Mater. **45**, 1821-1826 (2016).
- T12. “Enhanced thermoelectric properties of W and Fe substituted MnSi_y,” S. Ghodke, N. Hiroishi, A. Yamamoto, H. Ikuta, M. Matsunami, and T. Takeuchi, J. Elec. Mater. **45**, 5279-5284 (2016).
- T13. “Thermoelectric Properties of Al-Mn-Si Based C54 Phase Containing Small Amount of C40 Phase,” A. Yamamoto, S. Ghodke, H. Miyazaki, Y. Nishino, M. Matsunami and T. Takeuchi, Mater. Trans. **57**, 1055-1058 (2016).
- T14. “Development of Thermoelectric Materials Consisting Solely of Environmental Friendly Elements,” T. Takeuchi, A. Yamamoto and S. Ghodke, Mater. Trans. **57**, 1029-1034 (2016) (Review article). (*T1)
- T15. “Thermoelectric Properties Higher Manganese Silicide Containing Small Amount of MnSi/Si Nano-Particles,” Swapnil Ghodke, A. Yamamoto, H. Ikuta, T. Takeuchi, Proceedings of 11th International Conference on Ceramic Materials and Components for Energy and Environmental Applications, Ceramics for Energy Conversion, Storage, and Distribution Systems: Ceram. Trans. **255**, 115-122 (2016).
- T16. “The Potential of Maximal ZT-Value for Thermoelectric Materials of Mn₁₁Si₁₉ HMS Phase by Calculating Electronic Structure,” A. Yamamoto, K. Kitahara, H. Miyazaki, M. Inukai, and T. Takeuchi, Proceedings of 11th International Conference on Ceramic Materials and Components for Energy and Environmental Applications, Ceramics for Energy Conversion, Storage, and Distribution Systems: Ceram. Trans. **255**, 147-156 (2016).
- T17. “Thermoelectric Properties of Fe₂VAl-Based Thin-Films Deposited at High Temperature,” S. Hiroi, M. Mikami and T. Takeuchi, Mater. Trans. **57**, 1628-1632 (2016).
- T18. “Thickness dependence of thermal conductivity and electron transport properties of Fe₂VAl thin-films prepared by RF sputtering technique,” S. Hiroi, M. Mikami, K. Kitahara, and T. Takeuchi, International Journal of Nanotechnology **13**, 881-890 (2016).

法人番号	231023
プロジェクト番号	S1411027

- T19. "The Potential of FeVSb Half-Heusler Phase for Practical Thermoelectric Material," A. Yamamoto and T. Takeuchi, *J. Elec. Mater.* **46**, 3200-3206 (2017).
- T20. "Thermoelectric properties of p-type Cr doped MnSi_y prepared by liquid quenching technique," S. Ghodke, A. Yamamoto, M. Omprakash, H. Ikuta, and T. Takeuchi, *Mater. Trans.* **58**, 160-163 (2017).
- T21. "Doping effects of Mg for In on the thermoelectric properties of β -In₂S₃ bulk samples," Y.-X. Chen, A. Yamamoto, and T. Takeuchi, *J. Alloys Compounds* **695**, 1631-1636 (2017).
- T22. "Enhancement of power factor by energy filtering effect in hierarchical BiSbTe₃ nanostructures for thermoelectric applications," M. Sabarinathana, M. Omprakash, S. Harish, M. Navaneethan, J. Archana, S. Ponnusamy, H. Ikeda, T. Takeuchi, C. Muthamizhchelvan, and Y. Hayakawa, *Appl. Surf. Sci.* (2016), published electronically.
- T23. "Carrier concentration dependence of thermoelectric properties of Fe (V_{1-x}Ti_x) Sb half-Heusler phase," Kévin Delime-Codrin, Tatsuya Yamada, Akio Yamamoto, Robert Sobota, Masaharu Matsunami, Tsunehiro Takeuchi, *Japanese Journal of Applied Physics* **56**, 111202 (2017).
- T24. "Morphology dependent thermal conductivity of ZnO nanostructures prepared via a green approach," Pandiyarasan Veluswamy, Suhasini Sathiyamoorthy, Kalari Hanuman Chowdary, Omprakash Muthusamy, Karthikeyan Krishnamoorthy, Tsunehiro Takeuchi, Hiroya Ikeda, *Journal of Alloys and Compounds* **695**, 888-894 (2017).
- T25. "Control of Nano Structure by Multi Films for Nano-structured Thermoelectric Materials," M. Adachi, S. Fujii, M. Kiyama, Y. Yamamoto, Tsunehiro Takeuchi, *SEI Technical Review* **84**, 151 (2017).
- T26. "Direct observation of heterogeneous valence state in Yb-based quasicrystalline approximants," M. Matsunami, M. Oura, K. Tamasaku, T. Ishikawa, S. Ideta, K. Tanaka, Tsunehiro Takeuchi, T. Yamada, A. P. Tsai, K. Imura, K. Deguchi, N. K. Sato, T. Ishimasa, *Physical Review B* **96**, 241102 (2017).
- T27. "Analyzing the Boundary Thermal Resistance of Epitaxially Grown Fe₂VAl/W Layers by Picosecond Time-Domain Thermoreflectance," S. Hiroi, S. Choi, S. Nishino, O. Seo, Y. Chen, O. Sakata, Tsunehiro Takeuchi, *Journal of Electronic Materials* **47**, 3113-3118 (2018).
- T28. "High-Throughput Screening of Sulfide Thermoelectric Materials Using Electron Transport Calculations with OpenMX and BoltzTraP," Masanobu Miyata, Taisuke Ozaki, Tsunehiro Takeuchi, Shunsuke Nishino, Manabu Inukai, Mikio Koyano, *Journal of Electronic Materials* **47**, 3254-3259 (2018).

法人番号	231023
プロジェクト番号	S1411027

- T29. “Low Thermal Conductivity of Bulk Amorphous $\text{Si}_{1-x}\text{Ge}_x$ Containing Nano-Sized Crystalline Particles Synthesized by Ball-Milling Process,” Omprakash Muthusamy, Shunsuke Nishino, Swapnil Ghodke, Manabu Inukai, Robert Sobota, Masahiro Adachi, Makoto Kiyama, Yoshiyuki Yamamoto, Tsunehiro Takeuchi, Harish Santhanakrishnan, Hiroya Ikeda, Yasuhiro Hayakawa. *Journal of Electronic Materials* **47**, 3260-3266 (2018).
- T30. “Thermoelectric Properties of Nanograined Si-Ge-Au Thin Films Grown by Molecular Beam Deposition,” Shunsuke Nishino, Satoshi Ekino, Manabu Inukai, Muthusamy Omprakash, Masahiro Adachi, Makoto Kiyama, Yoshiyuki Yamamoto, Tsunehiro Takeuchi, *Journal of Electronic Materials* **47**, 3267-3272 (2018).
- T31. “Effective Decrease of the Thermal Conductivity Caused by Hf in Fe ($\text{V}_{0.955-x}\text{Hf}_{0.045}\text{Ti}_x$) Sb Half-Heusler Phase,” Kévin Delime-Codrin, Ghodke Swapnil, Dogyun Byeon, Robert Sobota, Masaharu Matsunami, Tsunehiro Takeuchi, *Materials Transactions* **59**, 1637-1644 (2018).
- T32. “Development of amorphous bulk Al-Mn-Si for nano-structured thermoelectric materials,” Masahiro Adachi, Shunsuke Fujii, Makoto Kiyama, Yoshiyuki Yamamoto, Shunsuke Nishino, Muthusamy Omprakash, Akio Yamamoto, Akihiro Makino, Tsunehiro Takeuchi, *Materials Today: Proceedings* **5**, 10291-10297 (2018).
- T33. “Discovery of colossal Seebeck effect in metallic Cu_2Se ,” Dogyun Byeon, Robert Sobota, Kévin Delime-Codrin, Seongho Choi, Keisuke Hirata, Masahiro Adachi, Makoto Kiyama, Takashi Matsuura, Yoshiyuki Yamamoto, Masaharu Matsunami, Tsunehiro Takeuchi, *Nature Communications* **10**, 72 (2019). (*T4)
- T34. “Effects of Re substitution for Mn on microstructures and properties in Re-substituted higher manganese silicide thermoelectric material,” T. Homma, T. Kamata, N. Saito, S. Ghodke, Tsunehiro Takeuchi, *Journal of Alloys and Compounds* **776**, 8-15 (2019).
- T35. “Large figure of merit $\text{ZT}=1.88$ at 873 K achieved with nanostructured $\text{Si}_{0.55}\text{Ge}_{0.35}(\text{P}_{0.10}\text{Fe}_{0.01})$,” Kévin Delime-Codrin, Muthusamy Omprakash, Swapnil Ghodke, Robert Sobota, Masahiro Adachi, Makoto Kiyama, Takashi Matsuura, Yoshiyuki Yamamoto, Masaharu Matsunami, Tsunehiro Takeuchi, *Applied Physics Express* **12**, 045507 (2019). (*T3)
- T36. “Optimization of thermoelectric properties achieved in Cu doped $\beta\text{-In}_2\text{S}_3$ bulks,” Yue-Xing Chen, Fu Li, Wenting Wang, Zhuanghao Zheng, Jingting Luo, Ping Fan, Tsunehiro Takeuchi, *Journal of Alloys and Compounds* **782**, 641-647 (2019). (*T2)

【界面・電極制御による電力損失の低減 - 界面制御磁性メモリ】

M1. 「電流駆動磁壁移動を用いた積層型 3 次元磁気メモリ」 栗野博之、日本磁気学会誌、**9**、275

法人番号	231023
プロジェクト番号	S1411027

(2014). (解説論文、査読なし)

- M2. 「希土類・遷移金属磁性細線における電流磁壁駆動効果の改善」 栗野博之、映像情報メディア学会技術報告、**39**、p.25-30、(2014). (解説論文、査読なし)
- M3. 「磁性細線における磁壁の電流駆動の基礎検討」 栗野博之、電子情報通信学会信学技法 IEIEC Technical Report、MR2014-11、p.17-22、(2014). (解説論文、査読なし)
- M4. “Domain wall motion in Tb/Co multilayer wire with a large domain wall depinning field,” Do Bang, H. Awano, J. Appl. Phys. **115**, 17D512 (2014).
- M5. “Investigation of domain wall motion in RE-TM magnetic wire towards a current driven memory and logic,” Hiroyuki Awano, Journal of Magnetism and Magnetic Materials **383**, 50 (2015). (*M2)
- M6. “Strain-induced reversible modulation of the magnetic anisotropy in perpendicularly magnetized metals deposited on a flexible substrate,” Shinya Ota, Yuki Hibino, Do Bang, Hiroyuki Awano, Takahiro Kozeki, Hirokazu Akamine, Tatsuya Fujii3, Takahiro Namazu, Taishi Takenobu, Tomohiro Koyama, and Daichi Chiba, Appl. Phys. Exp. **9**, 043004 (2015).
- M7. “High efficiency of the spin-orbit torques induced domain wall motion in asymmetric interfacial multilayered Tb/Co wires,” Do Bang, Hiroyuki Awano, J. Appl. Phys. **117**, 17D916 (2015).
- M8. “Current-induced dynamics of bubble domains in perpendicularly magnetized TbFeCo wires,” Masaaki Tanaka, Hiroki Kanazawa, Sho Sumitomo, Syuta Honda, Ko Mibu, and Hiroyuki Awano, Appl. Phys. Exp. **8**, 073002 (2015).
- M9. “Enhanced perpendicular coercive force of ultrathin perpendicularly,” Do Bang, Hiroyuki Awano, Journal of Science, Advanced Materials and Devices **1**, 57 (2016).
- M10. “Current-induced domain wall motion attributed to spin Hall effect and Dzyaloshinsky–Moriya interaction in Pt/GdFeCo (100 nm) magnetic wire,” Yuichiro Kurokawa, Masaya Kawamoto and Hiroyuki Awano, Jpn. J. Appl. Phys. **55**, 07MC02 (2016). (*M1)
- M11. “Enhancement of spin Hall effect induced torques for current-driven magnetic domain wall motion: Inner interface effect,” Do Bang, Jiawei Yu, Xuepeng Qiu, Yi Wang, Hiroyuki Awano, Aurelien Manchon, and Hyunsoo Yang, Phys. Rev. B **93**, 174424 (2016). (*M1)
- M12. “Thermal reduction of the threshold current density for current-induced domain wall motion in Tb-Co magnetic alloy wire,” Yuichiro Kurokawa, Ryogo Yoshimura, Satoshi Sumi, and Hiroyuki Awano, AIP Advances **7**, 035325 (2017).

法人番号	231023
プロジェクト番号	S1411027

- M13. "Electric-current-induced dynamics of bubble domains in a ferrimagnetic Tb/Co multilayer wire below and above the magnetic compensation point," Masaaki Tanaka, Sho Sumitomo, Noriko Adachi, Syuta Honda, Hiroyuki Awano, and Ko Mibu, *AIP Advances* **7**, 055916 (2017).
- M14. "Novel magnetic wire fabrication process by way of nanoimprint lithography for current induced magnetization switching," Tsukasa Asari, Ryosuke Shibata, and Hiroyuki Awano, *AIP Advances* **7**, 055930 (2017).
- M15. "Electric-field-induced on/off switching of the Faraday effect," Yuki Hibino, Tomohiro Koyama, Satoshi Sumi, Hiroyuki Awano, Kazumoto Miwa, Shimpei Ono, Makoto Kohda, and Daichi Chiba, *Appl. Phys. Exp.* **10**, 123201 (2017).
- M16. Masamichi Sakai, Hiraku Takao, Tomoyoshi MATsunaga, Makoto Nishimagi, Keitaro Iizasa, Takahito Sakuraba, Koji Higuchi, Akira Kitajima, Shigehiko Hasegawa, Osamu Nakamura, Yuichiro Kurokawa and Hiroyuki Awano, *Jpn. J. Appl. Phys.* **57**, 033001 (2018).
- M17. "Multilayered current-induced domain wall motion in Pt/Tb-Co/Ta/Tb-Co/Pt magnetic wire, Yuichiro Kurokawa and Hiroyuki Awano, *AIP Advances* **8**, 025309 (2018).
- M18. "Interface induced enhancement of magneto-optical Kerr effect in ultrathin magnetic films", Satoshi Sumi, Hiroyuki Awano, and Masamitsu Hayashi, *Scientific Reports* **8**, 776 (2018).
- M19. "Interface induced enhancement of magneto-optical Kerr effect in Pt/TbCo hetero-structureed films," Satoshi Sumi, Hiroyuki Awano, and Masamitsu Hayashi, *Crystals* **8**, 377 (2018)
- M20. "Long spin coherence length and bulk-like spin-orbit torque in ferrimagnetic multilayers," Jiwaei Yu, Do Bang, Rahui Mitshra, Rajaquopaian Ramaswamy, Jung Hyun Oh, Hyeon Jong Park, Yunboo Jeong, Pham Van Thach, dong Kyu Lee, Gyungchoon Go, Seo Won Lee, Yi Wang, Syuyuan Shi, Xuepeng Qiu, Hiroyuki Awano, Kyunng Jin Lee and Hyunson Yangi, *Nature Materials* **18**, 29-34 (2019). (*M1)
- M21. "Entropy production by thermodynamic currents in ambipolar conductors with identical spin dynamics characteristics between holes and electrons," Sanjida Aktar, Masamichi Sakai, Shigehiko Hasegawa, Osamu Nakamura, and Hiroyuki Awano, *Appl. Phys. Exp.* **12**, 053004 (2019).

【界面・電極制御による電力損失の低減 -光電・電光変換素子】

- P1. "Dilute nitride InNP quantum dots: Growth and photoluminescence mechanism," Y. J.

法人番号	231023
プロジェクト番号	S1411027

- Kuang, K. Takabayashi, S. Sukrittanon, J. L. Pan, I. Kamiya, and C. W. Tu, Appl. Phys. Lett. **105**, 173112 (2014).
- P2. “Formation of conductive spontaneous via holes in AlN buffer layer on n⁺Si substrate by filling the vias with n-AlGaN by metal chemical vapor deposition and application to vertical ultraviolet photo-sensor,” N. Kurose, N. Iwata, I. Kamiya, and Y. Aoyagi, AIP Advances **4**, 123007 (2014).
- P3. “Strain engineering of quantum dots for long wavelength emission: Photoluminescence from self-assembled InAs quantum dots grown on GaAs(001) at wavelengths over 1.55 μm,” Kenichi Shimomura and Itaru Kamiya, Appl. Phys. Lett. **106**, 082103 (2015). (*P7)
- P4. “Enhancement of the performance of GaP Solar cells by embedded In(N)P quantum dots,” Y. J. Kuang, K. Takabayashi, S. Sukrittanon, J. L. Pan, I. Kamiya, and C. W. Tu, Nano Energy **15**, 782-788 (2015).
- P5. “Femtosecond upconverted photocurrent spectroscopy of InAs quantum nanostructures,” Yasuhiro Yamada, David M. Tex, Itaru Kamiya, and Yoshihiko Kanemitsu, Appl. Phys. Lett. **107**, 013905 (2015). (*P6)
- P6. “Direct observation of strain in InAs quantum dots and cap layer during molecular beam epitaxial growth using *in situ* X-ray diffraction,” Kenichi Shimomura, Hidetoshi Suzuki, Takuo Sasaki, Masamitsu Takahashi, Yoshio Ohshita, and Itaru Kamiya, J. Appl. Phys. **118**, 185303 (2015). (*P7)
- P7. “InGaAs Triangular Barrier Photodiodes for High-Responsivity Detection of Near-Infrared Light,” Kazuya Sugimura, Masato Ohmori, Takeshi Noda, Tomoya Kojima, Sakunari Kado, Pavel Vitushinskiy, Naotaka Iwata, Hiroyuki Sakaki, Applied Physics Express **9**, 062101 (2016). (*P3)
- P8. “Realization of Conductive AlN Epitaxial Layer on Si Substrate using Spontaneously Formed Nano-Size Via-Holes for Vertical AlGaN High Power FET,” N. Kurose, K. Ozeki, N. Iwata, K. Shibano, T. Araki, I. Kamiya, and Y. Aoyagi, Proceedings of the 2016 28th International Conference on Indium Phosphide & Related Materials (IPRM)/43rd International Symposium on Compound Semiconductors (ISCS), UNSP ThD2-4 (2016). (*P5)
- P9. “Up-converted photoluminescence in InAs/GaAs heterostructures,” Yuwei Zhang and Itaru Kamiya, J. Cryst. Growth **477**, 54-58 (2017). (*P6)
- P10. “The g-C₃N₄ modified {001}-faceted TiO₂ nanosheet anodes for efficient quantum dot sensitized solar cells,” Qiqian Gao, Lianfeng Duan, Xueyu Zhang, Yue Yang, Itaru Kamiya, and Wei Lü, Superlattices and Microstructures **109**, 860-868 (2017).

法人番号	231023
プロジェクト番号	S1411027

P11. “Effect of substrate orientation on strain relaxation mechanisms of InGaAs layer grown on vicinal GaAs substrates measured by in situ X-ray diffraction,” Hidetoshi Suzuki, Takuo Sasaki, Masamitsu Takahashi, Yoshio Ohshita, Nobuaki Kojima, Itaru Kamiya, Atsuhiko Fukuyama, Tetsuo Ikari, and Masafumi Yamaguchi, *Jpn. J. Appl. Phys.* **56**, 08MA06 (2017). (*P2)

P12. “Band profiling of p-Si/ITO interface by Kelvin probe force microscopy under light controlled conditions,” Fumihiko Yamada, Takefumi Kamioka, Yoshio Ohshita, and Itaru Kamiya, *Proceedings of 2018 IEEE 7th World Conference on Photovoltaic Energy Conversion (WCPEC7)*, pp. 3315-3318 (2018). (*P1)

P13. “Laser-induced local activation of Mg-doped GaN with a high lateral resolution for high power vertical devices,” Noriko Kurose, Kota Matsumoto, Fumihiko Yamada, Teuku Muhammad Roffi, Itaru Kamiya, Naotaka Iwata, and Yoshinobu Aoyagi, *AIP Advances* **8**, 015329, 1-5 (2018). (*P5)

【界面・電極制御による電力損失の低減 -有機電子素子】

O1. “Effect of catalytic metals of various elements on synthesis of graphite-capped, vertically aligned carbon nanotube arrays,” Yuki Matsuoka and Masamichi Yoshimura, *Jpn. J. Appl. Phys.* **53**, 045501 (2014).

O2. “Low Density Growth of Graphene by Air Introduction in Atmospheric Pressure Chemical Vapor Deposition,” Seiya Suzuki, Kana Kiyosumi, Takashi Nagamori, Kei Tanaka, M. Yoshimura, *e-J. Surf. Sci. Nanotech.* **13**, 404-409 (2015). (*O1)

O3. “Macroscopic, Freestanding, and Tubular Graphene Architectures Fabricated via Thermal Annealing,” D. Dung, S. Suzuki, S. Kato, B. To, C. Hsu, H. Murata, E. Rokuta, N. Tai, M. Yoshimura, *ACS Nano* **9**(3), 3206-3214 (2015).

O4. “Graphene and graphene oxide for desalination,” Yi You, Veena Sahajwalla, Masamichi Yoshimura and Rakesh K. Joshi, *Nanoscale* **8**, 117-119 (2016).

O5. “Graphene/SiC(0001) interface structures induced by Si intercalation and their influence on electronic properties of graphene,” A. Visikovskiy, S. Kimoto, T. Kajiwara, M. Yoshimura, T. Iimori, F. Komori, S. Tanaka, *Phys. Rev. B* **94**, 245421 (2016).

O6. “On the mechanism of gas adsorption for pristine, defective and functionalized graphene,” Y. You, J. Deng, X. Tan, N. Gorjizadeh, M. Yoshimura, S. C. Smith, V. Sahajwalla and R. K. Joshi, *Phys. Chem. Chem. Phys.* **19**, 6051-6056 (2017).

O7. “Suppression of Graphene Nucleation by Turning Off Hydrogen Supply Just before

法人番号	231023
プロジェクト番号	S1411027

Atmospheric Pressure Chemical Vapor Deposition Growth,” S. Suzuki, Y. Terada, and M. Yoshimura, *Coatings* **7**, 206 (2017).(*O1)

O8. “Chemical Stability of Graphene Coated Silver Substrates for Surface-Enhanced Raman Scattering,” S. Suzuki, and M. Yoshimura, *Scientific Reports* **7**, 14851 (2017). (*O1)

O9. “Chemical reduction of graphene oxide using green reductants,” K. K. H. De Silva, H. H. Huang, R. K. Joshi, M. Yoshimura, *Carbon* **119**, 190-199 (2017).

O10. “Dependence on treatment ion energy of nitrogen plasma for oxygen reduction reaction of high ordered pyrolytic graphite,” Yuichi Hashimoto, Hsin-Hui Huang, Masamichi Yoshimura, Masanori Hara, Tamio Hara, Yasuhiro Hara, Manabu Hamagaki, *Jpn. J. Appl. Phys.* **57**, 125504 (2018). (*O2)

【界面・電極制御による電力損失の低減 -界面改質プロセス: 配向セラミックス薄膜の作製】

C1. “Formation of preferentially oriented $Y_3Al_5O_{12}$ film on a reactive sapphire substrate: Phase and texture transitions from Y_2O_3 ,” Shuichi Arakawa, Hiroaki Kadoura, Takeshi Uyama, Kazumasa Takatori, Yasuhiko Takeda, and Toshihiko Tani, *J. Eur. Ceram. Soc.* **36**, 663-670 (2016). (*C1)

C2. “Microstructural evolution of high purity alumina ceramics prepared by a templated grain growth method,” Kazumasa Takatori, Hiroaki Kadoura, Hidehito Matsuo, Shuichi Arakawa, and Toshihiko Tani, *J. Ceram. Soc. Japan* **124** (4), 432-441 (2016). (*C1)

<図書>

1. 「磁気便覧」 栗野博之

『光磁気記録材料』 第3章 p.370-380 日本磁気学会編、丸善出版、2016年1月刊

2. 「熱電変換材料 実用・活用を目指した設計と開発(書名)」 竹内恒博

『熱電材料の性能向上・コストダウンの為のポイント(分担章タイトル)』(第1章 第2節)、情報機構、2014年12月19日刊

3. 「フォノンエンジニアリング ~マイクロ・ナノスケールの次世代熱制御技術(書名)」竹内恒博

『異常電子熱伝導度と異常格子熱伝導度の発現機構と熱ダイオードへの応用(分担章タイトル)』(第3章 第4節)、(株)エヌ・ティー・エス、2017年9月刊

<学会発表>

国内

【先進エネルギー変換素子・材料 - 熱電材料、熱ダイオード, 熱スイッチ】

DT1. 「高性能熱電材料における界面の役割」(基調講演) 竹内恒博、日本金属学会 2014年春期(第154回)講演大会、東京工業大学、2014/3/23 (3/21-23)

法人番号	231023
プロジェクト番号	S1411027

- DT2. 「高性能熱電材料の開発における粉末冶金の重要性」(基調講演)竹内恒博、粉体粉末冶金協会平成 26 年度秋季大会、大阪大学、2014/10/29 (10/29-31)
- DT3. “Effect of silicon nano particles on thermoelectric properties of higher manganese silicide,” S. Ghodke, A. Yamamoto, H. Ikuta, and T. Takeuchi 第 62 回応用物理学会春期学術講演会、東海大学 湘南キャンパス、2015/3/12 (3/11-14)
- DT4. 「構成元素 Mn を重元素 Re で部分置換した高マンガンシリサイドの熱電物性」山本晃生、広石尚也、竹内恒博、第 62 回応用物理学会春期学術講演会、東海大学 湘南キャンパス、2015/3/12 (3/11-14)
- DT5. 「室温以上で動作する固体熱整流材料の開発」(招待講演) 竹内恒博、第 52 回伝熱シンポジウム、福岡国際会議場、2015/6/4 (6/3-5)
- DT6. 「Mn を重元素(Ta,W,Re)で微量置換した高マンガンシリサイドの熱電物性」山本晃生、広石尚也、竹内恒博、第 12 回日本熱電学会学術講演会、九州大学 筑紫地区総合研究棟、福岡、2015/9/7 (9/7-8)
- DT7. 「Fe₂VAI 系合金薄膜の成膜温度に伴う構造変化と熱電性能」廣井慧、三上祐史、竹内恒博、第 12 回日本熱電学会学術講演会、九州大学 筑紫地区総合研究棟、福岡、2015/9/8 (9/7-8)
- DT8. “Thermoelectric properties of bulk β-Indium sulfide with Mg doping,” Y. -X. Chen, K. Kitahara, T. Takeuchi 第 76 回応用物理学会秋季学術講演会、名古屋国際会議場、2015/9/13 (9/13-16)
- DT9. 「構成元素 Mn の一部を Ta で部分置換した HMS の熱電物性」山本晃生、広石尚也、竹内恒博 第 76 回応用物理学会秋季学術講演会、名古屋国際会議場、2015/9/13 (9/13-16)
- DT10. “Thermoelectric properties of W-substituted bulk higher manganese silicide,” S. Ghodke, N. Hiroishi, A. Yamamoto, and T. Takeuchi 第 76 回応用物理学会秋季学術講演会、名古屋国際会議場、2015/9/13 (9/13-16)
- DT11. 「Fe₂VAI 系薄膜熱電材料の熱電特性」竹内恒博、廣井慧、三上祐史、第 76 回応用物理学会秋季学術講演会、名古屋国際会議場、2015/9/13 (9/13-16)
- DT12. 「高マンガンシリサイド高性能熱電材料の創製」(招待講演) 竹内恒博、山本晃生、Swapnil Ghodke、第 26 回シリサイド系半導体研究会、ウィルあいち、名古屋、2015/9/16
- DT13. 「高性能マンガンシリサイド熱電材料の創製」山本晃生、スワプニルゴドゥケ、生田博志、竹内恒博日本金属学会・2015 年秋期講演大会、九州大学 伊都キャンパス、福岡、2015/9/17 (9/16-18)
- DT14. 「ホイスラー型 Fe₂VA 系合金の薄膜化による熱電性能向上の試み」廣井慧、三上祐史、竹内恒博、日本金属学会・2015 年秋期講演大会、九州大学 伊都キャンパス、福岡、2015/9/17 (9/16-18)

法人番号	231023
プロジェクト番号	S1411027

- DT15. 「Al-Cu-Fe 準結晶の熱伝導特性」 北原功一、竹内恒博 日本物理学会・2015 年秋季大会、関西大学 千里山キャンパス、2015/9/17 (9/16-19)
- DT16. 「Ag₂Ch (Ch = Te, Se, S)で観測される異常熱伝導度とそれを利用した固体熱流制御材料の創製」(シンポジウム講演) 竹内恒博、日本物理学会・2015 年秋季大会、関西大学 千里山キャンパス、2015/9/17 (9/16-19)
- DT17. 「MnSi_γ系高性能バルク熱電材料の開発」(招待講演) 竹内恒博、第 27 回排熱発電コンソーシアム、安保ホール、名古屋、2015/11/3
- DT18. 「精密電子構造解析に基づく熱電物性の理解と高性能熱電材料の設計指針」(招待講演) 竹内恒博、第 25 回日本 MRS 年次大会、横浜市開港記念会館、2015/12/8 (12/8-10)
- DT19. 「Al-Cu-Fe 準結晶の熱伝導特性に対する元素置換効果」 北原功一、竹内恒博、石切山守、木下洋平、大橋良央、吉永泰三、山口剛生、日本物理学会・第 71 回年次大会、東北学院大学 泉キャンパス、2016/3/22 (3/19-22)
- DT20. 「熱伝導度に異常な温度依存性を示す材料を利用した熱流ダイオードの開発」(シンポジウム講演) 竹内恒博 第 63 回応用物理学会春季学術講演会、東京工業大学 大岡山キャンパス、2016/3/22 (3/19-22)
- DT21. 「p 型及び n 型高性能 MnSi_γ (γ~1.73)系高マンガンシリサイド合金の創製」 山本晃生、竹内恒博 日本金属学会・2016 年春季(第 158 回)大会、東京理科大学 葛飾キャンパス、2016/3/24 (3/23-25)
- DT22. “Evolution of transport properties with microstructure in Re doped MnSi_γ,” Swapnil Ghodke, Akio Yamamoto, Hiroshi Ikuta, Tsunehiro Takeuchi 日本金属学会・2016 年春季(第 158 回)大会、東京理科大学 葛飾キャンパス、2016/3/24 (3/23-25)
- DT23. 「Fe₂VAl 系合金薄膜の熱電特性」 廣井慧、三上祐史、竹内恒博、日本金属学会・2016 年春季(第 158 回)大会、東京理科大学 葛飾キャンパス、2016/3/24 (3/23-25)
- DT24. 「Mn を(Ta,W,Re)で部分置換した HMS 相に対して Ag を少量添加したバルク体の熱電物性」 山本晃生、竹内恒博、第 13 回日本熱電学会学術講演会、東京理科大学 葛飾キャンパス、2016/9/5 (9/5-7)
- DT25. 「Fe₂VAl 層と重金属からなる多層膜の作成と熱伝導度へ影響」 廣井慧、竹内恒博、第 13 回日本熱電学会学術講演会、東京理科大学 葛飾キャンパス、2016/9/5 (9/5-7)
- DT26. “Amorphous Si_{1-x}Ge_x containing crystalline nano-particles prepared by high-energy planetary ball milling,” M. Omprakash, S. Nishino, M. Adachi, T. Takeuchi, 第 13 回日本熱電学会学術講演会、東京理科大学 葛飾キャンパス、2016/9/5 (9/5-7)
- DT27. “Nanostructured super-saturated solid solution of transition metal (Cr/Fe/W/Re)

法人番号	231023
プロジェクト番号	S1411027

- substituted higher manganese silicide,” (ポスター発表) Swapnil Ghodke, A. Yamamoto, H. Ikuta, T. Takeuchi, 第 13 回日本熱電学会学術講演会、東京理科大学 葛飾キャンパス、2016/9/6 (9/5-7)
- DT28. 「Yb 化合物の熱電材料探索」(ポスター発表)飯塚拓也、堀太郎、山本晃生、松波雅治、竹内恒博、第 13 回日本熱電学会学術講演会、東京理科大学 葛飾キャンパス、2016/9/6 (9/5-7)
- DT29. “Thermoelectric properties of lacunar spinel $\beta\text{-In}_{2-2x}\text{Cu}_x\text{Zn}_x\text{S}_3$,” K. Delime-Codrin, T. Takeuchi, 第 13 回日本熱電学会学術講演会、東京理科大学 葛飾キャンパス、2016/9/6 (9/5-7)
- DT30. 「2 種類の蔡型クラスターにおける電子状態の違い: Yb 系近似結晶の光電子分光」松波雅治、大浦正樹、出田真一郎、田中清尚、玉作賢治、石川哲也、竹内恒博、山田庸公、蔡安邦、出口和彦、佐藤憲昭、石政勉、日本物理学会・2016 年秋季大会、金沢大学 角間キャンパス、2016/9/14 (9/13-16)
- DT31. 「Fe₂VAl 系熱電材料の人工超格子による熱伝導度制御」廣井慧、竹内恒博、第 77 回応用物理学会秋季学術講演会、朱鷺メッセ、新潟コンベンションセンター、2016/9/15 (9/13-16)
- DT32. 「電子構造から予測した FeVSb half-Heusler の熱電物性」山本晃生、山田竜也、竹内恒博 第 77 回応用物理学会秋季学術講演会、朱鷺メッセ、新潟コンベンションセンター、2016/9/15 (9/13-16)
- DT33. 「周期加熱法を用いた MnSi₃リボン状試料の熱伝導度測定」西野俊佑、Swapnil Ghodk、山本晃生、竹内恒博 第 77 回応用物理学会秋季学術講演会、朱鷺メッセ、新潟コンベンションセンター、2016/9/15 (9/13-16)
- DT34. 「 $ZT > 2$ を実現する条件と新しい熱電材料の開発」(シンポジウム講演) 竹内恒博、第 77 回応用物理学会秋季学術講演会、朱鷺メッセ、新潟コンベンションセンター、2016/9/16 (9/13-16)
- DT35. 「異常電子熱伝導度と異常格子熱伝導度を利用した革新的熱利用材料」(招待講演) 竹内恒博 日本熱電学会東海支部主催第 27 回東海伝熱セミナー『エネルギー有効利用のための熱工学的アプローチ』、鳥羽シーサイドホテル、2016/9/17 (9/16-17)
- DT36. 「Fe₂VAl 系人工超格子の熱伝導度評価」廣井慧、竹内恒博、日本金属学会・2016 年秋期(第 159 回)大会、東京理科大学 葛飾キャンパス、2016/9/22 (9/21-23)
- DT37. 「微細電子構造とフォノンの散乱機構を考慮した環境調和型熱電材料の開発」(招待講演) 竹内恒博、平成 28 年度液体・非晶質研究会、エッサム神田ホール 401 会議室、東京、2017/3/13
- DT38. 「Fe₂VAl/重金属系人工超格子の熱伝導度低減効果」廣井慧、竹内恒博 第 64 回応用物理学会春季学術講演会、パシフィコ横浜、2017/3/14 (3/14-17).
- DT39. 「MBE 法で作製した Si-Ge 薄膜の熱電物性」西野俊佑、浴野哲史、犬飼 学、Muthusamy Omprakash、竹内恒博 第 64 回応用物理学会春季学術講演会、パシフィコ横浜、2017/3/15

法人番号	231023
プロジェクト番号	S1411027

(3/14-17)

- DT40. “Thermoelectric properties of half-Heusler $\text{FeV}_{1-x}\text{Ti}_x\text{Sb}$,” Kevin Delime-Codrin, A. Yamamoto, T. Yamada and T. Takeuchi 第 64 回応用物理学会春季学術講演会、パシフィコ横浜 2017/3/15 (3/14-17)
- DT41. “Enhancement of thermoelectric properties in amorphous $\text{Si}_{1-x}\text{Ge}_x$ synthesized by mechanical alloying process,” (ポスター講演) Omprakash Muthusamy, Shunsuke Nishino, Masahiro Adachi, Tsunehiro Takeuchi、第 64 回応用物理学会春季学術講演会、パシフィコ横浜、2017/3/16 (3/14-17)
- DT42. 「熱処理中その場 X 線回折測定による a-Si/Ge 薄膜中ナノ結晶の観察」(ポスター講演)足立真寛、豊島 遼、徳田一弥、斎藤吉広、藤井俊輔、木山 誠、山本喜之、西野俊佑、Omprakash Muthusamy、竹内恒博、第 64 回応用物理学会春季学術講演会、パシフィコ横浜、2017/3/16 (3/14-17)
- DT43. 「Si-Ge-Au 系ナノ構造薄膜の熱伝導率測定」西野俊佑, Muthusamy Omprakash, 竹内恒博, 第 78 回応用物理学会秋季学術講演会, 福岡国際会議場, 2017/9/5, (9/5-8).
- DT44. 「 α -SiGe: Au 薄膜における Au 凝集体の制御」(ポスター講演)足立真寛, 徳田一弥, 斎藤吉広, 木山誠, 上松康二, 山本善之, 西野俊佑, Omprakash Muthusamy, 竹内恒博, 第 78 回応用物理学会秋季学術講演会, 福岡国際会議場, 2017/9/6, (9/5-8)
- DT45. 「 Fe_2VAl /重金属系人工超格子界面でのフォノン散乱」廣井慧, Seongho Choi, 西野俊佑, Okkyun Seo, 竹内恒博, 第 78 回応用物理学会秋季学術講演会, 福岡国際会議場, 2017/9/7, (9/5-8).
- DT46. “Thermoelectric properties of Al-based ternary chalcopyrites: TAlTe_2 ($T = \text{Cu}, \text{Ag}$),” S. Choi, K. Kurosaki, M. Inukai, F. Nakamori, Y. Ohishi, H. Muta, S. Yamanaka, and T. Takeuchi, 第 78 回応用物理学会秋季学術講演会, 福岡国際会議場, 2017/9/7, (9/5-8).
- DT47. 「粒径を制御したバルク状高マンガンシリサイドの熱電物性」竹内恒博, Swapnil Ghodke, 山本晃生, 西野俊佑, 胡 玟雋, Robert Sobot, 日本金属学会 2017 年秋期講演大会, 北海道大学, 2017/9/8 (9/6-8).
- DT48. “Thermal conductivity of superlattices consisting of W/Ta-doped Fe_2VAl multilayers,” Seongho Choi, 廣井慧, 西野俊佑, 犬飼学, 竹内恒博, 第 14 回日本熱電学会学術講演会, 大阪大学, 豊中キャンパス, 2017/9/11 (9/11-13).
- DT49. 「SnSe と Cu_2Se 中の遷移金属の電子構造」犬飼学, 竹内恒博, 第 14 回日本熱電学会学術講演会, 大阪大学, 豊中キャンパス, 2017/9/11 (9/11-13).
- DT50. 「 $1 \text{ WK}^{-1}\text{m}^{-1}$ 以下の低熱伝導率を示すアモルファス Si-Ge 薄膜の作製」西野俊佑, Muthusamy

法人番号	231023
プロジェクト番号	S1411027

- Omprakash, 竹内恒博, 第 14 回日本熱電学会学術講演会, 大阪大学, 豊中キャンパス, 2017/9/11 (9/11-13).
- DT51. “Analysis of thermoelectric properties based on phase stability in complex $MnSi_y$,” (ポスター講演), S. Ghodke, R. Sobota, and T. Takeuchi, 第 14 回日本熱電学会学術講演会, 大阪大学, 豊中キャンパス, 2017/9/12 (9/11-13).
- DT52. 「 Yb_5Si_3 の熱電物性」(ポスター講演), 飯塚拓也, 堀太郎, 松波雅治, 竹内恒博, 第 14 回日本熱電学会学術講演会, 大阪大学, 豊中キャンパス, 2017/9/12 (9/11-13).
- DT53. “Giant reduction of thermal conductivity in amorphous with nano-crystalline P-doped $Si_{0.65}Ge_{0.35}$ prepared by ball milling process,” (ポスター講演), Omprakash Muthusamy, 西野俊佑, 足立真寛, 竹内恒博, 第 14 回日本熱電学会学術講演会, 大阪大学, 豊中キャンパス, 2017/9/12 (9/11-13).
- DT54. “Thermoelectric properties of FeVSb-based half Heusler alloys,” Kévin Delime-Codrin, A. Yamamoto, and T. Takeuchi, 第 14 回日本熱電学会学術講演会, 大阪大学, 豊中キャンパス, 2017/9/12 (9/11-13).
- DT55. “The thermoelectric properties of the densified nano-grained higher manganese silicide,” H.-C. Hu, S. Ghodke, and T. Takeuchi, 第 14 回日本熱電学会学術講演会, 大阪大学, 豊中キャンパス, 2017/9/12 (9/11-13).
- DT56. 「廃熱をエネルギーとして有効活用するための材料開発 ～研究開発の問題点と近年の技術進歩～」(招待講演) 竹内恒博, 平成 29 年度日本理化学協会東海ブロック研究会 第 23 回研究発表大会, 愛知県教育会館, 名古屋, 2017/10/20.
- DT57. 「省エネルギー社会のための新機能材料の開拓」(招待講演) 竹内恒博, 南山大学・豊田工業大学 連携講演会, 南山大学, 名古屋, 2017/11/12.
- DT58. 「 $1Wm^{-1}K^{-1}$ 以下の低熱伝導度を呈する Si-Ge 系非晶質熱電材料の開発」(招待講演) 竹内恒博, 第 58 回ガラスおよびフォトニクス材料討論会, 名古屋国際会議場, 名古屋, 2017/11/12.
- DT59. 「熱電材料に最適な電子構造・結晶構造と高性能熱電材料の開発」(招待講演) 竹内恒博, 日本表面科学会中部支部研究会, 静岡大学工学部, 浜松, 2017/11/24.
- DT60. “Thermoelectric properties of the $FeV_{0.955-x}Hf_{0.045}Ti_xSb$ half-Heusler phase,” K. Delime-Codrin, T. Takeuchi, D. Byeon, G. Swapnil, 第 65 回応用物理学会春季学術講演会, 早稲田大学 早稲田キャンパス, 2018/3/17 (3/17-20).
- DT61. “Effects of strain on thermal conductivity of Fe_2VAl -based superlattice thin film,” S. Choi, S. Hiroi, S. Nishino, M. Inukai, D. Byeon, M. MiKami, and T. Takeuchi, 第 65 回応用物理学会春季学術講演会, 早稲田大学 早稲田キャンパス, 2018/3/19 (3/17-20).

法人番号	231023
プロジェクト番号	S1411027

- DT62. 「自己発熱合成法により作製した X_2Ch ($X = Cu, Ag, CH = S, Se, Te$) の相変態過程と熱電物性」竹内恒博, 平田圭介, 松永卓也, 邊韜均, 日本金属学会 2017 年秋期講演大会, 千葉工業大学新習志野キャンパス, 2018/3/17 (3/15-17).
- DT63. “Thermoelectric power of Y-doped Bi₂Te₃ single crystals measured in strong magnetic field,” R. Sobota and T. Takeuchi, 日本物理学会 第 73 回年次大会, 東京理科大学 野田キャンパス, 2018/3/22 (3/22-25).
- DT64. 「電子構造, 電子散乱, フォノン分散, フォノン散乱を考慮した高性能熱電材料の開発」(招待講演), 竹内恒博, 長岡技術科学大学, 長岡, 2018/3/23.
- DT65. 「Yb-Si 系化合物の熱電物性」飯塚拓也, 加藤丈博, 堀太郎, 松波雅治, 竹内恒博, 日本物理学会 第 73 回年次大会, 東京理科大学 野田キャンパス, 2018/3/23 (3/22-25).
- DT66. “Thermal conductivity of Ta doped Fe₂VAl/(Mo,W) superlattice thin films,” Seongho Choi, Satoshi Hiroi, Shunsuke Nishino, Manabu Inukai, Okkyun Seo, Jae Myung Kim, Dogyun Byeon, Masashi Mikami, Masaharu Matsunami, Tsunehiro Takeuchi, 第 15 回日本熱電学会学術講演会 (TSJ2018) 東北大学, 青葉山キャンパス, 2018/9/13 (9/13-15).
- DT67. 「バイアス電圧で動作する熱スイッチ素子の作製」松永卓也, 平田圭佑, 崔城豪, 松波雅治, 竹内恒博, 第 15 回日本熱電学会学術講演会 (TSJ2018) 東北大学, 青葉山キャンパス, 2018/9/13 (9/13-15).
- DT68. 「Cu₂Se における自己キャリア濃度調整効果」竹内恒博, 邊韜均, 崔城豪, Robert Sobota, Kévin Delime-Codrin, 松波雅治, 足立真寛, 木山誠, 松浦尚, 山本喜之, 第 15 回日本熱電学会学術講演会 (TSJ2018) 東北大学, 青葉山キャンパス, 2018/9/13 (9/13-15).
- DT69. 「小型ヒーターと小型真空層を用いたゼーベック係数測定装置の開発」竹内恒博, 邊韜均, 第 15 回日本熱電学会学術講演会 (TSJ2018) 東北大学, 青葉山キャンパス, 2018/9/13 (9/13-15).
- DT70. 「Ag₂Ch (Ch = S, Se, Te) の相変態過程における熱電物性の挙動」(優秀講演賞受賞) 平田圭佑, 松永卓也, 崔城豪, Dogyun Byeon, 松波雅治, 竹内恒博, 第 15 回日本熱電学会学術講演会 (TSJ2018) 東北大学, 青葉山キャンパス, 2018/9/13 (9/13-15).
- DT71. 「体温や廃熱から電気をつくる材料(市民公開講座)」竹内恒博, 第 15 回日本熱電学会学術講演会 (TSJ2018) 東北大学, 青葉山キャンパス, 2018/9/15 (9/13-15).
- DT72. “High improvement of the figure of merit ZT in bulk amorphous-nanocrystalline Si_{0.55}Ge_{0.35}(Fe₁P_{0.10}),” (ポスター講演) Kévin Delime-Codrin, Muthusamy Omprakash, Ghodke Swapnil, Tsunehiro Takeuchi, 第 15 回日本熱電学会学術講演会 (TSJ2018) 東北大学, 青葉山キャンパス, 2018/9/14 (9/13-15).

法人番号	231023
プロジェクト番号	S1411027

- DT73. 「ZnO ナノ粒子添加による Zn_4Sb_3 の熱電性能向上」(ポスター講演) 松浦 佑哉, 佐藤 敦武, 田橋 正浩, 高橋 誠, 後藤 英雄, 崔 城豪, 竹内 恒博, 第 79 回応用物理学会秋季学術講演会, 名古屋国際会議場, 2018/9/19 (9/18-21).
- DT74. “Heavy-element dependence of thermoelectric properties in Fe_2VAl thin films,” Seongho Choi, Satoshi Hiroi, Dogyun Byeon, Masaharu Matsunami, Tsunehiro Takeuchi, 第 79 回応用物理学会秋季学術講演会, 名古屋国際会議場, 2018/9/20 (9/18-21).
- DT75. “Distinctive thermoelectric properties of P doped SiGe,” Swapnil Chetan Ghodke, Omprakash Muthusamy, Kevin Delime Codrin, Saurabh Singh, Masahiro Adachi, Tsunehiro Takeuchi, 第 79 回応用物理学会秋季学術講演会, 名古屋国際会議場, 2018/9/21 (9/18-21).
- DT76. 「 $Cu_{2-x}Se$ における自己キャリア濃度調整効果」(注目講演) 竹内 恒博, 邊 韜均, 崔 城豪, ロバート ソボタ, ケビン デリムコドリー, 松波 雅治, 足立 真寛, 木山 誠, 松浦 尚, 山本 喜之, 第 79 回応用物理学会秋季学術講演会, 名古屋国際会議場, 2018/9/21 (9/18-21).
- DT77. “Electron and heat transport properties in solid materials,” Tsunehiro Takeuchi, OIST Seminar, OIST, Okinawa, 2018/10/24.
- DT78. 「Si-Ge 系高性能バルク熱電材料の開発」竹内 恒博, Swapnil Ghodke, Muthusamy Omprakash, 足立 真寛, 山本 喜之, 粉体粉末冶金協会平成 30 年度秋季大会(第 122 回講演会), 朱鷺メッセ, 新潟, 2018/10/30. (10/30-31).
- DT79. 「カルコゲナイドで観測される巨大出力因子」竹内 恒博, 邊 韜均, Robert Sobota, 粉体粉末冶金協会平成 30 年度秋季大会(第 122 回講演会), 朱鷺メッセ, 新潟, 2018/10/30. (10/30-31).
- DT80. 「革新的熱スイッチ素子の開発」(ポスター発表) 松永卓也, 松波雅治, 竹内恒博, グリーン電子素子・材料研究センター 最終年度シンポジウム, 豊田工業大学, 2018/11/2.
- DT81. 「 Ag_2Ch ($Ch = S, Se, Te$) の異常熱伝導度を利用した熱ダイオードの開発」(ポスター発表) 平田 圭祐, 松波雅治, 竹内恒博, グリーン電子素子・材料研究センター 最終年度シンポジウム, 豊田工業大学, 2018/11/2.
- DT82. “Colossal Seebeck Effect in $Cu_{2-x}Se$,” (ポスター発表) Dogyun Byeon, Robert Sobota, Masaharu Matsunami, Tsunehiro Takeuchi, グリーン電子素子・材料研究センター 最終年度シンポジウム, 豊田工業大学, 2018/11/2.
- DT83. “Carrier Concentration Dependence of Electron Transport Properties of $Bi_2Sr_2CaCu_2O_{8+\delta}$,” (ポスター発表) Robert Sobota, Naoto Kubo, Masaharu Matsunami, Tsunehiro Takeuchi, グリーン電子素子・材料研究センター 最終年度シンポジウム, 豊田工業大学, 2018/11/2.

法人番号	231023
プロジェクト番号	S1411027

- DT84. “Thermoelectric Properties of (Mn,X)Si_{1.73} (X = Re, Fe, Co),” (ポスター発表) Swapnil Ghodke, Masaharu Matsunami, Tsunehiro Takeuchi, グリーン電子素子・材料研究センター 最終年度シンポジウム, 豊田工業大学, 2018/11/2.
- DT85. 「Effects of Grain Boundaries and Impurities on Thermal Conductivity」(ポスター発表) 崔城豪、松波雅治、竹内恒博, グリーン電子素子・材料研究センター 最終年度シンポジウム, 豊田工業大学, 2018/11/2.
- DT86. 「重い電子系化合物の熱電物性」(ポスター発表) 松波雅治、尾川史武、飯塚拓也、加藤丈博、堀太郎、竹内恒博, グリーン電子素子・材料研究センター 最終年度シンポジウム, 豊田工業大学, 2018/11/2.
- DT87. 「省エネルギー社会の構築に寄与する革新的熱利用材料・素子の研究」竹内恒博, グリーン電子素子・材料研究センター 最終年度シンポジウム, 豊田工業大学, 2018/11/2.
- DT88. 「自己キャリア濃度調整による巨大ゼーベック効果と超巨大出力因子」(招待講演) 竹内恒博, 第 39 回熱物性シンポジウム, ウィンク愛知, 名古屋, 2018/11/13. (11/13-15).
- DT89. 「Cu₂Se で観測される異常ゼーベック効果と巨大な出力因子(無次元性能指数)」(招待講演) 竹内恒博, 筑波大学第一回プレ戦略研究会「次世代物質・デバイス戦略開発拠点」, 第一回 TIA かけはし研究会「温度変化で発電するモバイル発電器」, 筑波大学, つくば, 2018/11/26.
- DT90. 「異常熱伝導度の実験的解明と機能性熱利用素子の創製」竹内恒博, 熱流制御・熱電変換材料研究会, 豊田工業大学, 2018/12/1.
- DT91. 「高性能熱電材料開発における放射光の利用」竹内恒博, 第 8 回名古屋大学シンクロトロン光研究センターシンポジウム, 名古屋大学, 2019/1/17.
- DT92. 「CePd₃ の熱電特性における元素置換効果」(ポスター講演) 尾川 史武, 松波 雅治, 竹内 恒博, 第 66 回応用物理学会春季学術講演会, 東京工業大学 大岡山キャンパス, 2019/3/9 (3/9-12).
- DT93. “Large evolution of ZT in p-type nanocrystalline bulk Si-Ge,” オムプラカシ ムサミー, ゴドケ スワプニル, デリムコドリ ケビン, 足立 真寛, 山本 喜之, 竹内 恒博, 第 66 回応用物理学会春季学術講演会, 東京工業大学 大岡山キャンパス, 2019/3/9 (3/9-12).
- DT94. 「Au と B を共添加した Si-Ge 系薄膜の熱電特性」廣瀬 光太郎, 足立 真寛, 西野 俊佑, 山本 喜之, 竹内 恒博, 第 66 回応用物理学会春季学術講演会, 東京工業大学 大岡山キャンパス, 2019/3/10 (3/9-12).
- DT95. 「重元素置換 Fe₂VAl 系超格子薄膜でのフォノン散乱」Choi Seongho, 廣井 慧, 犬飼 学, Byeon Dogyun, 松波 雅治, 竹内 恒博, 第 66 回応用物理学会春季学術講演会, 東京工業大学 大岡山キャンパス, 2019/3/9 (3/9-12).

法人番号	231023
プロジェクト番号	S1411027

DT96. 「外部電場で制御する熱流スイッチング素子の作製」松永 卓也, 平田 圭佑, 松波 雅治, 竹内 恒博, 第 66 回応用物理学会春季学術講演会, 東京工業大学 大岡山キャンパス, 2019/3/9 (3/9-12).

【界面・電極制御による電力損失の低減 - 界面制御磁性メモリ】

DM1. 「希土類磁性細線を用いたマルチレベルレーストラックメモリの検討」黒川雄一郎、栗野博 14p-p.10-30、第 64 回応用物理学会春季学術講演会、パシフィコ横浜、2016 年 3 月 14 日

DM2. 「希土類遷移金属合金 TbCo 磁性細線メモリの連続記録再生」吉村瞭吾、黒川雄一郎、鷺見聡、栗野博之、14p-p.10-33 第 64 回応用物理学会春季学術講演会、パシフィコ横浜、2016 年 3 月 14 日

DM3. “Effect of ultrathin Tb layer on current driven domain wall motion in Co/Tb magnetic bilayers.” Cheng Ying Wu, Hiroyuki Awano, 14p-P10-46、第 64 回応用物理学会春季学術講演会、パシフィコ横浜、2016 年 3 月 14 日

DM4. 「Pt/TbCo 薄膜の磁気光学特性」家元章吾、鷺見聡、栗野博之、林将光 14p-P10-34、第 64 回応用物理学会春季学術講演会、パシフィコ横浜、2016 年 3 月 14 日

DM5. “Domain wall dynamics in ferrimagnetic Tb/Co multilayer wires below and above the magnetic compensation point,” Hiroyuki Awano, Masaaki Tanaka, Sho Sumitomo, Noriko Adachi, Ko Mibu, Shuta Honda, 第 63 回応用物理学会春季学術講演会、東京工業大学 大岡山キャンパス、2016 年 3 月 19 日

DM6. 「TMR 磁気ヘッドを用いた希土類・遷移金属磁性細線の記録再生評価」鷺見聡、黒川雄一郎、栗野博之、第 32 回日本磁気学会光機能磁性デバイス・材料専門研究会、2017 年 03 月 13 日

DM7. 「希土類遷移金属/Pt ヘテロ界面細線における電流磁壁駆動と温度及び磁界の関係」黒川雄一郎、栗野博之、日本磁気学会光機能磁性デバイス・材料専門研究会、2017 年 01 月 20 日

DM8. 「希土類磁性細線を用いたマルチレベルレーストラックメモリの検討」黒川雄一郎、栗野博之、春季第 64 回応用物理学関係連合講演会、2017 年 3 月 14 日

DM9. 「希土類遷移金属合金 TbCo 磁性細線メモリの連続記録再生」吉村瞭吾、黒川雄一郎、鷺見聡、栗野博之、春季第 64 回応用物理学関係連合講演会、2017 年 3 月 14 日

DM10. “Effect of ultrathin Tb layer on current driven domain wall motion in Co/Tb magnetic bilayers,” Cheng Ying Wu, Yuichiro Kurokawa, Do Bang, Ko Wei Lin, Hiroyuki Awano, 春季第 64 回応用物理学関係連合講演会、2017 年 3 月 14 日

DM11. 「Pt/TbCo 薄膜の磁気光学特性」家元章吾、鷺見聡、栗野博之、林将光、春季第 64 回応用物

法人番号	231023
プロジェクト番号	S1411027

理学関係連合講演会、2017年3月14日

DM12. 「薄い Co 層を導入した Pt/Co/Tb-Co 多層膜の電流誘起磁壁移動」 栗野博之、第 41 回日本磁気学会学術講演会、2017年9月20日

DM13. 「(Tb/Co)/Pt ヘテロ界面磁性細線の電流磁壁駆動」 鷺見聡、ドバン、栗野博之、電気学会マグネティクス研究会、2017年11月16日

DM14. 「フレキシブルナノインプリントプラスチック基板を用いたバルクスピントルク磁化反転」 栗野博之、電子情報通信学会 IEICE、2018年3月9日

DM15. 「磁性層/重金属層ヘテロ構造の磁気光学効果」 松本 憩、鷺見 聡、田辺 賢士、栗野 博之、第 66 回応用物理学会春季学術講演会、2019年3月9日

DM16. 「電流磁壁駆動磁性細線の温度分布測定」 澤 拓哉、鷺見 聡、田辺 賢士、栗野 博之、第 66 回応用物理学会春季学術講演会、2019年3月9日

DM17. 「フェリ磁性体 GdFeCo の磁性共鳴によるスピン起電力」 福田 舜、高橋 晨、鷺見 聡、田辺 賢士、栗野 博之、第 66 回応用物理学会春季学術講演会、2019年3月9日

DM18. 「厚膜 GdFeCo 磁性細線における電流誘起磁壁移動」 高橋 晨、黒川 雄一郎、鷺見 聡、田辺 賢士、栗野 博之、第 66 回応用物理学会春季学術講演会、2019年3月9日

DM19. 「Pt/TbCo ヘテロ界面積層膜における磁気光学効果の波長依存性評価」 家元章吾、鷺見聡、Pham Van Thach, 栗野博之、林将光、電気学会マグネティクス研究会、MAG-18-105. 2018年11月1日

DM20. 「[Tb/Co]/Pt 磁性細線の電流磁壁駆動に関する研究」 栗野博之、Do Bang, Pham Van Thach, 電気学会マグネティクス研究会、MAG-19-023, EFM-19-010, (2019年3月8日)

【界面・電極制御による電力損失の低減 -光電・電光変換素子】

DP1. 「結晶成長その場 X 線回折装置(MBE-XRD)による InGaAs/GaAs(001)の緩和研究」 小寺大介、佐々木拓生、西俊明、鈴木秀俊、小島信晃、大下祥雄、山口真史、第 11 回次世代の太陽光発電システムシンポジウム、宮崎観光ホテル(2014年7月3日～4日)

DP2. 「GaAs(111)基板上に成膜した(In_xGa_{1-x})₂Se₃ 薄膜の構造評価」 中村紘也、小島信晃、大下祥雄、山口真史、第 11 回次世代の太陽光発電システムシンポジウム、宮崎観光ホテル(2014年7月3日～4日) (*P2)

DP3. 「GaAs 基板の傾斜方向が InGaAs 膜中緩和過程に与える影響 -X 線回折 その場観察」 小寺大介、佐々木拓生、高橋正光、鈴木秀俊、小島信晃、大下祥雄、神谷格、山口真史、第 75 回応用

法人番号	231023
プロジェクト番号	S1411027

物理学会秋季学術講演会、北海道大学 札幌キャンパス(2014年9月17日～20日)

- DP4. 「 $t\text{-C}_4\text{H}_9\text{GeH}_3$ を用いた Si および SiO_2 基板上への Ge 薄膜成長」 片山僚太、須田耕平、町田英明、須藤弘、石川真人、小椋厚志、大下祥雄、第 13 回次世代の太陽光発電システムシンポジウム、アオーレ長岡(2016年5月19日～20日)
- DP5. 「遷移金属酸化物/ SiO_2 /結晶 Si ヘテロ接合コンタクト界面における仕事関数」 神岡武文、林豊、磯貝勇樹、中村京太郎、大下祥雄、第 77 回応用物理学会秋季学術講演会、朱鷺メッセ(2016年9月13日～16日) (*P1)
- DP6. 「遷移金属酸化物/ SiO_2 /結晶 Si ヘテロ接合コンタクト界面における仕事関数(2):RPD-ITO」 神岡武文、山田郁彦、林豊、磯貝勇樹、リ ヒュンジュ、中村京太郎、大下祥雄、第 64 回応用物理学会春季学術講演会、パシフィコ横浜(2017年3月14日～17日) (*P1)
- DP7. 「 $\text{InP}(100)$ 基板上における $\text{InAs}/\text{InAlGaAs}$ 量子ロッド構造の形成」 大森雅登、野田武司、小嶋友也、杉村和哉、Pavel Vitushinskiy、岩田直高、榊裕之、第 76 回応用物理学会秋季学術講演会、名古屋国際会議場(2015年9月14日) (*P3)
- DP8. 「赤外用三角障壁フォトランジスタの暗電流低減と室温動作」 杉村和哉、大森雅登、野田武司、Vitushinskiy Pavel、岩田直高、榊裕之、第 76 回応用物理学会秋季学術講演会、名古屋国際会議場(2015年9月15日) (*P3)
- DP9. 「 HCl 表面処理とプラズマ励起原子層堆積 SiN_x 膜による $\text{AlGaIn}/\text{GaIn}$ HEMT の表面安定化」 鈴木貴之、土屋晃祐、大保崇博、赤澤良彦、下野貴史、松本滉太、江口卓也、岩田直高、第 64 回応用物理学会春季学術講演会、パシフィコ横浜、2017年3月16日 (*P4)
- DP10. 「プラズマ励起原子層堆積プラズマ励起原子層堆積保護膜による $\text{AlGaIn}/\text{GaIn}$ HEMT の表面安定化」 鈴木貴之、山田富明、河合亮輔、川口翔平、張東岩、岩田直高、第 77 回応用物理学会秋季学術講演会、朱鷺メッセ、新潟コンベンションセンター、2016年9月16日 (*P4)
- DP11. 「 Mg ドープ GaIn のレーザー誘起による活性化とその局所制御」 松本滉大、黒瀬範子、下野貴史、岩田直高、山田郁彦、神谷格、青柳克信、第 78 回秋季応用物理学会学術講演会、福岡国際会議場・国際センター・福岡サンパレス、2017年9月5日 (*P5)
- DP12. 「放射光 XRD・HAXPES による $\text{Al}/\text{Ti}/\text{AlGaIn}$ の界面反応層の結晶構造及び化学結合状態評価」 安野聡、小金澤智之、鈴木貴之、岩田直高、第 78 回秋季応用物理学会学術講演会、福岡国際会議場・国際センター・福岡サンパレス、2017年9月6日
- DP13. 「 Mg ドープ GaIn へのレーザー照射による局所活性化と結晶性のその場観測」 松本滉太、黒瀬範子、山田郁彦、神谷格、青柳克信、岩田直高、IEEE Metro Area Workshop in Nagoya、中京大学、2017年10月8日 (*P5)
- DP14. 「 p 型 GaIn ゲートを用いたノーマリオフ動作 $\text{AlGaIn}/\text{GaIn}$ 高電子移動度トランジスタ」 赤澤良彦、

法人番号	231023
プロジェクト番号	S1411027

近藤孝明、吉川慎也、岩田直高、榊裕之、第65回春季応用物理学会学術講演会、早稲田大学西早稲田キャンパス・ベルサール高田馬場、2018年3月17日 (*P5)

DP15. 「Mg イオン注入 GaN のフラッシュランプアニールによる活性化」 大森雅登、山田 隆泰、谷村 英昭、加藤 慎一、岩田 直高、塩崎 宏司、第 79 回応用物理学会秋季学術講演会、名古屋国際会議場、2018 年 9 月 18 日

DP16. 「選択ドライエッチングが p 型 GaN ゲート AlGaIn/GaN/GaN/GaN 高電子移動度トランジスタの特性へ及ぼす影響」 近藤孝明、赤澤良彦、岩田直高、第 79 回応用物理学会秋季学術講演会、名古屋国際会議場、2018 年 9 月 18 日 (*P4)

DP17. 「レーザを用いた局所 p-GaN オーミック電極形成法の開発」 川崎輝尚、黒瀬範子、松本晃太、岩田直高、青柳克信、第 79 回応用物理学会秋季学術講演会、名古屋国際会議場、2018 年 9 月 19 日 (*P5)

DP18. 「様々な p 型 GaN ゲート構造をドライエッチングで形成した AlGaIn/GaN/GaN/GaN 高電子移動度トランジスタ 高電子移動度トランジスタの特性」近藤孝明、赤澤良彦、岩田直高、春季第 66 回応用物理学関係連合講演会、東京工業大学、2019 年 3 月 11 日 (*P4)

DP19. 「フェムト秒励起光電流分光による InAs 量子構造の光キャリアアップコンバージョン過程と電子・正孔寿命の決定」 山田泰裕、David M. Tex、神谷格、金光義彦、日本物理学会 2014 年秋季大会 9pAD-2、中部大学 春日井キャンパス、2014 年 9 月 9 日 (9/7-10)

DP20. 「GaAs(001)上の InAs 量子ドットの 1.55 μm 以上での発光」下村憲一、神谷格、第 75 回応用物理学会秋季学術講演会 18p-A20-15 北海道大学 札幌キャンパス、2014 年 9 月 18 日 (9/17-20)

DP21. 「GaAs 基板の傾斜方向が InGaAs 膜中緩和過程に与える影響 – X 線回折その場観察」小寺大介、佐々木拓生、高橋正光、神谷格、大下祥雄、小島信晃、山口真史、鈴木秀俊、第 75 回応用物理学会秋季学術講演会 19a-S1-3 北海道大学 札幌キャンパス、2014 年 9 月 19 日 (9/17-20)

DP22. 「ケルビンプローブ顕微鏡を用いた Si ヘテロ接合 (SHJ) 太陽電池における表面構造界面の局所的仕事関数測定」 山田郁彦、神岡武文、立花福久、中村京太郎、神谷格、大下祥雄、第 75 回応用物理学会秋季学術講演会 19a-A25-8、北海道大学 札幌キャンパス、2014 年 9 月 19 日 (9/17-20) (*P1)

DP23. 「Si ヘテロ接合(SHJ)太陽電池におけるケルビンプローブ顕微鏡を用いた仕事関数測定の定量性検討」山田郁彦、高林紘、神岡武文、立花福久、中村京太郎、大下祥雄、神谷格、春季第 62 回応用物理学関係連合講演会 11p-C5-2、東海大学 湘南キャンパス、2015 年 3 月 11 日 (3/11-14)

DP24. 「Cu₂ZnSnS₄ ナノ粒子の液相合成における Cu²⁺還元過程」森下一喜、須藤裕之、神谷格

法人番号	231023
プロジェクト番号	S1411027

春季第 62 回応用物理学関係連合講演会、12p-C5-2、東海大学 湘南キャンパス、2015 年 3 月 12 日 (3/11-14)

DP25. 「GaAs(001)上の InAs 量子ドットの 1.55 μm 以上での発光(2)」下村憲一、神谷格、春季第 62 回応用物理学関係連合講演会 12p-C5-2、東海大学 湘南キャンパス、2015 年 3 月 14 日 (3/11-14) (*P7)

DP26. 「結晶 Si 太陽電池の断面仕事関数測定に適した観察研磨手法の検討」 山田郁彦、高林紘、神岡武文、大下祥雄、神谷格、須田耕平、中村京太郎、小椋厚志、春第 76 回応用物理学会秋季学術講演会、15a-2S-9、名古屋国際会議場、2015 年 9 月 15 日 (9/13-16) (*P1)

DP27. 「表面 In(Ga)As 量子ドット仕事関数の歪依存性 (注目講演)」小林知弘、高林紘、下村憲一、Yuwei Zhang、山田郁彦、神谷格、春季第 63 回応用物理学関係連合講演会 20a-S223-3、東京工業大学 大岡山キャンパス、2016 年 3 月 20 日 (3/19-22) (*P8)

DP28. “Up-converted photoluminescence in InAs QD-based structures with confined state,” Yuwei Zhang and Itaru Kamiya, 春季第 63 回応用物理学関係連合講演会 20a-S011-4、東京工業大学 大岡山キャンパス、2016 年 3 月 20 日 (3/19-22) (*P6)

DP29. 「太陽電池構造断面試料作製時のダメージが仕事関数測定に与える影響」 山田郁彦、神岡武文、大下祥雄、神谷格、春季第 63 回応用物理学関係連合講演会、20a-W611-9、東京工業大学 大岡山キャンパス、2016 年 3 月 20 日 (3/19-22) (*P1)

DP30. 「太陽電池構造評価に適した光照射が可能な AFM/KFM 装置の開発」 山田郁彦、神岡武文、大下祥雄、神谷格、第 77 回応用物理学会秋季学術講演会 15p-P13-14、朱鷺メッセ(新潟)、2016 年 9 月 15 日 (9/13-16) (*P1)

DP31. 「Si ドープによる InAs 量子ドットの仕事関数変化」小林知弘、高林紘、下村憲一、Yuwei Zhang、山田郁彦、神谷格、第 77 回応用物理学会秋季学術講演会、15p-A26-5、朱鷺メッセ、新潟コンベンションセンター、2016 年 9 月 15 日 (9/13-16) (*P8)

DP32. “Strain relaxation in submonolayer InAs/GaAs quantum structures,” Yuwei Zhang and Itaru Kamiya、第 77 回応用物理学会秋季学術講演会、16a-A26-2、朱鷺メッセ、新潟コンベンションセンター、2016 年 9 月 16 日 (9/13-16) (*P6)

DP33. 「KFM を用いた InAs 量子ドット表面近傍のバンド解析」小林知弘、高林紘、下村憲一、Yuwei Zhang、山田郁彦、神谷格、春季第 64 回応用物理学関係連合講演会、14p-E205-7、パシフィコ横浜、2017 年 3 月 14 日 (3/14-17) (*P8)

DP34. “Epitaxial growth of various InAs nanostructures by different growth methods,” Yuwei Zhang and Itaru Kamiya、春季第 64 回応用物理学関係連合講演会、15a-P9-1、パシフィコ横浜、2017 年 3 月 15 日 (3/14-17) (*P6)

法人番号	231023
プロジェクト番号	S1411027

- DP35. 「平坦な p-n 接合断面における局所仕事関数測定」(ポスター賞受賞) 山田郁彦、神岡武文、水野皓登、大下祥雄、神谷格、春季第 64 回応用物理学関係連合講演会、15a-P11-6、パシフィック横浜、2017 年 3 月 15 日 (3/14-17) (*P1)
- DP36. 「光制御下における p-型 Si/ITO 界面の断面仕事関数測定」 山田郁彦、神岡武文、大下祥雄、神谷格、第 78 回応用物理学会秋季学術講演会 5p-PB3-8、福岡国際会議場、2017 年 9 月 5 日 (9/5-8) (*P1)
- DP37. “Photon upconversion in InAs QDs and QWIs modeled by 8-band k·p theory,” Yuwei Zhang and Itaru Kamiya, 第 78 回応用物理学会秋季学術講演会 6p-PB3-8、福岡国際会議場、2017 年 9 月 6 日 (9/5-8) (*P6)
- DP38. 「InAs/GaAs サブモノレイヤー結晶成長の機構と制御」 水野皓登、Yuwei Zhang、神谷格、第 65 回応用物理学会春季学術講演会 17p-E314-6、早稲田大学西早稲田キャンパス、2018 年 3 月 17 日 (3/17-20) (*P6)
- DP39. 「コアシェル型酸化亜鉛ナノ粒子の作製と評価」 後藤直輝、奥山竜太、山田郁彦、神谷格、第 65 回応用物理学会春季学術講演会 19p-P8-13、ベルサール高田馬場、2018 年 3 月 19 日 (3/17-20)
- DP40. 「変調中間層による歪制御積層 InAs 量子ドット形状の変化」 鈴木幹人、神谷格、第 79 回応用物理学会秋季学術講演会 18p-234B-9、名古屋国際会議場、2018 年 9 月 18 日 (9/18-21) (*P7)
- DP41. 「サブモノレイヤー InAs 層を介した光アップコンバージョン」 水野皓登、Yuwei Zhang、神谷格、第 79 回応用物理学会秋季学術講演会 18p-234B-10、名古屋国際会議場、2018 年 9 月 18 日 (9/18-21) (*P6)
- DP42. 「InAs サブモノレイヤー構造における光アップコンバージョン過程」 水野皓登、Yuwei Zhang、神谷格、春季第 66 回応用物理学関係連合講演会 11p-PA4-6、東京工業大学(大岡山)、2019 年 3 月 11 日 (3/9-12) (*P6)
- DP43. 「変調中間層による歪制御積層 InAs 量子ドットの光学特性制御」 鈴木幹人、神谷格、春季第 66 回応用物理学関係連合講演会 11p-S422-6、東京工業大学(大岡山)、2019 年 3 月 11 日 (3/9-12) (*P7)
- DP44. 「ZnO/Zn_{1-x}Mg_xO ナノ粒子の作製」 後藤直輝、神谷格、春季第 66 回応用物理学関係連合講演会 11p-W833-11、東京工業大学(大岡山)、2019 年 3 月 11 日 (3/9-12)
- DP45. “Below-Bandgap Photoluminescence Emission from SI GaAs substrates subjected to pre-MBE-growth annealing,” Ronel Christian Roca, Hiroto Mizuno, Mikihiro Suzuki, and Itaru Kamiya, 春季第 66 回応用物理学関係連合講演会 11p-S422-10、東京工業大学(大岡山)、2019 年 3 月 11 日 (3/9-12)

法人番号	231023
プロジェクト番号	S1411027

【界面・電極制御による電力損失の低減 -有機電子素子】

- DO1. 「探針増強ラマン散乱分光法による酸化グラフェンの 2 次元マッピング」 稲葉 達郎、川畑 智雅、De Silva Kanishka、吉村 雅満、第 64 回応用物理学会春季学術講演会、パシフィコ横浜、2017 年 3 月 16 日 (*O2)
- DO2. 「2 層グラフェンによる SERS 基板内銀粒子の保護」 鈴木誠也、吉村 雅満、第 64 回応用物理学会春季学術講演会、パシフィコ横浜、2017 年 3 月 15 日
- DO3. “Reliable transfer of large-area single crystal CVD graphene for field effect transistor,” Liao YenChang、鈴木誠也、吉村 雅満、第 64 回応用物理学会春季学術講演会、パシフィコ横浜、2017 年 3 月 14 日(*11)
- DO4. 「チップ増強ラマン分光法による燃料電池触媒層の組成分布マッピング」池田英恵、稲葉達郎、川畑智雅、小澤誠也、高澤信明、任藤丈裕、吉村雅満、第 65 回応用物理学会春季学術講演会、早稲田大、2018 年 3 月 17 日(*O2)

【界面・電極制御による電力損失の低減 -界面改質プロセス:配向セラミックス薄膜の作製】

- DC1. 「サファイア基板を Reactive substrate として用いた YAG 配向膜の作製」 荒川修一、門浦弘明、宇山健、鷹取一雅、谷俊彦、日本セラミックス協会 2015 年年会、1P165、岡山大学、2015 年 3 月 18 日 (3/18-20) (*13)
- DC2. 「サファイア基板上 Y₂O₃ 薄膜から作製した YAG 薄膜の結晶配向性解析」 荒川修一、門浦弘明、宇山健、鷹取一雅、竹田康彦、谷俊彦、日本セラミックス協会 2016 年年会、1P195、早稲田大学、2016 年 3 月 14 日 (3/14-16) (*14)
- DC3. 「Reactive Substrate 上に合成した複酸化物薄膜の結晶配向性」 荒川修一、日本セラミックス協会 2019 年年会、1P227、工学院大学 新宿キャンパス、2019 年 3 月 24 日 (3/24-26) (*15)

国際会議

【先進エネルギー変換素子・材料 - 熱電材料、熱ダイオード、熱スイッチ】

- IT1. [Invited] “Development of thermal rectifier using unusual electron thermal conductivity of icosahedral quasicrystals,” T. Takeuchi, APS March Meeting, San Antonio, Texas, March 5, 2015 (March 2-6).
- IT2. “Thermoelectric properties of higher manganese silicide containing small amount of Re,” A. Yamamoto and T. Takeuchi, 11th International Conference on Ceramic Materials and Components for energy and Environmental Applications, Vancouver, Canada, June 16, 2015 (June 14-19).
- IT3. [Invited] “Development of thermoelectric materials using information about the electronic

法人番号	231023
プロジェクト番号	S1411027

structure near the chemical potential,” T. Takeuchi, A. Yamamoto, N. Hiroishi, S. Ghodke, and H. Ikuta, 34th Annual International Conference on Thermoelectrics & 13th European Conference on Thermoelectrics, Dresden, Germany, June 30, 2015 (June 28-July 2).

IT4. [Invited] “Development of high performance thermoelectric materials consisting solely of ubiquitous elements,” T. Takeuchi, 14th International Union of Materials Research Societies-International Conference on Advanced Materials, Jeju, Korea, October 29, 2015 (Oct. 25-29).

IT5. [Invited] “Thermoelectric properties of Heusler type Fe₂VAl thin-films deposited at high temperature,” S. Hiroi, M. Mikami and T. Takeuchi, International Congress on Small Science 2015, Phuket, Thailand, November 6, 2015 (Nov. 4-7).

IT6. [Invited] “Theories of thermoelectric properties and guiding principle for developing high-performance,” T. Takeuchi, International Conference on Thermoelectric Materials Science 2015, Nagoya Univ., November 9, 2015 (Nov. 9-11).

IT7. [Invited] “Unusual behaviors of thermal conductivity observed for icosahedral quasicrystals and approximants,” T. Takeuchi, Toyota RIKEN International Workshop on Strongly Correlated Electron Systems: Open Space between Heavy Fermions and Quasicrystals, Nagoya Univ., November 19, 2015 (Nov. 17-19).

IT8. [Invited] “Development of Bulk Thermal Rectifiers using Al-Cu-Fe Quasicrystals,” K. Kitahara and T. Takeuchi, The EMN Thermoelectric Materials Meeting 2016, Kissimmee, USA, February 23, 2016 (Nov. 21-25).

IT9. “Thermoelectric performance of higher manganese silicide containing a small amount of 5d transition metal elements,” A. Yamamoto, S. Ghodke, M. Matsunami, and T. Takeuchi, The 35th International Conference on Thermoelectrics & The 1st Asian Conference on Thermoelectrics (ICT/ACT 2016) Wuhan, China, May 31, 2016 (May 29-Jun. 2).

IT10. “Thermoelectric properties of lacunar spinel β -In_{2-2x}Cu_xZn_xS₃,” K. Delime-Codrin, A. Yamamoto, K. Kitahara, S. Hiroi, and T. Takeuchi, The 35th International Conference on Thermoelectrics & The 1st Asian Conference on Thermoelectrics (ICT/ACT 2016) Wuhan, China, May 31, 2016 (May 29-Jun. 2).

IT11. “Enhancement of power factor by energy filtering effect in Re substituted HMS,” Swapnil Ghodke, A. Yamamoto, H. Ikuta, and T. Takeuchi, The 35th International Conference on Thermoelectrics & The 1st Asian Conference on Thermoelectrics (ICT/ACT 2016) Wuhan, China, June 2, 2016 (May 29-Jun. 2).

IT12. “Development thermal rectifiers using thermoelectric chalcogenide Ag₂Ch (Ch = S, Se, and Te),” T. Takeuchi, Y. Kinoshita, Y. Ohashi, T. Yoshinaga, T. Yamaguchi, and M.

法人番号	231023
プロジェクト番号	S1411027

Ishikiriya, The 35th International Conference on Thermoelectrics & The 1st Asian Conference on Thermoelectrics (ICT/ACT 2016) Wuhan, China, May 31, 2016 (May 29-Jun. 2).

IT13. “Thermoelectric properties of full-Heusler Fe_2VAI -based thin-films,” S. Hiroi and T. Takeuchi, The 35th International Conference on Thermoelectrics & The 1st Asian Conference on Thermoelectrics (ICT/ACT 2016) Wuhan, China, May 30, 2016 (May 29-Jun. 2).

IT14. [Invited] “Development of high performance thermoelectric materials consisting solely of environmental friendly elements,” A. Yamamoto and T. Takeuchi, BIT's 5th Annual World Congress of Advanced Materials-2016, Chongqing, China, June 8, 2016 (Jun. 6-8).

IT15. [Invited] “Development of high performance thermoelectric materials using detailed information about electronic structure and local atomic arrangements,” T. Takeuchi, 2017 Spring Conference of the Korean Institute of Metals and Materials, Chongwang, Korea, April 27, 2017 (Apr. 26-28).

IT16. “Thermoelectric properties of half-Heusler $\text{FeV}_{1-x}\text{Ti}_x\text{Sb}$,” Kévin Delime-Codrin, A. Yamamoto, T. Yamada and T. Takeuchi, 8th International Conference on Electroceramics 2017 (ICE2017), Nagoya, Japan, May 28, 2017 (May 28-31).

IT17. “Reduction of thermal conductivity in amorphous $\text{Si}_{0.65}\text{Ge}_{0.35-x}\text{Cu}_x$ synthesized by mechanical alloying process for thermoelectric applications,” M. Omprakash, S. Nishino, M. Inukai, and T. Takeuchi, 8th International Conference on Electroceramics 2017 (ICE2017), Nagoya, Japan, May 30, 2017 (May 28-31).

IT18. “Thermoelectric Properties of Yb-based Heavy-Fermion System,” T. Iizuka, T. Hori. M. Matsunami and T. Takeuchi, 8th International Conference on Electroceramics 2017 (ICE2017), Nagoya, Japan, May 30, 2017 (May 28-31).

IT19. “Thermoelectric properties of Si-Ge-TM thin film (TM = Au, Cu) grown by molecular beam epitaxy method,” S. Nishino, S. Ekino, M. Inukai, M. Omprakash, T. Takeuchi, 8th International Conference on Electroceramics 2017 (ICE2017), Nagoya, Japan, May 31, 2017 (May 28-31).

IT20. “Electronic states of transition metal elements in Si-Ge alloys,” M. Inukai and T. Takeuchi, 8th International Conference on Electroceramics 2017 (ICE2017), Nagoya, Japan, May 31, 2017 (May 28-31).

IT21. [Invited] “Guiding principle to develop high-performance thermoelectric materials.” T. Takeuchi, 8th International Conference on Electroceramics 2017 (ICE2017), Nagoya, Japan, May 31, 2017 (May 28-31).

法人番号	231023
プロジェクト番号	S1411027

- IT22. [Invited] “Development of thermal diodes using Ag_2Ch (Ch = S, Se, Te),” T. Takeuchi, The 9th US-Japan Joint Seminar on Nanoscale Transport Phenomena, Tokyo, Japan, 5th July 2017 (July 2-5).
- IT23. “Ultra-Low Thermal Conductivity of Amorphous $\text{Si}_{0.65}\text{Ge}_{0.35-x}\text{Cu}_x$ Synthesized by Mechanical Alloying Process,” M. Omprakash, S. Nishino, M. Inukai, M. Adachi, M. Kiyama, Y. Yamamoto, T. Takeuchi, The 36th International Conference on Thermoelectrics (ICT2017) Pasadena, CA, USA, July 31st, 2017 (July 31 – Aug. 3)
- IT24. “Thermoelectric Properties of Nano-Grained Si-Ge-Au Thin Film Grown by Molecular Beam Epitaxy Method,” S. Nishino, S. Ekino, M. Inukai, M. Omprakash, M. Adachi, M. Kiyama, Y. Yamamoto, T. Takeuchi, The 36th International Conference on Thermoelectrics (ICT2017) Pasadena, CA, USA, July 31st, 2017 (July 31 – Aug. 3).
- IT25. “Development of high performance and cost-effective thermoelectric material,” S. Ghodke, A. Yamamoto, T. Takeuchi, The 36th International Conference on Thermoelectrics (ICT2017) Pasadena, CA, USA, July 31st, 2017 (July 31 – Aug. 3).
- IT26. “Development of (Si, Ge)-based high performance bulk thermoelectric materials,” T. Takeuchi, M. Inukai, M. Omprakash, S. Nishino, The 15th International Conference on Advanced Materials (IUMRS-ICAM 2017) , Kyoto, Japan, Aug. 31st 2017 (Aug. 27 – Sep. 1) .
- IT27. “Self-tuning carrier concentration effect of noble metal chalcogenides,” Dogyun Byeon, Robert Sobota, Kevin Delime-Codrin, Seongho Choi, Keisuke Hirata, Masahiro Adachi, Makoto Kiyama, Yoshiyuki Yamamoto, Takashi Matsuura, Masaharu Matsunami, and Tsunehiro Takeuchi, 37th International and 16th European Conference on Thermoelectrics, Caen, France, July 2, 2018, (July 1 – 5).
- IT28. “Thermal conductivity of Fe_2VAl -based superlattice thin film,” Seongho Choi, Satoshi Hiroi, Shunsuke Nishino, Manabu Inukai, Okkyun Seo, Jae Myung Kim, Dogyun Byeon, Masashi Mikami, Masaharu Matsunami, and Tsunehiro Takeuchi, 7th International and 16th European Conference on Thermoelectrics, Caen, France, July 4, 2018, (July 1 – 5).
- IT29. “The decreases of the lattice thermal conductivity of the $\text{FeV}_{0.955-x}\text{Hf}_{0.045}\text{Ti}_x\text{Sb}$ half-Heusler phases,” Kévin Delime-Codrin, Swapnil Ghodke, Dogyun Byeon, Robert Sobota, and Tsunehiro Takeuchi, 7th International and 16th European Conference on Thermoelectrics, Caen, France, July 4, 2018, (July 1 – 5).
- IT30. “Effect of element substitution on the phase stability of complex MnSi_x ,” Swapnil Ghodke, Robert Sabota, Tsunehiro Takeuchi, 7th International and 16th European Conference on Thermoelectrics, Caen, France, July 4, 2018, (July 1 – 5).

法人番号	231023
プロジェクト番号	S1411027

IT31. “Self-tuning carrier concentration effect and colossal value of ZT in Cu₂Se,” Tsunehiro Takeuchi, XVI Interstate Conference on Thermoelectrics and their Applications (ISCTA 2018), Sankt Peterburg, Russia, Oct. 10th 2018 (Oct. 8 – 12).

【界面・電極制御による電力損失の低減 - 界面制御磁性メモリ】

IM1. “Enhancement of spin Hall effect-induced torques for current driven magnetic domain wall motion,” Do Bang and Hiroyuki Awano, IEEE International Magnetics Conference GT-07 (2015).

IM2. “Inner interface effect enhances spin-orbit torques in Tb/Co multilayered wires,” Do Bang, Jiawei Yu, Xuepeng Qiu, Hiroyuki Awano, Aurelien Manchon, and Hyunsoo Yang, 61st Annual Conference on Magnetism and Magnetic Materials, BD-11 (2016).

IM3. “Novel magnetic wire fabrication process by way of nano-imprint lithography for current induced magnetization switching,” T. Asari, H. Awano and R. Shibata, 61st Annual Conference on Magnetism and Magnetic Materials, EU-03 (2016).

IM4. “Enhancement of spin orbit torques in a Tb-Co alloy magnetic wire by controlling its Tb composition,” Y. Kurokawa, A. Shibata, and H. Awano, 61st Annual Conference on Magnetism and Magnetic Materials, EU-03 (2016).

IM5. [Invited] “Magnetic recording on the RE-TM /Pt magnetic wire deposited on nano-imprinted plastic substrate,” Hiroyuki Awano, Satoshi Sumi, Yuichiro Kurokawa, Do Bang, Akihiko Moribayashi, Ryogo Yoshimura, and Tsukasa Asari, International conference of the Asian Union of Magnetic Societies, (DC-01) (2016).

IM6. “Extrodinary Hall Effect in GeTe/Sb₂Te₃ topological superlattice and perpendicular magnetic anisotropy Tb/Co films,” Do Bang, Hiroyuki Awano, Y. Saito, J. Tominaga, INTERMAG’ 2017 (2017).

IM7. [Invited] “Spin Orbitronics study in hetero- structure of ferri-magnetic (RE-TM) and heavy metal Pt,” Hiroyuki Awano, PIERS’2017 (Progress in electromagnetics Research Symposium) (2017).

IM8. “Enhancement of current induced-domain wall motion in Tb/Co multilayers sandwiched between heavy metal with opposite spin hall angles” Pham Van Thach, Do Bang, Hiroyuki Awano, International symposium on advanced magnetic materials and applications (2017).

IM9. “International symposium on advanced magnetic materials and applications,” Hiroyasu Kondo Yuichiro Kurokawa, Hiroyuki Awano, International symposium on advanced magnetic materials and applications (2017).

法人番号	231023
プロジェクト番号	S1411027

- IM10. “Temperature dependence of spin-polarized current-induced resistance switching in [(GeTe)₂/(Sb₂Te₃)] superlattices,” Do Bang, Hiroyuki Awano, Yuta Saito, Junji Tominaga, International symposium on advanced magnetic materials and applications (2017).
- IM11. “Magneto-optical characteristics of Pt/TbCo heterostructure films,” S. Iemoto, S. Sumi, Hiroyuki Awano, M. Hayashi, MORIS’ 2018 (Magnetics and Optics Research International Symposium (2018).
- IM12. “Damping coefficient enhancement evidence for spin orbit interaction on [(GeTe)₂/(Sb₂Te₃)₁]₂₀ superlattices,” Y. Hirano, S. Sumi, Do Bang, Hiroyuki Awano, Y. Saito, J. Tominaga, MORIS’ 2018 (Magnetics and Optics Research International Symposium (2018).
- IM13. “Fast current-induced domain wall motion in Tb/Co multilayered wires with symmetric structure,” Pham Van Thach, Do Bang, Hiroyuki Awano, MORIS’ 2018 (Magnetics and Optics Research International Symposium (2018).
- IM14. [Invited] “Spin orbit torque effect of TbCo/Pt magnetic wires,” Pham Van Thach, Do Bang, Hiroyuki Awano, ETOPI11, 2018.
- IM15. “Interference induced enhancement of magneto-optical effect in Pt/TbCo hetero-structured films,” S. Iemoto, S. Sumi, H. Awano, M. Hayashi, ETOPI11, 2018.
- IM16. [Invited] “Current driven domain wall motion study of magnetic wire with hetero-interface between RE-TM and heavy metal layers,” H. Awano, C. Y. Wu, H. Kondo, R. Yoshimura, S. Sumi, Y. Kurokawa, D. Bang, P. V. Thach, K. W. Lin, G1-1299, (2018).
- IM17. “Influence of the Tb layer on current driven domain wall motion in Pt/Co/Tb magnetic wire,” H. Awano, W.C. Ying, R. Yoshimura, S. Sumi, P.V. Thach, INTERMAG 2018, CD-11, (2018).
- IM18. “Magneto-optical properties of Pt/TbCo heterostructure films,” S. Iemoto, S. Sumi, H. Awano, M. Hayashi, INTERMAG 2018, GW-16, (2018).
- IM19. “Fast current-induced domain wall motion in symmetric ferrimagnetic Tb-Co alloy wires,” P. V. Thach, B. Do, S. Sumi, H. Awano, 2019 Joint MMM-INTERMAG, GN-10, (2019).
- IM20. “Observation of thermal distribution of magnetic nanowire memory by current injection,” T. Sawa, M. Kawamoto, S. Sumi, P. V. Thach, K. Tanabe, H. Awano, 2019 Joint MMM-INTERMAG, GN-05, (2019).

【界面・電極制御による電力損失の低減 -光電・電光変換素子】

- IP1. “In situ observation of strain relaxation during growth interruption in lattice-mismatched

法人番号	231023
プロジェクト番号	S1411027

III-V heteroepitaxy,” Y. Ohshita, T. Nishi, D. Koder, K. Ikeda, K. Shimomura, H. Suzuki, T. Sasaki, I. Kamiya, M. Takahasi, E-MRS 2014 SPRING MEETING, Congress Center, Lille, France (May 26-30, 2014).

IP2. “Growth of Layered $(\text{In}_x\text{Ga}_{1-x})_2\text{Se}_3$ Buffer Material for GaAs on Si System,” Nobuaki Kojima, Hiroya Nakamura, Yoshio Ohshita, Masafumi Yamaguchi, 40th IEEE Photovoltaic Specialists Conference (PVSC40), Colorado Convention Center, Denver, USA (Jun. 8-13, 2014) (*P2).

IP3. “In situ X-ray diffraction study of strain relaxation process of lattice-mismatched InGaAs/GaAs,” Daisuke Koder, Toshiaki Nishi, Kazuma Ikeda, Takuo Sasaki, Masamitsu Takahasi, Hidetoshi Suzuki, Hiroya Nakamura, Yoshio Ohshita, Nobuaki Kojima, Itaru Kamiya, Masafumi Yamaguchi, The 15th International Union of Materials Research Societies (IUMRS)-International Conference in Asia (IUMRS-ICA 2014), Fukuoka University, Japan, Aug. 27, 2015 (Aug. 24-30)

IP4. “Structural and Optical Characterization of MBE Grown $(\text{In}_x\text{Ga}_{1-x})_2\text{Se}_3$ on GaAs(111),” Hiroya Nakamura, Nobuaki Kojima, Yoshio Ohshita, Masafumi Yamaguchi, The 6th World Conference on Photovoltaic Energy Conversion (WCPEC-6), Kyoto International Conference Center, Kyoto, Japan (Nov. 23-27, 2014) (*P2).

IP5. “In Situ X-Ray Diffraction Study of Strain Relaxation Process of Lattice-Mismatched InGaAs/GaAs,” D. Koder, T. Nishi, K. Ikeda, T. Sasaki, M. Takahasi, H. Suzuki, H. Nakamura, Y. Ohshita, N. Kojima, I. Kamiya, M. Yamaguchi, The 6th World Conference on Photovoltaic Energy Conversion (WCPEC-6), Kyoto International Conference Center, Kyoto, Japan, Nov. 25, 2014 (Nov. 23-27, 2014).

IP6. “Lattice Relaxation Mechanism of InGaAs on Vicinal GaAs Substrate,” Kazuma Ikeda, Hidetoshi Suzuki, Daisuke Koder, Hiroya Nakamura, Nobuaki Kojima, Yoshio Ohshita, Masafumi Yamaguchi, 7th International Symposium on Innovative Solar Cells, ENEOS Hall, RCAST, Komaba II Research Campus, The University of Tokyo, Japan (Jan. 19-20, 2015).

IP7. [Invited] “Layered $(\text{In}_x\text{Ga}_{1-x})_2\text{Se}_3$ (III₂-VI₃) Compounds as Novel Buffer Layers for GaAs on Si System,” Nobuaki Kojima, Yoshio Ohshita, Masafumi Yamaguchi, The Energy, Materials, and Nanotechnology (EMN) Meeting, The Westin Resort & Spa, Cancun, Mexico (Jun. 8-11, 2015) (*P2).

IP8. “Suppression of Twin Formation in Layered In_2Se_3 Grown on GaAs(111),” Nobuaki Kojima, Hiroya Nakamura, Yoshio Ohshita, Masafumi Yamaguchi, 42th IEEE Photovoltaic Specialists Conference (PVSC42), Hyatt Regency-New Orleans, LA, USA (Jun. 14-19, 2015) (*P2).

法人番号	231023
プロジェクト番号	S1411027

- IP9. “Optical properties of layered $(\text{In}_x\text{Ga}_{1-x})_2\text{Se}_3$ buffer material deposited on GaAs(111) substrate for III-V/Silicon solar cell,” Li Wang, Hiroya Nakamura, Nobuaki Kojima, Yoshio Ohshita, Masafumi Yamaguchi, 25th International Photovoltaic Science & Engineering Conference (PVSEC-25), BEXCO, Busan, Korea (Nov. 15-20, 2015) (*P2).
- IP10. [Invited] “Real time study of strain relaxation in lattice mismatched InGaAs/GaAs for future tandem III-V solar cells,” Yoshio Ohshita, Hidetoshi Suzuki, Itaru Kamiya, Kazuma Ikeda, Takuo Sasaki, Masamitsu Takahashi, EMN Meeting on Photovoltaics 2016, Eaton Hotel, Hong Kong, China (Jan. 18-21, 2016).
- IP11. “Light-Induced Degradation and Thermal-Induced Recovery of PECVD- SiN_x :H Passivation: Reaction Kinetics and Interfacial Properties,” Yoshio Ohshita, Takefumi Kamioka, Taisei Iwahashi, Lee Hyunju, Yuri Sato, 6th International Conference on Crystalline Silicon Photovoltaics 2016 (Silicon PV 2016), Centre de congrès le Manège, Chambéry, France (Mar. 7-10, 2016).
- IP12. “Effects of light soaking and thermal treatment on PECVD- SiN_x passivation on n-type Si,” Takefumi Kamioka, Taisei Iwahashi, Lee Hyunju, Yuri Sato, Kyotaro Nakamura, Yoshio Ohshita, 8th International Symposium on Advanced Plasma Science and its Applications for Nitrides and Nanomaterials / 9th International Conference on Plasma-Nano Technology & Science (ISPlasma 2016 / IC-PLANTS 2016), Nagoya University, Japan (Mar. 10, 2016).
- IP13. “Ge thin film growth on Si and SiO_2 using $t\text{-C}_4\text{H}_9\text{GeH}_3$,” R. Katayama, N. Kojima, K. Suda, H. Machida, M. Ishikawa, H. Sudo, A. Ogura, Y. Ohshita, The 18th International Conference on Crystal Growth and Epitaxy (ICCGE-18), Nagoya Congress Center, Japan (Aug. 7-12, 2016).
- IP14. “N incorporation at the surface step in CBE grown GaAsN film on GaAs(111) vicinal substrate,” Ryota Katayama, Nobuaki Kojima, Yoshio Ohshita, Masafumi Yamaguchi, The 26th Photovoltaic Science and Engineering Conference (PVSEC-26), Marina Bay Sands, Sands Expo and Convention Centre, Singapore (Oct. 24-28, 2016).
- IP15. “Interfacial workfunctions of transition metal oxides in carrier-selective contact stacks,” Takefumi Kamioka, Yutaka Hayashi, Fumihiko Yamada, Yuki Isogai, Kyotaro Nakamura, Yoshio Ohshita, The 26th Photovoltaic Science and Engineering Conference (PVSEC-26), Marina Bay Sands, Sands Expo and Convention Centre, Singapore (Oct. 24-28, 2016) (*P1).
- IP16. “Realization of Conductive AlN Epitaxial Layer on Si Substrate using Spontaneously Formed Nano-Size Via-Holes for Vertical AlGaIn High Power FET,” Noriko Kurose, Kota Ozeki, Tsutomu Araki, Naotaka Iwata, Itaru Kamiya, and Yoshinobu Aoyagi, The 43rd International Symposium on Compound Semiconductors (ISCS), Toyama Japan, ThD2-4 (Jun. 30, 2016).

法人番号	231023
プロジェクト番号	S1411027

- IP17. "SiN_x Passivated GaN HEMT by Plasma Enhanced Atomic Layer Deposition," Takayuki Suzuki, Tomiaki Yamada, Ryosuke Kawai, Shohei Kawaguchi, Dongyan Zhang, and Naotaka Iwata, The 43rd International Symposium on Compound Semiconductors (ISCS), Toyama Japan, MoP-ISCS-086 (Jun. 27, 2016). (*P4)
- IP18. "AlGaAs/InGaAs HEMTs Passivated with Atomic Layer Deposited SiO₂ using Aminosilane Precursors," Takayuki Suzuki, Yousuke Takigawa, Naotaka Iwata, Zhang Dongyan, and Yoshio Ohshita, The 2015 International Meeting for Future of Electron Devices, Kansai (IMFEDK2015), 10.1109/IMFEDK.2015.715, 8492, IEEE, Kyoto, Japan, (Jun. 4, 2015).
- IP19. "A new laser induced local material engineering to convert from n-type to p-type nitride semiconductor to fabricate high power vertical AlGa_N/Ga_N devices on Si substrate," Yoshinobu Aoyagi, Noriko Kurose, Kota Matsumoto, Naotaka Iwata, and Itaru Kamiya, 22nd Advanced Materials 2018, Tokyo (September 19, 2018). (*P5)
- IP20. "Effect of inductively coupled plasma reactive ion etching on performances of p-GaN gate AlGa_N/Ga_N HEMTs," Yoshihiko Akazawa, Takaaki Kondo, and Naotaka Iwata, International Workshop on Nitride Semiconductors 2018, Kanazawa, Japan (Nov. 12, 2018). (*P4)
- IP21. [Invited] "Laser-induced local activation of Mg-doped GaN and AlGa_N for high power vertical devices," Noriko Kurose, Yoshinobu Aoyagi, Kota Matsumoto, Naotaka Iwata, and Itaru Kamiya, Photonics West 2019, Feb. 2, 2019, Moscone Center, San Francisco, CA, USA (Feb. 2-7, 2019). (*P5)
- IP22. "Effects of p-GaN gate structures and their fabrication process on performances of normally-off AlGa_N/Ga_N HEMTs," Takaaki Kondou, Yoshihiko Akazawa, and Naotaka Iwata, 11th International Symposium on Advanced Plasma Science and its Applications for Nitrides and Nanomaterials (ISPlasma2019), Nagoya, Japan (March 19, 2019). (*P4)
- IP23. "*In situ* XRD observation during various capping of InAs quantum dots by MBE," K. Shimomura, H. Suzuki, T. Sasaki, M. Takahashi, Y. Ohshita, and I. Kamiya, 8th International Conference on Quantum Dots, May 14, 2014, Palazzo dei Congressi, Pisa, Italy, W122 (May 11-15, 2014). (*P7)
- IP24. "nm-scaled workfunction mapping of the interfaces of silicon heterojunction (SHJ) solar cell using Kelvin probe force microscopy," Fumihiko Yamada, Takefumi Kamioka, Tomihisa Tachibana, Kyotaro Nakamura, Yoshio Ohshita and Itaru Kamiya, 40th IEEE Photovoltaics Specialists Conference, June 13, 2014, Colorado Convention Center, Denver, CO, U.S.A. P.860 I26 (June 8-13, 2014). (*P1)
- IP25. "Identification of trap states for two-step two-photon-absorption processes in InAs

法人番号	231023
プロジェクト番号	S1411027

quantum structures for intermediate-band solar cells,” David M. Tex, Itaru Kamiya, and Yoshihiko Kanemitsu, 40th IEEE Photovoltaics Specialists Conference, June 13, 2014, Colorado Convention Center, Denver, CO, U.S.A., O.1028 (June 8-13, 2014). (*P6)

IP26. “Fabrication of New Vertical AlGa_N Deep Ultra Violet Photo-detector on n⁺Si Substrate using Spontaneous Via Holes Growth Technique,” Kota Ozeki, Noriko Kurose, Naotaka Iwata, Kentaro Shibano, Tsutomu Araki, Itaru Kamiya, and Yoshinobu Aoyagi, 46th International Conference on Solid State Devices and Materials (SSDM 2014), September 11, 2014, Tsukuba International Congress Center, Japan, C-7-4 (September 8-11, 2014).

IP27. “Influence of trapping processes on photocurrent generation efficiencies in quantum-dot intermediate-band solar cells,” D. M. Tex, T. Ihara, I. Kamiya, and Y. Kanemitsu, The 6th World Conference on Photovoltaic Energy Conversion (WCPEC-6), November 26, 2014, Kyoto International Conference Center, Japan, 1WePo. 1.13 (November 23-27, 2014).

IP28. “Local workfunction mapping of interface on heterojunction Si solar cell using KFM,” Fumihiko Yamada, Takefumi Kamioka, Tomihisa Tachibana, Kyotaro Nakamura, Yoshio Ohshita and Itaru Kamiya, The 6th World Conference on Photovoltaic Energy Conversion (WCPEC-6), November 26, 2014, 2014, Kyoto International Conference Center, Japan, 4WePo. 7.55 (November 23-27, 2014).

IP29. “Local workfunction measurement of the interfaces of silicon heterojunction (SHJ) solar cell using Kelvin probe force microscopy,” Fumihiko Yamada, Takefumi Kamioka, Fukuhisa Tachibana, Kyotaro Nakamura, Yoshio Ohshita and Itaru Kamiya, Korea-Japan Top University League Workshop on Photovoltaics 2014 (Top-PV 2014), November 28, 2014, Hotel Marix, Miyazaki, Japan, A-1 (November 28-29, 2014). (*P1)

IP30. “Strain relaxation process of lattice mismatched InGaAs on miscut GaAs,” Daisuke Kodera, Toshiaki Nishi, Kazuma Ikeda Takuo Sasaki, Masamitsu Takahashi, Hidetoshi Suzuki, Hiroya Nakamura, Yoshio Ohshita, Nobuaki Kojima, Itaru Kamiya, Masafumi Yamaguchi, Korea-Japan Top University League Workshop on Photovoltaics 2014 (Top-PV 2014), November 28, 2014, Hotel Marix, Miyazaki, Japan, D-9 (November 28-29, 2014).

IP31. “Local workfunction mapping of the interface between surface layers on the Si heterojunction (SHJ) solar cell on nm scale using Kelvin probe force microscopy,” Fumihiko Yamada, Takefumi Kamioka, Tomihisa Tachibana, Kyotaro Nakamura, Yoshio Ohshita and Itaru Kamiya, 2014 Fall Mat. Res. Soc. Symposium, December 1, 2014, Hynes Convention Center, Boston, MA, U.S.A., PP 1.04 (Nov. 30 – Dec. 5, 2014). (*P1)

IP32. “*In situ* XRD observation during modulated InGaAs capping of InAs quantum dots on GaAs(001) by MBE,” K. Shimomura, H. Suzuki, T. Sasaki, M. Takahashi, Y. Ohshita, and I. Kamiya, 2014 Fall Mat. Res. Soc. Symposium, December 4, 2014, Hynes Convention Center, Boston, MA, U.S.A., OO 9.09 (Nov. 30 – Dec. 5, 2014), 2014). (*P7)

法人番号	231023
プロジェクト番号	S1411027

- IP33. “XRD transients during capping of different sized InAs quantum dots on GaAs(001),” K. Shimomura, H. Suzuki, T. Sasaki, M. Takahasi, Y. Ohshita, and I. Kamiya, 42nd Conference on Physics and Chemistry of Surfaces and Interfaces, January 20, 2015, Snowbird Ski & Resort, Snowbird, UT, U.S.A., Tu0930 (Jan. 18-22, 2015). (*P7)
- IP34. “Tuning the emission wavelength from self-assembled InAs quantum dots on GaAs(001) to over 1.55 μm by controlling the cap and barrier layers,” K. Shimomura and I. Kamiya, 42nd Conference on Physics and Chemistry of Surfaces and Interfaces, January 21, 2015, Snowbird Ski & Resort, Snowbird, UT, U.S.A., We1150 (Jan. 18-22, 2015). (*P7)
- IP35. “The reduction of Cu^{2+} and crystal growth processes during colloidal synthesis of $\text{Cu}_2\text{ZnSnS}_4$ nanoparticles,” Kazuki Morishita, Hiroyuki Suto, and Itaru Kamiya, 42nd IEEE Photovoltaics Specialists Conference, June 16, 2015, Hyatt Regency Hotel, New Orleans, LA, U.S.A., P.102.E21 (June 14-19, 2015).
- IP36. “Carrier dynamics of $\lambda > 1.55 \mu\text{m}$ PL from InAs quantum dots on GaAs(001),” K. Shimomura and I. Kamiya, Compound Semiconductor Week (CSW 2015), July 1, 2015, UCSB, Santa Barbara, CA, U.S.A., We GN7.5 (June 28 – July 2, 2015). (*P7)
- IP37. “Strain Control of InAs Quantum Dots on GaAs(001) by Molecular Beam Epitaxy,” K. Shimomura and I. Kamiya, 31st North American Molecular Beam Epitaxy Conference (NAMBE 2015), October 5, 2015, Iberostar Paraíso Beach Hotel, Riviera Maya, Mexico. Mo-08 (October 4-7, 2015). (*P7)
- IP38. “In situ XRD observation of strain in InAs quantum dots and InGaAs capping layers during MBE growth on GaAs(001),” Kenichi Shimomura, Hidetoshi Suzuki, Takuo Sasaki, Masamitu Takahasi, Yoshio Ohshita, and Itaru Kamiya, The 9th International Conference on Quantum Dots (QD2016), May 23, 2016, Ramada Plaza Jeju Hotel, Jeju, Korea, PM-058 (May 22-27, 2016). (*P7)
- IP39. “Achieving long wavelength emission from self-assembled InAs quantum dots by MBE through strain control,” Kenichi Shimomura, Hidetoshi Suzuki, Takuo Sasaki, Masamitu Takahasi, Yoshio Ohshita, and Itaru Kamiya, 33rd International Conference on the Physics of Semiconductors (ICPS2016), Aug. 1, 2016, Beijing International Convention Center, Beijing, China, Mo-P.028 (Jul. 31-Aug. 5, 2016). (*P7)
- IP40. “Upconverted photoluminescence in InAs/GaAs heterostructures,” Y. Zhang and I. Kamiya, 19th International Conference on Molecular Beam Epitaxy (MBE2016), September 6, 2016, Le Corum, Montpellier, France, Tu-P-9 (Sep. 4 – 9, 2016). (*P6)
- IP41. “Ring-like workfunction dip around In(Ga)As quantum dots,” T. Kobayashi, K. Takabayashi, K. Shimomura, Y. Zhang, F. Yamada, and I. Kamiya, 32nd North American

法人番号	231023
プロジェクト番号	S1411027

Molecular Beam Epitaxy Conference (NAMBE 2016), September 19, 2016, Gideon Putnam Hotel, Saratoga Springs, NY, U.S.A., MoP12 (September 18-21, 2016). (*P8)

IP42. “Simulation of RHEED Intensity Transients during MBE Growth of InAs Quantum Dots on GaAs(001),” Kenichi Shimomura and Itaru Kamiya, 32nd North American Molecular Beam Epitaxy Conference (NAMBE 2016), September 19, 2016, Gideon Putnam Hotel, Saratoga Springs, NY, U.S.A., MoP14 (September 18-21, 2016). (*P7)

IP43. “The influence of substrate orientation on strain relaxation mechanisms of InGaAs layer grown on vicinal GaAs substrates measured by *in situ* X-ray diffraction,” Hidetoshi Suzuki, Takuo Sasaki, Masamitsu Takahashi, Yoshio Ohshita, Nobuaki Kojima, Itaru Kamiya, A. Fukuyama, T. Ikari, and Masafumi Yamaguchi, 26th International Photovoltaic Science and Engineering Conference and Exhibition (PVSEC-26), October 26, 2016, Marina Bay Sands Expo and Convention Centre (MBS), 1.1.2f (October 24-28, 2016).

IP44. “Development of an AFM/KFM System Capable of Local Workfunction Mapping of Solar Cells under Light Illumination,” Fumihiko Yamada, Takefumi Kamioka, Kyotaro Nakamura, Yoshio Ohshita and Itaru Kamiya, 26th International Photovoltaic Science and Engineering Conference and Exhibition (PVSEC-26), October 27, 2016, Marina Bay Sands Expo and Convention Centre (MBS), 2_4-0057 (October 24-28, 2016). (*P1)

IP45. “Nanoscope Analysis of Semiconductor Heterointerfaces by Kelvin Probe Force Microscopy (KFM),” Fumihiko Yamada, Tomohiro Kobayashi, Ko Takabayashi, Kenichi Shimomura, Yuwei Zhang and Itaru Kamiya, Pacific Rim Symposium on Surfaces, Coatings & Interfaces (PACSURF 2016), December 14, 2016, Hapuna Beach Prince Hotel, Kohala Coast, HI, U.S.A., TF-WeM1 (Dec. 11-15, 2016). (*P8)

IP46. [Invited] “Understanding and Controlling Epitaxial Growth of Lattice Mismatched Materials Using InGaAs on GaAs,” Itaru Kamiya, Collaborative Conference on Crystal Growth (3CG 2014), Holiday Inn Resort, Phuket, Thailand, November 5, 2014, C11 (Nov. 4-7, 2014). (*P6,P7,P8)

IP47. [Invited] “Growth of InAs-based Quantum Structures and their Electronic Properties Controlled by Strain,” Itaru Kamiya, SemiconNano 2015, Lakeshore Hotel, Hsinchu, Taiwan, September 10, 2015, I-39 (Sep. 6 – 10, 2015). (*P6,P7,P8)

IP48. [Invited] “nm-scale Workfunction Measurements on the Interface between Si and Surface Layers on the Crystalline Si Solar Cell using Kelvin Probe Force Microscopy,” Fumihiko Yamada, Takefumi Kamioka, Kyotaro Nakamura, Yoshio Ohshita, and Itaru Kamiya, Energy Materials Nanotechnology (EMN) Meeting on Vacuum Electronics, New York Hotel & Casino, Las Vegas, NV, U.S.A., November 21, 2015, S05 (Nov. 21 – 24, 2015). (*P1)

IP49. [Invited] “Epitaxial Growth of InAs-based Quantum Structures on GaAs,” Itaru Kamiya,

法人番号	231023
プロジェクト番号	S1411027

Collaborative Conference on Crystal Growth (3CG 2015), Eaton Hotel Kowloong, Hong Kong, China, December 16, 2015, D29 (Dec. 13 – 17, 2015). (*P6,P7,P8)

IP50. [Invited] “Photon upconversion using InAs-based quantum structures and the control of intermediate states,” Itaru Kamiya, David M. Tex, Yuwei Zhang, Toshiyuki Ihara, Yasuhiro Yamada, and Yoshihiko Kanemitsu, SPIE Photonic West, San Francisco, U.S.A. (Jan. 31, 2017), 10099-15 (Jan. 28 – Feb. 2, 2017). (*P6)

IP51. [Invited] “Surfaces and Interfaces of Quantum Structures Prepared by Colloidal Synthesis and Epitaxial Growth,” Itaru Kamiya, Changchun Institute of Technology 長春工科大学 (July 29, 2017).

IP52. [Invited] “Epitaxial Growth and Characterization of InAs-based Structures on GaAs,” Itaru Kamiya, Waterloo Institute of Nanotechnology Seminar, University of Waterloo, Canada (September 7, 2017). (*P6,P7,P8)

IP53. [Invited] “Near-surface band structures of semiconductor nanostructures investigated by Kelvin probe force microscopy (KFM),” Itaru Kamiya, 6th International Workshop on Epitaxial Growth and Fundamental Properties of Semiconductor Nanostructures (SemiconNano 2017), Teatro di Como, Como, Italy, September 26, 2017 (Sep. 25–28, 2017). (*P8)

IP54. “Development of an AFM/KFM system capable of cross-sectional workfunction measurement of solar cell structures under light illumination,” Fumihiko Yamada, Takefumi Kamioka, Yoshio Ohshita and Itaru Kamiya, 33rd European PV Solar Energy Conference and Exhibition (EU PVSEC 2017), RAI Convention & Exhibition Centre, Amsterdam, The Netherlands, 2CV.2.52, September 27, 2017 (Sep. 25-29, 2017). (*P1)

IP55. “Band profiling of p-Si/ITO interface by Kelvin probe force microscopy under light controlled conditions,” Fumihiko Yamada, Takefumi Kamioka, Yoshio Ohshita and Itaru Kamiya, 7th World Conference on Photovoltaic Energy Conversion (WCPEC-7), June 14, 2018, Hilton Waikoloa Village, HI, USA (Jun. 10-15, 2018). (*P1)

IP56. [Invited] “Near-surface InAs/GaAs interfaces studied by KFM/AFM, XRD, and PL,” Itaru Kamiya, 14th International Conference on Beam Injection Assessment of Microstructures (BIAMS 2018), June 20, 2018, Koreana Hotel, Seoul, Korea (Jun. 18–21, 2018). (*P6,P7,P8)

IP57. “Cross-sectional workfunction measurements on solar cell structures under light-controlled conditions,” Fumihiko Yamada, Takefumi Kamioka, Yoshio Ohshita and Itaru Kamiya, 35th European PV Solar Energy Conference and Exhibition (EU PVSEC 2018), September 27, 2018, SQUARE – Brussels Meeting Centre, Brussels, Belgium, 2DV.3.15. (Sep. 24-28, 2018). (*P1)

法人番号	231023
プロジェクト番号	S1411027

【界面・電極制御による電力損失の低減 -有機電子素子】

- IO1. “Kelvin probe force microscopy study of the graphene oxide and reduced graphene oxide sheets,” Hsin-Hui Huang, T. Ikeda, M. Yoshimura, 24th International Colloquium on Scanning Probe Microscopy (ICSPM24), Honolulu, Hawaii (Dec. 14, 2016).
- IO2. “Controlled growth of carbon nanotube forest and graphene by chemical vapor deposition,” M. Yoshimura, 6th Global Experts Meeting on Nanomaterials and Nanotechnology, Dubai, UAE (Apr. 21-23, 2016). (*O1)
- IO3. “Effect of atomistic defects introduced in HOPG on oxygen reduction reaction,” M. Yoshimura, PGIS Research Congress 2016, Peradeniya, Sri Lanka, (Oct. 7-8, 2016).
- IO4. “Alcohol-Assisted Thermal Reduction of Graphene Oxide,” K. De Silva, H.H. Huang, S. Suzuki, M. Yoshimura, 25th International Colloquium on Scanning Probe Microscopy (ICSPM25), Atagawa, Japan (Dec. 7-9, 2017).
- IO5. “Two-dimensional mapping of graphene oxides by using tip-enhanced Raman scattering spectroscopy,” T. Inaba, K. De Silva, T. Kawabata, M. Yoshimura, 25th International Colloquium on Scanning Probe Microscopy (ICSPM25), Atagawa, Japan (Dec. 7-9, 2017). (*O2)
- IO6. “Formation Mechanism of Reduced Graphene Oxide Membrane,” H.H. Huang, R. Joshi, K. De Silva, M. Yoshimura, 25th International Colloquium on Scanning Probe Microscopy (ICSPM25), Atagawa, Japan (Dec. 7-9, 2017).

<研究成果の公開状況>(上記以外)

シンポジウム・学会等の実施状況、インターネットでの公開状況等

<既に実施しているもの>

シンポジウム

第1回 2015.8.3 開催, 第2回 2016.11.18 開催、

第3回 2017.10.13 開催、最終回 2018.11.2 開催

Website : <http://www.toyota-ti.ac.jp/kenkyu/greenelement.html>

<これから実施する予定のもの>

法人番号	231023
プロジェクト番号	S1411027

企業との共同研究

1. トヨタ自動車 2014/4/1-2017/3/31

熱制御技術の研究

2. 株式会社安永 2016/1/1-2018/3/31

高マンガンシリサイド(Higher Manganese Silicide、HMS)熱電変換材料・発電素子の高耐久化に関する研究

3. 住友電気工業株式会社 2016/10/1-

Si-Ge 系熱電変換材料・発電素子に関する研究

4. 三菱マテリアル株式会社 2019/1/1-

熱流制御素子に関する研究

法人番号	231023
プロジェクト番号	S1411027

15 「選定時」及び「中間評価時」に付された留意事項及び対応

<「選定時」に付された留意事項>

「開発すべき物を明確にして、目的をもって研究開発するよう努めて頂きたい。」

<「選定時」に付された留意事項への対応>

素子としては、1)熱電材料、2)光電・電光変換素子、3)低エネルギー消費メモリー、に注力している。界面・電極技術の確立は、こうした素子開発・性能向上に寄与する基盤と位置づけている。更に、これらの二本柱を支えるのが、マイクロ・メソ、という大きさの異なるレベルでの構造制御という基礎技術である。素子、界面共に、この異なるスケールでの構造制御が実現して始めて成り立つ。

本研究センターには基礎研究から開発に近いところまで幅広いスタンスの人材・研究が取り込まれており、これらを有機的機能させるため、グループミーティングで、特に若手研究者による最新の研究成果の紹介等を行なう事で、アイデアの交流を図る様に工夫をしてきている。従って、目的物としては上述の3種の素子開発・改良を実現しつつ、これを支える基盤技術についても劣らず成果を挙げている。

そして、熱電・GaN系・磁性メモリなどで、基礎的な研究成果に基き、デバイスのプロトタイプングを行い、実証をした。

<「中間評価時」に付された留意事項>

特になし。

<「中間評価時」に付された留意事項への対応>

N/A。

法人番号	231023
プロジェクト番号	S1411027

16 施設・装置・設備・研究費の支出状況(実績概要)

(千円)

年度・区分	支出額	内 訳						備考
		法人負担	私学助成	共同研究機関負担	受託研究等	寄付金	その他()	
平成26年度	施設	0						
	装置	0						
	設備	137,401	52,847	84,554				
	研究費	48,127	24,815	23,312				
平成27年度	施設	0						
	装置	0						
	設備	37,908	12,636	25,272				
	研究費	54,506	28,919	25,587				
平成28年度	施設	0						
	装置	0						
	設備	0	0	0				
	研究費	52,554	29,741	22,813				
平成29年度	施設	0						
	装置	0						
	設備	0	0	0				
	研究費	66,919	38,896	28,023				
平成30年度	施設	0						
	装置	0						
	設備	0	0	0				
	研究費	62,190	35,253	26,937				
総額	施設	0	0	0	0	0	0	0
	装置	0	0	0	0	0	0	0
	設備	175,309	65,483	109,826	0	0	0	0
	研究費	284,296	157,624	126,672	0	0	0	0
総計	459,605	223,107	236,498	0	0	0	0	

法人番号

231023

17 施設・装置・設備の整備状況（私学助成を受けたものはすべて記載してください。）

《施設》（私学助成を受けていないものも含め、使用している施設をすべて記載してください。）（千円）

施設の名 称	整備年度	研究施設面積	研究室等数	使用者数	事業経費	補助金額	補助主体
量子界面物性研究室・実験室	平成7年度	250m ²	1	12	不明	0	—
エネルギー材料研究室・実験室	平成7年度	250m ²	1	35	不明	0	—
情報記録材料研究室・実験室	平成7年度	250m ²	1	15	不明	0	—

※ 私学助成による補助事業として行った新增築により、整備前と比較して増加した面積

0 m²

《装置・設備》（私学助成を受けていないものは、主なもののみを記載してください。）

（千円）

装置・設備の名 称	整備年度	型 番	台 数	稼働時間数	事業経費	補助金額	補助主体
(研究装置) なし				h			
(研究設備) X線光電子分光装置	26	アルバックファイ社 PHI5000VersaProbeTI	1	2,500 h	38,000	23,415	私学助成
全自動多目的X線回折装置	26	Bruker D8 ADVANCE TKT	1	3,900 h	12,960	7,959	私学助成
熱拡散率測定装置	26	NETZSC LFA457	1	1,600 h	18,468	11,383	私学助成
超電圧計測装置用 ヘリウム再凝縮デ ュー	26	Quantum Design P935(A)SR	1	32,000 h	27,999	17,214	私学助成
磁化率測定装置	26	Quantum Design P525SR	1	800 h	10,999	6,756	私学助成
フローティング型アルゴンイオン銃	26	04-370Z	1	1,700 h	14,000	8,607	私学助成
小型・高性能エキシマーレーザ	26	ExciStar XS-500-ArF	1	1,480 h	8,495	5,241	私学助成
フォトルミネッセンス(PL)マッピング装置	26	PL-SMAP-RT100	1	2,000 h	6,480	3,979	私学助成
半導体エッチング装置	27	RIE-101iPH	1	2,524 h	37,908	25,272	私学助成
(情報処理関係設備) なし				h h			

18 研究費の支出状況

（千円）

年 度	平成 26 年度		
小 科 目	支 出 額	積 算 内 訳	
		主 な 使 途	金 額
教 育 研 究 経 費 支 出			
消 耗 品 費	12,904	研究用消耗品	12,904
光 熱 水 費	5,298	電気代	5,298
通 信 運 搬 費	2	書類郵送	2
印 刷 製 本 費	0		0
旅 費 交 通 費	1,574	国内外出張旅費	1,574
賃 借 料	10		10
報 酬 ・ 委 託 料	804	分析、ソフト保守	804
修 繕 費	6,769	装置設備修理	6,769
諸 会 費	281	学会参加費	281
(出版物費)	31	雑誌・資料	31
計	27,673		27,673
ア ル バ イ ト 関 係 支 出			
人 件 費 支 出 (兼務職員)	0		0
教 育 研 究 経 費 支 出	0		0
計	0		0
設 備 関 係 支 出 (1個又は1組の価格が500万円未満のもの)			
教 育 研 究 用 機 器 備 品	20,454		20,454
図 書	0		0
計	20,454		20,454
研 究 ス タ ッ フ 関 係 支 出			
リサーチ・アシスタント	0		0
ポスト・ドクター	0		0
研究支援推進経費	0		0
計	0		0

(千円)

年 度	平成 27 年度		
小 科 目	支 出 額	積 算 内 訳	
		主 な 使 途	金 額
教 育 研 究 経 費 支 出			
消 耗 品 費	9,388	研究用消耗品	9,388
光 熱 水 費	4,874	電気代	4,874
通 信 運 搬 費	11	書類郵送	11
印 刷 製 本 費	90	論文投稿、報告書印刷	90
旅 費 交 通 費	5,399	国内外出張旅費	5,399
賃 借 料	0		0
報 酬 ・ 委 託 料	220	分析、ソフト保守	220
修 繕 費	5,532	装置設備修理	5,532
諸 会 費	1,234	学会参加費	1,234
(出版物費・雑費)	102	雑誌・資料	102
計	26,850		26,850
ア ル バ イ ト 関 係 支 出			
人件費支出 (兼務職員)	0		0
教育研究経費支出	0		0
計	0		0
設 備 関 係 支 出(1個又は1組の価格が500万円未満のもの)			
教育研究用機器備品	20,992		20,992
図 書	0		0
計	20,992		20,992
研 究 ス タ ッ フ 関 係 支 出			
リサーチ・アシスタント			
ポスト・ドクター	6,664		6,664
研究支援推進経費			
計	6,664		6,664

(千円)

年 度	平成 28 年度		
小 科 目	支 出 額	積 算 内 訳	
		主 な 使 途	金 額
教 育 研 究 経 費 支 出			
消 耗 品 費	13,222	研究用消耗品	13,222
光 熱 水 費	3,474	電気代	3,474
通 信 運 搬 費	24	書類郵送	24
印 刷 製 本 費	94	報告書印刷、文献複写	94
旅 費 交 通 費	5,760	国内外出張旅費	5,760
賃 借 料	10		10
報 酬 ・ 委 託 料	784	分析、ソフト保守	784
修 繕 費	7,362	装置設備修理	7,362
諸 会 費	1,217	学会参加費	1,217
(出版物費)	179	雑誌・資料	179
(雑費)	31		31
(損害保険)	12		12
計	32,169		32,169
ア ル バ イ ト 関 係 支 出			
人件費支出 (兼務職員)	0		0
教育研究経費支出	0		0
計	0		0
設 備 関 係 支 出(1個又は1組の価格が500万円未満のもの)			
教育研究用機器備品	15,998		15,998
図 書			
計	15,998		15,998
研 究 ス タ ッ フ 関 係 支 出			
リサーチ・アシスタント			
ポスト・ドクター	4,387		4,387
研究支援推進経費			
計	4,387		4,387

法人番号

231023

年 度	平成 29 年度		
小 科 目	支 出 額	積 算 内 訳	
		主 な 使 途	金 額
教 育 研 究 経 費 支 出			
消 耗 品 費	20,139	研究用消耗品	20,139
光 熱 水 費	5,703	電気代	5,703
通 信 運 搬 費	18	荷物郵送	18
印 刷 製 本 費	71	報告書印刷	71
旅 費 交 通 費	2,708	国内外出張旅費	2,708
賃 借 料	10		10
報 酬 ・ 委 託 料	796	分析、ソフト保守	796
修 繕 費	10,045	装置設備修理	10,045
諸 会 費	457	学会参加費	457
(出版物費・雑費)	356	雑誌・資料	356
(会議費)	15		15
(損害保険)	10		10
計	40,328		40,328
ア ル バ イ ト 関 係 支 出			
人件費支出 (兼務職員)	0		0
教育研究経費支出	0		0
計	0		0
設 備 関 係 支 出 (1個又は1組の価格が500万円未満のもの)			
教育研究用機器備品	17,804		17,804
図 書	87		87
計	17,891		17,891
研 究 ス タ ッ フ 関 係 支 出			
リサーチ・アシスタント			
ポスト・ドクター	8,700		8,700
研究支援推進経費			
計	8,700		8,700

(千円)

年 度	平成 30 年度		
小 科 目	支 出 額	積 算 内 訳	
		主 な 使 途	金 額
教 育 研 究 経 費 支 出			
消 耗 品 費	19,666	研究用消耗品	19,666
通 信 運 搬 費	34	荷物郵送	34
印 刷 製 本 費	118	報告書印刷	118
旅 費 交 通 費	2,144	国内外出張旅費	2,144
賃 借 料	50		50
報 酬 ・ 委 託 料	2,775	分析、ソフト保守	2,775
修 繕 費	16,082	装置設備修理	16,082
諸 会 費	568	学会参加費	568
(出版物費)	997	雑誌・資料	997
(雑費)	176		176
(会議費)	21		21
(福利費)	53		53
(損害保険)	6		6
計	42,690		42,690
ア ル バ イ ト 関 係 支 出			
人件費支出 (兼務職員)	0		0
教育研究経費支出	0		0
計	0		0
設 備 関 係 支 出 (1個又は1組の価格が500万円未満のもの)			
教育研究用機器備品	15,092		15,092
図 書	15		15
計	15,107		15,107
研 究 ス タ ッ フ 関 係 支 出			
リサーチ・アシスタント			
ポスト・ドクター	4,393		4,393
研究支援推進経費			
計	4,393		4,393

Very large thermal rectification in bulk composites consisting partly of icosahedral quasicrystals

This content has been downloaded from IOPscience. Please scroll down to see the full text.

2014 Sci. Technol. Adv. Mater. 15 064801

(<http://iopscience.iop.org/1468-6996/15/6/064801>)

View [the table of contents for this issue](#), or go to the [journal homepage](#) for more

Download details:

This content was downloaded by: tsuneezo

IP Address: 211.9.37.141

This content was downloaded on 20/12/2014 at 00:34

Please note that [terms and conditions apply](#).

Very large thermal rectification in bulk composites consisting partly of icosahedral quasicrystals

Tsunehiro Takeuchi^{1,2,3}

¹Toyota Technological Institute, Nagoya 468-8511, Japan

²EcoTopia Science Institute, Nagoya University, Nagoya 464-8603, Japan

³PRESTO, JST, Tokyo 102-0076, Japan

E-mail: t_takeuchi@toyota-ti.ac.jp

Received 24 February 2014

Accepted for publication 30 October 2014

Published 25 November 2014

Abstract

The bulk thermal rectifiers usable at a high temperature above 300 K were developed by making full use of the unusual electron thermal conductivity of icosahedral quasicrystals. The unusual electron thermal conductivity was caused by a synergy effect of quasiperiodicity and by a narrow pseudogap at the Fermi level. The rectification ratio, defined by $TRR = |J_{\text{large}}|/|J_{\text{small}}|$, reached very large values exceeding 2.0. This significant thermal rectification would lead to new practical applications for the heat management.

Keywords: quasicrystal, thermal diode, electron thermal conductivity

1. Introduction

Thermal rectifiers [1] have attracted considerable interest because of their ability to manage heat, a large fraction of which is typically lost into the environment. After the first report of thermal rectification [2], several different mechanisms leading to the thermal rectification were reported: (a) a metal-insulator junction [2], (b) thermal wrapping [3–7], (c) thermal strain at the interface [8], (d) the thermal potential barrier [9], (e) inhomogeneous mass loading [10] and (f) composite of bulk materials possessing different temperature dependences of thermal conductivity [11–15]. Among these thermal rectifiers, (e) the composite of two bulk materials of different temperature dependences has attracted maximum attention because of its superior characteristics, which make it suitable for practical applications. One of these characteristics is tunable heat flux, controlled by the thickness of the composites. In addition, the geometry of the bulk thermal rectifier is not subject to any significant physical constraints, so it can

be easily incorporated into a wide range of mechanical components.

The principle of the bulk thermal rectifier, which is a composite consisting of two solid materials joined together, each possessing thermal conductivities (κ) with different temperature dependences, was theoretically proposed by two different groups in 2006 [11, 12]. These theoretical predictions were subsequently validated by experiments [13–15]. Despite the experimental confirmation of bulk thermal rectification, several problems prevent their use in practical applications. One of the most serious problems is the very low working temperature. Thermal rectification in a bulk material was first observed at low temperatures below 150 K [13–15] because these composites made use of the significant temperature dependence of lattice thermal conductivity, typically observed in crystalline materials below 100 K. Unfortunately, increasing the temperature range over which this large variation in lattice thermal conductivity occurs is difficult, especially up to room temperature (300 K). Another problem is the small magnitude of the thermal rectification ratio ($TRR = |J_{\text{large}}|/|J_{\text{small}}|$) observed for the bulk thermal rectifiers; the largest value observed is less than 1.45 [13–15], which would not be suitable for applications. To make a practical bulk thermal rectifier, we need to greatly increase both the working temperature and the magnitude of the TRR.



Content from this work may be used under the terms of the Creative Commons Attribution 3.0 licence. Any further distribution of this work must maintain attribution to the author(s) and the title of the work, journal citation and DOI.

We considered that the serious problems could be removed if we could employ an Al-based icosahedral quasicrystal (IQC) as a main component of the bulk thermal rectifier because it is characterized by drastically increasing thermal conductivity with an increasing temperature above 300 K [16, 17]. Indeed, by making composites consisting mainly of IQC, we succeeded in developing new thermal rectifiers that work at high temperatures above 300 K. In this paper, we shall report the performance of our newly developed thermal rectifier, together with the detailed information about the unusual thermal conductivity of Al-based IQC.

2. Unusual electron thermal conductivity of icosahedral quasicrystals

The thermal conductivity of Al-based IQC is characterized by its small magnitude at low temperatures below 300 K and the drastic increase with increasing temperatures (at high temperatures above 300 K). The former is caused by the small magnitude of both the lattice thermal conductivity and electron thermal conductivity. The small lattice thermal conductivity in IQCs is realized due to the quasiperiodicity and its corresponding phonon dispersions in which optical phonon branches exist in the low energy range [18], causing a significant reduction of group velocity and the enhancement of the Umklapp process of phonon scattering. The quasiperiodicity also contributes to the small electron thermal conductivity by enhancing the scattering probability of electrons into the strongest scattering limit known as the Mott–Ioffe–Regel limit [19]. The very small electronic density of states at the Fermi level [20–22] limits the number of conducting electrons and further reduces the magnitude of electron thermal conductivity [23, 24].

Despite that, the lattice thermal conductivity is kept small at high temperatures, and the magnitude of electron thermal conductivity of IQCs drastically increases with the increasing temperature. This unusual electron thermal conductivity is caused by the narrow, deep pseudogap at the Fermi energy.

The electron thermal conductivity is formulated in the context of the linear response theory [25].

$$\kappa_{\text{el}}(T) = \frac{1}{e^2 T} \int_{-\infty}^{\infty} \sigma(\varepsilon, T) (\varepsilon - \mu)^2 \left(-\frac{\partial f_{\text{FD}}(\varepsilon, T)}{\partial \varepsilon} \right) d\varepsilon - \frac{1}{e^2 T} \times \frac{\left\{ \int_{-\infty}^{\infty} \sigma(\varepsilon, T) (\varepsilon - \mu) \left(-\frac{\partial f_{\text{FD}}(\varepsilon, T)}{\partial \varepsilon} \right) d\varepsilon \right\}^2}{\int_{-\infty}^{\infty} \sigma(\varepsilon, T) \left(-\frac{\partial f_{\text{FD}}(\varepsilon, T)}{\partial \varepsilon} \right) d\varepsilon} \quad (1)$$

Here, $f_{\text{FD}}(\varepsilon, T)$, μ and e represent the Fermi–Dirac distribution function, the chemical potential and the unit charge of electron, respectively. The function $\sigma(\varepsilon, T)$ is known as the ‘spectral conductivity’ that represents the contribution of electronic states existing at ε to the electrical conductivity. If we use the relaxation time approximation with the isotropic electronic structure, the spectral conductivity is expressed by

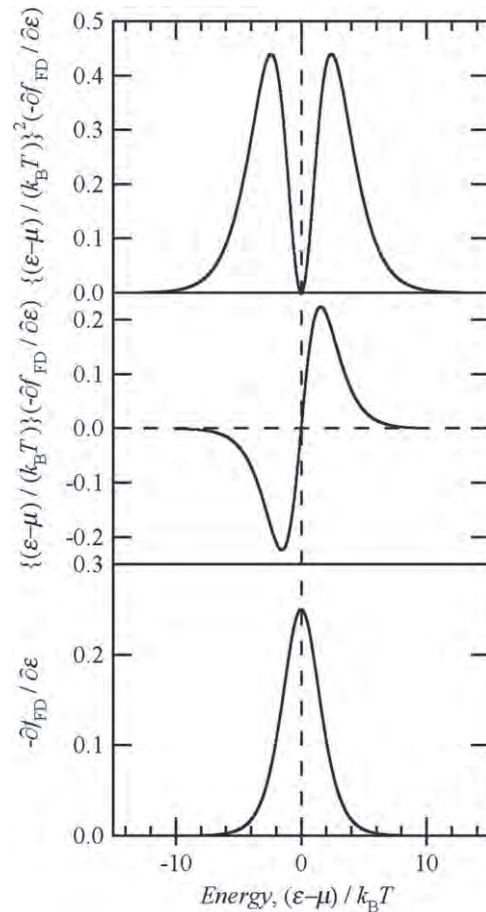


Figure 1. Three-window-functions limiting the energy range of electrons that contribute electron transport properties. The electron thermal conductivity is mainly determined by the function at the top panel.

the following equation

$$\sigma(\varepsilon, T) = \frac{e^2}{3} N(\varepsilon) v_G^2(\varepsilon) \tau(\varepsilon, T). \quad (2)$$

Here, $N(\varepsilon)$, $v_G(\varepsilon)$, and $\tau(\varepsilon)$ are the electronic density of states, the group velocity and the relaxation time, respectively. These three values generally vary with energy and temperature, and the resulting $\sigma(\varepsilon, T)$ also shows significant energy dependence and strong temperature dependence.

When the Seebeck coefficient is smaller than $100 \mu\text{V K}^{-1}$ [23, 24], the second term of equation (1) is small and can be safely ignored. In such a case, the behavior of electron thermal conductivity is accounted for solely with the first term of equation (1). The integrand in the first term of equation (1) contains $W_2(\varepsilon) = (\varepsilon - \mu)^2 (-\partial f_{\text{FD}}(\varepsilon, T) / \partial \varepsilon)$, which behaves as a window function and determines the energy range of electrons that contribute to the thermal conductivity, as shown in figure 1. Obviously, it has two peaks below and above the chemical potential μ at around $\varepsilon \sim \mu \pm 2.4k_B T$.

In the case of IQCs, $\sigma(\varepsilon, T)$ has almost temperature independence and becomes directly proportional to $N(\varepsilon)$ because of the quasiperiodicity and consequently introduces a strong scattering limit. Let us now assume that $N(\varepsilon)$ has a

deep, narrow pseudogap of a few hundred meV in width, and the Fermi energy is located at the energy where $N(\epsilon)$ possesses the smallest magnitude in the pseudogap. At a low temperature, κ_{el} should be kept very small because of the very small magnitude of $N(\epsilon)$ at $\epsilon \sim \mu \pm 2.4k_B T$, while it drastically increases with the increasing temperature because the electronic density of states drastically increases with being apart from the Fermi energy; consequently, $N(\epsilon)$ at $\epsilon \sim \mu \pm 2.4k_B T$ drastically increases with the increasing temperature. This is the reason why we observe a large evolution of electron thermal conductivity, and this mechanism was quantitatively investigated using the Al-Re-Si and Al-Mn-Si 1/1-cubic approximants [23, 24].

Dolinšek *et al* [26] reported that $L(T) = \kappa_{el}/(T\sigma(T))$ of Al-Cu-Fe IQC becomes almost constant above 300 K in their calculation using equation (1). Their result is certainly inconsistent with our interpretation of the unusual evolution of the thermal conductivity of IQCs. We should comment on this inconsistency and mention that the model of spectral conductivity used by Dolinšek *et al* was too simplified for estimating thermal conductivity at high temperatures above 300 K. Their spectral conductivity consisted of two Lorentzian functions in the same manner as that reported by Landauro and Solbrig [27], and the detailed shape was determined so as to reproduce the measured transport properties below 300 K using the equations deduced from the linear response theory. Their spectral conductivity should be highly reliable in the narrow energy range near the Fermi energy because of the function fitting on experimental data. However, it should not be reliable at the energy range apart from the Fermi energy where high temperature properties are determined because the transport properties below 300 K do not contain the information about the spectral conductivity at that energy range. This should be the reason why Dolinšek *et al* [26] reported behavior of electron thermal conductivity that is certainly inconsistent with our interpretation.

The reliability of our argument on the unusual increase of electron thermal conductivity can be confirmed in the experimental facts: (1) the magnitude of the Seebeck coefficient is closely related with the evolution of thermal conductivity at high temperatures [22], (2) the electron thermal conductivity of 1/1-cubic approximants shows almost the same behavior of that calculated from the electronic density of states determined theoretically and experimentally [23, 24] and (3) the behavior of thermal conductivity sensitively varies with carrier concentration [23, 24, 28]. These facts lend great support to our scenario of an unusual increase of electron thermal conductivity at high temperatures.

3. Thermal conductivity of Al-Cu-Fe icosahedral quasicrystals

As a result of the analyses on the electronic structure and its relation to the unusual behavior of electron thermal conductivity [23, 24], we realized that the Al-based IQC and their corresponding approximants show a significant increase of thermal conductivity with the temperature, provided that

those IQCs and their approximants contain 3d transition metal elements as one of the main constituent elements, rather than 4d or 5d transition metal elements. This tendency is caused by the narrower width of the pseudogap in IQC, which contains 3d transition metal elements. The narrower width of the pseudogap for the IQC and their approximants containing 3d transition metal elements is also understood from the behavior of the Seebeck coefficient, which increases with the increasing temperature and starts to decrease after becoming maximal at the T_{peak} . The peak temperature T_{peak} roughly represents the width of the pseudogap, and the IQCs and their approximants containing 3d elements possess lower T_{peak} than that those containing 4d and/or 5d elements [29, 30]. These considerations, together with the very small electronic density of states at the Fermi energy reported for Al-Cu-Fe IQC [20], prompted us to employ the Al-Cu-Fe IQC for the most appropriate material possessing a drastic increase of electron thermal conductivity with increasing temperatures.

Figure 2(a) shows the thermal conductivity of Al-Cu-Fe IQC. The mother ingots of Al-Cu-Fe IQC were prepared by induction melting under a pressurized argon atmosphere. The ingots were crushed into powders and sintered using a pulse-current sintering technique for making dense samples free of voids and cracks [28, 31]. Since electron thermal conductivity of IQC sensitively varies with the carrier concentration, we prepared several different samples possessing different carrier concentrations. We also measured the Seebeck coefficient of the samples (see figure 2(b)) because the magnitude of the Seebeck coefficient is supposed to be small when the electron thermal conductivity shows a drastic increase at high temperatures. The magnitude of the Seebeck coefficient becomes small at $Al_{61.5}Cu_{26.5}Fe_{12}$ where the ratio of thermal conductivity at 1000 K to that at 300 K, $\kappa_{1000K}/\kappa_{300K}$ possesses the largest value of 8.9 [28]. Therefore, we decided to employ this $Al_{61.5}Cu_{26.5}Fe_{12}$ IQC as one of the main components of the thermal rectifier.

4. Materials possessing thermal conductivity that decreases with increasing temperatures

We selected Si, Al_2O_3 , $CuGeTe_2$ and Ag_2Te as the materials possessing thermal conductivity that decrease with increasing temperatures. Figure 3 shows the thermal conductivity of these materials plotted as a function of temperature.

The downward trend in thermal conductivity with increasing temperatures observed for Al_2O_3 and Si is easily understood as a consequence of the lattice thermal conductivity of an insulator possessing a high Debye temperature (Θ_D). These values have been reported as $\Theta_D = 1000\text{--}1100$ K for Al_2O_3 [32] and $\Theta_D = 600\text{--}650$ K for Si [33]. In such materials, lattice thermal conductivity moderately decreases with the temperature as a result of the intensified Umklapp process of phonon-phonon scattering.

The temperature-dependent behavior of κ in $CuGaTe_2$, on the other hand, is difficult to interpret. Its Debye temperature was reported to be very low: $\Theta_D = 226$ K [34], and this low Θ_D indicates that lattice vibrations at high temperatures

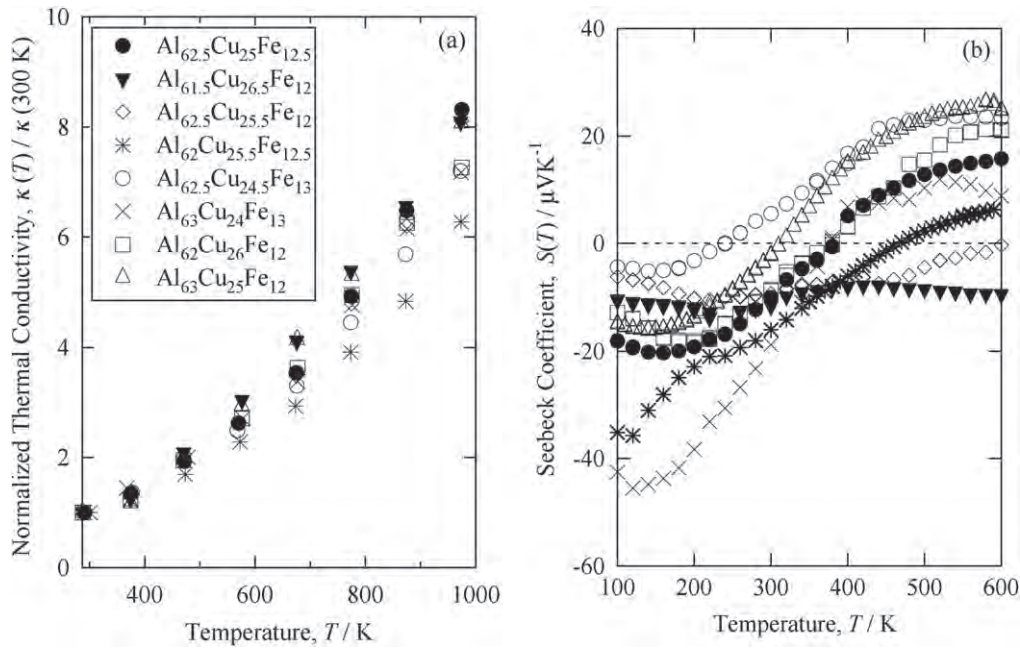


Figure 2. (a) Normalized thermal conductivity and (b) Seebeck coefficient of Al-Cu-Fe icosahedral quasicrystals. At the composition where the temperature dependence of the Seebeck coefficient becomes less significant, the thermal conductivity possesses the most significant increase with the increasing temperature.

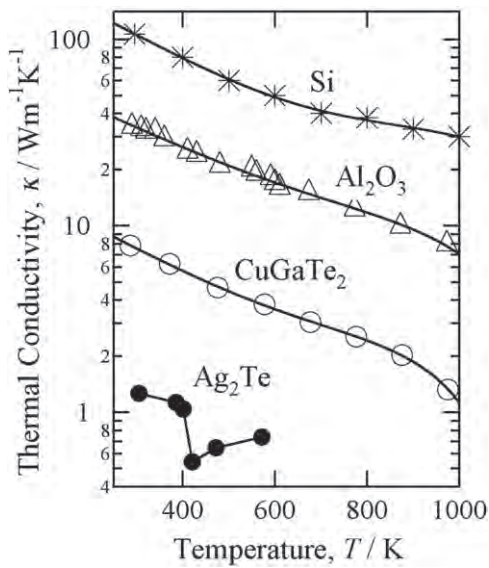


Figure 3. Thermal conductivity of Si, Al₂O₃, CuGeTe₂ and Ag₂Te. All of the samples possess a decreasing thermal conductivity with the increasing temperature.

(above 200 K) should not be considered as ‘conducting wave packets’ but rather as ‘intensely excited, localized oscillators.’ In materials such as these, the lattice thermal conductivity should have no temperature dependence at high temperatures ($T > \theta_D$), but this consideration is not the case with the experimentally observed variation of κ of CuGaTe₂. Although the mechanism that produces large reductions in κ with the increasing temperature is not yet well understood, we are justified in employing CuGaTe₂ as one of the components of our rectifier partly because its thermal conductivity varies with temperature more significantly than that of Al₂O₃ or Si

and partly because its κ is very small to be comparable with that of the IQC.

The thermal conductivity of Ag₂Te shows a big reduction at 420 K with increasing temperatures [35]. At temperatures above 420 K, silver ions start to wander in the samples [36]. The mobile silver ions presumably prevent the propagation of the wave packet or directly prohibit the existence of well-defined wave packets; therefore, the lattice thermal conductivity shows very small values.

5. Calculation of thermal rectification ratio TRR

$TRR = |J_{large}| / |J_{small}|$ is determined not only by the temperature dependence of the thermal conductivity of two constituent materials but also by their length ratio $x = L_{IQC} / (L_{IQC} + L_X)$ ($X = \text{Si, Al}_2\text{O}_3, \text{CuGeTe}_2, \text{or Ag}_2\text{Te}$). Before preparing the composite samples, we estimated the optimal length ratio x_{opt} for the maximum TRR obtainable for the given set of materials. The calculation method was reported previously [31].

The x dependence of TRR was calculated for the composite thermal rectifiers consisting of (a) Al_{61.5}Cu_{26.5}Fe₁₂ IQC/Si, (b) Al_{61.5}Cu_{26.5}Fe₁₂ IQC/Al₂O₃, (c) Al_{61.5}Cu_{26.5}Fe₁₂ IQC/CuGeTe₂ and (d) Al_{61.5}Cu_{26.5}Fe₁₂ IQC/Ag₂Te by assuming that the composites are placed between two heat reservoirs kept at $(T_H, T_L) = (900 \text{ K}, 300 \text{ K})$ for (a)–(c), and $(T_H, T_L) = (543 \text{ K}, 300 \text{ K})$ for (d). The resulting TRR is plotted as a function of x in figures 4(a1)–(a4).

The calculations predict that very large values of TRR exceeding 2.0 can be obtained in three composites: IQC/Si, IQC/Al₂O₃, and IQC/CuGaTe₂, placed between two heat

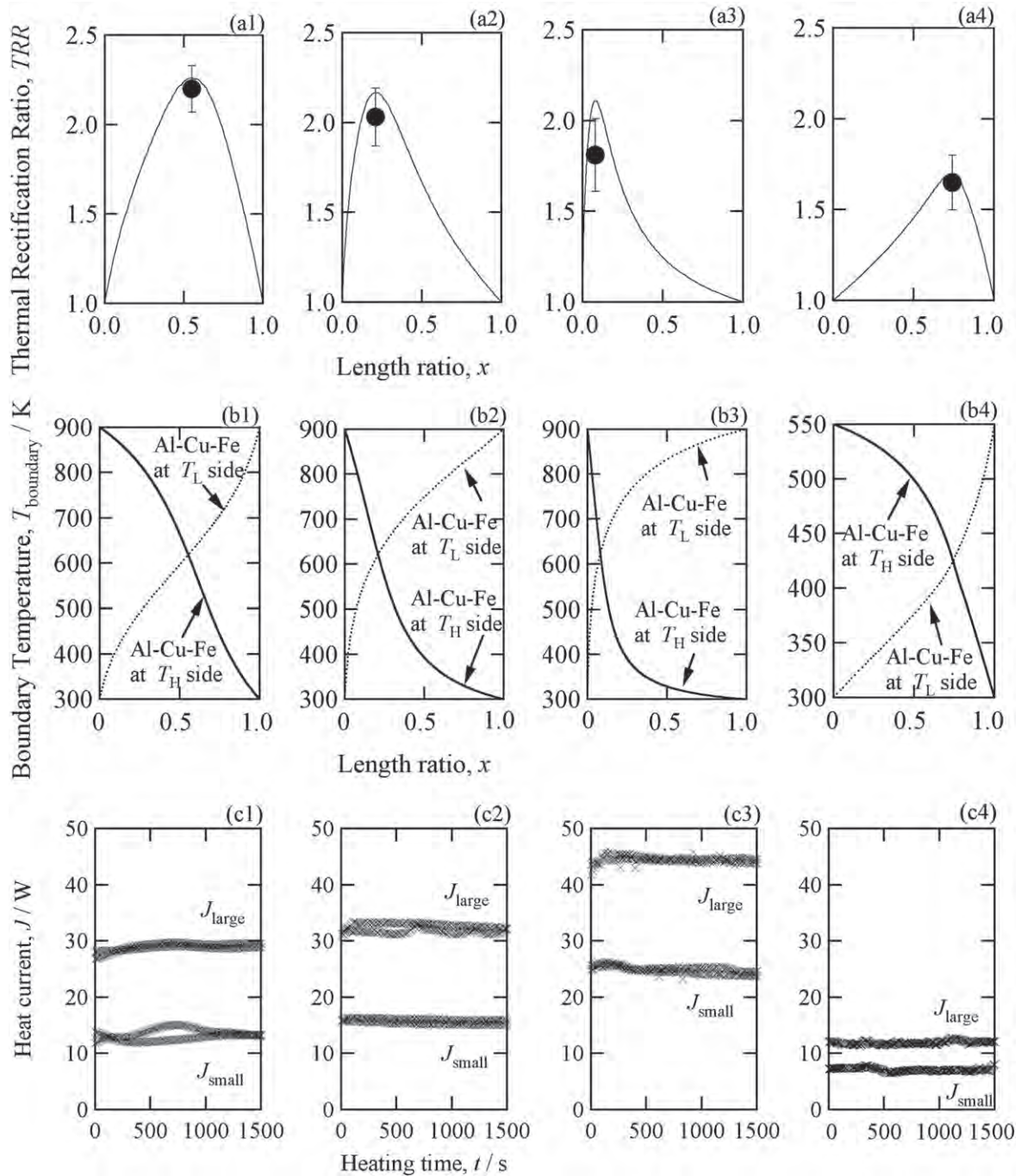


Figure 4. (a) Thermal rectification ratio, (b) boundary temperature and (c) measured heat flux of the (1) IQC/Si, (2) IQC/Al₂O₃, (3) IQC/CuGaTe₂ and (4) IQC/Ag₂Te composites.

reservoirs kept at 900 K and 300 K. Each composite has its own optimum value of x (x_{opt}) in which the largest value of TRR_{calc} is attained. The x_{opt} values were 0.08, 0.21 and 0.55 for IQC/Si, IQC/Al₂O₃ and IQC/CuGaTe₂, respectively.

It is also worthwhile to mention that the large value of TRR exceeding 1.75 is obtainable even at the small temperature difference from 543 K to 300 K in the composite of ICQ/Ag₂Te when the length ratio is $x=0.65$. Although the predicted value of $\text{TRR}_{\text{calc}}=1.75$ is slightly smaller than those of the other three composites, the much smaller temperature difference of $\Delta T=243$ K than $\Delta T=600$ K of the

other composites could have advantages in practical applications.

The conditions that determine x_{opt} are clearly understood from the x -dependence of the interface temperature, as shown in figures 4(b1)-(b4).

At x_{opt} , the interface temperature (T_{boundary}) possesses the same value for two different sample configurations: one configuration with the IQC at the high-temperature side and the other with the IQC at the low-temperature side. This result indicates that the ratio of the thermal resistance of the IQC at the high temperature side to that of the one of the other

Table 1. Thermal rectification ratio of the present composites.

Material A	Material B	T_H/K	T_L/K	TRR_{exp}	TRR_{calc}	TRR_{exp}/TRR_{calc}
$Al_{61.5}Cu_{26.5}Fe_{12}$ IQC	Si	900	~ 300	1.81 ± 0.16	2.10	0.86
$Al_{61.5}Cu_{26.5}Fe_{12}$ IQC	Al_2O_3	900	~ 300	2.01 ± 0.13	2.17	0.92
$Al_{61.5}Cu_{26.5}Fe_{12}$ IQC	CuGaTe ₂	900	~ 300	2.20 ± 0.13	2.26	0.97
$Al_{61.5}Cu_{26.5}Fe_{12}$ IQC	Ag ₂ Te	550	~ 300	1.65 ± 0.16	1.75	0.96

materials at the low temperature side becomes equal to the ratio of thermal resistance for the one of the other materials at the high temperature side to that of the IQC at the low temperature side.

In addition, x_{opt} requires a longer length of the material with the larger thermal conductivity, and vice versa. We obtained the smallest value of x_{opt} in the IQC/Si composites, because Si possesses a much larger κ than the $Al_{61.5}Cu_{26.5}Fe_{12}$ IQC. x_{opt} is in the vicinity of 0.5 for the IQC/CuGaTe₂ and IQC/Ag₂Te composites because of the comparable κ -values of the two components. The calculated x_{opt} , the boundary temperature at x_{opt} and the estimated maximum value of TRR_{calc} are listed in table 1.

6. Heat flux measurement for determining the TRR

To experimentally confirm the very large values of the TRR predicted from our calculations, we directly measured the heat flux in the IQC/Si, IQC/ Al_2O_3 , and IQC/CuGaTe₂ composites placed between two heat reservoirs kept at $T_L \approx 300$ K and $T_H = 900$ K in vacuum and that in the IQC/Ag₂Te placed at $T_L \approx 300$ K and $T_H = 550$ K.

The samples have cylindrical shapes 20 mm in height and 10 mm in diameter, and the length ratios x were fixed at x_{opt} for all of the composites. The heat flux J in the composite was estimated using a simple apparatus comprised of a heater, one of the composites, a copper block and a water-cooled block placed in a hand-press. The entire measurement system was sealed in a chamber, and the measurements were conducted under vacuum better than 10 Pa [28, 31]. To obtain good thermal contacts, both sides of the cylindrical ingots were carefully polished to a flat, mirror-like finish, and the cylindrical ingots were joined using a small amount of silver paste. We also used a thin carbon sheet (0.5 mm in thickness) at the interface between the sample and heater. A small amount of thermal grease was employed at the interfaces between the sample/copper block and the copper block/water-cooled block.

The measured heat fluxes are plotted in figures 4(c1)–(c4) as a function of heating time. Large differences in heat flux were observed between the measurements made in the two opposite directions, and the heat flux is always larger when the IQC is located at the high-temperature side. The experimentally observed TRR (TRR_{exp}) values for the IQC/Si, IQC/ Al_2O_3 , IQC/CuGaTe₂ and IQC/Ag₂Te composites were 1.81 ± 0.08 , 2.03 ± 0.16 , 2.20 ± 0.13 and 1.65 ± 0.20 , respectively. These values are much larger than

those of any other bulk thermal rectifiers previously reported [13–15, 28, 31, 37].

7. Discussions

The TRR_{exp} values were nearly consistent with the TRR_{calc} values for the IQC/CuGaTe₂ and IQC/Ag₂Te devices, whereas the other two rectifiers possessed TRR_{exp} values that were slightly smaller than TRR_{calc} . This fact is clearly confirmed by superimposing the TRR_{exp} data on the TRR_{calc} data in figure 4(a). Additionally, by calculating the ratio of TRR_{exp} to TRR_{calc} , we discovered that this ratio is closely related to the averaged thermal conductivities of component materials, estimated from the temperature distribution in the composites and the temperature dependence of κ for each material. The values of TRR_{exp}/TRR_{calc} were 0.97, 0.96, 0.92 and 0.86 for IQC/CuGaTe₂, IQC/Ag₂Te, IQC/ Al_2O_3 and IQC/Si, respectively. Their averaged κ for the two different directions of heat flow were calculated to be ($2.78 \text{ W m}^{-1} \text{ K}^{-1}$, $6.08 \text{ W m}^{-1} \text{ K}^{-1}$), ($1.55 \text{ W m}^{-1} \text{ K}^{-1}$, $2.63 \text{ W m}^{-1} \text{ K}^{-1}$), ($7.48 \text{ W m}^{-1} \text{ K}^{-1}$, $15.97 \text{ W m}^{-1} \text{ K}^{-1}$) and ($19.53 \text{ W m}^{-1} \text{ K}^{-1}$, $40.93 \text{ W m}^{-1} \text{ K}^{-1}$), respectively. Very small values of TRR_{exp}/TRR_{calc} were obtained for the IQC/Si composite, which possesses the largest values of averaged κ , whereas TRR_{exp}/TRR_{calc} reached nearly equal to unity in the IQC/CuGaTe₂ and IQC/Ag₂Te composites, which possess the very small values of averaged κ .

We firstly considered the effect of radiation emitted from the sidewall of the samples. The amount of radiation loss is not negligibly small but occasionally reaches a seriously large value. It is strongly affected by the dimension and thermal conductivity of the samples and becomes large for long, narrow samples of lower thermal conductivity. In the present samples with cylindrical shapes, we confirmed that the radiation loss was less than 10%, and the variation of TRR due to the radiation was less than a few %. Therefore, we safely ignored the effect of radiation loss in our samples.

We eventually realized that the departure of TRR_{exp}/TRR_{calc} from unity would be related to the contact resistance for heat flow at the interfaces between the heat reservoirs and the devices because it is capable of significantly reducing the highest temperature or significantly increasing the lowest temperature of the composite. The thermal conductivity of the $Al_{61.5}Cu_{26.5}Fe_{12}$ IQC and the CuGaTe₂ was small enough so that the effect of the contact resistance could be safely ignored; therefore, TRR_{exp}/TRR_{calc} was nearly equal to unity for the IQC/CuGaTe₂ composite. In the case of the IQC/Si composite, on the other hand, the thermal conductivity of Si is

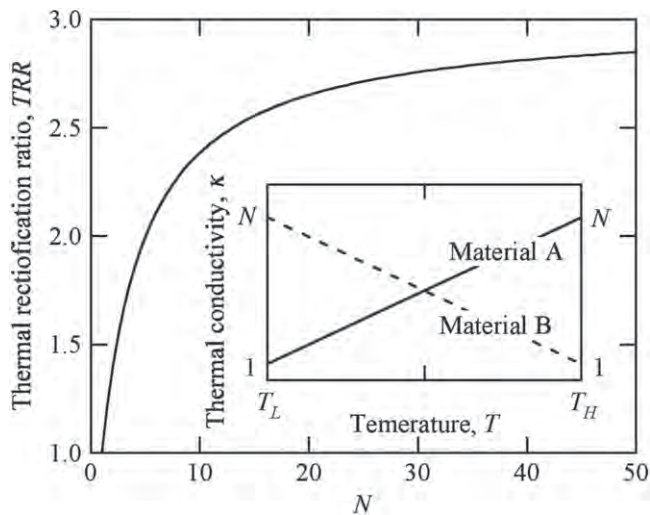


Figure 5. Thermal rectification ratio obtainable for composites consisting of material A and material B, which possess thermal conductivity that linearly varies with temperature.

so large that the temperature distribution in the samples is greatly affected under the presence of contact resistance. The highest temperature of the composite would be reduced significantly when Si is located at the hot side, while the lowest temperature would be increased at the opposite configuration. The temperature difference between the two edges of the composite is certainly reduced, and the value of the TRR is also reduced.

The contact resistance between two component materials, on the other hand, does not seriously affect the value of the TRR because the value is dominated by the thermal conductivity near the highest and lowest temperatures, whereas the interface of two component materials always stays in the middle temperature range.

If our consideration is correct, we still have a chance to observe a large TRR exceeding 2.0 even for the IQC/Si composite by tuning the heater power using the temperature exactly at the interface rather than that in the heater block. This requires the modified experimental setup; we are now in progress on it, and the results will be reported elsewhere in the near future.

Before the closing discussion, it would be worthwhile to mention the further increase of the TRR. Let us assume a composite consisting of two materials, one of which possesses thermal conductivity that linearly increases with temperature, and the other linearly decreases. For the sake of easy calculation, the increasing ratio and decreasing ratio of thermal conductivity in two materials were assumed to be the same as $[\kappa_{TH}/\kappa_{TL}]_{\text{Material A}} = [\kappa_{TL}/\kappa_{TH}]_{\text{Material B}} = N > 1$. The value of $\text{TRR}_{\text{model}}$ was calculated as a function of N under this condition, and the resulting values were plotted in figure 5.

Obviously, the TRR increases with increasing N and gradually approaches the maximal value 3. The Al-Cu-Fe IQC possesses $N=7.0$ under the condition of $T_H=900$ K and $T_L=300$ K, and the $\text{TRR} \sim 2.2$ observed for the composite consisting mainly of this IQC is very close to the $\text{TRR}_{\text{model}}$ at

$N=7.0$. These facts indicate that our samples have already stayed in very good condition for the thermal rectifier and that it would not be very easy to obtain much larger TRR values exceeding 3.0.

Nevertheless, if we employed materials possessing thermal conductivity that increases with temperature much more drastically than those with linear dependence, the maximum value should be increased to a value larger than 3.0. The thermal conductivity of IQCs possesses such a behavior; therefore, we keep studying toward the goal of developing a thermal rectifier possessing a TRR exceeding 3.0 using IQCs. The result will be reported elsewhere in the near future.

8. Conclusion

In this study, we developed a new thermal rectifier working at high temperatures above 300 K and possessing a large TRR exceeding 1.65 using $\text{Al}_{61.5}\text{Cu}_{26.5}\text{Fe}_{12}$ IQC together with one of the following materials: Si, Al_2O_3 , CuGeTe_2 or Ag_2Te . The values of TRR obtained in this study were definitely the largest among those ever reported; therefore, some of these composites could be used in practical applications, leading to the efficient use of energy.

Acknowledgments

This research was financially supported by both JST-PRESTO and the Ministry of Education, Science, Sports, and Culture, Japan (Grant-in-Aid for Scientific Research (B), no. 23360278). The author wishes to thank Mr Ryu-suke Nakayama of Nagoya University, Professor Yoichi Nishino and Professor Hidetoshi Miyazaki of Nagoya Institute of Technology for their help in conducting the experiment and Dr Atsushi Yamamoto of AIST for his valuable comments on heat current measurements.

References

- [1] Roberts N A and Walker D G 2011 *Int. J. Therm. Sci.* **50** 648
- [2] Starr C 1936 *J. Appl. Phys.* **7** 15
- [3] Barzelay M H, Tong K N and Holloway G F 1955 *NACA Technical Note* 3295
- [4] Powell R W, Tye R P and Jolliffe B W 1962 *Int. J. Heat and Mass Trans.* **5** 897
- [5] Lewis D V and Perkins H C 1968 *Int. J. Heat and Mass Trans.* **11** 1371
- [6] O'Callaghan P W, Probert S D and Jones A 1970 *J. Phys. D: Appl. Phys.* **3** 1352
- [7] Stevenson P F, Peterson G P and Fletcher L S 1991 *J. Heat Trans.* **113** 30
- [8] Clausing A M 1966 *Int. J. Heat and Mass Trans.* **9** 791
- [9] Rogers G F C 1961 *Int. J. Heat and Mass Trans.* **2** 150
- [10] Chang C W, Okawa D, Majumdar A and Zettl A 2006 *Science* **314** 1121
- [11] Peyrard M 2006 *Europhys. Lett.* **76** 49
- [12] Hu B, He D, Yang L and Zhang Y 2006 *Phys. Rev. E* **74** 060201

- [13] Kobayashi W, Teraoka Y and Terasaki I 2009 *Appl. Phys. Lett.* **95** 171905
- [14] Sawaki D, Kobayashi W, Moritomo Y and Terasaki I 2011 *Appl. Phys. Lett.* **98** 081915
- [15] Kobayashi W, Sawaki D, Omura T, Katsufuji T, Moritomo Y and Terasaki I 2012 *Appl. Phys. Express* **5** 027302
- [16] Janot C 1996 *J. Phys. Rev. B* **53** 181
- [17] Nagata T, Kirihara K and Kimura K 2003 *J. Appl. Phys.* **94** 6560
- [18] de Boissieu M, Currat R, Franconal S and Kats E 2004 *Phys. Rev. B* **69** 054205
- [19] Hussey N E, Takenaka K and Takagi H 2004 *Philos. Mag.* **84** 2847
- [20] Biggs B D, Li Y and Poon S J 1991 *Phys. Rev. B* **43** 8747
- [21] Biggs B D, Poon S J and Munirathnam N R 1990 *Phys. Rev. Lett.* **65** 2700
- [22] Takeuchi T 2003 *Phys. Rev. B* **68** 184203
- [23] Takeuchi T 2009 *Z. Krist.* **224** 35
- [24] Takeuchi T 2009 *J. Elec. Mater.* **38** 1354
- [25] For example, Ziman J M 1972 *Principle of the Theory of Solids* 2nd edn (Cambridge: Cambridge University Press)
- [26] Dolinšek J, Vrtnik S, Klanjšek M, Jagličič Z, Smontara A, Smiljanić I, Bilušić A, Yokoyama Y, Inoue A and Landauro C V 2007 *Phys. Rev. B* **76** 054201
- [27] Landauro C V and Solbrig H 2000 *Mater. Sci. Eng. A* **294–296** 600
- [28] Nakayama R and Takeuchi T 2014 *J. Elec. Mater.* at press (doi:10.1007/s11664-1014)
- [29] Takeuchi T, Otagiri T, Sakagami H, Kondo T, Mizutani U and Sato H 2004 *Phys. Rev. B* **70** 144202
- [30] Pope A, Tritt T, Chernikov M and Feuerbacher M 1999 *Appl. Phys. Lett.* **75** 1854
- [31] Takeuchi T, Goto H, Nakayama R and Terazawa Y 2012 *J. Appl. Phys.* **111** 093517
- [32] Hopkins P E, Norris P and Stevens R J 2008 *ASME Trans. J. Heat Transfer* **130** 022401
- [33] Desai P D 1986 *J. Phys. Chem. Ref. Data* **15** 967
- [34] Plirdpring T *et al* 2012 *Adv. Mater.* **24** 3622
- [35] Capps J, Drymiotis F, Lindsey S and Tritt T M 2010 *Philos Mag. Lett.* **90** 677
- [36] Fujikane M, Kurosaki K, Muta H and Yamanaka S 2005 *J. Alloys Compd.* **387** 297
- [37] Takeuchi T, Goto H, Toyama Y, Itoh T and Mikami M 2011 *J. Elec. Mater.* **40** 5

準結晶の異常電子熱伝導度が生み出す 巨大な熱整流効果

豊田工業大学 竹内恒博

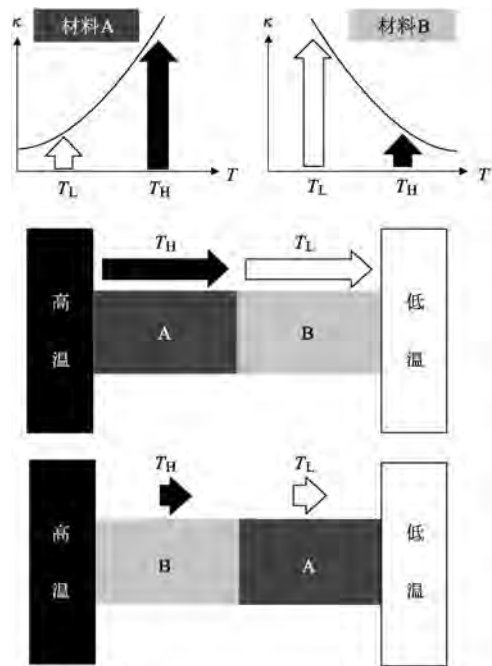
§1 はじめに

固体内を流れる熱流密度 J_Q は、一般的に、フーリエの法則 ($J_Q = -\kappa \nabla T$) により記述され、温度勾配の大きさ $|\nabla T|$ が同じであれば、熱流密度の大きさ $|J_Q|$ が方向依存性を有することはない。しかし、いくつかの“特殊な機構”を利用することで、同じ材料内においても熱流密度の大きさに方向依存性をもたせることが可能になる。このような材料は、熱整流材料 (Thermal rectifier)¹⁾ と呼ばれている。無駄に捨てられている廃熱を必要とされる箇所に移動して利用する熱マネジメントの概念が注目されており、実用温度域で再現性が高く大きな整流効果を示す熱整流材料があれば、熱マネジメントの中核をなす可能性が高い。しかし、残念ながら、その要求を満たす材料の開発に至っていない。

熱整流を生じさせる機構として、金属と非金属材料の界面の利用²⁾、熱膨張率の異なる2つの材料の界面の利用³⁻⁷⁾、ポテンシャル障壁の利用⁸⁾、質量が空間に分布する材料の利用^{9,10)}、熱伝導度の温度依存性の異なる2つの材料の利用¹¹⁻¹⁴⁾などが提案されている。金属と非金属の界面を利用した場合には、顕著な整流効果があることが報告されているが、その検証が行われた報告がなく、実際に熱整流特性を有するのか疑問が残る。熱膨張率の異なる2つの材料の界面の利用において最も顕著な整流効果が報告されているが、再現性が得られない問題がある。質量の空間分布が一樣でない場合の熱整流効果の場合には、カーボンナノチューブ⁹⁾や、グラフェン¹⁰⁾などが用いられており、他の機構に比べて性能が良くないことに加え、材

料の大きさが著しく小さく、実用化するためには技術のさらなる向上が必要とされるであろう。

筆者らは、熱伝導度の温度依存性の異なる2つの材料の利用¹¹⁻¹⁴⁾による熱整流機構に着目している。第1図に模式的に示すように、温度上昇に伴い熱伝導度が上昇する材料Aと温度上昇に伴い熱伝導度が減少する材料Bを組み合わせ、高温と低温に維持された熱浴の間に挟み込む場合を考える。材料AとBが、それぞれ、高温側と低温側に配置された場合、いずれの材料も大きな熱



第1図
固体熱整流材料の模式図。試料を入れ替えることで構成材料の温度と熱伝導度に変化し、熱整流効果が生み出される。

伝導度を示し、大きな熱流密度 J_{AB} が得られる。一方、逆に配置された場合には、2つの材料の熱伝導度は小さくなり、熱流の大きさ J_{BA} は小さくなる。この機構を利用すれば、熱整流材料の性能はバルクの物性で支配されることになり制御が容易である。さらに、熱流の機構が微視的に変化しない限りサイズ効果を持たず、かつ、熱流の大きさが素子の厚さで調整することも可能であることから、実用化における障壁が少ないと判断される。性能の高い熱整流材料を創製するためには、熱伝導度に顕著な温度依存性を示す材料を用いればよいことも自明である。

2009年、小林ら¹³⁾により、格子熱伝導度の顕著な温度依存性を利用してその機構が実証された。彼らは規則度の高い酸化物絶縁体 (LaCoO_3) と、 LaCoO_3 内の La の一部を Sr で置換することで構造の不規則性とホールを同時に導入した酸化物金属相 ($\text{La}_{1-x}\text{Sr}_x\text{CoO}_3$) を組み合わせることで熱整流材料を作製した。規則度の高い絶縁体 (LaCoO_3) では、低温において格子熱伝導度にピークが観測され、ピークより高温では昇温に伴い熱伝導度が減少する挙動を示す。一方、構造の不規則構造を有する金属相 $\text{La}_{1-x}\text{Sr}_x\text{CoO}_3$ では、おおむね、絶対温度に比例しながら昇温に伴い増大する熱伝導度が観測される。後者は、格子熱伝導度の絶対値が小さく、その温度依存性も顕著でないことから、熱伝導度の温度依存性は電子熱伝導度により決定されている。ビーデマン・フランツ則 $\kappa_{el} = L_0 \sigma T$ と不規則系に特有の温度依存性の小さい電気伝導度を $\sigma(T) \simeq \text{const.}$ 考慮すると、電子熱伝導度が絶対温度に比例することは容易に理解できるであろう。なお、 L_0 はローレンツ数と呼ばれる定数である。

小林らにより開発された固体熱整流材料の性能は、熱整流比 ($TRR = |J_{Q_{\text{large}}}| / |J_{Q_{\text{small}}}|$) が約 1.44 であった¹³⁾。理論的に予測された熱整流効果を実験的に証明し、かつ、比較的大きな熱整流効果を観測したことは意義深いだが、その動作温度は 150 K 以下の低温であった。格子熱伝導度で一般的に観測される低温のピークを利用しているために、性能を維持したまま動作温度を室温以上に上げることは難しいと判断される。

筆者らは、近年、AI 基準結晶や近似結晶が示す電子熱伝導度の異常な温度依存性^{15,16)}を利用すれば、性能を維持したまま熱整流材料の動作温度を上昇させることができると提案している¹⁷⁾。さらに、この考え方に基づいて、廃熱が存在する室温以上の温度領域で動作し、かつ、比較的高い性能を示す熱整流材料を開発に成功した¹⁸⁻²⁰⁾。本稿では、筆者らが開発した熱整流材料の動作原理、現状、および、今後の発展性を紹介する。

§2 格子熱伝導度と電子熱伝導度

廃熱利用に熱整流材料を活用するためには、室温以上の温度領域で熱伝導度の温度依存性が顕著な材料を開発する必要がある。一般的な材料では、室温以上の熱伝導度の温度依存性は、それほど顕著ではなく、室温以上で動作し、高い性能を示す熱整流材料を開発することは容易ではない。

フォノンの運動量およびエネルギーに対して平均値を用い、かつ、緩和時間近似を利用すると、格子熱伝導度は以下の式で表わされる。

$$\kappa_{\text{lat}} = \frac{1}{3} C v_G l \quad (1)$$

ここで、 C , v および l は、それぞれ、定積比熱、平均群速度、平均自由行程を表わしている。式 (1) で示される格子熱伝導度の温度依存性は、極低温で T^3 に比例し、昇温に伴いピークを有した後、ウムクラップ散乱過程の増大に伴い、おおむね $1/T$ で減衰することが知られている。ただし、高温でゼロに漸近するのではなく、平均自由行程がフォノンの波長よりも短くならない条件により導出される最小熱伝導度²¹⁾に漸近すると考えられている。廃熱が利用できる温度領域では、昇温に伴いおおむね $1/T$ で減衰する挙動が観測されることから、一般的に、この温度領域において温度依存性が顕著ではないことが理解される。ただし、上述した格子熱伝導度は、おおむねデバイ温度にスケールリングすることから、デバイ温度の高い材料を用いれば、室温以上の高温においても、昇温に伴う熱伝導度の減少を比較的大きくすることができる。たとえば、典型的な酸化物の Al_2O_3 では、デバイ温度が 1000 K を超える²²⁾ た

め、 $\kappa(300\text{ K})/\kappa(1000\text{ K})$ が4.8にも達する^{20,23}。さらに、また、具体的な材料については後ほど言及するが、非調和振動が顕著な材料などではフォノン分散から予想されるよりも格子熱伝導度が小さくなる傾向を示す。上記の特徴を有する材料を利用すれば、熱整流効果が得られると考えられるが、 $\kappa(300\text{ K})/\kappa(1000\text{ K})=4.8$ 程度では、大きな熱整流効果が得られるとは考えがたく、昇温に伴い熱伝導度が著しく増大する材料と複合化する必要があるのである。

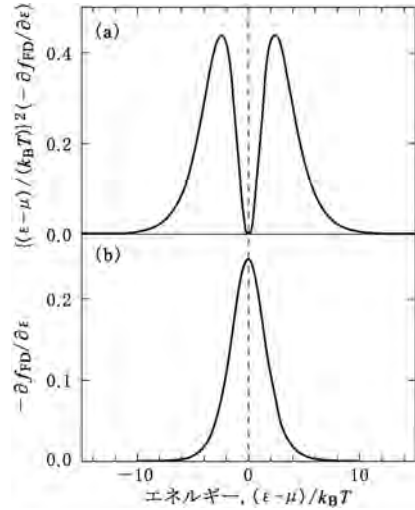
熱は電子にも運ばれることから、次に電子熱伝導度の特徴を簡単に述べる。線形応答理論を用いて電子熱伝導度と電気伝導度を下記の式で表わされる²⁴。

$$\begin{aligned} \sigma(T) &= \int_{-\infty}^{\infty} \sigma(\varepsilon, T) (-\partial f_{\text{FD}}/\partial \varepsilon) d\varepsilon \quad (2) \\ k_{\text{el}}(T) &= \frac{1}{e^2 T} \int_{-\infty}^{\infty} \sigma(\varepsilon, T) (\varepsilon - \mu)^2 (-\partial f_{\text{FD}}/\partial \varepsilon) d\varepsilon \\ &\quad \frac{1}{e^2 T} \frac{\left\{ \int_{-\infty}^{\infty} \sigma(\varepsilon, T) (\varepsilon - \mu) (-\partial f_{\text{FD}}/\partial \varepsilon) d\varepsilon \right\}^2}{\int_{-\infty}^{\infty} \sigma(\varepsilon, T) (-\partial f_{\text{FD}}/\partial \varepsilon) d\varepsilon} \quad (3) \end{aligned}$$

ここで、 f_{FD} , e , μ , k_{B} はそれぞれ、フェルミ・ディラック分布関数、電子の素電荷、化学ポテンシャル、ボルツマン定数を表わしている。スペクトル伝導度 $\sigma(\varepsilon, T)$ は、各エネルギーに存在する電子状態の電気伝導へ寄与する能力を現しており、緩和時間近似を用いれば、 ε に存在する電子状態の数、群速度 v_{G} 、および、緩和時間 τ から決定されると理解してよい。等方的な材料では、スペクトル伝導度 $\sigma(\varepsilon, T)$ は、以下の式で表現される。

$$\begin{aligned} \sigma(\varepsilon, T) &= \frac{e^2}{3} N(\varepsilon) v_{\text{G}}^2(\varepsilon) \tau(T) \\ &= \frac{e^2}{3} N(\varepsilon) v_{\text{G}}(\varepsilon) l(T) \quad (4) \end{aligned}$$

電子熱伝導度を表わす式(3)の第2項は第1項に比べて無視できる場合が多い²⁵ことから、ここでは、第1項のみを考慮する。電気伝導度は、 $\sigma(\varepsilon, T)$ とフェルミ・ディラック分布関数のエネルギーに対する1次導関数 $(-\partial f_{\text{FD}}/\partial \varepsilon)$ の積をエネルギーで積分することで得られていることがわか



第2図

(a) 熱伝導度と (b) 電気伝導度に寄与するエネルギー領域を指定する窓関数。

電気伝導度は化学ポテンシャル近傍の電子が、電子熱伝導度は化学ポテンシャルから $2.4 k_{\text{B}} T$ 程度離れたエネルギー領域に存在する電子により支配されていることがわかる。

る。同様に、 $\sigma(\varepsilon, T)$ と $(\varepsilon - \mu)^2 (-\partial f_{\text{FD}}/\partial \varepsilon)$ を被積分関数として有するエネルギーの積分で電子熱伝導度が計算される。第2図に示した $(-\partial f_{\text{FD}}/\partial \varepsilon)$ と $(\varepsilon - \mu)^2 (-\partial f_{\text{FD}}/\partial \varepsilon)$ は μ 近傍にしか有意な値を有していないために、積分のエネルギー領域を決定する窓関数になっていることがわかる。また、双方ともに $(\varepsilon - \mu)$ の偶関数になっている。また、それぞれの窓関数のみの積分は

$$\begin{aligned} \int_{-\infty}^{\infty} \left(-\frac{\partial f_{\text{FD}}}{\partial \varepsilon} \right) d\varepsilon &= 1 \quad (5) \\ \frac{1}{e^2 T} \int_{-\infty}^{\infty} (\varepsilon - \mu)^2 \left(-\frac{\partial f_{\text{FD}}}{\partial \varepsilon} \right) d\varepsilon &= \frac{\pi^2 k_{\text{B}}^2 T}{3e^2} = L_0 T \quad (6) \end{aligned}$$

になることも覚えておくとよい。ここで、 L_0 はローレンツ数と呼ばれる定数である。また、2つの窓関数に表われるピークのエネルギーは異なることから、電荷を運ぶ電子と熱を運ぶ電子は異なるエネルギー領域に存在することも理解できる。

一般的な金属材料では、スペクトル伝導度が化学ポテンシャル近傍の窓関数が有意な値を示す領域において $(\varepsilon - \mu)$ の1次関数として、 $\sigma(\varepsilon, T) = \sigma(\mu, T) + (\varepsilon - \mu) (\partial \sigma(\mu, T) / \partial \varepsilon)$ に近似できる。

偶関数である窓関数と $\sigma(\varepsilon, T)$ の積を積分する際に、奇関数である $\sigma(\varepsilon, T) = \sigma(\mu, T) + (\varepsilon - \mu) (\partial\sigma(\mu, T) / \partial\varepsilon)$ の第 2 項は消失する。結果として、 $\sigma(\varepsilon, T) = \sigma(\mu, T)$ および $\kappa_{el}(T) = L_0\sigma(\mu, T) T$ が得られる。また、これらの式から $\sigma(\mu, T)$ を消去すると、よく知られたビーデマン・フランツ則 $\kappa_{el}(T) = L_0\sigma(T) T$ が導出される。ここで示した式の展開から、ビーデマン・フランツ則は、スペクトル伝導度が化学ポテンシャル近傍でエネルギーの 1 次関数に近似できる場合のみ成立し、スペクトル伝導度に 2 次関数成分があると電子熱伝導度をうまく表現できないことがわかる。

$(-\partial f_{FD} / \partial\varepsilon)$ が $\varepsilon = \mu$ に単一のピークを有することに対し、 $(\varepsilon - \mu)^2 (-\partial f_{FD} / \partial\varepsilon)$ が $\varepsilon \approx \mu \pm 2.6 k_B T$ に 2 つのピークを呈することを考慮すると、 $\varepsilon \approx \mu \pm 2.6 k_B T$ 近傍のエネルギー領域において $\varepsilon = \mu$ 近傍よりも大きな状態密度を有する材料を用いた場合に、ビーデマン・フランツ則から予測されるよりもはるかに大きな電子熱伝導度が観測されることが容易に理解される^{15,16)}。すなわち、エネルギー幅が数百 meV 程度の幅を有する状態密度の窪みが存在し、化学ポテンシャルにおいて最も状態密度が小さくなる場合(典型的な 2 次関数でスペクトル伝導度が表現される場合)において、電子熱伝導度が高温で著しく増大するはずである。なお、ビーデマン・フランツ則では予測できないこの異常な電子熱伝導度の増大を顕著にするためには、化学ポテンシャルにおける状態密度 $N(\mu)$ は小さいほうがよく、 $N(\mu) = 0$ であってもまったく問題はない。

化学ポテンシャル近傍に狭い擬ギャップが存在している場合に、電子熱伝導度 $\kappa_{el}(T)$ が $L_0\sigma(\mu, T) T$ よりもはるかに大きくなることを述べたが、温度の上昇による電子散乱の増大に伴いスペクトル伝導度は高温で小さくなるので、狭い擬ギャップのみでは電子熱伝導度の増大が低減してしまう。一方、伝導電子が Mott-Ioffe-Regel 極限^{26,27)} として知られる強散乱極限にある場合には、緩和時間の温度依存性はなくなり、擬ギャップに起因した異常電子熱伝導度が顕著に観察されることになる。この機構を利用することで、室温以上の高温域で動作し、よい整流特性を示す熱整流材料を

開発することができる。

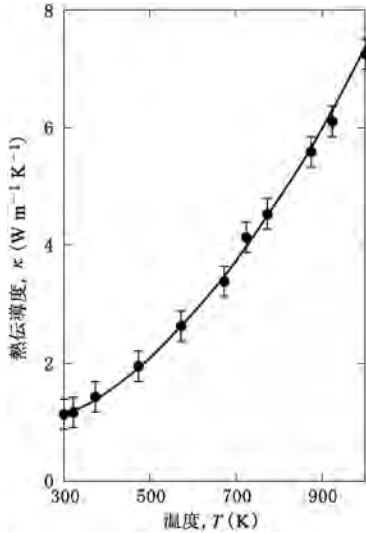
§3 準結晶の熱伝導度

Al 期準結晶の熱伝導度は低温においてガラス並に小さく^{29,30)}、また、高温では温度上昇に伴い増大することが報告されている^{31,32)}。熱伝導度における同様の傾向は、準結晶と同じ局所構造を有する近似結晶においても観測される²⁹⁾。われわれは構造解析が可能で、かつ、第一原理計算により電子構造の情報が得られる近似結晶の熱伝導度を解析することで、準結晶で観測される熱伝導度の特徴が、(i)準周期性と(ii)フェルミ準位近傍に形成する狭く深い擬ギャップにより生み出されている異常電子熱伝導度の特徴であることを明らかにした^{15,16)}。

準周期性が存在することで、フォノンが波束として伝播できなくなり、格子熱伝導度は著しく小さく抑制される。伝導電子も強散乱極限に達し、平均自由行程の温度依存性が無視できるほど小さくなる。先に述べたとおり、フェルミ準位近傍において状態密度が数 $k_B T$ 程度の温度領域にわたりエネルギーの 1 次関数で近似できる場合には、ビーデマン・フランツ則 $\kappa_{el} = L_0\sigma T$ が適用可能になるので、電子熱伝導度が絶対温度に比例することになる。しかし、ここに 100~200 meV 程度の幅をもつ深い擬ギャップが存在する場合には、高温における電子熱伝導度の増大が顕著に現れることになる。第 3 図に $\text{Al}_{62.0}\text{Cu}_{25.5}\text{Fe}_{12.5}$ 準結晶で観測された熱伝導度の温度依存性を示す¹⁸⁾。室温における熱伝導度が約 $1 \text{ W m}^{-1} \text{ K}^{-1}$ であるが、1000 K 付近では $7.5 \text{ W m}^{-1} \text{ K}^{-1}$ 程度にまで増大していることがわかる。

準結晶で観測される異常な熱伝導度の温度依存性が、前節で説明した擬ギャップに関連した異常電子熱伝導度により生み出されていることは、ゼーベック係数と熱伝導度の温度依存性からも確認できる。

ゼーベック係数は化学ポテンシャルの高エネルギー側と低エネルギー側の状態密度の差が大きい場合に増大する特徴を有している^{19,33)}。すなわち、電子熱伝導度の温度依存性が最も顕著になる組成

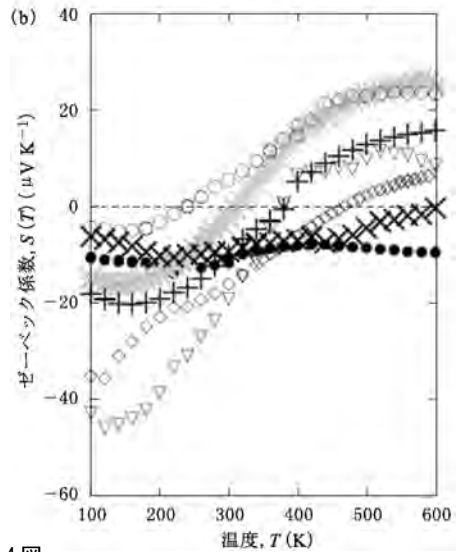
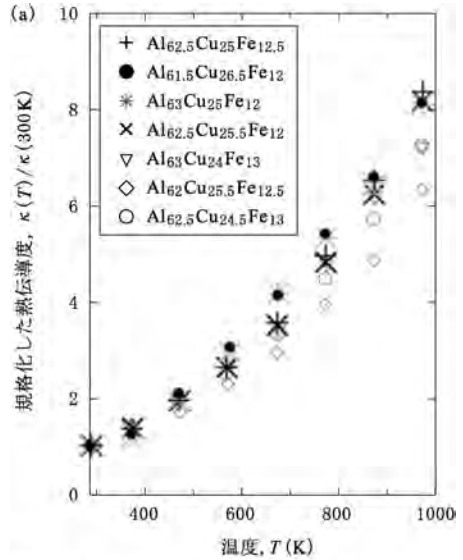


第3図 Al_{62.0}Cu_{25.5}Fe_{12.5}準結晶の熱伝導度の温度依存性. 昇温に伴い熱伝導度が著しく増大していることがわかる [文献18)より].

では、ゼーベック係数の値が小さくなることが予想される. 第4図(a)および(b)に組成をわずかに変化させることでキャリア濃度を調整したAl-Cu-Fe準結晶のゼーベック係数と、室温の値で規格化した熱伝導度の温度依存性を示す^{19,33)}. 広範囲で小さなゼーベック係数を示している組成において、熱伝導度の温度依存性が顕著になっていることがわかる. 準結晶における熱伝導度が高温において増大する機構として、比熱の増大³⁴⁾に伴う熱伝導度の増大や、準周期構造に由来して局在化していたフォノン³¹⁾の非局在化などによる可能性も示唆されているが、上記の実験結果を考慮すると、擬ギャップによる電子熱伝導度の増大と考えることが妥当であると判断される.

§4 Al 基準結晶を用いた熱整流特性の創製

Al 基準結晶の熱伝導度が高温において著しく増大することを紹介した. この特徴を利用することで、室温以上で動作し大きな整流効果を示す熱整流材料を開発できるはずである. 一方、Al 基準結晶と組み合わせる材料には、高温において熱伝導度が低下することが求められる. そのような



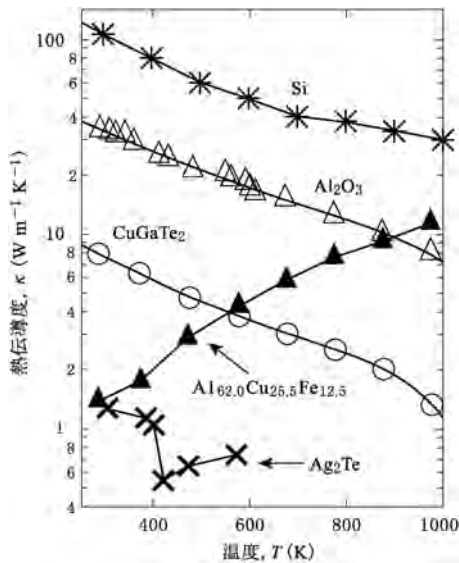
第4図 Al-Cu-Fe 準結晶の (a)室温で規格化した熱伝導度と (b)ゼーベック係数. ゼーベック係数の絶対値が小さい試料において熱伝導度の温度依存性が顕著になっている傾向がわかる [文献20)より].

特徴を持つ材料として、(i)デバイ温度の高い絶縁体、(ii)高温において非調和振動が顕著になる材料、および、(iii)規則-不規則相転移を伴う材料の利用を考えた.

デバイ温度が高い絶縁体では、電子の寄与がなく、かつ、昇温に伴いウムクラップ散乱が徐々に増大するために、緩やかに熱伝導度が低下す

る. この特徴を有する材料として Si と Al_2O_3 を利用することにした. それぞれの材料において, $\kappa(300\text{ K})/\kappa(1000\text{ K}) \approx 3.5$ と 4.8 が得られる²⁰⁾. また, CuGaTe_2 はデバイ温度が低い²³⁾にも関わらず, 高温まで熱伝導度の低下が観測され, $\kappa(300\text{ K})/\kappa(1000\text{ K}) \approx 6.9$ を示す²⁰⁾. Ag_2Te ³⁵⁻³⁷⁾ に代表されるカルコゲナイド化合物では Ag などのイオンがイオン伝導を生じやすいことを考慮すると, 昇温に伴う熱伝導度の低下は Cu 近傍において非調和振動が顕著になる結果であると予想される. Ag_2Te は約 400 K に構造変態を示し, 高温側では Ag がイオン伝導することが知られている. この特徴により, 狭い温度領域において大きく熱伝導度が増加し, $\kappa(400\text{ K})/\kappa(420\text{ K}) \approx 1.9$ が得られる. 構造相変態を伴うと体積変化により試料の形状を維持することが難しくなるが, ごく狭い温度領域で動作する熱整流材料を創製できると考えられる. 第 5 図に上述した材料群 (Si, Al_2O_3 , CuGaTe_2 , および, Ag_2Te) の $\text{Al}_{62.0}\text{Cu}_{25.5}\text{Fe}_{12.5}$ 熱伝導度を準結晶の熱伝導度とともに示した.

熱整流材料で得られる熱整流比 $TRR = |J_{e_{\text{large}}}| / |J_{e_{\text{small}}}|$ は, 組み合わせる 2 つの材料の長さ比にと



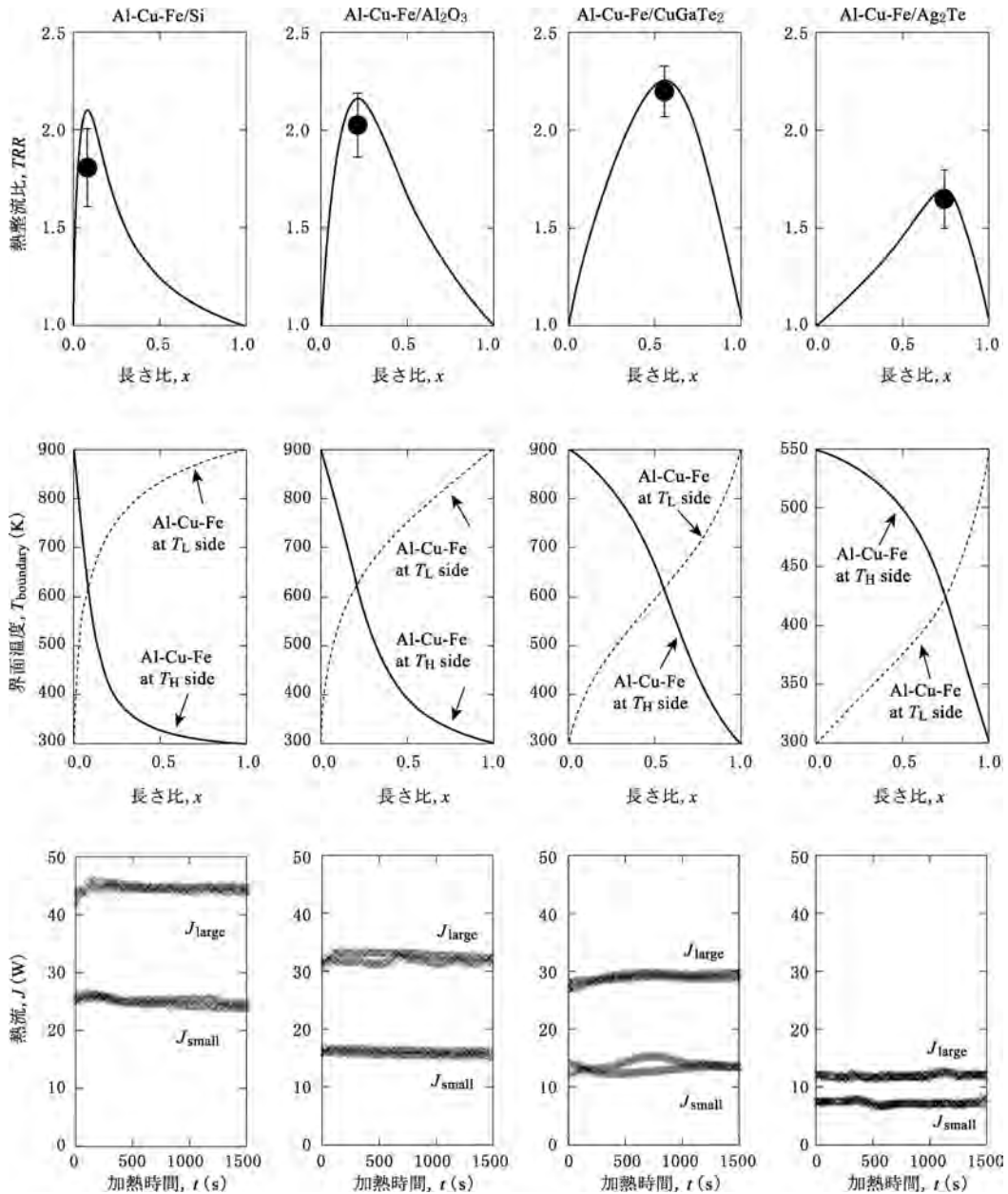
第 5 図

熱整流材料に用いた試料の熱伝導度. いずれの材料も室温以上の温度領域において熱伝導度に比較的顕著な温度依存性を有している [文献20) より].

もない変化する. 熱整流材料の側面から流出する熱量を無視した場合に得られる TRR をフーリエの法則を用いて計算し, 準結晶の相対長さ ($x = L_{\text{Al-Cu-Fe}}/L_{\text{total}}$) の関数として 第 6 図 上段に示した. Al-Cu-Fe 準結晶/ Ag_2Te を除き, 高温端 900 K, 低温端 300 K を仮定して計算を行った. また, Al-Cu-Fe 準結晶/ Ag_2Te では, 高温端 543 K, 低温端 300 K を仮定して計算した. 実線が計算値を示しており, Al-Cu-Fe 準結晶/Si, Al-Cu-Fe 準結晶/ Al_2O_3 , Al-Cu-Fe 準結晶/ CuGaTe_2 , Al-Cu-Fe 準結晶/ Ag_2Te において $x = 0.08, 0.21, 0.55$, および, 0.65 で TRR の最大値が得られ, その値は, Al-Cu-Fe 準結晶/Si, Al-Cu-Fe 準結晶/ Al_2O_3 , Al-Cu-Fe 準結晶/ CuGaTe_2 , Al-Cu-Fe 準結晶/ Ag_2Te において, $TRR_{\text{calc}} = 2.10, 2.17, 2.26$, および, 1.75 であることが予想される. 第 6 図中段に x の関数として示した界面温度からは, 2 つの異なる試料配置において, 界面温度が一致する場合に TRR_{max} が得られることがわかる. 別の言い方をすれば, 2 つの異なる試料配置において, 熱整流材料における高温側材料と低温側材料の熱抵抗の比が変化しない条件において TRR_{max} が得られると理解される.

$x = 0.08, 0.21, 0.55$, および, 0.65 で作製した Al-Cu-Fe 準結晶/Si, Al-Cu-Fe 準結晶/ Al_2O_3 , Al-Cu-Fe 準結晶/ CuGaTe_2 , Al-Cu-Fe 準結晶/ Ag_2Te において観測された熱流を加熱時間の関数として 第 6 図 下段に示した. 熱流は加熱時間に依存しておらず, 定常状態にあることがわかる. また, 試料配置を変化させた場合に, いずれの材料においても熱流が大きく変化していることが理解される. それぞれの材料において, $TRR = |J_{e_{\text{large}}}| / |J_{e_{\text{small}}}| = 1.81, 2.01, 2.20$, および 1.65 が観測された. これらの値は, すでに報告されている固体熱整流材料の TRR としては最大である. また, 動作温度が室温以上であることも応用の観点から極めて重要であると考えている. 測定結果は 第 1 表に示した.

実験値と計算値の比を計算すると, Al-Cu-Fe 準結晶/Si, Al-Cu-Fe 準結晶/ Al_2O_3 , Al-Cu-Fe 準結晶/ CuGaTe_2 , Al-Cu-Fe 準結晶/ Ag_2Te において, $TRR_{\text{exp}}/TRR_{\text{calc}} = 0.86, 0.92, 0.97$, および 0.96



第6図

Al₆₂Cu_{25.5}Fe_{12.5} 準結晶と Si, Al₂O₃, CuGaTe₂, および, Ag₂Te を組み合わせた複合材料の(上段)熱整流比の計算値と実測値(それぞれ実線と黒丸), (中段)界面温度の試料長さ比依存性. (下段)測定された熱流 [文献20]より].

が得られ, Si を用いた場合において熱整流比の値が小さくなっていることが確認できる. 簡単な計算を行うと, TRR_{exp} の低下は界面熱抵抗による試料端温度の低下に依存していることがわかる. Si を用いた材料では, Si の有する大きな熱

伝導度起因して熱整流材料の熱抵抗が小さくなる. この場合, 熱整流材料の熱抵抗に対して界面熱抵抗が相対的に大きくなっており, 熱浴と試料の界面において大きな温度勾配が生じることになる. その結果として, 熱整流材料にかかる実質的

第1表 Al 基準結晶を構成要素とする熱整流材料の性能.

材料 A	材料 B	T_H (K)	T_L (K)	TRR_{exp}	TRR_{calc}	TRR_{exp}/TRR_{calc}
Al _{61.5} Cu _{26.5} Fe _{12.0} 準結晶	Si	900	~300	1.81 ± 0.16	2.10	0.86
Al _{61.5} Cu _{26.5} Fe _{12.0} 準結晶	Al ₂ O ₃	900	~300	2.01 ± 0.13	2.17	0.92
Al _{61.5} Cu _{26.5} Fe _{12.0} 準結晶	CuGaTe ₂	900	~300	2.20 ± 0.13	2.26	0.97
Al _{61.5} Cu _{26.5} Fe _{12.0} 準結晶	Ag ₂ Te	543	~300	1.65 ± 0.16	1.75	0.96
Al _{60.5} Si _{0.5} Cu _{26.5} Fe _{11.5} Re _{0.5} 準結晶	CuGaTe ₂	900	~300	1.71 ± 0.13	1.75	0.97
Al _{60.5} Si _{0.5} Cu _{26.5} Fe _{11.5} Re _{0.5} 準結晶	Ag ₂ Te	543	~300	2.24 ± 0.14	2.30	0.97

な温度差が小さくなり、実験で得られる TRR が小さくなっている。Al-Cu-Fe 準結晶/CuGaTe₂ および Al-Cu-Fe 準結晶/Ag₂Te では、いずれの構成材料も熱伝導度が小さいために、熱整流材料の熱抵抗が大きく、熱整流材料の熱抵抗に対する界面熱抵抗の割合が小さくなっている。これが、 TRR_{exp}/TRR_{calc} が大きく保たれている理由である。なお、界面抵抗と同様に、2つの構成材料間の熱抵抗も存在するが、 TRR は熱浴付近の熱伝導度によって概ね決定されているために、 TRR の値に深刻な影響を与えない。

§5 熱整流材料をさらに高性能化させるために

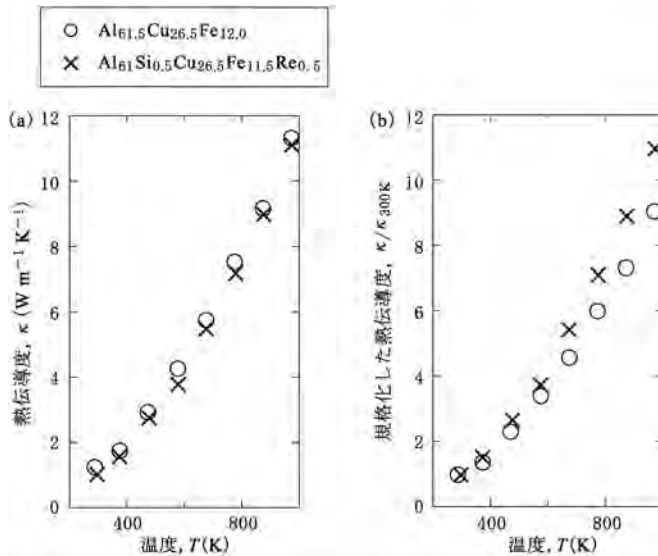
Al 基準結晶を利用した熱整流材料を高性能化するためには、準結晶の熱伝導度の温度依存性を顕著にすれば良い。室温において Al_{61.5}Cu_{26.5}Fe_{12.0} 準結晶の電子熱伝導度をビーデマン・フランツ則と比抵抗から大雑把に見積ると $\kappa_{el}(300\text{ K}) \approx 0.23\text{ W m}^{-1}\text{ K}^{-1}$ になる。観測されている熱伝導度の値は $\kappa_{meas}(300\text{ K}) = 0.9\text{ W m}^{-1}\text{ K}^{-1}$ であることから、室温における格子熱伝導度は $\kappa_{lat}(300\text{ K}) \approx 0.67\text{ W m}^{-1}\text{ K}^{-1}$ であると見積もられる。なお、格子熱伝導度は高温において増大しないと考えると、 $\kappa_{lat}(1000\text{ K}) \approx \kappa_{lat}(300\text{ K}) = 0.67\text{ W m}^{-1}\text{ K}^{-1}$ となることから、電子熱伝導度として $\kappa_{el}(1000\text{ K}) \approx 6.9\text{ W m}^{-1}\text{ K}^{-1}$ が得られる。すなわち、電子熱伝導度は1000 Kにおいて室温の値の約30倍にも達していると見積もられる。仮に電子構造を維持したまま、格子熱伝導度を1/2にすることができれば、 $\kappa_{lat}(1000\text{ K})/\kappa_{lat}(300\text{ K})$ は12.6程度にまで増大する可能性がある。このことを確認するために、Feの一部をReで置換した

試料を作製し、熱伝導度を測定した。

第7図(a)および(b)にReを置換した試料における熱伝導の変化を示す。FeをReで0.5 at.%置換した試料では、熱伝導度が測定した全温度領域にわたり低下していることがわかる。また、FeをReで置換した際に生じる電子の濃度の変化をSiでAlを置換することで補正している。300 Kにおいて熱伝導度を比較すると、Al_{61.0}Si_{0.5}Cu_{26.5}Fe_{11.5}Re_{0.5} 準結晶の熱伝導度はAl_{61.5}Cu_{26.5}Fe_{12.0} 準結晶の約65%にまで低減していることがわかる。この変化が格子熱伝導度の変化であると仮定してAl_{61.5}Cu_{26.5}Fe_{12.0} 準結晶の熱伝導度から計算すると、0.5 at.%Reの導入により、 $\kappa(1000\text{ K})/\kappa(300\text{ K}) \approx 12$ が得られると予想される。実際に、Al_{61.0}Si_{0.5}Cu_{26.5}Fe_{11.5}Re_{0.5} 準結晶において $\kappa(1000\text{ K})/\kappa(300\text{ K}) \approx 11$ が得られており、この値は計算値と良く一致している。

現状では、この試料が最も顕著な熱伝導度の温度依存性を示しているが、擬ギャップの形状を維持したまま重元素濃度を増やすことで、 $\kappa(1000\text{ K})/\kappa(300\text{ K})$ の値をさらに大きくすることは可能であろう。なお、実験データに関してはその記載を省略するが、Al_{61.0}Si_{0.5}Cu_{26.5}Fe_{11.5}Re_{0.5} 準結晶とCuGaTe₂を組み合わせた熱整流材料を、高温端900 Kと低温端300 Kに挟み込むことで、 $TRR = 2.24$ が得られている。同様に、Al_{61.0}Si_{0.5}Cu_{26.5}Fe_{11.5}Re_{0.5} 準結晶とAg₂Teを組み合わせた熱整流材料では、高温端543 Kと低温端300 Kに挟み込むことで、 $TRR = 1.71$ を実現した³⁸⁾。

最後に固体熱整流材料で得られる熱整流比の上限について考察する。熱整流比の大きさは用いる材料の熱伝導度の絶対値には依存せずに、その温度依存性のみから決定される¹⁸⁾。そこで、低温端と高温端において熱伝導度が n 倍増大する材料と



第7図
 $\text{Al}_{61.5}\text{Cu}_{26.5}\text{Fe}_{12.0}$ 準結晶と
 $\text{Al}_{61}\text{Si}_{0.5}\text{Cu}_{26.5}\text{Fe}_{11.5}\text{Re}_{0.5}$ 準結晶の熱伝導度と室温で規格化した熱伝導度. Reを導入することで格子熱伝導度が減少し、 $\kappa(1000\text{K})/\kappa(300\text{K})$ が増大していた.

$1/n$ に減少する材料を組み合わせた場合の熱整流比を計算した. 熱伝導度が温度の m 次関数で記述される場合には, TRR の上限値は $2^{m+1}-1$ になる. 用いる試料が1次関数的な熱伝導度の温度依存性を有していれば, TRR の上限は3であるが, 2次関数的な熱伝導度の温度依存性や3次関数的な温度依存性であれば TRR の上限は7と15にまで増大する. 実用化可能な熱整流材料の創製には, 急激に熱伝導度が増加する材料を用いることが望ましく, 固体熱整流材料の実用化のためには, 今後, そのような熱伝導度を示す材料を開発する必要がある.

§6 おわりに

本稿において, Al-Cu-Fe 準結晶を利用した熱整流材料の動作原理, 設計指針, および, 現状における性能を紹介した. 固体熱整流材料としては最も性能が高いこと(熱整流比 $TRR=2.24$), その動作温度が室温以上であること, また, 比較的安価で環境に優しい材料のみを用いても作製可能であることを考慮すると, 実用化も不可能ではないと判断される. 一方で, 熱浴温度($T_H=900\text{K}$, $T_L=300\text{K}$)や $TRR=2.24$ が熱整流材料のニーズに合致しているとは言い難く, 実用化のためには, さらなる性能向上が必要となることは間違い

ない. また, さらなる性能向上のためには, 新しい構成材料の開発が必須である. Al-Cu-Fe 準結晶は, 筆者が電子伝導機構およびフォノン伝導機構から考察する限り, 現状において最良の熱整流材料の構成材料である. しかし, Al-Cu-Fe 準結晶の利用は, 十分条件ではあるが必要条件ではないことから, 今後, 本稿で紹介したアイデアを下に, 新しい構成材料を用いた固体熱整流材料の開発が行われることを期待している.

【参考文献】

- 1) N. A. Roberts and D. G. Walker: Int. J. Therm. Sci. **50** (2011) 648.
- 2) C. Starr: J. Appl. Phys. **7** (1935) 15.
- 3) M. H. Barzelay, K. N. Tong, and G. F. Holloway: Technical Report **3295** (1955) NACA.
- 4) R. W. Powell, R. P. Tye, and B. W. Jolliffe: Int. J. Heat and Mass Trans. **5** (1962) 897.
- 5) D. V. Lewis and H. C. Perkins: Int. J. Heat and Mass Trans. **11** (1968) 1371.
- 6) P. W. O'Callaghan, S. D. Probert, and A. Jones: Journal of Physics D: Applied Physics **3** (1970) 1352.
- 7) P. F. Stevenson, G. P. Peterson, and L. S. Fletcher: J. Heat Trans. **113** (1991) 30.
- 8) A. M. Clausing: Int. J. Heat and Mass Trans. **9** (1966) 791.
- 9) C. W. Chang, D. Okawa, A. Majumdar, and A. Zettl: Science **314** (2006) 1121.
- 10) H. Tian, D. Xie, Y. Yang, T.-L. Ren, G. Zhang, Y.-F. Wang, C.-J. Zhou, P.-G. Peng, L.-G. Wang, and L.-T. Liu: Scientific Reports **2** (2012) 523.
- 11) M. Peyrard: Europhys Lett. **76** (2006) 49.

- 12) B. Hu, D. He, L. Yang, and Y. Zhang: Phys. Rev. E **74** (2006) 060201.
- 13) W. Kobayashi, Y. Teraoka, and I. Terasaki: Appl. Phys. Lett. **95** (2009) 171905.
- 14) D. Sawaki, W. Kobayashi, Y. Moritomo, and I. Terasaki: Appl. Phys. Lett. **98** (2011) 081915.
- 15) W. Kobayashi, D. Sawaki, T. Omura, T. Katsufuji, Y. Moritomo, and I. Terasaki: Appl. Phys. Express **5** (2012) 027302.
- 16) T. Takeuchi: Z. Krist. **224** (2009) 35.
- 17) T. Takeuchi: J. Elec. Mater. **38** (2009) 1354.
- 18) T. Takeuchi, H. Goto, Y. Toyama, T. Itoh, and M. Mikami: J. Erec. Mater. **40** (2011) 5.
- 19) T. Takeuchi, H. Goto, R. Nakayama, and Y. Terazawa: J. Appl. Phys. **111** (2012) 093517.
- 20) R. Nakayama and T. Takeuchi: Electrically published in J. Elec. Mater (2014), (10.1007/s11664-014-3204-4)
- 21) T. Takeuchi: Sci. Technol. Adv. Mater. (2014), in press.
- 22) D. G. Cahill and R. O. Pohl: Ann. Rev. Phys. Chem. **39** (1988) 93.
- 23) たとえば, P. E. Hopkins, P. Norris, and R. J. Stevens: ASME Trans. J. Heat Transfer **130** (2008) 022401.
- 24) T. Plirdpring, K. Kurosaki, A. Kosuga, T. Day, S. Firdosy, V. Ravi, G. J. Snyder, A. Harnwungmoung, T. Sugahara, Y. Ohishi, H. Muta, and S. Yamanaka: Advanced Materials **24** (2012) 3622.
- 25) たとえば, For example, J. M. Ziman: *Principle of the Theory of Solids*, 2nd ed. (Cambridge: Cambridge University Press, 1972).
- 26) 竹内恒博: 熱電学会誌 **8** No. 1 (2011) 17.
- 27) A. F. Ioffe and A. R. Regel: Prog. Semicond. **4** (1960) 237.
- 28) N. E. Hussey, K. Takenaka, and H. Takagi: Philos. Mag. **84** (2004) 2847.
- 29) T. Takeuchi: Phys. Rev. B **74** (2006) 054206.
- 30) A. Bilusic, Z. Budrovic, A. Smontara, J. Dolinsek, P. C. Canfield, and I. R. Fisher: J. Alloys. Compd. **342** (2002) 413.
- 31) C. Janot: J. Phys. Rev. B **53** (1996) 181.
- 32) T. Nagata, K. Kirihara, and K. Kimura: J. Appl. Phys. **94** (2003) 6560.
- 33) T. Takeuchi, T. Otagiri, T. Kondo, H. Sakagami, U. Mizutani, H. Sato, and R. Asahi: Phys. Rev. B **70** (2004) 144202.
- 34) K. Edagawa and K. Kajiyama: Mat. Sci. Eng. A **294** (2000) 646.
- 35) J. Capps, F. Drymiotis, S. Lindsey, and T. M. Tritt: Philos. Mag. Lett. **90** (2010) 677.
- 36) M. Ohto and K. Tanaka: J. Vac. Sci. Technol. B **14** (1996) 3452.
- 37) M. Fujikane, K. Kurosaki, H. Muta, and S. Yamanaka: J. Alloys Compd. **393** (2005) 299.
- 38) T. Takeuchi: unpublished.

Thermoelectric properties of supersaturated Re solid solution of higher manganese silicides

This content has been downloaded from IOPscience. Please scroll down to see the full text.

View [the table of contents for this issue](#), or go to the [journal homepage](#) for more

Download details:

IP Address: 211.9.37.141

This content was downloaded on 14/05/2016 at 08:52

Please note that [terms and conditions apply](#).



Thermoelectric properties of supersaturated Re solid solution of higher manganese silicides

Akio Yamamoto¹, Swapnil Ghodke², Hidetoshi Miyazaki³, Manabu Inukai³, Yoichi Nishino³, Masaharu Matsunami¹, and Tsunehiro Takeuchi^{1,4,5}

¹Toyota Technological Institute, Nagoya 468-8511, Japan

²Department of Crystalline Materials Science, Nagoya University, Nagoya 464-8603, Japan

³Department of Frontier Materials, Nagoya Institute of Technology, Nagoya 466-8555, Japan

⁴PRESTO, Japan Science and Technology Agency, Chiyoda, Tokyo 102-0076, Japan

⁵GREMO, Nagoya University, Nagoya 464-8603, Japan

Received September 23, 2015; accepted November 26, 2015; published online January 15, 2016

In this study, we developed a higher manganese silicide (HMS) that possesses a high dimensionless figure of merit ZT exceeding unity. HMSs containing a larger amount of Re than its solubility limit were prepared by the liquid quenching technique, and the obtained metastable HMSs showed good thermal stability to enable pulse current sintering at 1240 K. The lattice thermal conductivity was effectively reduced with increasing Re concentration, whereas the electron transport properties were not greatly affected. Consequently, the ZT of p-type HMS increased to 1.04 at 6 at. % Re from 0.4 of the Re-free sample. © 2016 The Japan Society of Applied Physics

Thermoelectric generators (TEG), which are capable of recovering waste heat into useful electricity, have attracted considerable interest given that their use is one of the promising techniques leading to an energy-saving society. The efficiency of energy conversion in thermoelectric generators increases with increasing magnitude of the dimensionless figure of merit, $ZT = S^2\sigma T/(\kappa_{\text{lat}} + \kappa_{\text{el}})$,¹⁾ where S , σ , κ_{el} , and κ_{lat} represent the Seebeck coefficient, electrical conductivity, electron thermal conductivity, and lattice thermal conductivity, respectively. To effectively recover energy from waste heat using TEG, we must develop thermoelectric materials possessing a large ZT . Additionally, the materials used in such TEGs are strongly required to consist solely of cheap and ubiquitous elements in order to reduce both the material cost and environmental pollution.

We consider that higher manganese silicide (HMS) stabilized at MnSi_γ ($1.73 \leq \gamma \leq 1.75$) is one of the most promising candidates for a practical thermoelectric material.^{2–7)} HMS is classified into the group of Nowotny Chimney Ladder Phases,⁸⁾ in which one of the constituent elements constructs square channels and the other element stays in the channels while forming helical chains.

One of the most important characteristics of p-type HMSs is their possession of high magnitudes both of the Seebeck coefficient ($S > 200 \mu\text{V}/\text{K}$) and electrical conduction ($\sigma > 200 \text{ S cm}^{-1}$).⁹⁾ These characteristics naturally lead to a large power factor $PF = S^2\sigma$ exceeding $1.5 \text{ mW m}^{-1} \text{ K}^{-2}$. Unfortunately, however, the lattice thermal conductivity of HMS was reported to stay above $2.5 \text{ W m}^{-1} \text{ K}^{-1}$ and this lattice thermal conductivity prevented us from obtaining a large ZT exceeding 0.5.

In our previous study, we succeeded in effectively reducing the lattice thermal conductivity of the Al–Mn–Si C54 phase and Al–Mn–Si C40 phase without affecting the electron transport properties.^{10–12)} This rather difficult mission was achieved through a small amount of heavy element substitution, with which the electronic structure near the chemical potential was not modified. Notably, HMS possesses very similar local atomic arrangements to those of the C54 phase and C40 phase. This suggests that the lattice thermal conductivity of HMS would be effectively reduced by a small amount of heavy element substitution in the same manner as that in the C54 phase and C40 phase. In this study, therefore, by sub-

stituting a small amount of heavy element, we tried to reduce the lattice thermal conductivity without affecting the electron transport properties of HMS to effectively increase the ZT .

We selected Re as a suitable substitute for Mn in HMS because Re substitution for Mn greatly reduces the lattice thermal conductivity without affecting the electron transport properties in the C54 phase, which also belongs to the Nowotny Chimney Ladder Phases and possesses similar local atomic arrangements to those of HMS. Notably, Re is in the same column as Mn in the periodic table, and almost the same carrier concentration was expected even with a finite amount of Re substitution for Mn. Unfortunately, however, the phase diagram reported previously¹³⁾ showed a very low solubility limit of Re in HMS, that is less than 2.5 at. %. Since large amounts of heavy elements should be required to effectively reduce the lattice thermal conductivity, we should find special techniques to increase the solubility of Re in HMS.

Chen et al. prepared HMSs containing 6.4 at. % Re by the mechanical alloying (MA) technique.¹⁴⁾ The main phase in their samples containing 1.4–6.4 at. % Re was HMS, but a large amount of ReSi_2 was precipitated as the secondary phase. This finding indicates that the mechanical alloying technique is not suitable for preparing a supersaturated Re solid solution of HMSs.

More recently, Ghodke et al. have reported that the solubility limit of W in HMS, which is less than 1 at. % under the thermodynamically stable condition, expanded to 3.6 at. % when they used the liquid quenching technique.¹⁵⁾ Moreover, their HMS containing 3.6 at. % W showed good thermal stability without any precipitation of secondary phases up to 1000 K. We expected this technique to be applicable even for Re substitution for Mn in HMS, and endeavored to prepare samples by the liquid quenching technique.

Powders of pure elements, 99.9% Mn, 99.9% Si, and 99.99% Re, were mixed together using an alumina mortar and pestle, and pressed into pellets at room temperature. The mother ingots were prepared by melting the pellets in an arc furnace. To obtain homogeneous samples, the alloys were repeatedly melted in the arc furnace with changing the position upside down. The prepared ingots were rapidly quenched into ribbons by the liquid quenching technique using a copper wheel of 200 mm diameter rotating at 4500 rpm. The arc-melting process and the liquid quenching process were

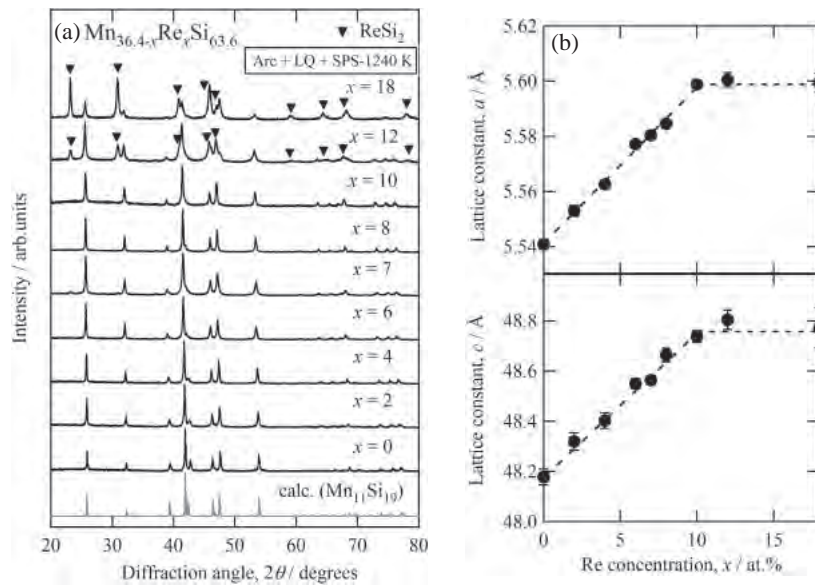


Fig. 1. (a) XRD patterns of $\text{Mn}_{36.4-x}\text{Re}_x\text{Si}_{63.6}$ ($x = 0, 2, 4, 6, 7, 8, 10, 12,$ and 18), prepared by arc melting, liquid quenching (LQ), and sintering (SPS) at 1240 K, at the nominal composition. (b) Re concentration dependence of the lattice constants of $\text{Mn}_{36.4-x}\text{Re}_x\text{Si}_{63.6}$.

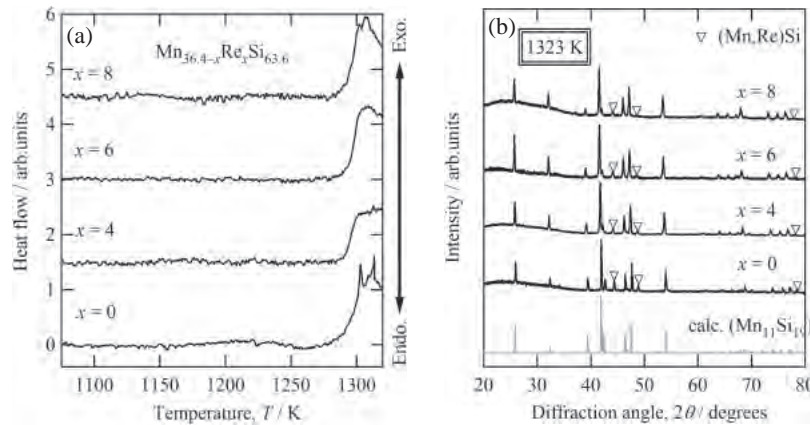


Fig. 2. (a) DTA curves of $\text{Mn}_{36.4-x}\text{Re}_x\text{Si}_{63.6}$ ($x = 0, 4, 6,$ and 8) in Ar atmosphere. The curves represent a heating cycle. (b) XRD patterns at $x = 0, 4, 6,$ and 8 measured at 300 K after DTA measurement.

performed under a pressurized argon gas atmosphere. The quenched, ribbon-shaped samples were ground into powders using an alumina mortar and pestle, and the obtained powders were sintered at 1240 K for 10 min under the pressure of 50 MPa in vacuum atmosphere by the pulsed current sintering technique.

The phases involved in samples were identified by conventional powder X-ray diffraction (XRD) measurements using the $\text{Cu-K}\alpha$ radiation source and a Bragg–Brentano-type diffractometer equipped in Bruker D8 Advance. The density of samples was evaluated by the Archimedes method, and it was confirmed that all the sintered samples were densely packed with more than 96% of the theoretical density. To investigate the grain size and composition of samples, we also employed scanning electron microscopy (SEM) and energy dispersive X-ray spectroscopy (EDX) measurements using JEOL JSM-6330F and JED-2140GS, respectively. To investigate the decomposition temperature of Re-substituted HMSs, differential thermal analysis (DTA) was carried out from 300 to 1340 K in Ar atmosphere using Rigaku TG8121.

The Seebeck coefficient and electrical resistivity of samples were measured in vacuum atmosphere by the steady-state method and the four-probe method, respectively, using ULVAC-Riko ZEM-3 M8. The thermal conductivity was measured in the temperature range from 300 to 1040 K by the laser-flash method using NETZSCH LFA457.

The powder XRD patterns and the lattice constants of quenched ribbon samples prepared at the nominal compositions of $\text{Mn}_{36.4-x}\text{Re}_x\text{Si}_{63.6}$ ($0 \leq x \leq 18$) are shown in Fig. 1. No evidence of an impurity phase was observed up to 10 at. % Re, whereas the samples prepared at 12 and 18 at. % Re clearly showed diffraction peaks from the secondary phase, ReSi_2 . The lattice constants monotonically increased with increasing Re concentration at $x \leq 10$, but became constant at $10 \leq x \leq 18$. Thus, the maximum solid solubility limit of Re in HMS prepared in our currently employed process was determined to be ~ 10 at. %.

The DTA curves observed for the $\text{Mn}_{36.4-x}\text{Re}_x\text{Si}_{63.6}$ samples ($x = 0, 4, 6, 8$) are shown in Fig. 2(a). A broad exothermic peak was observed for all the samples in the temperature range from 1273 to 1320 K. The precipitation of

Table I. Compositions obtained from EDX measurement.

Nominal comp.	Mn _{36.4} Si _{63.6}	Mn _{32.4} Re ₄ Si _{63.6}	Mn _{30.4} Re ₆ Si _{63.6}	Mn _{28.4} Re ₈ Si _{63.6}
Analyzed comp.				
Position #1	Mn _{35.8} Si _{64.2}	Mn _{32.0} Re _{4.0} Si _{64.0}	Mn _{30.5} Re _{6.2} Si _{63.3}	Mn _{28.3} Re _{8.2} Si _{63.5}
Position #2	Mn _{35.4} Si _{64.6}	Mn _{32.4} Re _{4.1} Si _{63.5}	Mn _{30.1} Re _{6.1} Si _{63.8}	Mn _{28.7} Re _{8.0} Si _{63.3}
Position #3	Mn _{36.8} Si _{63.2}	Mn _{32.7} Re _{3.9} Si _{63.4}	Mn _{29.9} Re _{5.8} Si _{64.3}	Mn _{27.7} Re _{7.6} Si _{64.7}
Position #4	Mn _{36.6} Si _{63.4}	Mn _{32.8} Re _{4.1} Si _{63.1}	Mn _{30.2} Re _{5.9} Si _{63.9}	Mn _{28.8} Re _{8.0} Si _{63.2}
Averaged value ^{a)}	Mn _{36.2±0.6} Si _{63.8±0.6}	Mn _{32.5±0.4} Re _{4.0±0.1} Si _{63.5±0.4}	Mn _{30.2±0.3} Re _{6.0±0.2} Si _{63.8±0.4}	Mn _{28.4±0.5} Re _{7.9±0.3} Si _{63.7±0.7}

a) The error values indicate the largest decimal place difference of measured composition from the averaged value.

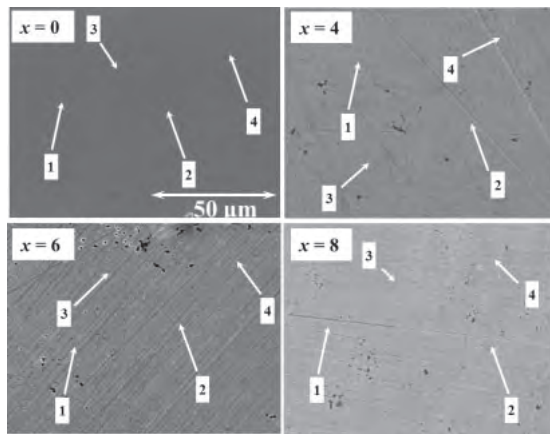


Fig. 3. SEM images obtained for the samples prepared at the nominal compositions of Mn_{36.4-x}Re_xSi_{63.6} ($x = 0, 4, 6,$ and 8). Positions 1, 2, 3, and 4 were used for the EDX analyses and the average results are shown in Table I.

manganese monosilicide occurred during this exothermic reaction. This was clearly confirmed in the XRD patterns of samples annealed at 1320 K [Fig. 2(b)].

The previously reported phase diagram suggested that the HMS containing more than 2.5 at. % Re was supposed to be metastable, but the present thermal analyses showed no critical difference in the DTA curve between the samples at $x \leq 2.5$ and those at $x > 2.5$. This experimental finding presumably indicates that the surface energy of HMS is lower than that of competitive phases, and the small size of grains produced by the liquid quenching technique stabilizes the HMS even with a large amount of Re exceeding 2.5 at. %. Further investigation with different grain sizes is required to investigate in more detail the stabilization mechanism of HMS containing Re atoms.

It should be noted that the decomposition temperature of supersaturated Re solid solution of HMS (1320 K) is much higher than that used for the sintering of HMS, and that helped us to obtain the bulk samples containing more than 2.5 at. % Re. Indeed, we did not observe any precipitation of impurity phases in the sintered samples of Mn_{36.4x}Re_xSi_{63.6} ($x \leq 10$).

Figure 3 shows the SEM image of Mn_{36.4-x}Re_xSi_{63.6}. Although the number of voids slightly increased with increasing Re concentration, no evidence of secondary phase was confirmed in the SEM images, consistent with the XRD measurement. We measured the composition at several different positions for all the samples, and the resulting values are summarized in Table I together with the averaged values. The error values shown for the averaged composition indicate the

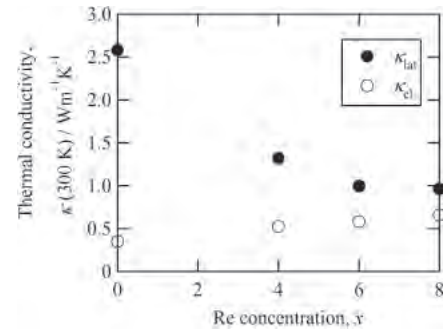


Fig. 4. Re concentration dependences of lattice thermal conductivity κ_{lat} ($= \kappa_{\text{measured}} - \kappa_{\text{el}}$) and electron thermal conductivity κ_{el} ($= L_0\sigma T - S^2\sigma$) for Mn_{36.4-x}Re_xSi_{63.6} ($x = 0, 4, 6,$ and 8) at 300 K calculated using Wiedemann-Franz law.

largest decimal place difference in the measured composition from the averaged value. Notably all the compositions determined at different positions stayed within the error of 0.7 at. % regardless of Re concentration. Furthermore, the averaged composition of each sample showed very good agreement with the nominal one. This result unambiguously indicated that the homogeneous samples were successfully obtained.

The Re concentration dependences of the lattice thermal conductivity κ_{lat} and the electron thermal conductivity κ_{el} of Mn_{36.4-x}Re_xSi_{63.6} ($x = 0, 4, 6, 8$) at 300 K are shown in Fig. 4. We used $\kappa_{\text{el}} = L_0\sigma T - S^2\sigma$ to roughly estimate the electron thermal conductivity. The second term $-S^2\sigma$ is generally small and ignored in metallic samples, but it is not negligibly small when the power factor is large, such as those in practical thermoelectric materials. It was clearly confirmed from the deduced κ_{el} and κ_{lat} that the lattice thermal conductivity at 300 K drastically decreased with increasing Re concentration, and eventually reached a small value of less than 1.0 W m⁻¹ K⁻¹ in the sample containing more than 6 at. % Re.

The temperature dependence of the thermoelectric properties of Mn_{36.4-x}Re_xSi_{63.6} ($x = 0, 4, 6, 8$) is shown in Fig. 5. The measured thermal conductivities drastically decreased with increasing x owing to the reduction in the lattice thermal conductivity. The absolute Seebeck coefficients, on the other hand, were kept almost unchanged over the whole range of measurement until the Re concentration reached 6 at. %, but decreased with increasing x at $x > 6$. The electrical resistivity slightly decreased with increasing x over the whole temperature range of measurement even at $x > 6$. The drastic reduction in lattice thermal conductivity together with the moderate reduction in electrical resistivity with the almost unchanged Seebeck coefficient naturally led to an effective increase in ZT . Consequently, the ZT of the p-type Mn_{30.4-}

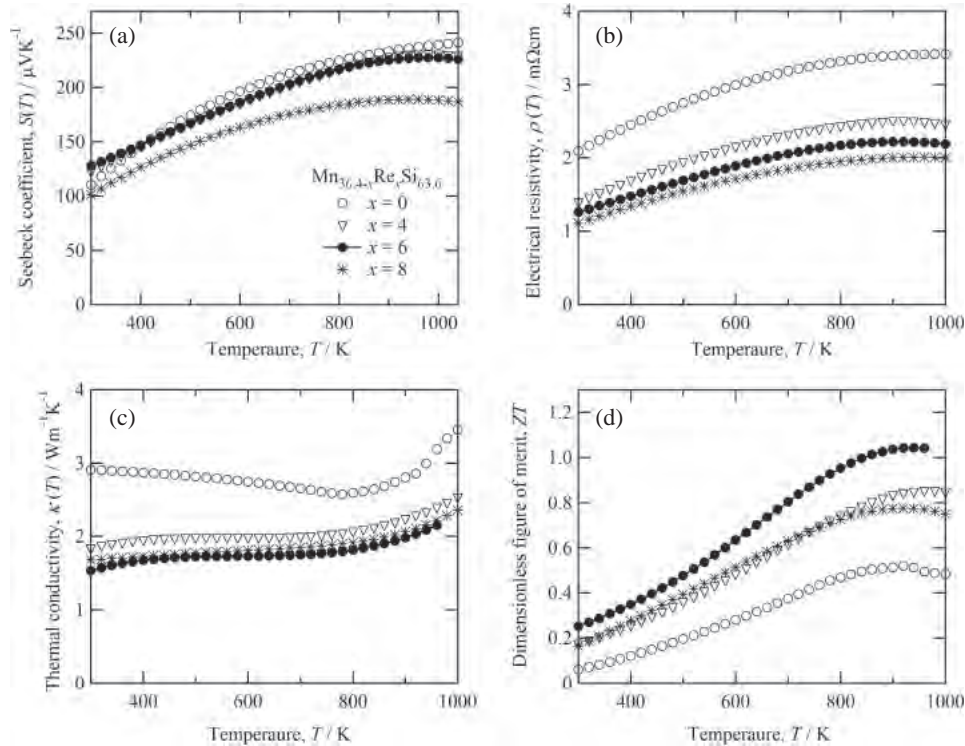


Fig. 5. Temperature dependences of thermoelectric properties [(a) Seebeck coefficient, (b) electrical resistivity, and (c) thermal conductivity] for $\text{Mn}_{30.4-x}\text{Re}_x\text{Si}_{63.6}$ ($x = 0, 4, 6,$ and 8). (d) Temperature dependence of dimensionless figure of merit ZT .

$\text{Re}_{6.0}\text{Si}_{63.6}$ HMS was increased to ~ 2.1 times larger than that of the Re-free sample, and it reached 1.04 at 920 K.

The ZT observed for the present $\text{Mn}_{30.4}\text{Re}_{6.0}\text{Si}_{63.6}$ HMS is comparable to that of TAGS ($= [\text{AgSbTe}]_{0.15}[\text{GeTe}]_{0.85}$) at 900 K,^{16,17} but the material cost of $\text{Mn}_{30.4}\text{Re}_{6.0}\text{Si}_{63.6}$ HMS is much cheaper than that of TAGS. The roughly estimated cost effectiveness (elements cost/maximal efficiency) of the present $\text{Mn}_{30.4}\text{Re}_{6.0}\text{Si}_{63.6}$ HMS is about 70% lower than that of TAGS. This value strongly suggests that p-type $\text{Mn}_{30.4}\text{Re}_{6.0}\text{Si}_{63.6}$ HMS is one of the candidates for practical thermoelectric materials.

Before finishing this discussion, we shall comment on the further increase in ZT for both n-type and p-type HMSs. The reduction in the Seebeck coefficient at $x > 8$ would be caused by the impurity states near the chemical potential.^{18–20} At small values of x , the effects of these states were negligible but became obvious at high values of x . To avoid the reduction of $|S|$, we propose the use of W together with Re, because the energy of impurity states varies with elements and a smaller amount of W would not seriously affect the transport properties of HMS, similarly to those of the Al–Mn–Si C40 phase.¹² This method would lead to an increase in ZT for both n- and p-type HMS.

In this study, by adopting the liquid quenching method, we prepared HMS with a larger amount of Re than the thermodynamical solubility limit. We found that the thermal stability of the metastable HMS was surprisingly good to be sintered at 1223 K, and that bulk samples with high density exceeding 96% of the theoretical one were successfully obtained. The lattice thermal conductivity of HMS was effectively reduced by the Re substitution for Mn, while the power factor was slightly increased. Consequently, we obtained a bulk p-type thermoelectric material, $\text{Mn}_{30.4}\text{Re}_{6.0}\text{Si}_{63.6}$, possessing $ZT = 1.04$ at 920 K.

Acknowledgments This work was conducted under the financial support of JSPS KAKENHI Grant Numbers 23360278 and 26630332. T. Takeuchi was supported financially by JST PRESTO.

- 1) A. F. Ioffe, *Semiconductor Thermoelements and Thermoelectric Cooling* (Infosearch, London, 1957) p. 1.
- 2) U. Gottlieb, A. Supuce, B. Lambert-Andron, and O. Laborde, *J. Alloys Compd.* **361**, 13 (2003).
- 3) O. Schwomma, H. Nowotny, and A. Wittman, *Monatsh. Chem.* **94**, 681 (1963).
- 4) H. W. Knott, M. H. Mueller, and L. Heaton, *Acta Crystallogr.* **23**, 549 (1967).
- 5) G. Zwilling and H. Nowotny, *Monatsh. Chem.* **104**, 668 (1973).
- 6) T. Itoh and M. Yamada, *J. Electron. Mater.* **38**, 925 (2009).
- 7) S. A. Barczak, R. A. Downie, S. R. Popuri, R. Decourt, and J. W. G. Bos, *J. Solid State Chem.* **227**, 55 (2015).
- 8) D. C. Fredrickson, S. Lee, R. Hoffmann, and J. Lin, *Inorg. Chem.* **43**, 6151 (2004).
- 9) Y. Miyazaki, Y. Saito, K. Hayashi, K. Yubuta, and T. Kajitani, *Jpn. J. Appl. Phys.* **50**, 035804 (2011).
- 10) A. Yamamoto and T. Takeuchi, *J. Electron. Mater.* **41**, 1743 (2012).
- 11) A. Yamamoto, H. Miyazaki, and T. Takeuchi, *J. Appl. Phys.* **115**, 023708 (2014).
- 12) A. Yamamoto, H. Miyazaki, M. Inukai, Y. Nishino, and T. Takeuchi, *Jpn. J. Appl. Phys.* **54**, 071801 (2015).
- 13) P. Villars, A. Prince, and H. Okamoto, *Handbook of Ternary Alloy Phase Diagrams* (ASM International, Materials Park, OH, 1995).
- 14) X. Chen, S. N. Girard, F. Meng, E. Lara-Curzio, S. Jin, J. B. Goodenough, J. Zhou, and L. Shi, *Adv. Energy Mater.* **4**, 14 (2014).
- 15) S. Ghodke, N. Hiroishi, A. Yamamoto, H. Ikuta, M. Matsunami, and T. Takeuchi, submitted to *J. Electron. Mater.*
- 16) E. A. Skrabek and D. S. Trimmer, in *CRC Handbook of Thermoelectrics*, ed. D. M. Rowe (CRC Press, Boca Raton, FL, 1995) p. 267.
- 17) A. Singh, S. Bhattacharya, C. Thinakaran, D. K. Aswal, S. K. Gupta, J. V. Yakhmi, and K. Bhanumurthy, *J. Phys. D* **42**, 015502 (2009).
- 18) T. Takeuchi, *Mater. Trans.* **50**, 2359 (2009).
- 19) T. Takeuchi, Y. Toyama, and A. Yamamoto, *Mater. Trans.* **51**, 421 (2010).
- 20) A. Yamamoto, K. Kitahara, H. Miyazaki, M. Inukai, and T. Takeuchi, to be published in Proc. 11th Int. Conf. Ceramic Materials and Components for Energy and Environmental Applications, 2015.

Development of Thermoelectric Materials Consisting Solely of Environmental Friendly Elements

Tsunehiro Takeuchi^{1,2,3}, Akio Yamamoto¹ and Swapnil Ghodke⁴

¹Toyota Technological Institute, Nagoya 468–8511, Japan

²PRESTO-JST, Tokyo 102–0076, Japan

³Green Mobility Collaborative Research Center, Nagoya University, Nagoya 464–8603, Japan

⁴Department of Crystalline Materials Science, Nagoya University, Nagoya 464–8603, Japan

A guiding principle for developing practical thermoelectric materials was constructed on the basis of simulations of thermoelectric properties using linear response theory. Al-Mn-Si C54-phase, Al-Mn-Si C40-phase and higher manganese silicide (HMS), all of which consist solely of cheap, environmentally friendly elements, were selected using the guiding principle. The validity of the strategy to develop practical thermoelectric material was clearly proved by our newly prepared HMS possessing a dimensionless figure of merit exceeding unity.

[doi:10.2320/matertrans.MF201610]

(Received January 6, 2016; Accepted February 25, 2016; Published April 15, 2016)

Keywords: thermoelectrics, electronic structure, electron transport properties, thermal transport properties

1. Introduction

Recently, thermoelectric generators have attracted considerable interest because of their ability in recovering energy from waste heat. Development of high-performance thermoelectric materials consisting solely of environment-friendly cheap-elements would lead us to the sustainable society in which all energy sources are effectively used.

Practical thermoelectric materials had been generally developed using degenerate semiconductors¹⁾ because the electronic structure of degenerate semiconductor is suitable for large magnitude of Seebeck coefficient and metallic electrical conduction, both of which together with low thermal conductivity are the necessities of high-performance thermoelectric materials. It would be natural to consider that the highly sophisticated theories of semiconductor developed for LSI, LED, Laser, solar cell, etc. could be applicable for the thermoelectric semiconductors. Indeed, the electron transport properties of thermoelectric materials were analyzed using the semiconductor-theory²⁾ in which carrier concentration, carrier mobility, and effective mass were employed as controlling parameters.

We should stress here, however, that the use of semiconductor-theory is often inappropriate for explaining the electron transport properties of thermoelectric materials, because the semiconductor-theory generally assumes the parabolic shape of energy-momentum ($\varepsilon - \mathbf{k}$) dispersion whereas the $\varepsilon - \mathbf{k}$ dispersion of thermoelectric materials is not well described with the parabolic shape near the chemical potential. Indeed, temperature dependence of Seebeck coefficient observed for practical thermoelectric materials cannot be often accounted for by the semiconductor-theory. This fact definitely indicates that the persistent use of carrier concentration, carrier mobility, and effective mass for analyzing electron transport properties would not lead us to the development of highly sophisticated thermoelectric materials.

The problem about the complicated electronic structure of thermoelectric materials is easily overcome by knowing the detailed information about the electronic structure near the

chemical potential. The first principles calculations and the highly developed experimental techniques, such as high-resolution photoemission spectroscopy, could greatly help us to obtain the reliable information about the electronic structure. In this paper, therefore, a guiding principle for developing high performance thermoelectric materials is proposed in terms of electronic structure, and its validity is demonstrated by showing the successfully developed high-performance thermoelectric materials.

2. Guiding Principle for Developing High-Performance Thermoelectric Materials

The electron transport properties of solids are usually calculated in the context of linear response theory, and electrical conductivity $\sigma(T)$, Seebeck coefficient $S(T)$, and electron thermal conductivity $\kappa_{el}(T)$ are expressed as eqs. (1)–(3).^{3–5)}

$$\sigma(T) = \int \sigma(\varepsilon, T) \left\{ -\frac{\partial f_{FD}(\varepsilon, T)}{\partial \varepsilon} \right\} d\varepsilon \quad (1)$$

$$S(T) = -\frac{1}{|e|T} \frac{\int \sigma(\varepsilon, T)(\varepsilon - \mu) \left\{ -\frac{\partial f_{FD}(\varepsilon, T)}{\partial \varepsilon} \right\} d\varepsilon}{\int \sigma(\varepsilon, T) \left\{ -\frac{\partial f_{FD}(\varepsilon, T)}{\partial \varepsilon} \right\} d\varepsilon} \quad (2)$$

$$\kappa_{el}(T) = \frac{1}{e^2 T} \int \sigma(\varepsilon, T)(\varepsilon - \mu)^2 \left\{ -\frac{\partial f_{FD}(\varepsilon, T)}{\partial \varepsilon} \right\} d\varepsilon - \frac{1}{e^2 T} \frac{\left\{ \int \sigma(\varepsilon, T)(\varepsilon - \mu) \left\{ -\frac{\partial f_{FD}(\varepsilon, T)}{\partial \varepsilon} \right\} d\varepsilon \right\}^2}{\int \sigma(\varepsilon, T) \left\{ -\frac{\partial f_{FD}(\varepsilon, T)}{\partial \varepsilon} \right\} d\varepsilon} \quad (3)$$

Here $\sigma(\varepsilon, T)$, e , $f_{FD}(\varepsilon, T)$, and μ represent spectral conductivity, unit charge of electron, Fermi-Dirac distribution function, and chemical potential, respectively.

The performance of thermoelectric materials is generally measured by the dimensionless figure of merit ZT ($= S^2 \sigma T / \kappa$).¹⁾ By knowing that the thermal conductivity is sum

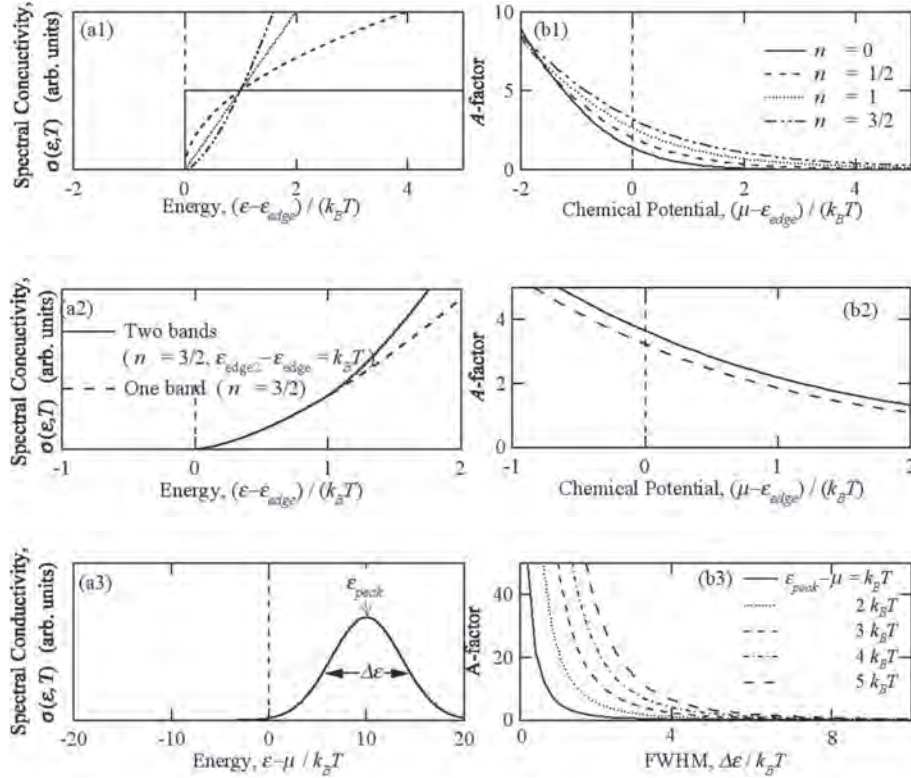


Fig. 1 (a) Model of spectral conductivity and (b) $A = S^2\sigma T/\kappa_{el}$ calculated using eqs. (1)–(3). The model 1 consists of one band, and the spectral conductivity is represented by $\sigma(\epsilon, T) = C(\epsilon - \epsilon_{edge})^n$. At a given chemical potential, A becomes larger with large number of n , and A is getting larger when the chemical potential is located in the band gap. The model 2 consists of 2 bands with $n = 3/2$. One of the bands is located $1k_B T$ above the others. The magnitude of A definitely becomes larger with two bands. The spectral conductivity of model 3 consists of a single gauss function, and the magnitude of A is calculated with two parameters: FWHM and peak energy.

of electronic contribution and lattice contribution as $\kappa = \kappa_{el} + \kappa_{lat}$, we transformed the equation of ZT into a slightly modified form,

$$ZT = \frac{S^2\sigma T}{\kappa_{el}} \left(\frac{1}{1 + \kappa_{lat}/\kappa_{el}} \right), \quad (4)$$

Two factors can be extracted from eq. (4). The first factor, $A = S^2\sigma T/\kappa_{el}$, is unambiguously calculated using eqs. (1)–(3) provided that spectral conductivity and chemical potential are obtained. Notably, the magnitude of A is less sensitive to the scattering phenomena because relaxation time τ , which generally possesses a very weak energy dependence in the narrow energy range of few $k_B T$ near the chemical potential, so τ comes out from the integrands and vanishes in the calculation of A .⁶⁾ It is also very important to note that the magnitude of second factor $B = 1/(1 + \kappa_{lat}/\kappa_{el})$ always stays below unity and increases with decreasing $(\kappa_{lat}/\kappa_{el})$. These facts indicate that the magnitude of A represents the largest value of ZT obtainable for the given electronic structure. It is explained, in other words, that for developing materials possessing a desired value of $ZT = a$, we should employ the materials possessing a value of A much larger than a .

We calculated the magnitude of A as a function of chemical potential using several different models of degenerate semiconductor possessing an energy gap near the chemical potential. As a consequence of calculations shown in Fig. 1, we found that the magnitude of A becomes extremely large when the chemical potential is located in the energy gap. This seemingly unusual situation is realized even for degenerate

semiconductors at high temperatures provided that the Fermi energy is located between band edge and a large peak existing in the electronic density of states near the band edge. In order to confirm this fact, the temperature dependence of chemical potential was calculated for two different models: single band model and two-band model consisting of wide and narrow bands. The Fermi energy was located so as to become the same carrier concentration in the both models.

If we assume that the spectral-conductivity is described as $\sigma(\epsilon, T) = C(\epsilon - \epsilon_{edge})^n$, the factor A at a given chemical potential possesses a larger value with the larger value of exponent n . The magnitude of constant parameter C , on the other hand, does not contribute to the variation of A , but affects the magnitude of B ; a large magnitude of C leads to an increase of B through the reduction of $(\kappa_{lat}/\kappa_{el})$. It would be also very important to note that the magnitude of B is further increased if the lattice thermal conductivity is greatly decreased by the complex structure⁷⁾, rattling mode⁸⁾, and/or anharmonic oscillation of lattice vibration.⁹⁾

On the basis of facts described above, we propose the necessities of electronic structure for high-performance thermoelectric materials possessing a large magnitude of A ; (a) large band gap exceeding $10 k_B T_A$ where T_A indicates the temperature of practical applications, (b) a large peak in electronic density of states staying at a few $k_B T_A$ apart from the edge of energy gap, and (c) multiple band existing near the band edge in the energy range where the electrons contribute the electrical properties. The condition (a) prohibits the reduction of Seebeck coefficient in association with bi-polar diffusion ef-

fect, and the condition (b) allows the chemical potential to move drastically with increasing temperature. The condition (c) is important for the large magnitude of Seebeck coefficient. The materials possessing these characteristics in their electronic structure must exhibit a large magnitude of A with an appropriate Fermi energy.

If the materials possessing the conditions (a)–(c) are further characterized by (e) the complex structure⁷⁾, (f) rattling mode⁸⁾, and/or (g) anharmonic oscillation of lattice vibration⁹⁾, the magnitude of ZT should be greatly increased through a large magnitude of $B = 1/(1 + \kappa_{\text{lat}}/\kappa_{\text{el}})$. Nevertheless, it would be very difficult to find such an ideal material possessing all the required conditions.

We should mention here that even without using the conditions (e)–(g) the magnitude of B could be effectively increased using the partial substitution of elements that have a large difference in atomic mass from that of constituent elements. We are not seriously concerned about the effect of disordering on the electron mean free path. In many thermoelectric materials, the conduction electrons stay near the strong scattering limit^{10,11)} due to the small Fermi surface and the chemical disordering introduced for carrier doping, because the long Fermi wavelength makes the conduction electrons near the Fermi level easily lose the coherence even under the small amount of impurity elements. In such a condition, the mean free path of electrons cannot be further shortened with the additionally introduced disordering, meanwhile the phonon mean free path, that is generally kept long in the degenerate semiconductors, should be greatly reduced by the partial substitution of elements possessing significantly different atomic mass.^{12–14)} Therefore, if impurity states are not produced near the chemical potential at the element substitution, the lattice thermal conductivity will be greatly reduced without seriously affecting the electron transport properties.

3. Al-Mn-Si C54-Phase (Si_2Ti Structure) and C40-Phase (CrSi_2 Structure)

According to the guiding principle described above, we selected two intermetallic compounds, Al-Mn-Si C54-phase (Si_2Ti structure, $oF24$) and Al-Mn-Si C40-phase (CrSi_2 structure, $hP9$) stabilized at around $\text{Al}_{32}\text{Mn}_{34}\text{Si}_{34}$ ¹⁵⁾ and $\text{Al}_{27.5}\text{Mn}_{33.0}\text{Si}_{39.5}$ ¹⁶⁾, respectively. Both materials are characterized by the two-dimensional honeycomb lattice consisting of Al and Si with Mn at the center of hexagon, and the two-dimensional planes are stacked with four different positions in C54-phase and three positions in C40-phase. The similarity in local atomic arrangements naturally leads to the similarity in electronic density of states as shown in Fig. 2. It is clearly confirmed that these selected materials possess the characteristics of electronic structure (a)–(c), which are the necessities of high-performance thermoelectric materials.

We found that these intermetallic compounds characterized by non-toxic, abundant constituent elements indeed possess a large magnitude of Seebeck coefficient $|S| > 200 \mu\text{VK}^{-1}$, metallic electrical conduction with a relatively low values of electrical resistivity $\rho < 10 \text{ m}\Omega\text{cm}$, and consequently large magnitude of A exceeding 2.^{15–17)} The magnitude of power factor $PF = S^2\sigma$ reaches $2.1 \text{ mWm}^{-1}\text{K}^{-2}$ at 500 K for n-type $\text{Al}_{33.0}\text{Mn}_{34.0}\text{Cr}_{1.0}\text{Si}_{30.0}$ C54-phase and 1.1 at 440 K for n-type

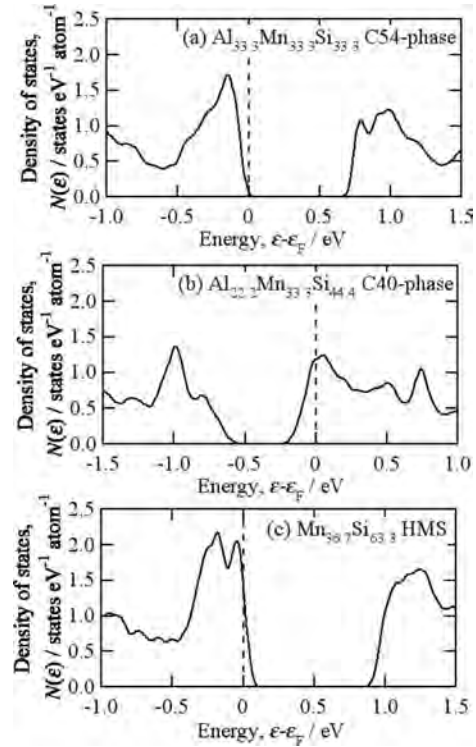


Fig. 2 Electronic density of states of (a) Al-Mn-Si C54-phase, (b) Al-Mn-Si C40-phase, and (c) HMS. A relatively wide band gap is formed in all the compounds. The peaks near the band edge indicate that these materials possess large magnitude of Seebeck coefficient, and rather complicated energy dependence means that the multiple bands near the band edges. The calculations were performed with FLAPW-GGA method.

$\text{Al}_{27.5}\text{Mn}_{31.0}\text{Cr}_{2.0}\text{Si}_{39.5}$ C40-phase. The large magnitude of power factor observed for the both compounds indicates that the conditions (a)–(c) of electronic structure are usable for easily finding materials possessing electron transport properties suitable for practical thermoelectric material.

Despite the electron transport properties suitable for thermoelectric materials, the large lattice thermal conductivity, $10 \text{ Wm}^{-1}\text{K}^{-1}$ of C54-phase¹⁷⁾ and $4.2 \text{ Wm}^{-1}\text{K}^{-1}$ of C40-phase¹⁶⁾ prevented us from obtaining a large magnitude of dimensionless figure of merit ZT . The magnitude of ZT was, hence, limited to less than 0.15. Note here that the difference of lattice thermal conductivity between C54-phase and C40-phase would be related to the number of atoms in the unit structure, $N = 6$ of C54-phase and 9 of C40-phase, because larger number of N naturally leads to enhanced umklapp process of phonon scatterings, reduced mean group velocity of phonons, and consequently to small magnitude of lattice thermal conductivity.⁷⁾

For effectively reducing lattice thermal conductivity of these compounds, we employed small amount of element substitutions using the heavy elements that do not produce any impurity states near the chemical potential at the substitution. The cluster calculations suggested us that (Re + Ru) and W produce no impurity states near the chemical potential when these elements were substituted for Mn in C54-phase and C40-phase, respectively.^{16,17)} The experimentally observed thermoelectric properties are shown in Fig. 3. The lattice thermal conductivity was reduced into $2.9 \text{ Wm}^{-1}\text{K}^{-1}$ for C54-phase and $1.9 \text{ Wm}^{-1}\text{K}^{-1}$ for C40-phase when small

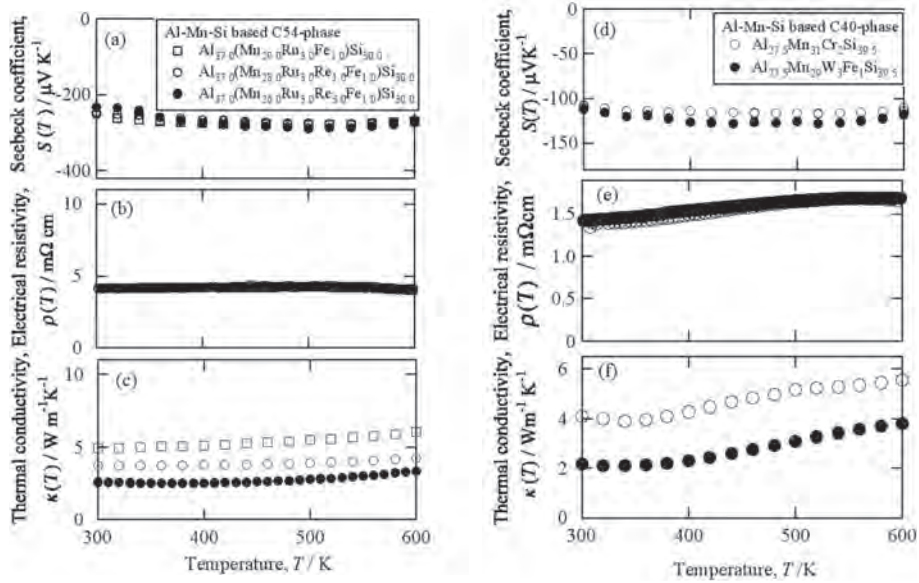


Fig. 3 (a) Seebeck coefficient. (b) electrical resistivity, and (c) thermal conductivity of Al-Mn-Si based C54-phase.¹⁷⁾ Those for Al-Mn-Si C40-phase were plotted in (d)–(f).¹⁶⁾ With increasing concentration of heavy elements, the lattice thermal conductivity were greatly reduced while the electron transport properties were essentially unchanged. Very small increase of scattering provability was found a in the electrical resistivity of Al-Mn-Si based C40-phase low temperatures where temperature coefficient of resistivity (*TCR*) was kept positive.

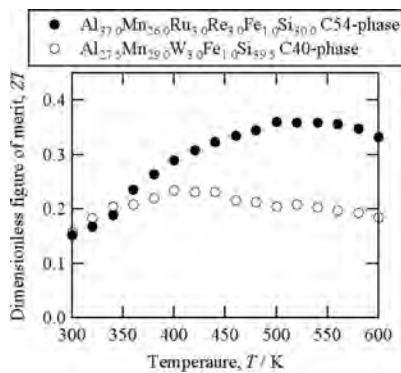


Fig. 4 Dimensionless figure of merit observed for $\text{Al}_{37.0}\text{Mn}_{26.0}\text{Ru}_{3.0}\text{Re}_{3.0}\text{Fe}_{1.0}\text{Si}_{30.0}$ C54-phase¹⁷⁾ and $\text{Al}_{27.5}\text{Mn}_{29.0}\text{W}_{3.0}\text{Fe}_{1.0}\text{Si}_{39.5}$ C40-phase.¹⁶⁾

amount of heavy elements were introduced in the samples. In sharp contrast to the large reduction in lattice thermal conductivity, the electron transport properties were essentially kept unchanged. The consequently obtained *ZT* was plotted as a function of temperature in Fig. 4. The maximum value of *ZT* was increased up to 0.38 (n-type) at 540 K and 0.24 (n-type) at 440 K for $\text{Al}_{37.0}\text{Mn}_{26.0}\text{Ru}_{3.0}\text{Re}_{3.0}\text{Fe}_{1.0}\text{Si}_{30.0}$ C54-phase¹⁷⁾ and $\text{Al}_{27.5}\text{Mn}_{29.0}\text{W}_{3.0}\text{Fe}_{1.0}\text{Si}_{39.5}$ C40-phase¹⁶⁾, respectively.

Although we succeeded in increasing *ZT* for both C54-phase and C40-phase, the resulting values of *ZT* were still smaller than unity mainly because the energy gap was smaller than that estimated from the first principles calculations. The difference in width of energy gap between the experiments and calculations was confirmed by comparing the temperature dependence of Seebeck coefficient. Figure 5 shows the temperature dependence of Seebeck coefficient obtained by both experiments and calculations. The experimentally obtained magnitude of Seebeck coefficient $|S|$ showed good

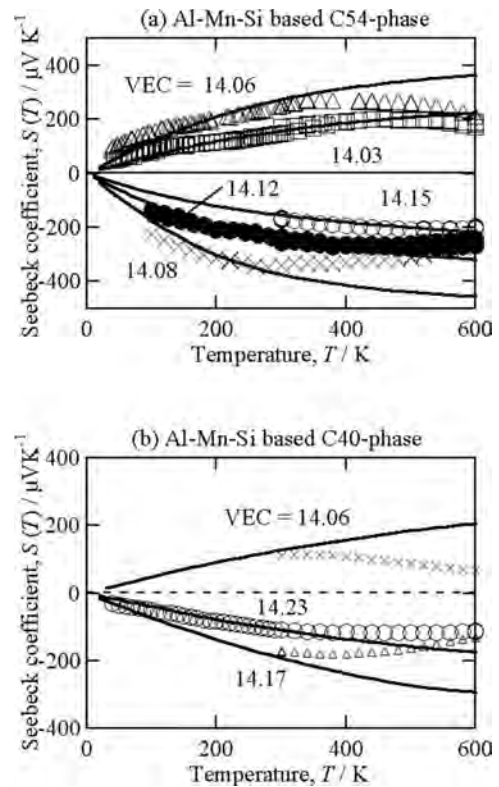


Fig. 5 Measured (markers) and calculated (solid lines) Seebeck coefficient of Al-Mn-Si based (a) C54-phase and (b) C40-phase. At low temperatures, the measured data showed very good consistency with the calculated one, but its magnitude becomes smaller at high temperature because of the bipolar diffusion effects. This fact definitely indicates that the calculated energy gap is overestimated presumably due to the hypothetical ordering between Al and Si used for the calculations.

agreement with the calculated ones at low temperatures, but became definitely smaller at high temperature regardless of the carrier concentrations. The reduction of $|S|$ at high tem-

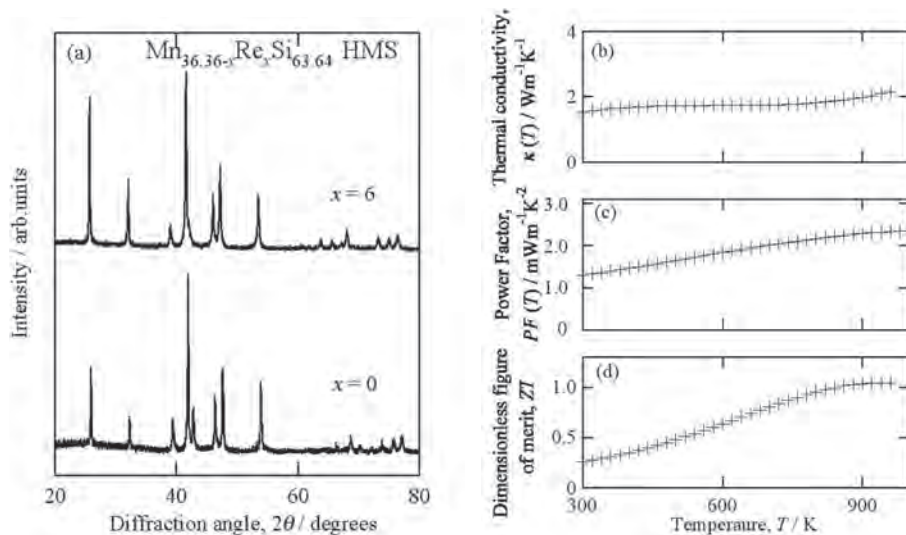


Fig. 6 (a) Powder XRD patterns of $\text{Mn}_{36.4}\text{Si}_{63.6}$ and $\text{Mn}_{30.4}\text{Re}_{6.0}\text{Si}_{63.6}$ HMS's. No impurity phase was found in the samples. (b) Thermal conductivity, (c) power factor, and (d) dimensionless figure of merit of $\text{Mn}_{30.4}\text{Re}_{6.0}\text{Si}_{63.6}$ HMS are plotted in (b)–(d), respectively. By using 6 at.% Re substitution for Mn in $\text{Mn}_{36.4}\text{Si}_{63.6}$ HMS, we succeed in obtaining sample possessing $ZT = 1.04$ at around 900 K. The information about sample preparation techniques and composition dependence of thermoelectric properties will be reported elsewhere.²¹⁾

peratures is caused by the bi-polar diffusion effect in association with the excitation of electrons from valence band to conduction band. The lower temperature of bi-polar diffusion effect definitely indicates that the energy gap of both compounds is smaller than that expected from the first principles band calculations. The unusual overestimation of energy gap in band calculations was presumably brought about by the inappropriate use of structure ordering between Al and Si, though the Al and Si are essentially coexist together in the same atomic sites in both compounds.

4. Higher Manganese Silicide

Higher manganese silicide (HMS) obtainable at around $\text{Mn}_{36.4}\text{Si}_{63.6}$ ($\text{MnSi}_{1.75}$) and Al-Mn-Si C54-phase are classified into the group of Nowotny chimney ladder phases¹⁸⁾ and consequently possess a good similarity in local atomic arrangements. The similar local atomic arrangements naturally lead to similarity in electronic structure as shown in Fig. 2., and hence similar electron transport properties. It would be very important to note that the temperature dependence of electron transport properties of HMS¹⁹⁾ indicates presence of a large energy gap of ~ 0.8 eV in width, which is comparable with that predicted by the band calculation. The consistency of energy gap between experiment and calculation would be closely related to the absence of chemical disordering between Al and Si in HMS.

The p-type HMS is known to possess a large value of $ZT \sim 0.46$ at around $\text{Mn}_{36.4}\text{Si}_{63.6}$ ¹⁹⁾ with its lattice thermal conductivity of $\kappa_{\text{lat}} \sim 2 \text{ Wm}^{-1}\text{K}^{-1}$.^{19,20)} This fact strongly let us believe that the value of ZT can be further increased provided that a small amount of 5d transition metal elements is substituted for Mn in the same manner as we performed for the Al-Mn-Si C54-phase and C40-phase.

We employed Re as the element of partial substitution for Mn, partly because Re stays in the same column in the periodic table to presumably produce no serious impurity states

in the energy gap, and partly because Re-substitution for Mn led the effective reduction of κ_{lat} without a serious variation in electron transport properties of Al-Mn-Si C54-phase.¹⁷⁾ By introducing 6 at.% Re in HMS, we succeeded in obtaining 60% reduction of κ_{lat} from that of Re-free sample.²¹⁾ Figure 6 (a) shows the powder XRD patterns of samples obtained at $\text{Mn}_{36.4}\text{Si}_{63.6}$ and $\text{Mn}_{30.4}\text{Re}_{6.0}\text{Si}_{63.6}$, and their thermal conductivity and power factor are shown in Fig. 6 (b) and (c), respectively. The maximum magnitude of ZT of $\text{Mn}_{30.4}\text{Re}_{6.0}\text{Si}_{63.6}$ shown in Fig. 6 (d) was increased up to 1.04 at around 920 K from 0.46 of $\text{Mn}_{36.4}\text{Si}_{63.6}$. The consequently obtained, large value of ZT for the HMS lends a great support to the validity of our newly constructed guiding principle for practical thermoelectric materials.

5. Discussions

In this section, the method to find the materials possessing (g) anharmonic oscillation of lattice vibration in crystal structure is discussed. The condition of (g) is realized when the atomic potential about some specific atomic sites in the lattice is rather shallow than that in usual materials. This characteristic in atomic potential sometime leads to ionic conduction, which is often observed in oxides and chalcogenides where some of the constituent elements are strongly connected by covalent bonding and some of atoms are connected by ionic bonds. If the ions in chalcogenides possess full filled d-bands near the Fermi energy, such as those in Cu and Ag, the atomic potential about the ions would become much shallower and the ions possess anharmonic oscillation even at low temperature. If these materials of ionic conduction possess the condition (a)–(c) in their electronic structure, we would have a large magnitude of both A and B and hence a large magnitude of ZT .

Indeed, bulk materials possessing an extremely large magnitude of $ZT > 1$ were found recently in chalcogenides such as Cu_2Se ²²⁾ and CuGaTe_2 ²³⁾. These materials are definitely char-

acterized by the very small magnitude of lattice thermal conductivity together with the large magnitude of power factor presumably due to the anharmonic lattice vibration. This fact indicates that both electronic structure and lattice vibrations of these compounds are best suited for the thermoelectric materials.

In the materials consisting both of metals and metalloids such as Cu₂Se and CuGaTe₂, several different chemical bonds exist to make the atomic potential anharmonic. This consideration was confirmed in our recent work on In₂S₃ possessing very small lattice thermal conductivity less than 1 W m⁻¹K⁻¹.²⁴ We selected this compound because it consists of metal (Indium) and metalloid (sulfur) and possesses the appropriate electronic structure for thermoelectricity. Consequently, it possessed relatively large dimensionless figure of merit exceeding 0.4.

We stress here that we could find other high-performance thermoelectric materials in chalcogenides if we carefully investigated their electronic structure using first principles calculations. Nevertheless, it would be mentioned before passing that even if the magnitude of ZT is very large, materials with ionic conduction cannot be used as practical thermoelectric materials because inhomogeneous distribution of ion caused by the electrical current would lead to serious effect on the phase stability and/or electron transport properties. We should, therefore, find the chalcogenides possessing atoms nearly conducting but staying in the specific sites in the unit cell.

6. Conclusion

In this paper, we proposed the conditions of electronic structure to developing practical thermoelectric materials together with the method for effectively reducing lattice thermal conductivity without seriously affecting electron transport properties. By using the proposed strategy, we succeeded in obtaining materials possessing a large magnitude of dimensionless figure of merit $ZT > 1.0$ in the alloy systems consisting solely of environmental-friendly elements, Mn, Si, and Re. This fact definitely indicated that our newly constructed guiding principle works for finding new thermoelectric materials of high performance.

Acknowledgements

This research was supported by the **JST PRESTO** pro-

gram (New Materials Science and Element Strategy) and supported by JSPS KAKENHI Grant Number 26630332 and 26289236.

REFERENCES

- 1) A. F. Ioffe: *Semiconductor Thermoelements and Thermoelectric cooling*, Infosearch limited, London, (1957).
- 2) G. Berns: *Solid State Physics*, Academic Press, Inc., Orland, FL, (1985).
- 3) N. F. Mott: *The Theory of the Properties of Metals and Alloys*, Dover Publications, Inc. New York, NY (1958).
- 4) J.M. Ziman: *Principles of the Theory of Solids*, Cambridge University Press, New York, NY (1972).
- 5) J. S. Dugdale: *The Electrical Properties of Metals and Alloys*, Edward Arnold, London, (1977).
- 6) T. Takeuchi: *New Thermoelectric Materials with Precisely Determined Electronic Structure and Phonon Dispersion in Thermoelectrics and its Energy Harvesting*, Ed. by D. Rowe, CRC press, Boca Raton, FL (2012).
- 7) T. Takeuchi, N. Nagasako, R. Asahi and U. Mizutani: *Phys. Rev. B* **74** (2006) 054206.
- 8) B.C. Sales, D. Mandrus, B.C. Chakoumakos, V. Keppens and J.R. Thompson: *Phys. Rev. B* **56** (1997) 15081.
- 9) Y. Wang, B. Qiu, A.J.H. McGaughey, X. Ruan and X. Xu: *J. Heat Transfer* **135** (2013) 091102.
- 10) A.F. Ioffe and A.R. Regel: *Prog. Semicond.* **4** (1960) 237.
- 11) N.E. Hussey, K. Takenaka and H. Takagi: *Philos. Mag.* **84** (2004) 2847.
- 12) P.G. Klemens: *Proc. Phys. Soc. Lond. A* **68** (1955) 1113.
- 13) Y. Nishino, S. Deguchi and U. Mizutani: *Phys. Rev. B* **74** (2006) 115115.
- 14) T. Takeuchi, Y. Terazawa, Y. Furuta, A. Yamamoto and M. Mikami: *J. Elec. Mater.* **42** (2013) 2084.
- 15) T. Takeuchi, Y. Toyama, A. Yamamoto, H. Hazama and R. Asahi: *Mater. Trans.* **51** (2010) 1127.
- 16) A. Yamamoto, M. Miyazaki, M. Inukai, Y. Nishino and T. Takeuchi: *Jpn. J. Appl. Phys.* **54** (2015) 071801.
- 17) A. Yamamoto, H. Miyazaki and T. Takeuchi: *J. Appl. Phys.* **115** (2014) 023708.
- 18) D.C. Fredrickson, S. Lee, R. Hoffmann and J. Lin: *Inorg. Chem.* **43** (2004) 6154.
- 19) Y. Miyazaki, Y. Saito, K. Hayashi, K. Yubuta and T. Kajitani: *Jpn. J. Appl. Phys.* **50** (2011) 035804.
- 20) V. Ponnambala, D.T. Morelli, S. Bhattacharya and T.M. Tritt: *J. Alloy. Compd.* **580** (2013) 598.
- 21) A. Yamamoto, S. Ghodke, H. Miyazaki, M. Inukai, Y. Nishino and T. Takeuchi: *Jpn. J. Appl. Phys.* **55** (2016) 020301.
- 22) X. Su, F. Fu, Y.-G. Yan, G. Zheng, T. Liang, Q. Zhang, X. Cheng, D.-W. Yang, H. Chi, X.-F. Tang, Q. Zhang and C. Uher: *Nature Communications* **5** (2014) 4908.
- 23) T. Plirdpring, K. Kurosaki, A. Kosuga, T. Day, S. Firdosy, V. Ravi, G.J. Snyder, A. Harnwungmoung, T. Sugahara, Y. Ohishi, H. Muta and S. Yamanaka: *Adv. Mater.* **24** (2012) 3622.
- 24) Y.X. Chen, K. Kitahara and T. Takeuchi: *J. Appl. Phys.* **118** (2015) 245103.

ARTICLE

DOI: 10.1038/s41467-017-02667-x

OPEN

Discovery of superconductivity in quasicrystal

K. Kamiya^{1,5}, T. Takeuchi², N. Kabeya³, N. Wada¹, T. Ishimasa⁴, A. Ochiai³, K. Deguchi¹, K. Imura¹ & N.K. Sato¹

Superconductivity is ubiquitous as evidenced by the observation in many crystals including carrier-doped oxides and diamond. Amorphous solids are no exception. However, it remains to be discovered in quasicrystals, in which atoms are ordered over long distances but not in a periodically repeating arrangement. Here we report electrical resistivity, magnetization, and specific-heat measurements of Al-Zn-Mg quasicrystal, presenting convincing evidence for the emergence of bulk superconductivity at a very low transition temperature of $T_c \cong 0.05$ K. We also find superconductivity in its approximant crystals, structures that are periodic, but that are very similar to quasicrystals. These observations demonstrate that the effective interaction between electrons remains attractive under variation of the atomic arrangement from periodic to quasiperiodic one. The discovery of the superconducting quasicrystal, in which the fractal geometry interplays with superconductivity, opens the door to a new type of superconductivity, fractal superconductivity.

¹Department of Physics, Graduate School of Science, Nagoya University, Nagoya 464-8602, Japan. ²Toyota Technological Institute, Nagoya 468-8511, Japan. ³Department of Physics, Graduate School of Science, Tohoku University, Sendai 980-8578, Japan. ⁴Toyota Physical and Chemical Research Institute, Aichi 480-1192, Japan. ⁵Present address: UACJ Corporation, Nagoya 455-8670, Japan. Correspondence and requests for materials should be addressed to N.K.S. (email: kensho@cc.nagoya-u.ac.jp)

In classical crystallography, a crystal was defined as a periodic arrangement of atoms with translational periodicity, leading to an infinitely extended crystal structure by aligning building blocks called unit cells; as an example, we illustrate a cubic unit cell (Fig. 1a), in which the corner and body-centered positions are occupied by the icosahedron. This traditional definition was forced to modify by the discovery of quasicrystal (QC) by Shechtman et al.¹, which led to a paradigm shift in science. Nowadays, QC is understood as a structure that is long-range ordered (as manifested in the occurrence of sharp diffraction spots) but not periodic (Fig. 1b)^{2–4}. Another characteristic of QC is the presence of a non-crystallographic rotational symmetry^{2,3}; whereas periodic crystals can possess only two-, three-, four-, and sixfold rotational symmetries, icosahedral QCs have fivefold symmetry (Fig. 1b). In recent years, cold atom gaseous QCs are formed in quasiperiodic optical potentials^{5,6}.

For simplicity, we consider a one-dimensional (1D) analog to QC known as the Fibonacci chain, *LSLSLSLSLSLS...* (see QC in Fig. 1c)⁷, where *L* and *S* are long and short segments with the ratio *L/S* equal to the golden mean $\tau \equiv (1 + \sqrt{5})/2$. This chain looks to have no order at a glance, but it has the perfect order as understood from the fact that it was created by successively applying the self-generation rule, $L \rightarrow LS$ and $S \rightarrow L$, onto the first generation sequence, *L*, as demonstrated below,

$$\begin{aligned} &L \text{ (1st)} \rightarrow LS \text{ (2nd)} \\ &\rightarrow LSL \text{ (3rd)} \rightarrow LSLS \text{ (4th)} \rightarrow LSLSLSL \text{ (5th)} \rightarrow \dots \end{aligned}$$

It may be noticed that *n*-th generation sequence is produced by placing (*n* – 2)-th one on the right-hand side of (*n* – 1)-th one. Then, the total number of the *L* and *S* segments of the *n*-th generation, F_n , follows the relation,

$$F_n = F_{n-1} + F_{n-2} \quad (n \geq 3). \quad (1)$$

This recurrence relation with $F_1 = 1$ and $F_2 = 1$ gives the Fibonacci sequence, 1, 1, 2, 3, 5, 8, ... A series of the successive Fibonacci number ratio, F_{n-1}/F_{n-2} , approximates the golden ratio; $1/1, 2/1, 3/2, 5/3, \dots, \lim_{n \rightarrow \infty} F_{n-1}/F_{n-2} = \tau (= 1.6180\dots)$. There is an actual material that corresponds to each rational ratio and is called approximant crystals (ACs). Examples are shown in Fig. 1c; 1/1AC is a periodic crystal consisting of the unit cell *LS*, 2/1AC consisting of *LSL*, and so on. In F_{n-1}/F_{n-2} AC, F_{n-1} and F_{n-2} indicate the number of *L* and *S* segments contained in the unit cell, respectively. (In the 3D case, for example, 1/1AC denotes cubic 1/1-1/1-1/1AC.) This means that the unit cell size of AC increases with the order of the rational approximant.

Reflecting such the unique geometry, QC is expected to have an electronic state called critical state that is neither extended nor localized. The existence of extended eigenstates in periodic crystals is a consequence of Bloch's theorem, whereas in random

systems, strong disorder can lead to the formation of localized eigenstates, i.e., Anderson localization, which occurs due to the interference effect between propagating and backwards scattered waves. In QCs, critical eigenstates emerge as a result of the competition between the broken translational invariance and the self-similarity of quasiperiodic structure⁸. Besides extensive studies, the electronic state of QCs is veiled in mystery⁹. For example, an electronic long-range-ordered state is not established yet although it was observed in ACs^{10,11}; to the best of our knowledge, there is no QC presenting the convincing evidence for bulk superconductivity^{12–14}, i.e., zero resistivity, Meissner effect, heat capacity jump, and the fivefold rotational symmetry as well. (In ref. ¹⁴, $\text{Mg}_3\text{Zn}_3\text{Al}_2$ was considered as a superconducting QC, but it seems to be AC according to the phase diagram given in ref. ¹⁵ and the present study, see below.) It is therefore interesting to discover superconductivity in QC. It is also interesting to examine whether the emerging superconductivity shows weak-coupling, spatially extended Cooper pairs or strong-coupling, local pairs (reflecting the critical state).

Here, we study the Al–Zn–Mg system as a test material owing to two reasons: First, it contains both QC^{15,16} and AC phases^{15,17,18}, and second, the AC phase exhibits superconductivity¹⁴. We show that bulk superconductivity emerges at $T_c \cong 0.05$ K in the Al–Zn–Mg QC, implying that it is not only the first superconducting QC but also the first QC exhibiting the electronic long-range order. We also show that temperature dependences of the thermodynamic properties and the upper critical field are understood within the weak-coupling framework of superconductivity, suggesting the formation of spatially extended pairs.

Results

Sample characterization. Samples prepared here are Al–Zn–Mg-based QC, 2/1AC, and 1/1ACs, which are summarized in the ternary phase diagram (Fig. 2). As reported in ref. ¹⁵, the 1/1ACs have a wide composition range. In this paper, each 1/1AC sample with different composition is identified using the alphabetical character, e.g., 1/1AC_A. The 1/1AC_G is a mother alloy of the QC and has almost the same composition as the 2/1AC. Note that the alloy $\text{Mg}_3\text{Zn}_3\text{Al}_2$ mentioned above is close to the 1/1AC_E sample.

The structure of the obtained samples was studied by X-ray and electron diffraction method. The lattice constant *a* of the 1/1AC samples is illustrated in Fig. 3a as a function of Al content. We note that *a* decreases almost linearly with the Al content.

For the QC, the following indexing scheme of the reflection vector **g** is used in this paper;

$$\mathbf{g} = \frac{1}{a_{6D}} \sum_{i=1}^6 m_i \mathbf{e}_{i||}. \quad (2)$$

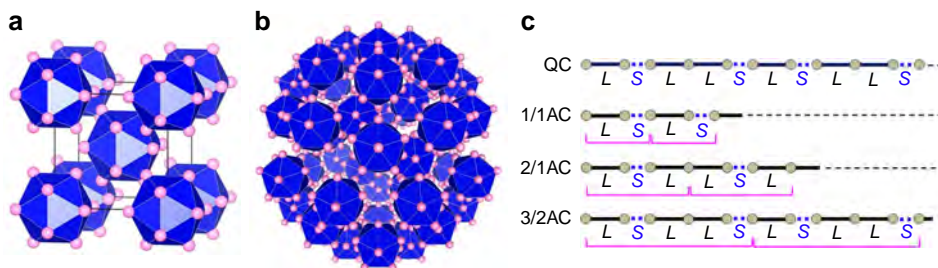


Fig. 1 Periodic and quasiperiodic arrangement of atoms. **a** An example of cubic unit cell in which the icosahedron occupies the corner and body-centered positions. Pink balls indicate atoms. **b** An example of the Tsai-type icosahedral quasicrystal. The fivefold rotational symmetry and the self-similarity may be observed. **c** Fibonacci sequence and its approximants. Atoms are denoted by circles, and the long and short interatomic segment is denoted by *L* and *S*, respectively. The bracket (e.g., *LS* for 1/1AC and *LSL* for 2/1AC) denotes the unit cell

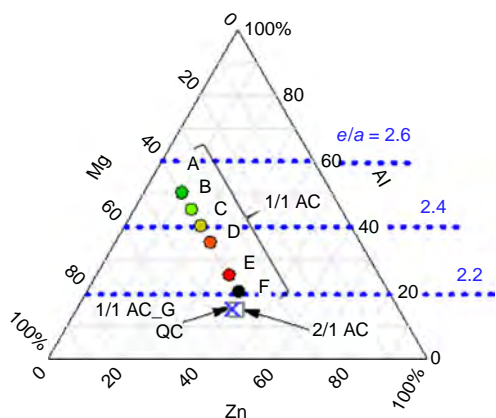


Fig. 2 Ternary phase diagram. The samples studied here are summarized in the ternary phase diagram. The 1/1AC samples have a wide composition range: Each 1/1AC sample with different composition is identified using the alphabetical character. The composition of both the QC and the 1/1AC_G (the mother alloy of the QC) is $\text{Al}_{14.9}\text{Mg}_{44.1}\text{Zn}_{41.0}$, and that of the 2/1AC is $\text{Al}_{14.9}\text{Mg}_{43.0}\text{Zn}_{42.1}$. The ratio e/a denotes electron number per atom

Here, the set of integers, m_i , represents reflection index. The vectors $\mathbf{e}_{i\parallel}$ have a length equal to $1/\sqrt{2}$, and they are parallel to the lines connecting the center of an icosahedron and the surrounding six vertices as in Fig. 6 of ref. ¹⁹. The lattice parameter a_{6D} of the 6D hypercubic lattice may be related to the edge length a_R of the rhombohedral cells of the 3D Penrose tiling as follows,

$$a_R = a_{6D}/\sqrt{2}. \quad (3)$$

In the following, we focus on the QC, the 2/1AC, and the 1/1AC_G (the mother alloy of the QC). The representative X-ray diffraction patterns of them are displayed in Fig. 3b, confirming almost the single phase. The diffraction peaks of the QC were indexed using the 6D lattice parameter, $a_{6D} = 0.7308 \pm 0.0001$ nm. Absence of any extinction condition indicates P-type of icosahedral QC. For the 2/1AC, the peaks are labeled using the lattice parameter, $a_{2/1} = 2.3006 \pm 0.0004$ nm, indicating P-type cubic phase. The intensity is strong for the 850 reflection ($d = 0.244$ nm) and the 583 reflection ($d = 0.232$ nm). Note that these indices are combination of successive Fibonacci numbers. For the 1/1AC_G, similar results are obtained: The peaks were indexed with the lattice parameter, $a_{1/1} = 1.4195 \pm 0.0003$ nm, for I-type cubic crystal. Note that the 530 reflection with the spacing $d = 0.243$ nm and the 352 reflection with $d = 0.230$ nm have a strong intensity. These indices are combination of the successive Fibonacci numbers again, and they correspond to 211111 and 221001 reflections of the QC, respectively.

The unit cell sizes obtained above satisfy the following equation^{20,21},

$$a_{F_{n-1}/F_{n-2}} = \sqrt{2/(2 + \tau)}(F_{n-1}\tau + F_{n-2})a_{6D}. \quad (4)$$

This ensures our assignment of the QC and the AC samples.

Using the X-ray diffraction peaks around $2\theta = 65^\circ$, we estimated the correlation length as 47, 85, and 28 nm for the QC, the 2/1AC, and the 1/1AC_G, respectively. Comparison between them suggests that the 1/1AC_G is meta-stable at the composition $\text{Al}_{14.9}\text{Mg}_{44.1}\text{Zn}_{41.0}$. For further comparison, we evaluated the correlation length of the 1/1AC_A as more than 65 nm, which is twice the 1/1AC_G value. This difference in the

sample quality would yield the sample dependence in the physical properties among the different ACs (Supplementary Figure 2).

Electron diffraction patterns of the QC, the 2/1AC, and the 1/1AC_G are demonstrated in Fig. 3c–g. Figure 3c displays a fivefold diffraction pattern of symmetry $m\bar{3}5$ of the QC. Indices of reflections A and B are 1220 $\bar{1}0$ and 221001, respectively. Magnified image (Fig. 3d) including reflection B shows deviation from the exact regular pentagon for weaker reflections, indicating the presence of linear phason strain²². Figure 3e shows a twofold diffraction pattern of the QC. Indices of reflections A and C are 1220 $\bar{1}0$ and 121 $\bar{1}11$, respectively. The τ^3 -scaling agrees with P-type of icosahedral QC. Figure 3f and g shows diffraction patterns of the 2/1AC and the 1/1AC_G, respectively, with the incident beam along each [001] direction. The 2/1 and 1/1ACs show no fourfold but twofold axis. In Fig. 3f, indices of reflections D and E are 10 00 and 850 of 2/1AC, respectively. We observe the reflection condition that h is even for $h00$ and $hk0$ reflections. The $0k0$ reflections with odd k should disappear following this reflection condition, but they are actually observed due to multiple diffraction effects. This observation is consistent with the space group $Pa\bar{3}$ proposed for the 2/1AC¹⁷. In Fig. 3g, reflections F and G correspond to 600 and 530 reflections of the 1/1AC, respectively. Note reflection condition of $h + k + l = \text{even}$ for hkl reflection, which is consistent with the reported space group $Im\bar{3}$ ¹⁸.

Electrical resistivity. Figure 4a shows the electrical resistivity normalized by the resistivity at $T = 280$ K, $\rho/\rho_{280\text{K}}$, as a function of temperature T in a logarithmic scale. Three points are to be noted. First, all the materials studied here show zero resistivity. Second, $\rho_{280\text{K}}$ of the QC and the 2/1AC amounts to $\sim 150 \mu\Omega\text{cm}$, greater than that of all the 1/1AC samples (inset of Fig. 4a). Third, while all the 1/1AC samples present the metallic behavior, the QC and the 2/1AC show the negative temperature coefficient of resistivity, $d\rho/dT < 0$ (Fig. 4b).

The normal state conductivity of QCs has been sometimes discussed using the concept of the Anderson localization⁹. For the present case, it remains open if the second and third points mentioned above show a precursor of the electron localization in the QC and the 2/1AC. This should be examined in the future by virtue of phason-strain-free samples; the present sample contains a linear phason strain as mentioned above.

Specific heat in normal state. The temperature dependences of the specific heat $C(T)$ in the normal state of the QC, the 2/1AC, and the representative 1/1AC samples are shown in Fig. 5a in the form of C/T vs T^2 . Using the relation, $\frac{C}{T} = \gamma + \beta T^2$, we obtain the coefficients γ and β for each sample. The Debye temperature Θ_D is deduced from β and plotted in Fig. 5b as a function of Al content, in good agreement with the previous report¹⁵. We confirm that Θ_D is almost independent of Al content. For the Al-content dependence of the electronic-specific heat coefficient γ , see below.

Relation between T_c and $1/\gamma$. Figure 6a shows the superconducting transition temperature T_c defined by zero resistivity as a function of Al content. Note that the zero resistivity corresponds to the heat capacity jump (see below) and hence shows the bulk transition of superconductivity. As Al content is decreased, T_c is monotonically decreased from ~ 0.8 to ~ 0.2 K, followed by the sudden drop down to ~ 0.05 K at 15% Al content (corresponding to the QC, the 2/1AC, and the 1/1AC_G).

Figure 6b shows the Al-content dependence of the electronic-specific heat coefficient γ deduced from Fig. 5a. We observe that γ monotonically decreases with Al content, suggesting that

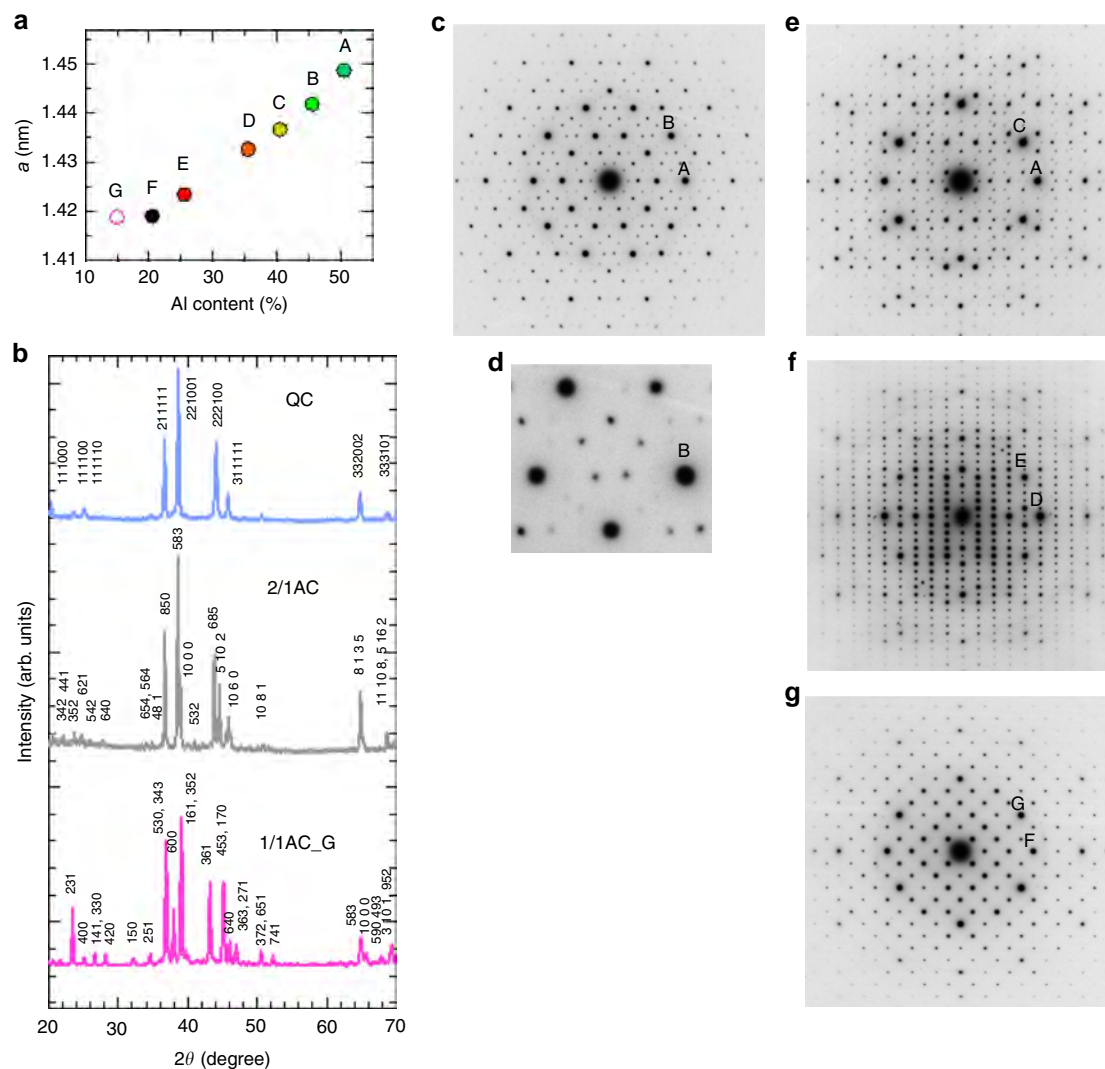


Fig. 3 Diffraction patterns. **a** Lattice parameter a of 1/1AC samples determined from X-ray diffraction method as a function of Al content. Note that a decreases almost linearly with Al content. **b** Representative X-ray diffraction patterns of the QC, the 2/1AC, and the 1/1AC_G. Note that six integers are needed to index the peak of the QC. **c, d** Fivefold electron diffraction patterns of the QC. Magnified image (**d**) shows deviation from the perfect regular pentagon for weaker reflections. **e** Twofold electron diffraction pattern of the QC. **f, g** Electron diffraction patterns of 2/1 and 1/1AC with the incident beam along each [001] direction

the density of states at the Fermi energy E_F , $D(E_F)$, decreases with Al content. Note that γ slightly drops at 15% Al content, which is likely related to the electronic stabilization effect, i.e., the pseudogap formation due to the so-called Hume–Rothery mechanism¹⁵.

To see the relation between T_c and γ , we plot $\ln T_c$ vs $1/\gamma$ in Fig. 6c with Al content as an implicit parameter. We find that all the samples lie on the straight line within an experimental uncertainty. According to the BCS theory, T_c is given as follows,

$$T_c = 1.14\Theta_D e^{-1/VD(E_F)}. \quad (5)$$

Here, V is the effective electron–electron interaction with the weak-coupling condition $|VD(E_F)| \ll 1$. As Θ_D is almost independent of Al content in the present system as mentioned above, Eq. (5) leads to the relationship, $\ln T_c \propto 1/\gamma$, if V is the same among the samples. This is just observed here, meaning that the effective interaction V remains attractive and unchanged in magnitude under variation of the atomic arrangement from the AC to the QC and T_c is fully determined by $D(E_F)$.

Bulk transition of superconductivity in QC. Let us focus on the superconducting transition of the QC. (See Supplementary Figure 2 for the AC samples.) At T_c marked by the resistivity drop (Fig. 7a), the real part of the ac magnetic susceptibility (χ') becomes negative (Fig. 7b), signaling the shielding effect associated with the zero resistivity. Upon cooling the sample through T_c under an external magnetic field, the dc magnetization M becomes diamagnetic (Fig. 7c), indicating the exclusion of the magnetic flux due to the Meissner effect. As seen in Fig. 7d, the specific heat divided by temperature C_e/T shows the large jump ($\delta C_e/T_c \sim 1.2\gamma$) at T_c , where C_e denotes the electronic part of specific heat, obtained by subtracting the lattice contribution from the measured specific heat, and δC_e indicates the jump height of C_e . This indicates that almost all mobile electrons in the sample participate in the superconductivity. These provide convincing evidence for the emergence of bulk superconductivity in the QC.

In Fig. 8, we show the normalized specific heat $C_e/\gamma T$ of the QC and the 1/1AC_A as a function of the reduced temperature $t = T/T_c$. (The QC sample presented here is different from that shown in Fig. 7d.) We observe that the data of the QC and the 1/1AC are in good agreement with each other. Note that both the

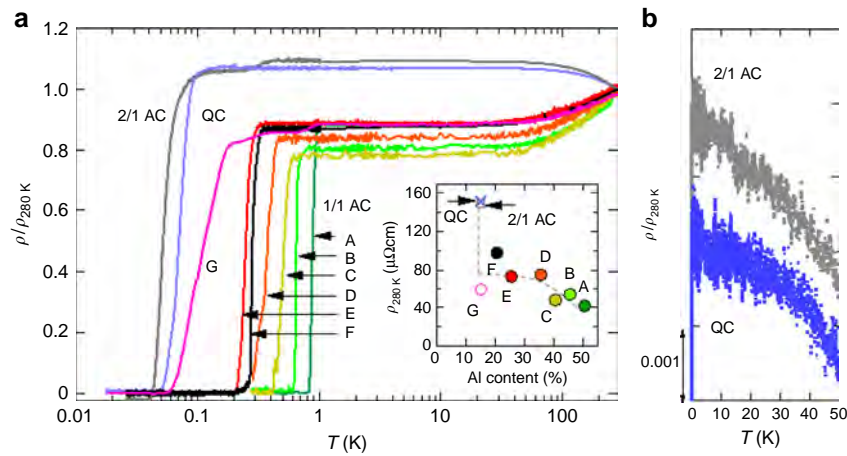


Fig. 4 Electrical resistivity. **a** Temperature dependence of normalized electrical resistivity. $\rho_{280\text{ K}}$ denotes the resistivity at $T = 280\text{ K}$. The samples plotted are the as-cast 1/1AC_A, E, F, G samples, the annealed 1/1AC_B, C, D samples, the 2/1AC sample, and the QC sample. The 1/1AC_G is a mother ingot of the QC. Inset: Electrical resistivity at $T = 280\text{ K}$ as a function of Al content. The broken line is a guide to the eyes: note that the resistivity of the QC and the 2/1AC is larger than that of the 1/1AC samples. **b** Temperature dependence of normalized resistivity of the QC and the 2/1AC in an expanded scale below 50 K. The data are shifted vertically for clarity. Note that they show the negative temperature coefficient of resistivity

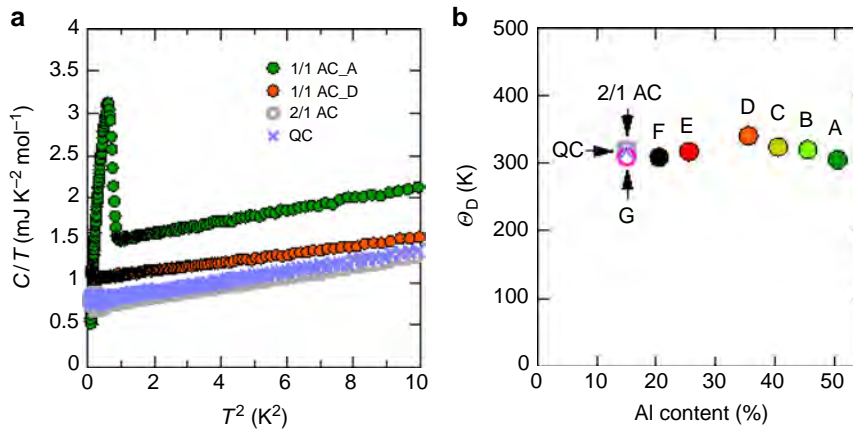


Fig. 5 Specific heat in normal state. **a** Temperature dependences of specific heat in the form of C/T vs T^2 in the range of $0 < T^2 < 10$. The results obtained here are consistent with the data in ref. ¹⁵. Note that all the samples show a conventional form of $\zeta = \gamma + \beta T^2$ in the normal state. The peak anomaly at low temperature is due to the onset of superconductivity. **b** Debye temperature Θ_D deduced from β . Note that Θ_D is almost independent of Al content

results are compatible with the BCS theory (see solid line), the only available theory at present for comparison with the experiment, although the base temperature of the experiment is not low enough to confirm the exponential tail of $C_e(t)$ at very low temperatures. The agreement with the theory signifies the onset of long-range order of Cooper pairs with opening of a full gap Δ characterized by the relation $2\Delta = 3.5k_B T_c$ (where k_B is the Boltzmann constant).

Superconducting critical field. The magnetic field dependence of the electrical resistivity $\rho(H)$ is demonstrated in Fig. 9. The zero resistivity defines the upper critical field H_{c2} shown in the inset of Fig. 10. Note that the 1/1AC_F has a several times larger H_{c2} than Al metal, while it has a several times lower T_c . This excludes the possibility that the superconductivity might arise from Al-derived impurity phase. Combining the relations, $\kappa = H_{c2}(0)/\sqrt{2}H_c(0)$ and $H_c(0) = T_c\sqrt{5.94\gamma}$ (where κ is the so-called GL parameter, $H_{c2}(0)$ and $H_c(0)$ are the upper and the thermodynamic critical fields extrapolated to zero temperature, respectively), we evaluate κ as 136, 128, and 337 for the QC, the 2/1AC, and the 1/1AC_F,

respectively. These values confirm that the present system is a type-II superconductor, in which the magnetic field penetrates the sample. The coherence length $\xi(0)$ was also evaluated from the relation $H_{c2}(0) = \phi_0/2\pi\xi(0)^2$ (where ϕ_0 is the flux quantum) as $\xi(0) \sim 139, 143,$ and 83 nm for the QC, the 2/1AC, and the 1/1AC_F, respectively.

The reduced upper critical field is defined as $h = -H_{c2}/(T_c dH_{c2}/dT|_{T=T_c})$, and is plotted in Fig. 10 as a function of the reduced temperature ($t = T/T_c$). We compare $h(t)$ with Werthamer–Helfand–Hohenberg (WHH) theory²³, which takes into account of electron mean free path (l), spin–orbit scattering, and spin paramagnetism. The experimental results are in good agreement with the theory (solid line) for the case of no spin paramagnetic or spin–orbit effects and in the dirty limit ($\xi(0) \gg l$), in which scattering from physical and chemical impurities is large compared with the superconducting energy gap. This dirty-limit superconductivity seems compatible with the large coherence length estimated above and the large residual resistivity (i.e., small mean path) shown in Fig. 4. On the other hand, the present system is distinguished from some dirty

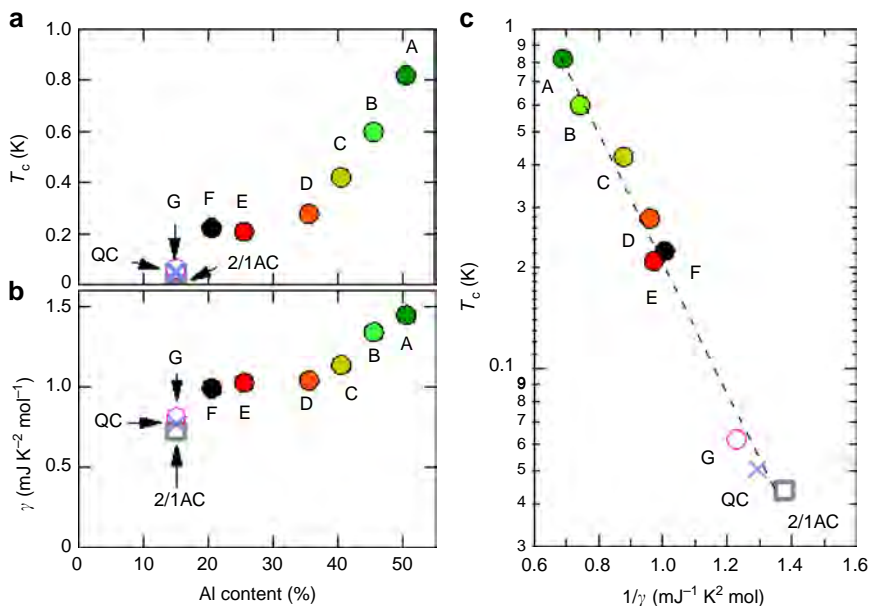


Fig. 6 Relation between transition temperature and γ coefficient. **a** Superconducting transition temperature T_c as a function of Al content. Note that T_c shows the sharp drop at Al content of about 15% corresponding to the QC and the 2/1AC. **b** Electronicspecific heat coefficient γ as a function of Al content. The slight drop at 15% Al content suggests the pseudogap formation. **c** Correlation between T_c and $1/\gamma$. The straight line denotes the interrelationship, $\ln T_c \propto 1/\gamma$, marking the constant pairing interaction

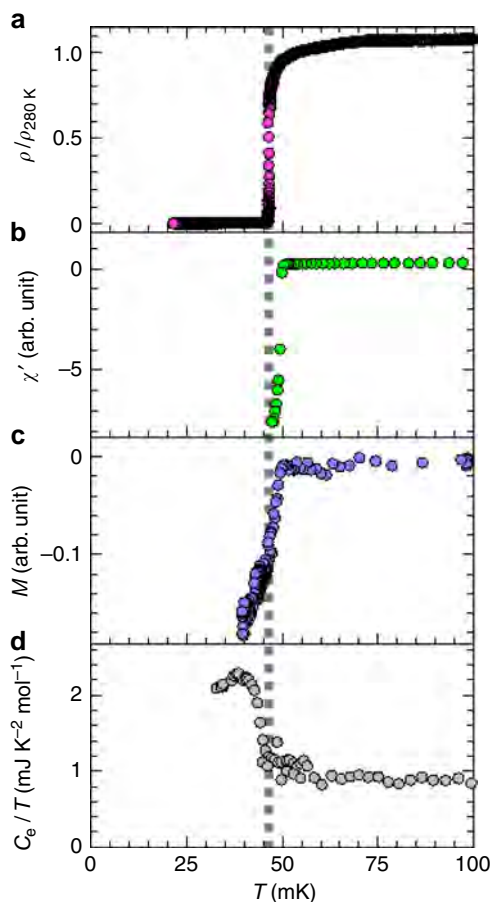


Fig. 7 Physical properties around T_c of quasicrystal. Temperature dependence of the normalized electrical resistivity (**a**), the real part of the ac magnetic susceptibility (**b**), the dc magnetization at external magnetic field of approximately 4 mOe (**c**), and the electronic part of the specific heat divided by temperature (**d**), for the QC sample. The broken line marks the transition temperature $T_c \approx 0.05$ K

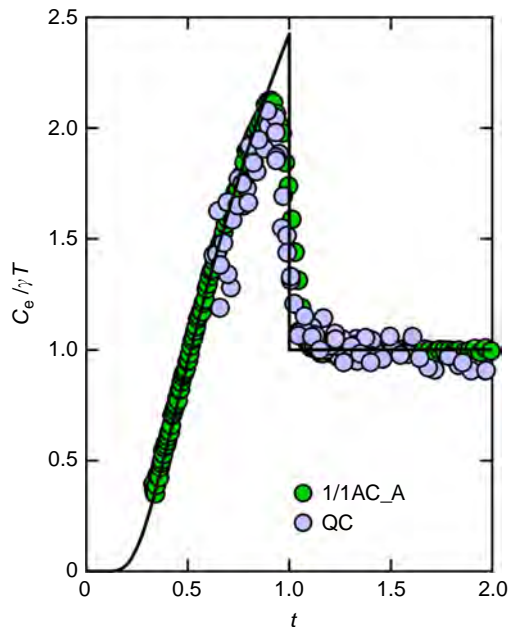


Fig. 8 Specific heat around superconducting transition. Normalized specific heat divided by temperature as a function of the reduced temperature $t = T/T_c$ for the QC (with $T_c \approx 0.05$ K) and the 1/1AC_A ($T_c \approx 0.8$ K). Here, C_e is the electronic part of the specific heat. The solid line denotes the weak-coupling BCS theory. Note that both results of the QC and 1/1AC samples are compatible with the weak-coupling theory

systems²⁴ in which $h(t)$ was enhanced over the WHH theory as a result of the field-induced suppression of localization.

Discussion

In general, superconductivity needs the attractive interaction among electrons and the finite density of states at the Fermi

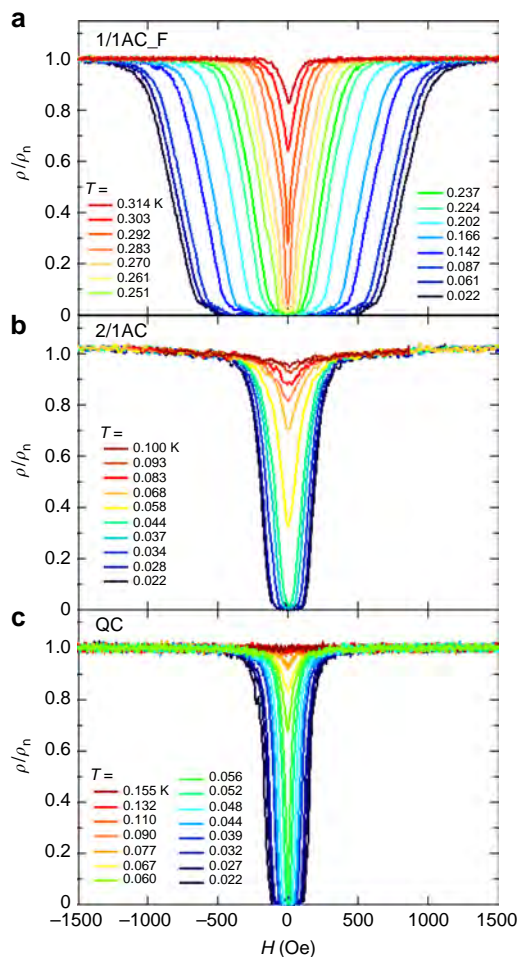


Fig. 9 Magnetoresistance at a constant temperature. Magnetic field dependence of normalized electrical resistivity of the 1/1AC_F sample (a), the 2/1AC sample (b), and the QC sample (c). ρ_n denotes the normal state resistivity

energy, i.e., $VD(E_F) > 0$ in Eq. (5). For the present QC case, two points are to be noted. First, $D(E_F)$ is reduced presumably due to the pseudogap formation, and T_c is much smaller than that of the ACs but remains finite. (The very low T_c due to the pseudogap may explain why superconductivity was hardly observed in QCs.) This situation resembles that in superconductors in which charge-density-wave (CDW) states coexist; the Cooper pairing and the CDW instabilities compete for the Fermi surface and so the presence of the CDW depresses T_c ²⁵. Second, the fact that V remains intact in the QC leads to the following discussion: The electron–electron interaction is expressed as $V = V_a - V_C$, where V_a is the attractive pairing interaction (mediated by phonons in conventional BCS superconductors) and V_C is the effective Coulomb repulsion. If the critical eigenstates of QCs would lead to the localization effect and, as a result, cause slow diffusion of electrons, then V_C could be enhanced and V would be reduced^{26,27}. The absence of such the reduction in V implies that the critical eigenstates would not have a dominant role in the superconductivity of the present QC.

In this study, we found no difference between the Al–Zn–Mg QC and other weak-coupling superconductors. According to a theoretical study by Sakai et al.²⁸, however, the Cooper pairs in the Penrose lattice are unconventional because the lack of the translational symmetry does not allow the conventional Cooper pairing formed at the opposite Fermi momenta, \mathbf{k} and $-\mathbf{k}$. It

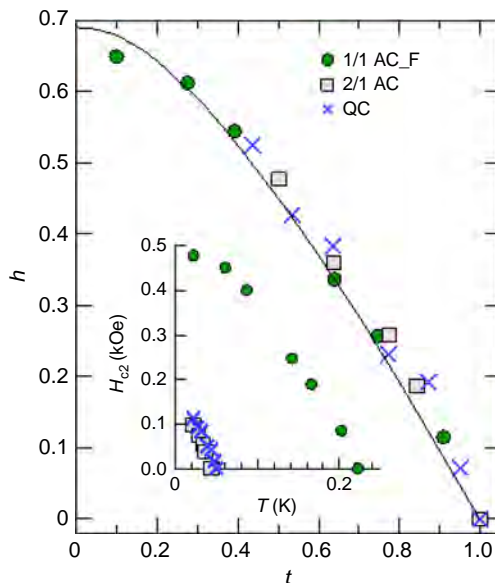


Fig. 10 Superconducting upper critical field. The superconducting upper critical fields H_{c2} of the QC, the 2/1AC, the 1/1AC_F are plotted in the form of $h = -H_{c2}/(T_c dH_{c2}/dT|_{T=T_c})$ vs $t = T/T_c$. The solid curve denotes the Werthamer-Helfand-Hohenberg theory in the dirty limit. The inset shows $H_{c2}(T)$ of the same samples as in the main frame. Note that the upper critical field in the limit of zero temperature of the 1/1AC_F ($H_{c2}(0) \cong 500$ Oe) substantially exceeds that of metal Al (~ 100 Oe), excluding the possibility that the superconductivity would arise from Al-derived impurity phase

would be challenging to detect the fractal superconducting order parameter as predicted by the theory. We hope that the present study stimulates a further work to reveal this new type of superconductivity.

Methods

Sample preparation. The 1/1AC samples were prepared by induction melting of appropriate amounts of constituent elements, 99.99% Al, 99.9% Mg, and 99.99% Zn, in a boron-nitride crucible under Ar atmosphere¹⁵. Some of them were annealed at 300 °C for 6 h or at 360 °C for 5 h. The mother alloys of the QC ($Al_{1.4,9}Mg_{44.1}Zn_{41.0}$) and the 2/1AC ($Al_{1.4,9}Mg_{43.0}Zn_{42.1}$) were first prepared by induction melting of the constituent elements. Then, by melt spinning of each mother alloy¹⁵, the ribbon specimens were fabricated. Finally, the QC samples were obtained by sintering the ribbons at 300 °C and at 50 MPa for 1 h using a spark plasma sintering apparatus, whereas the 2/1AC samples were obtained by sintering the ribbons at the same conditions as the above and subsequently annealing the sintered ribbons at 300 °C for 5 h. Some of the QC samples were annealed at 360 °C for 5 h, whose structure was confirmed to be kept in the QC.

Sample characterization. The composition of the obtained samples was analyzed by using inductively coupled plasma (ICP) spectroscopy and scanning electron microscope (SEM). For the ICP, the analyzed composition agreed well with the nominal one within the error <2%, and no segregation was detected for the SEM within the experimental accuracy (Supplementary Figure 1).

Selected-area electron diffraction patterns were observed using a JEOL JEM-200CS microscope with a double tilting stage at the acceleration voltage 200 kV. The alloy specimens were crushed into fragments using an agate mortar and pestle, and transferred on a micro-grid mesh for the electron microscopic observation.

X-ray diffraction patterns were obtained using a RIGAKU IIB diffractometer. Lattice parameters of the QC and the ACs were determined from angles of Bragg reflections, θ , using the extrapolation method: Least square fitting and extrapolation to $\theta = 90^\circ$ were carried out by assuming linear relationship between calculated lattice parameters and the following equation values,

$$\frac{\cos^2 \theta}{\sin \theta} + \frac{\cos^2 \theta}{\theta}$$

Correlation length, L (nm), was determined using the following relation,

$$L = \frac{\lambda}{2\Delta\theta\cos\theta}$$

Here, λ (nm) and $\Delta\theta$ (rad) denote wave length of X-rays and peak width (full width at half maxima), respectively. In this study, the following three reflections, 332002, 8 13 5, and 583 reflections, located approximately at $2\theta = 64.8^\circ$, were used for the QC, the 2/1 and 1/1ACs, respectively. To estimate $\Delta\theta$, the peaks were decomposed into two parts originating from Cu- $K\alpha_1$ ($\lambda = 0.15405$ nm) and $K\alpha_2$ by assuming pseudo-Voigt function for each peak shape.

Physical properties measurements. The physical properties were measured using one ^3He refrigerator and four $^3\text{He}/^4\text{He}$ dilution refrigerators (each having a different base temperature) installed at Nagoya and Tohoku Universities. Different measurement techniques were taken depending on the temperature region measured: for the electrical resistivity, a four-terminal dc or ac method was taken; for the ac magnetic susceptibility, the mutual inductance method or a SQUID magnetometer; for the heat capacity, the quasi-adiabatic heat-pulse, or relaxation method. The dc magnetization measurement was done using a SQUID magnetometer.

Data availability. The data that support the findings of this study are available from the corresponding author (kensho@cc.nagoya-u.ac.jp) upon request.

Received: 1 June 2017 Accepted: 18 December 2017

Published online: 11 January 2018

References

- Shechtman, D., Blech, D., Gratias, D. & Chan, J. W. Metallic phase with long-range orientational order and no translational symmetry. *Phys. Rev. Lett.* **53**, 1951–1953 (1984).
- Goldman, A. I. & Kelton, R. F. Quasicrystals and crystalline approximants. *Rev. Mod. Phys.* **65**, 213–230 (1993).
- Stadnik, Z. M. (ed). *Physical Properties of Quasicrystals* (Springer, Berlin, 1999).
- Takakura, H., Gomez, C. P., Yamamoto, A., de Boissieu, M. & Tsai, A. P. Atomic structure of the binary icosahedral Yb-Cd quasicrystal. *Nat. Mat.* **6**, 58–63 (2007).
- Sanchez-Palencia, L. & Santos, L. Bose-Einstein condensates in optical quasicrystal lattices. *Phys. Rev. A* **72**, 053607 (2005).
- Lang, L.-J., Chai, X. & Chen, S. Edge states and topological phases in one-dimensional optical superlattices. *Phys. Rev. Lett.* **108**, 220401 (2012).
- Steurer, W. & Haibach, T. in *Physical Properties of Quasicrystals* (ed. Stadnik, Z. M.) Ch. 3 (Springer, Berlin, 1999).
- H. Hafner, Jr. & Ktajčić, M. in *Physical Properties of Quasicrystals* (ed. Stadnik, Z. M.) Ch. 7 (Springer, Berlin, 1999).
- Fujiwara, T. in *Physical Properties of Quasicrystals* (ed. Stadnik, Z. M.) Ch. 6 (Springer, Berlin, 1999).
- Deguchi, K. et al. Superconductivity of Au-Ge-Yb approximants with Tsai-type clusters. *J. Phys. Soc. Jpn.* **84**, 023705 (2015).
- Tamura, R., Muro, Y., Hiroto, T., Nishimoto, K. & Takabatake, T. Long-range magnetic order in the quasicrystalline approximant Cd_6Tb . *Phys. Rev. B* **82**, 220201(R) (2010).
- Azhazha, V. et al. Superconductivity of Ti-Zr-Ni alloys containing quasicrystals. *Phys. Lett. A* **303**, 87–90 (2002).
- Wagner, J. L., Biggs, B. D., Wong, K. M. & Poon, S. J. Specific-heat and transport properties of alloys exhibiting quasicrystalline and crystalline order. *Phys. Rev. B* **38**, 7436–7441 (1988).
- Graebner, J. E. & Chen, H. S. Specific heat of an icosahedral superconductor, $\text{Mg}_5\text{Zn}_3\text{Al}_2$. *Phys. Rev. B* **58**, 1945–1948 (1987).
- Takeuchi, T. & Mizutani, U. Electronic structure, electron transport properties, and relative stability of icosahedral quasicrystals and their 1/1 and 2/1 approximants in the Al-Mg-Zn alloy system. *Phys. Rev. B* **52**, 9300–9309 (1995).
- Ramachandrarao, P. & Sastry, G. V. S. A basis for the synthesis of quasicrystals. *Pramana* **25**, L225–L230 (1985).
- Sugiyama, K., Sun, W. & Hiraga, K. Crystal structure of a cubic $\text{Al}_{17}\text{Zn}_{37}\text{Mg}_{46}$: a 2/1 rational approximant structure for the Al-Zn-Mg icosahedral phase. *J. Alloy. Comp.* **342**, 139–142 (2002).
- Bergman, G., Waugh, J. L. T. & Pauling, L. The crystal structure of the metallic phase $\text{Mg}_{32}(\text{Al}, \text{Zn})_{49}$. *Acta Crystallogr.* **10**, 254–259 (1957).
- Elser, V. Indexing problems in quasicrystal diffraction. *Phys. Rev. B* **32**, 4892–4898 (1985).
- Jarić, M. V. & Qiu, S.-Y. in *Proc. of the 12th Taniguchi Symposium, Shima, Japan, 14–19 Nov 1989* (eds Fujiwara, T. & Ogawa, T.) Springer-Series in Solid-State Sciences Vol. 93, 48–56 (Springer-Verlag, Heidelberg, 1990).
- Sato, N. K. et al. Quantum critical behavior in magnetic quasicrystals and approximant crystals. *J. Phys. Conf. Ser.* **868**, 012005 (2017).
- Socolar, J. E. S., Lubensky, T. C. & Steinhardt, P. J. Phonons, phasons and dislocations in quasicrystals. *Phys. Rev. B* **34**, 3345–3360 (1986).
- Werthamer, N. R., Helfand, E. & Hohenberg, P. C. Temperature and purity dependence of the superconducting critical field, H_{c2} . III. Electron spin and spin-orbit effects. *Phys. Rev.* **147**, 295–302 (1966).
- Coffey, L., Muttalib, K. A. & Levin, K. Theory of upper critical fields in highly disordered superconductors: localization effect. *Phys. Rev. Lett.* **52**, 783–786 (1984).
- Gabovich, A. M., Voitenko, A. I. & Ausloos, M. Charge- and spin-density waves in existing superconductors: competition between Cooper pairing and Peierls or excitonic instabilities. *Phys. Rep.* **367**, 583–709 (2002).
- Anderson, P. W. Theory of dirty superconductors. *J. Phys. Chem. Solids* **11**, 26–30 (1959).
- Feigel'man, M. V., Ioffe, L. B., Kravtsov, V. E. & Cuevas, E. Fractal superconductivity near localization threshold. *Ann. Phys.* **325**, 1390–1478 (2010).
- Sakai, S., Takemori, N., Koga, A. & Arita, R. Superconductivity on a quasiperiodic lattice: extended-to-localized crossover of Cooper pairs. *Phys. Rev. B* **95**, 024509 (2017).

Acknowledgements

We thank A. Yamamoto for his help of sample preparation and thank Y. Hara for his assistance of low-temperature magnetization measurement. We also thank H. Takakura for his help to create the figure of the QC geometrical structure, and S. Sakai & N. Takemori for useful discussions. This work was financially supported by JSPS KAKENHI (Nos. 26610100, 15H02111, 15H03685, and 16H01071), and Program for Leading Graduate Schools “Integrative Graduate Education and Research Program in Green Natural Sciences”, MEXT, Japan.

Author contributions

K.K. and T.T. carried out the sample preparation. K.K. and T.T. made the sample characterization. K.K., K.I. and K.D. carried out measurements of the electrical resistivity, specific heat, and ac magnetic susceptibility down to about 80 mK. N.K., K.K. and A.O. performed the measurements of heat capacity and the electrical resistivity down to 20–30 mK. N.W. measured the dc and ac magnetization down to about 40 mK. N.K.S. designed the project and drafted the manuscript together with T.I., K.D. and K.I. All authors participated in the writing and review of the final draft.

Additional information

Supplementary Information accompanies this paper at <https://doi.org/10.1038/s41467-017-02667-x>.

Competing interests: The authors declare no competing financial interests.

Reprints and permission information is available online at <http://npg.nature.com/reprintsandpermissions/>

Publisher's note: Springer Nature remains neutral with regard to jurisdictional claims in published maps and institutional affiliations.

 **Open Access** This article is licensed under a Creative Commons Attribution 4.0 International License, which permits use, sharing, adaptation, distribution and reproduction in any medium or format, as long as you give appropriate credit to the original author(s) and the source, provide a link to the Creative Commons license, and indicate if changes were made. The images or other third party material in this article are included in the article's Creative Commons license, unless indicated otherwise in a credit line to the material. If material is not included in the article's Creative Commons license and your intended use is not permitted by statutory regulation or exceeds the permitted use, you will need to obtain permission directly from the copyright holder. To view a copy of this license, visit <http://creativecommons.org/licenses/by/4.0/>.

© The Author(s) 2018

LETTER

Large figure of merit $ZT = 1.88$ at 873 K achieved with nanostructured
 $\text{Si}_{0.55}\text{Ge}_{0.35}(\text{P}_{0.10}\text{Fe}_{0.01})$

To cite this article: Kévin Delime-Codrin *et al* 2019 *Appl. Phys. Express* **12** 045507

View the [article online](#) for updates and enhancements.



Large figure of merit $ZT=1.88$ at 873 K achieved with nanostructured $\text{Si}_{0.55}\text{Ge}_{0.35}(\text{P}_{0.10}\text{Fe}_{0.01})$

Kévin Delime-Codrin^{1*}, Muthusamy Omprakash^{1†}, Swapnil Ghodke^{1†}, Robert Sobota¹, Masahiro Adachi², Makoto Kiyama², Takashi Matsuura², Yoshiyuki Yamamoto², Masaharu Matsunami¹, and Tsunehiro Takeuchi¹

¹Toyota Technological Institute, Nagoya 468-8511, Japan

²Sumitomo Electric Industries, Ltd, Japan

*E-mail: sd15602@toyota-ti.ac.jp

†These authors contributed equally to this work.

Received January 2, 2019; revised February 18, 2019; accepted February 20, 2019; published online March 27, 2019

High-performance Si–Ge-based thermoelectric materials were prepared simultaneously using nano-structuring and electronic structure modifications. Density functional theory calculations predicted that Fe atoms in the Si–Ge alloy would constructively modify the electronic structure to significantly increase the Seebeck coefficient, experimentally confirmed as $|S| > 517 \pm 20 \mu\text{V K}^{-1}$ at 673 K. Dense bulk samples made of nano-grains possessed very small thermal conductivity, $\kappa < 0.80 \pm 0.10 \text{ W m}^{-1} \text{ K}^{-1}$ at $T < 873 \text{ K}$. Very large ZT values exceeding 1.00 were obtained in the temperature range $710 \text{ K} < T < 873 \text{ K}$, with a maximal value of 1.88 at 873 K. © 2019 The Japan Society of Applied Physics

Thermoelectric generators, which are capable of generating electrical power from waste heat, are considered to be among the most promising technologies for the construction of a sustainable society. The efficiency of energy conversion in these devices is generally measured by the dimensionless figure of merit $ZT = S^2 T \rho^{-1} (\kappa_{el} + \kappa_{lat})^{-1}$ of their constituent materials, hereafter called thermoelectric materials. Here S , ρ , κ_{el} , and κ_{lat} represent the Seebeck coefficient, electrical resistivity, electron and lattice thermal conductivity, respectively. Typical examples of practical thermoelectric materials, such as Bi_2Te_3 -based¹⁾ and PbTe -based²⁾ alloys, exhibit large ZT values exceeding 1.86 at 320 K and 2.20 at 915 K,³⁾ respectively. However, these materials contain rare, expensive, and toxic elements that prohibit the wide use of thermoelectric generators for various applications. Therefore, the development of new, cheap, nontoxic, and high-performance thermoelectric materials is strongly desired.

The silicon–germanium alloys, $\text{Si}_{1-x}\text{Ge}_x$, are some of the cheapest and nontoxic thermoelectric materials working at high temperatures. They had been used as radioisotope thermoelectric generators (RTGs) for NASA space missions in the 1960s. Unfortunately, their ZT values were limited by their relatively large thermal conductivity, $\kappa > 5.0 \text{ W m}^{-1} \text{ K}^{-1}$, to less than 0.50 (p-type) and 0.90 (n-type).⁴⁾ Recently, nano-structuring^{5,6)} and nano-inclusion^{7,8)} approaches have been employed to reduce the thermal conductivity, and relatively low values of $\kappa < 2.3 \text{ W m}^{-1} \text{ K}^{-1}$ were reported for $\text{Si}_{0.80}\text{Ge}_{0.20}$ alloys without significant degradation of the power factor $PF = S^2/\rho$. As a result, the ZT values were increased up to 0.95⁹⁾ and 1.30¹⁰⁾ for p-type and n-type materials, respectively.

More recently, a significantly reduced $\kappa = 1.35 \text{ W m}^{-1} \text{ K}^{-1}$ over a wide temperature range from 300 K to 700 K was reported for bulk nano-structured $\text{Si}_{0.65}\text{Ge}_{0.35}$ prepared by means of ball milling and pulse-current sintering (PCS).¹¹⁾ Unfortunately, however, the power factor of the samples was lower than $0.03 \text{ W m}^{-1} \text{ K}^{-2}$, limiting the magnitude of ZT to less than 0.012.

In order to improve the power factor while retaining the small κ_{lat} of Si–Ge alloys, we consider a constructive modification of the electronic structure near the chemical potential (Fermi level)^{12,13)} to be one of the most effective

methods. Reference 14 proposed the use of resonance states to modify the density of states $N(\varepsilon)$, and reported that the ZT value of PbTe -based thermoelectric materials was raised considerably, from 0.7 (Na-PbTe) to 1.5 ($\text{Tl}_{0.02}\text{Pb}_{0.98}\text{Te}$) at 800 K, using a tiny amount of Tl which was supposed to produce some resonant states near the chemical potential.

Notably, this method has not been applied specifically for Si–Ge alloys, but previous results have reported its efficiency. As a typical example, Ref. 15 reported extremely large magnitudes of both Seebeck coefficient, $S > 4.8 \text{ mV K}^{-1}$, and power factor, $PF > 2.4 \times 10^{-2} \text{ W m}^{-1} \text{ K}^{-2}$, at 700 K for a p-type $\text{Si}_{0.50}\text{Ge}_{0.50}\text{Au}_{0.022}$ thin film. We speculate that these values were brought about by impurity states in association with the 5d orbitals of Au formed near the chemical potential, despite the fact that neither these huge values nor the presence of these impurity states have been confirmed by any other groups.¹⁶⁾

In this study, therefore, we attempt to greatly increase the ZT value of Si–Ge-based alloys using a nano-grained structure and by constructively modifying the electronic structure. The former condition was realized by high-energy ball milling and low-temperature sintering, and the latter by introducing transition metal (TM) elements that produce impurity states near the chemical potential in the electronic density of states.

The electronic structure was calculated using the projected augmented wave method included in the software package VASP.¹⁷⁾ An energy cutoff of 400 eV together with a $6 \times 9 \times 6$ k -point mesh was used in the irreducible edge of the first Brillouin zone. The correlation energy was calculated using the generalized gradient approximation functional developed in Ref. 18. A $3 \times 2 \times 3$ supercell of diamond structure, containing 143 Si atoms and one TM element substituted in a Si site, was employed as a model structure to estimate the eigenvalue energy of impurity states. In this model, the TM concentration corresponded to 0.7 at%. The density of states was calculated after a structure optimization so as to obtain the lowest total ground-state energy of the supercell. From calculations with all the 3d, 4d, and 5d TMs used as the impurity element, we found that Fe is one of the most plausible elements for improving the electron transport properties for n-type Si–Ge-based materials because it produces intense, sharp peaks at the bottom of conduction

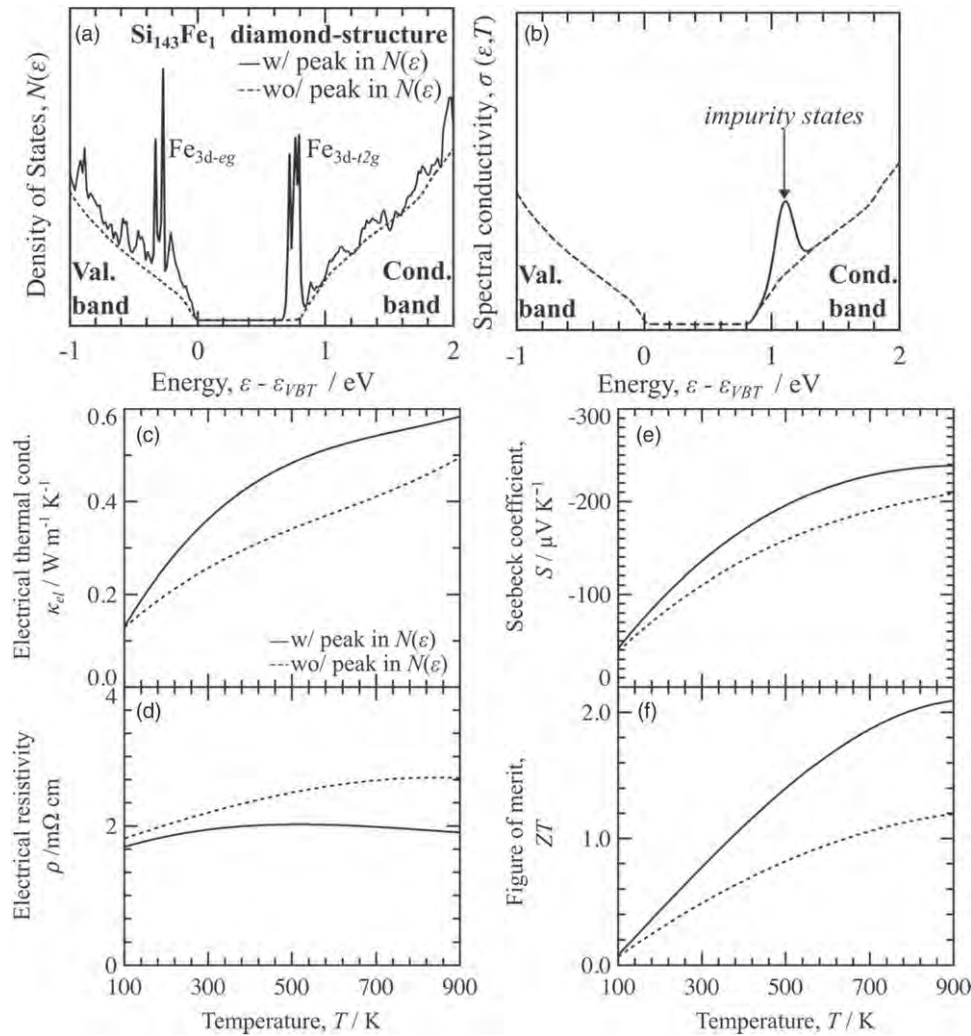


Fig. 1. (a) Electronic density of states $N(\varepsilon)$ of a $3 \times 2 \times 3$ supercell of diamond structure Si consisting of 143 Si and 1 Fe calculated by VASP (Ref. 17). (b) Spectral conductivity $\sigma(\varepsilon, T) = A_0 \times N(\varepsilon)$, with A_0 as constant, used to calculate the thermoelectric properties (c)–(f), $\kappa_e(T)$, $\rho(T)$, $S(T)$, and the consequently obtained ZT .

Table I. Chemical composition, density, carrier concentration, and carrier mobility measured at 300 K of $\text{Si}_{0.55}\text{Ge}_{0.35}(\text{P}_{0.10}\text{Fe}_{0.01})$.

Sintered conditions	Chemical composition	Density $d/\text{g cm}^{-3}$	Rel. density d/d_{th} (%)	Carrier conc. n/cm^{-3}	Carrier mobility $\mu/\text{cm}^2 \text{V}^{-1} \text{s}^{-1}$
873 K, 4 h	$\text{Si}_{0.51(7)}\text{Ge}_{0.31(7)}(\text{P}_{0.08(9)}\text{Fe}_{0.009(8)})$	3.40	95.74	1.24×10^{19}	1.2
1173 K, 5 min	$\text{Si}_{0.52(0)}\text{Ge}_{0.33(2)}(\text{P}_{0.06(8)}\text{Fe}_{0.005(8)})$	3.44	96.86	3.51×10^{19}	27.5

band, mainly consisting of $3d-t_{2g}$ orbitals of Fe, as illustrated in Fig. 1(a).

In order to confirm the impact of impurity states on thermoelectric properties, we calculated the electron transport properties of Si with and without the impurity states of Fe using the semi-classical Boltzmann transport equation and assuming diffusive electron conduction, where $A_0 \times N(\varepsilon)$ was used as a representative of spectral conductivity, $\sigma(\varepsilon, T)$. A_0 is a constant selected to obtain a similar electrical resistivity to amorphous Si. A Gaussian peak of 200 meV in full width at half maximum was artificially added as the Fe impurity states at the bottom of the conduction band of Si. The temperature dependence of electron thermal conductivity $\kappa_e(T)$, electrical resistivity $\rho(T)$, and Seebeck coefficient $S(T)$ were calculated by setting the Fermi energy at $E_F = 0.89$ eV and considering the temperature dependence of the chemical potential; the results are plotted in Figs. 1(c)–1(e). By additionally assuming

$\kappa_{lat} = 1 \text{ W m}^{-1} \text{ K}^{-1}$ over the whole temperature range, we also calculated the temperature dependence of ZT , plotted in Fig. 1(f). Clearly, the magnitude of both $\kappa_e(T)$ and $S(T)$ increased simultaneously with the presence of impurity states, while $\rho(T)$ decreased over the whole temperature range. As a result, ZT increased to 1.7 times larger than the value calculated without the impurity states. This result clearly proves that electronic structure modification using impurity states is one of the most useful methods for effectively increasing ZT .

To confirm the prediction, we prepared Si–Ge–Fe–P samples containing less than 1 at% Fe. A high-energy ball milling process was employed to make homogeneous nanocrystalline powders. Stainless steel balls and mill pods were specifically employed to introduce Fe-contamination into the sample during the milling process. The shortage of Fe was initially planned to be compensated for by additionally

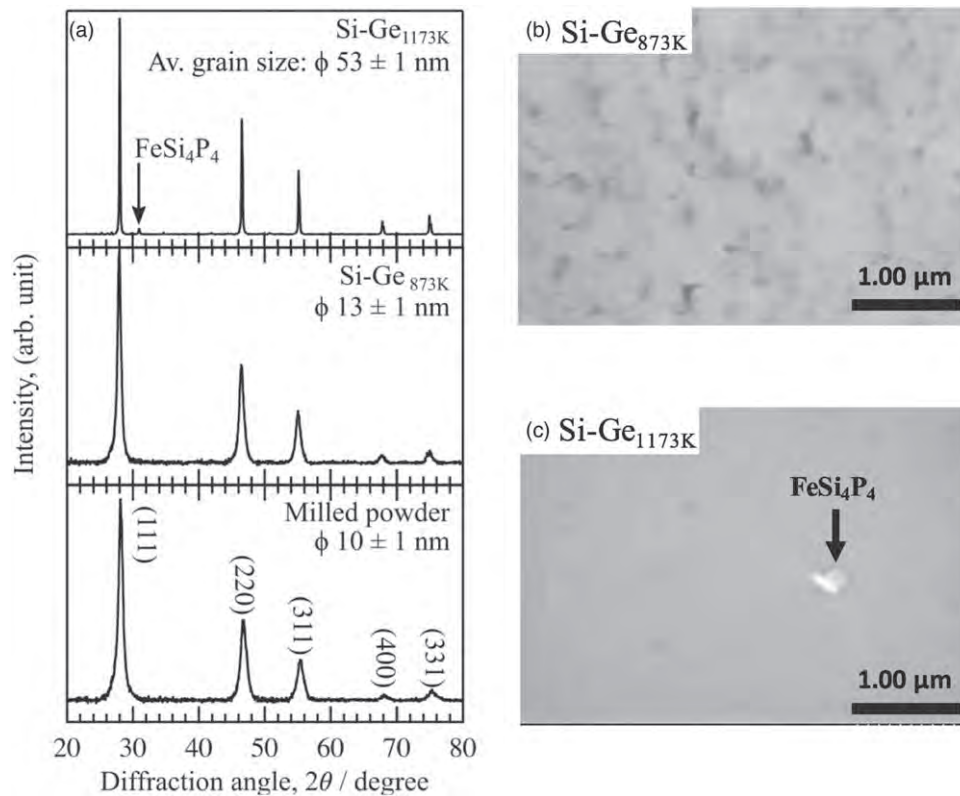


Fig. 2. (a) Powder XRD pattern of $\text{Si}_{0.55}\text{Ge}_{0.35}\text{P}_{0.10}\text{Fe}_{0.01}$ as-milled sample and bulk samples, Si-Ge_{873K} and Si-Ge_{1173K}. (b, c) Secondary electron images obtained by scanning electron microscopy of Si-Ge_{873K} and Si-Ge_{1173K} respectively. Arrows indicate the precipitated FeSi₄P₄.

introduced Fe but, fortunately, the preparation process provided the sample with a sufficient concentration of Fe, ~ 0.9 at%. The chemical composition of the bulks was estimated using energy dispersive X-ray (EDX) spectroscopy analyses, and the results are summarized in Table I. Since the composition of samples was selected so as to obtain n-type materials, the chemical potential was controlled by partial substitution of the pentavalent P for the tetravalent Si. Several samples of different P concentrations were prepared, but in this paper we concentrate solely on 10 at% P samples for reasons of space. The thermoelectric properties of Si-Ge alloys for different P concentrations will be reported elsewhere in the near future.

A powder of pure Si (99.99%), Ge (99.99%), and P (99.9999%) were weighed in the stoichiometric ratio of $\text{Si}_{0.55}\text{Ge}_{0.35}\text{P}_{0.10}$ so as to be 1 g in total weight, and thoroughly mixed with a mortar and pestle under 1 atm Ar gas in a glove box. The powder was subsequently sealed in a 40 ml stainless steel mill pod made of SUS304 with 6 mm stainless steel balls at a ball-to-powder weight ratio of 20:1. To prevent oxidation of the powder during milling, the mill pod was vacuumed and filled with 1 atm mixed gas of 60 vol% Ar and 40 vol% H every two hours. The powder was first milled at 600 rpm for six hours continuously without any interruption to synthesize a homogeneously alloyed Si-Ge-P powder. Then, to further reduce the size of the nano-grains, the powder was gently milled at 300 rpm for 50 hours with a 15 minute pause after every 30 minutes of milling.

The synthesized powder was carefully taken from the mill pod under 1 atm Ar in the glove box and placed into a cylindrical hardened stainless-steel die of 10 mm in diameter. The powder was sintered into bulk using PCS. A low

sintering temperature (T , $P = 873$ K, 400 MPa) was used with a very long duration of four hours to maintain the nanoparticle sizes in the densified bulk. For comparison, a high sintering temperature allowing grain growth with a relatively low pressure (T , $P = 1173$ K, 100 MPa) was also employed with a very short sintering duration (five minutes). The samples made by low- and high-temperature sintering are referred to as Si-Ge_{873K} and Si-Ge_{1173K}, respectively.

The density of the bulk samples was determined by Archimedes' method with ethanol as the working liquid, and the results are summarized in Table I. Both samples possessed a rather high density of $d_{\text{exp}} > 3.40$ g cm⁻³, corresponding to 95% of the theoretical density of $\text{Si}_{0.65}\text{Ge}_{0.35}$ crystal estimated from the empirical formula.¹⁹⁾

$$d_{\text{Si}_{1-x}\text{Ge}_x} = 2.39 + 3.493x - 0.499x^2. \quad (1)$$

The phases involved in each sample were analyzed by conventional powder X-ray diffraction (XRD) using Cu-K α radiation ($\lambda = 0.15418$ nm) in Bruker D8 Advance. The chemical composition was investigated by EDX spectrometry using a JEOL JED-2140GS equipped with a scanning electron microscope (SEM) JEOL JSM-6330F with an accelerating voltage of 15 kV. The Hall concentration of the bulk samples was measured at 300 K using the Quantum Design Inc. Physical Property Measurement System. The thermal conductivity, κ , was measured using a laser flash method in Netzsch LFA457 over the temperature range from 300 K to 873 K. The thermal diffusivity, α , was obtained using the method described in Ref. 20 The specific heat capacity, C_p , of the sample was measured using differential laser flash calorimetry using a standard pyroceram pellet.²¹⁾ Additionally, using the sample density d , we calculated the

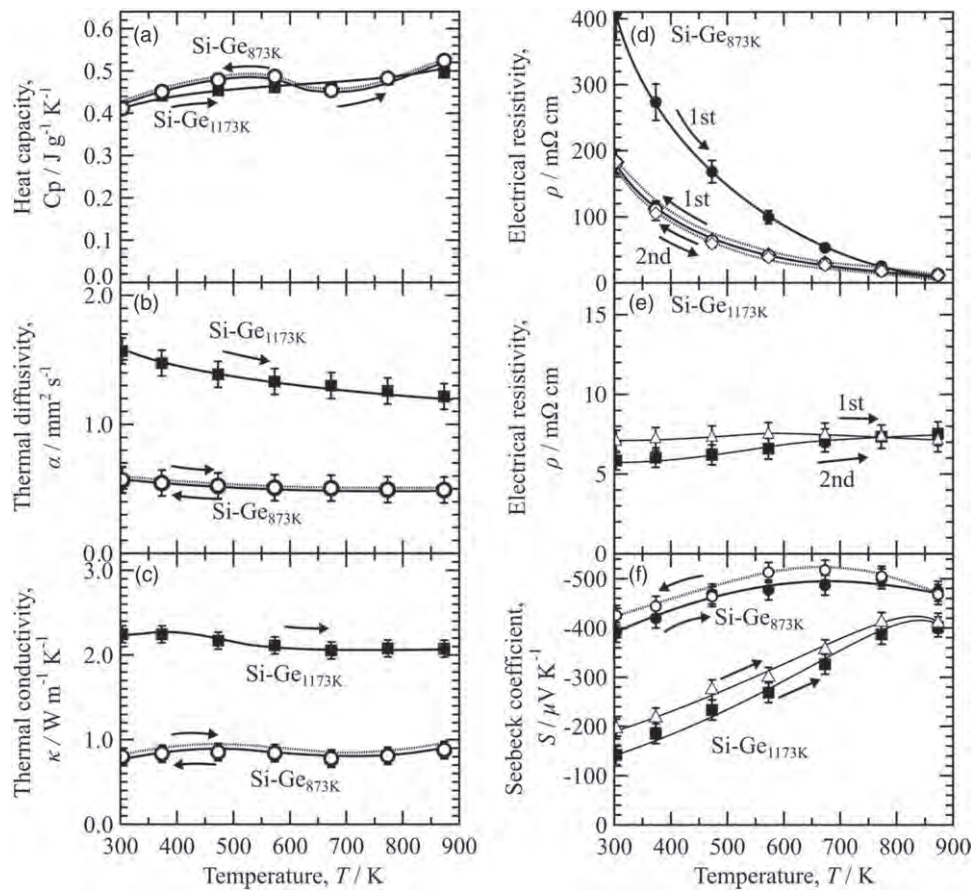


Fig. 3. (a) Heat capacity $C_p(T)$, (b) thermal diffusivity $\alpha(T)$, and (c) thermal conductivity $\kappa(T)$ of Si-Ge_{873K} and Si-Ge_{1173K}. Electrical resistivity (T) of Si-Ge_{873K} and Si-Ge_{1173K} is plotted in (d) and (e), respectively. The Seebeck coefficient $S(T)$ of both samples is plotted in (f). $S(T)$ and $\rho(T)$ were measured simultaneously under the same experimental conditions. Small arrows on the lines indicate heating or cooling conditions. $S(T)$ and $\rho(T)$ values were measured twice under the heating process for the Si-Ge_{1173K} samples. Si-Ge_{873K} had a smaller electrical resistivity after the first heating, but it stabilized, showing almost the same values in the first cooling curve, the second heating curve, and the second cooling curve.

thermal conductivity κ according to

$$\kappa = C_p \times d \times \alpha. \quad (2)$$

Electrical resistivity and the Seebeck coefficient were measured using a standard four-probe technique and steady state method, respectively, in the same temperature range under a vacuum atmosphere lower than 10^{-2} Pa.

The powder XRD patterns of the prepared samples are shown in Fig. 2(a). The XRD pattern of the ball-milled powder shows the homogeneous Si-Ge alloy consisting solely of a single phase of the diamond structure. In the low-temperature sintering sample, Si-Ge_{873K}, the phase in the as-milled powder remained without showing any precipitation of secondary phases. The average size of the crystalline nano-grains was roughly estimated from the XRD peaks using the Debye-Scherrer formula $D = K\lambda/\beta \cos(\theta)$, in which K , λ , β , and θ represent the Debye constant ($K=0.94$), X-ray wavelength ($\lambda=0.15418$ nm), line broadening, and Bragg angle, respectively. Nano-grains of $D=10 \pm 1$ nm were calculated for the milled powder, whereas a slightly larger grain size of $D=13 \pm 1$ nm was determined for Si-Ge_{873K}. This indicates that the small nano-grain size was maintained in the bulk samples, provided low-temperature sintering was employed. In sharp contrast to Si-Ge_{873K}, Si-Ge_{1173K} showed a significant grain growth to $D=53 \pm 1$ nm. Precipitation of FeSi₄P₄²²⁾ was confirmed from the XRD peak at $2\theta \approx 31^\circ$. Rietveld analysis

revealed that the volume fraction of FeSi₄P₄ was limited to values of less than 5.64%.

SEM-EDX measurements were also performed, and the secondary electron (SE) images are displayed in Figs. 2(b) and 2(c). The SE image of Si-Ge_{873K} definitely showed a large variation in grain size from a few tens to a few hundreds of nanometers in diameter. The presence of voids at the grain boundary of less than 20 nm was also confirmed in the highly densified bulk. The crystalline nanoparticles of average size 13 nm deduced by the Debye-Scherrer method indicates that the grains observed in the SE image were agglomerates of such nanocrystals. Despite the fact that P concentration far exceeded its solubility limit in Si,²³⁾ no evidence of a secondary phase was confirmed from the SE image, showing good consistency with the XRD measurement. Furthermore, the chemical composition of Si-Ge_{873K} determined by EDX showed a P concentration of 8.9 at%, close to nominal composition. This confirms the complete dissolution of P inside the amorphous Si-Ge phase. Also, EDX analysis showed the presence of 0.98 at% Fe, but no other impurity elements within the analysis sensitivity.

The SE image of Si-Ge_{1173K}, on the other hand, showed a relatively homogeneous structure without any clear evidence of a wide distribution of grain size. A small amount of FeSi₄P₄, approximately 20–100 nm in diameter, was confirmed in the SE image, in good agreement with XRD.

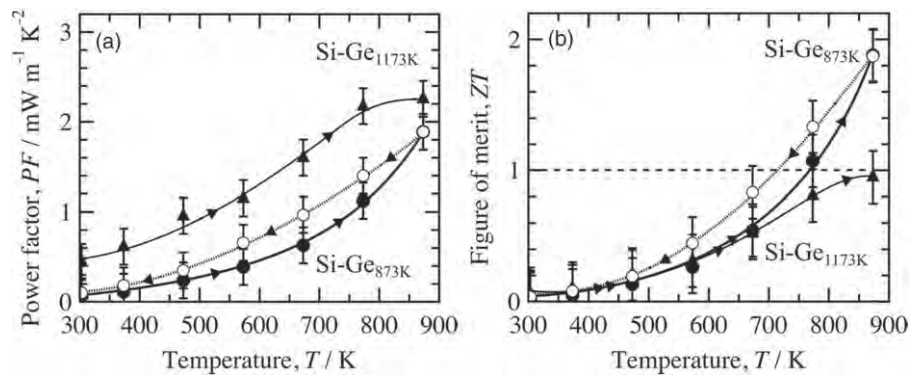


Fig. 4. (a) Power factor and (b) ZT of Si-Ge_{873K} and Si-Ge_{1173K} bulk samples. Small arrows on the lines indicate heating or cooling conditions. Si-Ge_{873K} has different values between the heating and cooling curves because of the variation in electrical resistivity. A maximal ZT value of 1.88 was observed for Si-Ge_{873K} at 873 K.

Unfortunately, the larger size of the electron beam in our SEM-EDX apparatus prevented us from precisely determining the composition of those nano-precipitates. The main portion of Si-Ge_{1173K}, where no precipitates were observed, possessed smaller amounts of Fe and P. This certainly lends great support to the precipitation scenario of FeSi₄P₄ for Si-Ge_{1173K}.

The heat capacity $C_p(T)$, thermal diffusivity $\alpha(T)$, and thermal conductivity $\kappa(T)$ are plotted as functions of temperature in Figs. 3(a)–3(c).

The heat capacity of Si-Ge_{873K} showed a slightly higher value, $C_p = 0.525 \text{ J g}^{-1} \text{ K}^{-1}$ at 873 K, than $C_p = 0.496 \text{ J g}^{-1} \text{ K}^{-1}$ of Si-Ge_{1173K}. We measured a smaller thermal diffusivity for Si-Ge_{873K} of $\alpha = 0.493 \text{ mm}^2 \text{ s}^{-1}$ at 873 K. This low thermal diffusivity led to an extremely low thermal conductivity, $\kappa < 0.88 \pm 0.10 \text{ W m}^{-1} \text{ K}^{-1}$ over the whole temperature range, much lower than $\kappa = 1.35 \text{ W m}^{-1} \text{ K}^{-1}$ previously reported for the nanostructured bulk Si_{0.65}Ge_{0.35}.¹¹⁾ This significant reduction of thermal conductivity was presumably caused by the various sizes of aggregates consisting of crystalline nanoparticles as observed in the SEM images, and by the slightly lower density associated with the voids.

In sharp contrast to the extremely small κ of Si-Ge_{873K}, Si-Ge_{1173K} showed a relatively large value: $\kappa = 2.25 \pm 0.10 \text{ W m}^{-1} \text{ K}^{-1}$ at 300 K. This large value is caused by the large $\alpha = 1.569 \text{ mm}^2 \text{ s}^{-1}$ at 300 K, presumably induced by the presence of larger crystal grains.

The Seebeck coefficient $S(T)$, and electrical resistivity $\rho(T)$ of Si-Ge_{873K} and Si-Ge_{1173K} are plotted as functions of temperature in Figs. 3(d)–3(f). All the prepared samples showed a negative sign of $S(T)$. Si-Ge_{873K} showed a high value of $S(T)$ over the whole measured temperature range with a maximal value of $517 \pm 20 \text{ } \mu\text{V K}^{-1}$ at 673 K. This value of $S(T)$ is more than double those of Si-Ge in RTGs,⁴⁾ for which $|S| > 213 \text{ } \mu\text{V K}^{-1}$ was observed at 673 K. As expected from our theoretical calculations, the enhancement of $S(T)$ is supposed to be brought about by the impurity states of Fe at the bottom of the conduction band. Si-Ge_{1173K}, on the other hand, possessed rather a smaller $S(T)$ with a maximum value of $|S| = 411 \pm 20 \text{ } \mu\text{V K}^{-1}$ at 873 K. This slightly reduced $S(T)$ would be related to the reduced amount of Fe in the Si-Ge matrix of Si-Ge_{1173K} in close accord with the precipitation of FeSi₄P₄ during the high-temperature sintering process.

The electrical resistivity of as-sintered Si-Ge_{873K} unfortunately was larger at room temperature, $\rho = 407 \pm 41 \text{ m}\Omega \text{ cm}$, but it drastically decreased with increasing temperature. The temperature dependence of $S(T)$ suggests that this reduction of $\rho(T)$ is not caused by electron-hole excitations, but by the delocalization of conduction electrons and/or the boundary resistance between nanocrystal agglomerates. At 873 K, it turns out to be small, less than $\rho < 12.4 \pm 1.2 \text{ m}\Omega \text{ cm}$.

It should be also mentioned that (T) of Si-Ge_{873K}, in the cooling process always had a smaller value than that in the first heating process. However, a second measurement of the sample showed the same values over the whole heating and cooling process, in good agreement with that of the first cooling process. This means that the microstructure of Si-Ge_{873K}, presumably at the grain boundaries, slightly varied in the first heating process, but became stable after reaching the highest temperature at 900 K.

The electrical resistivity of Si-Ge_{1173K}, on the other hand, had a less significant temperature dependence than that in disordered metals,²⁴⁾ and its average magnitude over the whole temperature range was $\rho \approx 7.50 \pm 0.75 \text{ m}\Omega \text{ cm}$. It showed no hysteresis during the heating and cooling processes.

Using the measured values of the thermoelectric properties, the power factor PF and the figure of merit ZT were calculated and are plotted in Figs. 4(a) and 4(b). The maximum power factors, $PF = 1.89 \pm 0.20 \text{ W m}^{-1} \text{ K}^{-2}$ and $2.26 \pm 0.20 \text{ W m}^{-1} \text{ K}^{-2}$ for Si-Ge_{873K} and Si-Ge_{1173K}, respectively, were observed at the highest temperature, 873 K. Because of their large electrical resistivity, these values are definitely smaller than the $2.96 \text{ W m}^{-1} \text{ K}^{-2}$ previously reported for Si_{0.80}Ge_{0.20}.⁴⁾ However, the much smaller thermal conductivity of our samples led to a superior value of ZT , exceeding unity at $T > 700 \text{ K}$, and eventually a maximum value of ZT , 1.88 ± 0.20 , was obtained for Si-Ge_{873K}.

Notably, $ZT = 1.88 \pm 0.20$ is the largest ever reported for Si-Ge-based materials. The wide temperature range from 710 K to 873 K where ZT exceeds unity is definitely important for practical applications. Strongly supported by cheap, environmentally friendly constituent elements, our new attainment of large ZT values should have a strong impact in the field of thermoelectricity, not only for developing a high-performance thermoelectric material but also proving the validity of the strategy to drastically improve the performance of any thermoelectric material.

The difference in Seebeck coefficient between Si-Ge_{1173K} and Si-Ge_{873K} is caused by the difference in carrier concentration and electronic structure associated with P and Fe: both P and Fe concentrations in the matrix were larger in Si-Ge_{873K} than in Si-Ge_{1173K} because of the absence of FeSi₄P₄ in Si-Ge_{873K}. The precipitation of FeSi₄P₄ naturally led us to expect a smaller amount of P in the main phase to reduce its carrier concentration in Si-Ge_{1173K}, but this was not the case. The carrier concentration estimated from the Hall coefficient was $n = 3.51 \times 10^{19} \text{ cm}^{-3}$ for Si-Ge_{1173K}, definitely larger than $n = 1.24 \times 10^{19} \text{ cm}^{-3}$ in Si-Ge_{873K}. The unexpected smaller carrier concentration in Si-Ge_{873K}, which contains more P in the matrix, would be brought about by the presence of impurity states of Fe 3d near the chemical potential. Therefore, we consider that the lower magnitude of $S(T)$ in Si-Ge_{1173K} is attributed partly to the larger carrier concentration and partly to the modified electronic structure near the chemical potential associated with the impurity states from Fe. We also consider that the effect of the precipitated FeSi₄P₄ particles themselves on the transport properties would be negligibly small, because their volume fraction was very small and each tiny particle was isolated.

Despite the fact that the smaller electrical resistivity of Si-Ge_{1173K} made its power factor larger than that of Si-Ge_{873K}, the simultaneously obtained larger magnitude of thermal conductivity led to smaller values of ZT , especially at high temperature, where the electrical resistivity of Si-Ge_{1173K} becomes comparable to that of Si-Ge_{873K}. This means that the σ/κ ratio is larger in Si-Ge_{873K} than in Si-Ge_{1173K}, especially at temperatures above 673 K. Strongly supported by the larger value of both the σ/κ ratio and S , the ZT value of Si-Ge_{873K} became much larger than that of Si-Ge_{1173K}.

In conclusion, we succeeded in improving the dimensionless figure of merit ZT of a Si-Ge-based material, Si_{0.55}Ge_{0.35}P_{0.10}Fe_{0.01}, by constructive modification of the electronic structure, and effectively reducing the lattice thermal conductivity by means of nano-structuring. Large power factors of $PF = 1.89 \text{ W m}^{-1} \text{ K}^{-2}$ and $2.26 \text{ W m}^{-1} \text{ K}^{-2}$ were observed at the highest temperature, 873 K, for Si-Ge_{873K} and Si-Ge_{1173K}, respectively, presumably due to the formation of 3d- t_{2g} orbitals of Fe as impurity states near

the bottom of the conduction band. The nano-structure, composed of various grain sizes, led to the low $\kappa < 0.88 \pm 0.05 \text{ W m}^{-1} \text{ K}^{-1}$ within the whole temperature range for Si-Ge_{873K}. As a result, a very high figure of merit, $ZT > 1.88$, was observed for Si-Ge_{873K} at 873 K.

Acknowledgements This work was partly supported by JSPS KAKENHI Grant Number JP18H01695 and partly by the Center of Innovation Program from Japan, Science and Technology Agency, JST, Grant Number JPMJCR18I2.

ORCID iDs Kévin Delime-Codrin  <https://orcid.org/0000-0003-1887-0621>

- 1) S. I. Kim et al., *Science* **348**, 109 (2015).
- 2) K. Biswas, J. He, I. D. Blum, C.-I. Wu, T. P. Hogan, D. N. Seidman, V. P. Dravid, and M. G. Kanatzidis, *Nature* **489**, 414 (2012).
- 3) M. Rull-Bravo, A. Moure, J. F. Fernandez, and M. Martin-Gonzalez, *RSC Adv.* **5**, 41653 (2015).
- 4) D. M. Rowe, *CRC Handbook of Thermoelectrics* (CRC Press, Boca Raton, FL, 1995).
- 5) G. Schierning, R. Theissmann, N. Stein, N. Petermann, A. Becker, M. Engenhorst, V. Kessler, M. Geller, H. Wiggers, and R. Schmechel, *J. Appl. Phys.* **110**, 113515 (2011).
- 6) A. Miura, S. Zhou, T. Nozaki, and J. Shiomi, *ACS Appl. Mater. Interfaces* **7**, 13484 (2015).
- 7) A. Nozariasbmarz, Z. Zamanipour, P. Norouzzadeh, J. S. Krasinski, and D. Vashaee, *RSC Adv.* **6**, 49643 (2016).
- 8) Z. Zamanipour and D. Vashaee, *J. Appl. Phys.* **112**, 093714 (2012).
- 9) G. Joshi et al., *Nano Lett.* **8**, 4670 (2008).
- 10) X. W. Wang et al., *Appl. Phys. Lett.* **93**, 4670 (2008).
- 11) O. Muthusamy et al., *J. Electron. Mater.* **47**, 3260 (2018).
- 12) L. D. Hicks and M. S. Dresselhaus, *Phys. Rev. B* **47**, 727 (1993).
- 13) B. Yu, M. Zebarjadi, H. Wang, K. Lukas, H. Wang, D. Wang, C. Opeil, M. Dresselhaus, G. Chen, and Z. Ren, *Nano Lett.* **12**, 2077 (2012).
- 14) J. P. Heremans, V. Jovovic, E. S. Toberer, A. Saramat, K. Kurosaki, A. Charoenphakdee, S. Yamanaka, and G. J. Snyder, *Science* **321**, 554 (2008).
- 15) H. Takiguchi, M. Aono, and Y. Okamoto, *Jpn. J. Appl. Phys.* **50**, 041301 (2011).
- 16) S. Nishino, S. Ekino, M. Inukai, M. Omprakash, M. Adachi, M. Kiyama, Y. Yamamoto, and T. Takeuchi, *J. Electron. Mater.* **47**, 3267 (2017).
- 17) G. Kresse and J. Furthmuller, *Phys. Rev. B* **54**, 11169 (1996).
- 18) J. P. Perdrew, K. Burkley, and M. Ernzerhof, *Phys. Rev. Lett.* **18**, 3865 (1996).
- 19) F. Schaffler et al. (ed.) *Properties of Advanced Semiconductor Materials GaN, AlN, InN, BN, SiC, Si_{1-x}Ge_x* (Wiley, New York, 2001), p. 149.
- 20) W. Parker, R. Jenkins, C. Butler, and G. Abott, *J. Appl. Phys.* **32** (1961)1679.
- 21) K. Shinzato and T. Baba, *J. Therm. Anal. Calorimetry* **64** (2001)413.
- 22) C. Perrier, H. Vincent, P. Chaudouet, B. Chenevier, and R. Madar, *Mater. Res. Bull.* **30**, 357 (1995).
- 23) R. W. Olesinski, N. Kanani, and G. J. Abbaschian, *J. Phase Equilib.* **6**, 130 (1985).
- 24) A. F. Ioffe and A. R. Regel, *Prog. Semicond.* **4**, 237 (1960).



Mechanical and *in vitro* study of an isotropic Ti6Al4V lattice structure fabricated using selective laser melting

Xingchen Yan^{a, b}, Qing Li^b, Shuo Yin^c, Ziyu Chen^d, Richard Jenkins^c, Chaoyue Chen^{e, *}, Jiang Wang^e, Wenyu Ma^b, Rodolphe Bolot^a, Rocco Lupoi^c, Zhongming Ren^e, Hanlin Liao^a, Min Liu^{b, **}

^a LERMPS, ICB UMR 6303, CNRS, Univ. Bourgogne Franche-Comté, UTBM, F-90010, Belfort, France

^b National Engineering Laboratory for Modern Materials Surface Engineering Technology, The Key Lab of Guangdong for Modern Surface Engineering Technology, Guangdong Institute of New Materials, Guangzhou, 510651, PR China

^c Trinity College Dublin, The University of Dublin, Department of Mechanical and Manufacturing Engineering, Parsons Building, Dublin 2, Ireland

^d Department of Orthopedics, The Third Affiliated Hospital of Southern Medical University, No. 183, Zhongshan West Avenue, Tianhe District, Guangzhou, 510630, Guangdong, PR China

^e State Key Laboratory of Advanced Special Steels, School of Materials Science and Engineering, Shanghai University, Shanghai, 200444, PR China

<https://doi.org/10.1016/j.jalcom.2018.12.220>
0925-8388/© 2018 Elsevier B.V. All rights reserved.

ARTICLE INFO

Article history:

Received 16 October 2018

Received in revised form

14 December 2018

Accepted 17 December 2018

Available online 18 December 2018

Keywords:

Lattice structure

Selective laser melting

Johnson-cook damage model

Ti6Al4V

Compression test

ABSTRACT

This study presents an evaluation of the effects of pore diameter and porosity on the mechanical properties and biocompatibility of Ti6Al4V ELI periodic lattice structures, fabricated using SLM technology. Lattice structures of titanium alloys are in high demand for biomedical applications and are particularly useful as bone substitutes. A series of lattice structures with pore diameters of 500, 600, and 700 μm and porosities of 60% and 70% were designed by repeating an octahedral unit cell. Based on SEM and micro-CT observations, good morphological agreement was detected between the original designs and the SLM-produced structures. Microstructural analysis using TEM showed that the typically acicular α' martensitic microstructure was obtained in the strut, which contributes to the brittle behavior of the lattice structure. Uniaxial compression tests were conducted, and the deformation behavior was recorded using a digital camera. Finite element analysis (FEA) of compression process was also conducted to enhance the understanding of the deformation mechanism. The surface chemistry of the lattice structure was analyzed using XPS methodology. The cytocompatibility of the lattice was also investigated with an *in vitro* test. The results show that the lattice structures with biocompatible surfaces have a comparable compressive strength (71–190 MPa) and elastic modulus (2.1–4.7 GPa) to trabecular bone.

© 2018 Elsevier B.V. All rights reserved.

1. Introduction

Metallic biomaterials play an essential role in assisting the repair or replacement of diseased or damaged bones in orthopaedics [1]. Among the commonly used metallic biomaterials such as Ti, Ta, Cr, Co, and stainless steel, Ti6Al4V ELI alloy has drawn increasing attention owing to its excellent mechanical and biological performance [2]. For metal implants, the elastic modulus is one of the most important mechanical properties. Although the elastic modulus of Ti6Al4V ELI alloy (100–140 GPa) [3,4] is lower than that

of other metals such as Co-based alloys (210–253 GPa) [5] and stainless steel (190–210 GPa) [6], it is still much higher than that of bone tissues (4–30 GPa) [7]. The elastic modulus mismatch between the Ti implant and bone tissue may cause stress shielding around the orthopaedic replacement, which can lead to bone atrophy and even implant loosening. Lattice structures have been recognized as an effective solution to narrow the elastic modulus difference and provide low density, high-surface-area ratio, and high energy absorption efficiency. Furthermore, the lattice structure can improve the ability of bone tissue in-growth and increase the rate of osteoblast differentiation [8–10]. Previous studies reported that the desirable pore diameter and porosity of a lattice structure for promoting bone tissue in-growth were 400–800 μm and 60–90%, respectively [8,11,12].

SLM is a novel powder bed additive manufacturing (AM) and 3D

* Corresponding author.

** Corresponding author.

E-mail addresses: cchen1@shu.edu.cn (C. Chen), liumin@gdas.gd.cn (M. Liu).

printing technology which has been used for the manufacture of custom implants. During this process, the metallic powder bed is selectively fused by a high-energy laser beam layer by layer. The resultant molten pool experiences rapid solidification (10^3 – 10^6 K/s) [12], offering tailored and ultrafine microstructure of the SLM parts. In contrast to traditional subtractive manufacturing techniques, SLM has the ability to directly fabricate the metallic cellular and lattice sample with complex interior structures without mold. With the direct fabrication from model, this technique can accelerate the procedure from model design, fabrication to sample test. The quality of the SLM lattice structures can be maximized by optimizing the laser power, laser scan speed, geometric design, and post-process treatment using parametric control. Thus, SLM is becoming an effective technique for the fabrication of customized human implants [2,13].

Currently, the studies of SLM lattice structures have mainly focused on their mechanical properties, with most of these lattice structures being employed in aeronautics and automobile industries. Lattice structures for biomedical applications such as the bone substitutes are complex, requiring different preferential dimensions of porosity and pore diameter. The characteristics of the unit cell that constitutes the lattice structure directly determine the mechanical and biological properties, such as the elastic modulus and tissue regeneration performance of the lattice structure [14,15]. So far, a relatively comprehensive unit cell library has been developed through numerical [16–18] and experimental analysis [10,19]. Unit cells with different shapes such as cube [11,20], dodecahedron [21,22], diamond [23], pyramidal [24], and tetrakaidecahedron [25,26] have been reported. Among all these unit cells, the octahedral unit cell is one of the most commonly used [27,28] owing to its spatial symmetry. The octahedral unit cell can be regarded as a body-centered cube (BCC) structure when the unit cell is extracted with the nodes. Very few studies have focused on the SLM BCC lattice structures. Smith et al. [20] studied the compressive response of the 316L stainless steel BCC and BCC-Z (BCC with vertical pillars) lattice structures produced by SLM. The results showed that the initial stiffness, yield strength, and energy absorption can be improved drastically by reducing the unit cell aspect ratio. Mines et al. [29] investigated the drop weight impact behavior of SLM Ti6Al4V sandwich-structured panels with BCC lattice cores. The authors found that the mechanical properties of the BCC Ti6Al4V structure was comparable to the aluminum honeycomb structure. Xiao et al. [28] used topology optimization technology to study the mechanical behavior and energy absorption properties of various SLM lattice structures including the face center cube (FCC), vertex cube (VC), and edge center cube (ECC). In addition, Sun et al. [30] found an exponential relationship between fracture load and porosity of SLM Ti6Al4V lattice, using the simplified octahedral model. Yan et al. [19] reported a good agreement in the geometry and mechanical properties of AlSi10Mg diamond lattice structures between designed structures and real structures manufactured using direct metal laser sintering (DMLS) method. Sun et al. [31] and Yang et al. [32] studied a simplified version of the octahedral unit cell where the horizontal struts were not considered. In addition, the horizontal struts of the octahedral can improve the isotropy of the lattice structure, which is helpful to the homogeneity mechanical behavior and can enhance the safety of bone implants. Hedayati et al. [15] studied the mechanical properties of the octahedral lattice structure with horizontal struts; however, an in-depth study on the effect of pore size and porosity was not included.

Although some studies have explored SLM lattice structures, the effect of pore size and porosity on the mechanical properties of the octahedral lattice structure and the corresponding biomedical performance are still not well understood. Moreover, most of

above-mentioned studies mainly focused on the mechanical performance of the lattice structure with varying geometry. Regarding the biomedical applications, few of them investigated the cell response for the lattice structure. Hence, it is necessary to investigate the effects of pore size and porosity on both the mechanical and biological properties of SLM lattice structure. Previous studies have demonstrated that optimum pore diameter and porosity are beneficial to the in-growth of bones and vessels [33]. Therefore, systematical investigation from the mechanical characteristics to biomedical properties of the SLM Ti6Al4V lattice structure has been conducted in this work. The octahedral lattice structures were fabricated using SLM with Ti6Al4V as feedstock material. The effects of pore size and porosity on the mechanical and biomedical properties were studied on the SLM Ti6Al4V lattice structure. Considering the biomedical application, a unit cell with pore sizes of 500, 600, and 700 μm and porosities of 60% and 70% were designed and manufactured with SLM [34–38].

2. Experimental details

2.1. Design and fabrication of Ti6Al4V lattice structures

Gas atomized spherical Ti Grade23 powder, also known as Ti6Al4V ELI (EOS GmbH, Germany), was used as the feedstock material. The surface morphology of the Ti6Al4V ELI powder is provided in Fig. 1a and b with different magnifications, and the cross-sectional view is shown in Fig. 1c where typically fine needle-like martensite can be observed. The highly spherical shape of the feedstock particles can facilitate the SLM process and help to produce dense Ti6Al4V samples. The powder size distribution ($d_{0.1} = 21.97 \mu\text{m}$, $d_{0.5} = 33.77 \mu\text{m}$ and $d_{0.9} = 51.43 \mu\text{m}$) was measured using a laser diffraction particle analyzer (Mastersizer 2000, Malvern Instruments Ltd., UK) and is shown in Fig. 1d.

The chemical composition of the Ti6Al4V ELI is listed in Table 1. According to supplier's information, the oxygen content of the Ti6Al4V powder is less than 0.13 wt%, which is below the minimum requirement in the biological industry (0.20 wt%). The Ti6Al4V samples were produced using a commercial EOS M290 system (EOS GmbH Germany) equipped with an Yb-Fiber laser (1070 nm), having a maximum power of 400 W. Due to the high reactivity of Ti6Al4V to interstitial elements, the oxygen content in the build chamber was maintained below 0.1% by using Ar gas as the protective atmosphere. Optimized SLM processing parameters were used in the experiments with a laser power of 240 W, scanning speed of 240 mm/s, layer thickness of 30 μm , laser spot size of 100 μm and hatch distance of 50 μm .

Various unit cells with different porosities (P), pore diameters (Dp), and strut thicknesses (St) were designed using a CAD software UG NX 10 (Siemens PLM, Germany). Fig. 2 shows the schematic and photo of the lattice structures manufactured in this work. As shown in Fig. 2a, a regular octahedron unit cell was used as the architecture of these lattice structures. The overhanging cuboid strut has an angle of 45° as shown in Fig. 2b. Six cubic lattice structures with dimensions of 10 mm \times 10 mm \times 15 mm were designed using a software of Magics (Materialise, Belgium). The pore diameter and porosity of each cubic lattice structure are listed in Table 2. The term of porosity (P) is defined as

$$P = \left(1 - \frac{\rho_p}{\rho_s}\right) \times 100\% \quad (1)$$

where ρ_s is the material density (4.43 g/cm³), ρ_p is the density of the porous structure which was measured based on the Archimedes principle using the following formula:

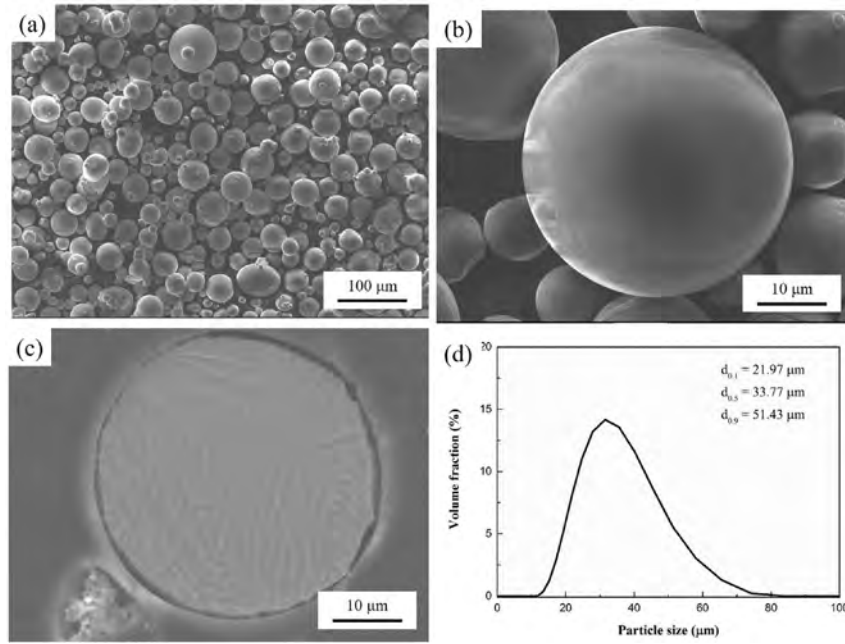


Fig. 1. SEM and particle size distribution of the feedstock used in this work. (a) overview and (b) high-magnification view of the spherical Ti6Al4V ELI powder, (c) cross-sectional view after etching, (d) particle size distribution.

Table 1
The chemical composition of the used Ti6Al4V ELI powder.

Element	Ti	Al	V	O	N	C	H	Fe
wt.%	Balance	5.5–6.5	3.5–4.5	<0.13	<0.03	<0.08	<0.012	<0.25

Table 2
Designation of the SLM-produced Ti6Al4V lattice structures.

Sample designation	A1	A2	A3	B1	B2	B3
Porosity (%)	60	60	60	70	70	70
Pore diameter (μm)	500	600	700	500	600	700

$$\frac{\rho_p}{\rho_s} = \frac{\rho_{\text{water}} \cdot m_{p(\text{air})}}{\rho_s \cdot (m_{p(\text{air})} - m_{p(\text{water})})} \quad (2)$$

where $m_{p(\text{air})}$ is the weight of SLM lattice structure sample in air; $m_{p(\text{water})}$ is the weight of a SLM lattice structure sample in water; ρ_{water} is the density of water. For the convenience of addressing, each sample was given a designation as shown in Table 2. Fig. 2c shows the photo of a lattice structure fabricated with SLM.

2.2. Microstructure, morphological and surface chemical characterization

The surface morphologies and cross-sectional microstructure of

the lattice structure samples were characterized using a scanning electron microscope (SEM, FEI Nova Nano SEM 450). As a preparation for the microstructure analysis, samples were polished using standard metallographic procedures with the final polishing applied using 0.05 μm alumina solution. The polished samples were etched in a solution of 50 ml H₂O, 25 ml HNO₃ and 5 ml HF to observe and study the grain structure. An optical microscope (OM, Leica Dmi5000m) was used for the metallographic analysis. The grain structure of the lattice structure sample was also characterized using Transmission Electron Microscopy (TEM, Titan Themis 200, FEI).

A randomly selected lattice structure sample was scanned using an X-computer tomography system (X5000, North Star Imaging, USA) with an acceleration voltage of 100 keV and a current of 90 μA

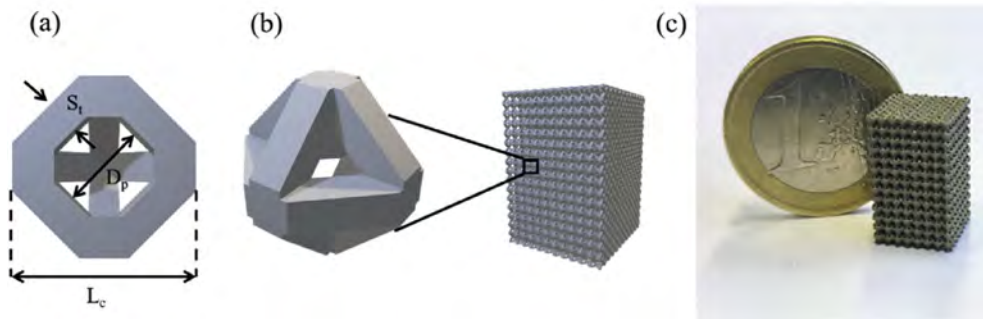


Fig. 2. Schematic and photograph of the lattice structures manufactured in this work. (a) cross-section of the B2 unit cell ($P = 70\%$ and $D_p = 600 \mu\text{m}$); (b) 3D view of the B2 unit cell (left) and cubic lattice structure made using the B2 unit cell (right); (c) digital photo of the SLM B2 cubic lattice structure.

to evaluate the pore diameter, porosity and strut thickness. A 2 mm × 2 mm × 2 mm unit cell was studied with a precision of 4 μm/voxel. The 3D volume was then reconstructed using the Amira-Avizo software (FEI Visualization Sciences Group, Software, Germany) and the porosity was computed based on the mean value of the entire volume.

X-ray photoelectron spectroscopy (XPS) Escalab 250Xi (Thermo Fisher Ltd), equipped with an Al Kα (λ = 1486.6 eV) X-ray source was adopted to characterize the surface chemical composition. The spectra were measured with an energy step of 0.05 eV and normalized to the binding energy of the C1s peak (284.8 eV). Distilled water and ethanol were used to thoroughly clean the porous sample before the XPS testing commenced.

2.3. Mechanical characterization

Static uniaxial compression tests were carried out using an Instron 8872 instrument at room temperature following the ISO 13314:2011 standard. A load of 50 kN was applied to each lattice structure sample at a constant deformation rate of 0.5 mm/min. Five samples of each lattice structure were tested. The load-displacement data during compression process were recorded to plot the stress-strain curve. In order to investigate the detailed deformation behavior, a digital video recorder was used to monitor the compression tests. Based on the ISO 13314:2011 standard, the first maximum compressive strength (σ_{\max}) corresponds to the first local maximum stress value in the stress-strain curve. Plateau stress (σ_{pl}) was the arithmetical mean of the stresses between 20% and 30% compressive strain. Plateau end stress (σ_{130}) was calculated as 1.3 times the σ_{pl} . The elastic gradient ($E\sigma_{20}-\sigma_{70}$) was determined by the gradient of the elastic straight line between two stress values of σ_{70} and σ_{20} (σ_{70} and σ_{20} correspond to 70% and 20%, respectively, of the plateau stress, σ_{pl}) [39].

2.4. Finite element analysis

To better understand the mechanical properties of the lattice structure samples, FEA was conducted to simulate the quasi-static compression test. A 3D explicit model was established using a commercial code (ABAQUS/explicit) by importing the CAD model of the lattice structure. The compression process was performed by a dynamic explicit procedure. In order to simplify the numerical model and improve the calculation efficiency, a lattice structure with a 5 mm × 5 mm × 5 mm unit cell was modelled as an assembled entity in the compression test. Such structural simplifications have been frequently applied in numerical studies by other researchers [40,41]. The geometry of the lattice structure was partitioned and meshed by four-node linear tetrahedral elements (C3D4). To develop the simulated compression process, two rigid shell plates were placed on the top and bottom of the lattice structure, and the interaction between the rigid plates with the lattice was defined as tie constrained. The rigid upper plate was gradually moved downwards at a vertical speed to crush the lattice structure. The reference point of the rigid upper plate was used to obtain the stress-strain curve of the numerical compression process. The lower plate was defined as a fixed substrate. Both rigid plates were meshed by bilinear rigid quadrilateral elements. The interaction within the lattice structure during crushing deformation was assessed by the penalty contact algorithm.

The Johnson-Cook plasticity model [42] was used to describe the plastic deformation and heat transfer, which accounts for the strain hardening, strain-rate (viscosity), and thermal softening. The yield stress can be expressed by the equation given below:

$$\sigma_y = [A + B(\dot{\epsilon}_e^p)^N] \cdot \left[1 + C \ln\left(\frac{\dot{\epsilon}^{pl}}{\dot{\epsilon}_0}\right)\right] \cdot [1 - (T^*)^M] \quad (3)$$

where A , B , N , C and M are material-related constants based on the flow stress data obtained from mechanical tests, $\dot{\epsilon}_e^p$ is the effective plastic strain, and $\dot{\epsilon}^{pl}$ is the equivalent plastic strain rate and $\dot{\epsilon}_0$ is the reference strain rate. T^* is a non-dimensional temperature defined as:

$$T^* \equiv \begin{cases} 0 & \text{for } T < T_{\text{transition}} \\ (T - T_{\text{transition}}) / ((T_{\text{melt}} - T_{\text{transition}})) & \text{for } T_{\text{transition}} \leq T \leq T_{\text{melt}} \\ 0 & \text{for } T > T_{\text{melt}} \end{cases} \quad (4)$$

A linear Mie–Grüneisen equation of state (EOS) was employed to account the material elasticity. The mechanical and thermal properties of the materials are assumed to be isotropic. The materials properties for the Johnson–Cook model describing the plasticity and fracture evolution of Ti6Al4V alloy are provided in Table 3 [43].

The fracture initiation and damage evolution were considered in this model by employing the fracture strain-based Johnson–Cook damage model. By enabling the status variable, the failure elements which exceed the limits can be deleted from the model. This Johnson–Cook damage model can be expressed as follows:

$$\bar{\epsilon}_f = \left[d_1 + d_2 \exp\left(d_3 \frac{p}{q}\right)\right] \cdot \left[1 + d_4 \ln\left(\frac{\dot{\epsilon}^{pl}}{\dot{\epsilon}_0}\right)\right] \cdot [1 - d_5 T^*] \quad (5)$$

where d_1 , d_2 , d_3 , d_4 , and d_5 are failure parameters in the Johnson–Cook damage model. d_1 , d_2 , and d_3 are damage parameters related to the relationships between failure strain and stress triaxiality, d_4 and d_5 depend on strain rate and temperature, respectively. The term of p/q is stress triaxiality parameter defined as the ratio between hydrostatic stress (p) and equivalent stress (q).

2.5. Cytocompatibility in vitro study

The SLM solid and porous plates with a dimension of 10 mm × 10 mm × 2 mm were used to assess the biocompatibility

Table 3
Johnson–Cook fracture model parameters for the Ti6Al4V alloy used in the simulation.

Properties	Value
Density, ρ (kg/m^3)	4430
Shear modulus, E (GPa)	110
Yield strength, A (MPa)	862
Hardening coefficient, B (MPa)	331
Strain-hardening exponent, N	0.34
Softening exponent, M	1.1
Melting temperature, T_m ($^\circ\text{C}$)	1630
Reference temperature, T_0 ($^\circ\text{C}$)	25
Strain rate constant, C	0.012
Conductivity, λ ($\text{W}/(\text{m} \times \text{K})$)	6.6
Specific heat, C_p ($\text{J}/(\text{kg} \times \text{K})$)	670
Inelastic heat fraction	0.9
Sound velocity, C_0 (m/s)	5.13
Slope in v_s versus v_p , S	1.03
Grüneisen coefficient, γ_0	1.23
d_1	−0.09
d_2	0.25
d_3	−0.5
d_4	0.014
d_5	3.87

of the material. All the samples were thoroughly cleaned and sterilized at 120 °C for 20 min. *In vitro* studies were performed using rat bone marrow mesenchymal stem cells (rBMSCs). The rBMSCs were resuspended in culture media including α -MEM (Gibco, USA) and 10% (v/v) fetal bovine serum (FBS, Gibco, USA). 5×10^4 cells were seeded directly onto the sterilized samples placed in 24-well cultivating plates and incubated at 37 °C in a humidified atmosphere with 5% CO₂. SEM observations were performed after the cells were cultured for 24 h to visualize the morphologies of cells attached to the surface of the samples. Three samples of each group were fixed with Karnovsky's fixative (2% formaldehyde, 2.5% glutaraldehyde and 2.5% sucrose in 0.2 M cacodylate buffer) for 1.5 h. Then, the samples were rinsed with 0.1 M cacodylate buffer and dehydrated in ethanol. Finally, these samples were covered with hexamethyldisilazane (100%, 2×10 min) and dried at 28 °C overnight. After coating with gold (10 nm), the samples were analyzed in the SEM. The Live/Dead Assay Kit (Thermo Fisher Scientific) was used to qualitatively evaluate the live and dead cells seeded on samples as per the manufacturer's instructions. The fluorescence images were photographed by an inverted fluorescence microscope.

3. Results

3.1. General characteristics of the SLM lattice structure

The photographs of the front and side views of the SLM lattice structure samples are shown in Fig. 3a and b, respectively. The SEM images of the B2 lattice structure are shown in Fig. 3c and d. The continuous geometric structure can be observed in Fig. 3c and the surface of the struts are sintered with partially melted particles as shown in Fig. 3d. A similar phenomenon was reported in previous studies [2,44]. It is generally considered that the waviness on the surface of the struts is caused by a combined effect of the 45° angle of the struts and the staircase performance of the SLM process. Besides, owing to the difference in the heat transfer process between the angled struts and other zones, particles tend to stick to the strut surface [45,46]. This appearance can lead to the mismatch between the original design and as-manufactured sample.

In order to assess the dimensional accuracy of the lattice structure samples, porosity was measured using the Archimedes method and micro-CT scanning. Table 4 lists nominal and measured porosity. The porosity calculated by the Archimedes method is about 0.8% lower than that of the nominal one for both group A and B. This may be explained by unavoidable errors associated with the Archimedes method due to the heterogeneous wettability of water into micro-sized pores within the lattice structure. Micro-CT scanning was conducted to further analyze the geometrical properties of the lattice structures. However, slightly higher porosity was detected by the micro-CT, with a deviation of ~1.3% for group A and ~4.5% for group B. The dross adhering to the strut surface and waviness are the reasons for the mismatch of the porosity between nominal values and measured values. In order to estimate the density of the lattice structure, the porosity value calculated by micro-CT was adopted.

3.2. Microstructure and phase constitution

The microstructures of the struts and unit nodes observed using SEM and TEM are shown in Fig. 4. The optimal processing parameters manufactured an intact strut without any defects as is shown in Fig. 4a. In Fig. 4b, partially melted particles that sintered on the edge of the strut were observed, which can increase the roughness of the strut surface. It is very difficult to remove welded particles using conventional methods without destroying the integrity of the strut. There is limited literature on the polishing of the internal lattice structure, and to the knowledge of the authors, there is no accepted method which does not damage the structure of the lattice. Fig. 4c shows the etched cross-sectional image of a node, where needle-like microstructures can be observed. The needle-like structure mainly consists of α' martensites due to the rapid solidification during the SLM process, which is a typical microstructure of the as-fabricated SLM Ti6Al4V alloy [47]. Moreover, internal defects such as cracks can be detected on the cross-sectional image, which can be caused by the lap joint of the angular strut. Back-scattered electron (BSE) image illustrated in Fig. 4d shows small residual pores within the strut. Although these residual pores have a size of approximately 1 μ m, they are still

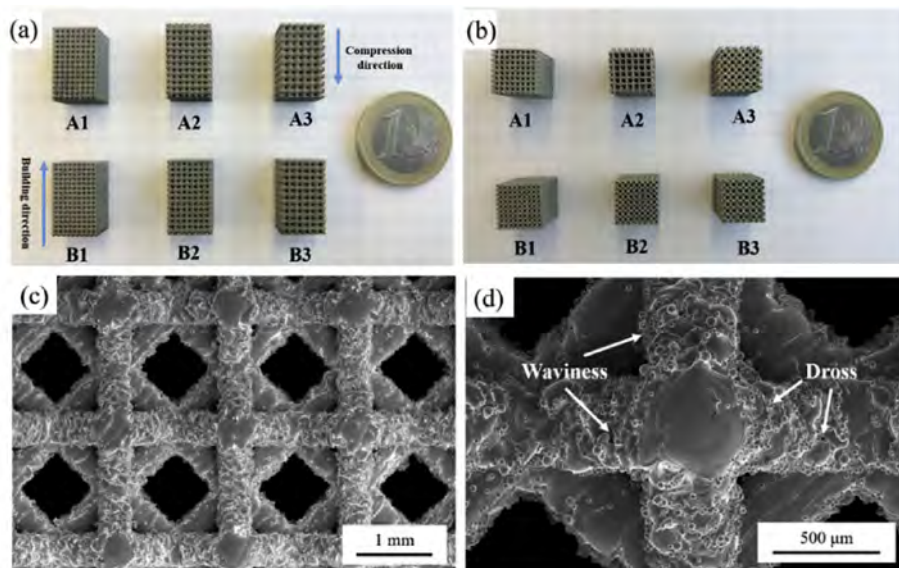


Fig. 3. Photographs and morphologies of the lattice structure samples. (a) side view, (b) front view, (c) overview morphology of B2 sample observed by SEM and (d) high-magnification morphology of the B2 sample observed using SEM.

Table 4
Porosity and density of the Ti6Al4V lattice structures (standard deviation in parentheses).

Series name	A1	A2	A3	B1	B2	B3
P, nominal (%)	60	60	60	70	70	70
P, Archimedes (%)	59.6 (± 3.7)	59.4 (± 2.5)	59.0 (± 3.3)	70.1 (± 4.2)	69.1 (± 1.7)	68.3 (± 2.9)
P, micro CT (%)	62.3 (± 1.3)	61.2 (± 2.2)	60.5 (± 1.7)	75.5 (± 3.1)	74.7 (± 2.7)	73.3 (± 2.3)
ρ_p (g/mm ³)	1.78 (± 0.3)	1.79 (± 1.3)	1.81 (± 1.3)	1.32 (± 1.3)	1.37 (± 1.3)	1.40 (± 1.3)

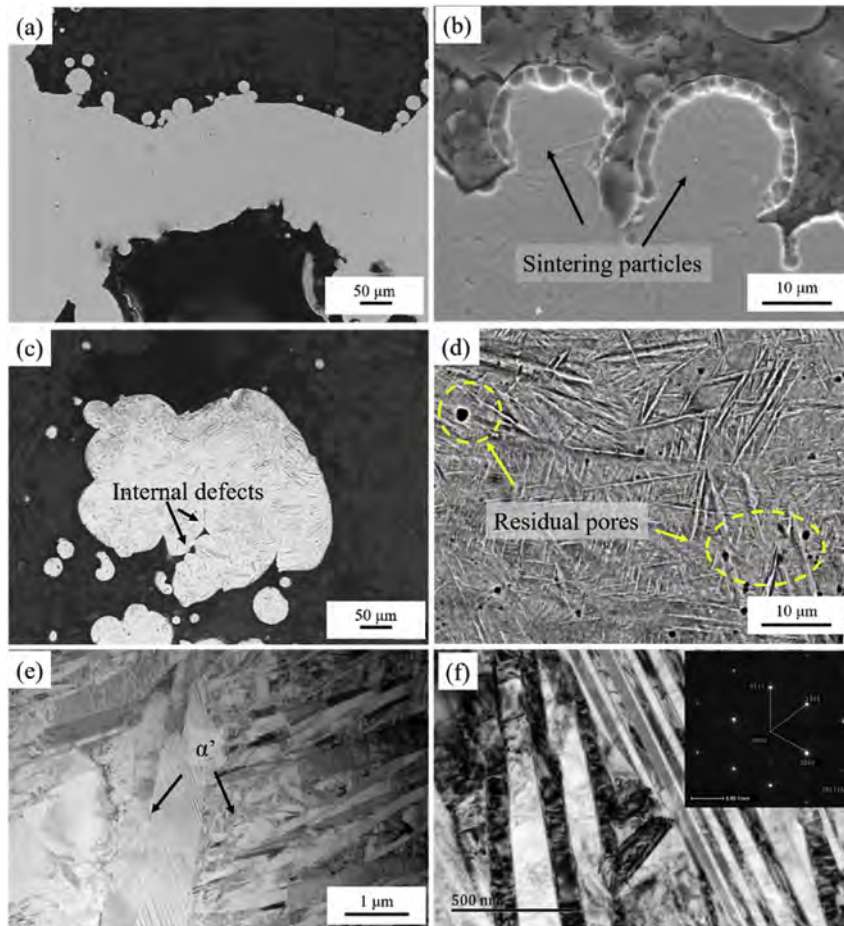


Fig. 4. Microstructure characterization of the SLM lattice structure: (a) Cross-sectional observations of a B1 strut; (b) welded powder on the strut surface; (c) the node image of the B1 unit cell after etching; (d) BSE image of B1 strut to observe the micro-residual pores; (e) STEM image and (f) BFI with the corresponding SAED patterns of the microstructure.

detrimental to the mechanical properties, especially under cyclical loading conditions. The scanning transmission electron microscopy (STEM) image and selected area electron diffraction (SAED) pattern shown in Fig. 4e and d further confirm the close-packed hexagonal (hcp) α' phase in the lattice structure. In addition, the TEM image in Fig. 4f also shows dense dislocations in the martensitic plates. This phenomenon can result in brittleness of the lattice structure during the compressive test. To further study the element composition of the lattice structure, EDS mapping of B1 sample is shown in Fig. 5 with the lattice structure containing only Ti, Al, and V.

3.3. Morphological characterization

Fig. 6a and b shows the initial design and CT-reconstructed 3D profile of a 2 mm \times 2 mm \times 2 mm array unit cell selected from sample A2. The CT-reconstructed 3D profile of the SLM sample matches well with the original drawing. In addition, no fractured unit cells but rough surfaces are observed on the CT-reconstructed

3D profile. Fig. 6c shows the CT detected residual pores within the selected A2 in Fig. 6b. The residual pores are uniformly distributed in the strut without any observable accumulation in any one area. This relatively even distribution is beneficial to the prevention of stress concentration, which can lead to premature failure during loading. Fig. 6d shows the size distribution of the residual pores within the strut. The equivalent diameter of the residual pores in the strut is approximately 6.5 μ m. It should be noted that the resolution of the CT reconstruction is 4 μ m; hence the quantitative analysis cannot account for the ultra-fine residual pores whose diameter is less than this value. Fig. 7 compares the pore diameter and strut thickness between the nominal values and experimental measurements of group A and B. In general, the measured values have no significant difference from the nominal values in both pore diameter and strut thickness. The measured pore diameters are slightly lower than those of the nominal ones, while the reverse is observed in the case of strut thickness.

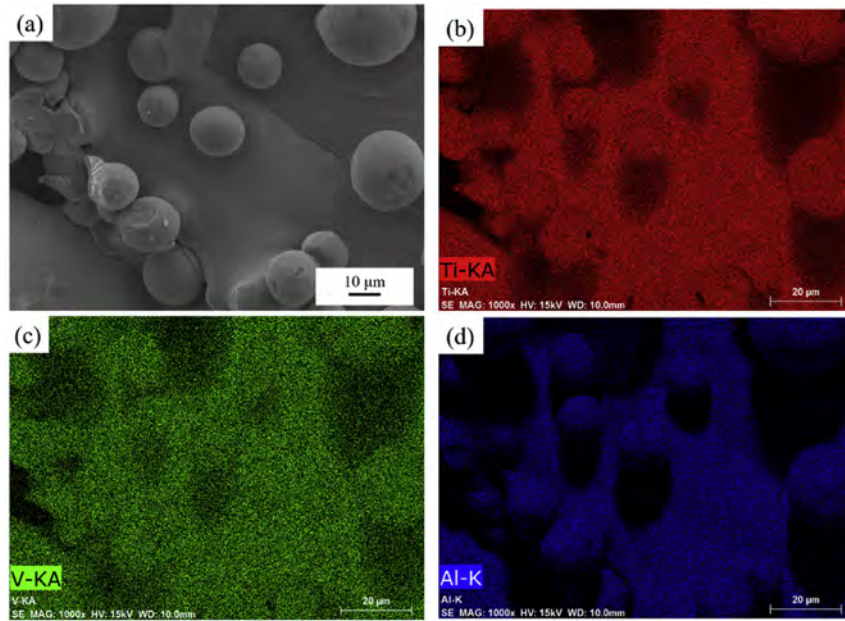


Fig. 5. EDS mapping of B1 sample showing the Ti, Al and V elements in the lattice structure.

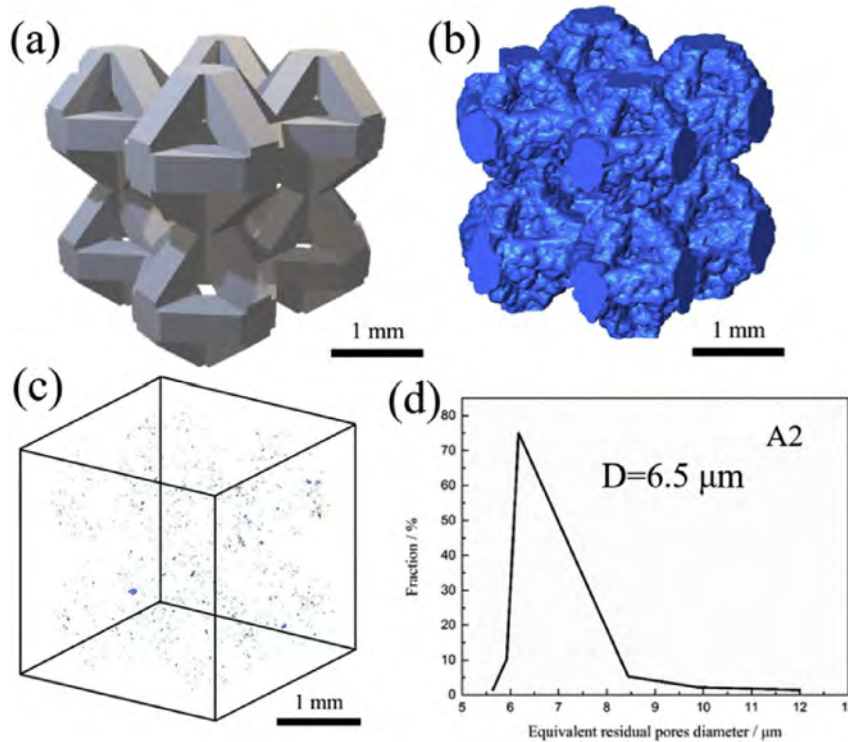


Fig. 6. Morphological characterization of the lattice structure: (a) A designed $2 \times 2 \times 2$ array of the A2 lattice structure, (b) 3D reconstruction of the micro-CT volumes of (a), (c) segmented residual pore within the struts, and (d) residual pore size distribution.

3.4. Mechanical properties

Fig. 8 shows the compressive stress-strain curves of all SLM lattice structure samples. The stress-strain curves can be categorized into three regions. Region I is an elastic region where the stress rises to the first peak. Region II shows an initial sharp decline in stress, followed by stress fluctuations. Finally, Region III shows a rapid stress increase due to densification effect. The stress

variations are in agreement with previous studies [27,31,48,49]. It is worth noting that the plateau region (Region II) with fluctuations is similar to that occurring in metallic foams, as reported previously [11].

The data on the mechanical properties related to the strain-stress curves are summarized in Table 5. Group A has relatively higher compressive and yield strength than Group B, which is in agreement with the observations of cellular materials previously

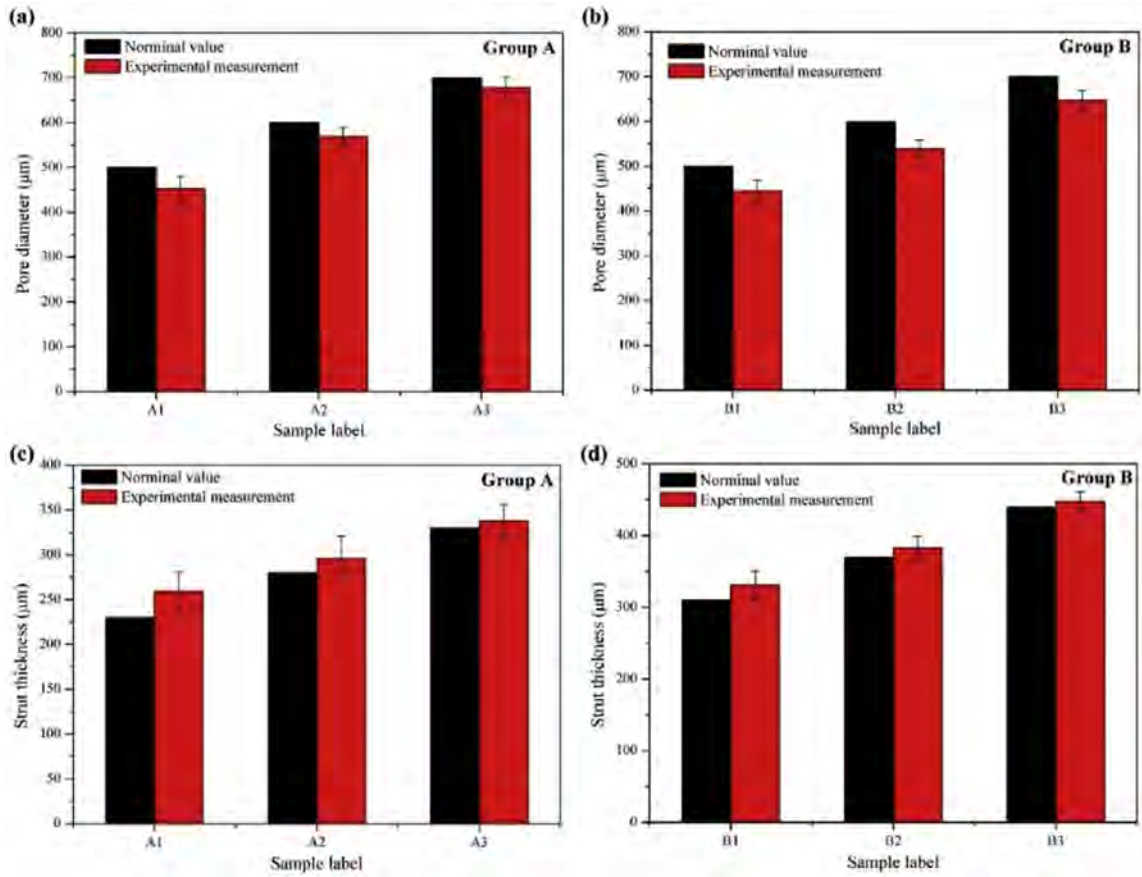


Fig. 7. Comparison of pore diameter and strut thickness between nominal and measured values.

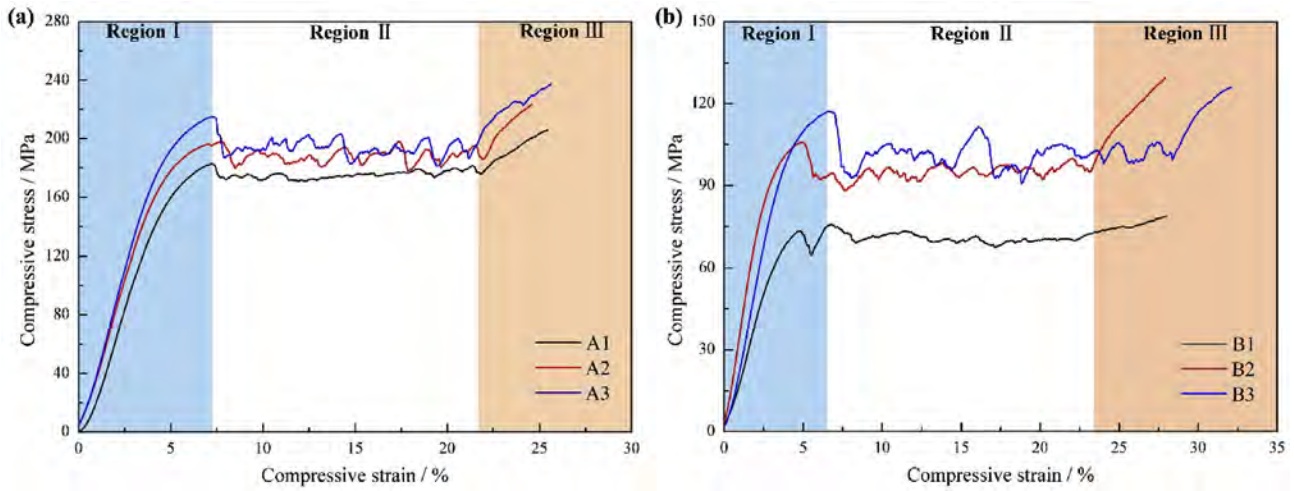


Fig. 8. Stress-strain curves for (a) group A samples and (b) group B samples.

Table 5
 Summarization of the mechanical properties of the lattice Ti6Al4V specimens, where E is elastic modulus, $\sigma_{y,0.2}$ the yield strength, σ_{max} the maximum strength (standard deviations in parentheses).

	A1	A2	A3	B1	B2	B3
σ_{max} (Mpa)	182 (± 3)	197 (± 5)	207 (± 10)	73 (± 3)	105 (± 9)	117 (± 4)
$\sigma_{y,0.2}$ (MPa)	174 (± 2)	187 (± 7)	192 (± 3)	71.8 (± 2)	92 (± 3)	102 (± 5)
E (Gpa)	4.2 (± 0.1)	4.7 (± 0.3)	4.6 (± 0.1)	2.1 (± 0.2)	3.2 (± 0.3)	2.9 (± 0.1)

reported [19]. The elastic modulus was determined as the gradient of the elastic straight line between two values of σ_{70} and σ_{20} . The elastic modulus values for both Group A and B fall in the range of human bone.

3.5. Energy absorption efficiency

During the compression process, the energy absorption efficiency (W_e) of the lattice structure can be described by the following equation [50]:

$$W_e = \frac{\int_0^{\varepsilon_n} \sigma d\varepsilon}{\sigma_n \varepsilon_n} \times 100\% \quad (6)$$

where σ_n is the stress value at the ε_n strain in the strain-stress compression diagram. In order to understand the energy absorption property of the lattice structure, the curves of the energy absorption efficiency versus compressive strain are plotted using Eq. (6) in Fig. 9. The samples of Group A and B show similar changes. Energy absorption efficiency experiences three different stages during the compressive response of the lattice structures. Regime I: elastic energy absorption regime. The energy absorption efficiency drastically decreases after primarily increasing to a peak at a strain of up to $\sim 0.5\%$. The energy absorbed in this regime can be partially recovered, and then the efficiency increases steadily until $\sim \varepsilon = 7.5\%$. Regime II: energy absorption plateau. With the increase in the strain from $\sim 7.5\%$ to $\sim 25.0\%$, significant fluctuations occur owing to the local collapse of brittle struts. In Regime III, the energy absorption decrease regime. With increasing strain in this regime, struts of each unit cell begin to interact with each other and the pores become gradually enclosed. Consequently, the energy absorption efficiency of the system decreases significantly as the densification process gradually eliminates the pores. Moreover, on comparing the energy absorption efficiency of Group A and B, it can be seen that Group B has better energy absorption efficiency than Group A. However, the fluctuation in energy absorption efficiency is more prominent in Group B than in Group A.

3.6. Finite element analysis

Fig. 10 shows the compressive stress-strain curves of the B1 sample obtained by simulation and experimental measurements,

with the inserted images showing the deformed lattice structures. In order to investigate the deformation behavior of the octahedron lattice structure, the compressive test of the B1 sample was recorded using a digital camera. Characteristic images from deformation process are also shown in Fig. 10. In Region I in the stress-strain curve (see Fig. 8), the samples deform uniformly without obvious fracture or collapse of lattice struts (see Fig. 10b). The simulation results are consistent with the experimental observation in the elastic regime and initial strength. In Region II, with increasing strain, the fracture initiates at the top surface of the specimen due to the failure of struts (see Fig. 10c and d). In this plastic regime, the simulation results demonstrate stress variations which are lower in amplitude than the experimental results. In Region III, a shear band is developed at an angle of around 45° to the compressive axis from the top to the side face of the sample (see Fig. 10e), resulting in the fracture of the lattice structure into two parts. The compression observation (Fig. 10) is in good agreement with the brittle characteristics of the lattice structure samples as indicated in the stress-strain curves (see Fig. 8). Based on the strain-stress curve, the simplified lattice structure of $5\text{ mm} \times 5\text{ mm} \times 5\text{ mm}$ unit can be successfully used to simulate the compression process of full structure. Finally, it can be seen that the numerical simulation predicts a similar deformation and collapse process as the experiments. Therefore, it can be concluded that FEA simulation can be used to analyze the failure mode and provide the guidance for structural optimization.

3.7. Chemical composition

The surface composition is crucial to the tissues as the biological environment interacts with the porous scaffold at the implant-tissue interface. Therefore, it is important to investigate the surface chemical composition of the SLM lattice structure. Fig. 11a illustrates the survey spectra of lattice structure A1 obtained by XPS analysis. The main element signals of titanium (Ti), oxygen (O), and carbon (C) can be detected. This indicates that the surface oxide forming on the lattice structure was mainly composed of Ti and O. In addition, it should be noted that the adsorption of organic molecules from the ambient atmosphere could be the reason behind the detection of C [51]. A signal for Al with weak intensity was also identified.

Detailed spectra of the main elements present on the surface of

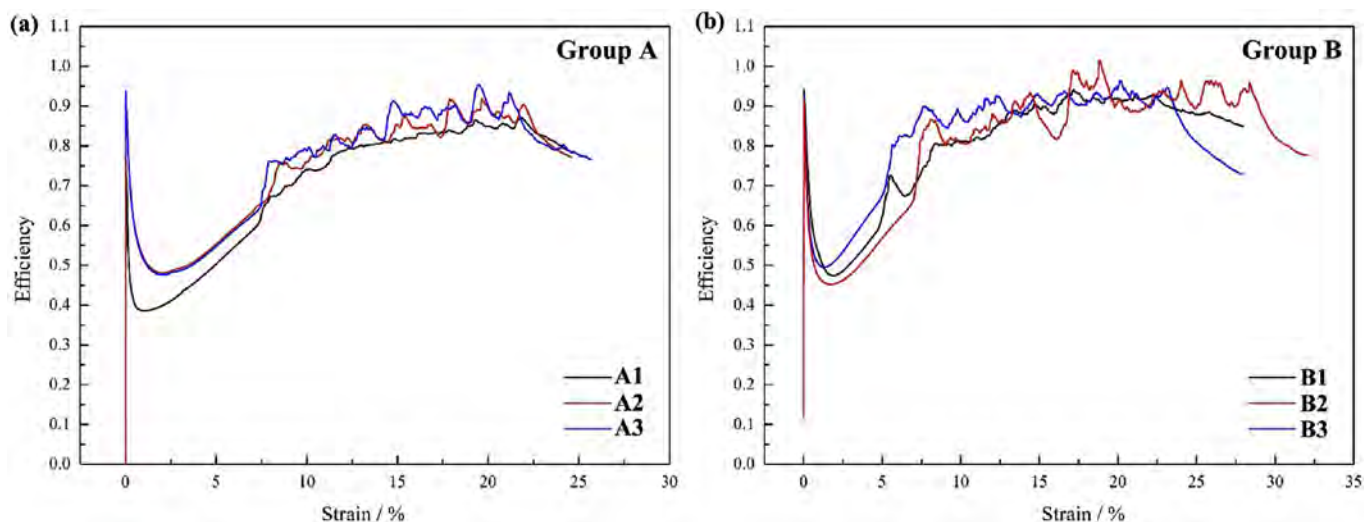


Fig. 9. Energy absorption efficiency as a function of the compressive strain for samples of (a) Group A and (b) Group B.

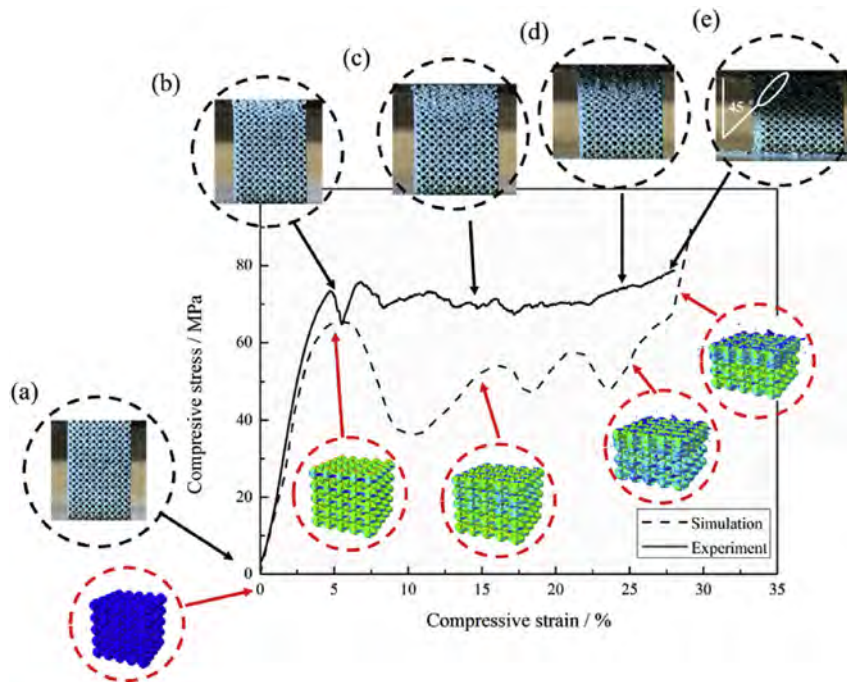


Fig. 10. Compressive stress-strain curves of the B1 sample obtained using simulations and experimental measurements, with the inserted images showing the deformed lattice structures.

the porous sample A1 are shown in Fig. 11b–c, where the Ti 2p, O 1s, and C 1s peaks of the sample are illustrated, respectively. The Ti 2p peak in Fig. 11b indicates the existence of titanium and its dioxide (mainly TiO_2) on the surface. On decomposing the O 1s peak in Fig. 11c, TiO_2 and H_2O were identified. Hence, the surfaces of SLM porous samples are mainly composed of TiO_2 [8]. The existence of a surficial TiO_2 layer on the SLM porous structure is believed to be favorable for its biological properties. In Fig. 11d, XPS detected carbon (like C–C and C=O bonds), which could have been introduced by atmospheric contamination or residual ethanol used for cleaning purposes.

3.8. Cytocompatibility

In order to evaluate the cytocompatibility of the SLM sample, rBMSCs were cultured on SLM solid (as the control group) and the porous plate B1 for 24 h. Fig. 12 shows the cell morphology results of SEM. In Fig. 12a, black arrows in the images refer to visible cells. As can be seen, cells seeded on the surface of the SLM samples were distributed with healthy cell morphology. The adhering powder particles on the surface are of approximately a 30- μm diameter, which can influence the preferential adsorption of cells. In Fig. 12b, the magnified view of the region in Fig. 12a, the cells are distributed with a polygonal shape. The preferential growth of the cells is obvious given the wavy surface, which means large adherent particles could hinder cell attachment [52]. Fig. 12c illustrates rBMSCs seeded on the porous sample B1. It should be noted that the cells can attach in the inner region of the structure. Fig. 12d shows the magnified view of the region in Fig. 12b where the cells grew among small particles (~10 μm).

Fig. 13 shows the fluorescence images of rBMSCs seeded on SLM solid plate and porous B1 sample after 24 h cultivation. Green fluorescence indicates live cells, while red color denotes dead cells. Very few dead cells can be detected on the samples, while the prevalence of live cells could be seen on the sample surfaces of all groups. In Fig. 13a, the live cells distributed on the SLM plate tend to

avoid the adherent particles (black region) on the surface. In Fig. 13b, the live cells remained along the strut surface and migrated to the inner space. Given its spatial 3D porous structure, the cells can also spread to the back of the strut, which cannot be directly observed. Note: due to the inclination of the strut and depth of field of the digital camera, the image becomes blurred at the intersection location.

4. Discussion

4.1. Morphology and microstructure analysis

In this study, SLM technology was used to prepare Ti6Al4V ELI periodic lattice structures. This type of lattice structure is suitable for bone implants or bone-grafting materials. In contrast to traditional methods, the pore size and porosity of the lattice structure can be accurately controlled using SLM technology, which can provide geometric space for the ingrowth of bone tissue. On the other hand, by using customized pore parameters, the lattice structures can have an elastic modulus similar to the replaced bone, which is important for the elimination of the stress-shielding effect.

Owing to the staircase and balling effect, powder adhesion is an inevitable side effect in the SLM fabrication process, which is unsafe due to the possibility of powders becoming dislodged after implantation. On the other hand, surface treatment both on the edges and within the lattice structure is complicated. Traditional grinding or sandblasting method have been adopted to remove the sintering surface particles [53,54]. Although, there are still numerous challenges associated with the polishing of SLM-produced parts which have difficult-to-access and complex internal geometries. In order to reduce the risk of the adhesive powders detaching, several researchers attempted to develop an internal structure polishing method. Xuan et al. [55] employed the abrasive flow machining (AFM) technique that offers better accuracy and efficiency for parts with complex structures. In the AFM polishing process, the abrasive media acts as the continuously deforming cutting tool which is

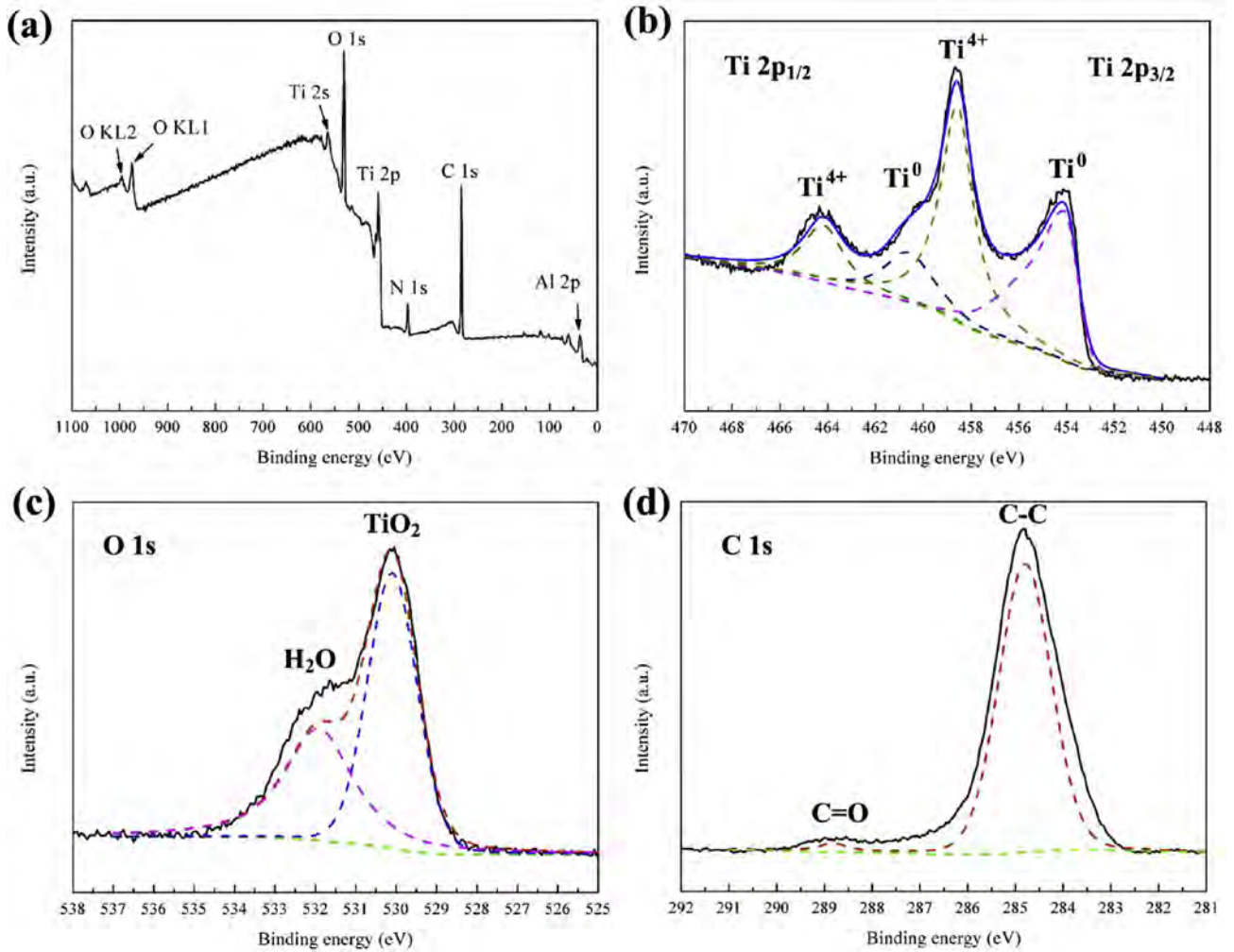


Fig. 11. (a) XPS survey spectra for the sample A1; (b) Ti 2p peak; (c) O 1s peak and (d) C 1s peak.

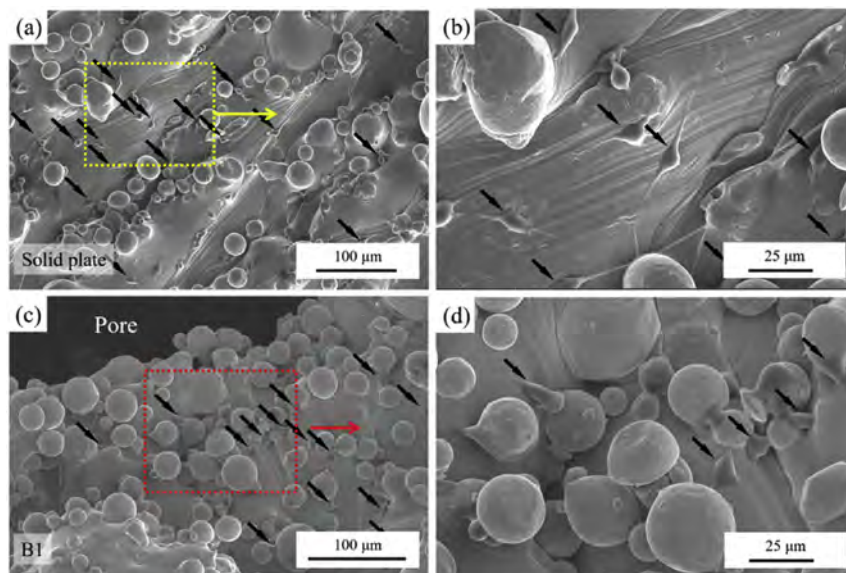


Fig. 12. SEM images of rBMSCs seeded on (a) SLM solid plate; (b) magnification view of the region marked in (a) by yellow dotted line; (c) porous sample B1; (d) magnification view of the region marked in (c) by red dotted line. (For interpretation of the references to color in this figure legend, the reader is referred to the Web version of this article.)

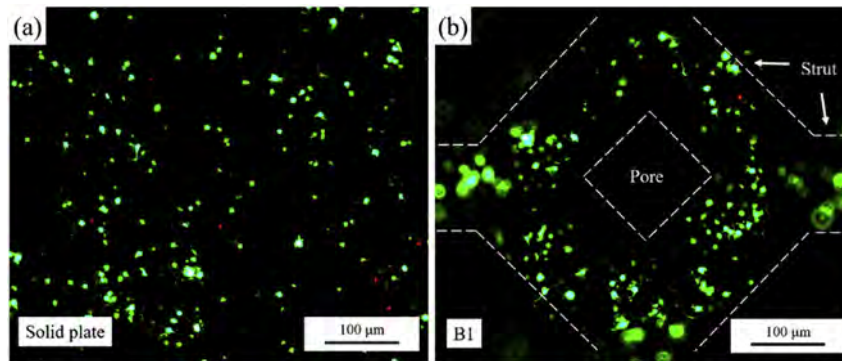


Fig. 13. Fluorescence images of rBMSCs seeded on (a) SLM solid plate and (b) SLM porous B1 sample after 24 h cultivation (Green and red represent live cells and dead cells, respectively). (For interpretation of the references to color in this figure legend, the reader is referred to the Web version of this article.)

composed of a polymer and abrasive grit. When abrasive media are extruded across the workpiece surface, the active abrasive grits scratch the surface and micro-chips are produced, leading to material removal. However, the grille workpiece (with open pores as the flow channel) manufactured using SLM in their work is a simpler geometric design than a lattice structure. Additionally, a special fixture must be tailored to the nonstandard samples, which leads to additional costs for an industrial application. Kim et al. [44] investigated the effect of a jet blasting process. The samples were cleaned through vigorous jet blasting using pellets that sublimate on impact. Once cleaned, the porous structures were subjected to a sintering process in high vacuum. The author concluded that jet blasting and sintering of the structures produced by SLM leads to localized removal of partially adhered Ti powder and weak lattice struts. However, unintended effects of the cleaning procedure were observed in the form of strut bending. The impact on mechanical performance after jet blasting and sintering is still unclear. Pyka et al. [56] developed a combination of chemical etching (CHE) and electrochemical polishing (ECP) using HF-based solutions for surface modification of 3D titanium alloyed-based open porous samples since the acid-based solutions can penetrate porous structures through interconnected pores. By applying this method, the heterogeneity of the surface roughness of the strut throughout the 3D structure is effectively removed. However, this kind of surface modification has advantages and drawbacks. The roughness of the strut decreases due to the reduction in average strut size after etching and polishing; meanwhile, the porous structure unit cell dimensions change significantly. Hence, the compressive strength of the surface-modified porous structures decreased by 50% as compared to the as-built samples. Until now, none studies in the literature have presented polishing methods for the entire lattice structure without hindering the mechanical properties.

The difference between the designed and experimental measurements (e.g., D_p , P and S_p , see Fig. 7a and b) can be attributed to two reasons. The first reason is the partially melted metal particles that adhered to the strut surfaces as shown in Fig. 2. The other reason is the scan vectors that describe the boundaries of a strut are much higher than the laser spot size although they are usually shifted half the size of laser spot inwards for compensation [46]. The internal defects (e.g., residual pores, see Fig. 4a–d) during the fabrication can influence the long-term service of the lattice structure. Compared to optical microscopy, micro-CT enables the evaluation of the spatial details of the entire lattice structure. However, the measurement accuracy is restricted by the resolution of the micro-CT as features smaller than the resolution ($4\ \mu\text{m}$) cannot be measured using this method. Therefore, the resolution must be taken into account when analyzing these results.

4.2. Compressive properties

The main deformation mechanism in the initial region I in Fig. 8 is the elastic bending of the strut. The external compressive force is converted into elastic deformation energy of the lattice structure sample. When the elastic strain increases to a certain value in region II, the stress-strain curve reaches the collapse-deformation stage. In this stage, the main processes are crack initiation and propagation of deformed struts where the stress variations are much lower. The horizontally distributed struts improve the spatial isotropy of the lattice structure and prevent unexpected shear failure [15]. With a further increase in compressive strain, the struts in the upper and lower layers of collapsed part approach each other, destroying the remainder structure. Owing to the slight change in the stress-strain curve in this stage, the struts are almost in the bending or yield stage when the collapse occurs [11,28]. In region III, the struts around the pores are in contact with each other and almost all pores in the lattice structure are crushed; hence the compression process enters the stage of densification. Therefore, the compressive stress greatly rises with the increase in strain. The above analysis shows that the compression properties of the SLM lattice structure produced in this study follow the classical theory of foam metals. In other words, there is a stable stress platform which acts as a cushion resisting the external shocks and preventing fracture.

In the restricted volume, more material means better compressive resistance. Thus, in Fig. 8a, the compressive and yield strength of Group A are higher than those of Group B. However, the elastic modulus is determined by the porosity of the structure [57]. Hence in b, the elastic modulus maintains a relatively stable value for both Group A and B samples. In addition, both groups have mechanical properties similar to those of human bone. Considering the typical range of elastic modulus and compressive strength of human bone being 1–27 GPa and ~107 MPa [58], respectively, Group A shows better mechanical strength than Group B.

It is known that the plastic deformation capacity of brittle metal materials is very low, despite the effects of friction and ballooning not being obvious (see Fig. 10) during the compression processing. Due to lower shear strength than compressive strength of a brittle material, shear fracture occurs in the direction of about $45\text{--}55^\circ$ to the compression axis (see Fig. 10d). Hence, a post-process heat treatment should be introduced to improve ductility. In the numerical model, the layer-by-layer collapse and failure of the lattice structure propagates from top to bottom. By applying damage revolution and element removal in the FEA simulation, the failed parts and resultant fragments are removed from the model to comply with the actual compression test in the experiment. Since

the broken parts and fragments are removed from the simulation the stress will be lower, which accounts for the difference between the simulation and experimental measurements. Differences between the simulation and experiment cannot be completely avoided. The discrepancies can be attributed to the manufacturing deviation in SLM parts; this is evident in the 3D reconstruction by micro-CT shown in Fig. 6. Furthermore, the adhered particles on the strut surface can also affect the mechanical behavior of the SLM lattice structure during the compression test. Thus, the author's plan is to conduct the FEA with the CT-constructed lattice structure in a future study, which can significantly improve the simulation accuracy.

The diagram of energy absorption efficiency can help designers select the correct structure, which provides the most appropriate configuration for a given application. In this work, the energy absorption efficiency of the SLM lattice structures provides useful information for practical biomedical applications. Generally, during compression processing, the lattice structures exhibit excellent energy absorption performance. Huge amounts of energy were absorbed in the initial stage of the compressive processing by the lattice structure. Then, the collapse of the structure occurred due to the diagonal 45–55° shear band failure, and the fracture was accompanied by fluctuation at the plateau region. The plateau region continues until the onset of densification at around 27% strain. Notably, Group A had improved mechanical properties but lower energy absorption efficiency than Group B. Within the safety strain rate (i.e., less than 10%), the strut can provide enough resistance against the catastrophic collapse of the lattice structure and the energy absorption efficiency implies the applicability of the lattice structure for the loading without deterioration.

4.3. Comparison with the classical model

The Gibson–Ashby model is widely applied to metallic lattice structures and was adopted to estimate the mechanical properties of the SLM Ti6Al4V lattice structures [57]. According to this model, the mechanical properties have the following relationship with the lattice structure parameters:

$$\frac{E_p}{E_s} = C_1 \cdot \left(\frac{\rho_p}{\rho_s}\right)^{n_1} \tag{7}$$

$$\frac{\sigma_{pl}}{\sigma_s} = C_2 \cdot \left(\frac{\rho_p}{\rho_s}\right)^{n_2} \tag{8}$$

where E_p and E_s are the elastic modulus of the lattice structure and bulk material, respectively, ρ_p and ρ_s are the lattice and dense material density, respectively, σ_{pl} is the plateau stress during the compression test, and σ_s is the yield strength of the fully dense Ti6Al4V material. Based on data from a previous study [14], the elastic modulus (E_s), yield strength (σ_s), and density (ρ_s) of the SLM Ti6Al4V are 120 GPa, 1064 MPa, and 4.43 g/cm³, respectively. C_1 , C_2 , n_1 , and n_2 can be calculated by fitting the test results into Eq. (7) and Eq. (8) [59].

In this work, n_1 and n_2 equaling to 1.81 and 2.51, respectively, are related to the unit cell of the as-built lattice structure [10]. The C_1 and C_2 of the SLM lattice samples produced in this work were computed as 0.20 and 1.66. The relative elastic modulus and compressive strength achieved through experimental measurement and the Gibson-Ashby model are shown in Fig. 14. A discrepancy between experimentally tested and the Gibson-Ashby model estimated elastic modulus (obtained by Eq. (7)) can be observed. Moreover, the elastic modulus of Group A is more dispersive than that of Group B (see Fig. 14a). However, a good agreement between compressive strength and fitting curve (obtained by Eq. (8)) is achieved (see Fig. 14b) in Group A and B. This is because the samples with higher porosity are not as strong as those with lower porosity.

The difference between the measured value and predicted value is mainly attributed to the following reasons. (i) Negative effect of residual pores within the struts (see Fig. 4d), (ii) the unreasonable assumption that the struts are uniform (see Fig. 4), (iii) manufacturing defects at the connecting nodes of the lattice structure (see Fig. 4c), and (iv) residual stress in the SLM lattice structure.

In summary, owing to the stair-stepping effect, the deformation behavior of the irregular strut cannot be assumed to be uniform in shape. Moreover, at the surface of the connecting nodes, the particles tend to bond, causing parts of the neighbor struts to be aggregated. Therefore, the space of free deformation of the strut is reduced. The resistance deformation ability of unit cell increases, which leads to an increase in the elastic modulus of the lattice structure. Finally, residual stress caused during the SLM processing

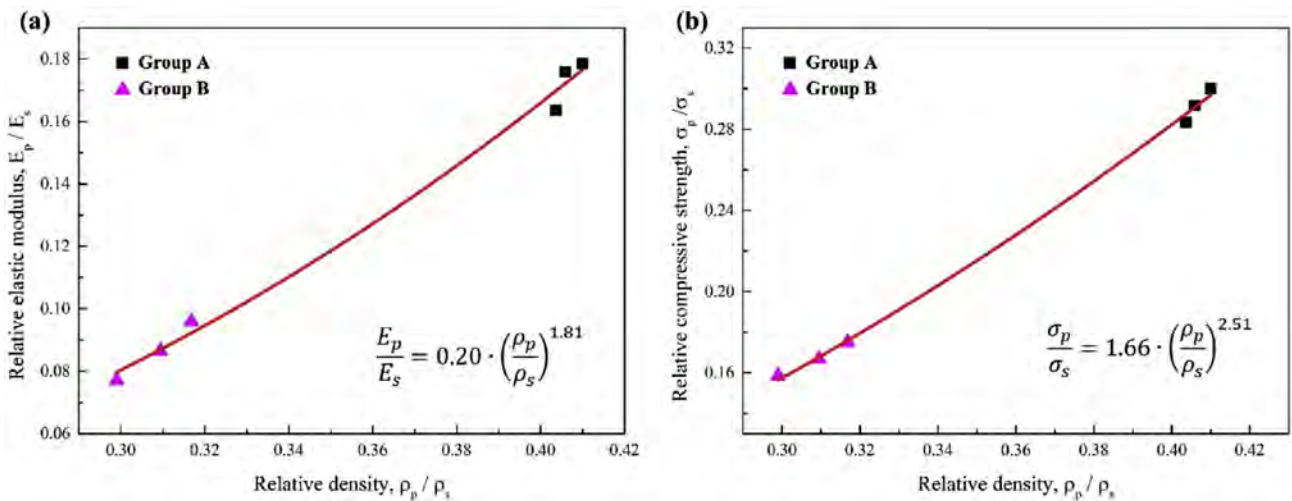


Fig. 14. Compression of experimental results and Gibson-Ashby model fittings for the lattice structure: (a) relative elastic modulus (E_p/E_s) and (b) relative compressive strength (σ_{pl}/σ_s).

on the lattice structure may lead to difference of compression behavior between theoretical and experimental measurements.

4.4. Cytocompatibility

Based on the result of XPS shown in Fig. 11, it should be noted that although the SLM process was conducted under the Ar atmosphere with oxygen concentrations lower than 0.1%, levels of oxidation cannot completely be avoided due to Ti's high affinity for oxygen. However, the appearance of superficial titanium oxide on the porous structures is thought to be beneficial for biological performances [60].

In Fig. 2, the rough strut surface is suggested to promote the attachment of osteoblasts and the function of cell osteogenesis, accelerating the healing of the defective tissue [8,35]. Firstly, the rough surface can increase the adhesion surface area of bone cells as well as the surface energy of the materials, which benefits the adsorption of macromolecules and the attachment of cells. Secondly, the rough interface has a similar curvature as bone cells, which helps the physical/chemical combination of the cells or macromolecules. Thirdly, the rough surface can improve the friction coefficient to a value higher than that of the traditional implant materials, which strengthens the initial fixation effect and amalgamation of implants and human tissues. Therefore, it is reasonable to consider that the rough surface is beneficial to the biological activity of the implant. However, on the other hand, large powders adhering to the strut surfaces can hinder cell attachment and may cause health risks to the human body due to the high possibility of peeling off from the surface after implantation.

The cytocompatibility of SLM porous structures was qualitatively assessed by *in vitro* studies. The cells on porous samples were a well-distributed and migrated to the inner space as the interconnected pore structure contributed to nutrient-waste exchange with the cultured cells. In addition, as can be observed in Fig. 13b, the cells on the porous structure can modify their morphology to match the topography of the space as opposed to those on the solid plate. Similar to the previous report, a porous structure with a large surface area and average curvature help induce tissue amplification *in vitro* [61,62]. In the future research, quantitative evaluation of cell proliferation and *in vivo* tests should be carried out to fully investigate the biocompatibility of SLM porous structures.

5. Conclusions

In this work, isotropic Ti6Al4V ELI octahedral lattice structures were primarily designed and then fabricated by SLM technology for application as human bone substitutes. The following conclusions can be drawn:

1. Based on micro-CT observation, the as-built lattice structures well with the original design. According to the morphology observation, such fabrication deviation is mainly caused by the adhered particle on struts and the staircase effect during laser melting process.
2. The SLM structure samples mainly consisted of acicular HCP α' martensite microstructure. Residual pores found within the struts are detrimental to long-term load bearing. This means post-treatments such as HIP treatment should be considered to control the microstructure and reduce the prevalence of the defects.
3. The effect of pore size doesn't seem to be a significant difference for the range that was studied. The mechanical properties of Group A are highly compatible with those of human bone; this means the stress-shielding effect can be reduced, ensuring longevity after implantation.

4. Titanium oxide appeared on the surface of the porous structures. Cells on porous samples were well distributed across the outer surface and also migrated to the inner surfaces of the lattice structure.
5. The Gibson-Ashby model could consistently predict the measured elastic modulus and yield strength of the as-built lattice structure.

Acknowledgements

As one of the authors, Xingchen Yan, is grateful for the financial support provided by the China Scholarship Council (No. 201504490031), the funds of Sciences Platform Environment and Capacity Building Projects of GDAS (2016GDASPT-0206, 2017GDASCX-0202, 2017GDASCX-0111, 2018GDASCX-0402 and 2018GDASCX-0111); Guangzhou Project of Science & Technology (201604016109, 201704030111); Guangdong province Science and Technology Plan Projects (2015B010122004, 2015B0909200032016B070701020, 2016B090916003, 2017A070702016, 2017B030314122 and 2017A070701027); Guangdong Natural Science Foundation (2016A030312015). Guangzhou Science and Technology Program (201510010095). As one of the authors, Chaoyue Chen is grateful for the support from the National Natural Science Foundation of China (No. U1560202, 51604171, No. 51690162, the Shanghai Science and Technology Committee (No. 17JC1400602), National Science and Technology Major Project of China "Aeroengine and Gas Turbine" (2017-VII-0008–0102).

References

- [1] Q. Chen, G.A. Thouas, Metallic implant biomaterials, *Mater. Sci. Eng. R Rep.* 87 (2015) 1–57.
- [2] D.K. Pattanayak, A. Fukuda, T. Matsushita, M. Takemoto, S. Fujibayashi, K. Sasaki, N. Nishida, T. Nakamura, T. Kokubo, Bioactive Ti metal analogous to human cancellous bone: fabrication by selective laser melting and chemical treatments, *Acta Biomater.* 7 (2011) 1398–1406.
- [3] B. Dutta, F.H. Froes, *The Additive Manufacturing (AM) of Titanium Alloys*, 2015, pp. 447–468.
- [4] M.C. Kruyt, J.D.d. Bruijn, C.E. Wilson, F.C. Oner, C.A.v. Blitterswijk, A.J. Verbout, W.J.A. Dhert, Viable osteogenic cells are obligatory for tissue-engineered ectopic bone formation in goats, *Tissue Eng.* 9 (2003) 327–336.
- [5] F.A. España, V.K. Balla, S. Bose, A. Bandyopadhyay, Design and fabrication of CoCrMo alloy based novel structures for load bearing implants using laser engineered net shaping, *Mater. Sci. Eng. C* 30 (2010) 50–57.
- [6] A. Goharian, M.R. Abdullah, 7 - bioinert metals (stainless steel, titanium, cobalt chromium), in: A. Goharian (Ed.), *Titanium Powder Metallurgy*, Elsevier, 2017, pp. 115–142.
- [7] P.K. Zysset, X. Edward Guo, C. Edward Hoffler, K.E. Moore, S.A. Goldstein, Elastic modulus and hardness of cortical and trabecular bone lamellae measured by nanoindentation in the human femur, *J. Biomech.* 32 (1999) 1005–1012.
- [8] M. Fousova, D. Vojtech, J. Kubasek, E. Jablonska, J. Fojt, Promising characteristics of gradient porosity Ti-6Al-4V alloy prepared by SLM process, *J. Mech. Behav. Biomed. Mater.* 69 (2017) 368–376.
- [9] Y. Li, C. Yang, H. Zhao, S. Qu, X. Li, Y. Li, New developments of Ti-based alloys for biomedical applications, *Materials (Basel)* 7 (2014) 1709–1800.
- [10] S.Y. Chen, J.C. Huang, C.T. Pan, C.H. Lin, T.L. Yang, Y.S. Huang, C.H. Ou, L.Y. Chen, D.Y. Lin, H.K. Lin, T.H. Li, J.S.C. Jang, C.C. Yang, Microstructure and mechanical properties of open-cell porous Ti-6Al-4V fabricated by selective laser melting, *J. Alloys Compd.* 713 (2017) 248–254.
- [11] S.J. Li, Q.S. Xu, Z. Wang, W.T. Hou, Y.L. Hao, R. Yang, L.E. Murr, Influence of cell shape on mechanical properties of Ti-6Al-4V meshes fabricated by electron beam melting method, *Acta Biomater.* 10 (2014) 4537–4547.
- [12] H.P. Tang, J. Wang, M. Qian, 28 - porous titanium structures and applications, in: M. Qian, F.H. Froes (Eds.), *Titanium Powder Metallurgy*, Butterworth-Heinemann, Boston, 2015, pp. 533–554.
- [13] I.A.J. van Hengel, M. Riol, L.E. Fratila-Apachitei, J. Witte-Bouma, E. Farrell, A.A. Zadpoor, S.A.J. Zaai, I. Apachitei, Selective laser melting porous metallic implants with immobilized silver nanoparticles kill and prevent biofilm formation by methicillin-resistant *Staphylococcus aureus*, *Biomaterials* 140 (2017) 1–15.
- [14] R. Gümrük, R.A.W. Mines, S. Karadeniz, Static mechanical behaviours of stainless steel micro-lattice structures under different loading conditions, *Mater. Sci. Eng., A* 586 (2013) 392–406.

- [15] R. Hedayati, M. Sadighi, M. Mohammadi-Aghdam, A.A. Zadpoor, Analytical relationships for the mechanical properties of additively manufactured porous biomaterials based on octahedral unit cells, *Appl. Math. Model.* 46 (2017) 408–422.
- [16] Z. Ozdemir, A. Tyas, R. Goodall, H. Askes, Energy absorption in lattice structures in dynamics: nonlinear FE simulations, *Int. J. Impact Eng.* 102 (2017) 1–15.
- [17] R. Hedayati, M. Sadighi, M. Mohammadi-Aghdam, A.A. Zadpoor, Mechanical properties of regular porous biomaterials made from truncated cube repeating unit cells: analytical solutions and computational models, *Mater. Biol. Appl.* 60 (2016) 163–183.
- [18] R. Hedayati, M. Sadighi, M. Mohammadi-Aghdam, A.A. Zadpoor, Mechanical behavior of additively manufactured porous biomaterials made from truncated cuboctahedron unit cells, *Int. J. Mech. Sci.* 106 (2016) 19–38.
- [19] C. Yan, L. Hao, A. Hussein, S.L. Bubb, P. Young, D. Raymont, Evaluation of light-weight AlSi10Mg periodic cellular lattice structures fabricated via direct metal laser sintering, *J. Mater. Process. Technol.* 214 (2014) 856–864.
- [20] M. Smith, Z. Guan, W.J. Cantwell, Finite element modelling of the compressive response of lattice structures manufactured using the selective laser melting technique, *Int. J. Mech. Sci.* 67 (2013) 28–41.
- [21] L. Xiao, W. Song, C. Wang, H. Tang, N. Liu, J. Wang, Yield behavior of open-cell rhombic dodecahedron Ti–6Al–4V lattice at elevated temperatures, *Int. J. Mech. Sci.* 115–116 (2016) 310–317.
- [22] L. Xiao, W. Song, C. Wang, H. Tang, Q. Fan, N. Liu, J. Wang, Mechanical properties of open-cell rhombic dodecahedron titanium alloy lattice structure manufactured using electron beam melting under dynamic loading, *Int. J. Impact Eng.* 100 (2017) 75–89.
- [23] S.M. Ahmadi, G. Campoli, S. Amin Yavari, B. Sajadi, R. Wauthle, J. Schrooten, H. Weinans, A.A. Zadpoor, Mechanical behavior of regular open-cell porous biomaterials made of diamond lattice unit cells, *J. Mech. Behav. Biomed. Mater.* 34 (2014) 106–115.
- [24] E. Ptochos, G. Labeas, Elastic modulus and Poisson's ratio determination of micro-lattice cellular structures by analytical, numerical and homogenisation methods, *J. Sandw. Struct. Mater.* 14 (2012) 597–626.
- [25] X. Zheng, H. Lee, T.H. Weisgraber, M. Shusteff, J. DeOtte, E.B. Duoss, J.D. Kuntz, M.M. Biener, Q. Ge, J.A. Jackson, S.O. Kucheyev, N.X. Fang, C.M. Spadaccini, Ultralight, ultrastiff mechanical metamaterials, *Science* 344 (2014) 1373–1377.
- [26] W.E. Warren, A.M. Kraynik, Linear elastic behavior of a low-density kelvin foam with open cells, *J. Appl. Mech.* 64 (1997) 787–794.
- [27] V. Crupi, E. Kara, G. Epasto, E. Guglielmino, H. Aykul, Static behavior of lattice structures produced via direct metal laser sintering technology, *Mater. Des.* 135 (2017) 246–256.
- [28] Z. Xiao, Y. Yang, R. Xiao, Y. Bai, C. Song, D. Wang, Evaluation of topology-optimized lattice structures manufactured via selective laser melting, *Mater. Des.* 143 (2018) 27–37.
- [29] R.A.W. Mines, S. Tsopanos, Y. Shen, R. Hasan, S.T. McKown, Drop weight impact behaviour of sandwich panels with metallic micro lattice cores, *Int. J. Impact Eng.* 60 (2013) 120–132.
- [30] J. Sun, Y. Yang, D. Wang, Mechanical properties of a Ti6Al4V porous structure produced by selective laser melting, *Mater. Des.* 49 (2013) 545–552.
- [31] J. Sun, Y. Yang, D. Wang, Mechanical properties of Ti-6Al-4V octahedral porous material unit formed by selective laser melting, *Adv. Mech. Eng.* 4 (2015) 427386.
- [32] L. Yang, Experimental-assisted design development for an octahedral cellular structure using additive manufacturing, *Rapid Prototyp. J.* 21 (2015) 168–176.
- [33] V. Karageorgiou, D. Kaplan, Porosity of 3D biomaterial scaffolds and osteogenesis, *Biomaterials* 26 (2005) 5474–5491.
- [34] G.E. Ryan, A.S. Pandit, D.P. Apatsidis, Porous titanium scaffolds fabricated using a rapid prototyping and powder metallurgy technique, *Biomaterials* 29 (2008) 3625–3635.
- [35] P. Heintz, L. Muller, C. Korner, R.F. Singer, F.A. Muller, Cellular Ti-6Al-4V structures with interconnected macro porosity for bone implants fabricated by selective electron beam melting, *Acta Biomater.* 4 (2008) 1536–1544.
- [36] P. Xiu, Z. Jia, J. Lv, C. Yin, Y. Cheng, K. Zhang, C. Song, H. Leng, Y. Zheng, H. Cai, Z. Liu, Tailored surface treatment of 3D printed porous Ti6Al4V by microarc oxidation for enhanced osseointegration via optimized bone in-growth patterns and interlocked bone/implant interface, *ACS Appl. Mater. Interfaces* 8 (2016) 17964–17975.
- [37] M. Kruyt, J.D. de Bruijn, C. Wilson, F. Oner, C. Van Blitterswijk, A. Verbout, W. Dhert, Viable osteogenic cells are obligatory for tissue-engineered ectopic bone formation in goats, *Tissue Eng.* 9 (2003) 327–336.
- [38] F. Li, J. Li, H. Kou, T. Huang, L. Zhou, Compressive mechanical compatibility of anisotropic porous Ti6Al4V alloys in the range of physiological strain rate for cortical bone implant applications, *Journal of materials science, Mater. Med.* 26 (2015) 233.
- [39] S.A. Yavari, R. Wauthle, J. van der Stok, A.C. Riemsag, M. Janssen, M. Mulier, J.P. Kruth, J. Schrooten, H. Weinans, A.A. Zadpoor, Fatigue behavior of porous biomaterials manufactured using selective laser melting, *Mater. Sci. Eng. C Mater. Biol. Appl.* 33 (2013) 4849–4858.
- [40] J. Kadkhodapour, H. Montazerian, A. Darabi, A.P. Anaraki, S.M. Ahmadi, A.A. Zadpoor, S. Schmauder, Failure mechanisms of additively manufactured porous biomaterials: effects of porosity and type of unit cell, *J. Mech. Behav. Biomed. Mater.* 50 (2015) 180–191.
- [41] N. Tanlak, D.F. De Lange, W. Van Paeppegem, Numerical prediction of the printable density range of lattice structures for additive manufacturing, *Mater. Des.* 133 (2017) 549–558.
- [42] G.R. Johnson, W.H. Cook, A constitutive model and data for metals subjected to large strains, high strain rates and high temperatures, in: *Proceedings of the 7th International Symposium on Ballistics*, 1983, pp. 541–547. The Hague, The Netherlands.
- [43] Y. Zhang, J.C. Outeiro, T. Mabrouki, On the selection of Johnson-cook constitutive model parameters for Ti-6Al-4V using three types of numerical models of orthogonal cutting, *Proc. CIRP* 31 (2015) 112–117.
- [44] T.B. Kim, S. Yue, Z. Zhang, E. Jones, J.R. Jones, P.D. Lee, Additive manufactured porous titanium structures: through-process quantification of pore and strut networks, *J. Mater. Process. Technol.* 214 (2014) 2706–2715.
- [45] D. Wang, Y. Yang, R. Liu, D. Xiao, J. Sun, Study on the designing rules and processability of porous structure based on selective laser melting (SLM), *J. Mater. Process. Technol.* 213 (2013) 1734–1742.
- [46] S. Van Bael, G. Kerckhofs, M. Moesen, G. Pyka, J. Schrooten, J.P. Kruth, Micro-CT-based improvement of geometrical and mechanical controllability of selective laser melted Ti6Al4V porous structures, *Mater. Sci. Eng., A* 528 (2011) 7423–7431.
- [47] W. Xu, M. Brandt, S. Sun, J. Elambasseril, Q. Liu, K. Latham, K. Xia, M. Qian, Additive manufacturing of strong and ductile Ti–6Al–4V by selective laser melting via in situ martensite decomposition, *Acta Mater.* 85 (2015) 74–84.
- [48] L.C. Montemayor, J.R. Greer, Mechanical response of hollow metallic nanolattices: combining structural and material size effects, *J. Appl. Mech.* 82 (2015), 071012.
- [49] C. Qiu, S. Yue, N.J.E. Adkins, M. Ward, H. Hassanin, P.D. Lee, P.J. Withers, M.M. Attallah, Influence of processing conditions on strut structure and compressive properties of cellular lattice structures fabricated by selective laser melting, *Mater. Sci. Eng., A* 628 (2015) 188–197.
- [50] M. Mohsenizadeh, F. Gasbarri, M. Munther, A. Beheshti, K. Davami, Additively-manufactured lightweight Metamaterials for energy absorption, *Mater. Des.* 139 (2018) 521–530.
- [51] J. Vaithilingam, E. Prina, R.D. Goodridge, R.J.M. Hague, S. Edmondson, F. Rose, S.D.R. Christie, Surface chemistry of Ti6Al4V components fabricated using selective laser melting for biomedical applications, *Mater. Biol. Appl.* 67 (2016) 294–303.
- [52] M. Wang, T. Chen, S. Lu, Y. Zhao, H. Chen, Y. Wu, Z. Tang, Osteogenic comparison on selective laser melting printed and sandblasting-acid-etching Ti substrates for customized implant applications, *Sci. Adv. Mater.* 9 (2017) 705–714.
- [53] W. Peng, L. Xu, J. You, L. Fang, Q. Zhang, Selective laser melting of titanium alloy enables osseointegration of porous multi-rooted implants in a rabbit model, *Biomed. Eng. Online* 15 (2016) 85.
- [54] J.R. Strub, E.D. Rekow, S. Witkowski, Computer-aided design and fabrication of dental restorations: current systems and future possibilities, *J. Am. Dent. Assoc.* 137 (2006) 1289–1296.
- [55] X. Wang, Y.F. ShichongLi, H. Gao, Finishing of additively manufactured metal parts by abrasive flow machining, in: *Proc. 27th Annu. Int. Solid Free. Fabr. Symp.*, 2016, pp. 2470–2472.
- [56] G. Pyka, A. Burakowski, G. Kerckhofs, M. Moesen, S. Van Bael, J. Schrooten, M. Wevers, Surface modification of Ti6Al4V open porous structures produced by additive manufacturing, *Adv. Eng. Mater.* 14 (2012) 363–370.
- [57] L.J. Gibson, M.F. Ashby, The mechanics of three-dimensional cellular materials, *Proc. Math. Phys. Eng. Sci.* 382 (1982) 43–59.
- [58] P.K. Zysset, X. Edward Guo, C. Edward Hoffler, K.E. Moore, S.A. Goldstein, Elastic modulus and hardness of cortical and trabecular bone lamellae measured by nanoindentation in the human femur, *J. Biomech.*, 32 1005–1012.
- [59] L.J. Gibson, M.F. Ashby, *Cellular Solids: Structure and Properties*, Cambridge University Press, 1997.
- [60] S.M. Thompson, L. Bian, N. Shamsaei, A. Yadollahi, An overview of Direct Laser Deposition for additive manufacturing; Part I: transport phenomena, modeling and diagnostics, *Addit. Manuf.* 8 (2015) 36–62.
- [61] W. Xue, B.V. Krishna, A. Bandyopadhyay, S. Bose, Processing and biocompatibility evaluation of laser processed porous titanium, *Acta Biomater.* 3 (2007) 1007–1018.
- [62] R. Stangl, B. Rinne, S. Kastl, C. Hendrich, The influence of pore geometry in cp Ti-implants – a cell culture investigation, *Eur. Cells Mater.* 2 (2001) 1–9.



Investigation of domain wall motion in RE-TM magnetic wire towards a current driven memory and logic



Hiroyuki Awano

Toyota Technological Institute, Tempaku, Nagoya 468-8511, Japan

ARTICLE INFO

Article history:

Received 20 June 2014

Received in revised form

29 December 2014

Accepted 31 December 2014

Available online 9 January 2015

Keywords:

Memory and logic

Magnetic wire

Spin logic

TbFeCo

Rare earth transition metal

Amorphous

ferrimagnetism

Critical current density

Low magnetization

Domain wall velocity

AND

OR

NOT

NAND

NOR

Polycarbonate substrate

Si substrate

Nano-imprint

ABSTRACT

Current driven magnetic domain wall (DW) motions of ferri-magnetic TbFeCo wires have been investigated. In the case of a Si substrate, the critical current density (J_c) of DW motion was successfully reduced to 3×10^6 A/cm². Moreover, by using a polycarbonate (PC) substrate with a molding groove of 600 nm width, the J_c was decreased to 6×10^5 A/cm². In order to fabricate a logic in memory, a current driven spin logics (AND, OR, NOT) have been proposed and successfully demonstrated under the condition of low J_c . These results indicate that TbFeCo nanowire is an excellent candidate for next generation power saving memory and logic.

© 2015 The Author. Published by Elsevier B.V. This is an open access article under the CC BY license (<http://creativecommons.org/licenses/by/4.0/>).

1. Introduction

Current driven domain wall (DW) motion has attracted much attention for new applications, such as low-power, high-speed, logic devices. Particularly, long-term preservation of data is possible because it does not have mechanical operation parts. DW displacement by spin polarized current was predicted by Berger [1]. Then, a lot of experimental results with in-plane magnetized FeNi magnetic wires have been reported [2–5]. The critical current density (J_c) of FeNi nanowire required large value of over 1×10^8 A/cm², and the J_c reduction was a big issue. Using FeNi nanowire, racetrack memory has been proposed [6] and demonstrated the accurate operation. Then several experiments have been conducted, J_c value was successfully reduced to 3×10^7 A/cm² by using a perpendicular magnetized Co/Ni nanowire [7–9]. As a reason of J_c reduction, it was considered that DW motion of Co/Ni nanowire is due to only intrinsic pinning effect [10,11]. It was very attractive to explain every experimental result

by theoretical analysis. Therefore, the wall pinning force of Co/Ni nanowire has a very low value, it is considered that Co/Ni nanowire is not suitable for external data storage. Because external storage material such as HDD and computer tape requires large DW pinning force to save data with high reliability. However, it was considered that J_c is proportional to DW pinning force [12]; it seems that coexistence of low J_c and large DW pinning force is difficult.

On the other hand, J_c of perpendicular magnetized TbFeCo has been reported [13–18] as 3×10^6 A/cm² which is lower than that of Co/Ni. The DW pinning force was over 1 kOe and it can be easily controlled by Tb composition. It seems that coexistence of low J_c and large DW pinning force is possible in the TbFeCo nanowire. Moreover, in the TbFeCo nanowire, there are high density and relatively uniform pinning sites. Therefore, arbitrary shape domain can be recorded. In the case of Co/Ni nanowire, it requires a lot of artificially fabricated notches at the wire edge to keep position of recorded domains [7]. From these results, it seems that rare earth

transition metal alloy such as TbFeCo is an attractive material for magnetic wire memory.

By the way, memory and logic are placed separately in the current computer, the memory and logic are connected by a data bus. Therefore, operation speed is rate-limiting in the communication speed between memory and logic. If memory and logic are prepared in the same area and directly connected each other, the operation speed would be improved. However, in the most spin logic reports [19–22], FeNi in-plane magnetized nanowires were used and most logics were operated by a rotational magnetic field from outside of the device. Therefore, current driven spin logic has been proposed. In this article, drastic J_c reduction of TbFeCo nanowire with PC substrate is reported, and low current driven AND, OR, and NOT operations with TbFeCo nanowire are presented.

2. Experimental procedure

The 0.3–1.5 μm -wide and 100- μm -length wire patterns were fabricated using electron beam lithography for a lift-off process as shown in Fig. 1(a). In this case, it is considered that the lift off process damages the magnetic film. Therefore, a new fabrication method with nanoimprint technique is proposed in Fig. 1(b). This method is similar to the optical disk fabrication and the substrate cost is very low compared with that of the Si substrate. When a magnetic film is deposited onto the grooved PC substrate, magnetic nanowire can be prepared without any damage. The 20-nm-thick $\text{Tb}_{26}\text{Fe}_{66.8}\text{Co}_{7.2}$ film was directly grown on SiO_2/Si substrate by RF magnetron sputtering. A Pt film with a thickness of 2 nm was subsequently capped on the film. The ultimate vacuum was less than 2×10^{-8} Torr and Ar sputtering gas pressure of 1 mTorr was kept during grown films. Ti/Al contacts were defined by optical lithography on top of each TbFeCo electrode. A scanning electron microscopy (SEM) image of the fabricated sample is shown in Fig. 2. The magnetic properties of the films and wires were measured using an alternating gradient force magnetometer

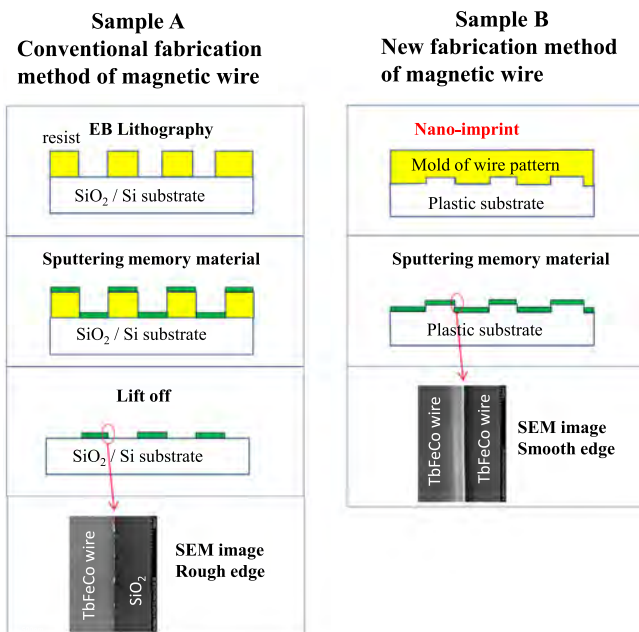


Fig. 1. Sample A: general fabrication process of magnetic nanowire. Sample B: proposed new fabrication process of magnetic nanowire. The feature is similar to the optical disk fabrication process. Therefore, the new fabrication process is attractive for low cost magnetic wire preparation and low J_c sample.

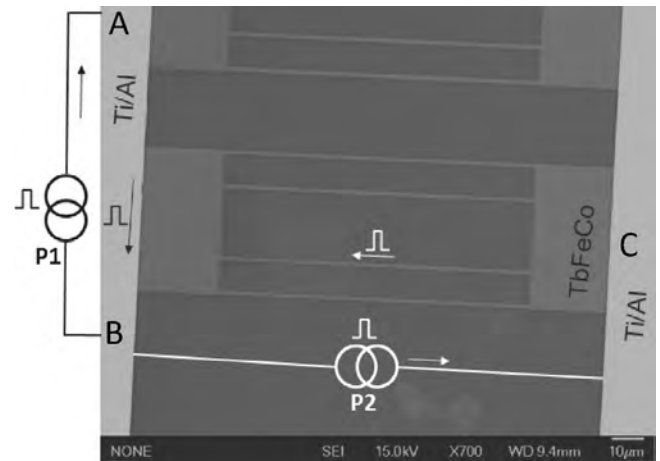


Fig. 2. SEM image of the Sample A set up for magnetic spin memory.

(AGFM) and anomalous Hall voltage measurement. When a domain wall motion of the sample is observed, magnetically initialize process is performed to the sample using larger external magnetic field over the coercive force (H_c). Then, the magnetic DWs were cleared in the wires by using an Oersted field which is generated by current flow from the electrode A to B in Fig. 3. The motion of DWs was driven by current flow from the electrode C to B. Pulse voltage duration was 100 ns. The DWs dynamics in the wires were directly observed using polar Kerr microscopy as shown in Fig. 4. Hysteresis loop measurement on the films using AGFM (data not shown) confirmed that the films had a good perpendicular magnetic anisotropy with a saturation magnetization of $M_s = 110 \text{ emu/cm}^3$.

3. Results and discussion

3.1. Very low current driven DW motion in TbFeCo wire

Using the sample of Fig. 2, current driven DW motions in

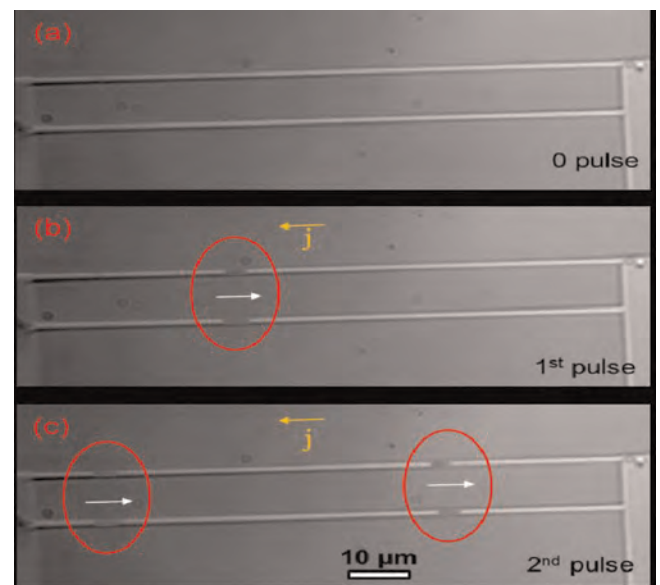


Fig. 3. Polar Kerr optical microscope image of TbFeCo magnetic nanowires on SiO_2/Si substrate. (a) After initialize process, (b) in each magnetic wire, one domain is recorded, then 1st pulse current is applied, each domain is displaced to the right hand side. (c) 2nd Domain is recorded at the left hand side, then injected 2nd pulse current drive both the 1st and 2nd recorded domains.

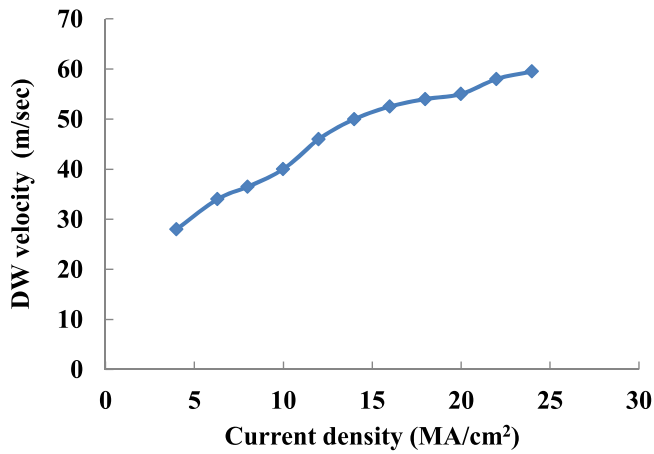


Fig. 4. Current density dependence of DW velocity in the TbFeCo wire.

TbFeCo wire were observed with Polar Kerr optical microscope. The observation results are shown in Fig. 3. The reason of utilizing two TbFeCo wires is to confirm the possibility of parallel data processing used by high-speed data transmission. After initialization of the TbFeCo was performed, there is no domain as shown in Fig. 3(a). Next, one domain is recorded on the left hand side of the TbFeCo wire, then one pulse current is applied to the wire from the electrode C to B. The recorded domain is displaced to the right hand side as shown in Fig. 3(b). The length of the displaced domain length is almost same as initial one. Moreover, one more domain is recorded to the TbFeCo wire, then the recorded 2 domains are shifted to the right hand side by applying 2nd current pulse as shown in Fig. 3(c). Two domain lengths and the interval length between them did not change even when 2nd current pulse is applied. This result indicates that current driven domain wall motion can be used as a memory device. The direction of the domain wall displacement is opposite to that of the current. Therefore, it is considered that the domain wall motion is caused by spin torque transfer effect [23].

Current density dependence of DW velocity is shown in Fig. 4. It indicates the DW motion of the flow regime. The critical current density (J_c) of the domain wall motion in TbFeCo wire was 5×10^6 A/cm². The value is relatively small compared with another magnetic material. The saturation magnetization (M_s) of the TbFeCo is 110 emu/cm³, it is very low compared with another current driven magnetic materials, because TbFeCo is ferri-magnetic material. Fig. 5 shows M_s dependence of J_c in several magnetic nanowires. It shows that J_c is proportional to M_s .

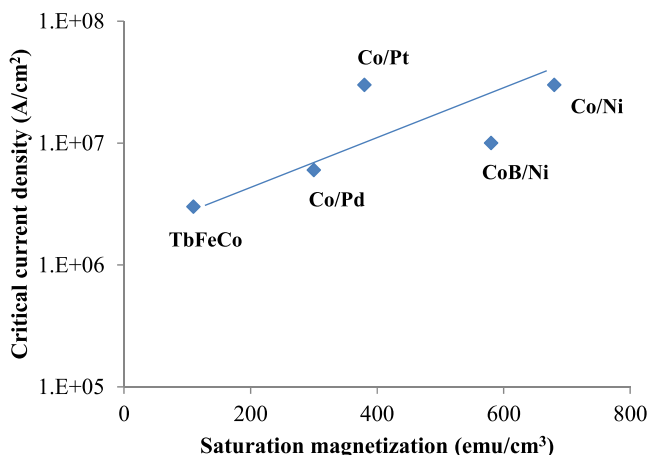


Fig. 5. Saturation magnetization (M_s) dependence of critical current density (J_c) on SiO₂/Si substrate for several kinds of magnetic nanowire.

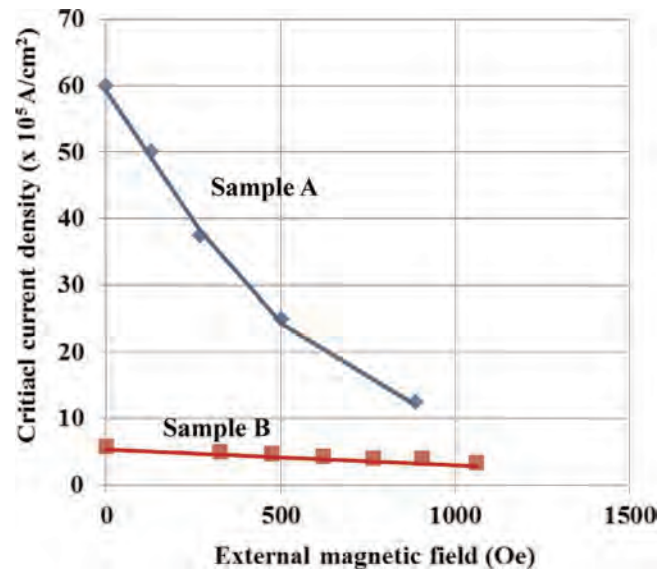


Fig. 6. External magnetic field dependence of J_c for Sample A (Si substrate) and Sample B (PC substrate).

3.2. Future potential estimation of low current driven TbFeCo spin memory with plastic low cost substrate

Thus, a rare-earth transition metal such as TbFeCo is very attractive material for low current driven memory device. For example, TbFeCo was used as a magneto-optical memory and the high durability and reliability of MO products has been demonstrated. The minimum recording domain length in the TbFeCo narrow track was around 40 nm. Also, narrow track pitch for the current driven spin memory can be produced with electron beam lithography technique. In the case of wire memory fabrication of Sample A in Fig. 1(a), both substrate cost and process cost are very high. However, in the case of Sample B in Fig. 1(b), both costs can be drastically reduced. Fig. 6 shows external magnetic field dependence of J_c for Sample A and B. In the case of the sample B with grooved PC substrate, J_c can be reduced to 6×10^5 A/cm². This result is also very attractive for spin memory. It seems that extrinsic pinning effect of PC substrate is much smaller than that of Si substrate. In the case of nanoimprint, thinner PC substrate also can be used. Moreover, nano-imprint can be pressed for both surfaces of the PC substrate. This means both side can be used for spin memory. In one side surface area of PC substrate (65 mm in width × 90 mm in length) which is similar area of SSD and 2.5" HDD form factor, data capacity of 40 nm bit and track pitch can be calculated as 450 GB. If both side spin memory with thinner PC substrate of 0.05 mm thickness can be adopted in the form factor, the data capacity would become to 100 TB. This is very attractive value. Thus, nano-imprint magnetic nanowire memory system should be investigated.

3.3. Proposal of low current driven spin logic

If memory and logic devices are designed with smart arrangement in a circuit, problem of interconnection delay can be reduced, it is very attractive for higher performance. Therefore, current driven spin memory and logic (AND, OR, NOT) should be proposed. If these 3 kinds of logic operation can be demonstrated, NAND, NOR, XOR could be also realized. Here, current driven AND, OR and NOT demonstrations with the same operating mechanism due to spin torque transfer effect are discussed. The operating mechanism of AND, OR, NOT are shown in Figs. 7–9, respectively.

In Fig. 7 current driven AND logic, 3 types of INPUT (1, 1), (1, 0),

Current driven AND LOGIC operations

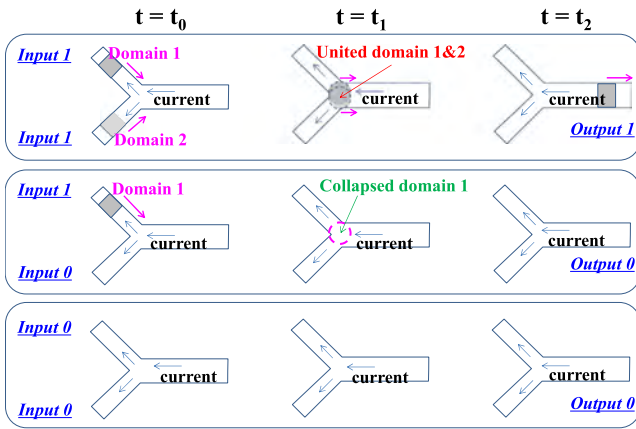


Fig. 7. Schematic figure of current driven AND type spin logic. Upper one is corresponding to the INPUT (1, 1), middle one INPUT (1,0), Lower one INPUT (0, 0).

Current driven OR LOGIC operations

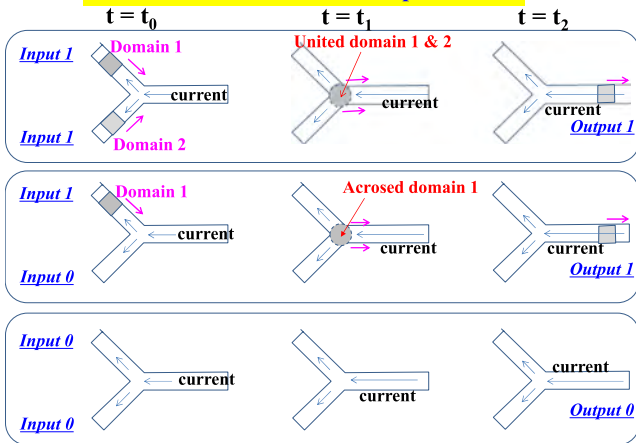


Fig. 8. Schematic figure of current driven OR type spin logic. Upper one is corresponding to the INPUT (1, 1), middle one INPUT (1,0), Lower one INPUT (0, 0).

Current driven NAND LOGIC with NOT GATE

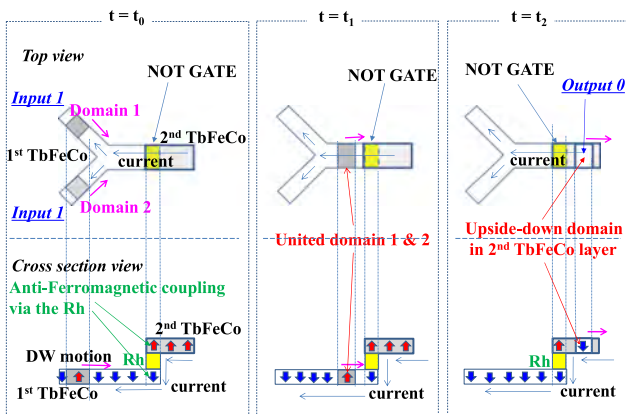


Fig. 9. Schematic figure of current driven NAND and NOT GATE type spin logic. Upper one is corresponding to the NAND process, lower one is corresponding to the NOT GATE.

(0, 0) are shown. For example, in the case of input (1, 1) at $t=t_0$, one domain is recorded on the each input port. When a current is applied from the output port to the input port, both recorded

domains in each input port are displaced to the confluence point. Then two domains are united each other at the confluence point ($t=t_1$). Finally, the united domain is thorough out to the output port ($t=t_2$). Thus, the AND logic operating result of input (1, 1) shows output (1).

On the other hand, in the case of input (1, 0), one domain is recorded on the upper input port ($t=t_0$). When current is flow from the right to the left of the Y-shaped sample, the right domain wall of the domain 1 gets trapped at the junction node, and as the left domain wall of the domain 1 moves toward the right, both domain walls are annihilated along with domain 1 ($t=t_1$). Therefore, output signal shows zero ($t=t_2$). The opposite input case of (0, 1) is also the same result as input (1, 0). It is clear that AND operating result of input (0, 0) is output (0).

In the same way, OR operation can be performed as shown in Fig. 8. The input (1, 1) operation is as same as that of the AND spin logic. On the other hand, in the case of the input (1, 0) case, the output signal should be (1). Therefore, the width of output port should be narrow because the right domain wall of the domain 1 do not be trapped at the junction node ($t=t_1$). In this case, the domain 1 can be flow out to the output port ($t=t_2$).

Finally, the schematic model of NOT function is shown in Fig. 9. Please look at the top view ($t=t_0$) of the NOT GATE and the cross section view. The layer stack structure is substrate/1st TbFeCo/Rh/2nd TbFeCo. In this case, spin direction in the 1st TbFeCo layer is opposite to that of the 2nd TbFeCo layer. This phenomena can be applied to the NOT function. In the figure upper area, current drive NAND logic circuit is indicated and the one part of the output port area works as a NOT GATE. In the figure lower part, a cross section image is represented. The NOT GATE area is composed of 3 layers. Both lower and upper layers are TbFeCo and the intermediate layer is Rh.

Fig. 10 shows Rh layer thickness dependence of remanent polar Kerr rotation angle. Total thickness of the 3 layers is less than 20 nm. The laser penetration depth into the film is about 100 nm. Therefore, the Kerr rotation signal involves magnetic properties of both TbFeCo layers. When the Rh layer is zero, both TbFeCo layers are coupled ferro-magnetically, therefore, the remanent Kerr rotation value is large.

However, when the Rh layer thickness is 0.4 nm, both TbFeCo layers are coupled ferri-magnetically, the remanent Kerr rotation shows very low because magnetization direction of the upper TbFeCo is opposite to that of lower TbFeCo layer. Here, to obtain a

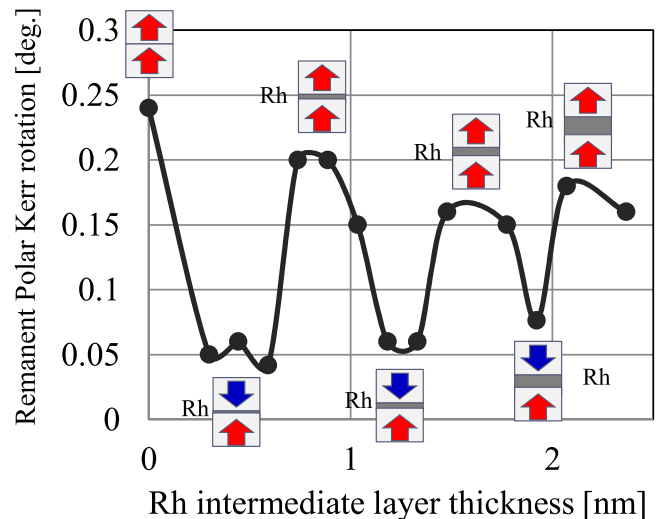


Fig. 10. Rh layer thickness dependence of remanent polar Kerr rotation angle in TbFeCo/Rh/TbFeCo multilayers. When Rh thickness is 0.4 nm, both TbFeCo layers coupled anti ferro-magnetically.

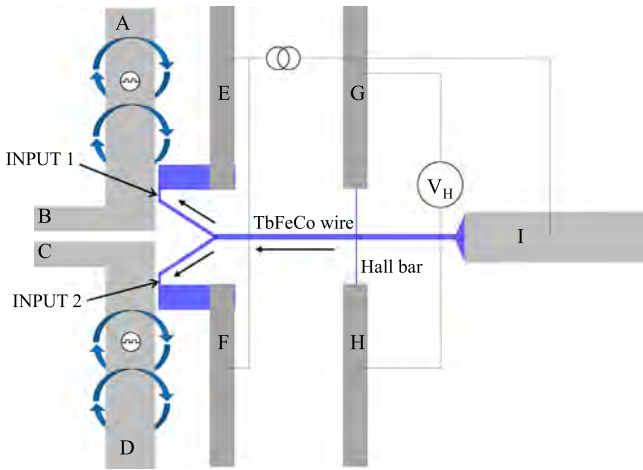


Fig. 11. Schematic figure of current driven AND type spin logic.

strong ferri-magnetic coupling in both TbFeCo layers, Rh layer of 0.4 nm in thickness is used for the NOT GATE sample. When the recorded domain is displaced to the right hand side by current flow as shown in Fig. 11 cross section view of the NOT GATE, the domain at the NOT GATE is copied to the upper TbFeCo layer. In the case, the copied magnetization can be reversed to that of the original domain, because of Rh thickness of 0.4 nm. Thus, the NOT function can be confirmed.

Fig. 11 is an image of current driven AND circuit. When current is applied between the electrode A and B, a domain at the INPUT 1 area of TbFeCo wire can be generated. In the same way, at the INPUT 2 area, a domain recording can be done. When current is applied from electrode I to E and F, the recorded domains at INPUT 1 and 2 area can be displaced to output area. The output signal can be reproduced by detecting anomalous Hall effect between the electrode G and H. The SEM image of AND spin logic experimental setup is shown in Fig. 12. Here, Input 1 and 2 signals are produced at the same time by applying Oersted field current from the electrode B to A. In the case of INPUT (1, 1) operation, If domain wall velocity at the INPUT 1 area is faster than 2 times compared with that of INPUT 2 area, it is difficult to become one output domain at the confluence point. In this case, there is no OUTPUT signal for any INPUT signals.

In order to confirm the current driven AND operation, AND demonstration circuit was prepared as shown in Fig. 13. Here, to simplify the experiment, simple electrode A to B is fabricated. Therefore, it is impossible to create domain corresponding to the INPUT (1, 0). However, In the case of INPUT (1, 1), when the current is applied from the electrode I to E, only one domain at the INPUT

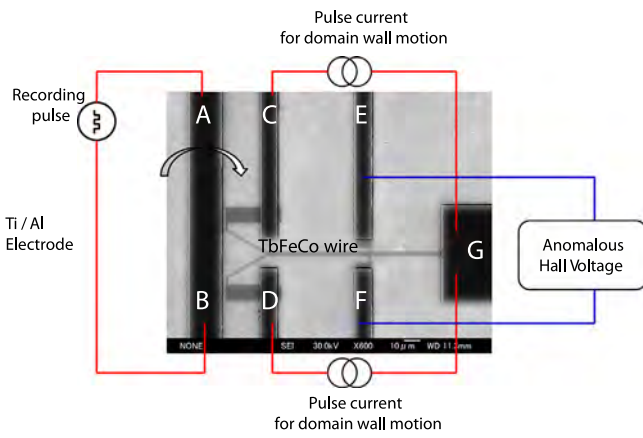


Fig. 12. SEM image of AND sample on SiO₂/Si substrate and experimental setup.

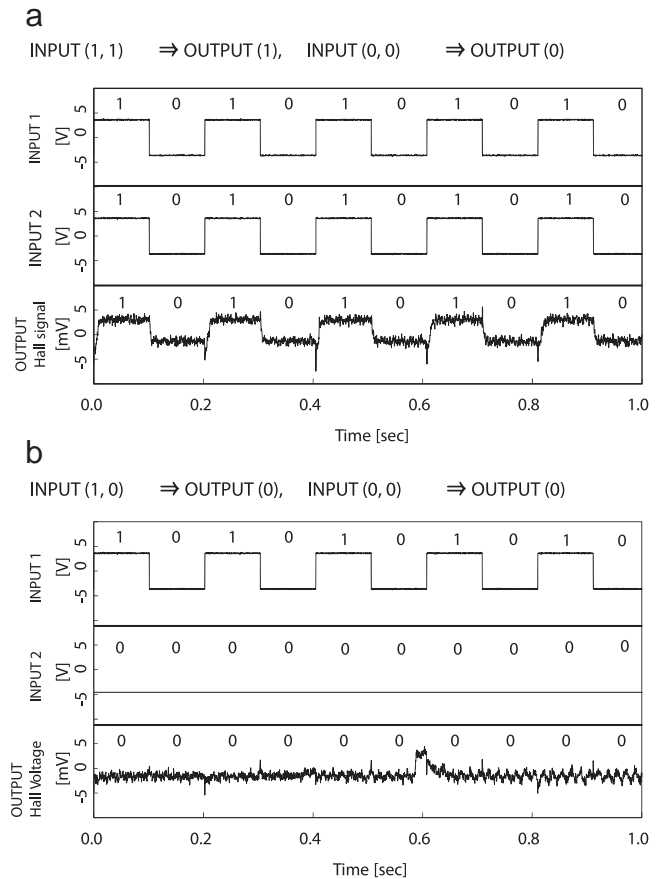


Fig. 13. Experimental result of current driven AND spin logic. (a) When INPUT signal is (1, 1), the operated OUTPUT result is (1). In case of INPUT (0, 0), the OUTPUT result is (0). (b) When INPUT signal is (1, 0), the operated OUTPUT result is (0).

1 area is displaced to the confluence point and collapsed.

Thus, the OUTPUT signal of the INPUT (1, 0) can be confirmed. The experimental result of the current driven AND circuit is shown in Fig. 13(a) INPUT (1, 1) and (0, 0), and (b) (1, 0), and (0, 0). In the case of Fig. 13(a), the upper one and middle one are corresponding to the signals of INPUT 1 and 2, the lower one is corresponding to the OUTPUT signal of Hall voltage. From those figures, it is found that the current driven AND circuit works exactly. In the case of OR circuit, it is more easy, because a domain collapse condition of INPUT (1, 0) at the confluence point can be easily fabricated. Thus, current driven DW memory and logic would be realized.

4. Conclusion

Current driven DW motions in TbFeCo magnetic nanowire were investigated. A critical current density (J_c) of TbFeCo which is prepared with lift off process and the substrate is Si was about 4×10^6 A/cm². It is considered that lower saturation magnetization (M_s) of the ferri-magnetic TbFeCo causes the decrease J_c . On the other hand, J_c of TbFeCo nanowire without any chemical process on PC substrate was 6×10^5 A/cm². This value is quite small compare to that of another magnetic nanowire. It is considered that in the Sample B preparation process named as nano-imprint method, extrinsic pinning sites can be reduced compared with that of the Sample A process named as etching method.

In order to realize current driven memory and logic, new spin logic of AND, OR, NOT have been proposed. These experimental

circuits were made and demonstrated. In these spin logic circuit, J_c was 1×10^6 A/cm². Thus, current driven spin memory and logic is very attractive for future memory and logic devices.

Acknowledgments

This work was performed by postdoctoral fellow Duc The Ngo and students Toma Kanehira, Jun Miyamoto, Masahiro Nomura of Toyota Technological Institute. This work was financially supported by the Ministry of Education, Culture, Sports, Science, and Technology, Japan – Supported Program for Strategic Research Foundation at Private University (2009–2013) and KAKENHI No. 24656219 (2012–2014) and No. 24360126 (2012–2015), No. 26630137 (2014–2016).

References

- [1] L. Berger, *Phys. Rev. B* 54 (1996) 9353–9358.
- [2] A. Yamaguchi, T. Ono, S. Nasu, K. Miyake, K. Mibu, T. Shinjo, *Phys. Rev. Lett.* 92 (2004) 077205.
- [3] M. Klaui, C.A.F. Vaz, J.A.C. Bland, W. Wernsdorfer, G. Faini, E. Cambril, L. Heyderman, F. Nolting, U. Rudiger, *Phys. Rev. Lett.* 94 (2005) 106601.
- [4] L. Thomas, M. Hayashi, X. Jiang, R. Moriya, C. Rettner, S.S.P. Parkin, *Nature* 443 (2006) 197.
- [5] L. Thomas, R. Moriya, C. Rettner, S.S.P. Parkin, *Science* 330 (2010) 1810.
- [6] S.S.P. Parkin, M. Hayashi, L. Thomas, *Magnetic domain-wall racetrack memory*, *Science* 320 (2008) 190–194.
- [7] T. Koyama, G. Yamada, H. Tnaniyawa, S. Kasai, N. Oshima, S. Fukami, N. Ishiwata, Y. Nakatani, T. Ono, *Appl. Phys. Express* 1 (2008) 101303.
- [8] H. Tanigawa, T. Koyama, G. Yamada, D. Chiba, S. Kasai, S. Fukami, T. Suzuki, N. Oshima, N. Ishiwata, Y. Nakatani, T. Ono, *Appl. Phys. Express* 2 (2009) 053002.
- [9] S. Fukami, Y. Nakatani, T. Suzuki, K. Nagahara, N. Oshima, N. Ishiwata, *Appl. Phys. Lett.* 95 (2009) 232504.
- [10] T. Koyama, et al., *Nat. Matter* 10 (2011) 194.
- [11] T. Koyama, K. Ueda, K.-J. Kim, Y. Yoshimura, D. Chiba, K. Yamada, J.-P. Jamet, A. Moughin, A. Thiavill, S. Mizukami, S. Fukami, N. Ishiwata, Y. Nakatani, H. Kohno, K. Kobayashi, T. Onol., *Nat. Nanotech.* 151 (2012) 1.
- [12] D. Ravelosona, D. Lacour, J.A. Katine, B.D. Terris, C. Chappert, *Phys. Rev. Lett.* 95 (2005) 117203.
- [13] S. Li, H. Nakamura, T. Kanazawa, X. Liu, A. Morisako, *IEEE. Trans. Mag.* 46 (2010) 1695.
- [14] D.-T. Ngo, K. Ikeda, H. Awano, *Appl. Phys. Express* 4 (2011) 093002.
- [15] D.-T. Ngo, K. Ikeda, H. Awano, *J. Appl. Phys.* 111 (2012) 083921.
- [16] D. Bang, H. Awano, *Appl. Phys. Express* 5 (2012) 125201.
- [17] D. Bang, H. Awano, *IEEE. Trans. Mag.* 49 (2013) 4390.
- [18] D. Bang, H. Awano, *Jpn. J. Appl. Phys.* 52 (2013) 123001.
- [19] D.A. Allwood, G. Xiong, C.C. Faulkner, D. Atkinson, D. Petit, R.P. Cowburn, *Science* 309 (2005) 1688.
- [20] H. Nomura, R. Nakatani, *Appl. Phys. Exp.* 4 (2011) 013004.
- [21] N. Ohshima, H. Numata, S. Fukami, K. Nagahara, T. Suzuki, N. Ishiwata, K. Fukumoto, T. Kinoshita, T. Ono, *J. Appl. Phys.* 107 (2010) 103912.
- [22] Y. Nakashima, K. Nagai, T. Tanaka, K. Matsuyama, *Appl. Phys. Lett.* 92 (2008) 022505.
- [23] J.C. Slonczewski, *Current-driven excitation of magnetic multilayers*, *J. Magn. Mater.* 159 (1996) L1–L7.

Enhancement of spin Hall effect induced torques for current-driven magnetic domain wall motion: Inner interface effect

Do Bang,^{1,2} Jiawei Yu,³ Xuepeng Qiu,³ Yi Wang,³ Hiroyuki Awano,¹ Aurelien Manchon,⁴ and Hyunsoo Yang³

¹*Toyota Technological Institute, Tempaku, Nagoya 468-8511, Japan*

²*Institute of Material Science, Vietnam Academy of Science and Technology, 18 Hoang Quoc Viet, Cau Giay, Ha Noi, Vietnam*

³*Department of Electrical and Computer Engineering, National University of Singapore, 117576, Singapore*

⁴*Division of Physical Science and Engineering, King Abdullah University of Science and Technology (KAUST), Thuwal 23955, Saudi Arabia*

(Received 3 February 2015; revised manuscript received 31 March 2016; published 23 May 2016)

We investigate the current-induced domain wall motion in perpendicular magnetized Tb/Co wires with structure inversion asymmetry and different layered structures. We find that the critical current density to drive domain wall motion strongly depends on the layered structure. The lowest critical current density ~ 15 MA/cm² and the highest slope of domain wall velocity curve are obtained for the wire having thin Co sublayers and more inner Tb/Co interfaces, while the largest critical current density ~ 26 MA/cm² required to drive domain walls is observed in the Tb-Co alloy magnetic wire. It is found that the Co/Tb interface contributes negligibly to Dzyaloshinskii-Moriya interaction, while the effective spin-orbit torque strongly depends on the number of Tb/Co inner interfaces (n). An enhancement of the antidamping torques by extrinsic spin Hall effect due to Tb rare-earth impurity-induced skew scattering is suggested to explain the high efficiency of current-induced domain wall motion.

DOI: [10.1103/PhysRevB.93.174424](https://doi.org/10.1103/PhysRevB.93.174424)

I. INTRODUCTION

The current-induced domain wall motion (CIDM) in thin perpendicular magnetized ferromagnetic wires sandwiched between a heavy metal and an oxide has been shown to be very efficient, yielding a high domain wall (DW) velocity at low current density enabling the development of spintronic devices [1–12]. In these asymmetric wires, inversion symmetry breaking together with strong spin-orbit interaction (SOI) has two major implications. First, it induces spin-orbit torques (SOTs) due to, on the one hand, the interfacial Rashba effect and, on the other hand, the spin Hall effect (SHE) present in the bulk heavy metal [13–17]. Both effects produce fieldlike and antidampinglike torques [18–20]. Second, it is also responsible for the emergence of interfacial Dzyaloshinskii-Moriya interaction (DMI), which promotes chiral magnetic textures. The concurrence of antidamping SOT and DMI-induced chiral textures results in fast DW motion in ultrathin layer structures [21–28].

Recently, a transition in the mechanism responsible for current-driven DW motion from bulk (spin-transfer) to interfacial (spin-orbit) torque has been confirmed as a change in the DW motion direction when reducing the layer thickness of Co/Ni multilayer down to 2.1 nm [29]. It is found that the adiabatic spin-transfer torque (STT) dominates the DW motion in the thick regime, while the antidamping SOT controls the DW motion in the thin regime. In an earlier study [30], on the other hand, SOTs-induced DW motion was observed up to a thickness of ~ 10 nm for the asymmetric interfacial wire with the layered structure of SiO₂/[Tb(3.2 Å)/Co(2.6 Å)]_{*n*}/Pt(20 Å). The high efficiency of SOTs in the wire can be attributed to an enhancement of antidamping SOT by inner Tb/Co interfaces. However, such an enhancement in thick multilayers has not yet been fully understood.

In this study, we present the current-induced DW motion in the Tb/Co wires with different layered structures. The

magnitude of the antidamping SOT by inner Co/Tb interfaces is tuned by changing the thickness of Co ultrathin sublayers, number of inner Co/Tb interfaces, and formation of Tb-Co alloy magnetic layer. Our results show that the efficiency of SOTs is highest for the samples with a larger number of inner Co/Tb interfaces and lowest for the one with Tb-Co alloy magnetic wire. DMI is found to be small in our samples. We suggest that the high efficiency of SOTs in our multilayers can be associated with extrinsic SHE due to Tb rare-earth impurity-induced skew scattering at inner Co/Tb interfaces [31,32].

II. SAMPLE PREPARATION AND MAGNETIC PROPERTIES

For this work, experiments are performed on three asymmetric magnetic wires with different layer structures [Fig. 1(a)], in which the total magnetic layer thickness is kept to be ~ 6 nm. Layers of A stack: [Tb(3.4 Å)/Co(3.2 Å)]₉/Pt(20 Å); B stack: [Tb(3.4 Å)/Co(6.5 Å)]₆/Pt(20 Å); and C stack: [Tb₄₅Co₅₅ alloy (60 Å)]/Pt(20 Å) are deposited on the thermally oxidized silicon substrates by dc and rf magnetron sputtering using high-quality Tb and Co targets. The base pressure of the growth chamber is $\sim 5 \times 10^{-8}$ mbar. The Ar (99.99%) gas pressure is kept at $\sim 3 \times 10^{-2}$ mbar during sputtering. The growth rates of Tb and Co sublayers are 0.56 and 0.53 Å/s, respectively. Therefore, it is expected that only a part of the first Tb sublayer is oxidized due to the minimal residual oxidation contamination from the SiO₂/Si substrate. The patterned wires have a width of 1.1 μ m and are fabricated by using electron-beam lithography and lift-off technique. The motion of DWs in the wires is driven by pulses of voltage between two Al/Ti electrodes, labeled as (1) and (2) in Fig. 1(b), and directly observed using polar Kerr microscopy [33]. All measurements shown in this work are performed at room temperature. Figure 1(b) shows the image of a scanning electron microscope (SEM) with the schematic

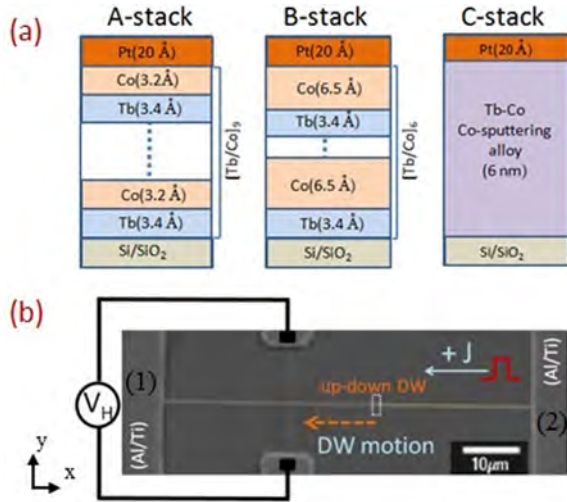


FIG. 1. (a) Schematic illustration of multilayered Tb/Co films with structural inversion asymmetry. (b) Scanning electron microscopy image of multilayered Tb/Co wire with Ti/Al electrodes for magnetotransport measurements.

electrical measurement setup. Both the film and patterned wires exhibit perpendicular magnetic anisotropy (PMA), which is confirmed by using an alternative gradient force magnetometer (AGFM) and anomalous Hall effect (AHE) measurements.

Figure 2(a) shows the hysteresis loops of the three magnetic films with different layered structures when the field is applied normal to the film plane, indicating that the films have perpendicular magnetic anisotropy. However, the magnetic films show different values of the coercivity (H_c) and saturation magnetization (M_s). The uniaxial anisotropy constant (K_u) is determined to be 1.44×10^5 , 2.8×10^5 , and 1.6×10^5 J/m³ from the M_s and saturation field (H_k) of in-plane (hard axis) hysteresis loops (not shown) for the A-, B-, and C-stack films, respectively. These different magnetic properties can be attributed to the different Tb-Co compositions, where the A stack has a rare-earth (RE)-rich composition, while B and C stacks have transition-metal (TM)-rich compositions, which can be qualitatively determined from the polarity of Kerr rotation angle from these films. In multilayers, Tb and Co moments are seen to be in the homogeneous antiferromagnetic state [34,35]. Therefore, the direction of the total magnetic moment in the whole stack depends on the moments of the Tb and Co sublattices: in a stack with Tb-rich composition, the moment of Tb sublattice is larger than that of the Co sublattice, while in a stack with Co-rich composition, the moment of Co sublattice is larger than that of the Tb sublattice. When the composition of the whole stack changes from Co rich to Tb rich, the direction of the total magnetic moment can be detected by a polarity change in the Kerr rotation angle.

Typical results for DW depinning field measurements for the three magnetic wires are shown in Fig. 2(b). As the out-of plane magnetic field changes from 0 to -2.5 kOe, the normalized Hall voltage (V_H) changes from 1 to -1 indicating that the magnetization is reversed in the Hall cross and the DW passes through the Hall cross region. Here, we define the DW depinning field (H_{dep}) as the magnetic field where V_H starts reducing from 1. Furthermore, it is found that H_{dep}

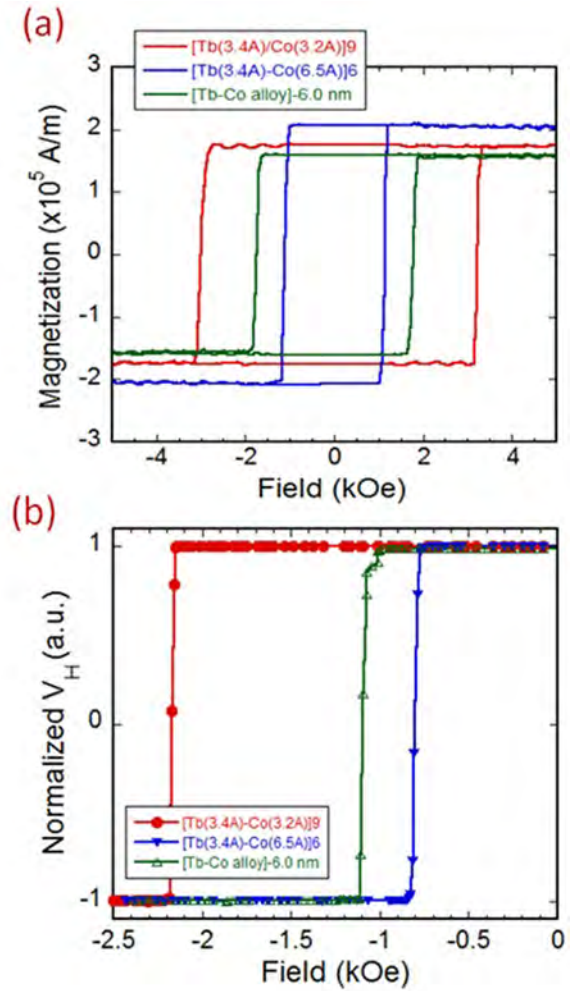


FIG. 2. (a) Magnetization curves of multilayered Tb/Co films. (b) Normalized anomalous Hall voltage as a function of the perpendicular field measured after the creation of a DW for different stack structures: A, B, and C stacks.

increases as the wire width of the A stack is reduced as shown in the inset of Fig. 3(a). The error bar was determined from five repeated measurements. It is clear that H_{dep} shows a linear dependence on $1/\text{width}$. Similar to the study of Co/Ni nanowires with perpendicular magnetic anisotropy [36], this size dependence of H_{dep} indicates that extrinsic pinning dominates field-induced DW motion in the wire.

III. CURRENT-DRIVEN DOMAIN WALL MOTION

A. Critical current density

We next investigate current-induced DW motion by applying voltage pulses of 100-ns duration between (1) and (2) electrodes. Figure 3(a) shows the critical current density (J_c) as a function of H_{dep} for the A-stack wire. Here, J_c is determined as the minimum current density required to drive DW with a depinning field of H_{dep} . The experiment was also repeated five times for each data point. Similar to a previous study [30], the DW moves along the direction of current flow ($+J$) in our asymmetric interfacial wires. This reversed DW motion with respect to electrons is explained by the concurrence of

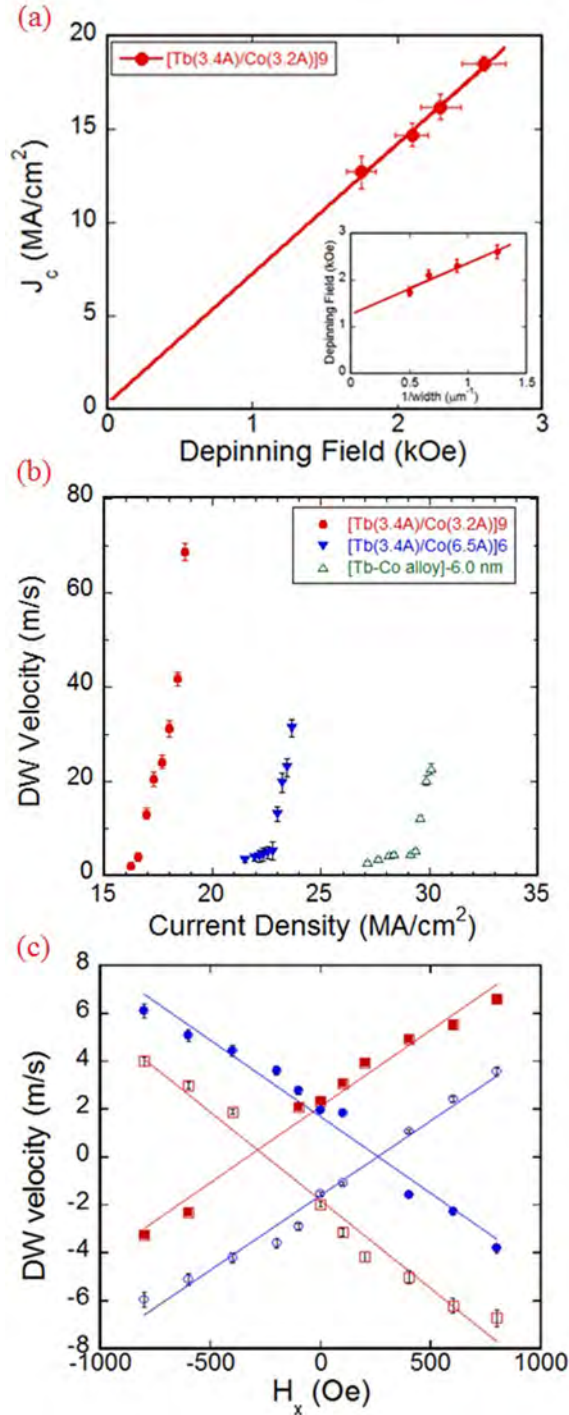


FIG. 3. (a) Critical current density (J_c) as a function of depinning field (H_{dep}) for the different widths of the A-stack wire. The inset shows the wire width dependence of depinning field. Solid lines are the linear fits. (b) Current density dependence of DW velocity for different magnetic wires (1.1- μm width) of A-, B-, and C-stack structures. (c) Measured DW velocity versus in-plane field (H_x) for A-stack wire. Red and blue symbols represent $\downarrow\uparrow$ and $\uparrow\downarrow$ DWs, respectively. Solid and open symbols correspond to positive and negative current directions, respectively. Lines are linear fits to the data to estimate crossing fields.

antidamping torque and DMI. It is clear that J_c is linearly proportional to H_{dep} . This observation suggests that current-

induced antidamping SOT can be regarded as an effective depinning field [9,15,25,37,38]. The contribution of antidamping SOT has been added to the Landau-Lifshitz-Gilbert equation to describe the time evolution of the magnetization by Haazen *et al.* [37]. Their results indicate that the H_{dep} can be tuned as a linear function of the current. Moreover, Emori *et al.* [9] also has showed that the current generates an effective field associated with a Slonczewski-like torque. The magnitude of the effective field induced by the current is estimated to be ~ 500 and ~ 2000 Oe per 10^{12} A.m⁻² for the Pt/CoFe/MgO and Ta/CoFe/MgO nanowires, respectively.

In order to study the effect of the layered structure on the current-induced DW motion, we have measured the DW velocity (v) as a function of the injected current density (J) for A, B, and C stacks, as sketched in Fig. 1(a). The results are shown in Fig. 3(b) for a wire width of 1.1 μm . J_c strongly increases for the wires of the B stack and C stack. In addition, the slope of v versus J curves gradually reduces in these wires. The highest slope was obtained for A-stack wire where there are more interfaces between Tb and Co, while the lowest slope was seen for the C-stack wire with a thick Tb₄₅Co₅₅ alloy magnetic layer.

B. Dzyaloshinskii-Moriya interaction

The effect of a longitudinal field (H_x) on the DW velocity is shown in Fig. 3(c) for A-stack wire (measured at 15.2 MA/cm²). Red and blue symbols represent $\downarrow\uparrow$ and $\uparrow\downarrow$ DWs, and solid and open symbols correspond to positive and negative current directions, respectively. One can see that DW velocity for both $\downarrow\uparrow$ and $\uparrow\downarrow$ DWs vanishes at a certain value of H_x ($H_{\text{cr}} \approx \pm 265$ Oe), which is associated with the DMI field [25].

To evaluate the effect of the number of inner Tb/Co interfaces on the DMI, we have measured the DMI constant and DMI effective field for the A stack with different repetition numbers ($n = 5$ and 6). The field-induced asymmetric DW expansion was investigated using a polar Kerr microscope, and the measurement schematic is presented in Fig. 4(a). The magnetic field was applied in plane with a small out-of-plane tilting ($\theta = 5^\circ$) to move the DW. As shown in Fig. 4(b), the DWs on the left edge of the circular domain moves faster than that on the right edge, indicating a left-handed Néel wall, which is stabilized by the presence of the DMI field [37,39]. We investigated systematically the DW velocities as a function of external field strength (not shown) then extracted DMI field as discussed in Ref. [40]. The extracted DMI constants (D) are shown at the bottom of each picture in Fig. 4(b), with the Co/Tb bilayer repetition numbers (n). We found that the extracted DMI field is comparable with the crossing field (H_{cr}), which is estimated from Fig. 3(c). One can see in Fig. 4(b) that the strength of DMI reduces with increasing n (i.e., with increasing the overall film thickness). This indicates that DMI in these films is controlled largely by the Co/Pt top interface.

C. Spin-orbit torque measurement

Using Hall voltage and lock-in measurements [41,43], both longitudinal (H_L) and transverse (H_T) SOT effective fields were estimated for the A-stack sample as shown in Fig. 4(c). It is reported in previous works [17,41,42] that

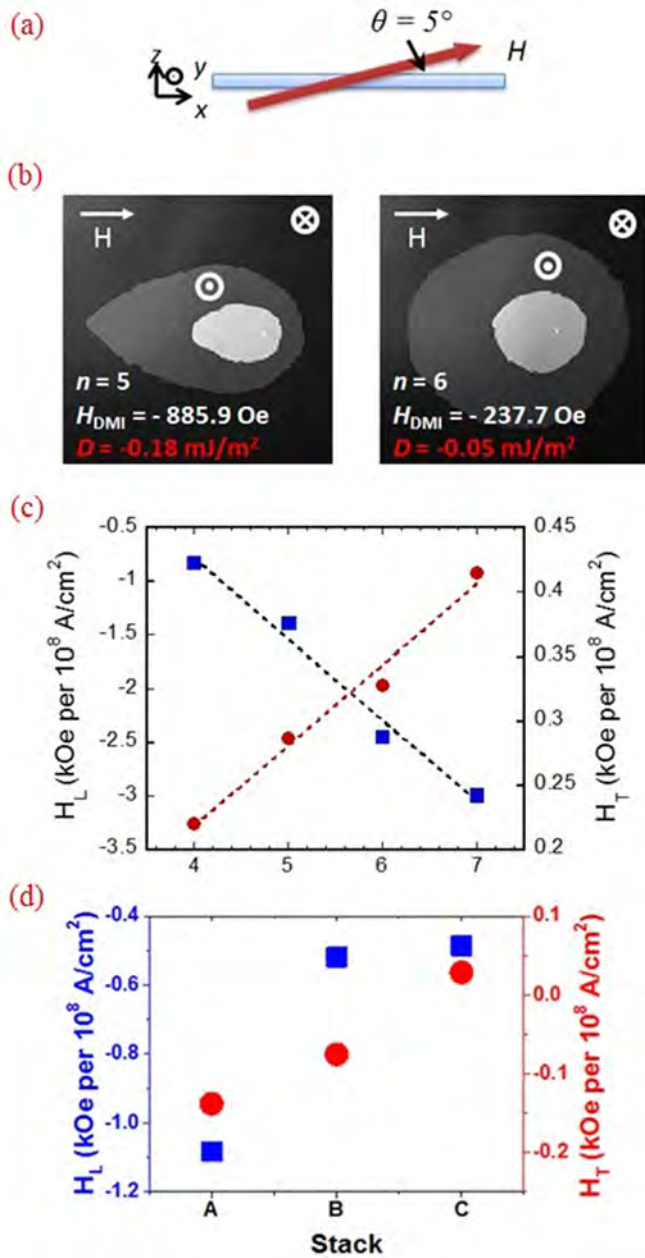


FIG. 4. (a) The lateral view of the DMI measurement schematic in the Kerr microscope. The blue horizontal box indicates the film and the red arrow presents the direction of the external field. (b) Anisotropic domain wall displacement under an in-plane magnetic field with a small out-of-plane angle for the A stack with repetition number $n = 5$ and 6. The magnetic field direction is indicated at the top of each picture. The initial domain position is indicated by the white area. (c) The dependence of longitudinal (H_L) and transverse (H_T) SOT effective fields on the number of repetitions n for the A-stack sample. (d) The H_L and H_T in A-, B-, and C-stack samples. In (c),(d), the square symbols are for H_L , and the circle symbols are for H_T .

SOT is purely an interfacial effect, inversely proportional to the film thickness. In our case, however, SOT increases with the number of interfaces, which strongly suggests significant contribution from the Co/Tb interfaces of the film. Our large SOT may be compared to those of Jamali *et al.* [43]

and Lee *et al.* [44], who found large effective fields with a [Co/Pd]₂₂ multilayered system and a bulk perpendicular magnetic anisotropy Pd/FePd/MgO system, respectively.

The SOT effective fields in A, B, and C stacks were also investigated as presented in Fig. 4(d). The largest SOT effective fields (H_L and H_T) are found in the A stack, which has the largest number of Co/Tb interfaces ($n = 9$). The SOT effective fields are found to be minimum in the C stack, which contains no Co/Tb interface ($n = 0$). The increase of SOT effective fields in Fig. 4(d) as well as the DW velocity in Fig. 3(b) with respect to the Co/Tb interface strongly indicates the contribution of SOTs from the inner Co/Tb interface. It is noted that H_T is about one order of magnitude smaller than H_L . This suggests that the antidamping torque, possibly arising from SHE, is dominant at Co/Tb inner interfaces.

IV. INTERPRETATION AND DISCUSSION

A. Thickness dependence of DMI and SOT

In Sec. III, we found that the DMI field decreases when increasing the number of repetition in the A stack, whereas the SOT effective fields increase. We now propose a toy model to interpret these behaviors. In magnetic multilayers, each magnetic layer i is embedded between two interfaces (top and bottom). Due to spin-orbit effects a current-driven SOT effective field is created at these two interfaces,

$$\vec{h}_{\text{SO}}^{\text{bottom}} = h_{\perp}^{b,i} \vec{y} + h_{\parallel}^{b,i} \vec{y} \times \vec{m}_i \quad (1)$$

$$\vec{h}_{\text{SO}}^{\text{top}} = -h_{\perp}^{t,i} \vec{y} - h_{\parallel}^{t,i} \vec{y} \times \vec{m}_i, \quad (2)$$

where $h_{\perp}^{\alpha,i}$ is the (out-of-plane and in-plane) SOT field at the interface α , and we chose the orientation $\vec{y} = \vec{z} \times \vec{j}_c / |\vec{z} \times \vec{j}_c|$ to comply with the symmetry of the system, without assuming any specific mechanism (spin Hall or inverse spin galvanic effects). Here, \vec{m}_i is the magnetization direction of layer i and the minus sign “-” in Eq. (2) emphasizes the fact that in the case layer i is embedded between symmetric interfaces, the current-driven SOT fields on both interfaces are equal and opposite. Hence, the torque on layer i reads

$$\vec{\tau}_i = \vec{m}_i \times [(h_{\perp}^{b,i} - h_{\perp}^{t,i}) \vec{y} + (h_{\parallel}^{b,i} - h_{\parallel}^{t,i}) \vec{y} \times \vec{m}_i]. \quad (3)$$

The same reasoning applies to the DMI field \vec{H}_{DM}^i felt by layer i (see, e.g., Ref. [38]),

$$\vec{H}_{\text{DM}}^i = \delta (h_{\text{DM}}^{b,i} - h_{\text{DM}}^{t,i}) \vec{m}_i \times [(\vec{z} \times \vec{\nabla}) \times \vec{m}_i]. \quad (4)$$

Here, δ is the domain wall width.

Let us now consider the stack $\text{SiO}_2/[\text{Tb}/\text{Co}]_n/\text{Pt}$, composed of a repetition of n bilayers. We assume that the magnetic layers composing the stack, Co and Tb, are antiferromagnetically aligned and can be treated as macrospins, forming a perfect ferrimagnet, i.e., $\vec{m}_{\text{Co}}^j = -\vec{m}_{\text{Tb}}^i = \vec{m}$. The total magnetization is therefore,

$$\vec{M} = \sum_i M_s^{\text{Tb},i} \vec{m}_{\text{Tb}}^i + \sum_j M_s^{\text{Co},j} \vec{m}_{\text{Co}}^j = M_s \vec{m}, \quad (5)$$

$$M_s = (n-1)(M_s^{\text{Co}} - M_s^{\text{Tb}}) + M_{s,\text{Top}}^{\text{Co}} - M_{s,\text{Bottom}}^{\text{Tb}}. \quad (6)$$

After some straightforward algebra, we obtain the Landau-Lifshitz-Gilbert (LLG) equation of the multilayer stack

$$\partial_t \vec{m} = -\gamma \vec{m} \times (\vec{H} + \Delta H_{\text{DM}}^{\text{eff}}[(\vec{z} \times \vec{\nabla}) \times \vec{m}]) + \alpha_{\text{eff}} \vec{m} \times \partial_t \vec{m} + \vec{m} \times [h_{\perp}^{\text{eff}} \vec{y} + h_{\parallel}^{\text{eff}} \vec{y} \times \vec{m}]. \quad (7)$$

In Eq. (7), we have defined the following effective DMI field, magnetic damping, and SOT fields,

$$\begin{aligned} H_{\text{DM}}^{\text{eff}} &= [M_{s,\text{Bottom}}^{\text{Tb}}(h_{\text{DM}}^{\text{SiO}_2/\text{Tb}} - h_{\text{DM}}^{\text{Tb/Co}}) + (n-1)(M_s^{\text{Tb}} - M_s^{\text{Co}})(h_{\text{DM}}^{\text{Co/Tb}} - h_{\text{DM}}^{\text{Tb/Co}}) + M_{s,\text{Top}}^{\text{Co}}(h_{\text{DM}}^{\text{Tb/Co}} - h_{\text{DM}}^{\text{Co/Pt}})]/M_s \\ \alpha_{\text{eff}} &= \alpha(M_{s,\text{Bottom}}^{\text{Tb}} + (n-1)M_s^{\text{Tb}} + M_{s,\text{Top}}^{\text{Co}} + (n-1)M_s^{\text{Co}})/M_s \\ h_{\perp}^{\text{eff}} &= [-M_{s,\text{Bottom}}^{\text{Tb}}(h_{\perp}^{\text{Tb/Co}} - h_{\perp}^{\text{SiO}_2/\text{Tb}}) + M_{s,\text{Top}}^{\text{Co}}(h_{\perp}^{\text{Tb/Co}} - h_{\perp}^{\text{Co/Pt}}) + (n-1)(M_s^{\text{Co}} - M_s^{\text{Tb}})(h_{\perp}^{\text{Tb/Co}} - h_{\perp}^{\text{Co/Tb}})]/M_s \\ h_{\parallel}^{\text{eff}} &= [M_{s,\text{Bottom}}^{\text{Tb}}(h_{\parallel}^{\text{Tb/Co}} - h_{\parallel}^{\text{SiO}_2/\text{Tb}}) + M_{s,\text{Top}}^{\text{Co}}(h_{\parallel}^{\text{Tb/Co}} - h_{\parallel}^{\text{Co/Pt}}) + (n-1)(M_s^{\text{Co}} + M_s^{\text{Tb}})(h_{\parallel}^{\text{Tb/Co}} - h_{\parallel}^{\text{Co/Tb}})]/M_s. \end{aligned}$$

The experimental data obtained in Sec. III indicate that DMI decreases with the number of repetitions, which suggests that DMI is solely due to the Pt/Co interface and absent at Co/Tb interfaces ($h_{\text{DM}}^{\text{Co/Tb}}, h_{\text{DM}}^{\text{Tb/Co}} \approx 0$), so that

$$H_{\text{DM}}^{\text{eff}} \approx -\frac{M_{s,\text{Top}}^{\text{Co}} h_{\text{DM}}^{\text{Co/Pt}}}{(n-1)(M_s^{\text{Co}} - M_s^{\text{Tb}}) + M_{s,\text{Top}}^{\text{Co}} - M_{s,\text{Bottom}}^{\text{Tb}}}. \quad (8)$$

We neglected the contribution of SiO₂/Tb interfaces due to the weak SOC of SiO₂. In contrast, SOT fields increase with the number of repetitions, which suggests that SOT fields are present at all the interfaces. Assuming that SiO₂/Tb interfaces do not produce significant SOT field ($h_{\text{DM},\perp,\parallel}^{\text{SiO}_2/\text{Tb}} \approx 0$), the total SOT fields read

$$h_{\perp}^{\text{eff}} = \frac{(n-1)(M_s^{\text{Co}} - M_s^{\text{Tb}})(h_{\perp}^{\text{Tb/Co}} - h_{\perp}^{\text{Co/Tb}}) - M_{s,\text{Bottom}}^{\text{Tb}} h_{\perp}^{\text{Tb/Co}} + M_{s,\text{Top}}^{\text{Co}}(h_{\perp}^{\text{Tb/Co}} - h_{\perp}^{\text{Co/Pt}})}{(n-1)(M_s^{\text{Co}} - M_s^{\text{Tb}}) + M_{s,\text{Top}}^{\text{Co}} - M_{s,\text{Bottom}}^{\text{Tb}}}, \quad (9)$$

$$h_{\parallel}^{\text{eff}} = \frac{(n-1)(M_s^{\text{Co}} + M_s^{\text{Tb}})(h_{\parallel}^{\text{Tb/Co}} - h_{\parallel}^{\text{Co/Tb}}) + M_{s,\text{Bottom}}^{\text{Tb}} h_{\parallel}^{\text{Tb/Co}} + M_{s,\text{Top}}^{\text{Co}}(h_{\parallel}^{\text{Tb/Co}} - h_{\parallel}^{\text{Co/Pt}})}{(n-1)(M_s^{\text{Co}} - M_s^{\text{Tb}}) + M_{s,\text{Top}}^{\text{Co}} - M_{s,\text{Bottom}}^{\text{Tb}}}. \quad (10)$$

This simple phenomenological model shows that the thickness dependence of the SOT fields depends on the relative magnitude of the torque at Co/Tb, Tb/Co, and Co/Pt interfaces. If the SOT field is dominated by Tb/Co and Co/Tb interfaces, $h_{\parallel,\perp}^{\text{Tb/Co}} - h_{\parallel,\perp}^{\text{Co/Tb}} \gg h_{\parallel,\perp}^{\text{Co/Pt}}$, one can expect that the overall SOT effective field increases with the number of repetitions, as observed in Sec. III.

B. DMI and SOT field at Co/Tb interfaces

The analysis provided above implies that DMI is weak at Co/Tb interfaces while SOT fields are sizable at these interfaces. This difference can be attributed to the nature of the electron orbitals involved in each mechanism.

DMI is the antisymmetric exchange between local spins and, as such, involves mainly localized electrons. In Tb, the magnetism is carried by 4*f* orbitals located far below Fermi energy, and therefore hybridizing only weakly to 3*d* orbitals of Co via 5*d* orbitals [45]. This is in sharp contrast with Pt/Co interfaces where 5*d* orbitals of Pt couple directly to 3*d* orbitals of Co, thereby acquiring magnetism by proximity effect. The magnetic coupling being much larger at Pt/Co interfaces than at Tb/Co interfaces, one can reasonably speculate that DMI should be larger in the former than in the latter.

In contrast with DMI, SOT is a nonequilibrium phenomenon that involves transport electrons at Fermi level. It has been recently showed that the Rashba effect at the surface of Tb layers and its monoxides is quite large [46], which should lead to sizable SOT fields. In addition, since Tb/Co interfaces are not sharp, Tb-Co intermixing is expected. Tb could act as an impurity in Co and one can envisage that it leads to the

emergence of extrinsic SHE due to rare-earth impurity-induced skew scattering in the ultrathin TM layer [31,32]. Such a resonant skew scattering results in a giant spin Hall effect, possibly an order of magnitude larger than in Pt [31,32]. In contrast, the Co impurity in Tb does not induce extrinsic SHE, which can be only realized in very low resistivity metals. Notice that this effect can only be significant as long as the magnetic exchange between itinerant and local spins is not too strong; otherwise, the itinerant spin remains aligned on the local magnetization.

C. Compensation between SOT and STT

To complete our study, we finally discuss the critical thickness where the DW stops moving under the SHE due to the cancellation of the SOTs and bulk STT in the A-, B-, and C-stack wires. Figure 5 shows the DW velocity as a function of current density in the Tb/Co multilayer of A stack and B stack with various Tb/Co repetition numbers (*n*). Seo *et al.* [8] reported that the magnitude of antidamping SOT is inversely proportional to the thickness of the ferromagnetic (FM) layer. Therefore, the SOT is expected to be compensated by the bulk STT at a critical thickness of the FM layer. We find that the critical thicknesses are ~13.2, 9.9, and 8 nm for the A, B, and C stack (not shown), respectively. The thickest magnetic layer to observe the SOT-induced DW motion is the A stack, which has the smallest J_c as shown in Fig. 3(b). This result suggests that the inner Tb/Co interfaces play a role for the DW motion in the A stack. As discussed above, DMI is negligible with increasing *n* as well as the thickness [Fig. 4(b)]. Therefore, DMI should not be strong enough to stabilize the Néel wall

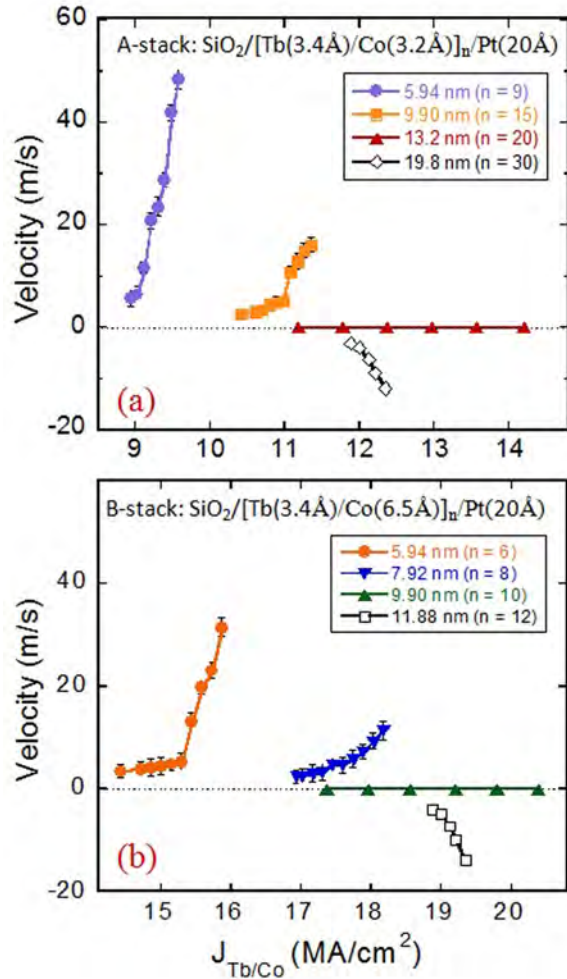


FIG. 5. (a) DW velocity as a function of current density in Co/Tb multilayer of (a) A stack and (b) B stack for various Co/Tb repetition number (n).

structure in thicker samples. In that case, the Bloch DWs would be moved in the direction of conduction electrons due to STT [$n > 20$ in Fig. 5(a)]. A high efficiency of current-induced SOTs has also been reported in 20 nm-thick Co/Pd multilayers with perpendicular magnetic anisotropy [43]. The authors concluded that the observed effect could not be explained only by SHE-induced torque at the outer interfaces.

V. CONCLUSION

In conclusion, we have studied the current-induced DW motion in the perpendicular magnetized Tb/Co wires with different layered structures. The critical current density was found to strongly depend on the layered structures. The lowest critical current density $\sim 1.5 \times 10^{11}$ A/m² and highest slope of DW velocity were obtained for the A-stack wire having thin Co sublayers and more Tb/Co interfaces, which suggests that (antidamping) SOT-induced DW motion is enhanced due to contributions from Tb/Co interfaces. We suggest that such an enhanced antidamping arises from skew scattering on Tb rare-earth impurities present in Co sublayers. Our study indicates an efficient way to reduce the critical current density for DW motion through inner interface engineering.

ACKNOWLEDGMENTS

This work was partially supported by the Ministry of Education, Culture, Sports, Science and Technology, Japan - Supported Program for Strategic Research Foundation at Private University (2014–2020) and KAKENHI No. 26630137, and the National Research Foundation (NRF), Prime Minister's Office, Singapore, under its Competitive Research Programme (CRP Award No. NRFCRP12-2013-01). H.Y. thanks the Singapore Spintronics Consortium (SG-SPIN) for support. A.M. acknowledges support from the King Abdullah University of Science and Technology (KAUST).

- [1] L. Berger, *Phys. Rev. B* **54**, 9353 (1996).
- [2] J. C. Slonczewski, *J. Magn. Magn. Mater.* **159**, L1 (1996).
- [3] J. Jaworowicz, N. Vernier, J. Ferré, A. Maziewski, D. Stanesco, D. Ravelosona, A. S. Jacqueline, C. Chappert, B. Rodmacq, and B. Diény, *Nanotechnol.* **20**, 215401 (2009).
- [4] L. Leem and J. S. Harris, *J. Appl. Phys.* **105**, 07D102 (2009).
- [5] L. Thomas, R. Moriya, C. Rettner, and S. S. P. Parkin, *Science* **330**, 1810 (2010).
- [6] I. M. Miron, T. Moore, H. Szabolcs, L. D. Buda-Prejbeanu, S. Auffret, B. Rodmacq, S. Pizzini, J. Vogel, M. Bonfim, A. Schuhl, and G. Gaudin, *Nature Mater.* **10**, 419 (2011).
- [7] K.-S. Ryu, L. Thomas, S. H. Yang, and S. S. P. Parkin, *Appl. Phys. Express* **5**, 093006 (2012).
- [8] S.-M. Seo, K.-W. Kim, J. Ryu, H.-W. Lee, and K.-J. Lee, *Appl. Phys. Lett.* **101**, 022405 (2012).
- [9] S. Emori, U. Bauer, S.-M. Ahn, E. Martinez, and G. S. D. Beach, *Nat. Mater.* **12**, 611 (2013).
- [10] T. Koyama, H. Hata, K.-J. Kim, T. Moriyama, H. Tanigawa, T. Suzuki, Y. Nakatani, D. Chiba, and T. Ono, *Appl. Phys. Express* **6**, 033001 (2013).
- [11] X. Qiu, K. Narayanapillai, Y. Wu, P. Deorani, D.-H. Yang, W.-S. Noh, J.-H. Park, K.-J. Lee, H.-W. Lee, and H. Yang, *Nature Nanotechnol.* **10**, 333 (2015).
- [12] W. Legrand, R. Ramaswamy, R. Mishra, and H. Yang, *Phys. Rev. Appl.* **3**, 064012 (2015).
- [13] S. Zhang, *Phys. Rev. Lett.* **85**, 393 (2000).
- [14] L. Liu, C.-F. Pai, Y. Li, H. W. Tseng, D. C. Ralph, and R. A. Buhrman, *Science* **336**, 555 (2012).
- [15] D. Bang and H. Awano, *Jpn. J. Appl. Phys.* **52**, 123001 (2013).
- [16] P. M. Haney, H.-W. Lee, K.-J. Lee, A. Manchon, and M. D. Stiles, *Phys. Rev. B* **88**, 214417 (2013).
- [17] X. Qiu, P. Deorani, K. Narayanapillai, K.-S. Lee, K.-J. Lee, H.-W. Lee, and H. Yang, *Sci. Rep.* **4**, 4491 (2014).
- [18] X. Wang and A. Manchon, *Phys. Rev. Lett.* **108**, 117201 (2012).
- [19] P. M. Haney, H.-W. Lee, K.-J. Lee, A. Manchon, and M. D. Stiles, *Phys. Rev. B* **87**, 174411 (2013).
- [20] F. Freimuth, S. Blügel, and Y. Mokrousov, *Phys. Rev. B* **90**, 174423 (2014).
- [21] T. Moriya, *Phys. Rev.* **120**, 91 (1960).
- [22] I. E. Dzyaloshinskii, *Sov. Phys. JETP* **19**, 1163 (1964).

- [23] M. Heide, G. Bihlmayer, and S. Blügel, *Phys. Rev. B* **78**, 140403(R) (2008).
- [24] A. V. Khvalkovskiy, V. Cros, D. Apalkov, V. Nikitin, M. Krounbi, K. A. Zvezdin, A. Anane, J. Grollier, and A. Fert, *Phys. Rev. B* **87**, 020402(R) (2013).
- [25] K.-S. Ryu, L. Thomas, S.-H. Yang, and S. S. P. Parkin, *Nature Nanotechnol.* **8**, 527 (2013).
- [26] O. Boulle, S. Rohart, L. D. Buda-Prejbeanu, E. Jué, I. M. Miron, S. Pizzini, J. Vogel, G. Gaudin, and A. Thiaville, *Phys. Rev. Lett.* **111**, 217203 (2013).
- [27] K.-S. Ryu, S.-H. Yang, L. Thomas, and S. S. P. Parkin, *Nature Commun.* **5**, 3910 (2014).
- [28] K. Di, V. L. Zhang, H. S. Lim, S. Choon Ng, M. H. Kuok, J. Yu, J. Yoon, X. Qiu, and H. Yang, *Phys. Rev. Lett.* **114**, 047201 (2015).
- [29] K. Ueda, K.-J. Kim, Y. Yoshimura, R. Hiramatsu, T. Moriyama, D. Chiba, H. Tanigawa, T. Suzuki, E. Kariyada, and T. Ono, *Appl. Phys. Express* **7**, 053006 (2014).
- [30] D. Bang and H. Awano, *J. Appl. Phys.* **117**, 17D916 (2015).
- [31] A. Fert and A. Friederich, *Phys. Rev. B* **13**, 397 (1976).
- [32] T. Tanaka and H. Kontani, *New J. Phys.* **11**, 013023 (2009).
- [33] A. Moore, I. M. Miron, G. Gaudin, G. Serret, S. Auffret, B. Rodmacq, A. Schuhl, S. Pizzini, J. Vogel, and M. Bonfim, *Appl. Phys. Lett.* **93**, 262504 (2008).
- [34] M. Nawate, T. Morikawa, S. Tsunashima, and S. Uchiyama, *IEEE Trans. Magn.* **26**, 2739 (1990).
- [35] L. Ertl, G. Endl and H. Hoffmann, *J. Magn. Magn. Mater.* **113**, 227 (1992).
- [36] K.-J. Kim, R. Hiramatsu, T. Moriyama, H. Tanigawa, T. Suzuki, E. Kariyada, and T. Ono, *Appl. Phys. Express* **7**, 053003 (2014).
- [37] P. P. J. Haazen, E. Mure, J. H. Franken, R. Lavrijsen, H. J. M Swagten, and B. Koopsman, *Nature Mater.* **12**, 299 (2013).
- [38] A. Thiaville, S. Rohart, É. Jué, V. Cros, and A. Fert, *Europhys. Lett.* **100**, 57002 (2012).
- [39] E. Martinez, S. Emori, and G. S. D. Beach, *Appl. Phys. Lett.* **103**, 072406 (2013).
- [40] A. Hrabec, N. A. Porter, A. Wells, M. J. Benitez, G. Burnell, S. McVitie, D. McGrouther, T. A. Moore, and C. H. Marrows, *Phys. Rev. B* **90**, 020402(R) (2014).
- [41] J. Kim, J. Sinha, M. Hayashi, M. Yamanouchi, S. Fukami, T. Suzuki, S. Mitani, and Ohno, *Nature Mater.* **12**, 240 (2013).
- [42] K. Garello, I. M. Miron, C. O. Avci, F. Freimuth, Y. Mokrousov, S. Blügel, S. Auffret, O. Boulle, G. Gaudi, and P. Gambardella, *Nature Nanotechnol.* **8**, 587 (2013).
- [43] M. Jamali, K. Narayanapillai, X. Qiu, L. M. Loong, A. Manchon, and H. Yang, *Phys. Rev. Lett.* **111**, 246602 (2013).
- [44] H. R. Lee, K. Lee, J. Cho, Y. H. Choi, C. Y. You, M. H. Jung, F. Bonell, Y. Shiota, S. Miwa, and Y. Suzuki, *Sci. Rep.* **4**, 6548 (2014).
- [45] I. A. Campbell, *J. Phys. F: Metal Phys.* **2**, L47 (1972).
- [46] O. Krupin, G. Bihlmayer, K. M. Döbrich, J. E. Prieto, K. Starke, S. Gorovikov, S. Blügel, S. Kevan, and G. Kaindl, *New J. Phys.* **11**, 013035 (2009).

Novel magnetic wire fabrication process by way of nanoimprint lithography for current induced magnetization switching

Tsukasa Asari, Ryosuke Shibata, and Hiroyuki Awano

Citation: *AIP Advances* **7**, 055930 (2017); doi: 10.1063/1.4977769

View online: <http://dx.doi.org/10.1063/1.4977769>

View Table of Contents: <http://aip.scitation.org/toc/adv/7/5>

Published by the [American Institute of Physics](#)

HAVE YOU HEARD?

Employers hiring scientists and
engineers trust

PHYSICS TODAY | JOBS

www.physicstoday.org/jobs



Novel magnetic wire fabrication process by way of nanoimprint lithography for current induced magnetization switching

Tsukasa Asari, Ryosuke Shibata, and Hiroyuki Awano

Information Storage Materials Laboratory, Toyota Technological Institute, 2-12-1 Hisakata, Tenpaku-ku, Nagoya Aichi 468-8511, Japan

(Presented 3 November 2016; received 23 September 2016; accepted 25 November 2016; published online 28 February 2017)

Nanoimprint lithography (NIL) is an effective method to fabricate nanowire because it does not need expensive systems and this process is easier than conventional processes. In this letter, we report the Current Induced Magnetization Switching (CIMS) in perpendicularly magnetized Tb-Co alloy nanowire fabricated by NIL. The CIMS in Tb-Co alloy wire was observed by using current pulse under in-plane external magnetic field (H_L). We successfully observed the CIMS in Tb-Co wire fabricated by NIL. Additionally, we found that the critical current density (J_c) for the CIMS in the Tb-Co wire fabricated by NIL is 4 times smaller than that fabricated by conventional lift-off process under $H_L = 200\text{Oe}$. These results indicate that the NIL is effective method for the CIMS. © 2017 Author(s). All article content, except where otherwise noted, is licensed under a Creative Commons Attribution (CC BY) license (<http://creativecommons.org/licenses/by/4.0/>). [<http://dx.doi.org/10.1063/1.4977769>]

I. INTRODUCTION

Nanoimprint lithography (NIL) process is easy to make the magnetic nanowire comparison with Electron Beam (EB) lithography.¹⁻³ EB lithography process needs expensive lithography systems and complex process. On the other hand, NIL is new method which is required only few processes and cheap stamper. It is required to reduce the bit-cost for the Internet of Things (IoT) applications.

Recently, magnetic materials have been investigated as future logic devices and storage devices.³⁻⁵ Especially, the current induced-domain wall motion (CIDWM) and the current induced magnetization switching (CIMS) in magnetic nanowire have attracted studies as a low power consumption memory such as race track memory and Magnetic Random Access Memory (MRAM).⁶⁻¹¹ As a future MRAM, Spin Torque Transfer (STT)-MRAM is also investigated.

A continuous growing interest in SOTs driven magnetization dynamics with out-of-plane magnetized films.¹²⁻¹⁴ The origin of SOTs is based on heavy metal and inversion asymmetry structure.^{15,16} In addition to that the pulse current injection in this structure, spin current is generated into the nanowire from the heavy metal layer.^{15,16}

In this work, we demonstrate magnetization switching with new fabrication process of magnetic nanowire by way of NIL with the pulse injection along the wire with substrate(SiO₂ or Plastic)/Al₂O₃ (10 nm)/Co-Tb (6 nm)/Pt (2 nm) wire.

II. EXPERIMENTS

Figure 1(a) indicates the fabrication process of the conventional way to make the magnetic nanowire, for example, EB lithography and lift-off procedures. The fabrication process of NIL is shown in Figure 1(b). Figure 1(c) shows the schematic image of the sample B. In the samples A and B, wire widths are 2 μm , lengths are 20 μm and pitches are 1 μm . The sample B has 200nm depth shown in Fig. 1(c).



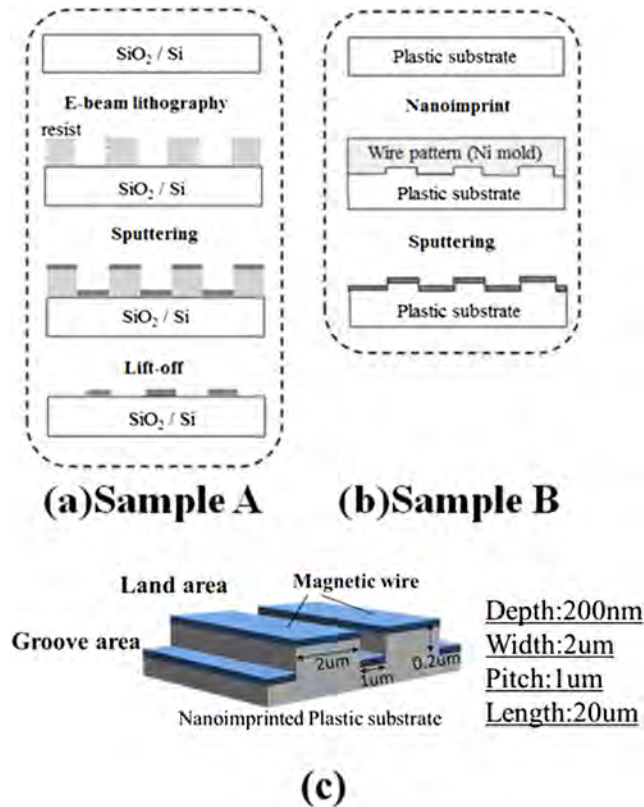


FIG. 1. (a) Schematic diagram of fabrication process by way of EB lithography. (b) Schematic diagram of the fabrication process by way of nanoimprint lithography and (c) the nanowires fabricated by the nanoimprint lithography.

The NIL was processed as follows. First, the mold was put on plastic substrate. Next, they were pressed at temperature $T = 453$ K. After that, we could obtain nanoimprinted plastic substrate after removing mold. Finally, Tb-Co alloy film was deposited on imprinted plastic substrate using sputtering. The wire could be obtained by only using sputtering because imprinted substrate already has wire pattern. On the other hand, we also fabricate wire on thermal oxide Si substrates using EB lithography and lift-off process. The Tb-Co alloy layer and Pt capping layer are deposited by DC magnetron sputtering. The buffer layer of Al₂O₃ was deposited by Atomic Layer Deposition (ALD). The CIMS in the Pt/Tb-Co wire is observed by the Magneto Optical Kerr Effect Microscope with the in-plane magnet (maximum field: ± 1 kOe). The composition of Tb-Co alloy wire was measured by Electron Probe Micro Analyzer (EPMA).

III. RESULTS AND DISCUSSION

Figure 2 shows magnetic field dependence on Polar Kerr rotation angle of the Tb₃₂Co₆₈ alloy films on Si and Plastic substrate as a function of perpendicular magnetic field. The sample structures are indicated in the figure. Both the coercive forces are almost 1.5 kOe. As shown in Fig. 2, both of loops are almost same. It indicates that magnetic properties of the wire on thermal oxide Si substrate and plastic substrate are almost same.

The CIMS was measured as follows. First, we applied an out-of-plane magnetic field to initialize the wire magnetization (-M). After that, the current pulses with 1μs duration were injected to wire under longitudinal magnetic field (H_L). Finally, we estimated switching probability by using switched area.

Figure 3(a) shows experimental set up. As shown in Fig. 3(a), the electrodes contact with the land areas and the current was applied to only these areas. Therefore, it is expected that there were no

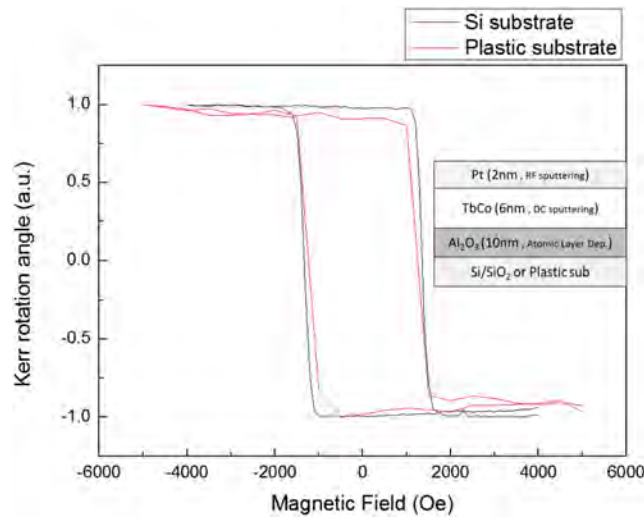


FIG. 2. Hysteresis loops of Tb-Co alloy films on Si and Plastic substrate measured by Magneto Optical Kerr Effect with Si and Plastic substrate.

coupling effects between groove and land areas. Figures 3(b) and 3(c) show Kerr images of Tb-Co alloy wire fabricated by NIL. The magnetization switching was induced by $1\mu\text{s}$ -wide current pulses under $H_L = 200$ Oe (X direction). According to Figs. 3(b) and 3(c), the almost all wire of magnetization is switched $-M$ (white) to $+M$ (black). The magnetization switching directions strongly depend on current and H_L direction. That phenomenon is the CIMS attributed to Spin Hall Effect.^{10,16} Therefore,

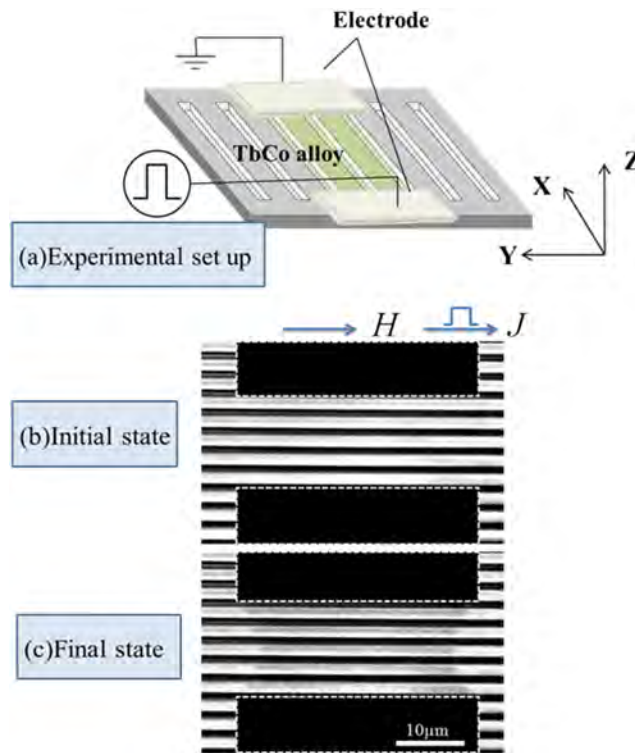


FIG. 3. (a) Schematic diagram of experimental set up. Kerr images of Tb-Co alloy wire on imprinted plastic substrate (b) before applying pulse current, and (c) after applying pulse current for $1\mu\text{s}$ pulse current of 7.1 MA/cm^2 under 200 Oe (X direction). Black area indicates the area which Tb-Co alloy film was not deposited.

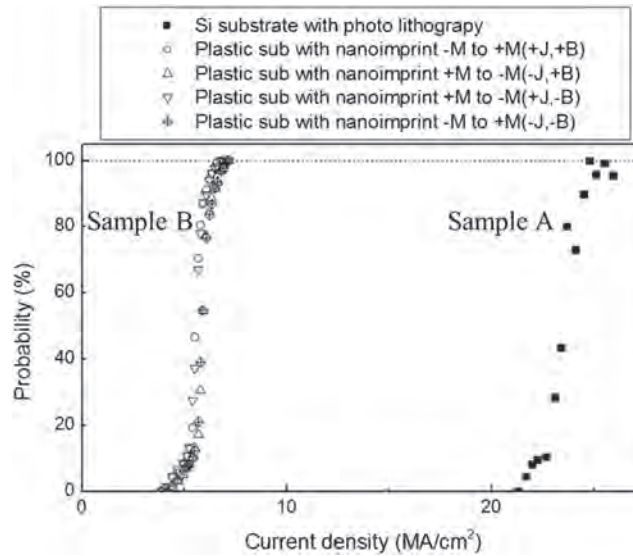


FIG. 4. Switching probabilities of the Tb-Co alloy wire on the Si substrate and imprinted plastic substrate as a function of current density.

we succeeded in observing the CIMS with wire fabricated by NIL. Figure 4 indicates switching probabilities as a function of current density. As shown in Fig. 4, the critical current density (J_c) for CIMS of Tb-Co wire on imprinted plastic and Si substrate are 24 MA/cm² and 5.5 MA/cm², respectively. The J_c of the Tb-Co wire on imprinted plastic substrate is 4 times smaller than that on Si substrate. That value of J_c is also smaller than another material, for example, MgO/FeCoB/Ta ($J_c = 20$ MA/cm²).¹⁰ Therefore, this result indicates that the imprinted plastic substrate is effectively induced CIMS.

One of the possibilities of reduction of the J_c for CIMS is thermal effect. The large current pulses usually generate Joule heating.¹⁷ The magnetic properties of rare-earth transition-metal magnetic material are greatly changed by changing temperature because its Curie temperature is near room temperature.^{18,19} Therefore, if the large current is applied to the wire the nucleation field (H_N) is decreased by the joule heating. Magnetization switching is occurred when values of effective magnetic field (H_{SHE}) generated by SHE is over the H_N . The thermal conductivity of plastic substrate is usually lower than Si substrate.^{20,21} It means the joule heating on the plastic substrate is more effective for heating up the wire than that on Si substrate.²² Therefore, since the reduction of H_N of Tb-Co wire on the plastic substrate is larger than that on Si substrate, the J_c for CIMS in Tb-Co wire on imprinted plastic substrate much lower than that on Si substrate.

IV. CONCLUSION

We investigated the current-induced magnetization switching with Tb-Co film. We succeeded in observing the CIMS with wire fabricated by nanoimprint lithography. The critical current density (J_c) for CIMS of Tb-Co wire on imprinted plastic and Si substrate are 24 MA/cm² and 5.5 MA/cm², respectively. The J_c of the Tb-Co wire on imprinted plastic substrate is 4 times smaller than that on Si substrate. Therefore, this result indicates that the imprinted plastic substrate is effectively induced CIMS.

ACKNOWLEDGMENTS

We thank Y. Kurokawa, D. Bang and S. Sumi for useful discussions and their technical help. This work was financially supported by the MEXT-Supported Program for Strategic Research Foundation at Private University (2014-2020).

- ¹ A. Bedoya-Pinto, M. Donolato, M. Gobbi, L. E. Hueso, and P. Vavassori, *Appl. Phys. Lett.* **104**, 062412 (2014).
- ² O. Lee, L. You, J. Jang, V. Subramanian, and S. Salahuddin, *Appl. Phys. Lett.* **107**, 252401 (2015).
- ³ H. Awano, *J. Magn. Magn.* **383**, 50–55 (2015).
- ⁴ A. Bedoya-Pinto, M. Donolato, M. Gobbi, L. E. Hueso, and P. Vavassori, *Appl. Phys. Lett.* **104**, 062412 (2014).
- ⁵ O. Lee, L. You, J. Jang, V. Subramanian, and S. Salahuddin, *Appl. Phys. Lett.* **107**, 252401 (2015).
- ⁶ S. S. P. Parkin, M. Hayashi, and L. Thomas, *Science* **320**, 190 (2008).
- ⁷ D. Bang and H. Awano, *J. Appl. Phys.* **117**, 17D916 (2015).
- ⁸ Y. Kurokawa, M. Kawamoto, and H. Awano, *Jpn. J. Appl.* **55**, 07MC02 (2016).
- ⁹ S. Ikeda, J. Hayakawa, Y. M. Lee, F. Matsukura, Y. Ohno, T. Hanyu, and H. Ohno, *IEEE Trans. Electron Devices* **54**(5), 991–1002 (2007).
- ¹⁰ R. Lo Conte, A. Hrabec, A. P. Mihai, T. Schulz, S.-J. Noh, C. H. Marrows, T. A. Moore, and M. Kläui, *Appl. Phys. Lett.* **105**, 122404 (2014).
- ¹¹ S. S. P. Parkin and S. H. Yang, *Nat. Nanotech* **10**, 195–198 (2015).
- ¹² R. Lo Conte, E. Martinez, A. Hrabec, A. Lamperti, T. Schulz, L. Nasi, L. Lazzarini, R. Mantovan, F. Maccherozzi, S. S. Dhesi, B. Ocker, C. H. Marrows, T. A. Moore, and M. Kläui, *Phys. Rev. B* **91**, 014433 (2015).
- ¹³ R. Lavrijsen, D. M. F. Hartmann, A. van den Brink, Y. Yin, B. Barcones, R. A. Duine, M. A. Verheijen, H. J. M. Swagten, and B. Koopmans, *Phys. Rev. B* **91**, 104414 (2015).
- ¹⁴ L. Liu, C.-F. Pai, Y. Li, H. W. Tseng, D. C. Ralph, and R. A. Buhrman, *Science* **336**, 555 (2012).
- ¹⁵ S. Emori, U. Bauer, S. M. Ahn, E. Martinez, and G. S. D. Beach, *Nat. Mater* **12**, 611 (2013).
- ¹⁶ I. Miron, G. Gaudin, S. Auffret, B. Rodmacq, A. Schuhl, S. Pizzini, J. Vogel, and P. Gambardella, *Nat. Mater* **9**, 230–234 (2010).
- ¹⁷ J. Torrejon, J. Kim, J. Sinha, S. Mitani, M. Hayashi, M. Yamanouchi, and H. Ohno, *Nat. Commun* **5**, 4655 (2012).
- ¹⁸ G. Garreau, E. Beaurepaire, K. Ounadjela, and M. Farle, *Phys. Rev. B* **53**, 1083 (1996).
- ¹⁹ W. C. Koehler, *J. Appl. Phys.* **36**, 1078 (1965).
- ²⁰ S. F. A. Taliba, W. H. Azmib, I. Zakariaa, W. Mohameda, A. M. I. Mamata, H. Ismaila, and W. R. W. Daud, *Energy Procedia* **79**, 366–371 (2015).
- ²¹ P. C. Chen, D. E. Nikitopoulos, S. A. Soper, and M. C. Murphy, *Biomedical Microdevices* **10**(2), 141–152 (2007).
- ²² C. Y. You, I. M. Sung, and B. K. Joe, *Appl. Phys. Lett.* **89**, 222513 (2006).

SCIENTIFIC REPORTS



OPEN

Interference induced enhancement of magneto-optical Kerr effect in ultrathin magnetic films

Satoshi Sumi¹, Hiroyuki Awano¹ & Masamitsu Hayashi^{2,3}

We have studied the magneto-optical spectra of ultrathin magnetic films deposited on Si substrates coated with an oxide layer (SiOx). We find that the Kerr rotation angle and the ellipticity of ~1 nm thick CoFeB thin films, almost transparent to visible light, show a strong dependence on the thickness of the SiOx layer. The Kerr signal from the 1 nm CoFeB thin film can be larger than that of ~100 nm thick CoFeB films for a given SiOx thickness and light wavelength. The enhancement of the Kerr signal occurs when optical interference takes place within the SiOx layer. Interestingly, under such resonance condition, the measured Kerr signal is in some cases larger than the estimation despite the good agreement of the measured and calculated reflection amplitude. We infer the discrepancy originates from interface states that are distinct from the bulk characteristics. These results show that optical interference effect can be utilized to study the magneto-optical properties of ultrathin films.

Thin film heterostructures with ultrathin magnetic layer(s) are attracting great interest owing to the strong interfacial effects found recently^{1,2}. The perpendicular magnetic anisotropy at the interface between a magnetic layer and an oxide layer has allowed development of magnetic storage elements for the spin transfer torque-magnetic random access memory (STT-MRAM) applications³⁻⁵. Layers with strong spin orbit interaction (e.g. 5d transition metals) can generate spin current and/or spin accumulation, which allows current controlled magnetization of the thin magnetic layer via spin orbit torques⁶⁻⁹. Chiral magnetic structure emerges in similar heterostructures due to the interface Dzyaloshinskii-Moriya interaction^{10,11}.

Magneto-optical Kerr effect provides a non-destructive approach to gaining information of the magnetization direction of magnetic materials¹²⁻¹⁵. It has been widely used recently to probe the magnetic state of thin film heterostructures to evaluate spin-orbit torques, chiral magnetism and related effects¹⁶⁻²⁵. More recently, the Kerr effect has also been used to reveal the magnetization of two-dimensional (2D) monoatomic van der Waals crystals^{26,27}. As the magnetic layer in many of the thin film heterostructures is only a few atomic layers thick and hardly reflects light, it is of interest to study how one can increase the Kerr signal from the heterostructures to allow evaluation of the magnetic states.

Optical interference effect has been commonly used to increase the Kerr signal from magnetic materials²⁸⁻³⁴. Dielectric materials with designed thickness (for a given wavelength) have been placed above or beneath the magnetic material so that multiple reflections occur at the top and bottom interfaces of the dielectric layer. If many reflections take place at the dielectric/magnetic layer interface, the effective Kerr rotation angle can be increased. Insertion of proper dielectric materials can boost the Kerr signal by more than a factor of ten^{29,33} and has been incorporated into magneto-optical storage technologies³⁵. However, this effect has not been confirmed for ultrathin magnetic layers which are almost transparent to visible light.

Here we study the magneto-optical Kerr spectrum of ultrathin magnetic films deposited on Si substrates coated with silicon oxide (SiOx) to identify the origin of the large Kerr signals found in such heterostructures. Even for films with magnetic layer of ~1 nm thickness, which is almost transparent to visible light, we find that the Kerr rotation angle and its ellipticity can be significantly enhanced by using optimal thickness of the SiOx for a given light wavelength. The Kerr signal of the ultrathin magnetic films is larger than that of the corresponding bulk value under certain conditions. The increase in the Kerr rotation angle and the ellipticity can be described with an analytical model that takes into account optical interference effect^{13,36-38} within the SiOx layer. These

¹Toyota Technological Institute, Nagoya, 468-8511, Japan. ²Department of Physics, The University of Tokyo, Bunkyo, Tokyo, 113-0033, Japan. ³National Institute for Materials Science, Tsukuba, 305-0047, Japan. Correspondence and requests for materials should be addressed to M.H. (email: hayashi@phys.s.u-tokyo.ac.jp)

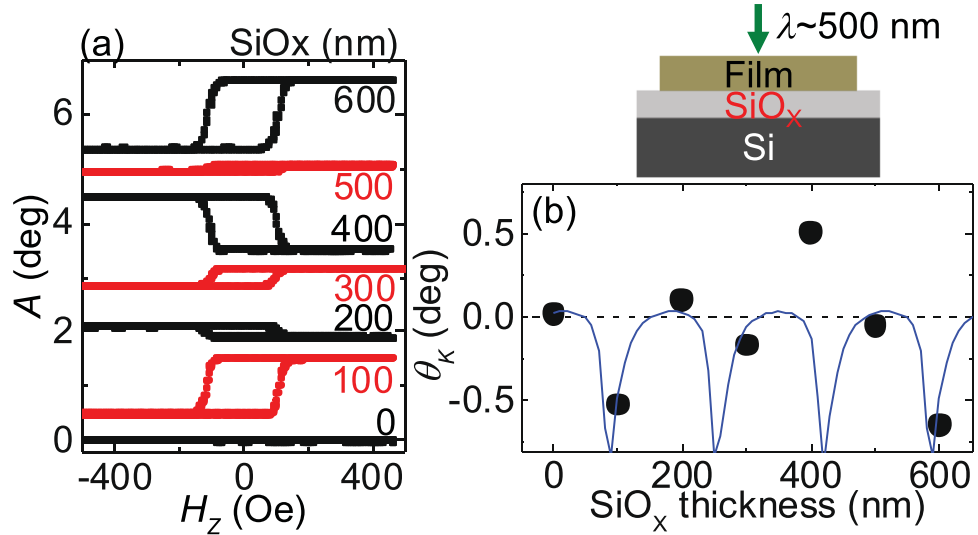


Figure 1. (a) Kerr signal (A) vs. out of plane magnetic field (H_z) for a film stack (Sub./0.5 Ta/1 CoFeB/2 MgO/1 Ta) deposited on Si substrates with different SiO_x thicknesses. The curves are shifted vertically by 1 deg for clarity. (b) The image shows a schematic illustration of the sample. The solid circles in the plot shows the Kerr rotation angle (θ_K) as a function of the SiO_x thickness. The laser wavelength (λ) is ~500 nm. The solid line represents calculation results using Eqs (5) and (6).

results show that the magnetic state of any ultrathin magnetic films, which hardly reflect light in the visible range, can be evaluated using the Kerr effect by properly choosing the substrate and the light wavelength.

Results

Films are deposited using RF magnetron sputtering. The heterostructure used here to study the magneto-optical Kerr effect is: Sub./0.5 Ta/1 CoFeB/2 MgO/1 Ta (thickness in nanometer). We use non-doped Si (100) substrates coated with SiO_x (thickness is t_{SiO_x}). The heterostructures are annealed at ~300 °C *ex-situ* in vacuum for 1 hour. The light wavelength dependence of the Kerr rotation angle and ellipticity are measured using a homemade Kerr spectroscopy. The refractive index of the substrate and the layers constituting the heterostructure are studied using an ellipsometry. We measure the refractive index of ~100 nm thick single layer films which we assume represent the dielectric properties of the corresponding layer in the heterostructure. See the Methods section for the details of the sample preparation and experimental setup.

Figure 1(a) shows the magnetization hysteresis loops obtained by sweeping the magnetic field directed along the film normal while the polar Kerr signal (A) is measured. As schematically shown to the right of Fig. 1(a), the light is incident from near film normal. The wavelength of the light is fixed to ~500 nm here. Clear Kerr signal from the magnetization of the CoFeB layer is found except for the film without the SiO_x layer ($t_{\text{SiO}_x} = 0$ nm). The amplitude of the Kerr rotation (θ_K) is defined as the difference in the signal when the magnetization (m_z) is reversed along its easy axis, i.e. $\theta_K \equiv A(m_z = -1) - A(m_z = 1)$. θ_K is plotted as a function of t_{SiO_x} in Fig. 1(b): the amplitude varies with the thicknesses of the SiO_x layer.

The wavelength dependence of the reflection amplitude is shown in Fig. 2(a–g) for the films with different t_{SiO_x} . The reflection amplitude shows an oscillatory dependence on the wavelength when t_{SiO_x} is non-zero. The corresponding Kerr rotation angle (θ_K) and the ellipticity (η_K) are plotted in Fig. 3(a–g) with black squares and red circles, respectively. The ellipticity is defined in units of angle. θ_K and η_K exhibit symmetric and/or asymmetric peak-like structures when the reflection amplitude takes a minimum. In order to account for the origin of the Kerr spectra's peaks, we calculate θ_K and η_K using the effective refractive index approach³⁶. Note that the matrix approach¹³ returns the same results.

The refractive index of a double layer system β/α (α is sitting on top of β) can be modeled as a single layer medium with an effective refractive index ($\tilde{n}_{\beta/\alpha}, \tilde{k}_{\beta/\alpha}$), which is defined as³⁶:

$$\tilde{n}_{\beta/\alpha} - i\tilde{k}_{\beta/\alpha} = (n_\alpha - ik_\alpha) \frac{1 - r_{\beta\alpha} \exp\left[2i(n_\alpha - ik_\alpha) \frac{2\pi t_\alpha}{\lambda}\right]}{1 + r_{\beta\alpha} \exp\left[2i(n_\alpha - ik_\alpha) \frac{2\pi t_\alpha}{\lambda}\right]} \quad (1)$$

Here λ is the wavelength of the light incident from medium α . t_α is the thickness of medium α . n_l and k_l ($l = \alpha, \beta$) are, respectively, the real and imaginary components of the refractive index of medium l . $r_{\beta\alpha}$ is the reflection amplitude of the light at the β/α interface and is defined as:

$$r_{\beta\alpha} = \frac{(n_\alpha - ik_\alpha) - (n_\beta - ik_\beta)}{(n_\alpha - ik_\alpha) + (n_\beta - ik_\beta)} \quad (2)$$

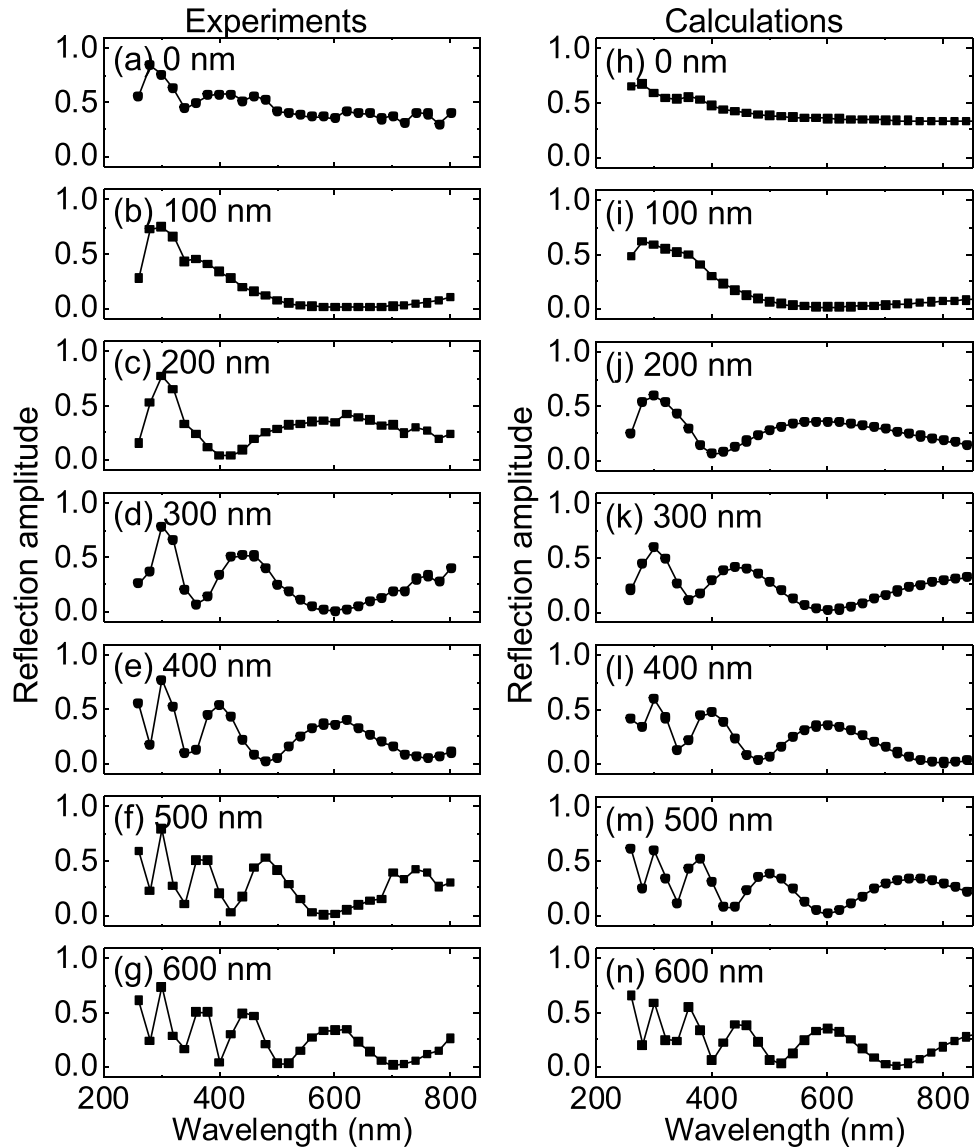


Figure 2. (a–n) Experimentally measured (a–g) and analytically calculated (h–n) reflection amplitude vs. laser wavelength for a film stack (Sub./0.5 Ta/1 CoFeB/2 MgO/1 Ta) deposited on Si substrates with different SiOx thicknesses.

To calculate the Kerr spectrum, we need values of the refractive index for the relevant layers. Here we assume that our system constitutes from three media, i.e., the Si substrate, the SiOx layer, and the thin film heterostructure. Although the thin film heterostructure includes four different layers, the dominant contribution to the magneto-optical properties arises from the magnetic (CoFeB) layer. The other layers are thin enough, compared to the light wavelength, such that interference effects within each layer can be neglected. In using Eqs (1) and (2) one must know the refractive index of three media.

The real (n_{Si}) and imaginary (k_{Si}) parts of the refractive index of the Si substrate without any SiOx layer ($t_{SiOx} \sim 0$ nm) is plotted in Fig. 4(a). A peak is found at low wavelength, a characteristic well known for Si (ref.³⁹). For the SiOx layer, we take a value ($n_{SiOx} = 1.5$, $k_{SiOx} = 0$) widely used in the literature and assume it is independent of the wavelength within the range studied. Figure 4(b) shows the refractive index (n_b , k_b) of a ~ 100 nm thick CoFeB film (Si/SiOx/0.5 Ta/100 CoFeB). Here the subscript “b” stands for *bulk* like CoFeB. The refractive index increases with increasing wavelength, typical of metallic films⁴⁰. As the refractive index of a magnetic material typically depends on the polarization of light we compute the refractive index (n_{CoFeB}^{\pm} , k_{CoFeB}^{\pm}) for both polarities (σ^{\pm}) using the refractive index (n_b , k_b) and the Kerr rotation angle (θ_b) and ellipticity (η_b) of the thick CoFeB film. σ^+ and σ^- correspond to right and left circularly polarized lights, respectively. θ_b and η_b are plotted in Fig. 4(c). It is interesting to note that some of the peak values of θ_K and η_K obtained from ~ 1 nm thick CoFeB layer shown in Fig. 3(a–g) are larger than the corresponding bulk limit shown in Fig. 4(c). n_{CoFeB}^{\pm} and k_{CoFeB}^{\pm} are expressed as:

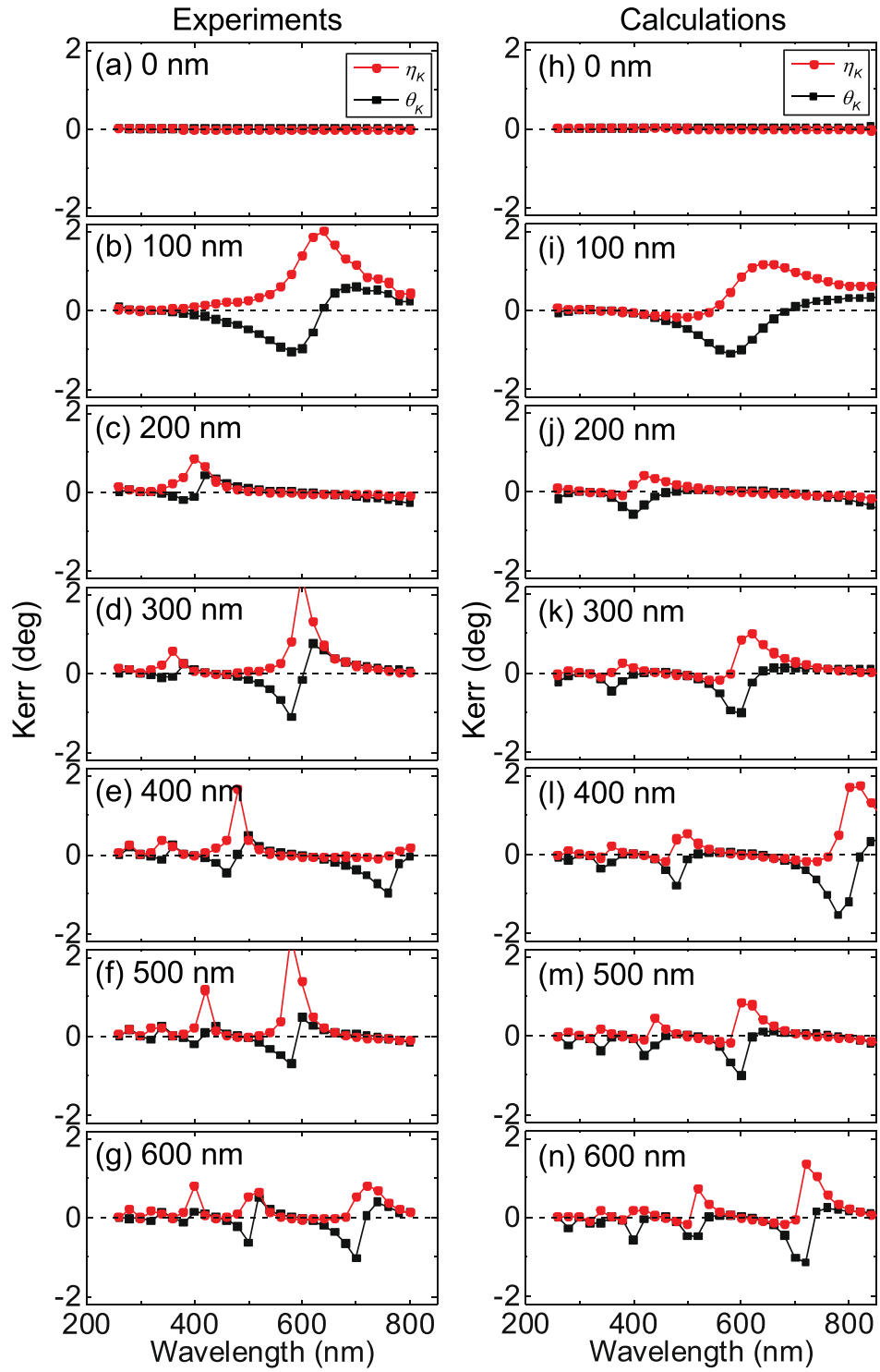


Figure 3. (a–n) Experimentally measured (a–g) and analytically calculated (h–n) Kerr rotation angle θ_K (black squares) and Kerr ellipticity η_K (red circles) vs. laser wavelength for a film stack (Sub./0.5 Ta/1 CoFeB/2 MgO/1 Ta) deposited on Si substrates with different SiOx thicknesses.

$$\begin{aligned}
 n_{\text{CoFeB}}^{\pm} &= n_b \pm \Delta n, \quad k_{\text{CoFeB}}^{\pm} = k_b \pm \Delta k \\
 \Delta n &= (k_b \text{Re}[\varepsilon_{XY}] - n_b \text{Im}[\varepsilon_{XY}]) / (n_b^2 + k_b^2) \\
 \Delta k &= (n_b \text{Re}[\varepsilon_{XY}] + k_b \text{Im}[\varepsilon_{XY}]) / (n_b^2 + k_b^2) \\
 \varepsilon_{XY} &= [n_b(1 - n_b^2 + 3k_b^2)\theta_b - k_b(1 - 3n_b^2 + k_b^2)\eta_b] \\
 &\quad + i[k_b(1 - 3n_b^2 + k_b^2)\theta_b + n_b(1 - n_b^2 + 3k_b^2)\eta_b]
 \end{aligned}
 \tag{3}$$

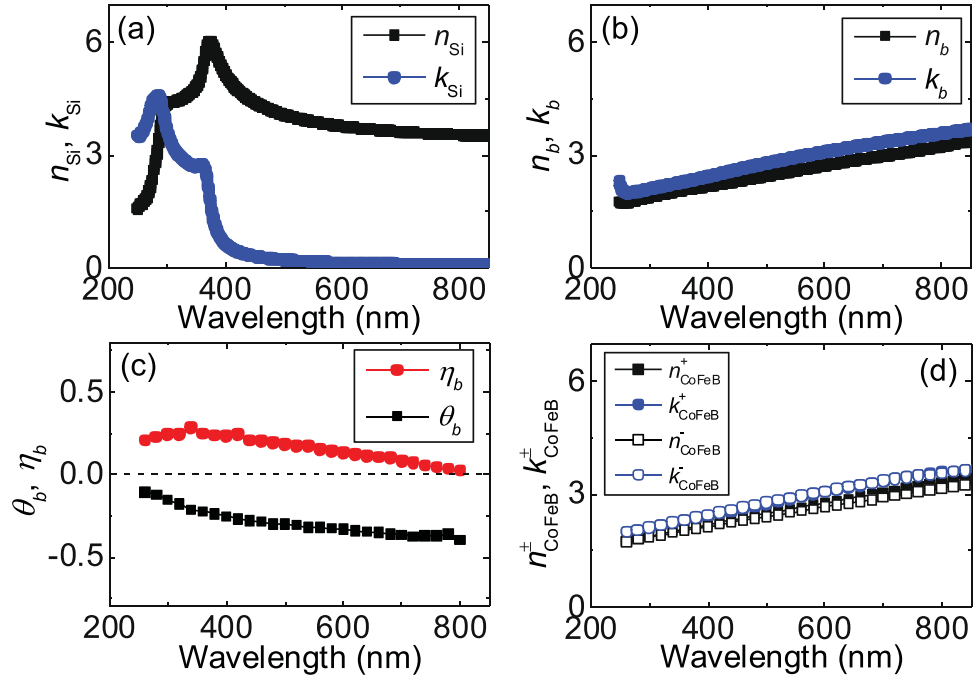


Figure 4. (a) Light wavelength dependence of the real (n_{Si}) and imaginary (k_{Si}) parts of the refractive index for Si substrate without SiOx. (b,c) Real (n_b) and imaginary (k_b) parts of the refractive index (b), Kerr rotation angle θ_b and ellipticity η_b (c) of a ~ 100 nm thick CoFeB film (Sub./0.5 Ta/100 CoFeB) deposited on a Si substrate with no SiOx. (d) Calculated real (n_{CoFeB}^{\pm}) and imaginary (k_{CoFeB}^{\pm}) parts of the refractive index of the thick CoFeB film for different light polarization. Equation (3) is used to obtain these results.

The calculated refractive index ($n_{CoFeB}^{\pm}, k_{CoFeB}^{\pm}$) is shown in Fig. 4(d). Although the difference of the refractive index for both polarities is small, such small difference causes the magneto-optical Kerr effect.

We first compute the effective refractive index of the Si substrate and SiOx layer, i.e. ($\tilde{n}_{Si/SiOx}, \tilde{k}_{Si/SiOx}$). Substituting $n_{SiOx}, k_{SiOx}, n_{Si}, k_{Si}$ into $n_{\alpha}, k_{\alpha}, n_{\beta}, k_{\beta}$ of Eq. (1), respectively, the effective refractive index of Si/SiOx ($\tilde{n}_{Si/SiOx}, \tilde{k}_{Si/SiOx}$) is obtained. Next we compute the effective refractive index of Si/SiOx and the thin film heterostructure (i.e. CoFeB layer). We substitute $n_{CoFeB}^{\pm}, k_{CoFeB}^{\pm}, \tilde{n}_{Si/SiOx}, \tilde{k}_{Si/SiOx}$ into $n_{\alpha}, k_{\alpha}, n_{\beta}, k_{\beta}$ of Eq. (1) to obtain the effective refractive index ($\tilde{n}_{Si/SiOx/CoFeB}^{\pm}, \tilde{k}_{Si/SiOx/CoFeB}^{\pm}$) of the entire structure. The polarization dependent reflection amplitude of the sample is defined as:

$$r^{\pm} = \frac{(n_0 - ik_0) - (\tilde{n}_{Si/SiOx/CoFeB}^{\pm} - i\tilde{k}_{Si/SiOx/CoFeB}^{\pm})}{(n_0 - ik_0) + (\tilde{n}_{Si/SiOx/CoFeB}^{\pm} - i\tilde{k}_{Si/SiOx/CoFeB}^{\pm})} \quad (4)$$

where n_0 and k_0 are the real and imaginary parts of the refractive index of air. Here we assume $n_0 \sim 1$ and $k_0 \sim 0$. The calculated average reflection amplitude ($\frac{r^+ + r^-}{2}$) is plotted as a function of light wavelength for different SiOx layer thicknesses in Fig. 2(h–n). The calculated curves resemble those of the corresponding experimental results. To gain insight into the underlying physics of the model calculations, Eq. (4) is rewritten more explicitly as the following:

$$r^{\pm} = \frac{r_{SiOx/CoFeB}^{\pm} + r_{CoFeB/Air}^{\pm} + r_{Si/SiOx}(1 + r_{SiOx/CoFeB}^{\pm} r_{CoFeB/Air}^{\pm}) \exp\left[4\pi i(n_{SiOx} + ik_{SiOx}) \frac{t_{SiOx}}{\lambda}\right]}{1 + r_{SiOx/CoFeB}^{\pm} r_{CoFeB/Air}^{\pm} + r_{Si/SiOx}(r_{SiOx/CoFeB}^{\pm} + r_{CoFeB/Air}^{\pm}) \exp\left[4\pi i(n_{SiOx} + ik_{SiOx}) \frac{t_{SiOx}}{\lambda}\right]} \quad (5)$$

We made the following assumption to derive Eq. (5) from Eq. (4), i.e. $\frac{t_{CoFeB}}{\lambda} \ll 1$: this is valid since the thickness of the heterostructure is much smaller than the wavelength. Equation (5) indicates that the reflection amplitude, and consequently the Kerr rotation angle and the ellipticity, will oscillate with the inverse of the light wavelength with a periodicity defined by $\frac{1}{2n_{SiOx}t_{SiOx}} \sim \frac{1}{3t_{SiOx}}$. In Fig. 5(a), we replot the calculated reflection amplitude (Fig. 2(m)) as a function of the inverse of the light wavelength (λ) for $t_{SiOx} = 500$ nm. The blue solid line is a fit to the results using a sinusoidal function with a linear background. The oscillation period of the reflection amplitude agrees with $\sim 1/3t_{SiOx}$.

The Kerr rotation angle and the ellipticity are defined using the reflection amplitude as the following:

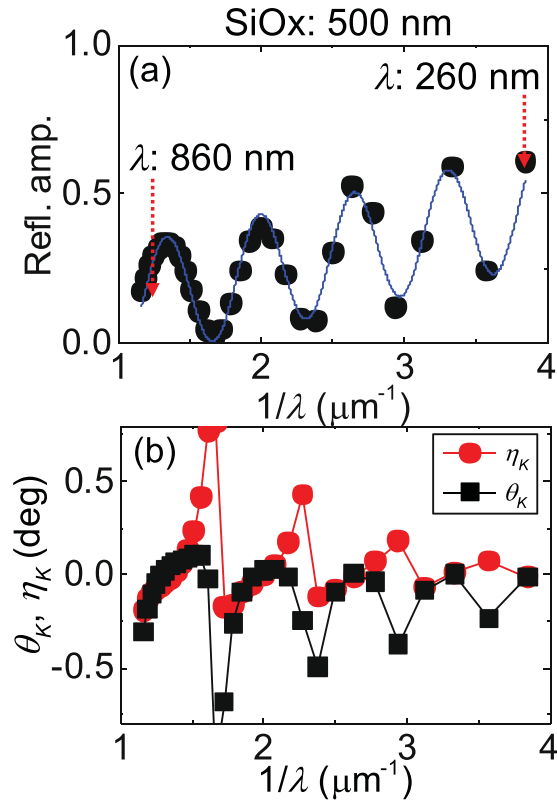


Figure 5. (a,b) Calculated reflection amplitude (a), Kerr rotation angle and ellipticity (b) plotted against the inverse of the light wavelength (λ). The blue line in (a) shows fit to the data using a sinusoidal function. The thickness of the SiOx layer is 500 nm.

$$\theta_K = \frac{1}{2} [\arg(r^+) - \arg(r^-)]$$

$$\eta_K = \arctan \left[\frac{|r^+| - |r^-|}{|r^+| + |r^-|} \right] \quad (6)$$

The calculated θ_K and η_K spectra for samples with various SiOx layer thicknesses are plotted in Fig. 3(h–n). We find good agreement between the calculation and the experimental results. The wavelength at which peaks in the θ_K and η_K occur coincides with that when the reflection amplitude takes a minimum. To show this more explicitly, we replot the results of Fig. 3(m) as a function of $1/\lambda$ in Fig. 5(b). The correspondence between the reflection amplitude and the Kerr signals are clear. These results suggest that when the light is confined within the SiOx layer and undergoes multiple reflection, the Kerr signal increases, however, with a reduction in the reflection amplitude.

Discussion

Finally we discuss the appropriate SiOx layer thickness for a given light wavelength to obtain the maximum Kerr signal output. We calculate θ_K as a function of t_{SiOx} to compare with the experimental results. The blue solid line in Fig. 1(b) shows the calculated results. Good agreement between the calculations and experiments are obtained except for $t_{\text{SiOx}} \sim 400$ nm (the deviation is also evident in Fig. 3(e) and (l) around $\lambda \sim 500$ nm). From the calculations shown in Fig. 1(b), one finds that there are optimum thicknesses for the SiOx layer under a given light wavelength. As the maximum Kerr signal occurs when the reflection amplitude takes a minimum, Eq. (5) indicates that the optimum condition to observe large Kerr signals is $4\pi n_{\text{SiOx}} \frac{t_{\text{SiOx}}}{\lambda} \sim \pi(2m - 1)$, where m is an integer. This in turn gives the optimum SiOx thickness $t_{\text{SiOx}}^* \sim \frac{\lambda}{4} \frac{2m-1}{n_{\text{SiOx}}}$ for a given wavelength. For a green light ($\lambda \sim 500$ nm), t_{SiOx}^* is ~ 80 nm, 250 nm, 420 nm, 580 nm, which are in good agreement with the SiOx thicknesses at which $|\theta_K|$ takes a maximum in the calculations (see Fig. 1(b)). Such interference condition is also required to visualize graphene sheets placed on Si/SiOx substrates using optical microscopes⁴¹.

It should be noted that the enhancement of θ_K is associated with a reduction in the reflected light amplitude. This is because multiple reflections occur at the Si/SiOx and SiOx/heterostructure interfaces under the interference condition, and as a result, there is a larger probability of the light being absorbed into the Si substrate and/or the heterostructure, resulting in a reduction of the light amplitude that reflects off the sample. The correspondence can be seen both in the experimental results and the simulated curves (see Figs 2 and 3). Significant effort

was placed in the past to maximize the Kerr rotation angle while maintaining a reasonable amount of reflected light amplitude to detect the magnetic state of the magneto-optic media³⁵.

We note that the optical interference effect may provide a useful means to study the interface states with magneto-optics. A common approach taken thus far is to use magnetic multilayers^{42–44} in which a large number of interfaces contribute to the overall signal and thereby increase the signal to noise ratio. Instead, one may use the optical interference within the oxide layer of the substrate and probe, for example, a single interface within the film many times via the multiple reflections associated with the interference. As we have shown here, even for an ultrathin film almost transparent to visible light (~1.5 nm thick metallic film), one can use conventional models^{13,36} to calculate the expected magneto-optical signal. Thus, this will allow a straightforward way to evaluate other contributions, if any, to the signal that may result from e.g. interface spin orbit coupling.

Experimentally, we find that the measured Kerr signals (rotation angle and ellipticity) at the resonance condition (when $t_{\text{SiOx}} \sim t_{\text{SiOx}}^*$) are in some cases larger in magnitude than those from the calculations. For example, the measured Kerr ellipticity at $t_{\text{SiOx}} \sim 100$ nm and $\lambda \sim 630$ nm (Fig. 3(b)) is nearly twice as large as that of the calculations (Fig. 3(i)). The reflection amplitude, in contrast, is better reproduced by the calculations. These results suggest that the Kerr signal of the heterostructure with the ultrathin magnetic film is enhanced compared to what is expected from the corresponding bulk properties. We infer that spin orbit coupling, magnetic moment, and/or magneto-optical coupling at the interface(s)⁴⁴ may be enhanced in the heterostructure, leading to larger Kerr signals.

In summary, we have studied conditions at which one can maximize the magneto-optical Kerr effect from an ultrathin magnetic layer, almost transparent to visible light, deposited on Si substrate coated with a SiOx layer. For a given light wavelength (λ), the thickness of the SiOx layer has to be set to one quarter of the effective wavelength (λ/n_{SiOx}) times an odd integer to observe the maximum Kerr signal (n_{SiOx} is the real part of the SiOx refractive index). Such condition fulfills the requirement to cause optical interference within the SiOx layer. Interestingly, we find that the Kerr signals are, for certain resonance conditions, larger than the estimation despite the good agreement of the measured and calculated reflection amplitude. The discrepancy may originate from interface states that are distinct from the bulk characteristics. These results show that optical interference effect can be utilized to study the magneto-optical properties of ultrathin films, including those of the interface states.

Methods

Sample preparation. RF magnetron sputtering is used for the film deposition. The substrate is non-doped Si(001) substrates coated with SiOx. Wet oxidation is used for the formation of SiOx. The SiOx thickness is determined by ellipsometry and its accuracy is $\sim \pm 10\%$. For the growth of heterostructures, relatively thick (~ 20 nm) calibration films are made to estimate the film deposition rate. Line profiling and x-ray resonant reflection are used to measure the thickness of the calibration films. The variation of the measured deposition rate is typically less than $\sim 10\%$.

Ellipsometry. Ellipsometry from JASCO (model M-150) is used. The angle of incidence is ~ 45 degree. A linearly polarized light is fed into a photo-elastic modulator (PEM) and the output from the PEM is irradiated on the sample. No magnetic field is applied during the ellipsometry measurements. The magnetization direction of the ~ 100 nm thick CoFeB film points along the film plane.

Kerr spectra. Magneto-optical Kerr spectrum is measured using a Xenon light source, a PEM and a photomultiplier detector. The angle of incidence is ~ 4 deg. Details of the setup are described in ref.⁴⁵.

References

- Brataas, A., Kent, A. D. & Ohno, H. Current-induced torques in magnetic materials. *Nat. Mater.* **11**, 372 (2012).
- Manchon, A., Koo, H. C., Nitta, J., Frolov, S. M. & Duine, R. A. New perspectives for rashba spin-orbit coupling. *Nat. Mater.* **14**, 871 (2015).
- Ikeda, S. *et al.* A perpendicular-anisotropy cofeb-mgo magnetic tunnel junction. *Nat. Mater.* **9**, 721 (2010).
- Worledge, D. C. *et al.* Spin torque switching of perpendicular ta[cofeb]mgo-based magnetic tunnel junctions. *Appl. Phys. Lett.* **98**, 022501 (2011).
- Thomas, L. *et al.* Perpendicular spin transfer torque magnetic random access memories with high spin torque efficiency and thermal stability for embedded applications (invited). *J. Appl. Phys.* **115**, 172615 (2014).
- Miron, I. M. *et al.* Perpendicular switching of a single ferromagnetic layer induced by in-plane current injection. *Nature* **476**, 189 (2011).
- Liu, L. *et al.* Spin-torque switching with the giant spin hall effect of tantalum. *Science* **336**, 555 (2012).
- Kim, J. *et al.* Layer thickness dependence of the current induced effective field vector in ta[cofeb]mgo. *Nat. Mater.* **12**, 240 (2013).
- Garello, K. *et al.* Symmetry and magnitude of spin-orbit torques in ferromagnetic heterostructures. *Nat. Nanotechnol.* **8**, 587 (2013).
- Heide, M., Bihlmayer, G. & Blugel, S. Dzyaloshinskii-moriya interaction accounting for the orientation of magnetic domains in ultrathin films: Fe/w(110). *Phys. Rev. B* **78**, 140403 (2008).
- Fert, A., Cros, V. & Sampaio, J. Skyrmions on the track. *Nat. Nanotechnol.* **8**, 152 (2013).
- Bader, S. D. & Erskine, J. L. In *Ultrathin magnetic structures ii: Measurement techniques and novel magnetic properties* (eds Bretislav Heinrich & J. Anthony C. Bland) 297 (Springer, Berlin Heidelberg, 1994).
- Qiu, Z. Q. & Bader, S. D. Surface magneto-optic kerr effect. *Rev. Sci. Instrum.* **71**, 1243 (2000).
- Hubert, A. & Schafer, R. *Magnetic domains: The analysis of magnetic microstructures*. (Springer-Verlag, 2001).
- Allwood, D. A. *et al.* Over 40% transverse kerr effect from ni(80)fe(20). *Appl. Phys. Lett.* **92**, 072503 (2008).
- Miron, I. M. *et al.* Current-driven spin torque induced by the rashba effect in a ferromagnetic metal layer. *Nat. Mater.* **9**, 230 (2010).
- Haazen, P. P. J. *et al.* Domain wall depinning governed by the spin hall effect. *Nat. Mater.* **12**, 299 (2013).
- Ryu, K.-S., Thomas, L., Yang, S.-H. & Parkin, S. Chiral spin torque at magnetic domain walls. *Nat. Nanotechnol.* **8**, 527 (2013).
- Emori, S., Bauer, U., Ahn, S.-M., Martinez, E. & Beach, G. S. D. Current-driven dynamics of chiral ferromagnetic domain walls. *Nat. Mater.* **12**, 611 (2013).
- Je, S.-G. *et al.* Asymmetric magnetic domain-wall motion by the dzyaloshinskii-moriya interaction. *Phys. Rev. B* **88**, 214401 (2013).

21. Torrejon, J. *et al.* Interface control of the magnetic chirality in cofeb/mgo heterostructures with heavy-metal underlayers. *Nat. Commun.* **5**, 4655 (2014).
22. Fan, X. *et al.* Quantifying interface and bulk contributions to spin-orbit torque in magnetic bilayers. *Nat. Commun.* **5**, 3042 (2014).
23. van't Erve, O. M. J., Hanbicki, A. T., McCreary, K. M., Li, C. H. & Jonker, B. T. Optical detection of spin hall effect in metals. *Appl. Phys. Lett.* **104**, 172402 (2014).
24. DuttaGupta, S. *et al.* Adiabatic spin-transfer-torque-induced domain wall creep in a magnetic metal. *Nat Phys* **12**, 333 (2016).
25. Safer, C. K. *et al.* Spin-orbit torque magnetization switching controlled by geometry. *Nat. Nanotechnol.* **11**, 143 (2016).
26. Gong, C. *et al.* Discovery of intrinsic ferromagnetism in two-dimensional van der waals crystals. *Nature* **546**, 265 (2017).
27. Huang, B. *et al.* Layer-dependent ferromagnetism in a van der waals crystal down to the monolayer limit. *Nature* **546**, 270 (2017).
28. Ahn, K. Y. & Fan, G. J. Kerr effect enhancement in ferromagnetic films. *IEEE Trans. Magn.* **2**, 678 (1966).
29. Qureshi, N., Schmidt, H. & Hawkins, A. R. Cavity enhancement of the magneto-optic kerr effect for optical studies of magnetic nanostructures. *Applied Physics Letters* **85**, 431 (2004).
30. Cantwell, P. R., Gibson, U. J., Allwood, D. A. & Macleod, H. A. M. Optical coatings for improved contrast in longitudinal magneto-optic kerr effect measurements. *J. Appl. Phys.* **100**, 093910 (2006).
31. Franken, J. H. *et al.* Effects of combined current injection and laser irradiation on permalloy microwire switching. *Appl. Phys. Lett.* **95**, 212502 (2009).
32. Moradi, M. & Ghanaatshoar, M. Cavity enhancement of the magneto-optic kerr effect in glass/al/sno2/ptmnsb/sno2 structure. *Opt. Commun.* **283**, 5053 (2010).
33. Zhang, S. Y. *et al.* Giant magneto-optical kerr effect in hfo2/co/hfo2/al/silicon structure. *J. Appl. Phys.* **114**, 064308 (2013).
34. Jaris, M. *et al.* Intrinsic spin dynamics in optically excited nanoscale magnetic tunnel junction arrays restored by dielectric coating. *Applied Physics Letters* **109**(5), 202403 (2016).
35. Ohta, K. *et al.* Magneto-optical disk with reflecting layers. *Proc. Soc. Photo-Opt. Instrum. Eng.* **382**, 252 (1983).
36. Egashira, K. & Yamada, T. Kerr-effect enhancement and improvement of readout characteristics in mnbi film memory. *J. Appl. Phys.* **45**, 3643 (1974).
37. Hubert, A. & Traeger, G. Magneto-optical sensitivity functions of thin-film systems. *Journal of Magnetism and Magnetic Materials* **124**, 185 (1993).
38. Kambersky, V., Wenzel, L. & Hubert, A. Magneto-optical interference and diffraction in isotropic and uniaxial multilayers. *Journal of Magnetism and Magnetic Materials* **189**, 149 (1998).
39. Palik, E. D. *Handbook of optical constants of solids.* (Academic Press, 1998).
40. Lange, R. J. *et al.* Ellipsometric and kerr-effect studies of pt-3-x (x = mn,co). *Phys. Rev. B* **58**, 351 (1998).
41. Blake, P. *et al.* Making graphene visible. *Appl. Phys. Lett.* **91**, 063124 (2007).
42. Weller, D., Reim, W., Spörl, K. & Brändle, H. Spectroscopy of multilayers for magneto-optic storage. *Journal of Magnetism and Magnetic Materials* **93**, 183 (1991).
43. Uba, S. *et al.* Optical and magneto-optical properties of co/pt multilayers. *Physical Review B* **53**, 6526 (1996).
44. Guo, G. Y. & Ebert, H. Band-theoretical investigation of the magneto-optical kerr effect in fe and co multilayers. *Physical Review B* **51**, 12633 (1995).
45. VanDrent, W. P. & Suzuki, T. Ultra-violet range magneto-optic study of fcc-co and co/pt multilayers. *J. Magn. Magn. Mater.* **175**, 53 (1997).

Acknowledgements

This work was partly supported by JSPS Grant-in-Aids for Scientific Research (16H03853), Specially Promoted Research (15H05702), MEXT Nanofab platform, the MEXT-Supported Program Research Foundation at Private University (2014-2020), and the Spintronics Research Network of Japan.

Author Contributions

M.H. and H.A. planned the study. M.H. prepared the films, S.S. measured the Kerr spectra and analyzed the results with inputs from H.A. and M.H. All authors have discussed the results and commented on the manuscript.

Additional Information

Competing Interests: The authors declare that they have no competing interests.

Publisher's note: Springer Nature remains neutral with regard to jurisdictional claims in published maps and institutional affiliations.



Open Access This article is licensed under a Creative Commons Attribution 4.0 International License, which permits use, sharing, adaptation, distribution and reproduction in any medium or format, as long as you give appropriate credit to the original author(s) and the source, provide a link to the Creative Commons license, and indicate if changes were made. The images or other third party material in this article are included in the article's Creative Commons license, unless indicated otherwise in a credit line to the material. If material is not included in the article's Creative Commons license and your intended use is not permitted by statutory regulation or exceeds the permitted use, you will need to obtain permission directly from the copyright holder. To view a copy of this license, visit <http://creativecommons.org/licenses/by/4.0/>.

© The Author(s) 2018

Long spin coherence length and bulk-like spin-orbit torque in ferrimagnetic multilayers

Jiawei Yu¹, Do Bang^{2,3,8}, Rahul Mishra^{1,8}, Rajagopalan Ramaswamy¹, Jung Hyun Oh⁴, Hyeon-Jong Park⁵, Yunboo Jeong⁶, Pham Van Thach^{2,3}, Dong-Kyu Lee⁴, Gyungchoon Go⁴, Seo-Won Lee⁴, Yi Wang⁶, Shuyuan Shi¹, Xuepeng Qiu⁷, Hiroyuki Awano², Kyung-Jin Lee^{4,5,6*} and Hyunsoo Yang^{1*}

Spintronics relies on magnetization switching through current-induced spin torques. However, because spin transfer torque for ferromagnets is a surface torque, a large switching current is required for a thick, thermally stable ferromagnetic cell, and this remains a fundamental obstacle for high-density non-volatile applications with ferromagnets. Here, we report a long spin coherence length and associated bulk-like torque characteristics in an antiferromagnetically coupled ferrimagnetic multilayer. We find that a transverse spin current can pass through >10-nm-thick ferrimagnetic Co/Tb multilayers, whereas it is entirely absorbed by a 1-nm-thick ferromagnetic Co/Ni multilayer. We also find that the switching efficiency of Co/Tb multilayers partially reflects a bulk-like torque characteristic, as it increases with ferrimagnet thickness up to 8 nm and then decreases, in clear contrast to the 1/thickness dependence of ferromagnetic Co/Ni multilayers. Our results on antiferromagnetically coupled systems will invigorate research towards the development of energy-efficient spintronics.

The spin-transfer torque (STT)^{1–4} acting on ferromagnets is a surface torque based on the averaging effect of STT^{5,6}. We note that the same averaging effect occurs regardless of the spin current source, and the spin-orbit torque (SOT)^{7,8}, which we use in our experiment, is also a surface torque for ferromagnets (Supplementary Note 1). When a transverse spin current with a spin orientation non-collinear with the magnetization is injected into a ferromagnet, the electron spin precesses rapidly in real space because the wavevectors of the majority (\uparrow) and minority (\downarrow) spins at the Fermi surface are different (that is, $k_F^\uparrow \neq k_F^\downarrow$). The precession wavelengths are different for different incident angles of electrons (that is, the direction of wavevector \mathbf{k}), leading to rapid spin dephasing when summing over all current-carrying \mathbf{k} states. As a result, the \mathbf{k} -integrated transverse spin current decays to zero within a distance from the ferromagnet surface called the ferromagnetic coherence length (spin coherence length, more generally), $\lambda_c = \pi/|k_F^\uparrow - k_F^\downarrow|$ (ref. ⁹). As $|k_F^\uparrow - k_F^\downarrow|$ becomes larger for larger exchange splitting, λ_c is only a few ångströms in strong ferromagnets (for example, cobalt or iron) for which the STT is almost a surface torque.

Theories have predicted that the spin coherence length is very long in antiferromagnets (AFMs) because of the staggered spin order on an atomic scale^{10–12}. We use the term ‘bulk-like torque’ to describe the characteristic of spin torque in AFMs (that is, spin-current absorption for a larger thickness), in contrast with the surface torque of ferromagnets. A semiclassical explanation of bulk-like torque is that conduction electron spins see the moments with alternating orientation on an atomic scale as exchange interactions with alternating signs. As a result, an ideal AFM has zero net effective exchange interaction when averaged over two sublattices and thus has an infinitely long λ_c , yielding the bulk-like torque characteristic.

Several experiments have investigated STT/SOT effects in systems including AFMs^{13–15} and more recently in ferrimagnetic alloys^{16–19}, but not on the long spin coherence length and associated bulk-like torque characteristic.

We qualitatively illustrate the spin coherence length in ferromagnets and antiferromagnetically coupled ferrimagnets (FIMs), based on the spin precession around the local exchange field. Neglecting the spin relaxation, the dynamics of non-equilibrium spin density \mathbf{s} is described by $\partial\mathbf{s}/\partial t = -\gamma\mathbf{s} \times \mathbf{H}_{\text{ex}}$, where γ is the gyromagnetic ratio and \mathbf{H}_{ex} is the effective exchange field that is aligned along the local spin moment \mathbf{S} . Assuming $\mathbf{s} = (\sin\theta, \cos\theta, 0)$ and $\mathbf{H}_{\text{ex}} = H\hat{z}$, this equation of motion transforms to $\partial\theta/\partial t = \delta\theta/\delta t = -\gamma H$, where the sign of the spin precession angle $\delta\theta$ follows the sign of H and thus the sign of \mathbf{S} (Fig. 1a,b). In a ferromagnet, an electron spin propagating along the x direction continuously precesses in the same sense because of the homogeneous exchange field (Fig. 1c). On the other hand, in a FIM, an electron spin precesses anticlockwise on a lattice corresponding to a positive exchange field, whereas it precesses clockwise on the next lattice corresponding to a negative exchange field. As a result, the period (or wavelength) of spin precession in FIMs is longer than that in ferromagnets, resulting in much less spin dephasing.

To verify the theoretical prediction of long spin coherence length, we performed experiments with a FIM, that is, Co/Tb multilayers where both the Co and Tb layers are atomically thin and their moments are coupled antiferromagnetically. We chose a FIM instead of an AFM for two reasons. First, the Co/Tb multilayers can have a longer λ_c than a ferromagnet because of the antiferromagnetic alignment of the Co and Tb moments, thereby exhibiting a feature of the bulk-like torque characteristic. As explained above, the STT

¹Department of Electrical and Computer Engineering, National University of Singapore, Singapore, Singapore. ²Toyota Technological Institute, Tempaku, Nagoya, Japan. ³Institute of Materials Science, Vietnam Academy of Science and Technology, Hanoi, Vietnam. ⁴Department of Materials Science and Engineering, Korea University, Seoul, Korea. ⁵KU-KIST Graduate School of Convergence Science and Technology, Korea University, Seoul, Korea. ⁶Department of Semiconductor Systems Engineering, Korea University, Seoul, Korea. ⁷Shanghai Key Laboratory of Special Artificial Macrostructure Materials and Technology and School of Physics Science and Engineering, Tongji University, Shanghai, China. ⁸These authors contributed equally: Do Bang, Rahul Mishra *e-mail: kj_lee@korea.ac.kr; eleyang@nus.edu.sg

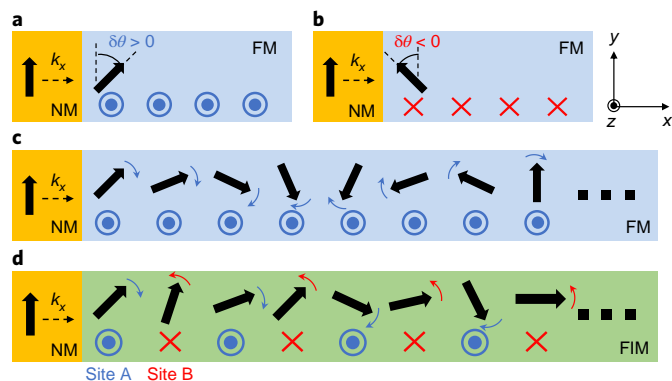


Fig. 1 | Semiclassical illustration of increased spin coherence length in FIMs compared to ferromagnets. **a,b**, Local spin precession angle $\delta\theta$ of a spin injected from a normal metal (NM) into a ferromagnet (FM) with up magnetic moment ($\mathbf{m} // +\hat{z}$) and down magnetic moment ($\mathbf{m} // -\hat{z}$), respectively. Note that \mathbf{m} is antiparallel to the local spin moment \mathbf{S} . Blue dots (red crosses) indicate the directions of magnetic moments along the $+\hat{z}$ ($-\hat{z}$) direction. **c,d**, Precession of an electron spin in the FM layer (**c**) and in the FIM layer (**d**). Blue and red curved arrows indicate $\delta\theta > 0$ and $\delta\theta < 0$, respectively.

efficiency of a ferromagnet is inversely proportional to the ferromagnet thickness²⁰, whereas that of an ideal AFM is independent of the AFM thickness. As the λ_c of a FIM is located between those for a ferromagnet and an AFM, it is expected that the STT efficiency of a FIM first increases and then decreases with FIM thickness. The second reason to choose a FIM is that various measurement methods established for ferromagnets are applicable to FIMs because of their non-zero net moment^{16,21}. However, the choice of a FIM also results in a difficulty. FIMs commonly show a thickness-dependent variation of their magnetic properties²², as also observed in Co/Tb multilayers (Supplementary Note 2), which makes a quantitative analysis of spin transport difficult. Even with this difficulty, our thickness-dependent SOT measurements combined with spin pumping measurements support a long spin coherence length and associated bulk-like torque characteristic in ferrimagnetic Co/Tb multilayers, as we show in the following.

Multilayer structures and harmonic Hall measurements

We fabricated perpendicularly magnetized ferromagnetic [Co/Ni]_N and ferrimagnetic [Co/Tb]_N multilayers (Fig. 2a,b; see Methods for details), where the total thickness varies with changing repetition number *N*. Both Co/Ni and Co/Tb multilayers have an additional Pt layer, and an in-plane current generates SOTs. We used harmonic Hall voltage measurements to quantify the strength of the SOT effective fields^{23–25}. The longitudinal and transverse measurement schematics are presented in Fig. 2c,d, respectively. Representative results for the longitudinal (blue line) and transverse (red line) second harmonic voltages (V_{2f}) from Co/Ni ($N=2$) and Co/Tb ($N=5$) devices are shown in Fig. 2e,f, respectively. The anomalous Nernst effect is corrected in the V_{2f} data²³. We observe a clear V_{2f} in the longitudinal configuration ($\mathbf{H} // \mathbf{I}$), which is mostly determined by the anti-damping SOT^{23,24}. The opposite V_{2f} signs in the $\mathbf{H} // \mathbf{I}$ case for Co/Ni and Co/Tb multilayers indicate that the Pt layer is the source of spin currents, as it is placed on top of the Co/Tb multilayer, but under the Co/Ni multilayer. To rule out the contribution from pure bulk Co/Tb to SOTs, we conducted a control experiment without and with the spin current source, Pt (Supplementary Note 3). We find that there is no noticeable current-induced SOT without the Pt layer, suggesting that the Co/Tb bulk itself cannot directly contribute to SOTs.

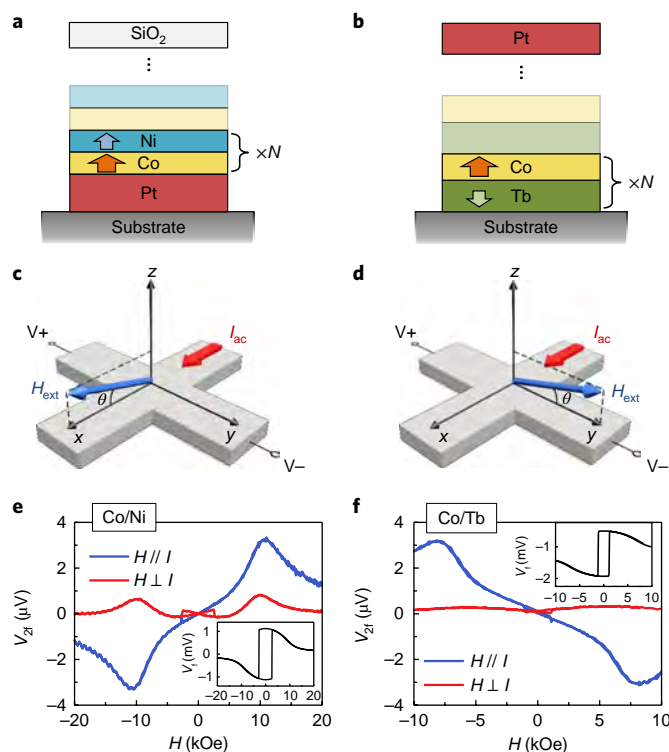


Fig. 2 | SOTs in ferromagnetic versus ferrimagnetic film stacks.

a,b, Illustrations of ferromagnetic Co/Ni (**a**) and ferrimagnetic Co/Tb (**b**) multilayers. The magnetizations of Co, Ni and Tb sublattices are presented by yellow, blue and green arrows, respectively. **c,d**, Measurement schematics for longitudinal (**c**) and transverse (**d**) SOT effective fields. $V_{+/-}$ represents the positive/negative port of a lock-in amplifier for voltage measurements. H_{ext} and I_{ac} are the external magnetic field and applied a.c. current, respectively. **e,f**, Second harmonic voltages (V_{2f}) obtained from Co/Ni (**e**) and Co/Tb (**f**) multilayer devices, with the blue curves representing the longitudinal signals and red curves representing the transverse signals. Insets, first harmonic voltages (V_{1f}). The units of the *x* axis are kOe.

SOT effective fields and spin Hall angles

We extracted the spin-orbit effective fields, H_L and H_T , by fitting V_{2f} (refs 24,26), where H_L and H_T correspond to the anti-damping (longitudinal) and field-like (transverse) components of SOTs, respectively. The planar Hall effect is considered for the fitting (Supplementary Note 4). Devices with different *N*, corresponding to different thicknesses of ferromagnetic Co/Ni (t_{FM}) or ferromagnetic Co/Tb (t_{FIM}) were measured. Absolute SOT effective fields normalized by the current density in the Pt layer ($H_{L/T}/J$) are presented in Fig. 3a,b for the Co/Ni and Co/Tb systems, respectively. We find that both H_L and H_T of Co/Ni multilayers decrease as t_{FM} increases, consistent with the surface torque characteristic expected for ferromagnets. However, Co/Tb multilayers show an entirely different trend, in which both H_L and H_T increase up to a t_{FIM} of 7.9 nm and then decrease for thicker samples.

We estimated the effective spin Hall angle $\theta_{\text{eff}} = H_L (2eM_S t_{\text{FM}/\text{FIM}} / \hbar J)$, where e is the electron charge and \hbar is the reduced Planck's constant, by considering the thickness-dependent variation of the saturation magnetization M_S and current density J in the Pt layer. The Co/Tb multilayer shows a significant M_S variation, with the minimum at $t_{\text{FIM}} = 6.6$ nm (inset of Fig. 3d). We find that θ_{eff} of the Co/Ni multilayer is nearly constant with t_{FM} (Fig. 3c). Similar to the trend for H_L/J , θ_{eff} of the Co/Tb

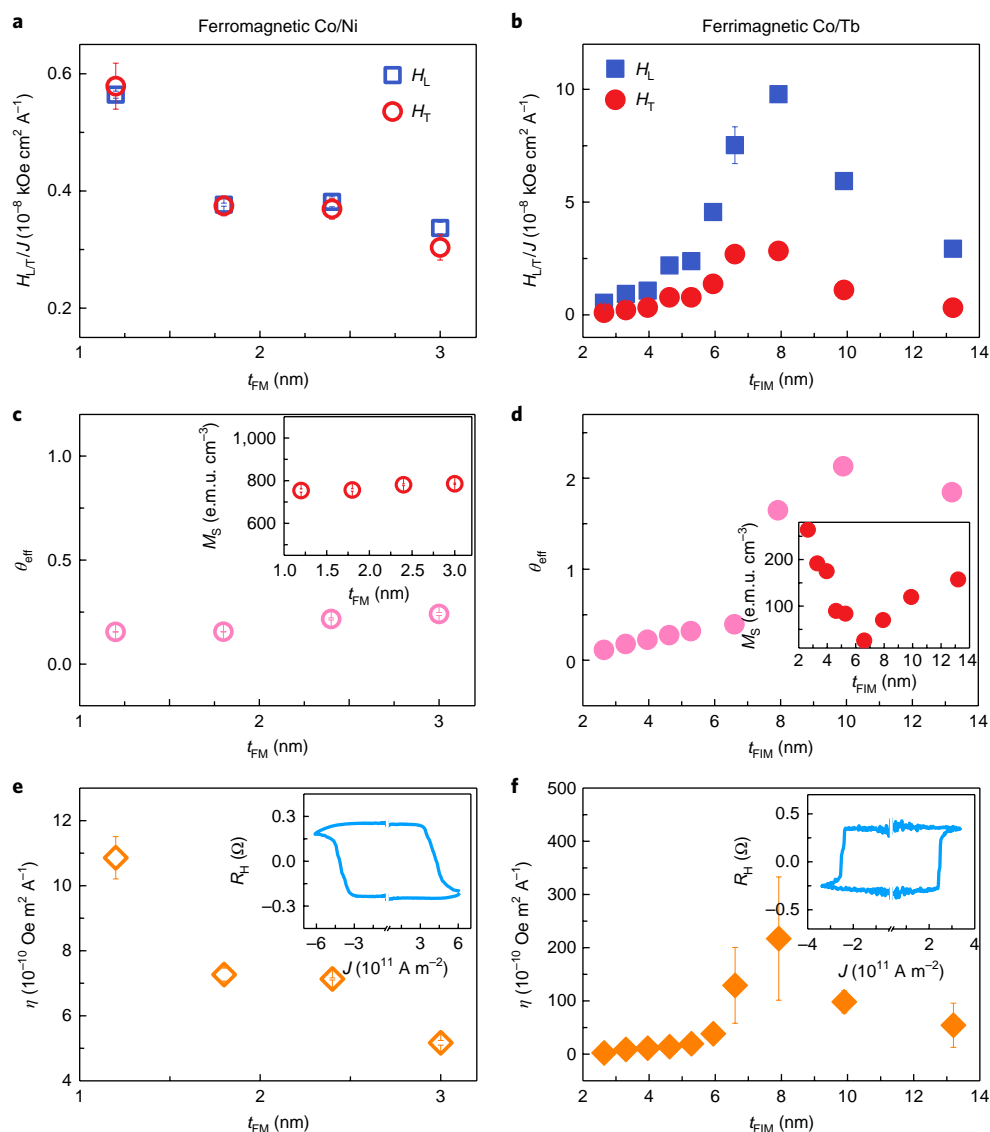


Fig. 3 | SOT effective fields and switching efficiencies in ferromagnetic versus ferrimagnetic multilayers. **a, b**, Longitudinal (H_L) and transverse (H_T) SOT effective fields as a function of ferromagnetic Co/Ni (**a**) or ferrimagnetic Co/Tb (**b**) thicknesses (t_{FM} or t_{FIM}). $H_{L,T}/J$ represents the SOT effective fields normalized by the current density in the heavy metal layer. **c, d**, Effective spin Hall angle (θ_{eff}) as a function of ferromagnetic or ferrimagnetic thickness. Insets (**c, d**), saturation magnetization (M_S) as a function of ferromagnetic or ferrimagnetic thickness. **e, f**, Switching efficiencies (η) as a function of Co/Ni (**e**) or Co/Tb (**f**) thicknesses. Insets (**e, f**), current-induced switching data, showing the Hall resistance (R_H) as a function of applied pulse current density (J). Error bars are calculated from repeated measurements in four different devices.

multilayer increases up to $t_{\text{FIM}}=9.9$ nm and then decreases for thicker samples (Fig. 3d). Apart from the distinct thickness dependence of θ_{eff} , another interesting observation is that the Co/Tb multilayer shows a larger θ_{eff} than the Co/Ni multilayer (θ_{eff} of the Co/Tb multilayer is 2.1 at $t_{\text{FIM}}=9.9$ nm and the average θ_{eff} of the Co/Ni multilayer is 0.2 ± 0.05). We note that a model calculation considering a thickness-dependent variation of the sd exchange in FIMs shows trends that are qualitatively similar to the experimental ones (Supplementary Fig. 2), even though the model is too simple to capture all the details of FIMs. Nevertheless, this qualitative agreement between model and experimental results indicates that the distinct behaviour of the θ_{eff} of the Co/Tb multilayer originates from a combined effect of long spin coherence length and thickness-dependent property variation, in which the thickness-dependent exchange coupling may be a possible origin for the unusual thickness dependence of the spin torque efficiency.

SOT switching experiments

As an independent test, we performed SOT switching experiments by applying an external field (H_{ext}) along the current direction ($\theta=0^\circ$) to achieve deterministic magnetization switching. The insets of Fig. 3e,f present representative current-induced switching data obtained from Co/Ni ($N=2$) and Co/Tb ($N=5$) samples, respectively. As the switching is governed by domain nucleation and propagation in large samples (that is, Hall bar width = $10 \mu\text{m}$), we estimate the STT efficiency to be $\eta=H_p/J$, where H_p is the domain wall depinning field^{16,27}. Figure 3e,f shows η as a function of t_{FM} and t_{FIM} , respectively. For the Co/Ni multilayers, η decreases with t_{FM} , whereas for Co/Tb multilayers it increases and then decreases with t_{FIM} , following similar trends to the SOT effective fields (Fig. 3a,b). We note that the recently reported fast dynamics at the angular momentum compensation condition in FIMs²¹ would affect the switching data, but not the harmonic Hall data.

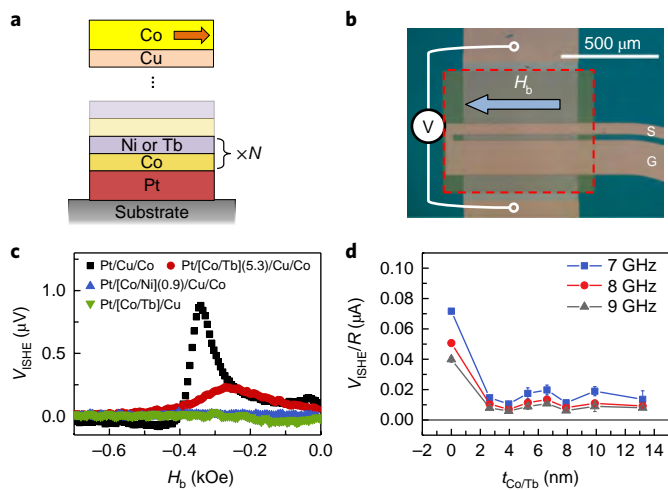


Fig. 4 | Spin pumping measurements. **a**, Spin pumping sample structure. The orange arrow represents the magnetization direction of the top Co layer. N is the repetition number of Co/Tb or Co/Ni bilayer pairs. **b**, Schematic of spin pumping measurements. Before making the copper waveguide on top of the device, a thick SiO_2 layer (~ 30 nm) is deposited (the translucent square highlighted by the red dashed box) on top of the multilayer stacks to isolate the waveguide. S and G indicate the signal and ground connections for high-frequency measurements. An in-plane bias field (H_b) along the waveguide direction is applied. Voltage is recorded by a lock-in amplifier. **c**, Spin pumping induced inverse spin Hall voltage (V_{ISHE}) with respect to H_b in various structures. **d**, Inverse spin Hall signal (V_{ISHE}/R , where R is the channel resistance) as a function of [Co/Tb] thickness ($t_{\text{Co/Tb}}$) in Pt/[Co/Tb]/Cu/Co structures at various frequencies. Error bars are calculated from repeated measurements in four different devices.

The fact that different approaches for the estimation of spin torque efficiency show qualitatively similar trends indicates that SOT for Co/Tb multilayers is not a surface torque. Moreover, the observed thickness dependence of spin torque efficiency is qualitatively consistent with the model calculation for the bulk-like torque characteristic in FIMs; it first increases and then decreases with FIM thickness. However, because of the thickness-dependent property variations in Co/Tb multilayers (inset of Fig. 3d and Supplementary Note 2) this result is not yet conclusive, and it is still possible that another unknown mechanism is responsible for the distinct thickness dependence observed in these Co/Tb multilayers.

Spin pumping experiments

To resolve this ambiguity we performed additional spin pumping experiments to estimate the spin coherence length λ_c . We measured a spin-pumping-induced inverse spin Hall voltage (V_{ISHE}) for substrate/Pt(10)/[FIM or FM]/Cu(2.4)/Co(20) structures (numbers are in nanometres; FIM = [Co(0.32)/Tb(0.34)] $_N$ and FM = [Co(0.3)/Ni(0.6)] $_N$, as shown in Fig. 4a). In these structures, the Co/Ni and Co/Tb multilayers are perpendicularly magnetized, whereas the top thick Co layer has an in-plane magnetization. In the spin pumping set-up (Fig. 4b; see Methods for details), the top Co layer generates a spin-pumping-induced spin current with an in-plane spin polarization (thus transverse to the Co/Ni or Co/Tb magnetization direction), which passes through the Cu layer and enters the Co/Ni or Co/Tb layer. If λ_c of the Co/Tb multilayer is long, it is expected that a transverse spin current passes through the Co/Tb layer without much spin dephasing and reaches the bottom spin sink, Pt, and subsequently V_{ISHE} is generated by the inverse spin Hall effect of Pt. On the other hand, V_{ISHE} is expected to be negligible for a thick

Co/Ni multilayer because a transverse spin current is almost absorbed at the [Co/Ni]/Cu interface. Therefore, the measurement of V_{ISHE} versus FIM or FM thickness provides an estimate of λ_c .

We find that the experimental results are consistent with this expectation. In Fig. 4c, black symbols are the data from a reference Pt/Cu/Co sample, which shows the largest V_{ISHE} signal at an in-plane bias field H_b . For the Co/Ni-based structure, the V_{ISHE} signal becomes negligible at a Co/Ni thickness of 0.9 nm (blue symbols). In contrast, the V_{ISHE} signal for the Co/Tb-based structure is finite for a much thicker Co/Tb (red symbols, Co/Tb thickness = 5.3 nm as an example). The V_{ISHE} signal disappears when excluding the top Co layer from the Co/Tb-based structure (green symbols), proving that the perpendicularly magnetized Co/Tb itself does not generate a V_{ISHE} signal. In Fig. 4d, spin pumping results are summarized for a wide thickness range of the Co/Tb multilayer. This shows that the inverse spin Hall signal (V_{ISHE}/R , where R is the channel resistance) is finite even for 13-nm-thick Co/Tb. This result is evidence of a long spin coherence length in ferrimagnetic Co/Tb multilayers.

The spin pumping and spin torque are connected through the Onsager reciprocity²⁸. Therefore, the long spin coherence length observed in spin pumping experiments suggests that the bulk-like torque characteristic must be present in spin torque experiments, at least partially. Given that the thickness-dependent change in the spin torque efficiency follows the trend expected for the bulk-like torque characteristic (Fig. 3), the spin pumping experiments combined with the spin torque experiments allow us to conclude that the antiferromagnetically coupled FIMs show a long spin coherence length and associated bulk-like torque characteristic.

SOT and spin coherence length in CoTb alloys

We also carried out experiments on the thickness dependence of the SOT efficiency and spin pumping signal for FIM alloys to find out if the long spin coherence length is a unique property of FIM multilayers or if it is also observed in FIM alloys. CoTb alloy/Pt (4 nm) samples with varying CoTb thicknesses were prepared. The Co and Tb ratio was kept similar to that in the multilayers for a fair comparison. Figure 5a shows saturation magnetization M_s as a function of alloy thickness. The M_s for the alloy samples shows minima for the thickness range 7–10 nm. Figure 5b shows H_L and H_T for the alloy as a function of thickness. While H_T for the alloy is close to zero, H_L shows a ‘bulk-like torque’ characteristic (that is, H_L does not follow the 1/CoTb thickness trend). This behaviour is qualitatively similar to a ‘partially random’ FIM (Supplementary Fig. 2b), indicating that the CoTb alloys have some ordering and thus would have a spin coherence length longer than ferromagnets. We also performed spin pumping experiments for CoTb alloys. The sample structure was Pt(10)/CoTb alloy(t_{CoTb})/Cu(2.4)/Co(20) (numbers are in nanometres), where the CoTb alloy was perpendicularly magnetized. Figure 5c shows that a transverse spin current originating from the spin pumping from a Co(20 nm) in-plane layer passes through a thick CoTb alloy, just like CoTb multilayers. This result provides evidence that the FIM alloy has a long spin coherence length possibly due to some ordering in the alloy^{29,30}. The results were supported by a model calculation using a ferrimagnetic alloy (Supplementary Fig. 2), where an ordered alloy shows a longer spin coherence length than a random alloy.

We speculate that this unexpectedly long spin coherence length in FIM alloys has the same origin as the perpendicular magnetic anisotropy that FIM alloys preserve even at large thicknesses. Previous X-ray studies on FeTb revealed a correlation between the structural ordering along the thickness direction and the large perpendicular magnetic anisotropy^{31,32}; more Tb–Fe ordering appears in the thickness direction than in plane. As a long spin coherence length is the only possible explanation for the spin pumping experiment with FIM alloys, we conclude that the spin coherence length of both the FIM multilayer and the FIM alloy

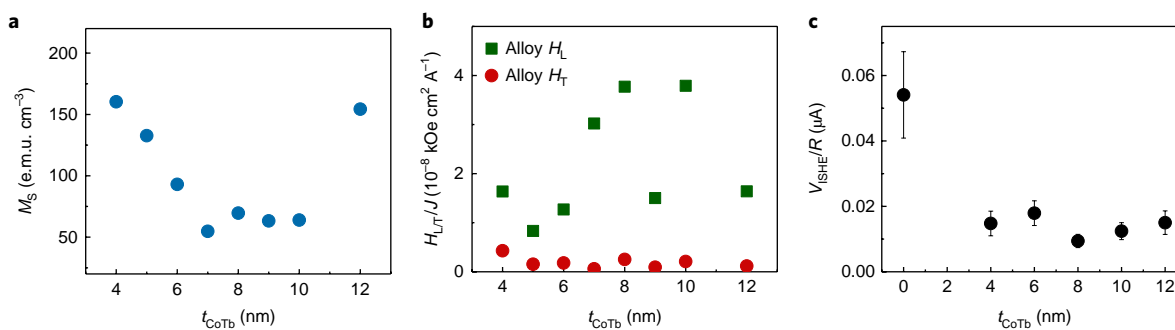


Fig. 5 | Characterizations of CoTb alloy samples. a, Saturation magnetization (M_s) as a function of CoTb alloy thickness (t_{CoTb}). **b,** Longitudinal (H_L) and transverse (H_T) SOT effective fields as a function of t_{CoTb} . **c,** Spin pumping signals in CoTb alloys with t_{CoTb} . Error bars are calculated from repeated measurements in four different devices.

can be much longer than that of the ferromagnet. These salient features make antiferromagnetically coupled FIMs attractive for low-power non-volatile applications. We expect that the bulk-like torque principle is also applicable to domain wall or skyrmion devices^{33–35} operated by SOTs. In this respect, our findings will motivate research activities to introduce FIMs as core elements in spintronics devices, which have so far been dominated by ferromagnets. Therefore, our result provides an important step towards ‘ferrimagnetic spintronics’.

Online content

Any methods, additional references, Nature Research reporting summaries, source data, statements of data availability and associated accession codes are available at <https://doi.org/10.1038/s41563-018-0236-9>.

Received: 31 July 2018; Accepted: 23 October 2018;
Published online: 3 December 2018

References

- Slonczewski, J. C. Current-driven excitation of magnetic multilayers. *J. Magn. Mater.* **159**, L1–L7 (1996).
- Berger, L. Emission of spin waves by a magnetic multilayer traversed by a current. *Phys. Rev. B* **54**, 9353–9358 (1996).
- Tsoi, M. et al. Excitation of a magnetic multilayer by an electric current. *Phys. Rev. Lett.* **80**, 4281–4284 (1998).
- Myers, E. B., Ralph, D. C., Katine, J. A., Louie, R. N. & Buhrman, R. A. Current-induced switching of domains in magnetic multilayer devices. *Science* **285**, 867–870 (1999).
- Waintal, X., Myers, E. B., Brouwer, P. W. & Ralph, D. C. Role of spin-dependent interface scattering in generating current-induced torques in magnetic multilayers. *Phys. Rev. B* **62**, 12317–12327 (2000).
- Stiles, M. D. & Zangwill, A. Anatomy of spin-transfer torque. *Phys. Rev. B* **66**, 014407 (2002).
- Miron, I. M. et al. Perpendicular switching of a single ferromagnetic layer induced by in-plane current injection. *Nature* **476**, 189–193 (2011).
- Liu, L. et al. Spin-torque switching with the giant spin hall effect of tantalum. *Science* **336**, 555–558 (2012).
- Kovalev, A. A., Bauer, G. E. W. & Brataas, A. Perpendicular spin valves with ultrathin ferromagnetic layers: magneto-electronic circuit investigation of finite-size effects. *Phys. Rev. B* **73**, 054407 (2006).
- Núñez, A. S., Duine, R. A., Haney, P. & MacDonald, A. H. Theory of spin torques and giant magnetoresistance in antiferromagnetic metals. *Phys. Rev. B* **73**, 214426 (2006).
- Haney, P. M. & MacDonald, A. H. Current-induced torques due to compensated antiferromagnets. *Phys. Rev. Lett.* **100**, 196801 (2008).
- Xu, Y., Wang, S. & Xia, K. Spin-transfer torques in antiferromagnetic metals from first principles. *Phys. Rev. Lett.* **100**, 226602 (2008).
- Wei, Z. et al. Changing exchange bias in spin valves with an electric current. *Phys. Rev. Lett.* **98**, 116603 (2007).
- Urazhdin, S. & Anthony, N. Effect of polarized current on the magnetic state of an antiferromagnet. *Phys. Rev. Lett.* **99**, 046602 (2007).
- Wadley, P. et al. Electrical switching of an antiferromagnet. *Science* **351**, 587–590 (2016).

- Mishra, R. et al. Anomalous current-induced spin torques in ferrimagnets near compensation. *Phys. Rev. Lett.* **118**, 167201 (2017).
- Finley, J. & Liu, L. Spin-orbit-torque efficiency in compensated ferrimagnetic cobalt-terbium alloys. *Phys. Rev. Appl.* **6**, 054001 (2016).
- Roschewsky, N., Lambert, C.-H. & Salahuddin, S. Spin-orbit torque switching of ultralarge-thickness ferrimagnetic GdFeCo. *Phys. Rev. B* **96**, 064406 (2017).
- Ueda, K., Mann, M., de Brouwer, P. W. P., Bono, D. & Beach, G. S. D. Temperature dependence of spin-orbit torques across the magnetic compensation point in a ferrimagnetic TbCo alloy film. *Phys. Rev. B* **96**, 064410 (2017).
- Fert, A., Emley, N. C., Myers, E. B., Ralph, D. C. & Buhrman, R. A. Quantitative study of magnetization reversal by spin-polarized current in magnetic multilayer nanopillars. *Phys. Rev. Lett.* **89**, 226802 (2002).
- Kim, K.-J. et al. Fast domain wall motion in the vicinity of the angular momentum compensation temperature of ferrimagnets. *Nat. Mater.* **16**, 1187–1192 (2017).
- Hebler, B., Hassdenteufel, A., Reinhardt, P., Karl, H. & Albrecht, M. Ferrimagnetic Tb–Fe alloy thin films: composition and thickness dependence of magnetic properties and all-optical switching. *Front. Mater.* **3**, 8 (2016).
- Garello, K. et al. Symmetry and magnitude of spin-orbit torques in ferromagnetic heterostructures. *Nat. Nanotech.* **8**, 587–593 (2013).
- Kim, J. et al. Layer thickness dependence of the current-induced effective field vector in Ta[CoFeB]MgO. *Nat. Mater.* **12**, 240–245 (2013).
- Jamali, M. et al. Spin-orbit torques in Co/Pd multilayer nanowires. *Phys. Rev. Lett.* **111**, 246602 (2013).
- Qiu, X. et al. Angular and temperature dependence of current induced spin-orbit effective fields in Ta/CoFeB/MgO nanowires. *Sci. Rep.* **4**, 4491 (2014).
- Lee, O. J. et al. Central role of domain wall depinning for perpendicular magnetization switching driven by spin torque from the spin Hall effect. *Phys. Rev. B* **89**, 024418 (2014).
- Brataas, A., Kent, A. D. & Ohno, H. Current-induced torques in magnetic materials. *Nat. Mater.* **11**, 372–381 (2012).
- Graves, C. E. et al. Nanoscale spin reversal by non-local angular momentum transfer following ultrafast laser excitation in ferrimagnetic GdFeCo. *Nat. Mater.* **12**, 293–298 (2013).
- Chimata, R. et al. All-thermal switching of amorphous Gd–Fe alloys: analysis of structural properties and magnetization dynamics. *Phys. Rev. B* **92**, 094411 (2015).
- Harris, V. G., Aylesworth, K. D., Das, B. N., Elam, W. T. & Koon, N. C. Structural origins of magnetic anisotropy in sputtered amorphous Tb–Fe films. *Phys. Rev. Lett.* **69**, 1939–1942 (1992).
- Hufnagel, T. C., Brennan, S., Zschack, P. & Clemens, B. M. Structural anisotropy in amorphous Fe–Tb thin films. *Phys. Rev. B* **53**, 12024–12030 (1996).
- Emori, S., Bauer, U., Ahn, S.-M., Martinez, E. & Beach, G. S. D. Current-driven dynamics of chiral ferromagnetic domain walls. *Nat. Mater.* **12**, 611–616 (2013).
- Ryu, K.-S., Thomas, L., Yang, S.-H. & Parkin, S. Chiral spin torque at magnetic domain walls. *Nat. Nanotech.* **8**, 527–533 (2013).
- Sampaio, J., Cros, V., Rohart, S., Thiaville, A. & Fert, A. Nucleation, stability and current-induced motion of isolated magnetic skyrmions in nanostructures. *Nat. Nanotech.* **8**, 839–844 (2013).

Acknowledgements

The authors acknowledge discussions with P.M. Haney. This research was supported by the National Research Foundation (NRF), Prime Minister’s Office, Singapore, under its Competitive Research Programme (CRP award no. NRCRP12-2013-01). K.-J.L. was

supported by the National Research Foundation of Korea (NRF-2015M3D1A1070465 and NRF-2017R1A2B2006119) and the KIST Institutional Program (project no. 2V05750) and Samsung Research Funding Center of Samsung Electronics under project no. SRFCMA1702-02.

Author contributions

J.Y. and H.Y. planned the project. J.Y., D.B. and P.V.T. deposited films. J.Y. and R.M. fabricated devices and performed the transport measurements. J.Y., R.R., R.M., Y.W. and S.S. carried out the spin pumping measurements. J.H.O., H.-J.P., Y.J., D.-K.L., S.-W.L., G.G. and K.-J.L. performed theoretical analysis. J.Y., D.B., X.Q., R.M., Y.J. and G.G. analysed the data with the help of H.A., K.-J.L. and H.Y. All authors discussed the results and commented on the manuscript. J.Y., K.-J.L. and H.Y. wrote the manuscript. H.Y. initiated the idea and led the project.

Competing interests

The authors declare no competing interests.

Additional information

Supplementary information is available for this paper at <https://doi.org/10.1038/s41563-018-0236-9>.

Reprints and permissions information is available at www.nature.com/reprints.

Correspondence and requests for materials should be addressed to K.-J.L. or H.Y.

Publisher's note: Springer Nature remains neutral with regard to jurisdictional claims in published maps and institutional affiliations.

© The Author(s), under exclusive licence to Springer Nature Limited 2018

Methods

Sample preparation. Substrate/(Tb(0.34 nm)/Co(0.32 nm))_N/Pt(4 nm) and substrate/MgO(2 nm)/Pt(4 nm)/(Co(0.3 nm)/Ni(0.3 nm))_N/SiO₂(3 nm) multilayers were fabricated on thermally oxidized silicon substrates using a radiofrequency and d.c. magnetron sputtering system with a base pressure of $\sim 1 \times 10^{-9}$ torr. N is the repetition number of the Tb/Co or Co/Ni bilayer pairs, and was varied from 4 to 20 for Co/Tb systems and from 2 to 5 for Co/Ni systems. For Co/Tb multilayers, a 4-nm-thick Pt layer was deposited on top as a spin current source, which also protected the multilayer from being oxidized. For Co/Ni multilayers, a bilayer of MgO(2 nm)/Pt(4 nm) was deposited on the bottom as a buffer and spin current source, and a SiO₂(3 nm) layer was deposited as a capping layer to prevent possible oxidation of the ferromagnet layer. Subsequent photolithography and ion milling processes were performed to fabricate the films into Hall bar devices with a width of 10 μm .

Second harmonic and spin pumping measurements. For the second harmonic measurements, an a.c. current I_{ac} with a frequency of 13.7 Hz and a peak-to-peak magnitude of 5 mA was injected into the channel of the device²⁶. An external magnetic field H_{ext} was applied along (orthogonal to) the current direction with a small out-of-plane tilting of $\theta = 4^\circ$ from the film plane in the longitudinal (transverse) configuration. The first and second harmonic Hall voltages were

recorded simultaneously by using two lock-in amplifiers triggered at the same frequency by the current source.

In the spin pumping measurements, a microwave with a magnitude of 17 dBm and frequencies of 7–9 GHz was applied to the asymmetric coplanar stripline waveguide by a signal generator. Before making the copper waveguide on top of the device, a thick SiO₂ layer (~ 30 nm) was deposited on top of the multilayer stacks to isolate the waveguide. An in-plane field (H_i) along the waveguide direction was swept around the resonance field (H_0) given by the Kittel formula $f = \frac{\gamma}{2\pi} \sqrt{H_0(H_0 + 4\pi M_s)}$, where γ is the gyromagnetic ratio and M_s is the saturation magnetization. The voltage (V) was recorded by a lock-in amplifier. V includes the asymmetric component (V_{asym}) from the anomalous Hall effect (AHE) and the anisotropic magnetoresistance, as well as the symmetric components (V_{sym}) from the spin pumping induced inverse spin Hall voltage (V_{ISHE}). Thus, the measured voltage was fitted by a sum of symmetric and asymmetric Lorentzian functions $V = V_{\text{sym}} \frac{\Gamma^2}{\Gamma^2 + (H - H_0)^2} + V_{\text{asym}} \frac{\Gamma(H - H_0)}{\Gamma^2 + (H - H_0)^2}$, from which V_{ISHE} was extracted as V_{sym} .

Data availability

The data supporting the findings of this study are available within the paper and other findings of this study are available from the corresponding author upon reasonable request.

Dilute nitride InNP quantum dots: Growth and photoluminescence mechanism

Y. J. Kuang, K. Takabayashi, S. Sukritanon, J. L. Pan, I. Kamiya, and C. W. Tu

Citation: [Applied Physics Letters](#) **105**, 173112 (2014); doi: 10.1063/1.4900960

View online: <http://dx.doi.org/10.1063/1.4900960>

View Table of Contents: <http://scitation.aip.org/content/aip/journal/apl/105/17?ver=pdfcov>

Published by the [AIP Publishing](#)

Articles you may be interested in

[Studies of InGaN/GaN multiquantum-well green-light-emitting diodes grown by metalorganic chemical vapor deposition](#)

Appl. Phys. Lett. **85**, 401 (2004); 10.1063/1.1773371

[Tuning of the electronic properties of self-assembled InAs/InP\(001\) quantum dots by rapid thermal annealing](#)

Appl. Phys. Lett. **84**, 3382 (2004); 10.1063/1.1715141

[Photoluminescence from quantum dots in cubic GaN/InGaN/GaN double heterostructures](#)

Appl. Phys. Lett. **79**, 1243 (2001); 10.1063/1.1396314

[Chemical beam epitaxy growth of self-assembled InAs/InP quantum dots](#)

J. Vac. Sci. Technol. B **19**, 1467 (2001); 10.1116/1.1376381

[Radiative recombination from InP quantum dots on \(100\) GaP](#)

Appl. Phys. Lett. **78**, 2163 (2001); 10.1063/1.1361277



Dilute nitride InNP quantum dots: Growth and photoluminescence mechanism

Y. J. Kuang (邝彦瑾),^{1,a)} K. Takabayashi (高林紘),^{2,a)} S. Sukritanon,³ J. L. Pan,⁴ I. Kamiya (神谷格),² and C. W. Tu⁴

¹Department of Physics, University of California, San Diego, La Jolla, California 92093, USA

²Quantum Interface Laboratory, Toyota Technological Institute, Nagoya 468-8511, Japan

³Material Science and Engineering Program, University of California, San Diego, La Jolla, California 92093, USA

⁴Department of Electrical and Computer Engineering, University of California, San Diego, La Jolla, California 92093, USA

(Received 5 October 2014; accepted 17 October 2014; published online 30 October 2014)

Self-assembled dilute nitride InNP quantum dots (QDs) in GaP matrix grown under the Stranski-Krastanov mode by gas-source molecular beam epitaxy are studied. The N-related localized states inside the InNP QDs provide a spatially direct recombination channel, in contrast to the spatially indirect channel through the strained In(N)P QDs/GaP interface states. The N incorporation into InP QDs therefore causes a blueshift and double-peak features in photoluminescence, which are not observed in other dilute nitride materials. © 2014 AIP Publishing LLC.

[<http://dx.doi.org/10.1063/1.4900960>]

Plagued by its indirect bandgap, GaP is not commonly used for traditional optoelectronics. However, recent development in light emitting diodes (LEDs)¹ and water splitting,² taking advantage of its transparency and band energy levels, raised interests in materials based on the GaP platform. The small difference in the lattice constants between GaP and Si (5.451 Å and 5.431 Å, respectively) also provides a III-V-on-Si integration opportunity.^{3,4} Functional optoelectronic nanostructures grown on GaP substrates are therefore attracting attention.⁵ The mismatch (7.7%) in lattice constant between InP and GaP allows for fabrication of InP self-assembled quantum dots (QDs) on GaP substrate by using the Stranski-Krastanov growth mode. Photoluminescence (PL) with a peak at about 2 eV from InP QDs grown on GaP substrate has been reported.⁶ The band alignment of InP QD/GaP has been found to be at the crossover of type I and type II depending on the QD size and strain.⁷ Such a band structure can be further tailored if N is incorporated during the QD assembling process to form dilute nitride InNP QDs.⁸ The wide freedom of bandgap engineering capability of N in dilute III-V nitrides enabled by band anti-crossing (BAC)⁹ has also attracted great interest because of their potential applications in telecommunications,¹⁰ thermoelectrics,^{11,12} intermediate band solar cells,^{13,14} defect engineering,^{15,16} and infrared photodetectors,¹⁷ among others. Previously, it was shown that the luminescence from N-incorporated GaInNAs QDs may be extended to 1.3–1.55 μm (Ref. 18) and these QDs have been fabricated into lasers.¹⁹ In contrast, there has been no report on InNP QDs and, consequently, on their optical properties.

In this letter, we report the study on the growth of InNP QDs on GaP (001) by gas-source molecular beam epitaxy (GSMBE) and their optical properties. In particular, the uniqueness of the InNP QDs will be discussed in comparison with InP QDs. Interestingly, in contrast to N-induced PL

redshifts and intensity decrease seen in GaInNAs QDs,¹⁸ the incorporation of N in InP QDs does not redshift the PL peaks solely due to N-induced bandgap reduction. Instead, N-related states inside QDs become effective recombination centers. This changes the PL mechanisms in the materials system and results in blueshift, emergence of double peaks, and considerable enhancement in the PL intensity not previously seen in other dilute nitrides.

All samples studied in this paper were grown on GaP (001) substrates in a Varian Gen-II MBE system modified to thermally crack gas-phase PH₃ to P₂ and H₂. Elemental Ga and In, and radio frequency (rf)-plasma activated radical N were used as group-III and N sources, respectively. After native oxide desorption under P₂ overpressure at ~580 °C, a 200 nm-thick GaP buffer layer was grown at a growth rate of 1 μm/h. Then growth was interrupted to lower the substrate temperature to 440–480 °C. The In flux was set to supply a deposition rate of 0.1 monolayer/s (ML/s) calibrated by reflection high energy electron diffraction (RHEED) oscillations.²⁰ The PH₃ flow rate was set at 4–6 sccm during the QD formation process. For the growth of InNP QDs, the N plasma was ignited and various plasma powers (220–280 W) and N₂ gas flow rates (0.6–1.2 sccm) were used. When the In (N)P wetting layer exceeded the critical thickness, the In(N)P QDs were formed under large compressive strain, and confirmed by the *in situ* RHEED pattern change from a streaky to a chevron, as well as *ex situ* atomic force microscopy (AFM) on the uncapped QD samples. A total of 2 MLs of In (N)P were deposited for all samples in this study. Samples for optical studies were all capped with a 20 nm-thick GaP layer grown at the QD formation temperature and a subsequent 30 nm-thick GaP layer grown at 580 °C. In the rapid thermal annealing (RTA) study, samples were annealed at various temperatures (750–850 °C) for 30 s with a GaP wafer placed on top for surface protection. For the PL studies, samples were cooled down to various temperatures in an evacuated cryostat. A 532 nm continuous wave semiconductor

^{a)}Y. J. Kuang and K. Takabayashi contributed equally to this work.

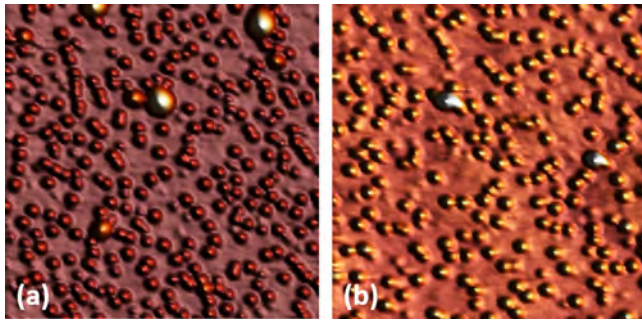


FIG. 1. $1 \times 1 \mu\text{m}^2$ AFM images of (a) InNP QDs and (b) InP QDs.

laser was used as an excitation source, and the power density was adjusted to $\sim 1 \text{ W/cm}^2$ for all the measurements.

The $1 \times 1 \mu\text{m}^2$ AFM images of InNP and InP QDs are shown in Figure 1. The QD densities for InNP and InP in this scanned area are found to be $230 \pm 34 \mu\text{m}^{-2}$ and $174 \pm 20 \mu\text{m}^{-2}$, respectively. The heights for InNP and InP QDs are $5.8 \pm 1.3 \text{ nm}$ and $4.5 \pm 1.1 \text{ nm}$, respectively. These dimensions are comparable to those of InP QD dimensions reported by Hatami *et al.* grown with a lower PH_3 flow rate (1.7 sccm).⁷ They have also reported that the size of InP QDs depends significantly on PH_3 flow rate when it is below 1.7 sccm. As the PH_3 flow is increased, the higher density of P adatom arrives at the surface and lowers the In mobility, resulting in larger QDs. However, our present study performed with various PH_3 flow rates shows that this is not necessarily the case in the higher range (4–6 sccm) either for InNP or InP QDs. The In surface mobility is inferred to become extremely low and becomes almost constant beyond a P flux threshold. Further increase in PH_3 flow rate therefore will not change the QD morphology. In addition, growth temperature variance from 440°C to 480°C , with other growth conditions fixed, does not seem to affect the QD morphology under a high PH_3 setting used in this experiment. Furthermore, we do not see a significant influence on the QD morphology from the presence of N plasma during the QD assembling process, although aggregated large clusters with diameter of $\sim 100 \text{ nm}$ and height of $\sim 30 \text{ nm}$ show up more frequently on the InNP QDs samples. These clusters, which

TABLE I. Growth conditions of each QD sample.

Sample	T_{sub} ($^\circ\text{C}$)	PH_3 flux (sccm)	N flux (sccm)	Plasma power (W)
InP	480	30
$\text{InN}_{0.014}\text{P}_{0.986}$	440	30	0.6	220
$\text{InN}_{0.017}\text{P}_{0.983}$	440	30	0.9	250
$\text{InN}_{0.02}\text{P}_{0.98}$	440	30	1.2	280

are formed as a result of increased nucleation rate by the reactive N plasma, are too large in size and do not contribute to the confinement energy in PL spectra.

Figure 2(a) shows the 4K PL spectra of InP QDs and InNP QDs grown with various N conditions (0.6 sccm, 220 W; 0.9 sccm, 250 W; and 1.2 sccm, 280 W). The growth conditions of each In(N)P sample are summarized in Table I. Based on the PL spectra, theoretical calculation²¹ and BAC model,⁹ the N contents of the three samples are estimated to be approximately 1.4%, 1.7%, and 2.0%. As more N atoms are incorporated, the 2ML InP QDs PL peak around 1.98 eV blueshifts to about 2.08 eV (1.4% N), then splits into multiple peaks with accompanying reduction in intensity (1.7% N), and further reduced (2.0% N). However, all InNP QDs showed higher PL intensity than InP, which is in clear contradiction to the reports on N incorporation in other direct-bandgap III-V materials. Generally speaking, introducing isovalent impurity N in III-V materials leads to bandgap reduction, which is well predicted by the BAC model.⁹ A large redshift is then expected for just a small amount of N added, i.e., 100–170 meV reduction for every percent of N added. On the other hand, N incorporation reduces the compressive strain endured by the InNP QDs due to the smaller N atom size, where further redshift was expected. The different PL features in peak position, intensity, and spectral shapes of InNP from InP shown in Figure 2(a) suggest that the radiative recombination mechanisms between the two are different. Such a distinctive difference is unlikely caused by QD size fluctuation nor strain variation because we observed small variance in the QD size under high PH_3 flow rate, and also because the results shown in Figure 2(a) are different

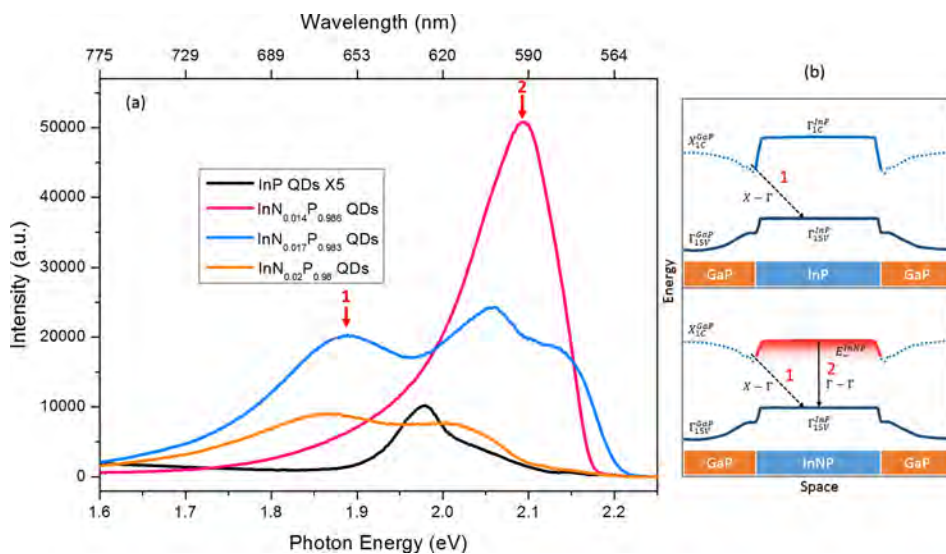


FIG. 2. (a) Low temperature (4K) PL spectra of InP QDs and InNP QDs with various N_2 flow rate and N plasma power conditions: $\text{InN}_{0.014}\text{P}_{0.986}$ QDs, 0.6 sccm, 220 W; $\text{InN}_{0.017}\text{P}_{0.983}$ QDs, 0.9 sccm, 250 W; and $\text{InN}_{0.02}\text{P}_{0.98}$ QDs, 1.2 sccm, 280 W. (b) Band diagrams of strained InP QDs and InNP QDs both in a GaP matrix. Arrows 1 and 2 in (a) indicate the X- Γ and Γ - Γ transitions shown in (b), respectively.

from the pressure-dependent PL study on InP QDs embedded in GaP.⁷

A band diagram of a strained In(N)P QDs is depicted in Figure 2(b) to explain the radiative mechanisms. The band alignment is based on the theoretical framework by Williamson *et al.*, taking into account the quantum confinement and strain effects.²¹ It is predicted that InP/GaP interface conduction (IC) states are formed in the strained InP/GaP QD system. Depending on the QD size, the Γ_{IC} -derived states inside the InP QDs can lie above the IC band edge or below the IC band edge. When the Γ_{IC} -derived states lie above the IC band edge, which is the case in Figure 2(b), photo-excited electrons will diffuse to the lower IC states, where electrons are localized and from where electrons recombine with heavy holes in the highest lying Γ_{15V} -derived states in the InP QDs. This type-II indirect transition is denoted as X- Γ in Figure 2(b). The PL lifetime of ~ 10 ns observed with our InP QDs is much longer than $\lesssim 2$ ns reported in Ref. 7, and suggests that the band alignment is likely type-II.

When N is incorporated, however, three things change this picture. First of all, dilute nitride alloy band, E_{-}^{InNP} , is formed via BAC.⁹ Second, due to its much higher electronegativity, N forms the highly localized states within InNP QDs. The exponential N-related band tail states²² are also denoted by the graded red region below the band edge in Figure 2(b). Third, N incorporation is also known to introduce N-related defects, such as DD1 non-radiative recombination centers,²³ which quench the PL intensity. These three factors all contribute to the change in the PL mechanisms. In InP QDs, the dipole transition matrix element between the IC states and the Γ -holes states is five orders of magnitude smaller than that of a typical type-I system.²¹ In contrast in InNP QDs, when electrons are excited into the conduction band, they are now more likely localized in the QDs due to the presence of N and then recombine with the heavy holes due to the stronger coupling between the dilute nitride states and the heavy hole states, within the QDs. This causes the blueshift and the much higher intensity (~ 25 fold) in the PL (InN_{0.014}P_{0.986} QDs). Recombination of the electrons in the IC states and the dilute nitride exponential band tail also contribute to the InN_{0.014}P_{0.986} QDs PL shoulder on the lower energy side. When more nitrogen is added, the E_{-}^{InNP} energy level is further shifted down. This accounts for the redshift of the peak positions of InN_{0.017}P_{0.983} QDs and InN_{0.02}P_{0.98} QDs (on the higher energy side marked by arrow 2), agreeing with the BAC model. At the same time, the higher N density generates more non-radiative defects, which reduces the radiative recombination rate of the Γ - Γ transition and makes it comparable to the recombination from the IC states (X- Γ transition). Therefore, a distinct peak is seen on the lower energy side in both InN_{0.017}P_{0.983} QDs and InN_{0.02}P_{0.98} QDs (marked by arrow 1). When the Γ - Γ -like transition rate is almost equal to that of the X- Γ -like transition, the convoluted PL just exhibits a flat plateau in InN_{0.02}P_{0.98} QDs. Although samples with higher N content than 2% are not available in this study, it is expected that the higher N density within InNP QDs results in more non-radiative centers and thus PL from the X- Γ -like transition becoming dominant. Note that there is a relatively large peak shift in X- Γ

transition in the InP reference sample and InNP samples. We attribute this peak shift to the variation of the strain and size since InP reference sample was grown at a higher temperature of 480 °C than that for InNP samples. However, further study needs to be done on this particular phenomenon.

To further confirm the origin of the two peaks in the PL, two separate studies were performed. One is a temperature-dependent PL study on an InN_{0.017}P_{0.983} sample showing the double peak feature. The evolution of the PL spectra between 4 K and 180 K is shown in Figure 3. At 4 K, the peaks 1 and 2, associated with the X- Γ - and Γ - Γ -transitions, respectively, show comparable intensities. As the sample temperature is elevated, the intensity of peak 2 (Γ - Γ) is reduced much quickly than peak 1 (X- Γ). At 100 K, peak 2 already becomes indiscernible. This can be explained with a physical picture similar to that employed to explain the S curve behavior in other dilute nitride materials.²⁰ At temperature lower than 20 K, the photo-excited electrons do not have enough thermal energy to escape the N-related localized states within the InNP QDs (PL at 4 K and 20 K are almost identical). When the temperature is elevated to above 20 K, these localized electrons have enough thermal energy to hop out and thermalize to the lower lying IC states, from where most transitions occur. Recombination from the E_{-}^{InNP} band hence decreases as observed in the peak 2 (Γ - Γ) intensity.

The other study is the low temperature PL on the RTA samples. PL spectra of an InNP as-grown samples and samples annealed at 700, 750, 800, and 850 °C (for 30 s) are shown in Figure 4. All PL spectra are normalized to the X- Γ -like transition peak for relative intensity comparison. RTA induced PL enhancement is expected on the QDs as well as on dilute nitrides, and more drastically on dilute nitrides, since RTA effectively removes the N-related non-radiative defects. As shown in Figure 4, intensity of transition associated with the N-related states (peak 2) is enhanced after RTA. For RTA at 700, 750, and 800 °C, the PL intensities of peak 1 (X- Γ) and peak 2 (Γ - Γ) are comparable. When the RTA temperature is raised to 850 °C, which is

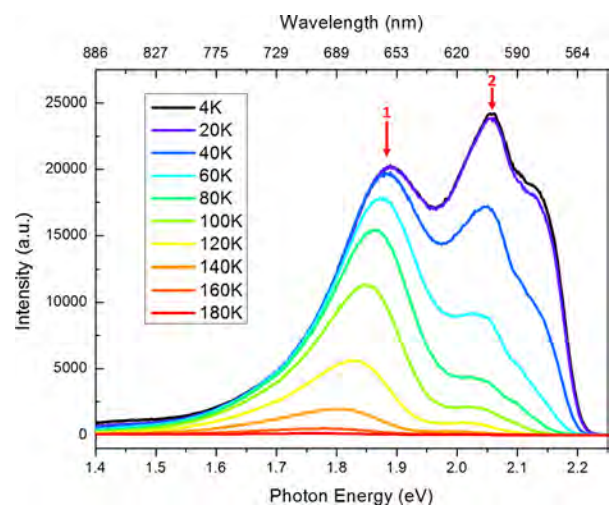


FIG. 3. Temperature dependent PL spectra of an InNP QD sample with double peak feature. The intensity of peak 2, associated with the Γ - Γ transition, decreases more quickly than peak 1 that is associated with the X- Γ transition, with rise in the temperature.

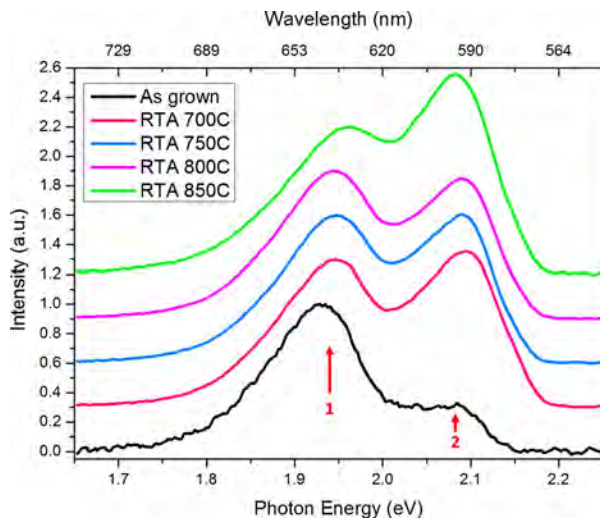


FIG. 4. 25 K PL spectra of an InNP QD as grown sample and a series samples annealed at 700, 750, 800, and 850 °C. Peak 1 and peak 2, associated with the X- Γ transition and the Γ - Γ transition, respectively, are also marked in the figure.

close to the reported optimal annealing temperature for dilute nitride optical quality enhancement,²⁴ the intensity of peak 2 (Γ - Γ) is noticeably higher than peak 1 (X- Γ). The similar response of PL intensity to RTA temperature as well as the peak intensity evolution in temperature dependent PL described above are strong evidences for the two transition pictures described in Figure 2(b).

Note that the N-induced blueshift and peak splitting observed in this study occur only under limited conditions. First of all, the Γ_{IC}^{InNP} band edge as well as the new InNP alloy E_{IC}^{InNP} band edge need to be above the IC band edge. If the Γ_{IC}^{InNP} band edge is lower than the IC band edge to start with, or in other words, the system is a clear type-I band alignment system, adding N in the QDs should result in PL redshift similar to GaInNAs. Second, the bandgap reduction induced by N in the InNP QDs should be smaller than the band offset between the Γ_{IC}^{InNP} band edge and the IC band edge. If the new alloy band E_{IC}^{InNP} is located well below the IC band edge, the double peak features are expected to disappear. For example, the Γ_{IC}^{InNP} band edge and the IC band edge offset is calculated to be ~ 300 meV for a QD with 6 nm diameter.²¹ If the InNP QDs contain more than 3% N, E_{IC}^{InNP} is expected to lie below the IC band edge, neglecting the strain condition. Then, the InNP QDs are not expected to show PL behavior seen in this study. The enhanced transition by N incorporation in InNP QDs can also enhance absorption. Since the transition matrix is symmetric, the significantly higher intensity in PL suggests that the absorption in InNP will be higher than in InP QDs. If InNP QDs are embedded in GaP based device, such as solar cell or water splitting cells, they are likely to perform much better than the indirect bandgap GaP alone.

In conclusion, the unusual PL features, such as blueshift, intensity increase, and double peaks in dilute nitride InNP

QDs are a result of the special band alignment and the N enhanced transition and localization within the QDs. When N is added into a type-II InP QD system, N changes the band structure and provides an efficient Γ - Γ -like recombination channel. If the IC states are located lower than the N induced alloy states, InNP QDs PL peaks show uncommon blueshift, intensity increase, and splitting behavior.

Material growth by GSMBE was supported by the National Science Foundation under Grant No. DMR-0907652 and DMR-1106369. S.S. acknowledges the financial support from the Royal Government of Thailand Scholarship. This work was partly supported by the Strategic Research Infrastructure Project, MEXT, and Toyooki Scholarship Foundation, Japan. J.L.P. was supported by ONR Grant No. N000141210457.

- ¹J. Chamings, S. Ahmed, S. J. Sweeney, V. A. Odnoblyudov, and C. W. Tu, *Appl. Phys. Lett.* **92**, 021101 (2008).
- ²S. Hu, M. R. Shaner, J. A. Beardslee, M. Lichterman, B. S. Brunswig, and N. S. Lewis, *Science* **344**(6187), 1005 (2014).
- ³T. Katoda and M. Kishi, *J. Electron. Mater.* **9**(4), 783 (1980).
- ⁴Y. J. Kuang, S. Sukritanon, H. Li, and C. W. Tu, *Appl. Phys. Lett.* **100**(5), 053108 (2012).
- ⁵Y. Song and M. L. Lee, *Appl. Phys. Lett.* **100**(25), 251904 (2012).
- ⁶F. Hatami, W. T. Masselink, and L. Schrottke, *Appl. Phys. Lett.* **78**(15), 2163 (2001).
- ⁷F. Hatami, W. T. Masselink, L. Schrottke, J. W. Tomm, V. Talalaev, C. Kristukat, and A. R. Goñi, *Phys. Rev. B* **67**(8), 085306 (2003).
- ⁸W. G. Bi and C. W. Tu, *J. Appl. Phys.* **80**(3), 1934 (1996).
- ⁹W. Shan, W. Walukiewicz, J. W. Ager III, E. E. Haller, J. F. Geisz, D. J. Friedman, J. M. Olson, and S. R. Kurtz, *Phys. Rev. Lett.* **82**(6), 1221 (1999).
- ¹⁰M. Kondow, K. Uomi, A. Niwa, T. Kitatani, S. Watahiki, and Y. Yazawa, *Jpn. J. Appl. Phys.* **35**(2B), 1273 (1996).
- ¹¹P. Pichanusakorn, Y. J. Kuang, C. J. Patel, C. W. Tu, and P. R. Bandaru, *Appl. Phys. Lett.* **99**(7), 072114 (2011).
- ¹²P. Pichanusakorn, Y. J. Kuang, C. Patel, C. W. Tu, and P. R. Bandaru, *Phys. Rev. B* **86**, 085314 (2012).
- ¹³Y. J. Kuang, K. M. Yu, R. Kudrawiec, A. V. Luce, M. Ting, W. Walukiewicz, and C. W. Tu, *Appl. Phys. Lett.* **102**(11), 112105 (2013).
- ¹⁴R. Kudrawiec, A. V. Luce, M. Gladysiewicz, M. Ting, Y. J. Kuang, C. W. Tu, O. D. Dubon, K. M. Yu, and W. Walukiewicz, *Phys. Rev. Appl.* **1**(3), 034007 (2014).
- ¹⁵A. Dobrovolsky, S. Sukritanon, Y. Kuang, C. W. Tu, W. M. Chen, and I. A. Buyanova, "Energy upconversion in GaP/GaN core/shell nanowires for enhanced near-infrared light harvesting," *Small* (published online).
- ¹⁶S. Filippov, S. Sukritanon, Y. Kuang, C. Tu, P. O. Å. Persson, W. M. Chen, and I. A. Buyanova, *Nano Lett.* **14**(9), 5264 (2014).
- ¹⁷E. Luna, M. Hopkinson, J. M. Ulloa, A. Guzman, and E. Munoz, *Appl. Phys. Lett.* **83**(15), 3111 (2003).
- ¹⁸M. Sopanen, H. P. Xin, and C. W. Tu, *Appl. Phys. Lett.* **76**(8), 994 (2000).
- ¹⁹Z. Z. Sun, S. F. Yoon, K. C. Yew, B. X. Bo, D. A. Yan, and T. Chih-Hang, *Appl. Phys. Lett.* **85**(9), 1469 (2004).
- ²⁰Y.-J. Kuang, S.-W. Chen, H. Li, S. K. Sinha, and C. W. Tu, *J. Vac. Sci. Technol. B* **30**(2), 02B121 (2012).
- ²¹A. J. Williamson, A. Zunger, and A. Canning, *Phys. Rev. B* **57**(8), R4253 (1998).
- ²²C. Karcher, K. Jandieri, B. Kunert, R. Fritz, M. Zimprich, K. Volz, W. Stolz, F. Gebhard, S. D. Baranovskii, and W. Heimbrodt, *Phys. Rev. B* **82**(24), 245309 (2010).
- ²³A. Dobrovolsky, J. E. Stehr, S. L. Chen, Y. J. Kuang, S. Sukritanon, C. W. Tu, W. M. Chen, and I. A. Buyanova, *Appl. Phys. Lett.* **101**, 163106 (2012).
- ²⁴H. P. Xin, K. L. Kavanagh, M. Kondow, and C. W. Tu, *J. Cryst. Growth* **201–202**, 419 (1999).

Strain engineering of quantum dots for long wavelength emission: Photoluminescence from self-assembled InAs quantum dots grown on GaAs(001) at wavelengths over 1.55 μm

K. Shimomura and I. Kamiya

Citation: [Applied Physics Letters](#) **106**, 082103 (2015); doi: 10.1063/1.4913443

View online: <http://dx.doi.org/10.1063/1.4913443>

View Table of Contents: <http://scitation.aip.org/content/aip/journal/apl/106/8?ver=pdfcov>

Published by the [AIP Publishing](#)

Articles you may be interested in

[Room temperature infrared photoresponse of self assembled Ge/Si \(001\) quantum dots grown by molecular beam epitaxy](#)

Appl. Phys. Lett. **96**, 233113 (2010); 10.1063/1.3446848

[The formation of self-assembled In As/Ga As quantum dots emitting at 1.3 \$\mu\text{m}\$ followed by photoreflectance spectroscopy](#)

J. Appl. Phys. **101**, 073518 (2007); 10.1063/1.2714686

[Long dephasing time in self-assembled InAs quantum dots at over 1.3 \$\mu\text{m}\$ wavelength](#)

Appl. Phys. Lett. **88**, 261907 (2006); 10.1063/1.2217156

[InAs self-assembled quantum dots grown on an InP \(311\)B substrate by molecular beam epitaxy](#)

J. Appl. Phys. **89**, 4186 (2001); 10.1063/1.1350616

[Self-assembled GaInNAs quantum dots for 1.3 and 1.55 \$\mu\text{m}\$ emission on GaAs](#)

Appl. Phys. Lett. **76**, 994 (2000); 10.1063/1.125917

The logo for Applied Physics Letters (AIP) is displayed in a white font against an orange background with a wavy, abstract pattern. The letters 'AIP' are large and bold, followed by a vertical bar and the words 'Applied Physics Letters' in a smaller font.

Meet The New Deputy Editors



Alexander A.
Balandin



Qing Hu



David L.
Price

Strain engineering of quantum dots for long wavelength emission: Photoluminescence from self-assembled InAs quantum dots grown on GaAs(001) at wavelengths over 1.55 μm

K. Shimomura^{a)} and I. Kamiya^{b)}

Toyota Technological Institute 2-12-1 Hisakata, Tempaku, Nagoya 468-8511, Japan

(Received 1 November 2014; accepted 11 February 2015; published online 23 February 2015)

Photoluminescence (PL) at wavelengths over 1.55 μm from self-assembled InAs quantum dots (QDs) grown on GaAs(001) is observed at room temperature (RT) and 4 K using a bilayer structure with thin cap. The PL peak has been known to redshift with decreasing cap layer thickness, although accompanying intensity decrease and peak broadening. With our strain-controlled bilayer structure, the PL intensity can be comparable to the ordinary QDs while realizing peak emission wavelength of 1.61 μm at 4 K and 1.73 μm at RT. The key issue lies in the control of strain not only in the QDs but also in the cap layer. By combining with underlying seed QD layer, we realize strain-driven bandgap engineering through control of strain in the QD and cap layers.

© 2015 AIP Publishing LLC. [<http://dx.doi.org/10.1063/1.4913443>]

Tuning the luminescence wavelength of self-assembled (SA) InAs quantum dots (QDs) grown by molecular beam epitaxy (MBE) to 1.3 μm and 1.55 μm has attracted great attention for telecommunication applications. While 1.3 μm emission has been accomplished from SA InAs QDs on GaAs(001),^{1,2} 1.55 μm emission has only been realized with use of InP substrates,^{3–5} or capping by GaAsSb.⁶ The emission wavelength of InAs QDs on GaAs(001) with GaAs cap had remained typically between 1.0 and 1.2 μm , and had been attributed to the strain in the QD in surrounded by lattice mismatched matrix. To redshift the emission, capping the InAs QDs with InGaAs layer instead of GaAs has been proposed.^{7–10} Two major effects of the InGaAs capping layer have been considered. The first is “strain reduction.”⁷ Because InGaAs has larger lattice constant than GaAs, capping by InGaAs reduces the strain of the QDs. The second is “mass transport.”¹¹ Nonuniformity in the strain field is induced within the InAs QDs, which leads to In migration and aggregation at the QD-cap interface during InGaAs layer growth. The In migration and aggregation increase the effective QD size and hence lowers the emission energy. Sun *et al.* have attributed the main effect of the capping layer, using InGaAs or InGaP of varied In contents, on the photoluminescence (PL) peak energy shift of InAs QDs to strain reduction rather than mass transport.¹⁰ They pointed out that the redshift is induced not only by the lower barrier height but also more due to the strain reduction of the QDs since InGaAs has larger lattice constant than GaAs. PL emission at 1.5 μm , at room temperature (RT), has been reported using 30% In InGaAs cap.¹² However, by increasing the In content of the capping layer, the lattice mismatch between the underlying buffer layer and the capping layer becomes larger, resulting in three dimensional (3D) growth of the capping layer.

According to former studies on the growth of InGaAs thin film on GaAs(001), it was found that the strain in the

InGaAs layer increases with increasing InGaAs thickness.^{13,14} Therefore, we deduced that a thin InGaAs capping layer should be effective in reducing the strain of InAs QDs on GaAs(001), thereby inducing further redshift in the PL emission wavelength of the QDs.

In addition, modifying the barrier layer with added features has also been shown to be effective for tuning the emission wavelength from InAs QDs. For instance, Ozaki *et al.* reported that the emission wavelength is redshifted by inserting a layer with small QDs between the layer with large QDs of concern, and the GaAs buffer layer grown on the substrate.¹⁵ In the present work, we show PL at wavelengths over 1.55 μm , even under cryogenic temperatures, from InAs QDs grown on GaAs(001) with modified barrier layers.

The samples were grown by MBE. After oxide removal at 600 °C, a 100 nm-thick undoped (u.d.) GaAs buffer layer is grown on semi-insulating (s.i.) GaAs(001) at a substrate temperature of 590 °C. Following 600 °C annealing of the u.d. GaAs buffer layer, the substrate temperature is lowered to 500 °C, at which reflection high-energy electron diffraction (RHEED) pattern changes from (2 × 4) to c(4 × 4) under As₄ flux (incorporation rate) of 1.0 ML/s. The InAs layer is grown on buffer layer at substrate temperature of 480 °C. Subsequently, the InAs QD layer is covered by GaAs with various thickness: 4, 9, 20, and 30 nm. The InAs growth rate is 0.021 ML/s and the As₄ flux is maintained at 1.0 ML/s. The formation of QDs is observed *in situ* by RHEED. The average height of the QDs observed by atomic force microscopy (AFM) is 6.2 nm. PL measurements are carried out at 4 K and RT using 780 nm light from a Ti:sapphire laser as excitation source at a power density of 5 W/cm².

To investigate the role of strain in the cap layer, InAs QDs directly covered by cap layer with varied thickness were grown. Figure 1 shows the PL spectra obtained from single 2.5 ML InAs QD layer covered by GaAs cap with thickness of 4, 9, 20, and 30 nm. The PL peak is redshifted with decreasing GaAs cap thickness. This result indicates that strain in the QDs can be controlled not only by the

^{a)}E-mail: sd12502@toyota-ti.ac.jp

^{b)}Author to whom correspondence should be addressed. Electronic mail: kamiya@toyota-ti.ac.jp

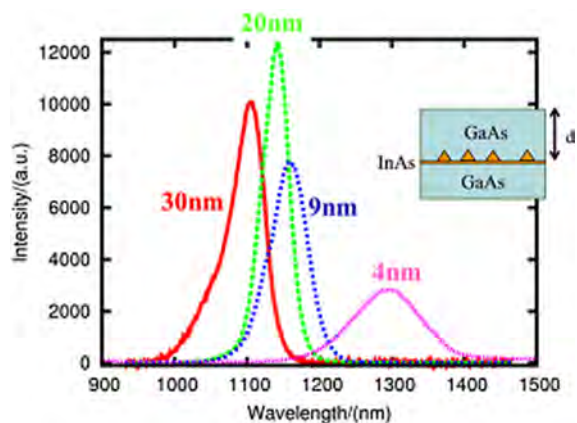


FIG. 1. 4 K PL spectra of single InAs QD layer grown on GaAs and capped by GaAs with various capping thickness (4 nm, 9 nm, 20 nm, and 30 nm) ($\lambda_{\text{ex}} = 780 \text{ nm}$ and 5 W/cm^2).

lattice constant of the capping layer but also by the cap thickness in the case of thin cap. In particular, a strong peak shift is observed when the cap thickness is reduced from 9 nm to 4 nm. This result indicates that the strain between the QDs and cap layer relaxed. However, the PL intensity also decreases and the full width at half maximum (FWHM) increases with decreasing cap thickness. It has been reported that during initial GaAs capping, InAs QDs are only partially covered and intermixing of Ga and In takes place.^{16–18}

We discuss the mechanisms of the peak shift with capping layer thickness by the following model. Without cap, the lattices of the relatively large InAs QDs are relaxed. At the early stage of capping, the lattices of the QDs are compressed by the cap layer which has a smaller lattice constant, and vice versa, the cap lattices are expanded by the QDs with a larger lattice constant. The strain energy between the QDs and the cap layer increases with the cap layer thickness. When the cap layer exceeds the critical thickness, strain relaxation of the cap layer, possibly accompanying Ga-In intermixing between the QDs and the cap layer, occurs thereby decreasing the strain energy. Both strain relaxation and intermixing induces the blueshift of the QD PL emission. This situation needs to be avoided for achieving $1.55 \mu\text{m}$ emission.

Another factor that needs to be considered is the unflatness of the cap layer. Since the QDs are not completely covered by the cap layer in the case of thin cap, strain distribution of the sample with thin cap is larger than that with thick cap. Therefore, the PL peak is broader with thinner cap. In addition, the carriers are likely to be captured by the non-radiative recombination centers at the surface in the case of the thin cap. Hence, the PL intensity from the 4 nm-thick capped QDs is weak.

Since the PL intensity is decreased, although the peak is redshifted, with decreasing cap thickness, we need to seek a way out from this dilemma. To achieve longer PL wavelength while increasing the intensity, we adopted a bilayered-QD structure, in which the second QD layer is grown on the cap, which also act as a spacer layer for covering the first (seed) QD layer. The QDs at the second layer are formed on top of the seed layer QDs due to the strain

induced in spacer layer by the seed QDs.¹⁹ Therefore, the first and second layer QDs are closely located allowing easy carrier transfer from the first to the second layer QDs, resulting in increased PL intensity from the second layer QDs. It has been reported that the QD height can be increased by this bilayer structure, but we point out that strain in the second layer can also be controlled by the seed layer in the bilayer system.¹⁹ Hence, this structure also provides us with the opportunity to further tune the emission wavelength on the second layer.

Figure 2 shows the sample structure that exhibited PL at peak wavelengths over $1.55 \mu\text{m}$ both at 4 K and RT using the bilayered-QD structure with thin cap. The first InAs layer is grown on a GaAs buffer layer. Subsequently, a 10 nm-thick GaAs spacer layer was deposited on the first InAs layer. Note that the use of GaAs in the spacer layer is the key for this bilayer system since the strain induced by the seed QDs is more likely to be accumulated on top of the seed QDs compared to InGaAs cap, and consequently, this enables the second QDs to form right above the seed layer QDs. The second InAs layer was grown followed by a 4 nm-thick $\text{In}_{0.19}\text{Ga}_{0.81}\text{As}$ cap for tuning the emission to longer wavelengths. The total amount of InAs deposited on the seed and the second layers are 2.0 and 2.8 ML, respectively. Higher size uniformity and longer emission wavelength have been reported to occur with increased amount of InAs on the second layer,¹⁹ in addition to larger QD heights.

Figure 3 shows the PL spectra obtained at 4 K and RT from the sample structure, as shown in Fig. 2. PL with an emission peak exceeding $1.7 \mu\text{m}$ is observed at RT. At 4 K, two peaks are observed. The peak at longer wavelength (around $1.6 \mu\text{m}$) is attributed to the emission from the second layer, while that at shorter wavelength (around $1.1 \mu\text{m}$) is due to the seed layer. The FWHM of the PL peak at around $1.6 \mu\text{m}$ from the second layer is broader than that at around $1.1 \mu\text{m}$ from the seed layer in agreement with the cap layer thickness dependence on the PL peak width, as shown in Fig. 1. From these results, we observe that the strain in the second layer QD is suppressed by the seed layer and cap layer thickness without increasing the In content of the capping layer. The use of QD bilayer system was already shown to allow control of the emission wavelength,^{15,20} but had not able to achieve $1.55 \mu\text{m}$ emission. Comparing these reports with our present result, we recognize that the key to realize emission at over $1.55 \mu\text{m}$ is suppressing the strain in the QDs by the cap layer.

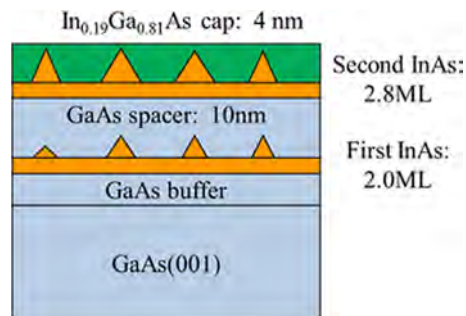


FIG. 2. The sample structure that exhibited luminescence at wavelength over $1.55 \mu\text{m}$.

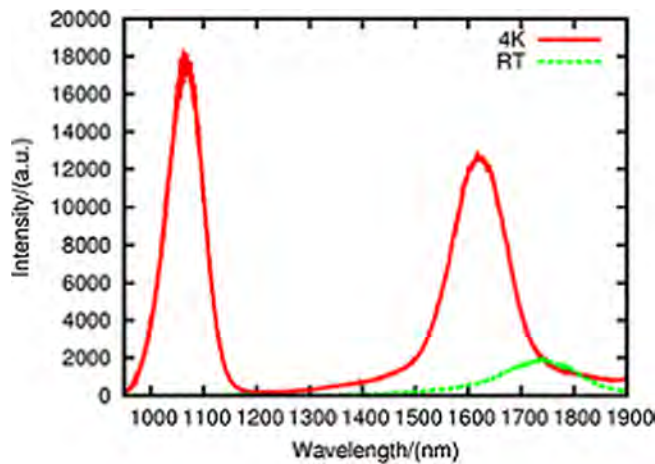


FIG. 3. 4 K and room temperature PL spectra of sample as shown in Fig. 2. PL with an emission peak exceeding $1.7 \mu\text{m}$ is observed at RT, while two peaks at around 1.1 and $1.6 \mu\text{m}$ are observed at 4 K ($\lambda_{\text{ex}} = 780 \text{ nm}$ and 5 W/cm^2).

The emission from the seed layer is not observed at RT, while the PL intensity from the second layer is weaker than that from the seed layer at 4 K. This result indicates that carrier transfer from the seed layer to the second layer QD involves thermal processes, although competing non-radiative processes exist. We also point out that the PL intensity at $1.61 \mu\text{m}$ at 4 K, shown in Fig. 3, is stronger than that from the single InAs QD layer directly covered by thin GaAs cap (4 nm) without the seed layer and spacer layer which is shown in Fig. 1. The PL intensity at such long wavelength is also increased using the bilayer system.²¹ The results of our temperature dependent PL measurement suggest that this is mainly due to carrier transfer from the seed QDs to the second QD layer. The details of this carrier transfer will be discussed in future publication. The increased carrier density in the second layer QDs results not only in increased radiative recombination but also possibly in reduced non-radiative recombination by filling of surface/interface states.

Non-radiative recombination via surface states may be further reduced by growing additional cap layer, while retaining the strain in the QDs, by alienating the QDs from the surface. The thickness of this extra cap layer needs to be determined from several other aspects as well: it needs to be thick enough that the QDs are thoroughly capped, but thin enough to allow vertical current flow, particularly if the QDs are to be applied to lasers operated by carrier injection. The actual design of the extra cap layer based on these criteria is underway.

We also point out that the fundamental concept of strain control described here is not limited to quantum dots, and can be applied to various structures and materials system. Thus, we expect strain control to play an important role in the preparation of advanced devices.

In conclusion, PL emission at wavelengths over $1.55 \mu\text{m}$ has been obtained from our strain-controlled bilayer structure. We find that the crucial issue for realizing such long wavelength emission is strain control, suppressing the strain in the QDs by the cap layer, in particular, that can only be achieved by simultaneously tuning the lattice constant of the capping layer and the cap thickness. The PL peak is

redshifted with decreasing cap thickness by the weaker strain suffered by the QDs, although the PL intensity decreases and the FWHM increases. PL emission at wavelengths over $1.55 \mu\text{m}$ as well as enhanced PL intensity has been obtained from our stacked InAs QD structure grown on GaAs(001). PL with an emission peak exceeding $1.7 \mu\text{m}$ is observed at RT, while two peaks at around 1.1 and $1.6 \mu\text{m}$ are observed at 4 K. The emission from the seed layer is not observed at RT, while the PL intensity from the seed layer is higher than that from the second layer at 4 K. It is suggested that thermally assisted carrier transfer from the seed layer to the second layer is involved. By this carrier transfer, the intensity at longer wavelength is increased. However, for further improving the PL intensity and peak width, further studies on strain control is underway. For instance, the cap needs to be thin enough to allow current flow vertically and thick enough that all QDs are thoroughly covered for laser structure that operates by current injection. From the present study, it has been seen that while the PL intensity increases, the emission wavelength is blueshifted with increasing thickness of the cap layer. Therefore, it is necessary to compensate the strain between the QDs and the cap layer using cap layer which has large lattice constants, i.e., high In content, for realizing long wavelength emission under increased cap thickness.

This work was supported by the Strategic Research Infrastructure Project, MEXT, Japan.

- ¹V. M. Ustinov, N. A. Maleev, A. E. Zhukov, A. R. Kovsh, A. Yu. Egorov, A. V. Lunev, B. V. Volovik, I. L. Krestnikov, Yu. G. Musikhin, N. A. Bert, P. S. Kop'ev, Zh. I. Alferov, N. N. Ledentsov, and D. Bimberg, *Appl. Phys. Lett.* **74**, 2815 (1999).
- ²K. Mukai, N. Ohtsuka, M. Sugawara, and S. Yamazaki, *Jpn. J. Appl. Phys., Part 2* **33**, L1710 (1994).
- ³S. Fréchengues, N. Bertru, V. Drouot, B. Lambert, S. Robinet, S. Loualiche, D. Lacombe, and A. Ponchet, *Appl. Phys. Lett.* **74**, 3356 (1999).
- ⁴C. Paranthoen, N. Bertru, O. Dehaese, A. Le Corre, S. Loualiche, B. Lambert, and G. Patriarche, *Appl. Phys. Lett.* **78**, 1751 (2001).
- ⁵M. Gendry, C. Monat, J. Brault, P. Regreny, G. Hollinger, B. Salem, G. Guillot, T. Benyattou, C. Bru-chevallier, G. Bremond, and O. Marty, *J. Appl. Phys.* **95**, 4761 (2004).
- ⁶H. Y. Liu, M. J. Steer, T. J. Badcock, D. J. Mowbray, M. S. Skolnick, F. Suarez, J. S. Ng, M. Hopkinson, and J. P. R. David, *J. Appl. Phys.* **99**, 046104 (2006).
- ⁷K. Nishi, H. Saito, S. Sugou, and J. S. Lee, *Appl. Phys. Lett.* **74**, 1111 (1999).
- ⁸D. Litvinov, H. Blank, R. Schneider, D. Gerthsen, T. Vallaitis, J. Leuthold, T. Passow, A. Grau, H. Kalt, C. Klingshirn, and M. Hetterich, *J. Appl. Phys.* **103**, 083532 (2008).
- ⁹K. Mukai and M. Sugawara, *Appl. Phys. Lett.* **74**, 3963 (1999).
- ¹⁰Z. Z. Sun, S. F. Yoon, W. K. Loke, and C. Y. Liu, *Appl. Phys. Lett.* **88**, 203114 (2006).
- ¹¹M. V. Maximov, A. F. Tsatsul'nikov, B. V. Volovik, D. S. Sizov, Yu. M. Shernyakov, I. N. Kaiander, A. E. Zhukov, A. R. Kovsh, S. S. Mikhrin, V. M. Ustinov, Zh. I. Alferov, R. Heitz, V. A. Shchukin, N. N. Ledentsov, D. Bimberg, Yu. G. Musikhin, and W. Neumann, *Phys. Rev. B* **62**, 16671 (2000).
- ¹²L. Seravalli, P. Frigeri, M. Minelli, P. Allegri, V. Avanzini, and S. Franchi, *Appl. Phys. Lett.* **87**, 063101 (2005).
- ¹³C. W. Snyder, B. G. Orr, and H. Munekata, *Appl. Phys. Lett.* **62**, 46 (1993).
- ¹⁴T. Sasaki, H. Suzuki, A. Sai, J. H. Lee, M. Takahashi, S. Fujikawa, K. Arafune, I. Kamiya, Y. Ohshita, and M. Yamaguchi, *Appl. Phys. Express* **2**, 085501 (2009).
- ¹⁵N. Ozaki, Y. Nakatani, S. Ohkouchi, N. Ikeda, Y. Sugimoto, K. Asakawa, E. Clarke, and R. A. Hogg, *J. Cryst. Growth* **378**, 553 (2013).

- ¹⁶J. M. García, G. Medeiros-Ribeiro, K. Schmidt, T. Ngo, J. L. Feng, A. Lorke, J. Kotthaus, and P. M. Petroff, *Appl. Phys. Lett.* **71**, 2014 (1997).
- ¹⁷I. Kamiya, I. Tanaka, and H. Sakaki, *J. Cryst. Growth* **201/202**, 1146 (1999).
- ¹⁸F. Ferdos, S. Wang, Y. Wei, A. Larsson, M. Sadeghi, and Q. Zhao, *Appl. Phys. Lett.* **81**, 1195 (2002).
- ¹⁹I. Mukhametzhanov, R. Heitz, J. Zeng, P. Chen, and A. Madhukar, *Appl. Phys. Lett.* **73**, 1841 (1998).
- ²⁰E. Clarke, P. Spencer, E. Harbord, P. Howe, and R. Murray, *J. Phys.: Conf. Ser.* **107**, 012003 (2008).
- ²¹C. Y. Ngo, S. F. Yoon, H. Tanoto, H. K. Hui, D. R. Lim, V. Wong, and S. J. Chua, *J. Cryst. Growth* **323**, 167 (2011).

Femtosecond upconverted photocurrent spectroscopy of InAs quantum nanostructures

Yasuhiro Yamada, David M. Tex, Itaru Kamiya, and Yoshihiko Kanemitsu

Citation: *Applied Physics Letters* **107**, 013905 (2015); doi: 10.1063/1.4926569

View online: <http://dx.doi.org/10.1063/1.4926569>

View Table of Contents: <http://scitation.aip.org/content/aip/journal/apl/107/1?ver=pdfcov>

Published by the *AIP Publishing*

Articles you may be interested in

[Competitive carrier interactions influencing the emission dynamics of GaAsSb-capped InAs quantum dots](#)
Appl. Phys. Lett. **101**, 231109 (2012); 10.1063/1.4769431

[Photocurrent spectroscopy of intersubband transitions in GaInAsN/\(Al\)GaAs asymmetric quantum well infrared photodetectors](#)

J. Appl. Phys. **112**, 084502 (2012); 10.1063/1.4754573

[Properties of the SiO₂- and SiN_x-capped GaAs\(100\) surfaces of GaInAsN/GaAs quantum-well heterostructures studied by photoelectron spectroscopy and photoluminescence](#)

Appl. Phys. Lett. **99**, 102105 (2011); 10.1063/1.3634046

[Structural and optical properties of vertically stacked triple InAs dot-in-well structure](#)

J. Appl. Phys. **103**, 096107 (2008); 10.1063/1.2921266

[Carrier relaxation in InGaN/GaN quantum wells with nanometer-scale cluster structures](#)

Appl. Phys. Lett. **85**, 1371 (2004); 10.1063/1.1784033

The advertisement features a dark blue background with three panels. The first panel shows an AFM with the text 'Frustrated by old technology?'. The second panel shows a tombstone with 'RIP My Old AFM 1994-2015' and the text 'Is your AFM dead and can't be repaired?'. The third panel shows a man shouting with the text 'Sick of bad customer support?'. To the right, a large text block reads 'It is time to upgrade your AFM' followed by 'Minimum \$20,000 trade-in discount for purchases before August 31st' and 'Asylum Research is today's technology leader in AFM'. The Oxford Instruments logo and tagline 'The Business of Science' are at the bottom right, along with the email 'dropmyoldAFM@oxinst.com'.

Femtosecond upconverted photocurrent spectroscopy of InAs quantum nanostructures

Yasuhiro Yamada,¹ David M. Tex,^{1,2} Itaru Kamiya,³ and Yoshihiko Kanemitsu^{1,2,a)}

¹*Institute for Chemical Research, Kyoto University, Uji, Kyoto 611-0011, Japan*

²*Japan Science and Technology Agency, CREST, Kyoto University, Uji, Kyoto 611-0011, Japan*

³*Toyota Technological Institute, Nagoya, Aichi 468-8511, Japan*

(Received 8 January 2015; accepted 28 June 2015; published online 8 July 2015)

The carrier upconversion dynamics in InAs quantum nanostructures are studied for intermediate-band solar-cell applications via ultrafast photoluminescence and photocurrent (PC) spectroscopy based on femtosecond excitation correlation (FEC) techniques. Strong upconverted PC-FEC signals are observed under resonant excitation of quantum well islands (QWIs), which are a few monolayer-thick InAs quantum nanostructures. The PC-FEC signal typically decays within a few hundred picoseconds at room temperature, which corresponds to the carrier lifetime in QWIs. The photoexcited electron and hole lifetimes in InAs QWIs are evaluated as functions of temperature and laser fluence. Our results provide solid evidence for electron–hole–hole Auger process, dominating the carrier upconversion in InAs QWIs at room temperature. © 2015 AIP Publishing LLC.

[<http://dx.doi.org/10.1063/1.4926569>]

The quantum confinement of electrons in nanostructures enhances dynamical electron-electron interactions, thereby leading to many-body processes such as quantized Auger recombination (AR) and carrier multiplication (CM).^{1–6} In AR process, the recombination energy of an electron–hole (e–h) pair is transferred to a third electron or hole which results in a carrier with large kinetic energy, i.e., a so-called hot carrier.^{5,6} In CM process, a single high-energy photon creates two or more e–h pairs.^{2–6} Unique solar-cell concepts based on these AR and CM processes in nanostructures have attracted considerable attention because of the high theoretical conversion-efficiency limit beyond that of conventional single p–n junction solar cells. For instance, confined photocarriers in semiconductor nanostructures embedded in bulk crystals can be efficiently extracted above the potential barrier via upconversion through multi-carrier interactions, which can assist in realizing efficient intermediate-band solar cells (IBSCs).^{7–10}

InAs quantum nanostructures such as quantum dots (QDs) have tremendous potential for future SC applications. In the case of IBSCs, low-energy infrared photons can be absorbed by InAs nanostructures embedded in GaAs, and two-step excitation of charge carriers to higher energy levels enables enhanced photocurrent (PC).^{9–12} While the efficiency of this upconversion process is a core requirement for IBSCs, the currently achieved efficiencies are far from that needed for practical SC applications. We found that disk-like InAs nanostructures embedded in AlGaAs, which are referred to as quantum well islands (QWIs), exhibit efficient upconverted PC, and that the large efficiency of the PC cannot be explained by conventional thermal and two-step photoabsorption processes.^{9,10} Although it has been suggested that the enhanced PC is caused by upconversion of photocarriers through the AR process, no direct evidence has been presented experimentally,^{8,9} and the detailed mechanism

remains unclear. It is necessary to clarify the physical mechanism of the efficient carrier upconversion in QWIs to realize efficient IBSCs. In addition, an evaluation of electron and hole lifetimes to gain a thorough understanding of the upconversion process in InAs nanostructures can aid in arriving at the design principles required for the development of highly efficient SCs based on quantum nanostructures.^{12,13}

Time-resolved spectroscopy is one of the most important techniques to investigate the dynamical behaviors of photocarriers that determine the photovoltaic characteristics of SCs.^{14,15} Popular techniques based on femtosecond photoluminescence (PL) and transient absorption (TA) have been used to investigate the ultrafast response of photocarriers in various kinds of SC materials including nanostructures.^{16,17} Further, time-resolved PC measurement is a powerful tool for analyzing carrier dynamics.^{18–21} In particular, the PC measurement directly probes the charge carriers extracted from the nanostructures in IBSCs, and thus, we can obtain essential information about the carrier generation and extraction processes. However, the ultrafast response of PC measurements has not been fully investigated thus far when compared with PL and TA spectroscopies because the fabrication of complex device structures such as the Auston switch is necessary for PC measurements.^{22,23}

In this letter, we investigated the ultrafast upconverted PC dynamics in InAs quantum nanostructures by femtosecond excitation correlation (FEC) spectroscopy to unveil the carrier upconversion processes. We observed efficient upconverted PC and PC-FEC signals upon excitation of shallow InAs QWIs. The room-temperature PC-FEC decay time was typically ~ 100 ps, depending on the excitation laser fluence. We evaluated the photoexcited electron and hole lifetimes based on PL- and PC-FEC measurements as functions of temperature and laser fluence. The strong dependence of the carrier lifetime on laser fluence provides solid evidence that the three-carrier AR process dominates the carrier upconversion process in InAs QWIs at room temperature.

^{a)}E-mail: kanemitsu@scl.kyoto-u.ac.jp

The sample was prepared by molecular beam epitaxy under conditions similar to those described in our previous publication.⁹ A nominally undoped structure was grown on top of a semi-insulating GaAs (001) substrate and a GaAs buffer. The sample contains an AlGaAs layer with an InAs layer nominally two monolayer (ML) thick. It was confirmed that the PC signals from this layer are dominant and therefore this layer will be discussed in detail. It is known that one ML wetting layers (WLs) and QDs are self-organized in the thin InAs layer. In addition, disk-like InAs nanostructures (QWIs) that are a few MLs high are also formed.^{8,9,24} The sample structure and the energy diagram are schematically illustrated in Fig. 1(a).²⁵ For this sample, we have determined the resonance energy of InAs QD, 2 ML-QWI, 3 ML-QWI, and WL in AlGaAs barrier by means of conventional PL and PC spectroscopy.^{8–10} For instance, the resonance energy for 2-ML QWIs at room temperature is 1.37 eV, and QD resonance energy widely ranges below 1.25 eV.⁹ (For more details of this sample, see Ref. 25.)

For PC measurements, an open-rectangular-shaped gold electrode was evaporated on the GaAs top layer and excitation laser beam was focused on the sample surface surrounded by the electrode [see Fig. 1(b)]. Indium metal was attached on the GaAs substrate as a bottom electrode. For ultrafast time-resolved PC measurements, we applied the FEC technique, which is often used in PL spectroscopy.^{26,27} A positive bias voltage of 0.2 V was applied to the indium electrode to gain sufficient PC. We confirmed that the FEC profile is independent of the bias voltage. The excitation laser source was a wavelength-tunable femtosecond laser system (pulse duration: 250 fs and repetition rate: 200 kHz). As shown in Fig. 1(b), two femtosecond pulses, modulated at different frequencies ($f_1 = 391$ Hz and $f_2 = 326$ Hz), were focused on the sample surface. The FEC signal was detected by a lock-in amplifier with a differential frequency of $|f_1 - f_2|$ as a function of the delay time between the two pulses, τ . The FEC signal arises due to the temporal overlap of the PC

induced by the first and second pulses via a nonlinear response, as schematically described in Fig. 1(c). For a carrier lifetime of $\tau_c \ll \tau$, there is no temporal overlap between the carriers induced by the first and second pulses, and thus, the FEC signal intensity is zero. Conversely, when $\tau_c \sim \tau$, a temporal overlap between carriers generated by the first and second pulses occurs, and this overlap results in a variation in the total PC intensity because of the nonlinear interaction between the carriers. If we assume that the PC intensity is proportional to the carrier density and shows weak nonlinearity on excitation intensity, the FEC signal intensity is approximately written as²⁵

$$\text{FEC} \propto n(N_1, t)N_2. \quad (\text{for } N_1 \ll N_2). \quad (1)$$

Here, $n(N, t)$ represents the carrier density at time t after the initial carrier density N induced by photoexcitation at time 0. N_1 and N_2 denote the initial photocarrier densities generated by the first and second pulses. Note that the FEC signal intensity is zero when $n(N, t)$ depends linearly on N , and positive (negative) FEC signal corresponds to sublinear (superlinear) excitation-intensity dependence, as schematically shown in the inset of Fig. 1(c). According to Eq. (1), the FEC profile corresponds to the population dynamics of carriers that contribute to the PC.

For the temperature dependence of the PC-FEC profile, the excitation photon energy was tuned to the QWI resonance energy at each temperature. PL signals were detected by an InGaAs photodiode, and PL-FEC signals were obtained in a similar manner with PC-FEC. The time-resolutions of PC- and PL-FEC measurements were approximately 250 fs, which is determined by the duration of the excitation laser pulse.

Figure 2(a) shows the PC-FEC profiles at room temperature under different excitation photon energies. The PC-FEC profiles are normalized and offset for clarity. The first and second pulse fluences were 3.2 and $20 \mu\text{J}/\text{cm}^2$, respectively.

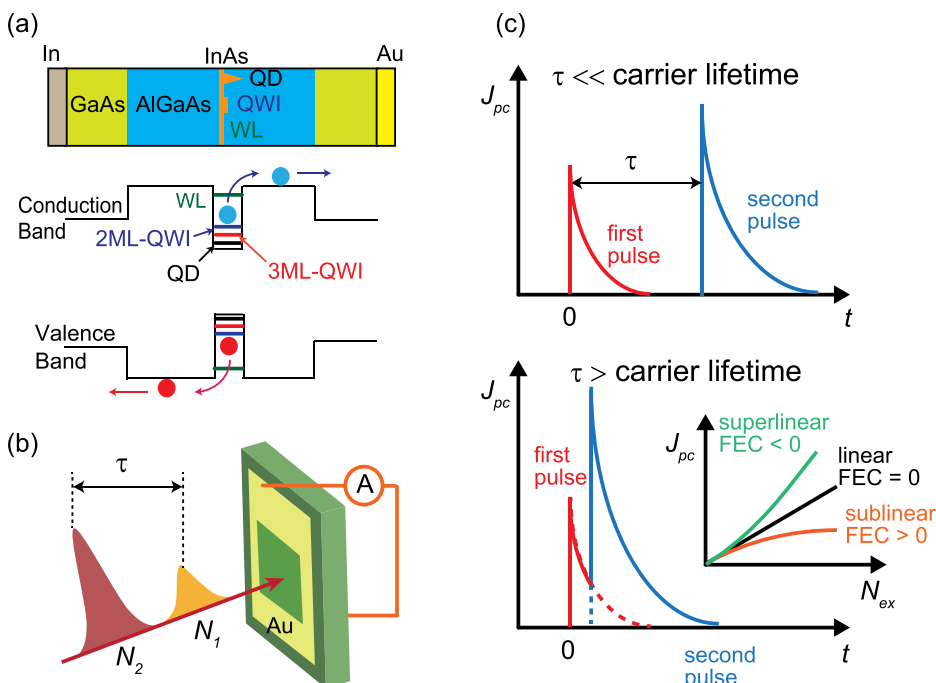


FIG. 1. (a) Schematic illustration of sample structure and energy diagram. Electrons and holes photoexcited in QWIs are upconverted to AlGaAs barrier layers and contribute to PC. (b) Experimental setup for PC-FEC measurements. (c) Schematic of FEC signal interpretation. Decay dynamics of carrier density under excitation by first and second pulses are shown for $\tau \ll$ carrier lifetime and $\tau >$ carrier lifetime. The inset shows excitation-fluence dependence of PC. The sign of FEC signal is determined whether PC superlinearly or sublinearly depends on excitation-fluence according to Eq. (1).

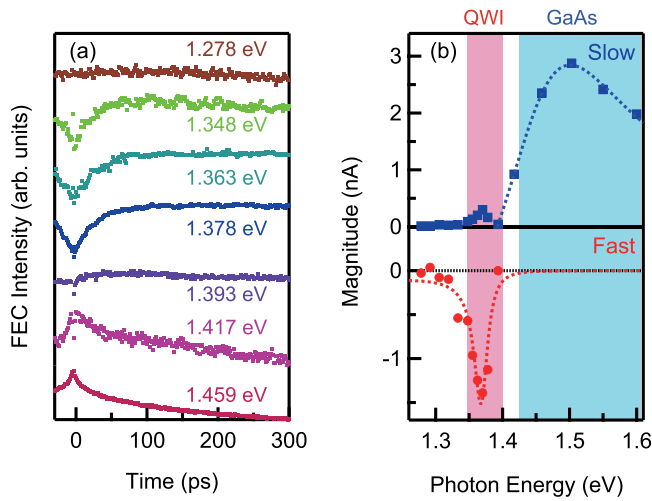


FIG. 2. (a) Excitation photon energy dependence of PC-FEC profiles. (b) Magnitudes of slow and fast components as a function of excitation photon energy.

Above the excitation energy of the GaAs substrate (around 1.42 eV), the FEC signal exhibits a positive slow-decay component. The decay profile is non-exponential and well reproduced by a double exponential function, $I_{s1} \exp(-t/\tau_{s1}) + I_{s2} \exp(-t/\tau_{s2})$. The mean lifetime, $(I_{s1}\tau_{s1} + I_{s2}\tau_{s2}) / (I_{s1} + I_{s2})$, was ~ 700 ps and almost independent of the excitation photon energy above 1.42 eV. The positive FEC signal indicates a sublinear excitation-fluence dependence of the PC. We observed strong PC and PC-FEC signals under excitation at 1.37 eV, which correspond to the 2 ML-QWI resonance.^{8,9} Here, we remark that we observed considerably smaller PC and PC-FEC signals under resonant excitation of QDs (> 1.25 eV) compared with those of QWIs, thereby indicating that efficient upconversion occurs in QWIs. Therefore, we hereafter focus on the QWI.

Under QWI resonant excitation, a fast and negative decay component appears. The fast decay time, τ_f , was on the timescale of several tens of picoseconds, depending on the laser fluence; this is discussed later. We fitted the experimental data by a triple exponential function, $I_{s1} \exp(-t/\tau_{s1}) + I_{s2} \exp(-t/\tau_{s2}) + I_f \exp(-t/\tau_f)$ for $t > 0$, where $I_f < 0$, $I_{s1} > 0$, and $I_{s2} > 0$. The magnitudes of the slow ($I_{s1} + I_{s2}$) and fast (I_f) components are shown in Fig. 2(b). The positive slow-decay component is mainly observed above the bandgap energy of GaAs (1.42 eV). Thus, the slow-decay time corresponds to the photocarrier lifetime in GaAs. The fast-decay component has a peak at 1.37 eV, which corresponds to the QWI resonance energy,⁹ thereby indicating that the fast-decay time is the photocarrier lifetime in QWIs. The negative FEC intensity appearing at the excitation energy of the QWIs indicates a superlinear excitation-fluence dependence of the PC, which can be caused by the upconversion of carriers to GaAs through the AR process.

Since the AR rate is sensitive to the number of photoexcited carriers,^{1,5,6} we studied the excitation-fluence dependence of the PC-FEC profiles under resonant excitation of QWIs, as shown in Fig. 3(a). The PC-FEC profiles are normalized and offset for clarity. Here, the excitation photon energy was tuned to 1.37 eV, which is the resonance energy of the QWI. The second pulse fluence was fixed at $20 \mu\text{J}/\text{cm}^2$. The

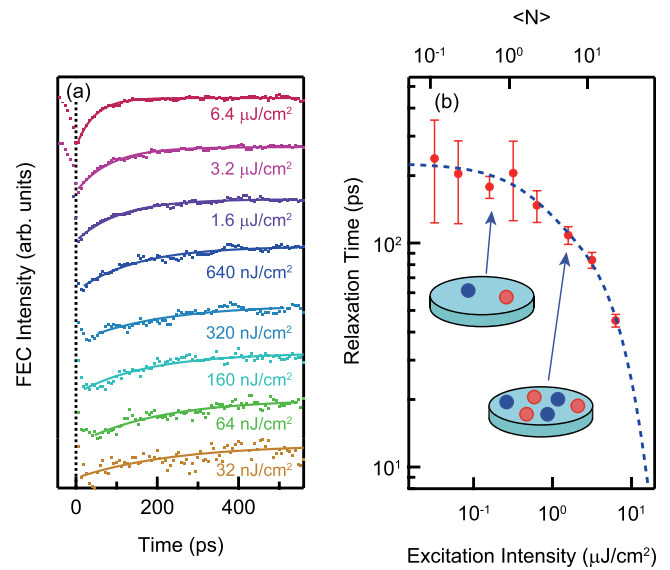


FIG. 3. (a) Excitation-laser-fluence dependence of PC-FEC profiles. (b) Relaxation time as a function of excitation laser fluence. The estimated carrier density per QWI is represented along the top x-axis.

time constant of the fast-decay component is plotted as a function of the first pulse fluence in Fig. 3(b). Here, we roughly estimated the mean number of e-h pairs photogenerated in a QWI, $\langle N \rangle$. We used a QWI with a diameter of 100 nm, and we assumed that 1% of the excitation light was absorbed (assuming almost bulk-like absorption). Below a laser fluence of $500 \text{ nJ}/\text{cm}^2$, the relaxation time is nearly constant at ~ 200 ps. This means that multi-carrier interactions are negligible and indicates that the relaxation time at low excitation densities represents the intrinsic carrier lifetime in QWIs. This is consistent with the estimated number of $\langle N \rangle < 1$. Above $500 \text{ nJ}/\text{cm}^2$, the relaxation time decreases with increasing excitation intensity. Under high-fluence excitation, a large number of electrons and holes are photogenerated in a QWI, and the AR process dominates the carrier recombination dynamics. Such excitation-density dependent carrier dynamics cannot be accounted for by two-step two-photon absorption process because two-step two-photon absorption process occurs within the pulse duration and never affect the carrier dynamics after pulse excitation. It should be noted that the assessment of the carrier lifetime in QWIs plays a key role for the design of devices based on InAs nanostructures.

The PC can arise from both electrons and holes. Thus, it is necessary to verify whether the observed lifetime corresponds to that of electrons or holes. For this purpose, we compared the PC-FEC results with the PL-FEC results. The PL from the QWI was observed only at low temperatures below 100 K because of thermal quenching. The excitation photon energy was 1.49 eV, which is close to the QWI resonance energy (1.46 eV) at low temperatures below 100 K. The PL was monitored at 1.43 eV. The normalized PL- and PC-FEC profiles at 12 K are plotted in Fig. 4(a). The excitation fluences were 5 and $60 \mu\text{J}/\text{cm}^2$ for the first and second pulses, respectively. The PL-FEC profile shows a single decay component with a lifetime of ~ 100 ps. On the other hand, the PC-FEC profile exhibits two components. The fast PC component is similar to the PL decay profile and the

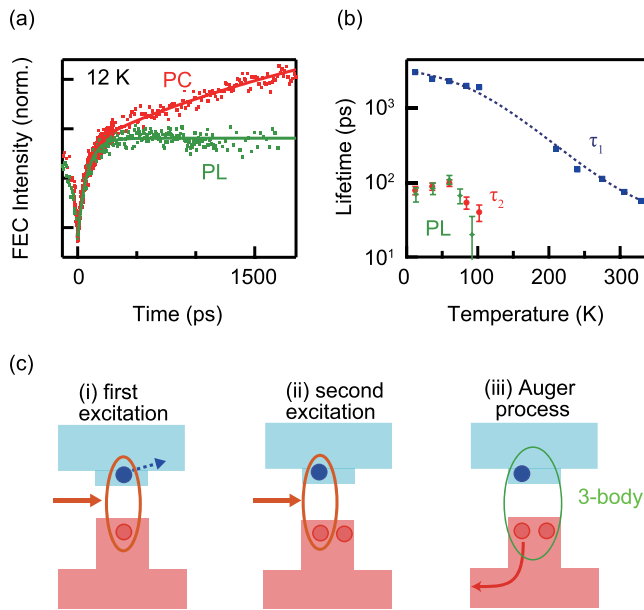


FIG. 4. (a) PC- and PL-FEC profiles at 12 K. (b) Temperature dependence of the decay times (τ_1 , τ_2 , and PL lifetime). (c) Schematics of room-temperature relaxation and upconversion processes involving photoexcited electrons and holes. (i) An electron photoexcited by the first pulse is thermally upconverted to the barrier and a photoexcited hole is left behind in the QWI. (ii) Via the second-pulse excitation, an electron-hole-hole state is realized in the QWI. (iii) The hole is upconverted to the barrier via the three-carrier Auger process.

slow decay is of the order of nanoseconds. Note that the directions of the left and right axes in Fig. 4(a) are opposite, i.e., the PL-FEC signal is plotted upside down. Hence, PL-FEC has a positive decaying component, while PC-FEC shows a negative component. This is because AR process causes a reduction of the PL efficiency, and therefore, PL shows the sublinear excitation-fluence dependence, which results in the positive FEC signals.

The fast (τ_1) and slow (τ_2) PC lifetimes and the PL lifetime are plotted as a function of temperature in Fig. 4(b). The fast PC lifetime τ_1 increases monotonically with decreasing temperature and reaches a value of 3 ns at 12 K. On the other hand, τ_2 is about 100 ps below 50 K and decreases at higher temperatures. The temperature dependence of τ_2 shows good agreement with that of the PL lifetime. It is noteworthy that the FEC signal intensity is strongly reduced at around 200 K because of the weak nonlinear response. At high temperatures, the upconverted PC exhibits sublinear power dependence while a superlinear power dependence appears below 200 K.²⁸

The PL lifetime reflects that of the minority (short-lived) carriers in the radiative two-carrier (electron-hole) recombination process. We assume that τ_2 represents the lifetime of photoexcited electrons in QWIs because the electron's effective mass is less than that of the hole.²⁹ The thermal activation energy derived from the temperature dependence of the PL lifetime and τ_2 , which is ~ 20 meV,³⁰ is consistent with the expected barrier height for electrons in QWIs,^{31,32} thereby suggesting that τ_2 is determined by the thermal upconversion of electrons to the barrier at high temperatures above 60 K, in which temperature region τ_2 decreases with temperature. Consequently, τ_1 is attributed to the hole

lifetime in QWIs. Because of the very short electron lifetime and the relatively long hole lifetime at high temperatures, we consider that the photoexcited electron is extracted above the potential barrier immediately after the e-h pair generation, leaving behind a photoexcited hole in the QWI. When a second e-h pair is excited in the QWI, an electron-hole-hole state is realized, which leads to the carrier upconversion through the three-carrier AR process, as illustrated in Fig. 4(c).

Based on the above reasoning, we conclude that the room-temperature upconversion rate is dominated by the hole lifetime in InAs QWIs. The very small PL efficiency at room temperature indicates that the radiative recombination rate is negligibly small. We speculate that the long hole lifetime is due to it being trapped at nonradiative recombination centers in QWIs or its migration into deep InAs QDs through the WLs.³³ The observed carrier lifetimes in QWIs are considerably smaller than the reported carrier lifetimes in QDs despite the relatively higher QWI upconversion efficiencies.^{9,34,35} This indicates that QWIs exhibit a large AR coefficient, and thus, the upconversion efficiency can be improved by suppressing the nonradiative relaxation rate. This suppression can be achieved by fabricating high-quality InAs layers and ensuring the spatial separation of QWIs and QDs.

Finally, it is worth mentioning the potential application of QWIs into IBSCs. We have previously estimated the maximum conversion efficiency of the AlGaAs single junction SC (28.2%) including ideal QWIs under 1-sun illumination as 35.7% under assumption of 100% AR upconversion efficiency in the QWI.⁹ However, an upconversion efficiency of only 2% is currently achieved in our samples for moderate continuous-wave excitation (1.37 eV, 0.5 W/cm², corresponding to about 42 sun) at room temperature.⁹ Since the upconversion rate is dominated by the hole lifetime in QWIs, IBSCs based on the QWI concept will become practical after improvement of the hole lifetime by at least one order of magnitude.

In conclusion, we investigated the ultrafast carrier upconversion dynamics in InAs QWIs embedded in Al_xGa_{1-x}As by PC-FEC. We estimated the hole lifetime at room temperature in a QWI to be ~ 200 ps, which is reduced under high-density excitation due to the AR process. The large difference between the electron and hole lifetimes suggests that the three-body upconversion process (electron-hole-hole) plays a dominant role in carrier upconversion through the AR process at room temperature. Our results provide insights into the physics underlying the carrier dynamics in quantum nanostructures, which would enable us to deduce suitable design principles for efficient IBSCs utilizing carrier upconversion processes.

This work was supported by the Sumitomo Electric Industries Group CSR Foundation, JST-CREST, and KAKENHI (25247052).

¹V. I. Klimov, A. A. Mikhailovsky, D. W. McBranch, C. A. Leatherdale, and M. G. Bawendi, *Science* **287**, 1011 (2000).

²R. D. Schaller and V. I. Klimov, *Phys. Rev. Lett.* **92**, 186601 (2004).

- ³R. J. Ellingson, M. C. Beard, J. C. Johnson, P. R. Yu, O. I. Micic, A. J. Nozik, A. Shabaev, and Al. L. Efros, *Nano Lett.* **5**, 865 (2005).
- ⁴A. Ueda, K. Matsuda, T. Tayagaki, and Y. Kanemitsu, *Appl. Phys. Lett.* **92**, 233105 (2008).
- ⁵Y. Kanemitsu, *Acc. Chem. Res.* **46**, 1358 (2013).
- ⁶J. T. Stewart, L. A. Padilha, W. K. Bae, W.-K. Koh, J. M. Pietryga, and V. I. Klimov, *J. Phys. Chem. Lett.* **4**, 2061 (2013).
- ⁷A. Luque and A. Martí, *Phys. Rev. Lett.* **78**, 5014 (1997).
- ⁸D. M. Tex and I. Kamiya, *Phys. Rev. B* **83**, 081309(R) (2011).
- ⁹D. M. Tex, I. Kamiya, and Y. Kanemitsu, *Phys. Rev. B* **87**, 245305 (2013).
- ¹⁰D. M. Tex, I. Kamiya, and Y. Kanemitsu, *Sci. Rep.* **4**, 4125 (2014).
- ¹¹A. Martí, E. Antolín, C. R. Stanley, C. D. Farmer, N. López, P. Díaz, E. Cánovas, P. G. Linares, and A. Luque, *Phys. Rev. Lett.* **97**, 247701 (2006).
- ¹²Y. Okada, T. Morioka, K. Yoshida, R. Oshima, Y. Shoji, T. Inoue, and T. Kita, *J. Appl. Phys.* **109**, 024301 (2011).
- ¹³K. Nishikawa, Y. Takeda, T. Motohiro, D. Sato, J. Ota, N. Miyashita, and Y. Okada, *Appl. Phys. Lett.* **100**, 113105 (2012).
- ¹⁴Y. Yamada and Y. Kanemitsu, *Appl. Phys. Lett.* **101**, 133907 (2012).
- ¹⁵Y. Yamada, T. Nakamura, M. Endo, A. Wakamiya, and Y. Kanemitsu, *J. Am. Chem. Soc.* **136**, 11610 (2014).
- ¹⁶F. Rossi and T. Kuhn, *Rev. Mod. Phys.* **74**, 895 (2002).
- ¹⁷J. Shah, *Ultrafast Spectroscopy of Semiconductors and Semiconductor Nanostructures*, Springer Series in Solid-State Sciences (Springer, New York, 1999).
- ¹⁸A. Solbrand, H. Lindstrom, H. Rensmo, A. Hagfeldt, S. E. Lindquist, and S. Sodergren, *J. Phys. Chem. B* **101**, 2514 (1997).
- ¹⁹N. M. Gabor, Z. Zhong, K. Bosnick, and P. L. McEuen, *Phys. Rev. Lett.* **108**, 087404 (2012).
- ²⁰L. Q. Phuong, M. Okano, Y. Yamada, A. Nagaoka, K. Yoshino, and Y. Kanemitsu, *Appl. Phys. Lett.* **103**, 191902 (2013).
- ²¹M. Freitag, T. Low, F. N. Xia, and P. Avouris, *Nat. Photon.* **7**, 53 (2013).
- ²²C. H. Lee, *Picosecond Optoelectronic Devices* (Academic Press, Inc., New York, 1984).
- ²³L. Prechtel, L. Song, S. Manus, D. Schuh, W. Wegscheider, and A. W. Holleitner, *Nano Lett.* **11**, 269 (2011).
- ²⁴R. Heitz, T. R. Ramachandran, A. Kalburge, Q. Xie, I. Mukhametzhanov, P. Chen, and A. Madhukar, *Phys. Rev. Lett.* **78**, 4071 (1997).
- ²⁵See supplementary material at <http://dx.doi.org/10.1063/1.4926569> for sample characteristics and FEC measurement principle.
- ²⁶D. von der Linde and J. Kuhl, *J. Lumin.* **24–25**, 675 (1981).
- ²⁷Y. Miyauchi, K. Matsuda, and Y. Kanemitsu, *Phys. Rev. B* **80**, 235433 (2009).
- ²⁸D. M. Tex, T. Ihara, I. Kamiya, and Y. Kanemitsu, *Jpn. J. Appl. Phys., Part 1* **53**, 05FV01 (2014).
- ²⁹C. E. Pryor and M.-E. Pistol, *Phys. Rev. B* **72**, 205311 (2005).
- ³⁰The thermal activation energy for electrons was estimated using Arrhenius plots of τ_2 and τ_{PL} .
- ³¹The QWI confinement energy (~ 230 meV) is the sum of the electron and hole barrier heights. Due to momentum conservation, the energy is differently distributed. Based on the electron and hole effective masses in InAs ($m_e^* = 0.026m_0$ and $m_h^* = 0.04m_0$) according to Ref. 32, we can calculate the electron barrier height as ~ 14 meV.
- ³²M. Fox, *Optical Properties of Solids* (Oxford University Press, Inc., New York, 2010).
- ³³W.-H. Chang, T. M. Hsu, C. C. Huang, S. L. Hsu, C. Y. Lai, N. T. Yeh, T. E. Nee, and J.-I. Chyi, *Phys. Rev. B* **62**, 6959 (2000).
- ³⁴D. Sato, J. Ota, K. Nishikawa, Y. Takeda, N. Miyashita, and Y. Okada, *J. Appl. Phys.* **112**, 094305 (2012).
- ³⁵T. E. J. Campbell-Ricketts, N. A. J. M. Kleemans, R. Nötzel, A. Yu. Silov, and P. M. Koenraad, *Appl. Phys. Lett.* **96**, 033102 (2010).

Direct observation of strain in InAs quantum dots and cap layer during molecular beam epitaxial growth using in situ X-ray diffraction

Kenichi Shimomura, Hidetoshi Suzuki, Takuo Sasaki, Masamitsu Takahashi, Yoshio Ohshita, and Itaru Kamiya

Citation: [Journal of Applied Physics](#) **118**, 185303 (2015); doi: 10.1063/1.4935456

View online: <http://dx.doi.org/10.1063/1.4935456>

View Table of Contents: <http://scitation.aip.org/content/aip/journal/jap/118/18?ver=pdfcov>

Published by the [AIP Publishing](#)

Articles you may be interested in

[Investigation of single-layer/multilayer self-assembled InAs quantum dots on GaAs_{1-x}Sb_x/GaAs composite substrates](#)

J. Appl. Phys. **118**, 094303 (2015); 10.1063/1.4929639

[The effect of InGaAs strain-reducing layer on the optical properties of InAs quantum dot chains grown on patterned GaAs\(100\)](#)

J. Appl. Phys. **111**, 014306 (2012); 10.1063/1.3675271

[In situ mask designed for selective growth of InAs quantum dots in narrow regions developed for molecular beam epitaxy system](#)

Rev. Sci. Instrum. **78**, 073908 (2007); 10.1063/1.2756624

[Molecular beam epitaxy growth of novel double-layer InAs quantum dot structures and their optical properties](#)

J. Vac. Sci. Technol. B **23**, 1240 (2005); 10.1116/1.1926308

[InAs self-assembled quantum dots grown on an InP \(311\)B substrate by molecular beam epitaxy](#)

J. Appl. Phys. **89**, 4186 (2001); 10.1063/1.1350616

The logo for AIP APL Photonics is displayed. It features the letters 'AIP' in a large, white, sans-serif font on the left, followed by a vertical line and the words 'APL Photonics' in a smaller, white, sans-serif font on the right. The background is a dark red with a bright yellow sunburst effect in the upper right corner.

APL Photonics is pleased to announce
Benjamin Eggleton as its Editor-in-Chief



Direct observation of strain in InAs quantum dots and cap layer during molecular beam epitaxial growth using *in situ* X-ray diffraction

Kenichi Shimomura,¹ Hidetoshi Suzuki,² Takuo Sasaki,³ Masamitsu Takahashi,³ Yoshio Ohshita,¹ and Itaru Kamiya^{1,a)}

¹Toyota Technological Institute, 2-12-1 Hisakata, Tempaku, Nagoya 468-8511, Japan

²Faculty of Engineering, University of Miyazaki, 1-1 Gakuen Kibanadai-nishi, Miyazaki 889-2192, Japan

³Quantum Beam Science Center, Japan Atomic Energy Agency, Koto 1-1-1, Sayo-cho, Hyogo 679-5148, Japan

(Received 7 August 2015; accepted 28 October 2015; published online 12 November 2015)

Direct measurements on the growth of InAs quantum dots (QDs) and various cap layers during molecular beam epitaxy are performed by *in situ* X-ray diffraction (XRD). The evolution of strain induced both in the QDs and cap layers during capping is discussed based on the XRD intensity transients obtained at various lattice constants. Transients with different features are observed from those obtained during InGaAs and GaAs capping. The difference observed is attributed to In-Ga intermixing between the QDs and the cap layer under limited supply of In. Photoluminescence (PL) wavelength can be tuned by controlling the intermixing, which affects both the strain induced in the QDs and the barrier heights. The PL wavelength also varies with the cap layer thickness. A large redshift occurs by reducing the cap thickness. The *in situ* XRD observation reveals that this is a result of reduced strain. We demonstrate how such information about strain can be applied for designing and preparing novel device structures. © 2015 AIP Publishing LLC.

[<http://dx.doi.org/10.1063/1.4935456>]

I. INTRODUCTION

Application of quantum dots (QDs) to optoelectronic devices has attracted great attention ever since the concept of QDs was proposed.¹ One of the potential applications that utilizes the unique electronic properties of QDs has been emitter/detector of photons at the telecommunication wavelengths of 1.3 or 1.55 μm . Self-assembled (SA) InAs QDs grown epitaxially on GaAs by molecular beam epitaxy (MBE) or metal-organic chemical vapor deposition (MOCVD) have been one of the strongest candidates. Since the bandgaps of InAs and GaAs are approximately 0.35 and 1.42 eV, respectively, at room temperature (RT), and from the reported ideal band alignment,² it looks straightforward and easy to tune the luminescence/absorption wavelength to 1.5 μm or even to 2 μm by bandgap engineering. However, it has been reported that the strain induced at the InAs-GaAs interface alters both the band alignment and the bandgap of these materials.³ The luminescence wavelength of InAs QDs on GaAs(001) with GaAs cap had remained typically between 1.0 and 1.2 μm even when the size and the shape of the QDs were controlled. Studies have been performed to quantitatively account for this limitation in the wavelength tunability for the InAs QDs.⁴

The luminescence wavelength from SA InAs QDs has been reported to redshift when capped by InGaAs instead of GaAs.⁵⁻⁸ In the case of InGaAs cap, the luminescence wavelength is also varied by its In content,^{8,9} and photoluminescence (PL) emission at 1.5 μm at RT has been reported using 30% In InGaAs, i.e., $\text{In}_{0.3}\text{Ga}_{0.7}\text{As}$, cap.¹⁰ These results can be understood by the lowering of the barrier height with increasing In content in the InGaAs cap, leading to lower

quantized energies. However, it has been reported that the luminescence wavelength can be further redshifted by eliminating the cap.¹¹ According to bandgap engineering, if the QDs are exposed directly to vacuum, the barrier height should be higher than having any semiconductor materials, and result in blueshift of the luminescence compared to having GaAs as the cap. In fact, Sun *et al.*, by comparing QDs capped by InGaAs or InGaP of varied In contents, showed that the main cause of the PL peak redshift of InAs QDs is strain reduction rather than lowered barrier height of the cap or exchange of materials.⁸ They pointed out that while redshift can be induced by lowering the barrier height, strain reduction of the QDs by changing the lattice constant of the barrier plays a far more significant role. InGaAs has a lattice constant larger than that of GaAs, therefore induces less strain on InAs. These results have led the society to realize the importance of strain control.

Although the strain in the QDs and consequently their emission wavelengths have been discussed in connection to the lattice constants of the cap layer, information about the strain in the QDs and the cap layer during growth has been limited since it is not easy to perform direct measurement on buried structures. Reflection high-energy electron diffraction (RHEED)¹²⁻¹⁵ has been one of the most popular techniques for *in situ* MBE growth monitoring. With RHEED, the atomic arrangements of the growth surfaces have been extensively studied, but it is difficult, if not impossible, to gain information about the subsurface on an atomic scale. On the other hand, our previous work using *in situ* X-ray diffraction (XRD) revealed that strain in buried layers can evolve as lattice-mismatched overlayers are grown.^{16,17} Hence, it is imperative to follow and understand how the cap layer grows and also what influence it has on the underlying layers for controlling the emission wavelength from InAs QDs.

^{a)}Author to whom correspondence should be addressed. Electronic mail: kamiya@toyota-ti.ac.jp

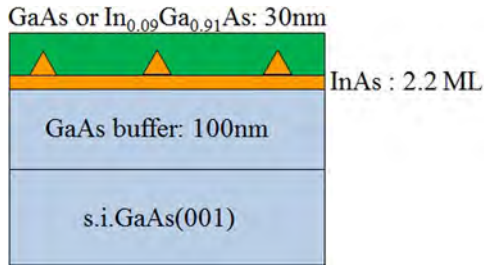


FIG. 1. The fundamental structure of the samples used in the present XRD studies. An InAs layer 2.2 ML in thickness is grown on a GaAs buffer, and subsequently covered by a cap layer of GaAs, InGaAs, or a combination of the two.

In situ monitoring by XRD is a powerful tool for studying the growth mechanisms not only on the surface but also on the subsurface layers.^{18–21} Besides, XRD is one of the very few techniques that can observe lattice strain on an atomic scale. The structural properties, including internal strain and chemical composition, which cannot be determined by electron diffraction nor scanning-probe microscopy, can be revealed by X-ray techniques.^{22–25} In fact, *in situ* XRD measurements have not only been successfully employed for the study of strain during InAs growth^{18–21} but also for GaAs capping on InAs QDs.^{18,20} We hence performed *in situ* XRD measurements during GaAs and InGaAs cap layer growth on InAs QDs for understanding the influence of the strain on the PL emission wavelength.

II. EXPERIMENTS

The experiments were performed at SPring-8 (BL11XU), Japan, using a MBE-X-ray diffractometer (MBE-XRD) system. After oxide removal at 600 °C, a 100-nm-thick undoped (u.d.) GaAs buffer layer was grown on semi-insulating (s.i.) GaAs(001) at a substrate temperature of 550 °C. Following 570 °C annealing of the u.d. GaAs buffer layer, the substrate temperature was lowered to 480 °C, at which RHEED pattern changes from (2 × 4) to c(4 × 4) under an As₄ beam equivalent pressure of 3.0 × 10^{−4} Pa. The InAs layer was grown on the buffer layer at a substrate temperature of 470 °C at a growth rate of 0.017 ML/s. The X-rays 10 keV in energy with an incident angle of 0.2° were reflected by the (220) planes and monitored by a charge coupled device (CCD) detector during the InAs QD and cap layer growth. The total amount of InAs deposition for the growth of QDs was either 2.2 ML, and the 30-nm-thick GaAs or In_{0.09}Ga_{0.91}As cap layers were grown (Fig. 1). The cap layer growth rate was about

0.05 nm/s. A two-dimensional reciprocal space map (2D-RSM) at the vicinity of 220 diffraction spot could be obtained in about 8 s. The average height of the surface QDs observed by atomic force microscopy (AFM) is 3.6 nm.

III. RESULTS AND DISCUSSIONS

Figure 2 shows typical XRD CCD images obtained from InAs QDs with a total deposition of 2.2 ML InAs (a) before and after capping by (b) 6 nm, (c) 12 nm, or (d) 30 nm GaAs. The vertical axis represents the relative lattice constant, defined as the in-plane lattice constant normalized by that of bulk GaAs

$$a_{R[110]} = \frac{a_{\text{InGaAs}[110]}}{a_{\text{GaAs}[110]}}, \quad (1)$$

where $a_{\text{InGaAs}[110]}$ is the lattice constant of InAs QDs and the (In)GaAs cap layer along [110] and $a_{\text{GaAs}[110]}$ is that of bulk GaAs. The $a_{R[110]}$ of the InAs bulk and 9% In InGaAs (In_{0.09}Ga_{0.91}As) are 1.072 and 1.006, respectively. The XRD signals collected for 1.01 ≤ $a_{R[110]}$ < 1.08 are selectively displayed to focus on the signals arising from the strained layer.

The horizontal axis represents the outgoing angle α normalized by the critical angle for total reflection of X-ray α_c . The intensity variation along α is due to generalized optical functions, including the interference effects of the incident and totally-reflected X-rays.²² While a sharp maximum is attained at α_c for a scatterer located exactly at the surface, the peak position is shifted to a lower angle with increasing vertical position of the scatterers above the surface. This trend for the peak is recognizable in Fig. 2(a), where the gradient of the lattice constant along the growth direction within an uncapped QD results in the peak shift correlated with the relative lattice constant. In other words, higher relative lattice constants tend to be observed at lower α , i.e., closer to the apex of the QDs. With increasing GaAs cap thickness, the XRD intensities decrease. The XRD signals are hardly observed from the relative lattice constants 1.01 ≤ $a_{R[110]}$ < 1.08 after capping the QDs by 30-nm-thick GaAs.²⁶

In this study, we focus on the XRD intensity transients from relative lattice constants partitioned in 0.01 step to investigate the evolution of the strain in both the QDs and cap layer during growth. The XRD intensities from relative lattice constants sectioned by 0.01, such as those between 1.01 and 1.02, 1.02 and 1.03, and so forth, are integrated and plotted as a function of the growth time as shown in

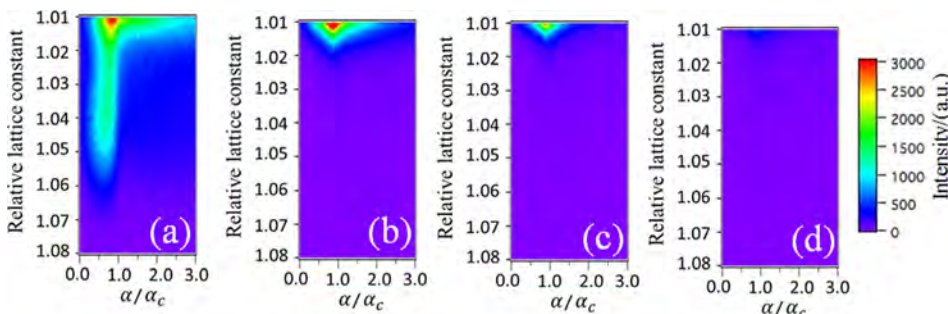


FIG. 2. XRD CCD images (around (220)) of InAs QDs with total deposition of 2.2 ML (a) before and after growing cap layers of (b) 6 nm, (c) 12 nm, or (d) 30-nm-thick GaAs.

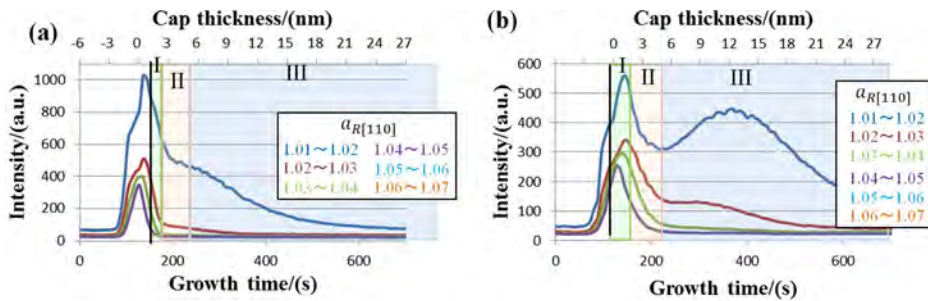


FIG. 3. Integrated XRD intensity transients observed from various relative lattice constants during InAs QD layer and (a) GaAs and (b) $\text{In}_{0.09}\text{Ga}_{0.91}\text{As}$ cap growth. Black line indicates the end of InAs growth and the beginning of GaAs or $\text{In}_{0.09}\text{Ga}_{0.91}\text{As}$ cap layer growth. Green, pink, and blue region correspond to stages I, II, and III, respectively.

Fig. 3(a). The black vertical line indicates the end of InAs growth and the beginning of GaAs cap layer growth. In the early stage of cap layer growth, the intensities from $1.01 \leq a_{R[110]} < 1.03$ increase. In contrast, those from $a_{R[110]} \geq 1.04$ decrease as soon as the cap layer growth starts. These results are in agreement with the previous *in situ* XRD results during GaAs cap growth.²¹ With further growth, the intensities from all lattice constants decrease monotonously with GaAs cap thickness. The rate of decrease in the intensities becomes smaller after capping by 4 nm-thick GaAs which is comparable to the average surface QD height, as observed by AFM, suggesting that the cap layer has covered the QDs completely. It has been reported that below sufficient cap thickness, the QDs remain partly uncapped, forming a pit-and-mound structure.^{27–29}

Figure 3(b) shows the integrated XRD intensity transients during InAs and 9% In InGaAs ($\text{In}_{0.09}\text{Ga}_{0.91}\text{As}$) cap growth. In the early stage of cap growth, the intensities from small lattice constants increase as was the case with GaAs cap. After this initial stage, the intensities from all lattice constants first decrease, then the intensity from $a_{R[110]} \sim 1.01$ increases between cap thickness of 4 and 12 nm, and decreases again with increasing InGaAs cap thickness. In addition, the decrease in the XRD intensity from various $a_{R[110]}$ during InGaAs cap growth is slower than that during GaAs cap growth. We believe this is because the strain in the QDs is smaller when capped with InGaAs instead of GaAs, which accounts for the redshift of emission wavelength of the QDs.

To understand the growth mechanisms of capping, we divide the XRD intensity transients into three stages as shown in Figs. 3(a) and 3(b).

(Stage I) The intensities from small lattice constants increase, whereas those from large lattice constants decrease during both GaAs and InGaAs cap growth.

(Stage II) The intensities from all lattice constants decrease.

(Stage III) The rate of decrease in intensities becomes smaller during GaAs cap growth, and the intensity from $a_{R[110]} \sim 1.01$ increases during InGaAs cap growth.

Based on these *in situ* XRD observations, we discuss the growth mechanisms of the cap layer as illustrated in Fig. 4. Before capping (Fig. 4(a)), it has been reported that the QD lattice constants spatially vary and larger lattices appear with increasing QD size from RHEED and XRD observations.^{21,30} In the early stage of cap layer growth, the intensities from small ($1.01 \leq a_{R[110]} < 1.03$) relative lattice constants increase, whereas those from large lattice constants decrease with both GaAs and InGaAs caps. In addition, the

increase in XRD intensity from small relative lattice constant lasts longer for InGaAs capping due to the difference in the lattice constants between InGaAs and GaAs. These results suggest that the lattices of the QDs are compressed by the cap layer. This is supported by the observation by Saito *et al.*¹¹ where unburied QDs exhibited a large PL redshift

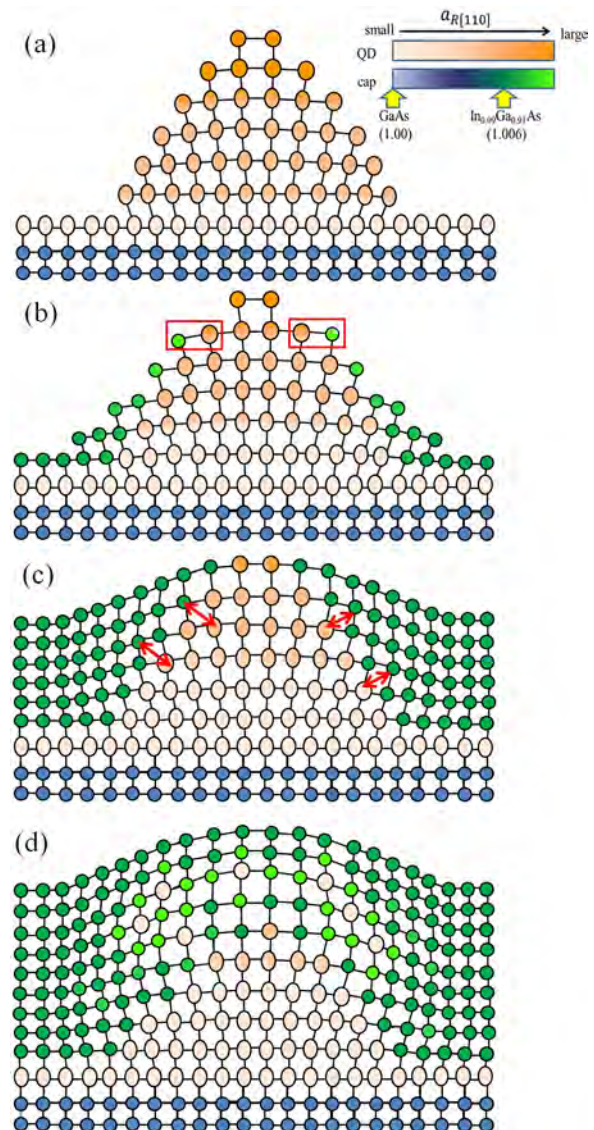


FIG. 4. Schematic illustration of InAs QDs and cap layer during the cap layer growth: (a) before growth, (b) partially covered, (c) fully covered, and (d) excessively covered. When partially covered, the QD lattices are compressed by the cap layer. In return, the cap layer lattices are expanded by the QDs. When excessively covered, the cap layer lattices are expanded due to In-Ga intermixing during capping.

with respect to the buried. In return, the lattices of the cap layer are expanded by the QDs (Fig. 4(b)). The elastic strain energy per atom E is given by

$$E = \frac{V}{2} C_{11} (\epsilon_{xx}^2 + \epsilon_{yy}^2 + \epsilon_{zz}^2) + \frac{V}{2} C_{44} (\epsilon_{xy}\epsilon_{yz} + \epsilon_{yz}\epsilon_{zx} + \epsilon_{zx}\epsilon_{xy}) + VC_{12} (\epsilon_{xx}\epsilon_{yy} + \epsilon_{yy}\epsilon_{zz} + \epsilon_{zz}\epsilon_{xx}), \quad (2)$$

where V is the equilibrium volume, C_{ij} are cubic elastic constants, and ϵ_{ij} are elements of strain tensor. Ga-As bond has a larger elastic constant than In-As bond as shown in Table I.³¹ In the absence of shear strain ϵ_{ij} ($i \neq j$),³¹ the strain components are

$$\epsilon_{xx} = \epsilon_{yy} = \frac{a_{R[110]} - \alpha_{eq}}{\alpha_{eq}}, \quad \epsilon_{zz} = \frac{a_{R[001]} - \alpha_{eq}}{\alpha_{eq}}, \quad (3)$$

where α_{eq} is the equilibrium lattice constant of the unstrained cap or QD layer, and $a_{R[001]}$ is the lattice constant along [001] normalized by that of bulk GaAs. The elastic strain energy E_{inter} at the interface of the QDs and the cap layer, which is depicted by the red squares in Fig. 4(b), is defined as

$$E_{inter} = (E_{(In)GaAs} + E_{InAs})/2, \quad (4)$$

which is the average of elastic strain energy of the InAs QD and (In)GaAs cap lattices. E_{inter} is minimized when $a_{R[110]}$ and $a_{R[001]}$ at the interface with GaAs cap are 1.032 and 1.031, and those with $\text{In}_{0.09}\text{Ga}_{0.91}\text{As}$ cap are 1.036 and 1.037, respectively. Hence, the (In)GaAs cap layer lattices are expanded and the QD lattices are compressed, resulting in the increase in XRD intensities from $1.01 \leq a_{R[110]} < 1.03$ in the early stage of cap layer growth.

With further capping, the cap layer grows preferentially on the wetting layer rather than on the QDs in order to suppress the increasing strain energy. The out-of-plane lattices of the QDs are not compressed since the QDs are not completely covered. On the other hand, with increasing cap layer thickness, all in-plane lattices of the QDs are compressed by the cap layer, and the expanded cap layer lattices shown in Fig. 4(b) begin to regain the original cap layer lattice constant. Therefore, the XRD intensities from all lattice constants decrease as cap layer growth proceeds in stage II.

Eventually, the QDs are completely covered by the cap layer as shown in Fig. 4(c). Here, the out-of-plane lattices are also strained, resulting in rapid increase in strain energy accumulated in the QDs. To reduce this rapidly increasing strain energy, In-Ga intermixing and/or In segregation may also occur between the QDs and the cap layer (Fig. 4(d)), consequently expanding the cap layer lattices. Here, In-Ga intermixing means the mixing of In and Ga atoms between the QDs and cap layer, whereas In segregation describes the

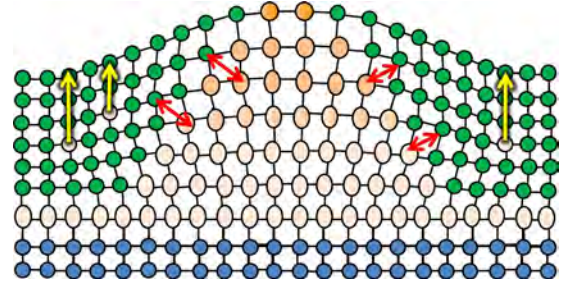


FIG. 5. Schematic illustration of In-Ga intermixing and in segregation defined in this report. Red arrows indicate In-Ga intermixing in which In and Ga atoms mix between the QDs and cap layer. Yellow arrows indicate In segregation in which In atoms diffuse to surface.

diffusion of In atoms in the cap layer to the surface as shown by the yellow arrows in Fig. 5.

To clarify the dominant mechanism that explains the experimental results, we further studied the evolution of the lattices during growth of modulated cap layers. The structures of the modulated cap layers are shown in Figs. 6(a) and 6(b). The thickness 4 nm of the first cap layer corresponds to the end of stage II, during which the intensities from all lattice constants decrease after the initial intensity increase from $1.01 \leq a_{R[110]} < 1.03$ in both GaAs and $\text{In}_{0.09}\text{Ga}_{0.91}\text{As}$ cap in stage I (Figs. 3(a) and 3(b)). By further depositing 26 nm cap layer of different In content, the total thickness reaches 30 nm, which corresponds to the thickness in stage III, when intensities from all lattice constants gradually decrease. Figures 7(a) and 7(b) show the XRD intensity transients during 4 nm-thick $\text{In}_{0.09}\text{Ga}_{0.91}\text{As}$ followed by 26 nm-thick GaAs cap (Fig. 6(a)) and 4 nm-thick GaAs followed by 26 nm-thick $\text{In}_{0.09}\text{Ga}_{0.91}\text{As}$ cap growth (Fig. 6(b)), respectively. The XRD intensities from almost all lattice constants decrease monotonously with increasing cap layer thickness in the case of 4 nm-thick GaAs followed by 26 nm-thick InGaAs cap. This trend is similar to that during the unmodulated 30 nm-thick GaAs cap layer growth. In contrast, the intensities from $a_{R[110]} \geq 1.04$ decrease with cap layer thickness, while those from $a_{R[110]} \sim 1.01$ increase, and decrease again during 4 nm-thick $\text{In}_{0.09}\text{Ga}_{0.91}\text{As}$ followed by 26 nm-thick GaAs cap growth as was the case with unmodulated 30 nm-thick $\text{In}_{0.09}\text{Ga}_{0.91}\text{As}$. The relative lattice constant of GaAs is $a_{R[110]} = 1.00$, and that of $\text{In}_{0.09}\text{Ga}_{0.91}\text{As}$ is $a_{R[110]} \sim 1.0065$. The intensity at $a_{R[110]} \sim 1.01$ should increase if In segregates to the surface terminated with either GaAs or $\text{In}_{0.09}\text{Ga}_{0.91}\text{As}$, and more readily with the latter. However,

TABLE I. Elastic constants of bulk GaAs and InAs.³¹

	C11	C12	C44
	(10^{11} dyne/cm)		
GaAs	12.03	5.70	5.20
InAs	8.53	4.90	3.14

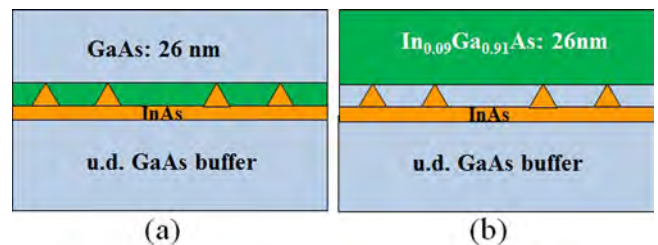


FIG. 6. The sample structures with modulated cap layers. (a) 4 nm-thick $\text{In}_{0.09}\text{Ga}_{0.91}\text{As}$ followed by 26 nm-thick GaAs cap and (b) 4 nm-thick GaAs followed by 26 nm-thick $\text{In}_{0.09}\text{Ga}_{0.91}\text{As}$ cap are grown on InAs QDs.

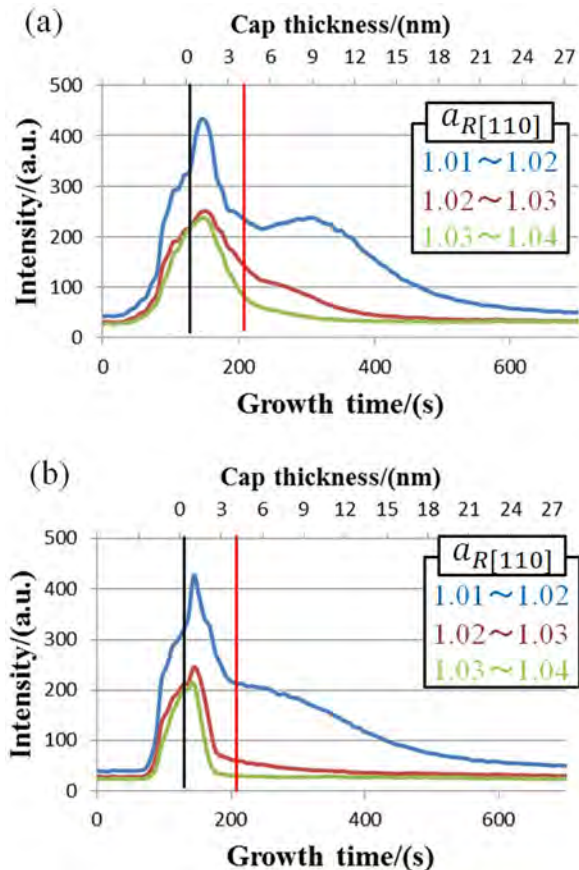


FIG. 7. Integrated XRD intensity transients from various relative lattice constants during growth of InAs QD layer and modulated (a) 4 nm-thick $\text{In}_{0.09}\text{Ga}_{0.91}\text{As}$ followed by 26 nm-thick GaAs cap or (b) 4 nm-thick GaAs followed by 26 nm-thick $\text{In}_{0.09}\text{Ga}_{0.91}\text{As}$ cap.

while we observe increase in the intensity at $a_{R[110]} \sim 1.01$ during growth of 26 nm-thick GaAs on 4 nm-thick $\text{In}_{0.09}\text{Ga}_{0.91}\text{As}$ (Fig. 6(a)), we do not observe increase during growth of 26 nm-thick $\text{In}_{0.09}\text{Ga}_{0.91}\text{As}$ on 4 nm-thick GaAs not only at $a_{R[110]} \sim 1.01$ but at any of the lattice constants (Fig. 6(b)). Therefore, surface segregation of In cannot account for the results.

In contrast, In-Ga intermixing at the InAs-cap interface, followed by In diffusion in the cap, can explain the XRD transients. In this case, the cap layer lattices near the interface between the QDs and cap layer, rather than the surface, are expanded. Once again, since $\text{In}_{0.09}\text{Ga}_{0.91}\text{As}$ ($a_{R[110]} = 1.006$) has a lattice constant larger than GaAs ($a_{R[110]} = 1.0$), increase in the intensity from $a_{R[110]} \sim 1.01$ is readily observed during InGaAs cap growth due to intermixing, but not with GaAs cap.

Further evidence that supports In-Ga intermixing being the dominant process can be found in the unmodulated InGaAs capping transients (Fig. 3(b)). After the growth of 12 nm-thick $\text{In}_{0.09}\text{Ga}_{0.91}\text{As}$ cap, the layer includes an equivalent of 3.8 ML InAs and 38.4 ML GaAs. Since the amount of InAs deposition for QD growth is 2.2 ML, the average InAs content in the cap layer and the QD layer added together is 13.5% at the cap thickness of 12 nm. The relative lattice constant of 13.5% In InGaAs ($\text{In}_{0.135}\text{Ga}_{0.865}\text{As}$) is $a_{R[110]} \sim 1.01$. This deficiency in In may account for the gradual decrease in

the intensity from $a_{R[110]} \sim 1.01$ beyond 12 nm of $\text{In}_{0.09}\text{Ga}_{0.91}\text{As}$ cap thickness even if In-Ga intermixing occurs.

The same argument can be applied to the unmodulated GaAs capping (Fig. 3(a)). The average InAs content in the cap layer and the QD layer added together becomes 13.5% at the cap thickness of approximately 4 nm. It is seen in Fig. 3(a) that the intensity from $a_{R[110]} \sim 1.01$ does not increase beyond 4 nm of GaAs cap thickness.

As discussed above, it is suggested that the strain in the QDs increases with increasing cap layer thickness, inducing In-Ga intermixing, based on *in situ* XRD observation during cap layer growth. Here, the relation between the cap layer thickness and PL emission wavelength is studied. Figure 8(a) shows the PL results at 4 K from InAs QDs covered by 7% In InGaAs ($\text{In}_{0.07}\text{Ga}_{0.93}\text{As}$) cap of various thickness. Red, green, blue, and pink lines describe the results obtained from those with cap thickness of 4, 9, 20, and 30 nm, respectively. The PL emission is redshifted with decreasing InGaAs cap thickness. This result suggests that strain in the QDs can be controlled not only by the lattice constant of the cap layer but also by the cap thickness in the case of thin cap. In particular, a large redshift is observed when the cap thickness is reduced from 9 to 4 nm. These results are in agreement with the previous work on PL emission from QDs covered by GaAs of various thicknesses as shown in Fig. 8(b).³² This redshift is induced by decreasing the strain in the QDs and/or In-Ga intermixing between the QDs and cap layer, as observed from *in situ* XRD measurements. The PL peak lies

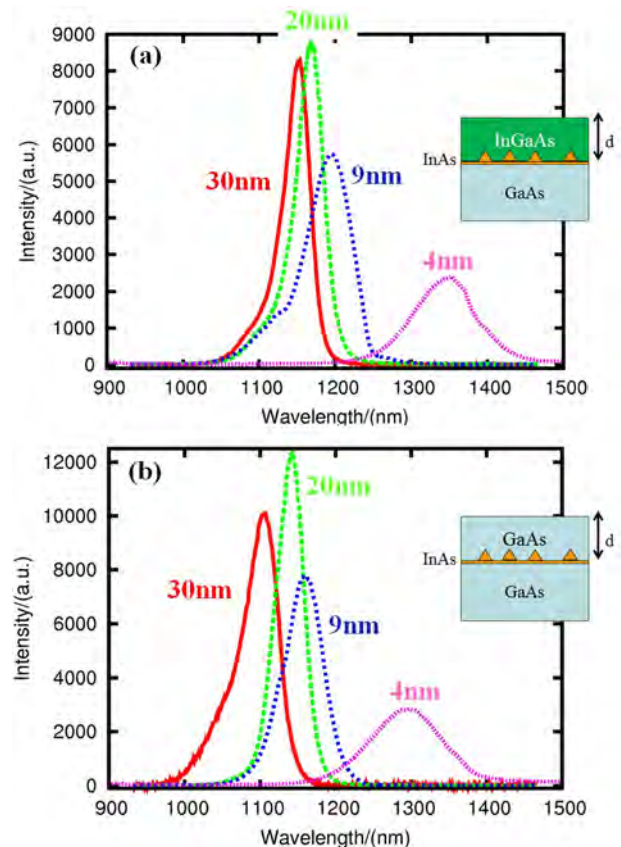


FIG. 8. 4 K PL spectra of a single InAs QD layer grown on GaAs and capped by (a) $\text{In}_{0.07}\text{Ga}_{0.93}\text{As}$ and (b) GaAs of various thicknesses (4 nm, 9 nm, 20 nm, and 30 nm).³² ($\lambda_{\text{ex}} = 780 \text{ nm}$, 5 W/cm^2).

at about $1.35\ \mu\text{m}$ with 4 nm-thick $\text{In}_{0.07}\text{Ga}_{0.93}\text{As}$ cap at 4 K, and further PL redshift of over 200 nm is reported when 23% In InGaAs ($\text{In}_{0.23}\text{Ga}_{0.77}\text{As}$) cap is used instead.¹⁰ By preparing a thin InGaAs cap with high In content, PL emission at wavelength over $1.55\ \mu\text{m}$, at cryogenic or RT, should be possible. Using thin cap in a QD bilayer structure, in which smaller seed QDs are inserted between the larger QDs of concern and buffer layer, we have indeed demonstrated PL emission at wavelength over $1.55\ \mu\text{m}$ at both 4 K and RT.²⁹ However, the PL intensity decreases and the peak width measured by full width at half maximum (FWHM) increases with decreasing cap thickness. As discussed above, it has been reported that during initial GaAs cap layer growth, InAs QDs are only partially covered and intermixing of Ga and In takes place actively.^{27,29–32} Surface states formed on such surfaces tend to capture the carriers generated in the device, resulting in enhanced nonradiative recombination. The rate of carriers being captured by such sites is likely to increase with decreasing cap thickness. In addition, the spatial variation of the strain in the sample with thin cap is larger than that with thick cap since the QDs are only partially covered by the cap layer. Therefore, the PL peak FWHM increases with decreasing cap thickness. For enhancing the PL intensity and narrowing peak width simultaneously, further studies on strain control are warranted inclusive of those by *in situ* XRD.

IV. CONCLUSIONS

The evolution of strain induced in the QDs and cap during the cap layer growth has been studied using *in situ* XRD. Strain in the QDs is found to increase with increasing cap thickness in both GaAs and 9% In InGaAs cap. In the early stage of the cap layer growth, the intensities from small lattices increase, whereas those from large lattices decrease. After that, the intensities from $a_{R[110]} \sim 1.01$ decrease until the cap is 4 nm-thick, then increase up to 12 nm-thick, and decrease again during InGaAs cap growth. The increase in the intensities from $a_{R[110]} \sim 1.01$ between 4 and 12 nm cap thickness is attributed to In-Ga intermixing between the QDs and cap layer, and the total In content in these layers limits the XRD intensity beyond the thickness of 12 nm. In the case of GaAs cap, the rate of decrease in the intensities becomes smaller at around 4 nm-thick, and the intensities from all lattice constant decrease monotonously. This difference in the XRD intensity transients between GaAs and InGaAs cap suggests In-Ga intermixing taking place during the cap growth under limited supply of In. The supply of In is not sufficient to enhance the XRD signal at $a_{R[110]} \sim 1.01$ in the case of GaAs cap, while the cap layer lattices are expanded by incorporating In atoms due to the intermixing in the case of InGaAs cap.

The relation between the cap layer thickness and PL emission wavelength has been discussed incorporating the information about strain observed by *in situ* XRD. The emission wavelength from InAs QDs is redshifted with decreasing thickness of the $\text{In}_{0.07}\text{Ga}_{0.93}\text{As}$ cap. It is suggested that strain in the QDs can be controlled not only by the lattice constant of the cap layer but also by the cap thickness.

Moreover, PL emission at $1.35\ \mu\text{m}$ is observed at 4 K when capped by 4 nm-thick $\text{In}_{0.07}\text{Ga}_{0.93}\text{As}$, although the intensity decreases and FWHM increases with decreasing cap thickness. Increasing the PL intensity and narrowing the width are imperative for device applications, and further work in better controlling the strain is awaited.

ACKNOWLEDGMENTS

This work was supported by the Strategic Research Infrastructure Project, MEXT, and KEKENHI No. 25289362, JSPS, Japan. The synchrotron radiation experiments were performed at BL11XU of JAEA in SPring-8 under the Shared Use Program of JAEA Facilities (Nos. 2012B-E02, 2013A-E15, 2013B-E01, 2014A-E01) with the approval of Nanotechnology Platform project supported by MEXT (Nos. A-12-AE-0002, A-13-AE-0010, A-13-AE-0022, and A-14-AE-0001), Japan at JAEA beamline BL11XU in SPring-8 (Nos. 2012B3512, 2013A3512, 2013B3511, and 2014A3511).

¹Y. Arakawa and H. Sakaki, *Appl. Phys. Lett.* **40**, 939 (1982).

²S. P. Kowalczyk, W. J. Schaffer, E. A. Kraut, and R. W. Grant, *J. Vac. Sci. Technol.* **20**, 705 (1982).

³K. Hirakawa, Y. Hashimoto, K. Harada, and T. Ikoma, *Phys. Rev. B* **44**, 1734 (1991).

⁴M. Grundmann, O. Stier, and D. Bimberg, *Phys. Rev. B* **52**, 11969 (1995).

⁵K. Nishi, H. Saito, S. Sugou, and J. S. Lee, *Appl. Phys. Lett.* **74**, 1111 (1999).

⁶D. Litvinov, H. Blank, R. Schneider, D. Gerthsen, T. Vallaitis, J. Leuthold, T. Passow, A. Grau, H. Kalt, C. Klingshirn, and M. Hetterich, *J. Appl. Phys.* **103**, 083532 (2008).

⁷K. Mukai and M. Sugawara, *Appl. Phys. Lett.* **74**, 3963 (1999).

⁸Z. Z. Sun, S. F. Yoon, W. K. Loke, and C. Y. Liu, *Appl. Phys. Lett.* **88**, 203114 (2006).

⁹L. Seravalli, P. Frigeri, M. Minelli, P. Allegri, V. Avanzini, and S. Franchi, *Appl. Phys. Lett.* **87**, 063101 (2005).

¹⁰T. Sengoku, R. Suzuki, K. Nemoto, S. Tanabe, F. Koyama, and T. Miyamoto, *Jpn. J. Appl. Phys. Part 2* **48**, 070203 (2009).

¹¹H. Saito, K. Nishi, and S. Sugou, *Appl. Phys. Lett.* **73**, 2742 (1998).

¹²F. Patella, F. Arciprete, M. Fanfoni, A. Balzarotti, and E. Placidi, *Appl. Phys. Lett.* **88**, 161903 (2006).

¹³M. Yakimov, V. Tokranov, G. Agnello, J. V. Eisdien, and S. Oktyabrsky, *J. Vac. Sci. Technol. B* **23**, 1221 (2005).

¹⁴K. Shimomura, T. Shirasaka, D. M. Tex, F. Yamada, and I. Kamiya, *J. Vac. Sci. Technol. B* **30**, 02B128 (2012).

¹⁵K. Shimomura, T. Shirasaka, D. M. Tex, and I. Kamiya, *J. Cryst. Growth* **378**, 41 (2013).

¹⁶T. Sasaki, H. Suzuki, M. Inagaki, K. Ikeda, K. Shimomura, M. Takahashi, M. Kozu, W. Hu, I. Kamiya, Y. Ohshita, and M. Yamaguchi, *IEEE J. Photovoltaics* **2**, 35 (2012).

¹⁷H. Suzuki, T. Sasaki, A. Sai, Y. Ohshita, I. Kamiya, M. Yamaguchi, M. Takahashi, and S. Fujikawa, *Appl. Phys. Lett.* **97**, 041906 (2010).

¹⁸M. Takahashi and J. Mizuki, *J. Cryst. Growth* **275**, e2201 (2005).

¹⁹M. Takahashi, T. Kaizu, and J. Mizuki, *Appl. Phys. Lett.* **88**, 101917 (2006).

²⁰M. Takahashi and T. Kaizu, *J. Cryst. Growth* **311**, 1761 (2009).

²¹M. Takahashi, *J. Cryst. Growth* **401**, 372 (2014).

²²I. Kegel, T. H. Metzger, A. Lorke, J. Peisl, J. Stangl, G. Bauer, K. Nordlund, W. V. Schoenfeld, and P. M. Petroff, *Phys. Rev. B* **63**, 035318 (2001).

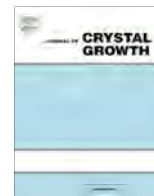
²³A. A. Darhuber, P. Schittenhelm, V. Holý, J. Stangl, G. Bauer, and G. Abstreiter, *Phys. Rev. B* **55**, 15652 (1997).

²⁴T. U. Schüllli, M. Sztucki, V. Chamard, T. H. Metzger, and D. Schuh, *Appl. Phys. Lett.* **81**, 448 (2002).

²⁵A. Malachias, S. Kycia, G. Medeiros-Ribeiro, R. Magalhães-Paniago, T. I. Kamins, and R. Stanley Williams, *Phys. Rev. Lett.* **91**, 176101 (2003).

²⁶Obviously, a strong XRD signal is detected at $a_{R[110]} \sim 1.00$ from the GaAs. This is not shown due to the significant difference in the intensity with respect to the signals of concern.

- ²⁷J. M. García, G. Medeiros-Ribeiro, K. Schmidt, T. Ngo, J. L. Feng, A. Lorke, J. Kotthaus, and P. M. Petroff, *Appl. Phys. Lett.* **71**, 2014 (1997).
- ²⁸I. Kamiya, I. Tanaka, and H. Sakaki, *J. Cryst. Growth* **201/202**, 1146 (1999).
- ²⁹F. Ferdos, S. Wang, Y. Wei, A. Larsson, M. Sadeghi, and Q. Zhao, *Appl. Phys. Lett.* **81**, 1195 (2002).
- ³⁰T. Hanada, B. H. Koo, H. Totsuka, and T. Yao, *Phys. Rev. B* **64**, 165307 (2001).
- ³¹C. Pryor, J. Kim, L. M. Wang, A. J. Williamson, and A. Zunger, *J. Appl. Phys.* **83**, 2548 (1998).
- ³²K. Shimomura and I. Kamiya, *Appl. Phys. Lett.* **106**, 082103 (2015).



Up-converted photoluminescence in InAs/GaAs heterostructures



Yuwei Zhang^{*}, Itaru Kamiya

Quantum Interface Laboratory, Toyota Technological Institute, Nagoya, Aichi 468-8511, Japan

ARTICLE INFO

Article history:

Available online 7 May 2017

Communicated by Jean-Baptiste Rodriguez

Keywords:

- A3. Molecular beam epitaxy
- B2. Semiconducting III–V materials
- A3. Quantum wells
- A1. Optical properties
- B3. Intermediate band solar cell

ABSTRACT

Up-converted photoluminescence (UPL) in InAs/GaAs heterostructures has been investigated. Relaxation process imposes a great challenge for efficient UPL. It is found that efficient UPL can be detected by the luminescence from InAs/GaAs multi quantum well (MQW), and that the intensity could be enhanced by further improving crystalline quality of GaAs barrier. In addition, choosing proper energy states as intermediate states is another important issue to enhance UPL. We describe how the overall UPL efficiency can be controlled by the epitaxial growth and selection of intermediate states.

© 2017 Elsevier B.V. All rights reserved.

Up-converted photoluminescence (UPL) in semiconductor quantum dots (QDs) and quantum wells (QWs) has attracted much attention in recent years. The striking observation of photoluminescence (PL) signal at energy higher than the excitation energy makes it promising for applications such as intermediate band solar cells, unconventional lasers, or displays [1–3]. Although numerous investigations have been performed to elucidate the mechanisms of UPL, where Auger recombination and two-step two-photon absorption through intermediate state are proposed, less information is available on the competing mechanisms between carrier extraction and relaxation processes which impose a great challenge for the observation of UPL [4–6]. We recently reported the importance of introducing confinement states for overcoming such difficulties and enhancing UPL [7]. In this paper, we discuss how the growth of such structures can influence the efficiency of UPL and introduce quantum well islands (QWIs), island structure of InAs with thickness of a few MLs, as confinement state, to further enhance UPL.

A series of samples were grown on semi-insulating GaAs (001) substrates by molecular beam epitaxy (MBE). Sample A consists of InAs/GaAs single QW (SQW) with one monolayer (ML) InAs and 20 nm GaAs cap layer. Sample B has an increased number of QWs with three periods of 1 ML InAs/20 nm GaAs QWs, *i.e.*, multi quantum wells (MQWs). Sample C has a structure identical to sample B except that the GaAs barrier layers, both below and on top of the MQWs were grown at a higher substrate temperature of 560 °C. In sample D, a QD layer with 1.5 ML InAs is inserted between the MQW and the GaAs cap layer of sample C. Samples

E, F and G consist of MQWs identical to sample B, grown beneath and on top of a QD layer with 1.7 ML, 1.75 ML, and 1.8 ML InAs, respectively. It should be noted that the growth of samples C and D proceeds as follows: after growing the GaAs buffer layer at 580 °C, the temperature was lowered to 480 °C to grow 1 ML InAs QW layer. Then the temperature was raised to 560 °C gradually to grow the 20 nm GaAs barrier layer followed by lowering of temperature to 480 °C and then deposit of InAs QW layer. The 20 nm GaAs cap layer was also grown at a gradually raised substrate temperature. However, all the layers of samples A, B, E, F, and G were grown at 480 °C except that of the GaAs buffer grown at 580 °C. The sample structures are shown in Fig. 1. PL measurement were carried out using a cw beam of Ti:sapphire laser for excitation and a liquid nitrogen cooled InGaAs diode array detector.

Fig. 2 shows the PL spectra of samples A and B with excitation wavelength of 780 nm and 930 nm at 4 K, respectively. For sample A, when excited at an energy above GaAs band gap ($\lambda_{\text{ex}} = 780$ nm), emission from GaAs layer is observed at 818 nm and 832 nm which relate to GaAs free exciton and donor-to-acceptor recombination, respectively. The emission at 845 nm originates from the InAs SQW. When the excitation energy is reduced to below the GaAs band gap ($\lambda_{\text{ex}} = 930$ nm), UPL signal is observed at 845 nm which corresponds to the recombination in InAs SQW. Since the excitation energy is below the GaAs band transition or the QW transitions, energy states such as those induced by impurities within the GaAs bandgap might be acting as intermediate state to up-convert carriers which are then captured by the QWs and exhibit UPL. It should be noted that UPL is also observed in GaAs without structures [8,9]. However, the impurities introduced during MBE growth in the present sample only allow limited up-converted carriers to be captured, resulting in a relatively weak UPL. To enhance

^{*} Corresponding author.

E-mail address: yuwei.zhang@toyota-ti.ac.jp (Y. Zhang).

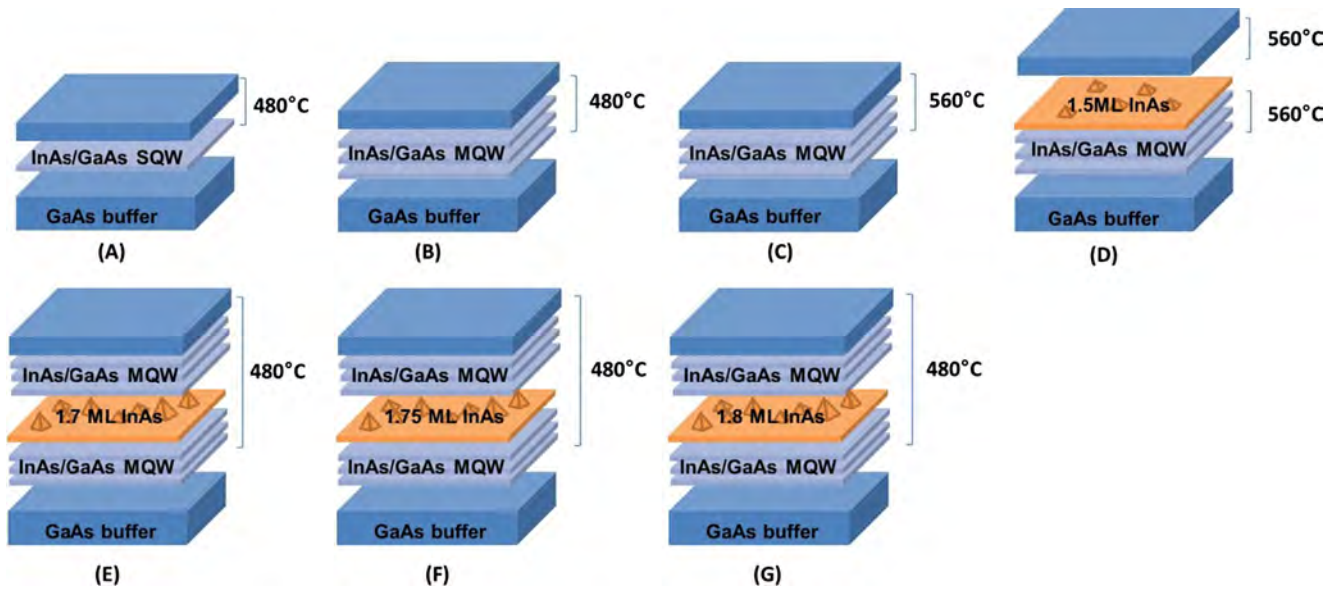


Fig. 1. Structures of samples A–G. The indicated temperature corresponds to the growth temperature of GaAs in the MQW and cap layer.

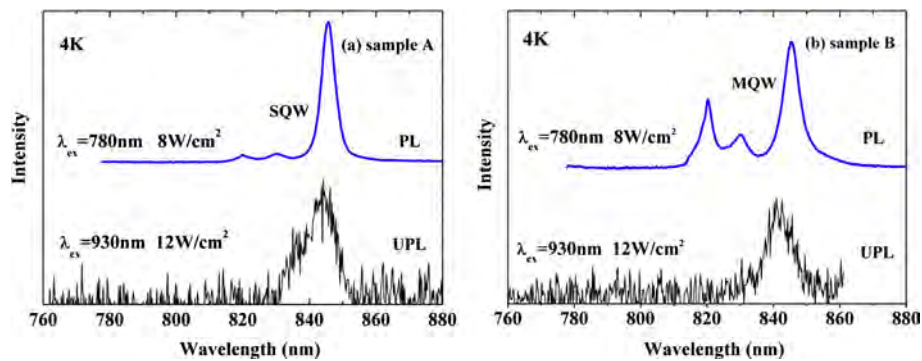


Fig. 2. PL and UPL spectra of (a) sample A and (b) sample B at 4 K with excitation wavelengths of 780 nm and 930 nm, excitation intensity 8 and 12 W/cm², respectively.

the luminescence from the QWs, one straightforward approach is to increase the density of the QW, the luminescing states. Hence, sample B with three periods of InAs/GaAs QW, *i.e.*, triple QW, was grown. While UPL from InAs/GaAs MQW is observed at 845 nm, the enhancement of UPL was not up to the expectation. We believe this is due to the formation of non-radiative centers in GaAs barriers during the growth of three layers of SQW, as discussed below. Note that the slight shift in the emission peak of the UPL spectra from the PL spectra is due to the experimental artifact introduced by the use of different gratings. In order to reduce the non-radiative centers in the GaAs barriers, sample C was grown at a higher substrate temperature for the GaAs barriers. As shown in Fig. 3(a), a narrow and strong peak from MQW is observed in PL spectra (note that the excitation intensity is weaker than for those in Figs. 2 and 4), implying an efficient capture of carriers being realized as a consequence of improved crystal quality. In the UPL spectra with an excitation wavelength of 930 nm, sample C displays a more intense UPL than sample B. In this sample, we believe that the elevated growth temperature of 560 °C for the GaAs barriers within the MQWs resulted in improved crystal quality, which plays an important role for the UPL enhancement. We further note that neither PL nor UPL spectra exhibit luminescence from GaAs. This may also be due to the high quality GaAs crystal, not trapping any carriers within the GaAs but rather passing them into lower energy states in the MQWs.

Based on the results obtained from sample C, we prepared sample D, in which 1.5 ML InAs layer is introduced as confinement states for enhancing UPL. QWIs can be formed when the InAs deposition amount is close to that of critical thickness of 1.7 ML or less, and are reported to act as efficient intermediate states for UPL [10–13]. However, their role of relaxation pathway through which UPL would be weakened should also be considered. As shown in Fig. 4, sample D displays a strong UPL which is comparable to that of sample C at the same excitation energy (930 nm), in which UPL peaks not only from the MQW (845 nm) but also from the GaAs layer (donor-to-acceptor recombination; 832 nm) are observed. We attribute the observation of 832 nm peak in the UPL of sample D to the defects which are formed during GaAs capping. The lattice of the GaAs cap layer is distorted by the underlying InAs QWIs. Surprisingly, neither PL nor UPL is observed from the QWIs themselves, whose peak should lie at around 870 nm, longer wavelength than that of MQWs. The results suggest that the QWIs may act as efficient intermediate states. This is probably achieved by the quantized electronic states of QWIs weakly confining the excited carriers for a limited period of time without recombining until they are transferred into the QWs, the luminescing sites. The relatively long survival time might be due to the phonon bottleneck which inhibits the excited carriers relax into the ground state but being injected into the MQW [14] or due to the relatively large carrier separation that could be achieved in the QWIs. The

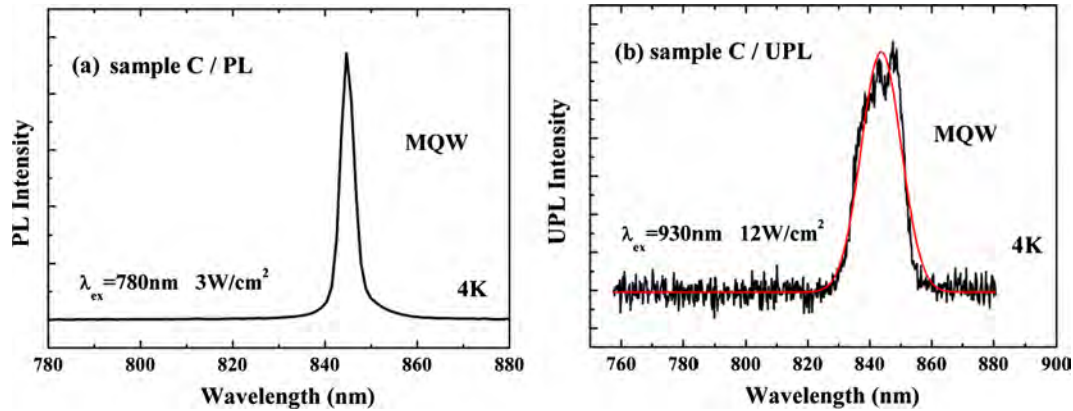


Fig. 3. (a), PL and (b), UPL spectra of sample C with $\lambda_{ex} = 780$ nm and 930 nm, at excitation intensity 3 and 12 W/cm², respectively at 4 K.

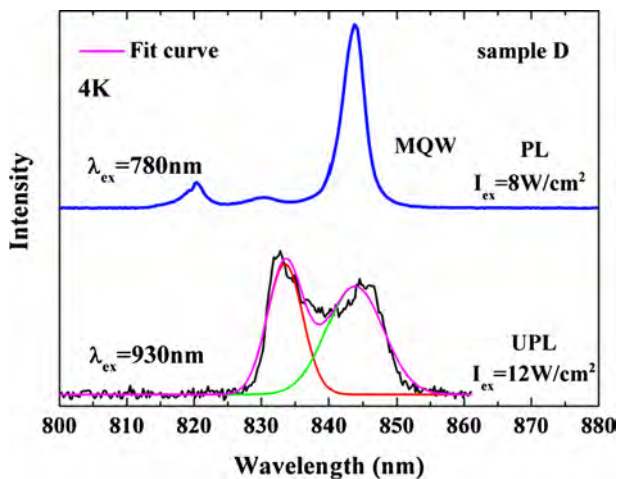


Fig. 4. PL and UPL spectra of sample D with $\lambda_{ex} = 780$ nm and 930 nm, at excitation intensity 8 and 12 W/cm², respectively at 4 K.

QWIs are about 100 nm in lateral size, although the thickness is typically 2 or 3 MLs [15,16]. Consequently, the carriers generated in the QWIs are quantum confined vertically (thickness direction), but only classically confined laterally, and are less likely to recombine radiatively due to the spatial spread compared to those in QDs.

In order to explain the up-conversion and relaxation processes, a schematic band diagram in the above discussed structures is depicted in Fig. 5. In principle, the process starts with generation

of electron-hole pairs at the intermediate state, followed by a second excitation process to transit carriers into the GaAs barrier layer. Those up-converted carriers are either trapped by the QWs or QWIs embedded in the GaAs barriers. Those that are captured by the QWs recombine radiatively directly giving rise to UPL, as observed in samples A, B and C. However, in sample D, some carriers can be trapped by the QWIs and the accompanying WL, formed by SK growth, can proceed through two possible paths; (1) relax to the ground state of the QDs and recombine, or (2) be ejected after a period of time. In sample D, a strong UPL is observed indicating that the role of QWIs as relaxation path way is not prominent and UPL maybe further enhanced through a careful control of energy states in QWI structures.

Our results demonstrate that for efficient UPL it is essential to choose proper intermediate states through which up-conversion dominates over relaxation. The up-conversion is limited by the wavefunction overlap between the intermediate states and the conduction band (CB). As shown in Fig. 6, when the QDs are excited, up-conversion is weak because the wavefunction of the electrons in QDs is confined both in the growth and lateral directions while the wavefunction of the electrons in the CB of GaAs is delocalized. In contrast, when QWIs act as the intermediate states, the wavefunction overlap between intermediate states and CB can be increased in the lateral direction as a result of the large lateral size of QWI with thinner GaAs barrier in between leading to delocalization of wavefunction. Hence, UPL is expected to be enhanced. Up-conversion can be further enhanced by increasing the density of QWIs by controlled growth. Inspired by this idea, we grow and compare UPL in the InAs QWI structures.

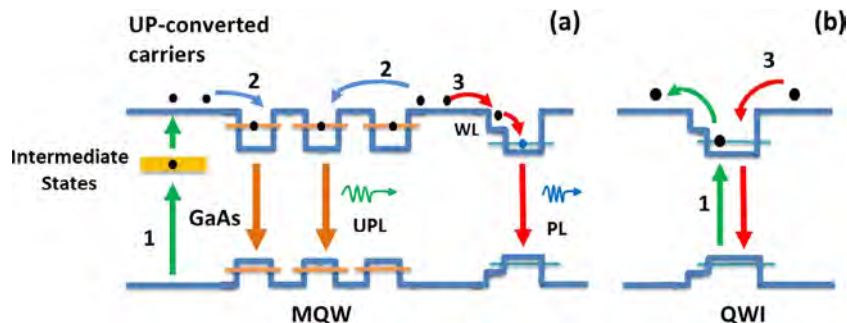


Fig. 5. (a) Schematic illustration of up-conversion and relaxation processes in InAs quantum structures which consists of (1) (green), up-conversion of carriers to above bandgap of GaAs, followed by (2), capture of the carriers by either by MQW (direct UPL) or QWIs. (b) Two competing processes through QWIs. QWIs can act either as intermediate states for up-conversion (green) or relaxation pathway (red). (For interpretation of the references to color in this figure legend, the reader is referred to the web version of this article.)

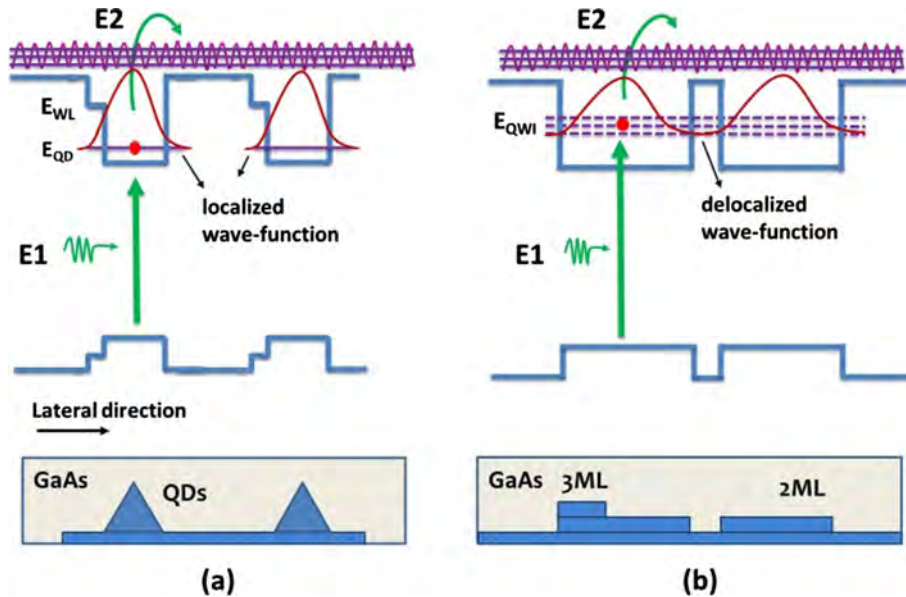


Fig. 6. Schematic illustration of up-conversion through (a) QDs and (b) QWIs as intermediate states in InAs/GaAs quantum structures. The wavefunction of electrons in the intermediate states of QDs is localized while that in QWIs is delocalized along the lateral direction. The morphology of QDs and QWIs are also shown, respectively.

Sample E was grown with 1.7 ML InAs layer, that contains QDs, sandwiched between InAs/GaAs MQW at both sides. Fig. 7 shows the PL spectra of sample E with excitation wavelength of 780 nm, 850 nm, and 900 nm, respectively. The PL spectra with excitation wavelength of 780 nm and 850 nm are nearly alike. The PL signal only arises from the QDs. (The 850 nm peak in Fig. 7(b) is due to the scattered excitation beam.) The subtle redshift and shoulder at around 950 nm arising in Fig. 7(c) is due to the direct excitation of the QDs since at 900 nm, neither GaAs nor InAs WL can be excited. When the 3 ML QWIs are excited at 900 nm in this sample E, UPL from MQW at around 850–855 nm can be observed as shown in Fig. 8(bottom). It is encouraging that the QWI structures with weak electron confinement, as confirmed from PL spectra that only emission from QDs are observable, exist even when the QDs are formed near the critical InAs deposition thickness for QD formation. With increased InAs deposition, the density of 3 ML QWIs increases as the InAs layer develops from 1 or 2 ML structures. In order to prepare a high density of QWIs for achieving efficient UPL, we prepared samples with InAs deposited near the critical thickness (1.7 ML) of QD formation. Samples F and G consist of structures identical to sample E but with 1.75 ML and 1.8 ML InAs, respectively. As can be seen from Fig. 8, with increased InAs deposition, UPL from MQW is enhanced. We attribute the enhancement to the increased density of intermediate states at these InAs coverages. However, with further InAs deposition, the QWIs convert to

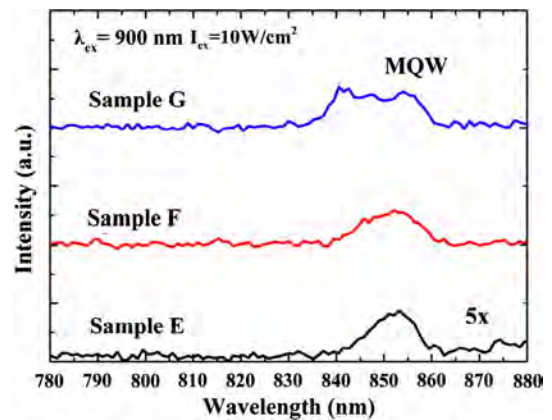


Fig. 8. UPL spectra of samples E, F, and G with $\lambda_{\text{ex}} = 900$ nm at excitation intensity 10 W/cm^2 at 4 K. Note that the spectrum for sample E is magnified fivefold.

QDs, thus decreasing the UPL intermediate states. Further study is necessary to confirm this model. The peak at a shorter wavelength (ca. 840 nm) in sample G is assumed to arise from the distorted lattice of GaAs by the underlying InAs QWIs, which can capture part of the up-converted carriers only if the up-

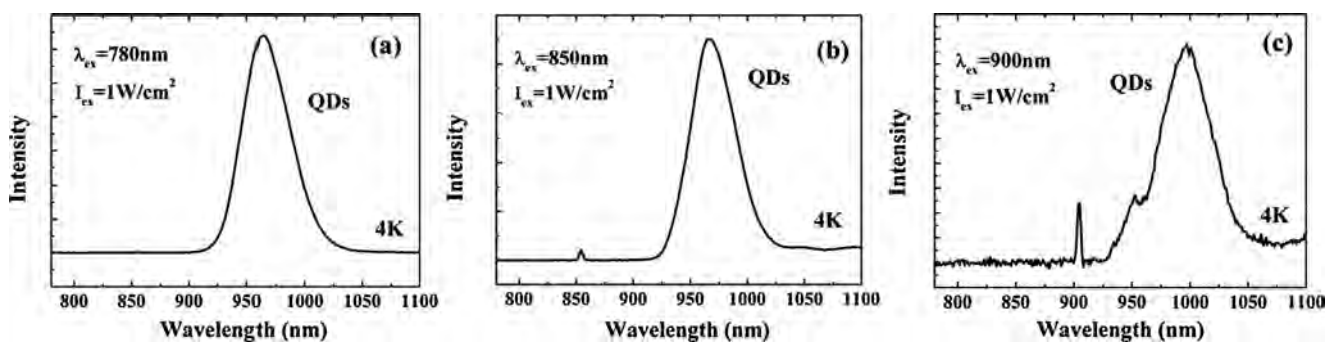


Fig. 7. PL spectra of sample E with (a) $\lambda_{\text{ex}} = 780$ nm, (b) $\lambda_{\text{ex}} = 850$ nm, and (c) $\lambda_{\text{ex}} = 900$ nm, respectively, at excitation intensity 1 W/cm^2 at 4 K.

conversion becomes significant with more up-converted carriers available in CB. This can also explain the absence of the corresponding peak in samples D and F.

In summary, we have investigated UPL in InAs/GaAs heterostructures. It is found that preparing the samples with high crystal quality is a crucial factor to enhance UPL. We also showed that the up-conversion through QWIs lead to efficient UPL compared with QDs due to the increased wave-function overlap between the intermediate states and CB. We found that InAs deposited near InAs QD formation thickness is crucial for efficient UPL.

Acknowledgement

This work was supported by the Strategic Research Infrastructure Project, MEXT, Japan.

References

- [1] A. Luque, A. Marti, C. Stanley, *Nat. Photon.* 6 (2012) 146.
- [2] G. Chen, H. Qiu, P.N. Prasad, X. Chen, *Chem. Rev.* 114 (2014) 5161.
- [3] A. Baumgartner, A. Chaggar, A. Patane, L. Eaves, M. Henini, *Appl. Phys. Lett.* 92 (2008) 091121.
- [4] W. Seigel, A. Titkov, J.P. Andre, P. Voisin, M. Voos, *Phys. Rev. Lett.* 73 (1994) 2356.
- [5] D.M. Tex, I. Kamiya, Y. Kanemitsu, *Phys. Rev. B* 87 (2013) 245305.
- [6] R. Hellmann, A. Euteneuer, S.G. Hense, J. Feldmann, P. Thomas, E.O. Gobel, D.R. Yakovlev, A. Waag, G. Landwehr, *Phys. Rev. B* 51 (1995) 18053.
- [7] Y. Zhang, I. Kamiya, (submitted for publication).
- [8] L.G. Quagliano, H. Nather, *Appl. Phys. Lett.* 45 (1984) 555.
- [9] D.M. Tex, I. Kamiya, *J. Vac. Sci. Technol. B* 30 (2012) 02B120.
- [10] P.P. Paskov, P.O. Holtz, B. Monemar, J.M. Garcia, W.V. Schoenfeld, P.M. Petroff, *Appl. Phys. Lett.* 77 (2000) 812.
- [11] D.M. Tex, I. Kamiya, *Phys. Rev. B* 83 (2011) 081309(R).
- [12] C. Kammerer, G. Cassabois, C. Voisin, C. Delalande, Ph. Roussignol, *Phys. Rev. Lett.* 87 (2001) 207401.
- [13] G. Cassabois, C. Kammerer, R. Sopracase, C. Voisin, C. Delalande, Ph. Roussignol, J.M. Gerard, *J. Appl. Phys.* 91 (2002) 5489.
- [14] R. Heitz, M. Grundmann, N.N. Ledentsov, L. Eeckey, M. Veit, D. Bimberg, V.M. Ustinov, A.Y. Egorov, A.E. Zhukon, P.S. Kopev, Zh.I. Alferov, *Appl. Phys. Lett.* 68 (1996) 361.
- [15] R. Heitz, T.R. Ramachandran, A. Kalburge, Q. Xie, I. Mukhametzhanov, P. Chen, A. Madhukar, *Phys. Rev. Lett.* 78 (1997) 4071.
- [16] D.M. Tex, T. Ihara, I. Kamiya, Y. Kanemitsu, *Phys. Rev. B* 89 (2014) 125301.

Laser-induced local activation of Mg-doped GaN with a high lateral resolution for high power vertical devices

Noriko Kurose, Kota Matsumoto, Fumihiko Yamada, Teuku Muhammad Roffi, Itaru Kamiya, Naotaka Iwata, and Yoshinobu Aoyagi

Citation: *AIP Advances* **8**, 015329 (2018);

View online: <https://doi.org/10.1063/1.5009970>

View Table of Contents: <http://aip.scitation.org/toc/adv/8/1>

Published by the [American Institute of Physics](#)

HAVE YOU HEARD?

Employers hiring scientists and
engineers trust

PHYSICS TODAY | JOBS

www.physicstoday.org/jobs



Laser-induced local activation of Mg-doped GaN with a high lateral resolution for high power vertical devices

Noriko Kurose,¹ Kota Matsumoto,² Fumihiko Yamada,²
Teuku Muhammad Roffi,² Itaru Kamiya,² Naotaka Iwata,²
and Yoshinobu Aoyagi^{1,a}

¹Ritsumeikan University, 1-1-1, Noji-Higashi, Kusatsu, Shiga 525-8577, Japan

²Toyota Technological Institute, Tempaku-ku, Nagoya, Aichi 468-8511, Japan

(Received 21 October 2017; accepted 19 January 2018; published online 31 January 2018)

A method for laser-induced local p-type activation of an as-grown Mg-doped GaN sample with a high lateral resolution is developed for realizing high power vertical devices for the first time. As-grown Mg-doped GaN is converted to p-type GaN in a confined local area. The transition from an insulating to a p-type area is realized to take place within about 1–2 μm fine resolution. The results show that the technique can be applied in fabricating the devices such as vertical field effect transistors, vertical bipolar transistors and vertical Schottkey diode so on with a current confinement region using a p-type carrier-blocking layer formed by this technique. © 2018 Author(s). All article content, except where otherwise noted, is licensed under a Creative Commons Attribution (CC BY) license (<http://creativecommons.org/licenses/by/4.0/>). <https://doi.org/10.1063/1.5009970>

Many studies have been reported on the development of high-power devices using materials such as GaN/AlGaN, Ga₂O₃ and diamond.^{1–3} High-power vertical GaN devices, such as vertical field effect transistors (FETs), vertical bipolar transistors, and vertical Schottkey diode so on are the main applications of GaN-related materials. In case of vertical FETs the source–drain current should be confined to the gate region to control the current by the gate. To achieve this confinement, a local carrier-blocking layer of p-GaN has been proposed.⁴ Crystal regrowth⁵ or ion implantation⁶ into the n-type layer are commonly employed methods to achieve such a current-blocking layer.

Crystal regrowth is a complicated technique in which lithography needs to be performed during the interruption of crystal growth. In this process, the regrown crystal surface is exposed to air and contaminated by the lithography processes. Consequently, the quality of the regrown crystals is unsatisfactory.

Ion implantation needs a high-vacuum system, and spatial control of the implanted dopants is difficult. Furthermore, damage caused during the ion implantation is a serious problem. In order to reduce this damage, annealing processes are required.

In conventional p activation of Mg-doped as-grown GaN, a hot wall furnace or rapid thermal annealing processes are used for the annealing. However, the as-grown Mg-doped GaN is uniformly activated and locally confined activation is impossible. In contrast, the laser-induced local activation (LILA) process developed here for the first time allows the preparation of local p-activated regions without any damage or dopant migration. LILA is a technique for converting locally as-grown Mg-doped GaN or AlGaN epitaxial layers grown by metal organic chemical vapor deposition (MOCVD) to p-type GaN or AlGaN using excimer laser irradiation while conducting *in situ* monitoring of the surface during the process. It is demonstrated that it is possible to locally convert the as-grown n⁻-type or insulating region to p-type in a conversion transition region of approximately 1–2 μm accuracy using LILA. Especially this LILA can control the areas to be activated as a fashion of area-by-area using a computer control system.

^aE-mail: yaoyagi@gst.ritsumei.ac.jp



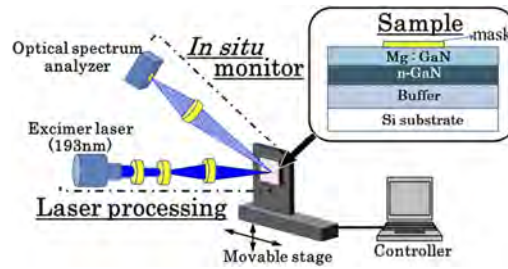


FIG. 1. Experimental setup of LILA. The sample placed on the X–Y stage was scanned using a controller. The PL and scattered light from the processing region of the GaN were monitored *in situ* to feed the actual irradiation conditions back to the laser. The inset shows a typical sample used for measurement. In our experiment Mg-doped GaN was epitaxially grown on the top of the n-GaN without an AlGaIn layer.

Here, local activation in Mg-doped GaN to p-type GaN from n⁻-type as-grown GaN using LILA is reported. The sample used was a Mg-doped GaN layer epitaxially grown on a Si (111) substrate by MOCVD. On the Si substrate, a buffer layer (2 μm), a non-doped (4 μm) layer and a Mg-doped GaN (1 μm) layer were grown, successively. The Mg doping was $2.6 \times 10^{19}/\text{cm}^3$.

Excimer laser light (193 nm, 10–500 Hz, 0.1–7 mJ/pulse, 10 ns pulse width) was collimated with a pin hole and lenses to a size of 1 mm \times 0.2 mm on the sample surface. The profile of the laser intensity was observed using a knife edge method. The sample, on a stage, was scanned horizontally and vertically to obtain uniform and/or local irradiation. The optimum scanning speed for obtaining uniform irradiation was determined by simulation using the experimentally observed beam profile pattern. Photoluminescence (PL) and scattered light from the surface were observed *in situ* during the laser irradiation using an optical spectrum analyzer to control the irradiation condition as shown in Fig. 1.

The optical micrographs of the surface under laser irradiation at high and low power intensities are shown in Fig. 2. At an irradiation of 0.7 mJ laser power, the surface was mirror-like with p-type conversion (Fig. 2(a)). Under this condition, the *in situ* monitored PL and scattered light were identical to those of the unprocessed sample.

However, when the laser intensity was increased to 1.8 mJ, the scanning pattern of the laser can clearly be seen due to surface ablation and the surface is no longer mirror-like (Fig. 2(b)). A new spectrum appeared on the optical spectrum analyzer, which may have come from the surface modified by the laser. The details of the spectrum will be reported elsewhere.

The carrier types, the carrier density and mobility of the samples activated by LILA and the samples annealed using a conventional hot wall furnace were determined using Van der Pauw–Hall measurements. The experimental results are summarized in Table I. In the as-grown sample, the Hall effect could not be measured because of the high resistivity of the sample, but it was assigned as n-type from Seebeck effect measurements. The carrier type obtained by LILA processing was p-type; this was the same as that obtained by conventional heat treatment. The carrier density and mobility were comparable but the mobility obtained LILA method is higher than that obtained by

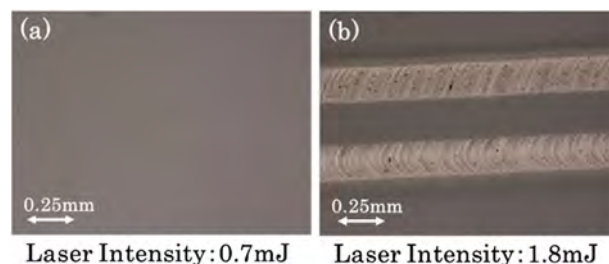


FIG. 2. Optical micrographs of the surface under laser irradiation at (a) low power (0.7 mJ) and (b) high power (1.8 mJ).

TABLE I. Carrier density and mobility of Mg-doped GaN activated by LILA and conventional hot wall furnace annealing determined by Van der Pauw–Hall effect measurements.

Treatment Method	Carrier type	Carrier density (cm ⁻³)	Mobility (cm ² /V·sec)
As grown	n ⁻ -type ^a	NA	NA
Laser activation (1.1mJ, 150Hz in Air)	p-type	3.3×10^{16}	4.7
Conventional Furnace activation (950°C, 20min in N ₂)	p-type	5.5×10^{16}	4.1

^aFrom Seebeck effect measurement.

conventional furnace activation method. In this region of carrier concentration of order of $10^{16}/\text{cm}^3$, phonon scattering may be a main scattering mechanism but not electron-ionized acceptor scattering. So, laser annealing phenomena to improve the crystal quality may happen.

In LILA process the process is confined in a small local area and the crystal quality may be better than original one as discussed in previous paragraph. The spread of the heat generated by the laser is less than 1 to 2 micron meter as proved in Kelvin probe measurement shown in Fig. 4. So, this LILA process does not effect to other processes carried out for device fabrication such as ohmic contact formation and/or hetero structure interface.

For confirming local activation of as-grown Mg-doped GaN, LILA was conducted on a sample with a mask of 3-mm Si stripe patterns on the surface. As shown in Fig. 3(a), the laser irradiated the whole area of the sample with the mask, and the mask was then removed after irradiation to measure the conductance profile of the sample. The irradiated area changed to p-GaN and the non-irradiated area remained n⁻-type as-grown GaN, which was confirmed by Seebeck effect measurements. Two microprobe measurements were carried out as shown in Fig. 3(b). Two microprobes separated at a distance of 0.3 mm were moved together to the perpendicular direction of the p–n⁻ junction interface. The current between the two probes was measured after removing the mask.

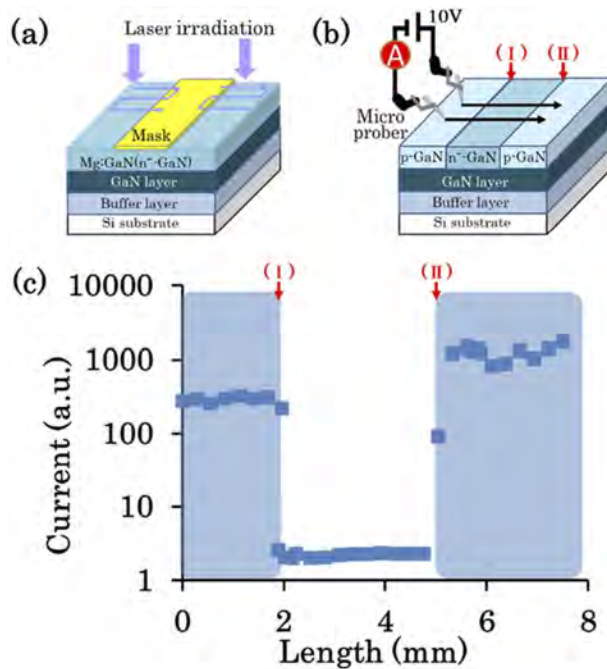


FIG. 3. Two-probe conductance measurements on the LILA-treated surface using a mask. (a) Sample used for local activation by LILA with the mask. (b) Schematic view of the two-probe measurement of the local conductance. The two probes were moved on the surface in the direction perpendicular to the p–n⁻ junction. (c) Current observed by the two-probe measurements as a function of distance.

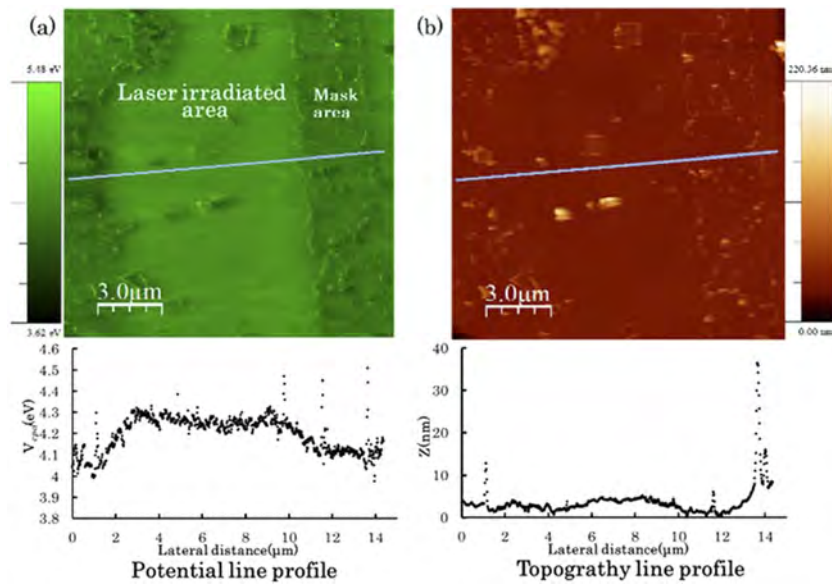


FIG. 4. (a) Observed KFM image and line profile of the contact potential difference V_{cpd} along the blue line in the image. (b) Corresponding AFM image and line profile of the topography along the blue line in the image. The images and the blue lines are of identical areas.

The current observed as a function of the distance of the movement across the p–n⁻ junction is shown in Fig. 3(c). At the interfaces of the p–n⁻ junction (I) and (II), an abrupt conductance change was observed. The abrupt change was more than two orders of magnitude greater on conductance in the p-GaN compared to that in the n⁻-type as-grown GaN. The conduction transition width between the non-irradiated and the irradiated regions was determined to be less than the resolution limit of 70 μm in this two-probe method. This meant that the Mg did not diffuse under laser irradiation, the laser did not penetrate in the horizontal direction and local activation was enabled by LILA. The steepness of the interface was less than the resolution limit of 70 μm of this measurement.

To clarify the spatial resolution limit of LILA in the conversion region at a finer scale, Kelvin probe force microscopy (KFM) was performed, with which atomic force microscopy (AFM) could be performed simultaneously. Typical results are shown in Fig. 4.

The 4- μm Ti stripe metal masks at an interval of 8 μm were deposited on the as-grown surface using lithography for this experiment. After uniform irradiation on this sample, the Ti metal masks were removed. The Ti metal masked (non-irradiated) and unmasked (irradiated) regions can clearly be distinguished in the KFM image and line profile, where a potential difference of the laser-irradiated region and non-irradiated region of approximately 200 meV was observed (Fig. 4(a)).

This clear contact potential difference of about 200 meV arose from the work function difference between the p-type converted Mg-doped GaN by laser irradiation and the n⁻-type as-grown Mg-doped GaN. The value was smaller than that expected from the work function difference between ideal p- and n⁻-type GaN. The reason for the discrepancy is not clear at the moment, but the same phenomenon has been observed in other materials. In particular, the measurements on pure n- and p-type GaAs showed a work function difference of 260 meV.⁷ This was tentatively attributed to the surface states changing their degree of charging when the Kelvin force measurements were performed using AFM cantilevers, thereby inducing an uneven field at the surface.

The simultaneously observed AFM image is shown in Fig. 4(b). The surface was almost flat and the root mean square roughness of the surface was 9.5 nm. (The spikes observed in the KFM and AFM cross-sections were not noise, but were due to surface contamination during the processes.) This image confirms the boundaries of the masked and unmasked regions, agreeing well with the KFM results.

From these results, it can be concluded that the conversion transition from p- to n⁻-GaN occurs over a distance of about 1–2 μm. The laser light was absorbed just on the surface because of the high optical absorption coefficient of GaN for 193 nm light ($\sim 7 \times 10^5/\text{cm}$)⁸ and the heat generated at the surface diffused isotropically. The observed transition region of about 1–2 μm suggests that the thermal diffusion length in which p-type conversion takes place from the as-grown sample is about 1–2 μm. As the thermal conductivity of GaN is 1.0 W/K·cm,⁹ the temperature at a depth of 1–2 μm below the surface is about 10–20°C lower than the temperature at the surface.

The carrier-blocking layer of p-GaN is underneath the GaN and AlGaIn for vertical FETs. However, the thickness of AlGaIn is about 10–20 nm and the thickness of the GaN is expected to be about 0.3 μm, depending on the device design. So, the Mg-doped GaN inside the device can be activated locally using this LILA method, and vertical FETs with a p-GaN carrier-blocking layer can be developed. When it is necessary for activation at deeper Mg-doped GaN layers locally, activation can be achieved using a multi-irradiation technique.

The present results show the strong potential for fabrication of vertical devices with p-GaN without using any regrowth or ion implantation techniques. In addition to this advantage LILA method makes possible to fabricate repeated and complicated small cells of devices using computer control system by positioning the local activating spots one by one and/or large area batch treatment for the activation.

In conclusion, a new technique, called LILA, has been established for the first time. This has achieved local activation of Mg-doped GaN using an excimer laser operating at 193 nm together with *in situ* observations of the surface during laser processing. Using this method, local activation of carriers with a lateral resolution of about 1–2 μm was possible, thus establishing the potential for fabricating vertical high-power devices without using any other fabrication techniques such as crystal regrowth, ion implantation or mesa structures.

¹ S. Chowdhury and U. K. Mishra, *IEEE Trans. Electron Devices* **60**, 3060 (2013).

² M. Higashiwaki, K. Sasaki, H. Murakami, Y. Kumagai, A. Koukitu, A. Kuramata, T. Masui, and S. Yamakoshi, *Semicond. Sci. Technol.* **31**, 034001 (2016).

³ H. Umezawa, M. Nagase, Y. Kato, and S. Shikata, *Diamond Rel. Mater.* **24**, 201 (2012).

⁴ R. Yeluri, J. Lu, C. A. Jumi, D. A. Browne, S. Chowdhury, S. Keller, J. S. Speck, and U. K. Mishra, *Appl. Phys. Lett.* **106**, 183502 (2015).

⁵ H. Nie, Q. Diduck, B. Alvarez, A. P. Edwards, B. M. Kayes, M. Zhang, G. Ye, T. Prunty, D. Bour, and I. C. Kizilyalli, *IEEE Electron Device Lett.* **35**, 939 (2014).

⁶ M. Kodama, M. Sugimoto, E. Hayashi, N. Soejima, O. Ishiguro, M. Kanechika, K. Itoh, H. Ueda, T. Uesugi, and T. Kachi, *Appl. Phys. Express* **1**, 021104 (2008).

⁷ T. Kobayashi, MS Thesis, Toyota Technological Institute (2017); F. Yamada, T. Kamioka, K. Nakamura, Y. Ohshita, and I. Kamiya, Proceeding of 26th International Photovoltaic Science and Engineering Conference, to be published.

⁸ B. B. Kosicki, R. J. Powell, and J. C. Burgiel, *Phys. Rev. Lett.* **24**, 1421 (1970).

⁹ E. K. Sichel and J. I. Pankove, *J. Phys. Chem. Solids* **38**, 330 (1977).

Suppression of Twin Formation in Layered In_2Se_3 Grown on GaAs(111)

Nobuaki Kojima, Hiroya Nakamura, Yoshio Ohshita, and Masafumi Yamaguchi

Toyota Technological Institute, 2-12-1 Hisakata, Tempaku, Nagoya 468-8511, JAPAN

Abstract — We propose novel buffer layers consisting of the layered defect zincblende ($\text{In}_x\text{Ga}_{1-x}$) $_2\text{Se}_3$ compounds for the GaAs on Si(111) system. The layered structured materials are suitable for lattice mismatch and thermal expansion mismatch buffer layers. However, weak van der Waals bonding may cause twin crystal domain formation during the crystal growth. We investigated In_2Se_3 growth on GaAs(111) just and vicinal substrates by MBE and compared twin crystal formation, surface morphology and crystal quality. The vicinal substrates suppress twin formation by predominating the step-flow growth at the surface step edge. To eliminate twin crystal domains and to improve crystal quality, the optimization of the surface step structure is necessary.

Index Terms — Epitaxial layers, Photovoltaic cells, Gallium arsenide.

I. INTRODUCTION

The defect zincblende structured III-VI compounds ($\text{In}_x\text{Ga}_{1-x}$) $_2\text{Se}_3$ are attractive materials as novel buffer layer for GaAs on Si system. ($\text{In}_x\text{Ga}_{1-x}$) $_2\text{Se}_3$ has the lattice constant between that of Si and GaAs, depending on In content, and can have layered structure with loose van der Waals gaps as described below. The layered structured materials are suitable for lattice mismatch and thermal expansion mismatch buffer layers.

The defect zincblende structure is basically a zincblende structure, in which one third of III group atoms are vacant. In this structure, the native vacancies are known to be spontaneously ordered. In Ga_2Se_3 , vacancies order along [1-10] direction of the zincblende lattice.^[1] On the other hand, in In_2Se_3 , vacancies form planes every three indium planes along the (111) plane of the zincblende lattice.^[2] Thus, defect zincblende In_2Se_3 exhibits layered structure with van der Waals gaps.

We proposed novel buffer layers consisting of ($\text{In}_x\text{Ga}_{1-x}$) $_2\text{Se}_3$ compounds for the GaAs on Si(111) system.^[3-5] In this crystallographic orientation, the layered defect zincblende ($\text{In}_x\text{Ga}_{1-x}$) $_2\text{Se}_3$ can be grown on Si epitaxially with the van der Waals gaps aligned parallel with the Si(111) substrate surface. The van der Waals interface of the layered structure should absorb any strain caused by lattice mismatch and thermal expansion coefficient difference between Si and GaAs.

However, weak van der Waals bonding may cause twin crystal domain formation during the crystal growth. Such twin defects should be eliminated from the epi-layer for use of the buffer layer between GaAs and Si.

In this study, we grew In_2Se_3 films on GaAs(111)B just and vicinal substrates. The vicinal substrates may prevent the twin formation by predominating the step-flow growth at the

surface step edge. We compare twin crystal formation, surface morphology and crystal quality of the In_2Se_3 films.

II. EXPERIMENTAL PROCEDURE

In_2Se_3 films were grown on GaAs(111)B just and vicinal substrates by molecular beam epitaxy (MBE). The offcut angle of the vicinal substrate is 2° toward the [2-1-1] direction. The growth temperature (T_g) and growth time were fixed at 450°C and 1.5 h, respectively. VI/III beam flux ratio was adjusted to around 150. Prior to growing process, the GaAs substrates were chemically etched with Semico-23-clean and rinsed with deionized water, and then heated at 590°C under As beam irradiation for 10 min in the MBE growth chamber to remove surface oxides. In the above growth conditions, the film thickness is typically around 150 nm.

Twin crystal formation was evaluated by electron back scatter diffraction (EBSD) using a scanning electron microscope (SEM) equipped with an EBSD detector. Surface morphology was observed by SEM and atomic force microscope (AFM). Crystal quality was measured by X-ray diffraction (XRD).

III. RESULTS AND DISCUSSION

Twin crystal formation was evaluated by EBSD as shown in Fig. 1. The area enclosed by red or black line corresponds twin crystal domain. The area ratio of twin crystal is around 39% for In_2Se_3 on GaAs(111)B just, and 12% for In_2Se_3 on GaAs(111)B vicinal, respectively.

Surface morphology was observed by SEM and AFM as shown in Fig. 2 and 3. From SEM images for both GaAs(111) just and vicinal substrates in Fig. 2, stripe contrast is seen

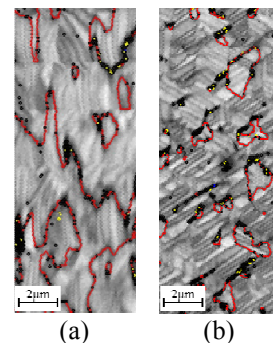


Fig. 1. EBSD images of In_2Se_3 films (a) on GaAs(111) just substrate. (b) on GaAs(111) vicinal substrate.

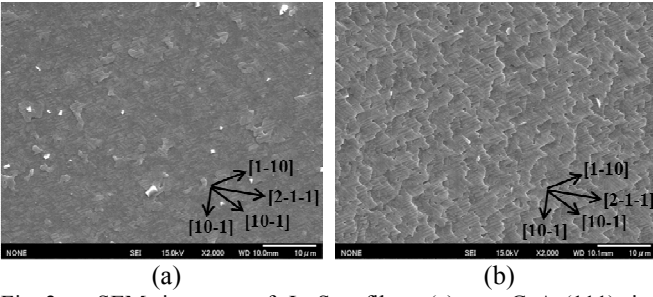


Fig. 2. SEM images of In₂Se₃ films (a) on GaAs(111) just substrate. (b) on GaAs(111) vicinal substrate.

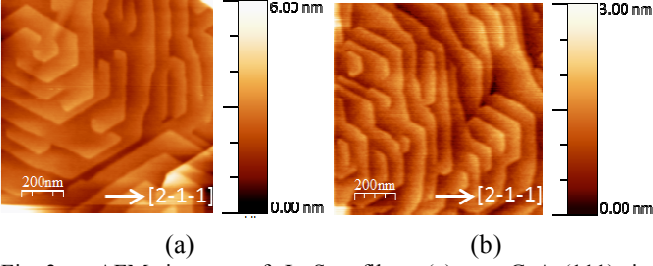


Fig. 3. AFM images of In₂Se₃ films (a) on GaAs(111) just substrate. (b) on GaAs(111) vicinal substrate.

along equivalent $\langle 1-10 \rangle$ directions. In addition, clear crystal surface morphology with straight edges along three equivalent $\langle 1-10 \rangle$ directions is seen in GaAs(111) vicinal substrate. These edges make stair-like step structure toward substrate off direction.

From AFM images in Fig. 3, surface steps are directed to three equivalent $\langle 2-1-1 \rangle$ directions, and the step height is around 9.4 Å, corresponding to mono-unit layer of In₂Se₃. In GaAs(111) just substrate, spiral growth structure is seen. By contrast, in GaAs(111) vicinal substrate, mono-unit layer steps make stair-like step structure toward substrate off direction in the flat area of SEM image, suggesting step-flow growth at the surface step edge. Deep steep structure is also observed in places in both GaAs(111) just and vicinal substrates (not shown in figure). The height of steeps are around 3 to 10 nm for GaAs(111) just substrate and 10 to 40 nm for GaAs(111) vicinal substrate. Such steep structure corresponds to straight edges in SEM images and may be caused by grain boundaries or dislocations.

Fig. 4 shows X-ray reciprocal space mapping of In₂Se₃ films on GaAs(111) just and vicinal substrates. The peak located just above GaAs(111) diffraction peak can be attributed to (0 0 3L) diffraction of layered In₂Se₃, where L is the number of van der Waals unit layers contained within a crystallographic unit cell and cannot be defined from only this XRD data. The (0 0 2L) diffraction of layered In₂Se₃ were also measured. [111] and [2-1-1] directions in Fig. 4 correspond respectively c-axis and a-axis direction of the In₂Se₃ hexagonal lattice. The In₂Se₃ (0 0 2L) and (0 0 3L) diffraction peak on the vicinal substrate shifts from the [111] direction, which indicate crystal plane tilting.

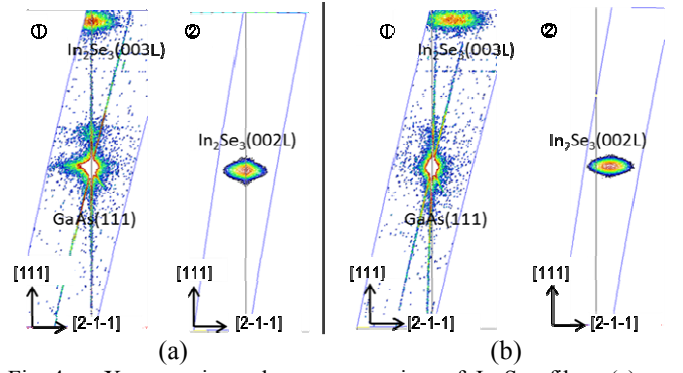


Fig. 4. X-ray reciprocal space mapping of In₂Se₃ films (a) on GaAs(111) just substrate. (b) on GaAs(111) vicinal substrate.

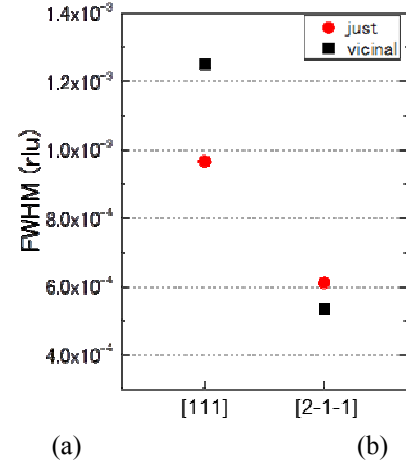


Fig. 5. FWHM values of the In₂Se₃ (0 0 2L) diffraction peak in Fig. 4 along [111] and [2-1-1] direction.

Fig. 5 shows the full width at half maximum (FWHM) values of the In₂Se₃ (0 0 2L) diffraction peak in Fig. 4 along [111] and [2-1-1] direction. FWHM values of the In₂Se₃ (0 0 2L) diffraction peak on the vicinal substrate is narrower along [111] (In₂Se₃ c-axis) direction and wider along [2-1-1] (In₂Se₃ a-axis) direction than (111) just substrate.

From the results of EBSD, SEM, AFM and XRD, we can conclude that the vicinal substrates can suppress twin formation by predominating the step-flow growth at the surface step edge. It is thought that the X-ray diffraction peak FWHM along c-axis broadens due to the existence of screw dislocations of the spiral growth for GaAs(111) just substrate, and the FWHM along a-axis broadens due to the existence of grain boundaries or dislocations for GaAs(111) vicinal substrate. To eliminate twin crystal domains and to improve crystal quality, the optimization of the surface step structure is necessary.

IV. CONCLUSIONS

We investigated In₂Se₃ growth on GaAs(111) just and vicinal substrates by MBE and compared twin crystal formation, surface morphology and crystal quality of the

In₂Se₃ films. The vicinal substrates suppress twin formation by predominating the step-flow growth at the surface step edge. It is thought that the X-ray diffraction peak FWHM along c-axis broadens due to the existence of screw dislocations of the spiral growth for GaAs(111) just substrate, and the FWHM along a-axis broadens due to the existence of grain boundaries or dislocations for GaAs(111) vicinal substrate. To eliminate twin crystal domains and to improve crystal quality, the optimization of the surface step structure is necessary.

ACKNOWLEDGEMENT

This work was supported in part by the New Energy and Industrial Technology Development Organization (NEDO) under the Ministry of Economy, Trade and Industry (METI), Japan, and by the Strategic Research Infrastructure Project, MEXT, Japan.

REFERENCES

- [1] K. Ueno et al., Journal of Crystal Growth 237-239 (2002) 1610.
- [2] T. Okamoto et al., Journal of Crystal Growth 175/176 (1997) 1045.
- [3] N. Kojima, H. Nakamura, Y. Ohshita, M. Yamaguchi, Proc. 40th IEEE Photovoltaic Specialist Conference, 2014.
- [4] N. Kojima, H. Nakamura, Y. Ohshita, M. Yamaguchi, Proc. 29th European PV Solar Energy Conference, 2014.
- [5] H. Nakamura, N. Kojima, Y. Ohshita, M. Yamaguchi, Tech. Digest 6th World Conference on Photovoltaic Energy Conversion, 2014.

● **Area 1: Crystalline and Thin Film Silicon PV**

ANALYSIS OF WORKFUNCTION OF MOOX AT MOOX/SIO2 INTERFACE BY CAPACITANCE-VOLTAGE MEASUREMENT

Takefumi Kamioka¹, Yutaka Hayashi¹, Yuki Isogai¹, Kyotaro Nakamura², Yoshio Ohshita¹
¹Toyota Technological Institute, Japan, ²Meiji University, Japan
t-kamioka@toyota-ti.ac.jp

Short summary: The "interface workfunction" of MoO_x at the MoO_x/SiO₂ interface is experimentally extracted by our C-V analysis. The dependence on post-deposition annealing temperature was also obtained, showing the monotonically decrease with temperature by about 500 meV from as-deposition to 300 °C.

Introduction: Workfunction of transition-metal oxide (TMO) at a TMO/insulator interface, which is referred here as an interface workfunction, is an important factor to determine silicon (Si) solar cells with so-called carrier-selective contact (CSC), since a workfunction difference between a TMO and Si determines the surface potential of Si. So far, we have reported our analysis of an interface workfunction of reactive-plasma-deposited indium-tin-oxide (RPD-ITO) at the ITO/SiO₂ interface, by capacitance-voltage (C-V) analysis [1,2]. This analysis is not limited to ITO and can be applied to other TMO/insulator stacks.

In this work, the interface workfunction of molybdenum oxide (MoO_x) at the MoO_x/SiO₂ interface was extracted by applying our C-V analysis. Its dependence on post-deposition annealing temperature was also obtained. MoO_x has been expected to be utilized for a hole-selective contact since its workfunction is well below the valence-band maximum in Si [3]. It is noted again, however, that the reported values were only limited to bulk ones measured by x-ray and/or ultraviolet photoelectron spectroscopy (XPS/UPS) [4,5].

Experimental: ITO/MoO_x/SiO₂/Si/Al MOS structure devices were fabricated for C-V analysis as follows. Boron-doped p-type Si(100) wafers were thermally oxidized. The thicknesses of oxide (t_{ox}) were about 10, 20 and 30 nm. The MoO_x film was thermally deposited about 30 nm, followed by the 50-nm-thick ITO layer deposition by RPD at 160 °C. The samples were annealed in a forming-gas (4% H₂ in N₂) for 15 min at 200, 250 and 300 °C. The C-V measurement were performed and the flat-band voltage (V_{FB}) were analyzed as a function of oxide thickness. The interface workfunction was determined by the extrapolation of V_{FB}-t_{ox} plot (the detail will be described elsewhere).

Results and Discussion: The estimated interface workfunction of MoO_x is shown in Fig. 1, as a function of temperature during the post-deposition annealing (PDA). For ITO/MoO_x stack, the workfunction values were about 5.7 eV after ITO deposition. The workfunction decreased with temperature and became about 5.2 eV after 300 °C PDA. The interface workfunction of MoO_x capped by Al (Al/MoO_x) is also plotted, showing about 5.8 eV. For low-temperature PDA condition, the interface workfunction values seem to kept high independent of the capping layer (Al and ITO).

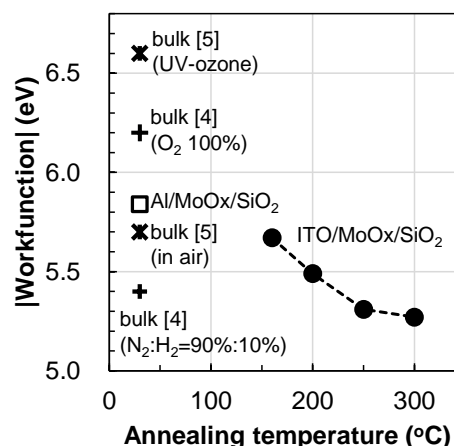
For comparison, reported bulk workfunction values are also plotted although the data were reported only for as-deposition. The bulk workfunction varies largely depending on the stoichiometry [4]. Also, the bulk workfunction strongly depends on the surface treatment [5], indicating the importance of the interface workfunction analysis presented here. In their works [4,5], V_{OC} were also shown, however, there is no information on workfunction during the fabrication process. Since the annealing process will lead to changes in the interface properties as well as bulk properties (structure, composition etc), it is important to obtain its temperature dependence. In the presentation, the relation between the interface workfunction and V_{OC} of our cells will be also discussed.

Acknowledgements

This work was supported by the NEDO project, Japan. We also acknowledged to M. Morimura, N. Maeda for their help fabricating devices.

References

[1] T. Kamioka et al., The 7th SiliconPV (2017). [2] T. Kamioka et al., The 64th JSAP Spring Meeting (2017). [3] J. Ballock et al., Nature Energy **1**, 15031 (2016). [4] M. Vasilopoulou et al., J. Am. Chem. Soc. **134**, 16178 (2012). [5] C. Battaglia et al., Nano Lett. **14**, 967 (2014).



workfunction values of MoO_x as a function of post-deposition annealing temperature.

XRD Pole Figure Analysis of In₂Se₃ Zinc-Blende Like (ZBL) Van der Waals Template for Epitaxial GaAs Lift Off

Nobuaki Kojima, Yu-Cian Wang, Kei Kawakatsu, Yoshio Ohshita, Masafumi Yamaguchi

Toyota Technological Institute, Nagoya, 468-8511, Japan

Abstract — Double layers of In₂Se₃ and GaAs were grown on GaAs (111) just and 2° off substrates by MBE. The crystal structure and crystallographic orientation distribution were characterized by the 2θ-ω scan and pole figure of X-ray diffraction (XRD). Single domain growth of α-In₂Se₃ was obtained by using GaAs (111) 2° off substrate. The vicinal substrates can suppress twin formation by predominating the step-flow growth at the surface step edge, and the crystallographic orientation of In₂Se₃ is defined at the hetero-interface. From the dominant three α-In₂Se₃(1 0 17) plane peaks, the interface structure is estimated.

I. INTRODUCTION

The defect zincblende structured III-VI compounds (In_xGa_{1-x})₂Se₃ are attractive materials as novel buffer layer for GaAs on Si system. (In_xGa_{1-x})₂Se₃ has the lattice constant between that of Si and GaAs, depending on In content, and can have layered structure with loose van der Waals gaps as described below. The layered structured materials are suitable for lattice mismatch and thermal expansion mismatch buffer layers.

The defect zincblende structure is basically a zincblende structure, in which one third of III group atoms are vacant. In this structure, the native vacancies are known to be spontaneously ordered. In Ga₂Se₃, vacancies order along [1-10] direction of the zincblende lattice.^[1] On the other hand, in In₂Se₃, vacancies form planes every three indium planes along the (111) plane of the zincblende lattice.^[2] Thus, defect zincblende In₂Se₃ exhibits layered structure with van der Waals gaps.

We reported this novel buffer layers consisting of (In_xGa_{1-x})₂Se₃ compounds are capable for the GaAs growth on Si(111) system.^[3] In this crystallographic orientation, the layered defect zincblende (In_xGa_{1-x})₂Se₃ can be grown on Si epitaxially with the van der Waals gaps aligned parallel with the Si(111) substrate surface. The van der Waals interface of the layered structure should absorb any strain caused by lattice mismatch and thermal expansion coefficient difference between Si and GaAs. We named (In_xGa_{1-x})₂Se₃ buffer “Zinc-Blende Like (ZBL) Van der Waals template”.

We also reported new layer transfer technique for the fabrication of thin film flexible multi-junction solar cells by using the ZBL van der Waals template.^[4] The III-V overlayer on (In_xGa_{1-x})₂Se₃ template can be transferred onto a support substrate by peeling from Si or GaAs substrate via van der Waals interface of (In_xGa_{1-x})₂Se₃. Therefore, thin film flexible III-V solar cells can be fabricated more easily than usual epitaxial lift-off (ELO) technique using selective etching by aqueous acid.

However, weak van der Waals bonding may cause twin crystal domain formation during the crystal growth. Such twin defects should be eliminated from the epi-layer for the high-quality GaAs overlayer growth.

In this study, the crystallographic orientation distribution of In₂Se₃ ZBL van der Waals template on GaAs(111) substrate were characterized by the pole figure of X-ray diffraction (XRD). We expect that the crystallographic orientation of In₂Se₃ align in the same direction with the polar GaAs surface at the hetero-interface. We found the suppression of twin formation in In₂Se₃ by using GaAs (111) vicinal substrate.

II. EXPERIMENTAL PROCEDURE

Double layers of In₂Se₃ and GaAs were grown on GaAs(111)B just and vicinal substrates by molecular beam epitaxy (MBE). The offcut angle of the vicinal substrate is 2° toward the [2-1-1] direction. The growth temperature and growth time were fixed at 450°C and 1hr for both In₂Se₃ and GaAs layers. VI/III and V/III beam flux ratios for In₂Se₃ and GaAs were 140 and 20, respectively. The typical growth rate for In₂Se₃ and GaAs was 150 to 200 nm/hr.

The crystal structure and crystallographic orientation distribution were characterized by the 2θ-ω scan and pole figure of X-ray diffraction (XRD). In the pole figure, the diffraction peaks from GaAs(331) and α-In₂Se₃(1 0 17) planes were measured to confirm the twin crystal domain formation.

III. RESULTS AND DISCUSSION

The crystallographic orientation distribution for In₂Se₃ films grown on GaAs(111) just and 2° off substrates was characterized by the XRD pole figure measurement. Figure 1 shows the pole figures for α-In₂Se₃(1 0 17) planes grown on GaAs(111)B just and 2° off substrate. The epitaxial α-In₂Se₃(1 0 17) planes grown on GaAs(111)B just substrate show sixfold symmetry, although it should have threefold symmetry. The such sixfold symmetry suggests the 60° rotation twin formation in α-In₂Se₃. On the other hand, three α-In₂Se₃(1 0 17) plane peaks along [1 1 -2] are dominant in the α-In₂Se₃ grown on GaAs(111)B 2° off substrate. This result shows the vicinal substrates suppress twin formation by predominating the step-flow growth at the surface step edge, and the crystallographic orientation of In₂Se₃ is defined at the hetero-interface. From the dominant three α-In₂Se₃(1 0 17) plane peaks, we estimated the interface structure as shown in Fig. 2. The crystallographic

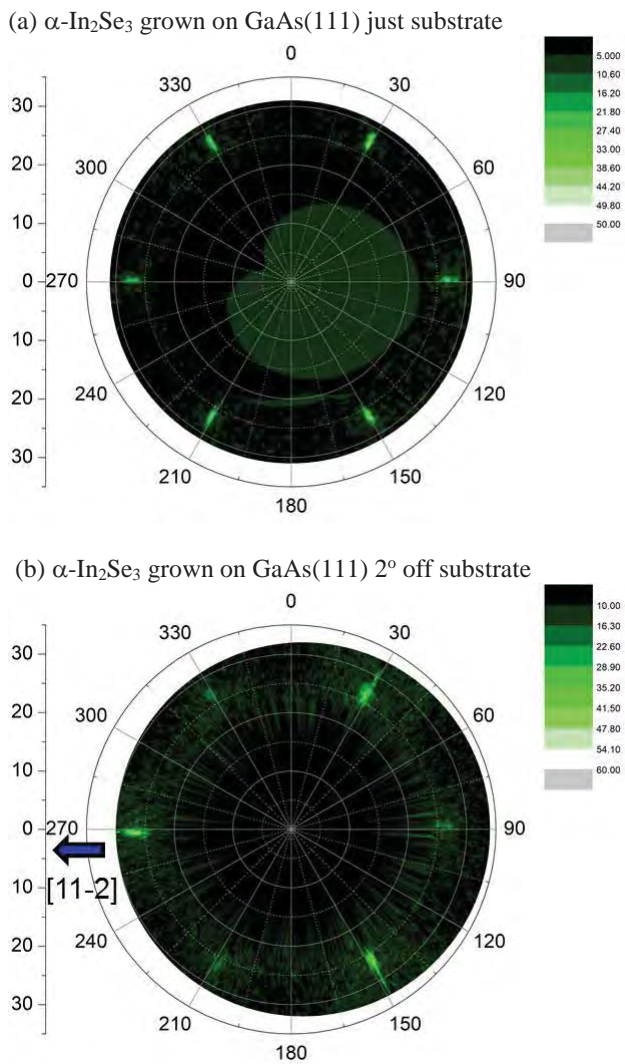


Figure 1: XRD pole figures for α - $\text{In}_2\text{Se}_3(1\ 0\ 17)$

orientation of In_2Se_3 align in the same direction with the polar GaAs surface at the hetero-interface.

IV. CONCLUSIONS

Double layers of In_2Se_3 and GaAs were grown on GaAs (111) just and 2° off substrates by MBE. The crystal structure and crystallographic orientation distribution were characterized by the 2θ - ω scan and pole figure of X-ray diffraction (XRD). Single domain growth of α - In_2Se_3 was obtained by using GaAs (111) 2° off substrate. The vicinal substrates can suppress twin formation by predominating the step-flow growth at the surface step edge, and the crystallographic orientation of In_2Se_3 is defined at the hetero-interface. From the dominant three α - $\text{In}_2\text{Se}_3(1\ 0\ 17)$ plane peaks, the interface structure is estimated.

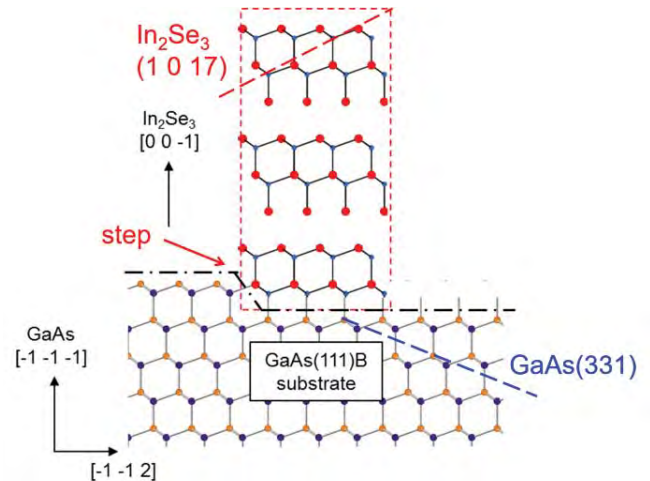


Figure 2: The estimated interface structure between GaAs and In_2Se_3 .

ACKNOWLEDGEMENT

This work was supported in part by the New Energy and Industrial Technology Development Organization (NEDO) under the Ministry of Economy, Trade and Industry (METI), Japan and by JSPS KAKENHI Grant Numbers JP15K05998 and by the Strategic Research Infrastructure Project, MEXT, Japan.

REFERENCES

- [1] K. Ueno, S. Tokuchi, K. Saiki, A. Koma, "Epitaxial growth of a vacancy-ordered Ga_2Se_3 thin film on a vicinal $\text{Si}(001)$ substrate", *Journal of Crystal Growth*, vol. 237-239, pp.1610-1614, 2002.
- [2] T. Okamoto, A. Yamada, M. Konagai, "Growth and characterization of In_2Se_3 epitaxial films by molecular beam epitaxy", *Journal of Crystal Growth*, vol. 175-176, pp.1045-1050, 1997.
- [3] N. Kojima, C. Morales, Y. Ohshita, M. Yamaguchi, *AIP Conference Proceedings*, vol. 1556, pp. 38-40, 2013.
- [4] Nobuaki Kojima, Li Wang, Yoshio Ohshita, Masafumi Yamaguchi, "Novel Epitaxial GaAs Lift-Off Approach via van der Waals Interface in In_2Se_3 Buffer Layer", *Proceedings of the 33rd European Photovoltaic Solar Energy Conference*, pp.1295-1297, 2017.

ITO reactive plasma deposition damage analysis by C-V and QSSPC measurement

Yuki Isogai^{1*}, Takefumi Kamioka^{1,2}, Yutaka Hayashi¹ and Yoshio Ohshita¹

¹ Toyota Technological Institute, Nagoya 468-8511, Japan

² Meiji University, Kawasaki 214-8571, Japan

* E-mail: sd17407@toyota-ti.ac.jp, Tel & Fax: +81-52-809-1877

Introduction

Indium tin oxide (ITO) is widely used as a transparent electrode layer material for heterojunction solar cells [1,2]. A reactive plasma deposition (RPD) technique is widely used to deposit ITO films [3]. This method offers the advantages of relatively low ion damage [4]. However, the effective minority carrier lifetime for ITO/SiO₂/Si decreases after the ITO film is deposited by this process [5]. This suggests that some crystalline defects are formed due to the ITO deposition, and that they act as recombination centers. However, the detail about this degradation phenomenon is not clear yet.

In this work, we discuss the effect of the defect density of the Si interface (D_{it}) and the total charge (Q_{tot}) i.e. the sum of the interface trap charges and the fixed charges in the SiO₂ film, on the surface recombination velocity (SRV). D_{it} and Q_{tot} are obtained by capacitance-voltage (C-V) measurement [6]. Based on the extended SRH model [7], SRV is estimated by D_{it} and Q_{tot} which determines the surface carrier density. The SRV is also derived from lifetime measured by quasi-steady-state photoconductance (QSSPC) measurement. The relationships between SRVs, D_{it} and Q_{tot} as a function of anneal temperature are studied. The result indicates that the D_{it} increase induced by the RPD process is the main reason of the SRV increase.

Experimental

The ITO/SiO₂/Si/SiO₂/ITO structure samples for minority carrier lifetime measurement and the ITO/SiO₂/Si/Al structure samples for C-V measurement were fabricated as follows. Boron-doped p-type Cz Si(100) wafers with 4 - 6 Ωcm resistivity were used as substrates. The wafers were chemically cleaned and thermally oxidized in dry oxygen (O₂) at 950 °C for 12, 32 and 62 min to grow 12.3, 20.0 and 30.5 nm-thick SiO₂, respectively. The oxidized wafers were then annealed in nitrogen gas (N₂) ambient at 950 °C for 15 min to obtain the Si/SiO₂ interface with small D_{it} values of the order of 10¹⁰ cm⁻²eV⁻¹. The SiO₂ thickness was determined by a single wavelength ellipsometer. For the fabrication of lifetime samples, the ITO film was then deposited on the SiO₂ at the both sides by RPD. For C-V samples, ITO film was then deposited on the SiO₂ at the front side by the RPD. The ITO (5 wt % Sn) target was used for this purpose. The flow rate of argon (Ar) and O₂ gases were 85 and 20 sccm, respectively. The thickness of ITO was about 80 nm, estimated by a stylus profilometer. Al was thermally evaporated on the rear surface of Si substrate to form Ohmic contact.

C-V curves for the MOS devices were obtained at small-signal frequencies (100 Hz and 100 kHz). The sum of Q_{it} and $Q_f(Q_{tot})$ was estimated from the obtained C-V curves as follows [6]. The relation between flat-band voltage (V_{FB}) and SiO₂ thickness (t_{ox}) for experimental samples was plotted. The value of V_{FB} was determined as the voltage at which the measured capacitance becomes the flat-band capacitance (C_{FB}). Here the C_{FB} was calculated according to the following equation, [8]

$$\frac{C_{FB}}{C_{ox}} = \left(1 + \frac{136\sqrt{T/300}}{t_{ox}\sqrt{N_A}} \right)^{-1}, \quad (1)$$

where C_{ox} denotes the oxide capacitance calculated by the measured oxide thickness, and T the lattice temperature. The dopant

(acceptor) concentration in the Si substrate (N_A) was determined from the minimum capacitance of a high-frequency C-V curve. There exist charges in the SiO₂ layer, and defect states at the SiO₂/Si interface. In a case where distributed charges like sodium (Na) ions in SiO₂ can be neglected, V_{FB} is described as, [8]

$$V_{FB} = \phi_{ITO-Si} - \frac{Q_f}{C_{ox}} - \frac{Q_{it}(\phi_s)}{C_{ox}}, \quad (2)$$

Where ϕ_{ITO-Si} is the difference between the workfunction of ITO (ϕ_{ITO}) and Fermi level of Si (ϕ_{Si}), Q_f denotes the fixed charge density located near the Si/SiO₂ interface, Q_{it} is the interface trapped charge at the in SiO₂/Si interface (trapped charge in the interface defect with the density of D_{it}), and ϕ_s the surface potential of Si. This equation means that when Q_f and Q_{it} are independent of SiO₂ thickness, the V_{FB} - t_{ox} plot follows a linear relation, and the value of slope corresponds to sum of Q_{it} and Q_f (Q_{tot}).

As the damage induced by the RPD of ITO, the D_{it} generated during the RPD of ITO was extracted from the measured C-V curves as follows. Here, so-called "high-low frequency" method was adopted, as following equation, [9]

$$D_{it} = \frac{C_{ox}}{q^2} \left(\frac{\frac{C_{lf}}{C_{ox}}}{1 - \frac{C_{lf}}{C_{ox}}} - \frac{\frac{C_{hf}}{C_{ox}}}{1 - \frac{C_{hf}}{C_{ox}}} \right), \quad (3)$$

where C_{hf} and C_{lf} denote the capacitances measured at a high- and low-frequency, respectively. It is noted that C_{hf} is used as an alternative of the ideal capacitance in this equation. As C_{hf} , the value obtained at 100 kHz is used in the experiments, although the 100 kHz C-V curve is still slightly deviated from the ideal C-V one. This means that the estimated D_{it} values are slightly under-estimated.

In order to evaluate the effect of post-deposition annealing on the D_{it} and Q_{tot} , the samples were obtained after annealing in N₂ ambient at different temperatures ranging from 120 to 200 °C for 5 min.

The lifetime was measured by QSSPC. SRV was calculated by the following equation [7]

$$SRV = \frac{W}{2} \left(\frac{1}{\tau_{eff}} - \frac{1}{\tau_{bulk}} \right), \quad (4)$$

where W denotes the substrate thickness, τ_{eff} the effective carrier lifetime and τ_{bulk} the bulk carrier lifetime.

On the other hand, the SRV was calculated by the obtained D_{it} and Q_{tot} [7] by the following equation

$$SRV = \frac{(n_s p_s - n_i^2)}{\Delta n} \times \int_{E_v}^{E_c} \frac{v_{th} D_{it}(E_t) dE_t}{[n_s + n_i(E_t)] \sigma_p^{-1}(E_t) + [p_s + p_i(E_t)] \sigma_n^{-1}(E_t)}, \quad (5)$$

where n_s or p_s is the electron or hole density at the surface, D_{it} is the interface defect density, E_t are the defect levels, n_i or p_i is the SRH densities and σ_n or σ_p is the capture cross-sections for electron or hole. The calculated SRV was compared with the experimental one to understand the main factor for ITO-RPD damage.

n_s is calculated to get the experimental SRV. The surface carrier density Q_{sc} (C/cm²) at the surface of the semiconductor is induced by the charge in SiO₂ Q_{tot} (C/cm²) by the following equation

$$Q_{sc} = Q_{tot} - Q_d \sim Q_{tot}, \quad (6)$$

Since the charge density in the depletion layer, Q_d , is negligible. Here the polarity of Q_{tot} is positive, n_s or p_s is represented as,

$$n_s = \frac{Q_{sc}}{q d_0} + \Delta n, \quad (7) \quad p_s = N_A + \Delta n, \quad (8)$$

where d_0 is the thickness of the excess carrier layer at the semiconductor surface. The electric field at the semiconductor surface, E_{surf} , is described as,

$$\epsilon_0 \epsilon_{Si} E_{surf} = Q_{tot}, \quad (9)$$

where ϵ_0 is permittivity of vacuum and ϵ_{Si} is relative permittivity of Si.

At the surface, E_{surf} is almost constant and d_0 is then as follows.

$$d_0 = \frac{kT}{q} \frac{1}{E_{surf}} = \frac{kT}{q} \frac{\epsilon_0 \epsilon_{Si}}{Q_{tot}}. \quad (10)$$

where, k is Boltzmann constant, T is temperature, q is elementary charge. n_s is given by,

$$n_s = \frac{Q_{tot}^2}{\epsilon_0 \epsilon_{Si} k T} + \Delta n. \quad (11)$$

Results and discussion

The effective minority carrier lifetimes of the ITO/SiO₂/Si/SiO₂/ITO samples (ITO samples) and the SiO₂/Si/SiO₂ samples (SiO₂ samples) as a function of PDA temperature are shown in Fig. 1. The lifetime of the SiO₂ sample is much higher than that of ITO sample without PDA. This suggests some damage were induced by the RPD process and that they act as recombination centers. While the lifetimes of the SiO₂ samples are almost constant independent of PDA temperature, the lifetime of ITO sample is recovered as about two orders of magnitude by the PDA at 200 °C. Many of induced damage were annihilated due to the 200 °C annealing. The calculated SRV of the ITO samples as a function of PDA temperature is shown in Fig. 2. The SRV is 3×10^3 cm/s without PDA. As the PDA temperature increases, the SRV decreases and becomes low about two orders of magnitude at 200 °C.

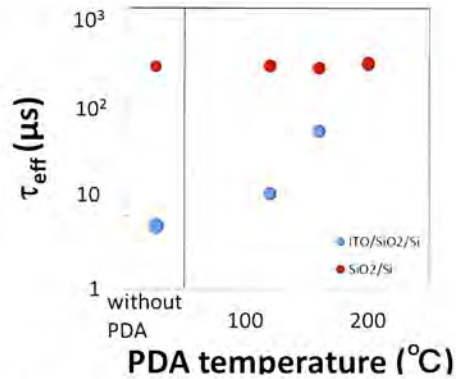


Fig. 1 Effective minority carrier lifetime of the ITO and SiO₂ samples as a function of PDA temperature.

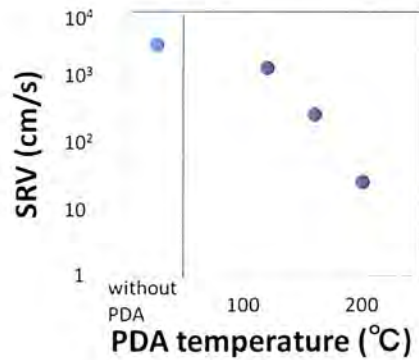


Fig. 2 SRV of the ITO samples as a function of PDA temperature.

C-V curves for ITO/SiO₂/Si stack obtained at different PDA temperatures are shown in Fig. 3. Without PDA, the C-V curve obtained at 100 Hz shows a hump in the transition region and is largely deviated from the ideal C-V curve. Also, a small hysteresis exists between the forward and reverse bias sweeps. These humps and hysteresis were caused due to the damage induced by the RPD process.

The extracted D_{it} at the SiO₂/Si interface and the Q_{tot}/q as a function of PDA temperature are shown in Fig. 4. The value of D_{it} is about 2.0×10^{11} cm²eV⁻¹ for the Al/SiO₂/Si sample. That is about 1.1×10^{12} cm²eV⁻¹ for the as-deposited ITO/SiO₂/Si sample. The obtained value of Q_{tot}/q for the Al/SiO₂/Si sample is about 3.7×10^{11} cm⁻². That for the ITO/SiO₂/Si sample is about 1.3×10^{12} cm⁻². These results mean that the RPD process increased the D_{it} and Q_{tot}/q values, as the relatively large amount of damages generated at the interface, and that they increased the SRV.

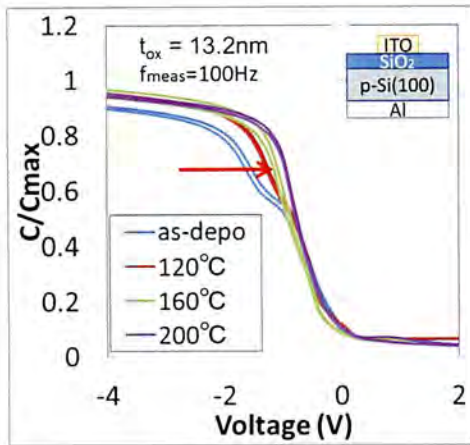


Fig. 3 C-V curves for ITO/ SiO₂/Si stack obtained at different PDA temperatures.

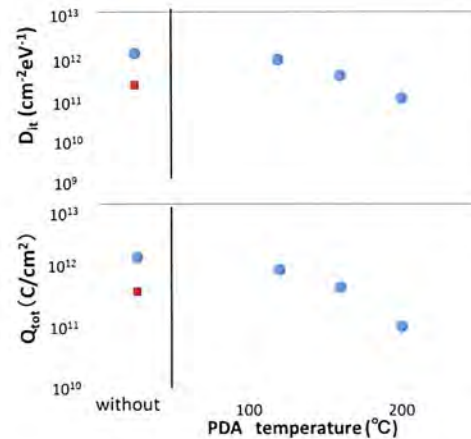


Fig. 4 Extracted D_{it} and Q_{tot}/q as a function of PDA temperature.

The SRVs evaluated by the data of C-V (SRV_{C-V}) and QSSPC (SRV_{LT}) were compared to study the ITO deposition damage. SRV_{C-V} was obtained by eq. (5) using n_s , p_s , $\sigma_n=6 \times 10^{-15} \text{ cm}^2$, $\sigma_p=1 \times 10^{-16} \text{ cm}^2$, $\Delta n=10^{15} \text{ cm}^{-3}$ and the obtained D_{it} . The n_s was calculated by eq. (8) using the obtained Q_{tot}/q . On the other hand, SRV_{LT} was estimated by eq. (4) using lifetime data.

The effects of Q_{tot}/q and D_{it} on SRV_{C-V} are shown in Figs. 5 and 6. When D_{it} is constant, the SRVs are almost constant independent of Q_{tot}/q , and are strongly affected by D_{it} , as lines shown in Fig. 5. Figure 6 shows that the SRV dramatically increases as the increase in D_{it} . The SRV_{LT} is explained by the change of D_{it} . These results suggest that ITO reactive plasma deposition-induced damage is the defect appeared as D_{it} and Q_{tot}/q . D_{it} increase mainly increased the SRV and that the recovery of the lifetime by the PDA is explained as the decrease of D_{it} .

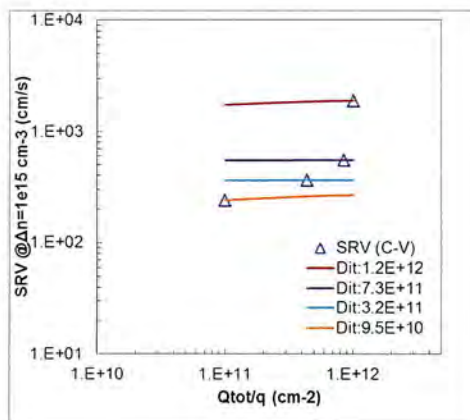


Fig. 5 SRV_{C-V} as functions of D_{it} and Q_{tot}/q (horizontal axis: D_{it}). SRV lines were obtained as a function of Q_{tot}/q for the constant D_{it} .

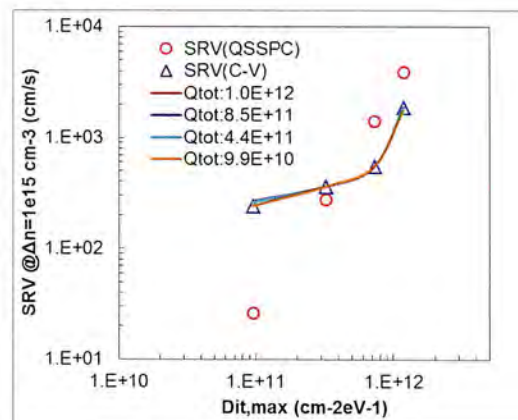


Fig. 6 The SRV_{C-V} and The SRV_{LT} as functions of D_{it} and Q_{tot}/q (horizontal axis: Q_{tot}/q).

Summary

The effects of D_{it} and Q_{tot} on the SRV were discussed. Some damages were induced by ITO deposition process and they appeared as the decrease in lifetime and the increase in D_{it} and Q_{tot}/q . By the PDA, the damages decreased because lifetime, D_{it} and Q_{tot}/q

recovered. The SRV_{C-V} was obtained using D_{it} and Q_{tot} estimated by C-V measurement. The SRV_{LT} was derived from the lifetime measured by QSSPC technique. The SRVs were almost constant independent of Q_{tot}/q , and were mainly determined by D_{it} . This is because n_s ($\sim 10^{18} \text{ cm}^{-3}$) is much larger than p_s ($\sim 10^{15} \text{ cm}^{-3}$) in the range of $10^{11} < Q_{tot}/q < 10^{12}$. These results suggested that ITO deposition-induced damage was the defects appeared as D_{it} and Q_{tot}/q . D_{it} increase mainly increased the SRV and that the recovery of the lifetime by the PDA was explained as the decrease of D_{it} .

Acknowledgment

This work was partly supported by the New Energy and Industrial Technology Development Organization (NEDO) under the Ministry of Economy, Trade and Industry of Japan. We thank M. Morimura at Toyota Technol. Inst. for their help in fabricating samples.

References

- 1) M. Taguchi, A. Yano, S. Tohoda, K. Matsuyama, Y. Nakamura, T. Nishiwaki, K. Fujita, and E. Maruyama "24.7% record efficiency HIT solar cell on thin silicon wafer," IEEE J. Photovolt., vol. 4, no. 1, 2014.
- 2) H. Imran, T.M. Abdolkader, N.Z. Butt, "Carrier-selective NiO/Si and TiO₂/Si contacts for silicon heterojunction solar cells," IEEE Trans. Ele. Dev, vol. 63, no. 9, pp. 3584-3590, Sep. 2016.
- 3) H. Kitami, M. Miyashita, T. Sakemi, Y. Aoki, and T. Kato, "Quantitative analysis of ionization rates of depositing particles in reactive plasma deposition using mass-energy analyzer and Langmuir probe," J. Appl. Phys., vol. 54, 01AB05 (5 pages), 2015.
- 4) K. Sakai, T. Kakeno, T. Ikari, S. Shirakata, T. Sakemi, K. Awai, and T. Yamamoto, "Defect centers and optical absorption edge of degenerated semiconductor ZnO thin films grown by a reactive plasma deposition by means of piezoelectric photothermal spectroscopy," J. Appl. Phys., vol. 99, 043508, 2006.
- 5) Y. Isogai, T. Kamioka, L. Hyunju, N. Kojima, Y. Ohshita, "Influence of ITO-RPD process on effective minority carrier lifetime in reactive plasma deposited ITO/SiO₂/Si structure," in the 27th Photovoltaic Science and Engineering Conference (PVSEC), 2017.
- 6) T. Kamioka, Y. Hayashi, Y. Isogai, K. Nakamura, and Y. Ohshita, "Analysis of interface workfunction and process-induced damage of reactive-plasma-deposited ITO/SiO₂/Si stack," AIP Adv., vol. 7, 095212, 2017.
- 7) S. Rein, *Lifetime spectroscopy*, (Springer), 2005.
- 8) D. K. Schroder, *Semiconductor Material and Device Characterization*, 3rd ed., (Wiley & Sons, New Jersey), 2006.
- 9) R. Castagne and A. Vapaille, "Description of the SiO₂/Si interface properties by means of very low frequency MOS capacitance measurements," Surf. Sci., vol. 28, no. 157, 1971.

Low Density Growth of Graphene by Air Introduction in Atmospheric Pressure Chemical Vapor Deposition

Seiya Suzuki,* Kana Kiyosumi, and Takashi Nagamori
*Graduate School of Engineering, Toyota Technological Institute,
2-12-1 Hisakata, Tempaku, Nagoya 468-8511, Japan*

Kei Tanaka
Daido Bunseki Research, Inc., 2-30 Daido-cho, Minami-ku, Nagoya 457-8545, Japan

Masamichi Yoshimura
*Graduate School of Engineering, Toyota Technological Institute,
2-12-1 Hisakata, Tempaku, Nagoya 468-8511, Japan*

(Received 20 April 2015; Accepted 27 June 2015; Published 22 August 2015)

Chemical vapor deposition (CVD) is a promising method to produce large-size single-crystal graphene, and further increase in domain size is desirable for electro/optic applications. Here we studied the effect of low amount of air introduction by intentional leak on graphene growth in atmospheric pressure CVD. The air introduction at the heating process resulted in roughening of Cu surface induced by oxygen, while air introduction at the annealing under H₂ ambient drastically decreased graphene density due to reduction of active sites for graphene nucleation both by surface oxidation and enlargement of Cu domain. Although air introduction only at the growth stage was ineffective for graphene nucleation, air introduction for both annealing and growth provided great enhancement of domain growth without increasing the density of graphene, which is an optimized condition to obtain a large single-crystal. This controlled introduction of air in atmospheric pressure CVD provided ~ 2.5 mm hexagonal single layer graphene with high quality. [DOI: 10.1380/ejsnt.2015.404]

Keywords: Carbon; Copper; Nucleation; Growth; Graphene; Air

I. INTRODUCTION

High quality graphene provided by mechanical exfoliation from bulk graphite [1-5] has demonstrated attractive fundamental properties such as extraordinary carrier mobility approaching $200,000 \text{ cm}^2\text{V}^{-1}\text{s}^{-1}$ [1-5], universal 2.3% optical absorption from mid-infrared to UV light [6], and high Young's modulus of 1 TPa [7]. Regardless of these excellent works, flake size and layer number of graphene formed by the exfoliation method are neither uniform nor controllable, limiting the practical use. In contrast, chemical vapor deposition (CVD) can produce large-area and uniform graphene on catalytic metal surfaces [8, 9], and CVD graphene growth on copper (Cu) shows preferential single layer formation [10] which is suitable for mass production. However, the CVD graphene is generally polycrystalline [11, 12], and its domain boundaries degrade electronic properties such as carrier mobility. Thus, it is desirable for graphene applications [13-18] to grow large single-crystal graphene by improving CVD growth conditions.

Several effective methods to enlarge single-crystal size of graphene/Cu in CVD growth on Cu has been reported such as prolonged annealing [19], electrochemical polishing [20], high pressure annealing [21,22], and suppression of evaporation loss of Cu by wrapping the foil [23]. With these methods, millimeter size graphene domain was achieved. More recently, oxygen was found to play an important role in suppressing graphene nucleation [24,25], and centimeter size graphene was successfully obtained

through the oxygen passivation [25]. Here, we report that a low amount of air introduction during atmospheric pressure CVD processes suppresses graphene nucleation similar to the oxygen passivation. It is found that the air introduction highly affected morphology of Cu surface. The air introduction at each stage of heating, annealing and growth was in detail investigated to clarify the role of the air introduction. By the optimized CVD condition we achieved to obtain millimeter-size hexagonal graphenes. It is noted that our technique neither require any vacuum pump, high quality Cu foils, nor special equipment for air introduction, which is practical for mass production of large single crystal graphenes at a low cost.

II. EXPERIMENTAL

Commercially available Cu foils (Nilaco No. 113321, 100- μm -thick and 99.96% in purity) were electropolished by a custom-built electrochemistry cell. Two Cu foils with the sizes of $\sim 3.5 \text{ cm} \times 10 \text{ cm}$ were placed into a water solution of 500 mL of 1 M KOH in a glass beaker, and were used as anode and cathode. A DC voltage of 4.5 V was applied for 5 min during the polishing process. The Cu foil on the anode was cut into a piece of $\sim 3.5 \text{ cm} \times 2.5 \text{ cm}$ and rinsed with 500 mL deionized (DI) water (2 \times), further washed with 50 mL methanol (2 \times), and dried by blowing air, and was then introduced in the CVD chamber to grow graphene.

Graphenes were prepared on electropolished Cu foils in lateral quartz-tube CVD equipment (Fig. 1(a)) under nearly ambient pressure (standard atmospheric pressure (P_{atm}) plus $\sim 0.023 \text{ MPa}$). This nearly ambient pres-

* Corresponding author: seiya09417@gmail.com

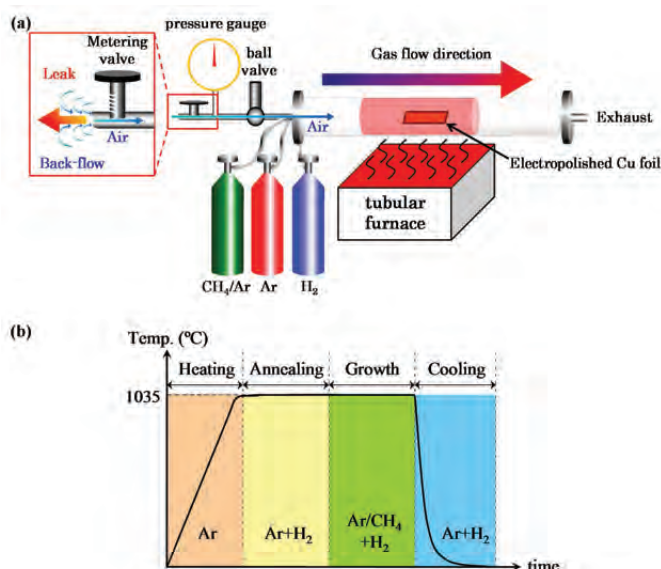


FIG. 1. (a) A schematic illustration of CVD setup and air introduction through back-flow of leak (red rectangular) (b) A schematic illustration of the CVD growth process. CVD process is divided for 4 parts which are heating, annealing, growth, and cooling.

sure was achieved by suppressing the amount of exhaust gasses. Prior to graphene growth, an electropolished Cu foil was heated to 1035°C under Ar flow (1000 standard cubic centimeter per minute: (sccm)) for ~ 45 min, and then annealed under Ar (500 sccm) and H₂ (100 sccm) flows for desirable time, which allows to form nucleation seeds of a large sized graphene [24]. After reducing the H₂ flow rate to be 9 sccm, the graphene growth was initiated by flowing 10 ppm of CH₄ diluted in Ar (500 sccm). Subsequently, the Cu foil was rapidly cooled from 1035°C down to room temperature within less than 30 min under Ar (1000 sccm) and H₂ (9 sccm) flows. The whole CVD process is schematically summarized in Fig. 1(b), and is divided by 4 stages, heating, annealing, growth, and cooling.

Air introduction was performed by intentional leak through a ball valve (BV) and a normally-open metering valve (MV), as schematically shown in Fig. 1(a). When we open the BV, the gasses are leaked through the MV since the pressure of the CVD chamber is higher than atmospheric pressure. At the same time, there must be unavoidable very low amount back-flow of air into the chamber. To confirm the back-flow of air by leak, we monitored the oxygen concentration under Ar ambient by a zirconia oxygen sensor (Toray Engineering LC 750 L). As a result, oxygen concentration increased ~ 1.5 ppm via the leak with closing MV and opening BV (low leak), while oxygen concentration showed lower than 0.1 ppm without leak, proving the existence of low amount of air introduction by the back flow. The amount of air introduction can be varied by adjusting the MV. When the MV has been closed (low leak) and opened for 10° (high leak), approximately 0.02 and 0.04 cm³ in volume of oxygen (in 1000 sccm Ar flow) have been introduced during the leak process, respectively. In addition, flow rates of

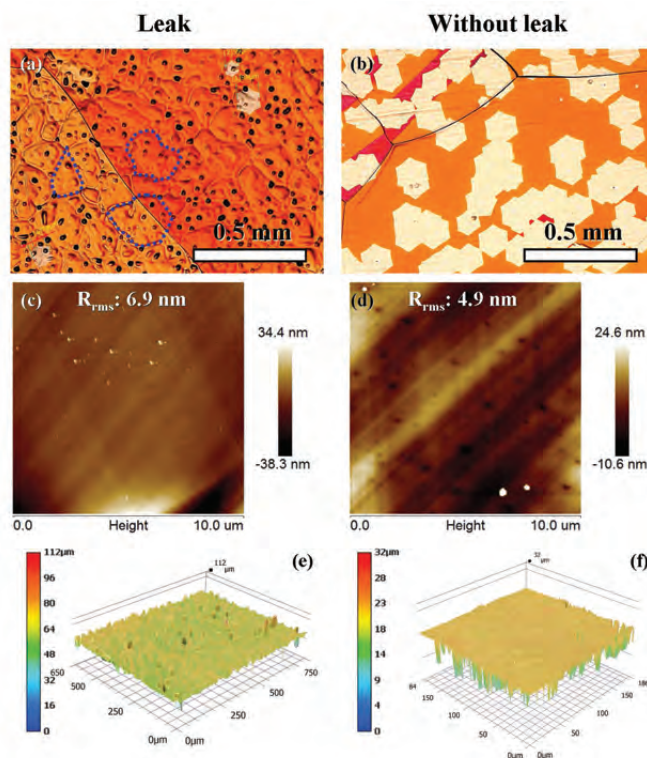


FIG. 2. Effect of leak on graphene growth and surface morphology. Optical microscope images of visualized graphene on Cu which are grown with (a) and without leak (b). Typical AFM images of Cu surface after CVD with (c) and without leak (d). 3D optical images showing large scale morphology of Cu surface after CVD with (e) and without leak (f).

leak which can be used as a parameter for adjusting the amount of air were estimated by monitoring the decay of pressure with time after filling Ar gas and closing the BV.

The graphene on Cu was heated to around 200°C for 2 min in air, which oxidizes only exposed Cu surface, leading large contrast between graphene and Cu in optical microscope image (Keyence Digital Microscope VHX-5000). Detailed surface morphology was observed using an atomic force microscope (AFM; Bruker Multi-Mode 8) in a ScanAsyst[®] mode. X-ray photoelectron spectroscopy (XPS, ULVAC-PHI PHI5000 Versa Probe II) and Auger electron spectroscopy (AES, ULVAC-PHI PHI700 Xi) were used for surface elemental analysis. The graphenes were wet-transferred from the Cu foils onto the SiO₂/Si substrates with a spin-coated poly (methyl methacrylate) (PMMA) film as a mechanical support [9,26]. Raman spectra and mapping images of the transferred graphene were obtained to characterize the quality of graphene by a commercial Raman microscope (Renishaw InVia) using a 532 nm excitation laser.

III. RESULTS AND DISCUSSIONS

Figures 2(a) and 2(b) show optical microscope images of visualized CVD graphenes on Cu with and without leak, respectively. The leak was conducted during all

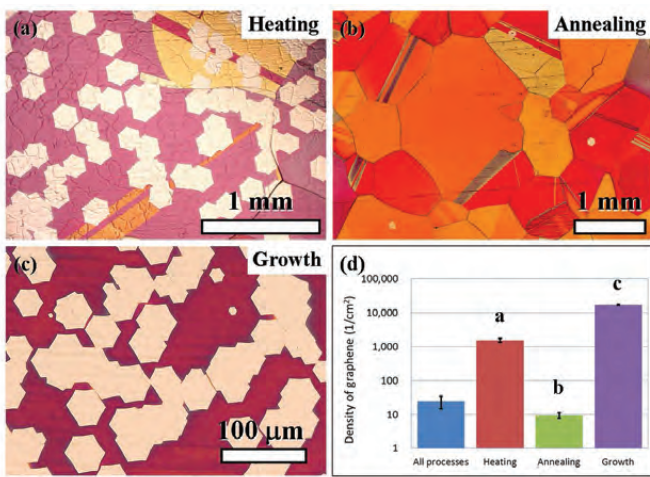


FIG. 3. Effect of leak term on graphene growth. Optical microscope images of visualized graphene on Cu after CVD with leak during heating (a), annealing (b), and growth (c). (d) Comparison of term of air introduction for graphene density.

CVD processes (heating, annealing, growth, and cooling Fig. 1(b)). Hexagonal graphenes showing white contrast in optical images are observed in Figs. 2(a) and (b). The CVD processes with leak produce apparently lower density of graphene than those without leak. The thus drastic change empirically indicates suppression of graphene nucleation by the air introduction. On the other hand, island-like shapes (guided by dotted lines) and black dots are observed in Fig. 2(a) while smooth surface is formed in Fig. 2(b).

Figures 2(c) and 2(d) show typical AFM images of Cu surface after CVD growth with and without leak, respectively. Figures 2(e) and 2(f) show typical 3D optical images showing large scale morphology of Cu surface after CVD growth with and without leak, respectively. The root mean squared roughness (R_{rms}) measured for Fig. 2(c) and Fig. 2(d) shows 6.9 and 4.9 nm, respectively. The values are almost similar in this short range ($< 10 \mu m$), but are much smoother than that of the electropolished Cu (R_{rms} : 93.3 nm), presumably by virtue of annealing in Ar/H₂ [9]. On the other hand, many protrusions (more than 10 μm in height) corresponding to the black dots in Fig. 2(a) were observed only on the Cu surface with leak in the 3D optical image (Fig. 2(e)), indicating that the leak affected Cu morphology on a large scale ($> 100 \mu m$).

To understand the role of leak, we conducted the leak only at a specified process (heating, annealing or growth) during CVD. Figures 3(a-c) show optical microscope images of CVD graphene with leak only at heating, annealing, and growth, respectively. Figure 3(d) summarizes the graphene density in each figure. Since the leak process at the annealing process only showed low graphene density with similar magnitude of leak at all processes, low amount air introduction at annealing is an effective process for suppressing graphene nucleation.

To clarify the reason of the lowered graphene density by air introduction at annealing, we characterized the surface of annealed Cu foils (45 min at 1035°C) before growth.

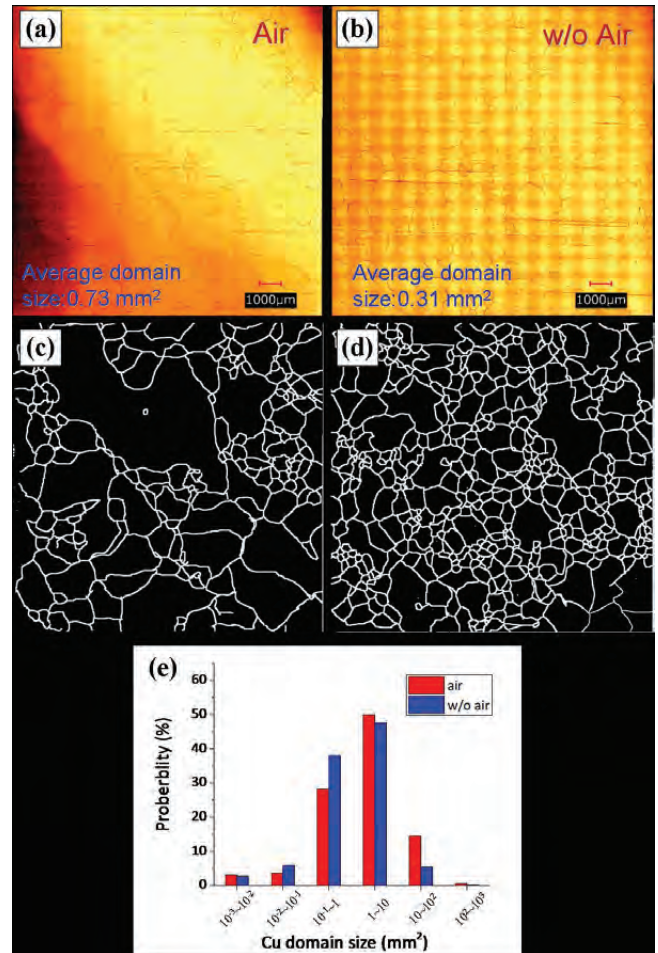


FIG. 4. Optical images of annealed Cu surface with (a) and without (b) air introduction. (c,d) Binarized images converted from (a) and (b) to emphasize domain boundaries of Cu. (e) Histogram of Cu domain size extracted from (c) and (d).

TABLE I. Elemental composition of annealed Cu surface with (air) and without air (w/o air). O/Cu is relative atomic ratio of oxygen for Cu.

	C1s (%)	O1s (%)	Cu2p _{3/2} (%)	O/Cu
air	22.6±0.4	27.8±0.7	49.5±0.6	0.56±0.02
w/o air	19.8±0.3	24.4±0.5	55.7±0.7	0.44±0.01

Figures 4(a) and 4(b) show optical images of Cu surface after annealing with and without leak. Cu crystal domains was be observed for both samples (Figs. 4(a) and 4(b)). Figures 4(c) and 4(d) show binarized images of Figs. 4(a) and 4(b). Figure 4(e) shows the size distribution of the Cu domains extracted from the corresponding optical microscope images. The probability of large Cu domain ($> 1mm^2$) apparently increased by air introduction. In addition, average size of Cu domain also increased by air introduction. Since domain boundary is an active site for graphene nucleation [27], the enlargement of Cu domain by air would be attributed to the lowered graphene density.

The elemental composition of annealed Cu surface was

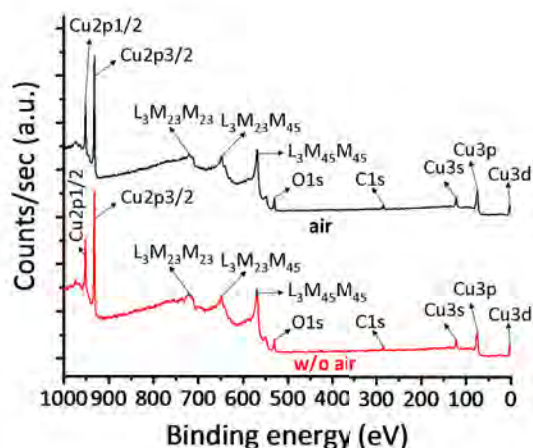


FIG. 5. Representative XPS survey spectra of annealed Cu foils with (black) and without air (red) using 25 W, Al K α (1486.6 eV) radiation.

further examined by XPS. Since Cu surface is oxidized and the chemical state gradually changes with time under ambient air [28], we immediately transferred the annealed Cu foils from CVD to XPS chamber with the same time span (< 10 min). Figure 5 shows representative XPS survey spectra of the annealed Cu foils with and without air introduction. Core-level lines (Cu2p $_{1/2}$, Cu2p $_{3/2}$, Cu3s, Cu3p, Cu3d) and Auger peaks (LMM) of Cu are present. Oxygen (O1s) at 530.5 eV and carbon (C1s) at 285 eV corresponded to oxidation of Cu and adventitious contamination from air on the surface. Table I shows elemental composition of annealed Cu surface with (air) and without air (w/o air) extracted from C1s, O1s, and Cu2p $_{3/2}$ peaks in XPS spectra. The atomic ratio of oxygen of the annealed Cu with air is higher than that without air, which is clearer in O/Cu relative atomic ratios. This indicates that air introduction at annealing oxidized Cu surface. The surface oxidation by air at annealing would passivate active sites for graphene, resulting in suppressing graphene nucleation, which is similar to passivation by oxygen reported in Ref. 25.

On the other hand, a rough Cu surface such like in Fig. 2(a) is only observed after CVD with leak at heating (Fig. 3(a)). This result empirically showed that the air introduction at heating causes roughening of Cu surface which is not desirable for graphene growth.

To investigate the roughening of Cu, we examined the protrusion and flat surface in Fig. 2(a) by AES. As a result, copper, carbon and oxygen signals were detected but no significant difference between the protrusion and the flat region. This result indicates that the surface roughening was not caused by impurities such from the Cu substrate or the quartz tube in CVD furnace but from the main components of the air such as nitrogen, H $_2$ O, and oxygen. Although we cannot exclude intermediate chemical reaction during CVD by nitrogen and H $_2$ O in air, no trace of nitrogen after CVD indicates that surface morphology was affected by oxidation process [24, 29, 30] by H $_2$ O and oxygen in air. Therefore, surface roughening in the present study would be caused by oxidation because

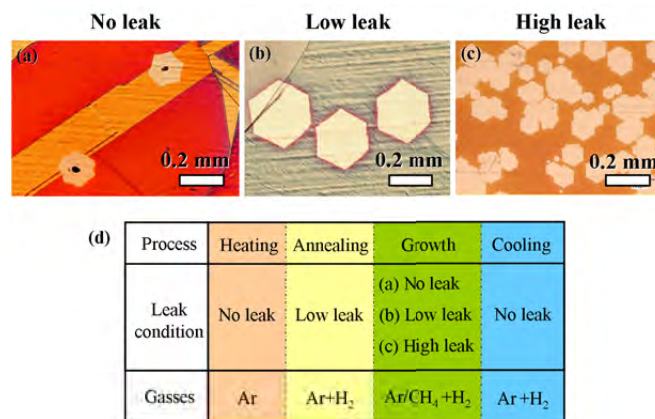


FIG. 6. Comparison of amount of air during the growth stage. Optical images of visualized graphene with different leak conditions during growth stage: (a) no leak; (b) low leak; (c) high leak. (d) Schematic summary of CVD conditions for (a), (b) and (c).

of the absence of reduction gas like at the H $_2$ heating.

To further investigate the effect of air on growth stage, we prepared three different conditions of no, low, and high leaks by closing BV, MV, and opening MV for 10 $^\circ$, respectively. Figures 6(a-c) show graphenes grown for 40 min with no, low, and high leak conditions on Cu that are annealed for 45 min with low leak. Figure 6(d) shows the summary of the process for Figs. 6(a-c). The average diameter and density of graphene domains are measured from optical images and summarized in Table II. The low leak (Fig. 6(b)) leads to twice larger graphene growth than that of no (Fig. 6(a)) and high leak conditions (Fig. 6(c)), even in the same growth time. This acceleration of graphene growth in Fig. 6(c) would be due to growth kinetics change from edge-attachment-limited to diffusion-limited by oxygen, as reported in Ref. 25. On the other hand, high leak (0.20 \pm 0.01 sccm) led to dense growth of graphene in Fig. 6(c). This result indicates only very low amount of air introduction (0.14 \pm 0.01 sccm) can achieve high growth rate and low density of graphene. The reason for the dense growth in Fig. 6(c) might be that nanoscale dusts in air were introduced by opening MV valve.

Since annealing and growth with low leak resulted in large graphene domain sizes with low density, this condition is used hereafter to obtain large size graphene. Figure 7(a) shows dependence of graphene density on annealing time with low leak during the annealing and growth processes. Graphene nucleation is drastically suppressed by annealing up to 60 min, and becomes lower than 10 (cm $^{-2}$) with gradual decay after 180 min annealing. Figure 7(b) shows an optical microscope image of the graphene with long time annealing (4 h) and growth (3.5 h). Approximately 2.5 mm graphenes were observed in a magnified image (Fig. 7(c)), and the hexagonal shape of domains indicates a single crystal [24, 25].

Figures 8 show Raman spectroscopy analysis for millimeter-scale graphene transferred onto a SiO $_2$ /Si substrate. Figure 8(a) shows an optical microscope image of a single hexagonal graphene domain. Figure 8(b) shows

TABLE II. Summary of graphene growth with different leak conditions during growth stage.

Sample	Valve conditions	Leak rate (sccm)	Average diameter of graphene (μm)	Density ($1/\text{cm}^3$)
No leak	BV close	0	81 ± 22	14 ± 7
Low leak	MV close	0.14 ± 0.01	179 ± 15	27 ± 8
High leak	10° open (MV)	0.20 ± 0.01	75 ± 3	14100 ± 500

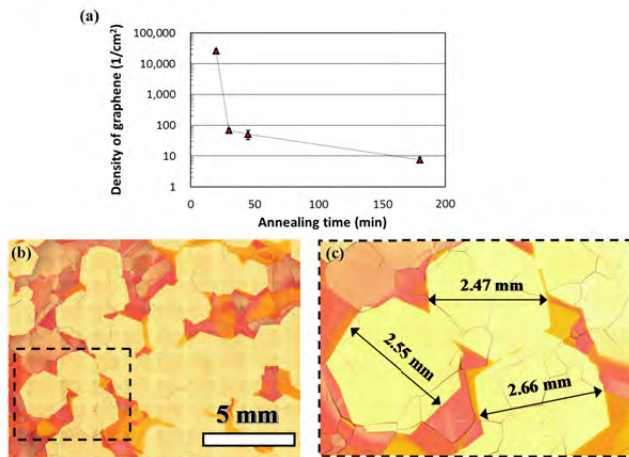


FIG. 7. Large scale graphene growth. (a) Dependence of graphene density on annealing time with leak. (b) Optical image of visualized large-size graphene grown by 4 h annealing and 3.5 h growth. (c) Enlarged view of (b).

TABLE III. Average peak properties of Raman spectra in Fig. 6(b). Each peak was analyzed by fitting with a Lorentzian curve. Width means full width at half maximum.

G center (cm^{-1})	G width (cm^{-1})	G' center (cm^{-1})	G' width (cm^{-1})	G/D	G'/G
1588.9 ± 0.4	12.3 ± 0.3	2679.1 ± 0.5	31.2 ± 0.2	63 ± 5	2.4 ± 0.1

Raman spectra taken at position 1-6 in Fig. 8(a). Each spectra show similar features of D, G, and G' peaks, indicating uniform quality and layer numbers of graphene in a large domain. Average peak properties of the six spectra are summarized in Table III. Narrow G' peak width ($< 40 \text{ cm}^{-1}$), low G' peak center position ($< 2700 \text{ cm}^{-1}$), and high G'/G peak intensity ratio (> 2) indicates single layer [31]. High G/D peak intensity ratio indicates excellent quality of graphene [31, 32]. Figures 8(c-f) show a magnified optical microscope image, D, G, and G' peak maps around the corner of the graphene domain, respectively, showing high uniformity both in quality and in number of layer on a short scale.

IV. CONCLUSIONS

Effect of low amount of air introduction in atmospheric pressure CVD on graphene growth was studied. Air introduction for all the CVD processes leads to low graphene

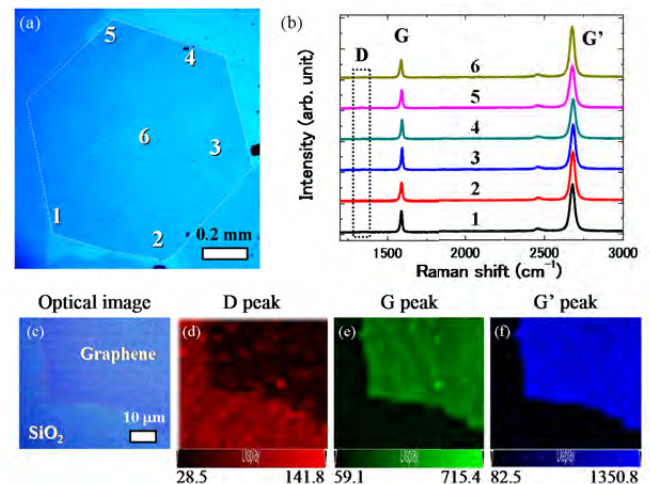


FIG. 8. Raman spectroscopic analysis for large-size transferred graphene on SiO₂/Si. (a) Optical microscope image of a single hexagonal graphene domain. The domain shape is guided by white dotted lines. (b) Stacked Raman spectra taken at 6 different points in a graphene domain. Numbers (1-6) are corresponding to the position in (a). (c) Magnified optical microscope image around the corner of the graphene domain in (a). (d-f) Raman mappings of (c) for D, G, and G' peak show uniformity in quality and layer number of graphene. The mapping images are shown in color scale, and high intensity correspond to red, green, and blue for D, G, and G' as shown in color bars at the bottom of each image. Numerical values at the lower left and right of the mapping images correspond to the lowest and highest peak intensity in each mapping image, respectively.

nucleation, but rough surface is formed by oxidation of Cu. By limiting the air introduction at a specified process (heating, annealing or growth), it was revealed that the roughening was caused by excess oxidation of Cu at the heating, and the graphene nucleation was effectively suppressed due to the reduction of active sites for graphene nucleation both by surface oxidation and enlargement of Cu domain. Although air introduction only at the growth stage was ineffective for graphene nucleation, air introduction for both annealing and growth provided enhancement of domain growth without increasing the density of graphene. Finally, $\sim 2.5 \text{ mm}$ hexagonal graphenes were successfully obtained by low amount air introduction in atmospheric pressure CVD. On the other hand, the fact that back-flow of air readily changes graphene growth claims the importance of careful control of air in a CVD chamber. A careful control of air in CVD chamber will minimize day to day variation of the graphene growth and will be more important for large-size graphene growth

beyond millimeter scale. To our knowledge, it is the first report of air introduction for suppressing nucleation in atmospheric pressure CVD on a Cu foil. It is also noted that this low amount air introduction is effective and practical for the scalable production of high quality large-size single-crystal graphene at low cost.

ACKNOWLEDGMENTS

This study was supported in part by Grant-in-Aid for Japan Society for the Promotion of Science (JSPS)

Fellows (25 · 10897), and Strategic Research Foundation Grant-aided Project for Private Universities from the Ministry of Education, Culture, Sport, Science, and Technology, Japan (MEXT).

-
- [1] A. K. Geim and K. S. Novoselov, *Nat. Mater.* **6**, 183 (2007).
- [2] K. S. Novoselov, A. K. Geim, S. V. Morozov, D. Jiang, Y. Zhang, S. V. Dubonos, I. V. Grigorieva, and A. A. Firsov, *Science* **306**, 666 (2004).
- [3] K. S. Novoselov, A. K. Geim, S. V. Morozov, D. Jiang, M. I. Katsnelson, I. V. Grigorieva, S. V. Dubonos, and A. A. Firsov, *Nature* **438**, 197 (2005).
- [4] Y. Zhang, Y. W. Tan, H. L. Stormer, and P. Kim, *Nature* **438**, 201 (2005).
- [5] P. Avouris, Z. Chen, and V. Perebeinos, *Nat. Nanotechnol.* **2**, 605 (2007).
- [6] R. R. Nair, P. Blake, A. N. Grigorenko, K. S. Novoselov, T. J. Booth, T. Stauber, N. M. R. Peres, and A. K. Geim, *Science* **320**, 1308 (2008).
- [7] C. Lee, X. Wei, J. W. Kysar, and J. Hone, *Science* **321**, 385 (2008).
- [8] X. S. Li, W. Cai, J. An, S. Kim, J. Nah, D. Yang, R. Piner, A. Velamakanni, I. Jung, E. Tutuc, S. K. Banerjee, L. Colombo, and R. S. Ruoff, *Science* **324**, 1312 (2009).
- [9] A. Reina, X. Jia, J. Ho, D. Nezich, H. Son, V. Bulovic, M. S. Dresselhaus, and J. Kong, *Nano Lett.* **9**, 30 (2009).
- [10] X. Li, W. Cai, L. Colombo, and R. S. Ruoff, *Nano Lett.* **9**, 4268 (2009).
- [11] X. S. Li, C. W. Magnuson, A. Venugopal, J. H. An, J. W. Suk, B. Y. Han, M. Borysiak, W. W. Cai, A. Velamakanni, Y. W. Zhu, L. F. Fu, E. M. Vogel, E. Voelkl, L. Colombo, and R. S. Ruoff, *Nano Lett.* **10**, 4328 (2010).
- [12] P. Y. Huang, C. S. Ruiz-Vargas, A. M. van der Zande, W. S. Whitney, M. P. Levendorf, J. W. Kevek, S. Garg, J. S. Alden, C. J. Hustedt, Y. Zhu, J. Park, P. L. McEuen, and D. A. Muller, *Nature* **469**, 389 (2011).
- [13] P. Avouris, Z. Chen, and V. Perebeinos, *Nat. Nanotechnol.* **2**, 605 (2007).
- [14] M. Liu, X. Yin, E. U. Avila, B. Geng, T. Zentgraf, L. Ju, F. Wang, and X. Zhang, *Nature* **474**, 64 (2011).
- [15] M. Liu, X. Yin, and X. Zhang, *Nano Lett.* **12**, 1482 (2012).
- [16] L. Ren, Q. Zhang, J. Yao, Z. Sun, R. Kaneko, Z. Yan, S. Nanot, Z. Jin, I. Kawayama, M. Tonouchi, J. M. Tour, and J. Kono, *Nano Lett.* **12**, 3711 (2012).
- [17] C. C. Lee, S. Suzuki, W. Xie, and T. R. Schibli, *Opt. Express* **20**, 5264 (2012).
- [18] C. C. Lee, C. Mohr, J. Bethge, S. Suzuki, M. E. Fermann, I. Hartl, and T. R. Schibli, *Opt. Lett.* **37**, 3084 (2012).
- [19] H. Wang, G. Wang, P. Bao, S. Yang, W. Zhu, X. Xie, and W. J. Zhang, *J. Am. Chem. Soc.* **134**, 3627 (2012).
- [20] Y. H. Zhang, Z. Y. Chen, B. Wang, Y. W. Wu, Z. Jin, X. Y. Liu, and G. H. Yu, *Mater. Lett.* **96**, 149 (2013).
- [21] Z. Yan, J. Lin, Z. Peng, Z. Sun, Y. Zhu, L. Li, C. Xiang, E. L. Samuel, C. Kittrell, and J. M. Tour, *ACS Nano* **6**, 9110 (2012).
- [22] S. Suzuki, T. Nagamori, Y. Matsuoka, and M. Yoshimura, *Jpn. J. Appl. Phys.* **53**, 095101 (2014).
- [23] S. Chen, H. Ji, H. Chou, Q. Li, H. Li, J. W. Suk, R. Piner, L. Liao, W. Cai, and R. S. Ruoff, *Adv. Mater.* **25**, 2062 (2013).
- [24] L. Gan and Z. Luo, *ACS Nano* **7**, 9480 (2013).
- [25] Y. Hao, M. S. Bharathi, L. Wang, Y. Liu, H. Chen, S. Nie, X. Wang, H. Chou, C. Tan, B. Fallahzad, H. Ramnarayan, C. W. Magnuson, E. Tutuc, B. I. Yakobson, K. F. McCarty, Y.-W. Zhang, P. Kim, J. Hone, L. Colombo, and R. S. Ruoff, *Science* **342**, 720 (2013).
- [26] H. J. Jeong, H. Y. Kim, S. Y. Jeong, J. T. Hana, K.-J. Baeg, J. Y. Hwang, and G.-W. Lee, *Carbon* **66**, 612 (2014).
- [27] G. H. Han, F. Güneş, J. J. Bae, E. S. Kim, S. J. Chae, H.-J. Shin, J.-Y. Choi, D. Pribat, and Y. H. Lee, *Nano Lett.* **11**, 4144 (2011).
- [28] I. Platzman, R. Brenner, H. Haick, and R. Tannenbaum, *J. Phys. Chem. C* **112**, 1101 (2008).
- [29] P. Klapetek, I. Ohlídal, and K. Navrátil, *Microchim. Acta* **147**, 175 (2004).
- [30] J. Kraft and F. P. Netzer, *Surf. Sci.* **357**, 740 (1996).
- [31] L. M. Malard, M. A. Pimenta, G. Dresselhaus, and M. S. Dresselhaus, *Phys. Rep.* **473**, 51 (2009).
- [32] A. C. Ferrari and J. Robertson, *Philos. Trans. R. Soc. London, Ser. A* **362**, 2477 (2004).

Cite this: *Nanoscale*, 2016, 8, 117

Graphene and graphene oxide for desalination

Yi You,^a Veena Sahajwalla,^a Masamichi Yoshimura^b and Rakesh K. Joshi*^aReceived 8th September 2015,
Accepted 8th November 2015

DOI: 10.1039/c5nr06154g

www.rsc.org/nanoscale

There is a huge scope for graphene-based materials to be used as membranes for desalination. A very recent study has confirmed that 100% salt rejection can be achieved for commonly used ions by utilizing single layer nonporous graphene. However, the cost effective fabrication procedure for graphene oxide membranes with precise control of pore size can offer a practical solution for filtration if one can achieve 100% percent salt rejection.

Desalination is defined as the process that isolates pure water from seawater and it is proposed to be an effective solution to water scarcity. In any desalination process, the role of a membrane is crucial. Though various materials have been exploited as membranes for desalination, such as polymers and ceramics (e.g. organosilica, zeolites),^{1–3} graphene-based materials have recently emerged as potential candidates with excellent desalination characteristics.^{4–9} Pristine graphene is extremely impermeable to liquid and gases, therefore the possibilities to create water pathways through the material are either the stacking of graphene oxide sheets (Fig. 1a)^{10–14} or the generation of nanopores in monolayer graphene (Fig. 1b).^{6,15}

The use of graphene oxide as a feasible membrane was firstly developed by Nair *et al.*,¹⁰ and they discovered that stacking the graphene oxide film allows a unique water permeation pathway but selectively hinders the motion of gases and non-aqueous solutions.¹⁰ After that, there were several attempts towards the development of graphene oxide based membranes.^{4,5,11–14,16} Meanwhile, graphene with artificially created nanosized holes finds application as a molecular and ionic sieving membrane, thanks to the development of technology for the fabrication of high quality graphene with a large size.¹⁷ After some nanopores are created, the inherent hydrophobia of the parent graphene can exhibit a capillary force for water permeation.⁶ Recent discoveries have addressed the capability of nanoporous graphene as a reverse osmosis membrane in terms of both mechanical aspects and desalination performances, such as salt rejection and water flux.^{6,18} Surwade *et al.* have experimentally demonstrated the possibility of desalination using single layer graphene with a few controllable holes¹⁵ and proved the theoretical predictions.⁶

This is a major breakthrough for the application of graphene in desalination.¹⁵ The authors engineered the nanopores by treating the CVD grown graphene layers with oxygen plasma with the nanoporosity being varied by altering the oxygen exposure time, and the nanoporous graphene was then tested for desalination.¹⁵ This article has put forth several possibilities to perform more desalination experiments using the membranes for large scale desalination.¹⁵ We certainly believe that there is a huge scope for further research on the utilization of single layers with artificially created defects as pores for desalination. The current density measurements performed by the authors are indeed a good tool to qualitatively understand the possible permeation mechanisms. However, at this point, experiments related to the chemical analysis of solutions in feed and permeate are essential to estimate the exact rejection ratios for the application of porous graphene in large scale desalination. One must take a quantity of solutions from feed and permeate at regular intervals in order to perform the chemical analysis of the solutions with the highest possible detection limit. Based on the past investigations on graphene-based desalination membranes, herein we provide brief comparisons between nanoporous graphene and graphene oxide layers employed for desalination.

Nanoporous graphene is expected to excel as a potential candidate due to the following characteristics. Firstly, the sub-nanometre sized pores in the graphene can be defined with high precision by the oxidative etching method and ion bombardment.^{15,17} Secondly, nanoporous graphene demonstrates the high possibility to achieve 100% salt rejection because the only translocation pathways for water molecules and ions are the nanopores.¹⁵ Third, the water permeation rate can be governed by managing the porosity on the graphene. Fourth, various functional groups can be employed to terminate the bare carbon atoms in the holes, thereby diversifying the desalination performance.^{4,6} However, some disadvantages and experimental challenges are also associated with the nanoporous graphene membrane for desalination. Despite advance-

^aCentre for Sustainable Materials Research and Technology, School of Materials Science and Engineering, University of New South Wales, NSW 2052, Australia.
E-mail: veena@unsw.edu.au, r.joshi@unsw.edu.au

^bSurface Science Laboratory, Toyota Technological Institute, Nagoya 468-8511, Japan

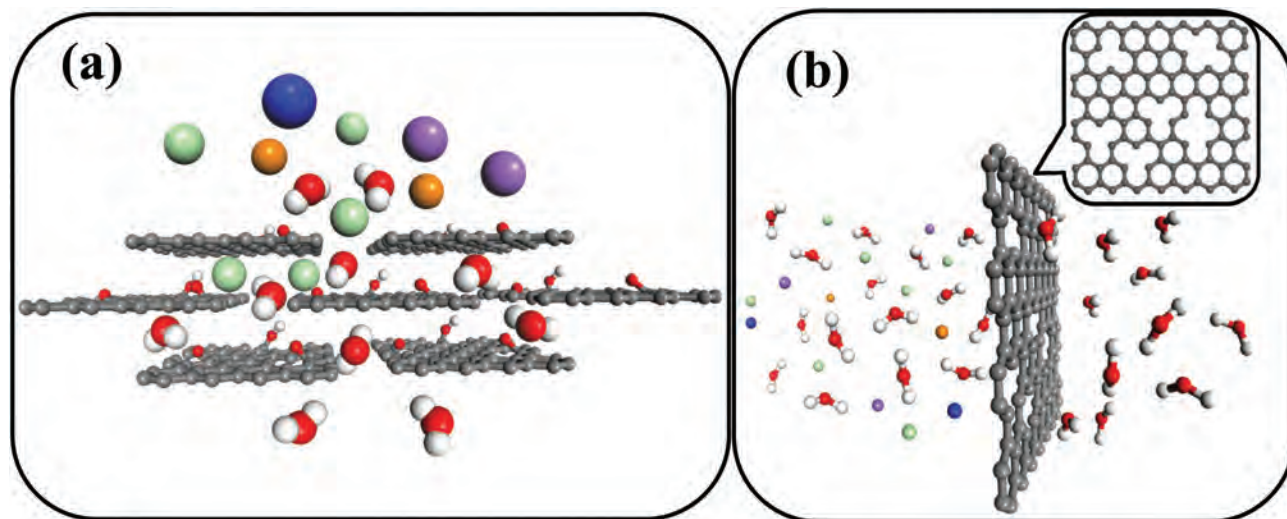


Fig. 1 (a) A stacked graphene oxide layer membrane in which water molecules permeate through the developed nanochannels between each graphene oxide layer, while hydrated salt ions are blocked.¹⁰ (b) A nanoporous graphene membrane, in which water molecules pass through deliberately created nanopores in the graphene with a specific size, hindering the permeation of large hydrated salt ions.⁶ (C: black, H: white, O: red, K⁺: blue, Na⁺: purple, Mg²⁺: orange, Cl⁻: cyan).

ments in the methods for producing pores in graphene, it is an extremely daunting challenge to achieve a high density of holes with a narrow size distribution.⁴ Besides, the tiny nanoscale holes generated in graphene restrict the amount of water permeation. Even if high water permeability is achieved, the high density of holes in the graphene may result in unexpected reductions in mechanical properties or even the destruction of the whole structure. Additionally, the complexity of obtaining continuous large-area perfect graphene and subsequent generation of holes limit the scaling up of production. Furthermore, the whole process of composing the nanoporous graphene should be conducted with extreme caution. Last but not least, the design of high quality graphene, the oxidative etching technique and ion bombardment are expensive methods.

Compared to nanoporous graphene, the stacking of graphene oxide membranes has been proposed to exhibit superiorities in the following aspects. Firstly, unlike the artificially created holes in graphene, graphene oxide membranes rely on tortuous routes in the interconnected nanochannels that serve as a water permeation route.^{19,20} These nanochannels are actually the spaces between each graphene oxide layer, which can be regulated through the creation of stabilizing force between the layers.^{11,19} Furthermore, the high surface area in the twisted nanochannels ensures that a high water flux can be achieved. Secondly, the preparation of graphene oxide is cost effective in terms of both raw materials and methodology. For instance, the typical starting material for graphene oxide is graphite, which is abundant and cheap.¹⁹ Additionally, the entire synthesis process can be performed in solution. As well as the low cost, this wet chemical synthesis can be performed at the expense of minimum energy and it is facile to control.¹³ Further, the solution synthesis offers the possibility of surface

functionalization with a variety of groups for an efficient catalyst attachment, thereby imparting the graphene oxide membranes with diverse functions, such as sterilization. Besides, these diverse functional groups also provide a foundation for composite constructions such as graphene oxide–polymer composites, which are found to reinforce the mechanical stability and further enhance the membrane properties.¹⁶ In addition, the oxygenated functional groups endow graphene oxide with hydrophilicity and pH sensitivity.^{19,21} Since the hydrophobic region regulates the water flow, the functional group density should be well controlled during the fabrication. The linear distribution of the hydrophobic region will ensure fast water permeation.¹¹ Moreover, despite some defects being introduced during the preparation of the graphene oxide, the stacked layer structure will counter this effect and prevent any unexpected diffusion through these sites.¹⁹ On the other hand, as a desalination membrane, stacking graphene oxide necessitates further improvements. The spacing (mesh size) in graphene oxide membranes is the critical parameter that determines the desalination property,²⁰ therefore it should be properly controlled. The uncertainty in the chemical synthesis may introduce several unwanted groups and cause unpredictable swelling effects. Therefore, the challenge of handling functional groups needs to be addressed. On a final note, achieving 100% salt rejection is a daunting task for graphene oxide membranes.¹¹

In summary, graphene-based materials exhibit unlimited potential to be used as membranes for desalination. Recent discovery¹⁵ has proved that a membrane with nanoporous graphene can exhibit 100% salt rejection. However, compared to nanoporous graphene, the simple and cost-effective fabrication of graphene oxide membranes with precise control of pore size can be a practical solution for filtration, providing

that the salt rejection could match that of nanoporous graphene membranes.

Acknowledgements

This work was supported by the Australian Research Council Laureate Fellowship awarded to Prof. Veena Sahajwalla. RKJ acknowledges Start-Up Research Grant (PS38305) from the University of New South Wales.

References

- 1 K. P. Lee, T. C. Arnot and D. Mattia, A review of reverse osmosis membrane materials for desalination—Development to date and future potential, *J. Membr. Sci.*, 2011, **370**, 1–22.
- 2 Y. Chua, *et al.*, Mesoporous organosilica membranes: Effects of pore geometry and calcination conditions on the membrane distillation performance for desalination, *Desalination*, 2015, **370**, 53–62.
- 3 B. Zhu, *et al.*, Application of robust MFI-type zeolite membrane for desalination of saline wastewater, *J. Membr. Sci.*, 2015, **475**, 167–174.
- 4 M. Hu and B. Mi, Enabling graphene oxide nanosheets as water separation membranes, *Environ. Sci. Technol.*, 2013, **47**, 3715–3723.
- 5 Y. Han, Z. Xu and C. Gao, Ultrathin graphene nanofiltration membrane for water purification, *Adv. Funct. Mater.*, 2013, **23**, 3693–3700.
- 6 D. Cohen-Tanugi and J. C. Grossman, Water Desalination across Nanoporous Graphene, *Nano Lett.*, 2012, **12**, 3602–3608.
- 7 D. Konatham, *et al.*, Simulation Insights for Graphene-Based Water Desalination Membranes, *Langmuir*, 2013, **29**, 11884–11897.
- 8 E. N. Wang and R. Karnik, Water desalination: Graphene cleans up water, *Nat. Nanotechnol.*, 2012, **7**, 552–554.
- 9 A. K. Mishra and S. Ramaprabhu, Functionalized graphene sheets for arsenic removal and desalination of sea water, *Desalination*, 2011, **282**, 39–45.
- 10 R. Nair, *et al.*, Unimpeded permeation of water through helium-leak-tight graphene-based membranes, *Science*, 2012, **335**, 442–444.
- 11 R. Joshi, *et al.*, Precise and ultrafast molecular sieving through graphene oxide membranes, *Science*, 2014, **343**, 752–754.
- 12 P. Sun, *et al.*, Selective Trans-Membrane Transport of Alkali and Alkaline Earth Cations through Graphene Oxide Membranes Based on Cation- π Interactions, *ACS Nano*, 2014, **8**, 850–859.
- 13 P. Sun, *et al.*, Selective ion penetration of graphene oxide membranes, *ACS Nano*, 2012, **7**, 428–437.
- 14 A. Nicolăi, B. G. Sumpter and V. Meunier, Tunable water desalination across graphene oxide framework membranes, *Phys. Chem. Chem. Phys.*, 2014, **16**, 8646–8654.
- 15 S. P. Surwade, *et al.*, Water desalination using nanoporous single-layer graphene, *Nat. Nanotechnol.*, 2015, **10**, 459–464.
- 16 H. M. Hegab and L. Zou, Graphene oxide-assisted membranes: Fabrication and potential applications in desalination and water purification, *J. Membr. Sci.*, 2015, **484**, 95–106.
- 17 S. P. Koenig, *et al.*, Selective molecular sieving through porous graphene, *Nat. Nanotechnol.*, 2012, **7**, 728–732.
- 18 D. Cohen-Tanugi and J. C. Grossman, Mechanical Strength of Nanoporous Graphene as a Desalination Membrane, *Nano Lett.*, 2014, **14**, 6171–6178.
- 19 B. Mi, Graphene oxide membranes for ionic and molecular sieving, *Science*, 2014, **343**, 740–742.
- 20 D. W. Boukhvalov, M. I. Katsnelson and Y. W. Son, Origin of anomalous water permeation through graphene oxide membrane, *Nano Lett.*, 2013, **13**, 3930–3935.
- 21 B. Ganesh, A. M. Isloor and A. Ismail, Enhanced hydrophilicity and salt rejection study of graphene oxide-polysulfone mixed matrix membrane, *Desalination*, 2013, **313**, 199–207.

Article

Suppression of Graphene Nucleation by Turning Off Hydrogen Supply Just before Atmospheric Pressure Chemical Vapor Deposition Growth

Seiya Suzuki *, Yoshifumi Terada and Masamichi Yoshimura

Graduate School of Engineering, Toyota Technological Institute, 2-12-1 Hisakata, Tempaku, Aichi, Nagoya 468-8511, Japan; teranisuta@gmail.com (Y.T.); yoshi@toyota-ti.ac.jp (M.Y.)

* Correspondence: seiya09417@gmail.com; Tel.: +81-52-809-1852

Academic Editor: Maria Miritello

Received: 17 October 2017; Accepted: 9 November 2017; Published: 20 November 2017

Abstract: To exploit the extraordinary property of graphene in practical electrical and optical devices, it is necessary to produce large-sized, single-crystal graphene. Atmospheric pressure chemical vapor deposition (APCVD) on polycrystalline Cu surface is a promising scalable route of graphene synthesis but the unavoidable multiple nucleation limits their reachable domain size. Here, we report that effective suppression of nucleation was achieved by only turning off hydrogen supply before introduction of the carbon source for graphene growth. The density of graphene decreased from 72.0 to 2.2 domains/cm² by turning off hydrogen for 15 min. X-ray photoelectron spectroscopy and Raman spectroscopy studies show that the Cu surface was covered with 3–4 nm thick highly crystalline Cu₂O, which would be caused by oxidation by residual oxidative gasses in the chamber during the turning off period. It was also revealed that elevating the temperature in Ar followed by annealing in H₂/Ar before turning off hydrogen led to the enlargement of the Cu domain, resulting in the further suppression of nucleation. By optimizing such growth parameters in the CVD process, a single-crystal graphene with ~2.6 mm in diameter was successfully obtained.

Keywords: graphene; atmospheric pressure chemical vapor deposition; copper surface

1. Introduction

Graphene is an atomic sheet of carbon atoms densely packed in a honeycomb structure and has attracted plenty of attention [1–3]. The extraordinary performance of graphene in optoelectronic and electronic applications has been shown by theoretical and experimental investigations using mechanically exfoliated graphene [4–6]. However, the mechanical exfoliation method has no controllability for the flake size and the layer number of graphene, limiting the practical use. A promising scalable route of graphene synthesis is chemical vapor deposition (CVD) on catalytic metal surfaces (Cu [7–15], Ni [14–17], Pt [18], Ir [19], and Ru [20]). Among these, Cu has prominent advantages in terms of cost of production and the preference formation of a single layer originating from the low solubility of carbon [14]. However, the grown CVD graphene is generally polycrystalline [10,21], and its domain boundaries degrade electronic properties such as carrier mobility [22]. Thus, the growth of large-sized graphene with a single crystal domain is highly needed for practical graphene applications.

A strategy to obtain such a large-sized crystal domain is to reduce the nucleation density of graphene. The nucleation density is strongly affected by the amount of carbon supply during the graphene growth [10,23,24] and the number of active sites for graphene nucleation [25,26]. As for the carbon supply, a reduced supply of carbon sources is required to achieve the effective suppression of nucleation [10,23]. In the latter aspect, atomic steps, point defects, impurities, and the grain

boundaries on the Cu surface may act as the potential nucleation sites [26,27]. Many approaches have been performed to reduce the active sites by pretreatment of Cu [13,28], resulting in the growth of millimeter-size single crystal graphene [11,23,24,29,30]. Further increase of domain size was demonstrated by utilizing oxygen in the CVD process. Gan et al. reported that oxygen plays a role to control nucleation seeds in the preheating process, giving subcentimeter single-crystal by controlling the seeding process [31]. Hao et al. reported that surface oxygen plays roles in the passivation of active sites as well as in the acceleration of domain growth by reducing the attachment barrier of carbon to the edge of the domain, resulting in a centimeter single-crystal [32].

Although the technique to grow a large-sized graphene has been steadily advanced, further enlargement in the domain size is desirable for practical use. In addition, the wide variation in domain size, shape, density, and film quality from lab to lab suggests that the growth mechanism of graphene has not been comprehensively understood. Therefore, effective and reproducible methods for suppressing nucleation should be established with understanding of the growth mechanism. Here, we report that the effective suppression of nucleation can be achieved by only turning off hydrogen supply before the introduction of the carbon source for graphene, resulting in the growth of single crystal graphene up to 2.6 mm. The effect of the Ar annealing to the physical property of the substrate surface was studied by depth-profiling X-ray photoelectron spectroscopy (XPS) and Raman spectroscopy. It was revealed that a very thin Cu_2O (3–4 nm thick) layer was formed after the Ar annealing, suggesting the existence of residual oxidative gasses such as oxygen and water vapor in the CVD chamber. The present report proposes the utilization of the residual oxidative gasses for large size graphene growth, and clarifies the reason for the wide variation in graphene growth from lab to lab. It was also revealed that elevating temperature in the Ar followed by annealing in H_2/Ar before turning off hydrogen led to enlargement of the Cu domain, resulting in further suppression of nucleation. The present APCVD process neither requires any special gasses, high quality Cu foils, nor vacuum pumps, which is ideal for mass production of large single crystal graphenes at a low cost.

2. Materials and Methods

The APCVD system for graphene growth consists of an inner 30 mm and outer 36 mm diameter quartz tubes as a sample holder and a chamber, respectively (Figure 1a). The purities of H_2 and Ar gasses are higher than 99.9999% (7N), and 99.9999% (6N), respectively. The chamber pressure has been kept at a slightly higher pressure than atmospheric pressure (0.123–0.128 MPa) during the CVD process. Commercially available 100 μm thick Cu foils (#113321, Nilaco, Tokyo, Japan) with a size of $\sim 2.2\text{ cm} \times 10\text{ cm}$ were used as catalytic substrates for the growth.

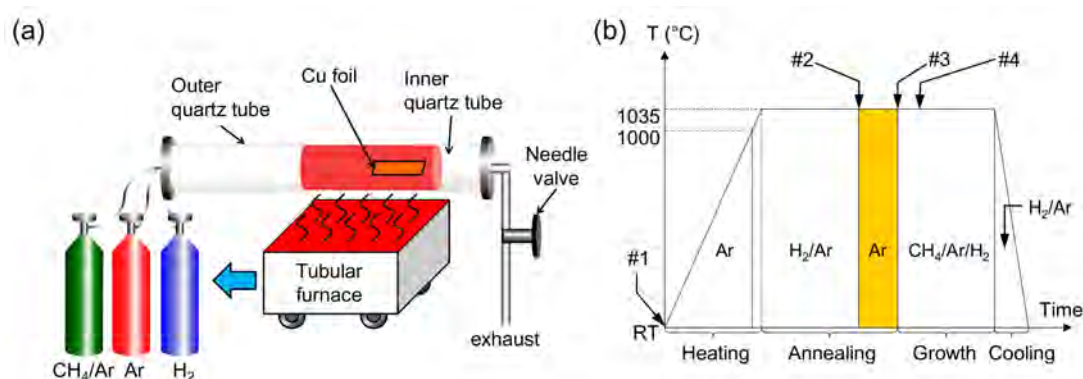


Figure 1. (a) A schematic illustration of the CVD setup; (b) A schematic illustration of a typical CVD growth process. The Cu foil was heated with Ar flow (1000 sccm) until 1000 °C (Ar heating) and with H_2/Ar flow (100/500 sccm) until the reaction temperature (1035 °C). The heating process takes ~ 50 min to elevate the temperature until reaching 1035 °C. The annealing process can be divided by Ar heating, H_2/Ar annealing, Ar annealing, growth, and cooling.

The concentration of residual oxygen in the CVD chamber under Ar flow was measured by a zirconia oxygen sensor (LC-750 L, Toray Engineering, Tokyo, Japan). The zirconia oxygen sensor was placed downstream of the heating furnace. Optical microscopy (Digital Microscope VHX-5000, Keyence, Osaka, Japan) and field emission scanning electron microscopy (S4700, Hitachi High-Technologies Corporation, Tokyo, Japan) were used to obtain the density and the size of graphenes. To visualize graphene in the optical image, Cu foils were oxidized in air around 200 °C. Then the graphene nucleation density was measured by counting the amount of graphene in an optical microscope image. The average nucleation densities were obtained from several different optical images on the same sample. Surface analysis of Cu foils was performed by XPS (PHI 5000 VersaProbe II, ULVAC-PHI, Kanagawa, Japan) under a base pressure of $\sim 6 \times 10^{-8}$ Pa and a monochromatized Al K α (1486.6 eV) X-ray source. Energy calibration was performed using the position of the primary C 1s peak at 284.8 eV. Atomic concentrations were calculated using the ratio of integrated spectral areas for C1s, O1s, and Cu2p_{3/2} from high resolution scans and the relative sensitivity factors inherent to the instrument. The accuracy of the atomic concentration is up to 10% of the measured value. Cu foils were sputtered by using accelerated Ar ions with 1 kV for the depth profiling of XPS. The sputtering depth of Cu by 1 kV Ar ions was calibrated by using Cu thin films deposited by vacuum evaporation. We calculated the difference of the expected sputtered depth between low index Cu crystal planes such as (100), (110), and (111) by 1 kV Ar ions as shown in Table S1. As a result, (100) and (111) showed the smallest and the largest depth, and the depth ratio of (100) to (111) is 0.77 to 0.85, indicating that the crystal plane does not largely affect the depths sputtered by 1 kV Ar ions. The transfer from the CVD to the XPS chamber was performed within 10 min to minimize the gradual change of the chemical state of the Cu surface by ambient air and water [33]. Raman microscopy (InVia Reflex, Renishaw, Gloucestershire, UK) with a 532 nm laser was used to characterize crystal quality of Cu foils and CVD graphene samples.

3. Results and Discussion

A typical CVD process in the present study is schematically shown in Figure 1b. The Cu foil was heated with Ar flow (1000 standard cubic centimeter per minute: (sccm)) until 1000 °C (Ar heating) and with H₂/Ar flow (100/500 sccm) until the reaction temperature (1035 °C). The elevation to the reaction temperature from room temperature takes ~ 50 min. Then the Cu was annealed for 15–45 min with H₂/Ar flow (H₂/Ar annealing). The hydrogen flow was turned off for 0–20 min before introducing CH₄ (Ar annealing). Subsequently, to initiate the growth, the pure Ar flow was replaced by the 10 ppm CH₄ diluted in Ar (500–1000 sccm) and the H₂ (15–20 sccm). Finally, the CVD chamber was rapidly cooled down to room temperature within 30 min.

Figure 2a–c shows optical microscope images of CVD graphene grown on Cu with different Ar annealing times. The preceding H₂/Ar annealing and the subsequent growth time were fixed at 15 and 150 min, respectively. It is obvious that the density of graphene was reduced by increasing the Ar annealing time. Figure 2e shows the dependence of average density of graphene domains on Ar annealing time for two different growth conditions. The numerical values of the average densities of the graphene domains in Figure 2e are summarized in Table S2. Square (corresponding to Figure 2a–c) and circle plots in Figure 2e correspond to 15/500 and 15/1000 for the gas flow ratios of H₂ and diluted CH₄ in Ar (H₂/CH₄) during the growth. The density of graphene decreased rapidly with increasing Ar annealing time for both growth conditions (Figure 2e). For instance, the density of graphene decreased from 72.0 to 2.2 domains/cm² by 15-min Ar annealing for the H₂/CH₄ of 15/1000. The decrease in the density of graphenes implies that the Ar annealing is effective for suppressing graphene nucleation. Figure 2d shows an optical microscope image of CVD graphene grown after longer annealing in H₂/Ar for 45 min without Ar annealing. Since the density of graphene in Figure 2c is smaller than that in Figure 2d, Ar annealing is more effective for suppressing graphene nucleation than extending H₂/Ar annealing time.

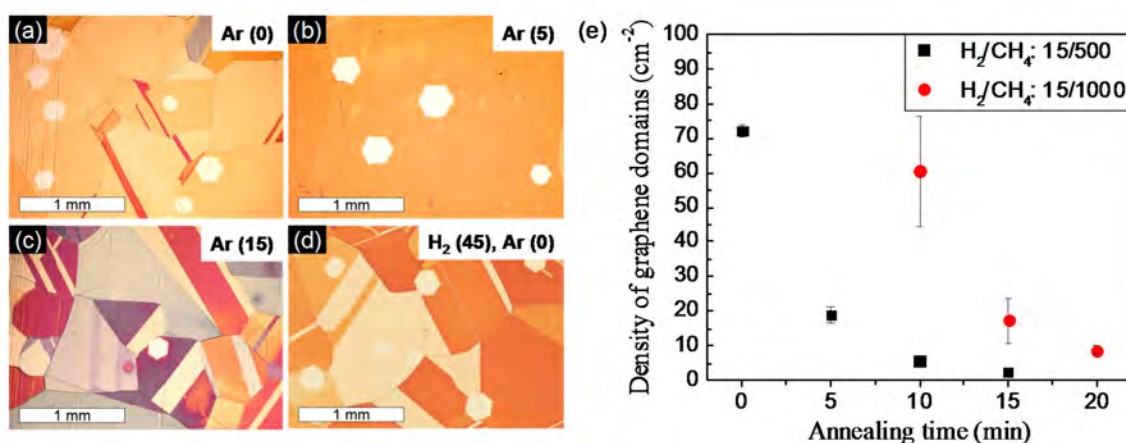


Figure 2. Effect of Ar annealing on density of graphene domains. (a–c) Optical microscope images of CVD graphene on Cu with different Ar annealing time (0, 5, and 15 min), while H₂ annealing time was fixed at 15 min; (d) CVD graphene grown after H₂/Ar annealing for 45 min without Ar annealing; (e) Dependence of average density of graphene domains on Ar annealing time with two different flow rates for the growth. Square (black) and circle (red) plots correspond to the gas flows of 15/500 and 15/1000 sccm of H₂/diluted CH₄ in Ar (H₂/CH₄), respectively. Density of graphene domains is drastically decreased by Ar annealing for both growth conditions.

In addition, the standard errors in Figure 2e were larger in the gas follow ratio of H₂/CH₄ of 15/1000 than that of 15/500 (see Table S2). The H₂/CH₄ of 15/1000 was used for the high speed growth. The large standard errors in Figure 2e indicate that the high speed growth results in a large distribution in density of the graphene domain. The variation of the density of graphene obtained by 15/1000 at different locations can be seen in optical microscope images of graphene/Cu in Figures S1–S3.

To understand the suppressed nucleation caused by the Ar annealing, we examined annealed Cu surfaces before growth by XPS. The samples were prepared with a fixed H₂/Ar annealing time (15 min) and a different Ar annealing time (0–20 min), and were then cooled down under Ar ambient without growth process. Since the Cu surface is easily oxidized in air and the chemical state gradually changes with time [33], we immediately transferred the annealed Cu foils to the XPS chamber to minimize the effect. Figure 3a,b show high-resolution O1s and Cu2p_{3/2} XPS spectra taken at different depths (0–4 nm) in the 5 min-annealed Cu foil, respectively. In O1s depth profiling (Figure 3a), the major (530.6 eV) and the second peaks (532.1 eV) at 0 nm (black) represent the Cu₂O and hydroxyl (OH⁻) group due to the humidity in ambient, respectively, which is in good agreement with the previous results [33]. The O1s spectra at 1 nm (red online) showed a single peak at 530.3 eV also corresponding to Cu₂O as previously reported in the electrodeposited copper oxide film after Ar sputtering [34]. The observed Cu2p_{3/2} spectra showed a single peak at 932.6 eV for all depths, corresponding to Cu₂O [33,35], consistent with O1s spectra. The formation of Cu₂O is consistent with the result of Cu LMM which is shown in Figure S4. Figure 3c shows the dependence of oxygen concentrations on the depth from surface of Cu foils with different Ar annealing times. It was found that the oxygen concentration was increased at deeper positions (1–4 nm) by increasing the Ar annealing time. Wrong call-out order.

To find the reason for Cu₂O formation during Ar annealing, we measured the oxygen concentration in the CVD chamber under Ar flow. Figure S5a showed the transition of residual oxygen in the CVD chamber. Ar flowing (1000 sccm) and elevating the temperature were started at 0 and 1 min, respectively. The chamber pressure was kept at ~0.12 MPa. The temperature was reached at 1035 °C after 50 min. The chamber pressure was ~0.12 MPa. The oxygen concentration was suddenly decreased after flowing Ar (Figure S5a). When the temperature was reached at 1035 °C, the oxygen concentration showed ~10 ppm. With continuing heating in the Ar, the oxygen concentration gradually increased as shown in Figure S5b, which is an enlarged graph of Figure S5a. The oxygen concentration

increased to ~4.2 ppm for 20 min after reaching the minimum concentration, which is a typical time for Ar annealing. Thus, the residual oxygen concentration during Ar annealing would be 10–20 ppm.

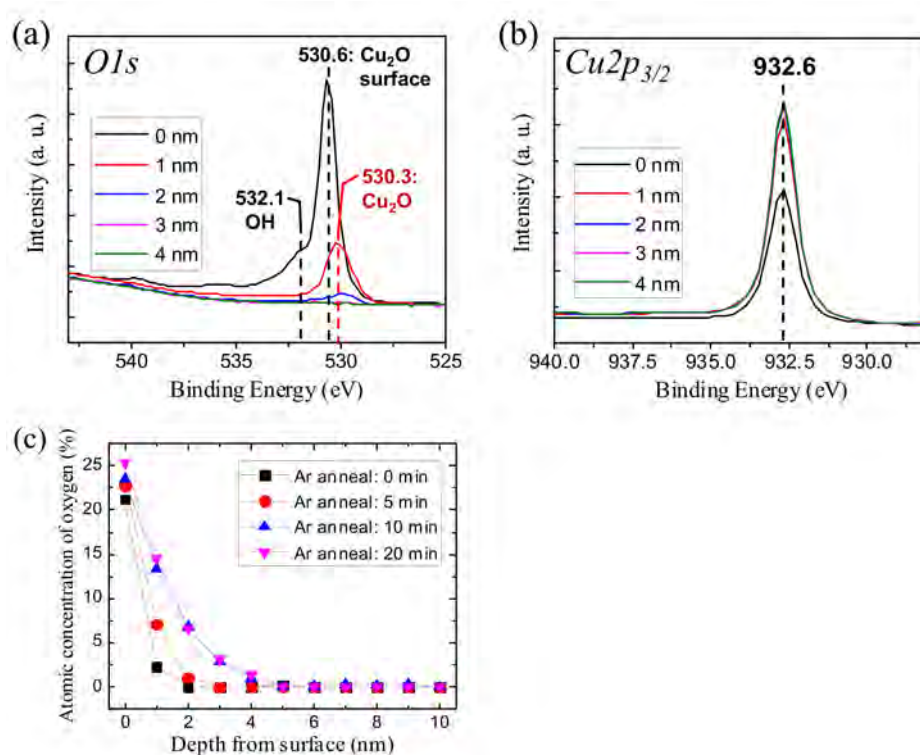


Figure 3. XPS analysis of annealed Cu foils without growth of graphene. (a,b) High-resolution O1s and Cu2p_{3/2} XPS depth profiling of Cu foils with Ar annealing for 5 min; (c) Dependence of oxygen concentration on depth from surface of Cu foils with different Ar annealing time.

In the gas-phase reaction, the following equilibrium must be considered for Cu₂O formation:



Based on thermodynamics, the equilibrium oxygen partial pressure is about 0.1 Pa at 1035 °C [37], which is lower than the partial pressure of the residual oxygen (~1 Pa). Therefore, the residual oxygen can provide surface oxidation to form the Cu₂O during the Ar annealing. On the other hand, dissociation of Cu₂O at the metal oxide interface (Cu₂O(s) → 2Cu(s) + O) would also be happening at a high temperature [38–40]. In addition, the segregation of oxygen during the cooling process is not likely for the formation of the Cu₂O (Figure S6). The observed difference in thickness of the Cu₂O in Figure 3c and Figure S7b would imply that surface oxidation is faster than the dissociation of the oxide during the Ar annealing.

To clarify the crystal structure of the Cu₂O layer, Raman spectroscopy was performed for a CVD-treated Cu foil with Ar annealing for 20 min (H₂/Ar annealing and growth for 45 and 150 min, respectively). However, any peaks of Cu₂O were not observed in the Ar-annealed Cu foil since the thickness of the Cu₂O layer is too thin to detect by Raman spectroscopy. To gain Raman signals, the CVD-treated Cu foil was intentionally oxidized at ~200 °C for 3 min in air (Oxi-CVD), and was measured by Raman spectroscopy. The thickness of the oxide layer was more than 100 nm which was confirmed by XPS depth profiling. To compare Raman spectra, an oxidized as-received Cu foil was also prepared (Oxi-foil).

Figure 4a shows Raman spectra of the Oxi-foil (red) and the Oxi-CVD (blue). All peaks in Figure 4a can be assigned to the phonon energies of Cu₂O: (i) Γ₂₅⁻ (90 cm⁻¹) and Γ₁₂⁻ (110 cm⁻¹), which are silent

modes [41,42]; $\Gamma_{15}^{-(1)}$ (150 cm^{-1}) and $\Gamma_{15}^{-(2)}$ (TO (625 cm^{-1}) and LO (648 cm^{-1})), which are infrared active [41,42]; (iii) Γ_{25}^{+} (521 cm^{-1}), which is the Raman-active mode [41,42]; (IV) $2\Gamma_{12}^{-}$ (217 cm^{-1}) [42] and $2\Gamma_{12}^{-} + \Gamma_{25}^{-}$ (300 cm^{-1}) [43], which are an overtone and combination of them. The appearances of modes Γ_{12}^{-} and Γ_{15}^{-} are derived from the activation by defects or resonance effects [41,44,45]. Thus, the Cu_2O formation by oxidation in the air was clearly observed and detectable by Raman spectroscopy for both the Oxi-CVD and Oxi-foil. Figure 4b shows high resolution Raman spectra around the intense peaks of $\Gamma_{15}^{-(1)}$ and $2\Gamma_{12}^{-}$ modes. Table 1 summarizes peak positions and the full width at half maximum (FWHM) of these peaks for the Oxi-CVD and Oxi-foil samples. These statistical data were extracted from 36 Raman spectra with peaks fitted by a mixture of Lorentzian and Gaussian functions. The peak positions of $\Gamma_{15}^{-(1)}$ and $2\Gamma_{12}^{-}$ modes in the Oxi-CVD are nearly the same as that of Oxi-foil. On the other hand, the FWHM of $\Gamma_{15}^{-(1)}$ and $2\Gamma_{12}^{-}$ modes in the Oxi-CVD were smaller than that of the Oxi-foil, indicating the higher crystallinity of Cu_2O in Oxi-CVD, as reported by Solache-Carranco et al. [46]. This result indicated that the present Ar annealing formed a Cu_2O thin layer with high crystallinity.

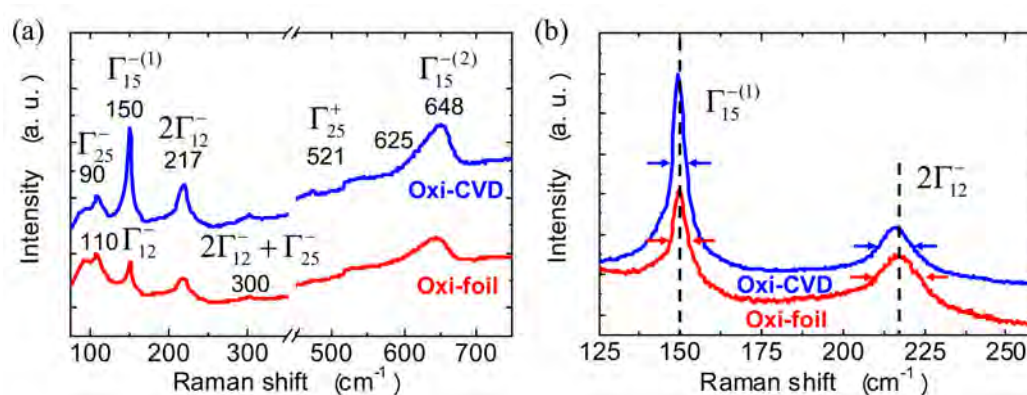


Figure 4. Raman spectroscopy of Cu foils after intentional oxidization in air. (a) Raman spectra of the Oxi-foil (red line) and the Oxi-CVD (blue line). The Raman spectrum of the Oxi-CVD was taken at the Cu surface uncovered by grapheme; (b) High resolution Raman spectra around the peaks of 150 and 217 cm^{-1} . Vertical broken lines and cursors are eye guides to compare Raman peaks.

Table 1. Comparison of Raman peaks in Figure 4b.

Sample	$\Gamma_{15}^{-(1)}$		$2\Gamma_{12}^{-}$	
	Peak Position (cm^{-1})	FWHM (cm^{-1})	Peak Position (cm^{-1})	FWHM (cm^{-1})
Oxi-CVD	149.6	5.0	216.1	13.8
Oxi-foil	149.9	5.7	216.9	17.9

Figure S8a,b is a representative SEM image and electron backscatter diffraction (EBSD) orientation map of a Cu surface which was heated at elevated temperatures in Ar following by H_2/Ar annealing for 2.5 h. The color in Figure S8b represents the fcc crystalline orientation of Cu as shown in Figure S8c. Figure S8d is the area ratio of low index faces for the annealed Cu obtained by statistical analysis of EBSD orientation maps such as Figure S8b. The major crystal face of Cu is (111), and the second (001) as shown in Figure S8b. It is reported that the oxidation of Cu (111) and Cu (001) results in epitaxial Cu_2O [47]. Therefore, the Cu_2O formed by the present Ar annealing would be mainly (111) and (001) surfaces.

To gain full understanding of the evolution of the chemical states of the Cu surface, XPS depth profile measurement was performed on Cu foils which were cooled down after a specific CVD process. These Cu foils are “raw Cu”, “ H_2 : 15 min”, “Ox: 10 min”, and “Red: 5 min” corresponding to the timing of #1–4 shown in Figure 1b, respectively. Figure 5a shows the evolution of the depth profile of oxygen in Cu foils by the CVD process. It was found that the “raw Cu” contains abundant oxygen

inside the foil. The oxygen signals in the “H₂: 15 min” and “Red: 5 min” samples disappeared around 2 nm in depth. Since the oxygen near the surface would come from native oxide formed during the transferring of the sample, the surface of “H₂: 15 min” and “Red: 5 min” samples would be completely reduced to the metallic Cu. The “Ox: 10 min” sample showed detectable oxygen signals until 4 nm from surface, being consistent with Figure 3c.

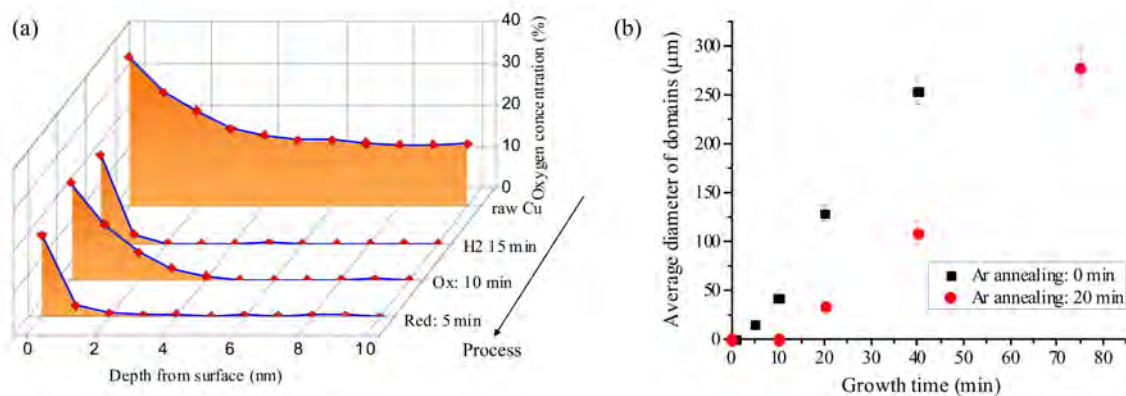


Figure 5. (a) Evolution of an XPS depth profile of oxygen in Cu foil by CVD process. Cu foils of “raw Cu”, “H₂: 15 min”, “Ox: 10 min”, and “Red: 5 min” were obtained after cooling down at #1–4 shown in Figure 1b, respectively; (b) Dependence of the average domain diameter of graphene grown with Ar annealing for 0 and 20 min on growth time.

In addition, the initial growth behavior of graphene has been examined. Figure 5b shows a dependence of the average diameter of the graphene domain on growth time for the substrates without and with 20 min annealing in Ar. Incubation times were observed of around 1 and 10 min for the CVD samples with the 0 and 20 min-Ar annealing, respectively. This indicates that the nucleation of graphene is delayed by the existence of a Cu₂O layer, probably due to the less catalytic activity of Cu₂O for decomposing CH₄.

Although we revealed that surface oxidation by Ar annealing is an efficient way to reduce the density of the nucleation of graphene, the role of Ar heating and H₂/Ar annealing before Ar annealing remains unclear. To reveal them, the graphene was grown with a fixed Ar annealing time (20 min) after heating and annealing (15 min) in H₂/Ar or Ar ambient, and the density of graphene and the morphology of Cu were compared to the present process (Ar heating and H₂/Ar annealing followed by Ar annealing). Figure 6a–f show high and low magnification optical microscope images of CVD graphene obtained by Ar heating followed by H₂/Ar annealing (Figure 6a,d), heating and annealing in H₂/Ar (Figure 6b,e), and heating and annealing in Ar (Figure 6c,f). It can be seen that the present Ar heating followed by H₂/Ar annealing (Figure 6a) provided the largest domain of Cu, and the lowest density of graphene among these processes, proving the present process is the best condition of the heating and annealing process. Since the surface oxidation condition (Ar annealing for 20 min) were the same for all samples in Figure 6, the reduction of the graphene density in the present heating and annealing was mainly caused by lowering the number of domain boundaries of Cu, which are active sites for graphene nucleation [26]. On the other hand, the other two processes did not provide the largest domain size of Cu, indicating that the solely H₂/Ar or Ar annealing is not an effective way to form a large domain of Cu. Although the detailed mechanism of the large domain formation of Cu is not clear, it would be related to Cu transport, which can be changed by the chemisorption of oxygen [48,49]. The present Ar heating followed by H₂/Ar annealing would provide higher mobility of Cu atoms, and resulted in large size Cu domains.

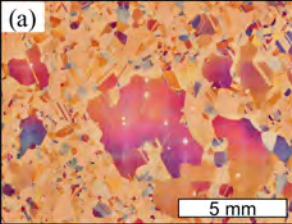
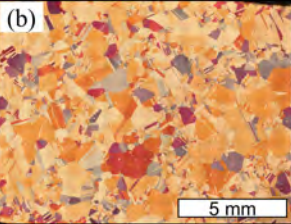
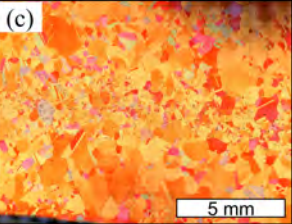
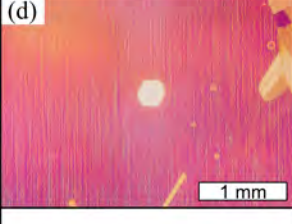
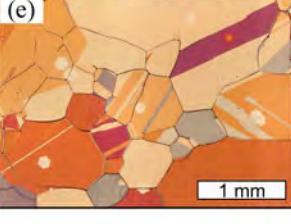
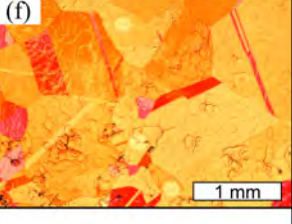
Process	Heating Ar → Annealing H ₂ /Ar	Heating H ₂ /Ar → Annealing H ₂ /Ar	Heating Ar → Annealing Ar
Low Mag.	(a) 	(b) 	(c) 
High Mag.	(d) 	(e) 	(f) 
Density of graphene (cm ⁻¹)	9±1	90±10	15±1

Figure 6. Effect of gas ambient on the heating and annealing process before Ar annealing on the morphology of Cu and the density of graphene. Low (a–c) and high magnification (d–f) optical microscope images of CVD graphene on Cu obtained by the Ar heating followed by H₂/Ar (a,d); heating and annealing in H₂/Ar (b,e); and heating and annealing in Ar (c,f).

Figure 7a shows an optical microscope image of large-sized graphene domains by a CVD process with the H₂/Ar and the Ar annealing for 100 and 35 min, respectively. The isolated hexagonal shape in Figure 7a corresponds to a single crystal domain of graphene [12,23], and single crystal with a size of up to 2.6 mm in diameter was obtained. The single crystallinity of the hexagonal domain was also experimentally confirmed by low-energy electron diffraction (LEED) pattern (Figure S9). Figure 7b shows a Raman spectrum of a millimeter scale CVD graphene transferred to a SiO₂/Si substrate, where G', G, and D peaks were observed around 2685, 1590, and 1345 cm⁻¹, respectively. The higher intensity of G' than G and negligible small D peak indicated the single layer formation and high quality crystallinity of the graphene, respectively [50–52]. Thus, the present modified CVD process successfully demonstrated a large-sized, single-layer graphene formation with high quality.

From the aforementioned results, the evolution of the Cu surface is schematically summarized in Figure 8. At the beginning, the as-received Cu foil has abundant oxygen inside Cu (“Initial” in Figure 8, and #1 in Figure 1b). During H₂/Ar annealing at 1035 °C for 15 min, the oxygen concentration in the Cu suddenly decreases and the crystallization of Cu occurs (“H₂/Ar annealing” in Figure 8, and #2 in Figure 1b). Subsequent Ar annealing provides surface oxidation (“Ar annealing” in Figure 8, and #3 in Figure 1b). The thin layer Cu₂O formed by Ar annealing has high crystallinity since it was formed on crystalline Cu, as observed by Raman spectroscopy (Figure 4 and Table 1). After the initiation of the growth process, the reduction of the surface is started again due to the presence of H₂, and is completed within 5 min (“Incubation time” in Figure 8, and #4 in Figure 1b). Finally, the nucleation of graphene occurs after the supersaturation of active carbons [8], and then domain growth is started (“Growth” in Figure 8).

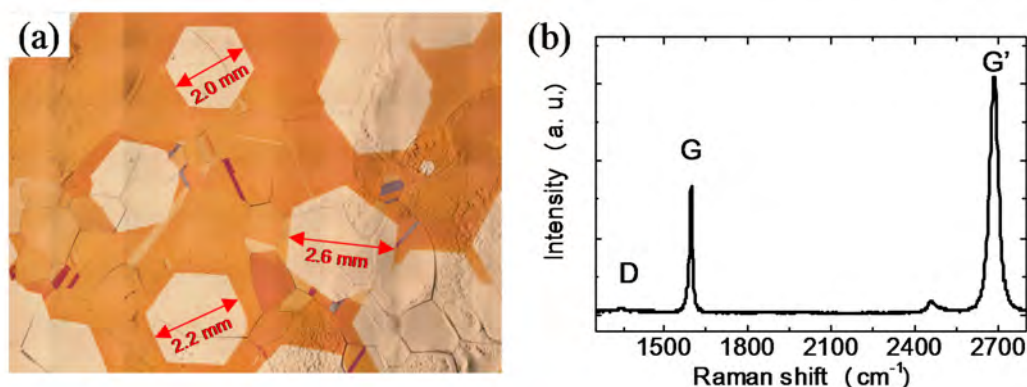


Figure 7. (a) Optical microscope image of large-sized single-crystal graphene. The graphene was grown by a CVD with the H₂/Ar and the Ar annealing for 100 and 35 min, respectively; (b) Raman spectrum of a millimeter scale CVD graphene transferred on a SiO₂/Si substrate.

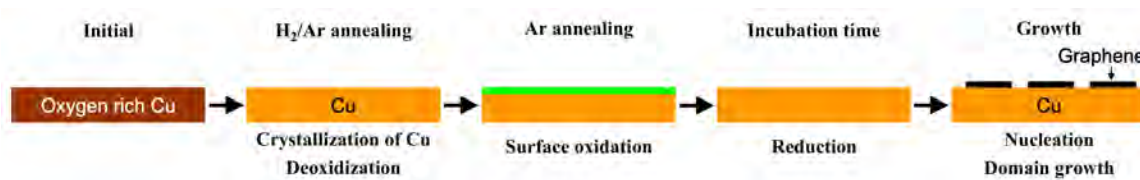


Figure 8. Schematic illustration of the evolution of the Cu surface during the CVD. The initial, H₂/Ar annealing, Ar annealing, and incubation time correspond to the CVD process at #1–4 in Figure 1b, respectively.

The most important process for suppressing nucleation is Ar annealing, which provides surface oxidation. The surface oxidation was reported to remove carbon impurities [53,54] and to passivate active sites [32], resulting in suppressed graphene nucleation. The removal of carbon impurities happens not only from the surface, but also in the bulk Cu through the dissociation of Cu₂O and the diffusion of dissolved atomic oxygen [54]. The highly crystalline Cu₂O observed in the present study may also be attributed to the passivation of active sites, since structural defects in the preformed Cu₂O layer would not possess a sufficient passivation effect. By prolonged Ar annealing, both the removal of carbon impurities and the passivation effects are enhanced, resulting in suppressed graphene nucleation. In addition, Ar heating followed by H₂/Ar annealing contributes to the enlargement of the Cu domain, resulting in the additional suppression of nucleation by reducing active sites such as domain boundaries of Cu.

4. Conclusions

We investigated the effect of turning off hydrogen (Ar annealing) before the growth process on Cu, and engineered it for large size graphene growth. We first revealed that the Ar annealing oxidizes the Cu surface by residual oxidant, which results in the effective suppression of graphene nucleation. The enlargement of the Cu domain by Ar heating, followed by H₂/Ar annealing before Ar annealing was ascribed to the extra suppression of graphene nucleation. Finally, single crystal graphene of ~ 2.6 mm diameter was successfully grown by utilizing the Ar annealing. This study demonstrated that a large-sized single crystal graphene can be grown by utilizing oxidative gasses in the CVD chamber. We expect that the existence of the oxidative gasses is one of the reasons for the wide variation in graphene growth from lab to lab. It is also noted that our modified APCVD process requires neither vacuum pumps nor high-quality Cu, and it is compatible for industrial scale mass production of large-sized single crystal graphene.

Supplementary Materials: Supplementary materials are available online at <http://www.mdpi.com/2079-6412/7/11/206/s1>.

Acknowledgments: The authors thank Yoshimi Horio at Daido University for his help with the LEED measurements. This work was supported in part by the Grant-in-Aid for Young Scientist (Start-up) (No. 15H06723), Research Center for Green Electronic Devices and Materials (S1411027), and Strategic Research Foundation Grant-aided Project for Private Universities from the Ministry of Education, Culture, Sport, Science, and Technology, Japan (MEXT).

Author Contributions: Seiya Suzuki conceived, designed, and performed the experiments; Yoshifumi Terada provided primitive important experiments for the paper. Masamichi Yoshimura contributed reagents/materials/analysis tools; Seiya Suzuki wrote the paper. Masamichi Yoshimura contributed revision and collection of the paper.

Conflicts of Interest: The authors declare no conflict of interest.

References

1. Geim, A.K.; Novoselov, K.S. The rise of graphene. *Nat. Mater.* **2007**, *6*, 183–191. [[CrossRef](#)] [[PubMed](#)]
2. Novoselov, K.; Geim, A.K.; Morozov, S.; Jiang, D.; Katsnelson, M.; Grigorieva, I.; Dubonos, S.; Firsov, A. Two-dimensional gas of massless Dirac fermions in graphene. *Nature* **2005**, *438*, 197–200. [[CrossRef](#)] [[PubMed](#)]
3. Zhang, Y.; Tan, Y.-W.; Stormer, H.L.; Kim, P. Experimental observation of the quantum Hall effect and Berry's phase in graphene. *Nature* **2005**, *438*, 201–204. [[CrossRef](#)]
4. Xia, F.; Mueller, T.; Lin, Y.-M.; Valdes-Garcia, A.; Avouris, P. Ultrafast graphene photodetector. *Nat. Nanotechnol.* **2009**, *4*, 839–843. [[CrossRef](#)] [[PubMed](#)]
5. Liu, M.; Yin, X.; Ulin-Avila, E.; Geng, B.; Zentgraf, T.; Ju, L.; Wang, F.; Zhang, X. A graphene-based broadband optical modulator. *Nature* **2011**, *474*, 64–67. [[CrossRef](#)] [[PubMed](#)]
6. Wilmart, Q.; Berrada, S.; Torrín, D.; Nguyen, V.H.; Fève, G.; Berroir, J.-M.; Dollfus, P.; Plaças, B. A Klein-tunneling transistor with ballistic graphene. *2D Mater.* **2014**, *1*, 011006. [[CrossRef](#)]
7. Bae, S.; Kim, H.; Lee, Y.; Xu, X.; Park, J.-S.; Zheng, Y.; Balakrishnan, J.; Lei, T.; Kim, H.R.; Song, Y.I. Roll-to-roll production of 30-inch graphene films for transparent electrodes. *Nat. Nanotechnol.* **2010**, *5*, 574–578. [[CrossRef](#)] [[PubMed](#)]
8. Kim, H.; Mattevi, C.; Calvo, M.R.; Oberg, J.C.; Artiglia, L.; Agnoli, S.; Hirjibehedin, C.F.; Chhowalla, M.; Saiz, E. Activation energy paths for graphene nucleation and growth on Cu. *ACS Nano* **2012**, *6*, 3614–3623. [[CrossRef](#)] [[PubMed](#)]
9. Li, X.; Cai, W.; An, J.; Kim, S.; Nah, J.; Yang, D.; Piner, R.; Velamakanni, A.; Jung, I.; Tutuc, E. Large-area synthesis of high-quality and uniform graphene films on copper foils. *Science* **2009**, *324*, 1312–1314. [[CrossRef](#)] [[PubMed](#)]
10. Li, X.; Magnuson, C.W.; Venugopal, A.; An, J.; Suk, J.W.; Han, B.; Borysiak, M.; Cai, W.; Velamakanni, A.; Zhu, Y. Graphene films with large domain size by a two-step chemical vapor deposition process. *Nano Lett.* **2010**, *10*, 4328–4334. [[CrossRef](#)] [[PubMed](#)]
11. Li, X.; Magnuson, C.W.; Venugopal, A.; Tromp, R.M.; Hannon, J.B.; Vogel, E.M.; Colombo, L.; Ruoff, R.S. Large-area graphene single crystals grown by low-pressure chemical vapor deposition of methane on copper. *J. Am. Chem. Soc.* **2011**, *133*, 2816–2819. [[CrossRef](#)] [[PubMed](#)]
12. Vlasiouk, I.; Regmi, M.; Fulvio, P.; Dai, S.; Datskos, P.; Eres, G.; Smirnov, S. Role of hydrogen in chemical vapor deposition growth of large single-crystal graphene. *ACS Nano* **2011**, *5*, 6069–6076. [[CrossRef](#)] [[PubMed](#)]
13. Wang, H.; Wang, G.; Bao, P.; Yang, S.; Zhu, W.; Xie, X.; Zhang, W.-J. Controllable synthesis of submillimeter single-crystal monolayer graphene domains on copper foils by suppressing nucleation. *J. Am. Chem. Soc.* **2012**, *134*, 3627–3630. [[CrossRef](#)] [[PubMed](#)]
14. Li, X.; Cai, W.; Colombo, L.; Ruoff, R.S. Evolution of graphene growth on Ni and Cu by carbon isotope labeling. *Nano Lett.* **2009**, *9*, 4268–4272. [[CrossRef](#)] [[PubMed](#)]
15. Sun, Z.; Yan, Z.; Yao, J.; Beitler, E.; Zhu, Y.; Tour, J.M. Growth of graphene from solid carbon sources. *Nature* **2010**, *468*, 549–552. [[CrossRef](#)] [[PubMed](#)]
16. Kim, K.S.; Zhao, Y.; Jang, H.; Lee, S.Y.; Kim, J.M.; Kim, K.S.; Ahn, J.-H.; Kim, P.; Choi, J.-Y.; Hong, B.H. Large-scale pattern growth of graphene films for stretchable transparent electrodes. *Nature* **2009**, *457*, 706–710. [[CrossRef](#)] [[PubMed](#)]

17. Reina, A.; Jia, X.; Ho, J.; Nezich, D.; Son, H.; Bulovic, V.; Dresselhaus, M.S.; Kong, J. Large area, few-layer graphene films on arbitrary substrates by chemical vapor deposition. *Nano Lett.* **2009**, *9*, 30–35. [[CrossRef](#)] [[PubMed](#)]
18. Gao, L.; Ren, W.; Xu, H.; Jin, L.; Wang, Z.; Ma, T.; Ma, L.-P.; Zhang, Z.; Fu, Q.; Peng, L.-M. Repeated growth and bubbling transfer of graphene with millimetre-size single-crystal grains using platinum. *Nat. Commun.* **2012**, *3*, 699. [[CrossRef](#)] [[PubMed](#)]
19. Pletikosić, I.; Kralj, M.; Pervan, P.; Brako, R.; Coraux, J.; N'diaye, A.; Busse, C.; Michely, T. Dirac cones and minigaps for graphene on Ir (111). *Phys. Rev. Lett.* **2009**, *102*, 056808. [[CrossRef](#)] [[PubMed](#)]
20. Sutter, P.W.; Flege, J.-I.; Sutter, E.A. Epitaxial graphene on ruthenium. *Nat. Mater.* **2008**, *7*, 406–411. [[CrossRef](#)] [[PubMed](#)]
21. Huang, P.Y.; Ruiz-Vargas, C.S.; van der Zande, A.M.; Whitney, W.S.; Levendorf, M.P.; Kevek, J.W.; Garg, S.; Alden, J.S.; Hustedt, C.J.; Zhu, Y. Grains and grain boundaries in single-layer graphene atomic patchwork quilts. *Nature* **2011**, *469*, 389–392. [[CrossRef](#)] [[PubMed](#)]
22. Yu, Q.; Jauregui, L.A.; Wu, W.; Colby, R.; Tian, J.; Su, Z.; Cao, H.; Liu, Z.; Pandey, D.; Wei, D. Control and characterization of individual grains and grain boundaries in graphene grown by chemical vapour deposition. *Nat. Mater.* **2011**, *10*, 443–449. [[CrossRef](#)] [[PubMed](#)]
23. Yan, Z.; Lin, J.; Peng, Z.; Sun, Z.; Zhu, Y.; Li, L.; Xiang, C.; Samuel, E.L.; Kittrell, C.; Tour, J.M. Toward the synthesis of wafer-scale single-crystal graphene on copper foils. *ACS Nano* **2012**, *6*, 9110–9117. [[CrossRef](#)] [[PubMed](#)]
24. Zhang, Y.; Chen, Z.; Wang, B.; Wu, Y.; Jin, Z.; Liu, X.; Yu, G. Controllable growth of millimeter-size graphene domains on cu foil. *Mater. Lett.* **2013**, *96*, 149–151. [[CrossRef](#)]
25. Lin, L.; Li, J.; Ren, H.; Koh, A.L.; Kang, N.; Peng, H.; Xu, H.; Liu, Z. Surface engineering of copper foils for growing centimeter-sized single-crystalline graphene. *ACS Nano* **2016**, *10*, 2922–2929. [[CrossRef](#)] [[PubMed](#)]
26. Han, G.H.; Güneş, F.; Bae, J.J.; Kim, E.S.; Chae, S.J.; Shin, H.-J.; Choi, J.-Y.; Pribat, D.; Lee, Y.H. Influence of copper morphology in forming nucleation seeds for graphene growth. *Nano Lett.* **2011**, *11*, 4144–4148. [[CrossRef](#)] [[PubMed](#)]
27. Kim, S.M.; Hsu, A.; Lee, Y.-H.; Dresselhaus, M.; Palacios, T.; Kim, K.K.; Kong, J. The effect of copper pre-cleaning on graphene synthesis. *Nanotechnology* **2013**, *24*, 365602. [[CrossRef](#)] [[PubMed](#)]
28. Suzuki, S.; Nagamori, T.; Matsuoka, Y.; Yoshimura, M. Threefold atmospheric-pressure annealing for suppressing graphene nucleation on copper in chemical vapor deposition. *Jpn. J. Appl. Phys.* **2014**, *53*, 095101. [[CrossRef](#)]
29. Chen, S.; Ji, H.; Chou, H.; Li, Q.; Li, H.; Suk, J.W.; Piner, R.; Liao, L.; Cai, W.; Ruoff, R.S. Millimeter-size single-crystal graphene by suppressing evaporative loss of cu during low pressure chemical vapor deposition. *Adv. Mater.* **2013**, *25*, 2062–2065. [[CrossRef](#)] [[PubMed](#)]
30. Suzuki, S.; Kiyosumi, K.; Nagamori, T.; Tanaka, K.; Yoshimura, M. Low density growth of graphene by air introduction in atmospheric pressure chemical vapor deposition. *e-J. Surf. Sci. Nanotechnol.* **2015**, *13*, 404–409. [[CrossRef](#)]
31. Gan, L.; Luo, Z. Turning off hydrogen to realize seeded growth of subcentimeter single-crystal graphene grains on copper. *ACS Nano* **2013**, *7*, 9480–9488. [[CrossRef](#)] [[PubMed](#)]
32. Hao, Y.; Bharathi, M.; Wang, L.; Liu, Y.; Chen, H.; Nie, S.; Wang, X.; Chou, H.; Tan, C.; Fallahzad, B. The role of surface oxygen in the growth of large single-crystal graphene on copper. *Science* **2013**, *342*, 720–723. [[CrossRef](#)] [[PubMed](#)]
33. Platzman, I.; Brener, R.; Haick, H.; Tannenbaum, R. Oxidation of polycrystalline copper thin films at ambient conditions. *J. Phys. Chem. C* **2008**, *112*, 1101–1108. [[CrossRef](#)]
34. Zhu, C.; Osheroov, A.; Panzer, M.J. Surface chemistry of electrodeposited Cu₂O films studied by XPS. *Electrochim. Acta* **2013**, *111*, 771–778. [[CrossRef](#)]
35. Moulder, J.F.; Stickle, W.F.; Sobol, P.E.; Bomben, K.D. *Handbook of X-ray Photoelectron Spectroscopy: A Reference Book of Standard Spectra for Identification and Interpretation of XPS Data*; Ulvac-PHI Inc.: Kanagawa, Japan, 1995.
36. Hono, K.; Pickering, H.; Hashizume, T.; Kamiya, I.; Sakurai, T. Oxygen segregation and oxidation on a copper surface. *Surf. Sci.* **1989**, *213*, 90–102. [[CrossRef](#)]
37. Wang, J.-P.; Cho, W. Oxidation behavior of pure copper in oxygen and/or water vapor at intermediate temperature. *ISIJ Int.* **2009**, *49*, 1926–1931. [[CrossRef](#)]

38. Lee, S.; Mettlach, N.; Nguyen, N.; Sun, Y.; White, J. Copper oxide reduction through vacuum annealing. *Appl. Surf. Sci.* **2003**, *206*, 102–109. [[CrossRef](#)]
39. Rao, D.B.; Heinemann, K.; Douglass, D. Oxide removal and desorption of oxygen from partly oxidized thin films of copper at low pressures. *Oxid. Met.* **1976**, *10*, 227–238.
40. Cho, J.; Gao, L.; Tian, J.; Cao, H.; Wu, W.; Yu, Q.; Yitamben, E.N.; Fisher, B.; Guest, J.R.; Chen, Y.P. Atomic-scale investigation of graphene grown on Cu foil and the effects of thermal annealing. *ACS Nano* **2011**, *5*, 3607–3613. [[CrossRef](#)] [[PubMed](#)]
41. Peter, Y.Y.; Shen, Y. Resonance Raman studies in Cu₂O. I. The phonon-assisted 1s yellow excitonic absorption edge. *Phys. Rev. B* **1975**, *12*, 1377.
42. Gao, H.; Zhang, J.; Li, M.; Liu, K.; Guo, D.; Zhang, Y. Evaluating the electric property of different crystal faces and enhancing the Raman scattering of Cu₂O microcrystal by depositing Ag on the surface. *Curr. Appl. Phys.* **2013**, *13*, 935–939. [[CrossRef](#)]
43. Reimann, K.; Syassen, K. Raman scattering and photoluminescence in Cu₂O under hydrostatic pressure. *Phys. Rev. B* **1989**, *39*, 11113. [[CrossRef](#)]
44. Compaan, A. Surface damage effects on allowed and forbidden phonon Raman scattering in cuprous oxide. *Solid State Commun.* **1975**, *16*, 293–296. [[CrossRef](#)]
45. Williams, P.; Porto, S. Symmetry-forbidden resonant Raman scattering in Cu₂O. *Phys. Rev. B* **1973**, *8*, 1782. [[CrossRef](#)]
46. Solache-Carranco, H.; Juárez-Díaz, G.; Esparza-García, A.; Briseño-García, M.; Galván-Arellano, M.; Martínez-Juárez, J.; Romero-Paredes, G.; Pena-Sierra, R. Photoluminescence and X-ray diffraction studies on Cu₂O. *J. Lumin.* **2009**, *129*, 1483–1487. [[CrossRef](#)]
47. Luo, L.; Kang, Y.; Yang, J.C.; Zhou, G. Effect of oxygen gas pressure on orientations of Cu₂O nuclei during the initial oxidation of Cu (100), (110) and (111). *Surf. Sci.* **2012**, *606*, 1790–1797. [[CrossRef](#)]
48. Guillemot, L.; Bobrov, K. Morphological instability of the Cu(110)–(2 × 1)–O surface under thermal annealing. *Phys. Rev. B* **2011**, *83*, 075409. [[CrossRef](#)]
49. Gottardi, S.; Müller, K.; Bignardi, L.; Moreno-López, J.C.; Pham, T.A.; Ivashenko, O.; Yablonskikh, M.; Barinov, A.; Björk, J.; Rudolf, P. Comparing graphene growth on Cu (111) versus oxidized Cu (111). *Nano Lett.* **2015**, *15*, 917–922. [[CrossRef](#)] [[PubMed](#)]
50. Ferrari, A.; Meyer, J.; Scardaci, V.; Casiraghi, C.; Lazzeri, M.; Mauri, F.; Piscanec, S.; Jiang, D.; Novoselov, K.; Roth, S. Raman spectrum of graphene and graphene layers. *Phys. Rev. Lett.* **2006**, *97*, 187401. [[CrossRef](#)] [[PubMed](#)]
51. Ferrari, A.C.; Robertson, J. Raman spectroscopy of amorphous, nanostructured, diamond-like carbon, and nanodiamond. *Phil. Trans. R. Soc. A* **2004**, *362*, 2477–2512. [[CrossRef](#)] [[PubMed](#)]
52. Malard, L.; Pimenta, M.; Dresselhaus, G.; Dresselhaus, M. Raman spectroscopy in graphene. *Phys. Rep.* **2009**, *473*, 51–87. [[CrossRef](#)]
53. Kraus, J.; Böbel, M.; Günther, S. Suppressing graphene nucleation during CVD on polycrystalline Cu by controlling the carbon content of the support foils. *Carbon* **2016**, *96*, 153–165. [[CrossRef](#)]
54. Braeuninger-Weimer, P.; Brennan, B.; Pollard, A.J.; Hofmann, S. Understanding and controlling Cu-catalyzed graphene nucleation: The role of impurities, roughness, and oxygen scavenging. *Chem. Mater.* **2016**, *28*, 8905–8915. [[CrossRef](#)] [[PubMed](#)]



REGULAR PAPERS

Dependence on treatment ion energy of nitrogen plasma for oxygen reduction reaction of high ordered pyrolytic graphite

To cite this article: Yuichi Hashimoto *et al* 2018 *Jpn. J. Appl. Phys.* **57** 125504

View the [article online](#) for updates and enhancements.



Dependence on treatment ion energy of nitrogen plasma for oxygen reduction reaction of high ordered pyrolytic graphite

Yuichi Hashimoto^{1*}, Hsin-Hui Huang², Masamichi Yoshimura², Masanori Hara², Tamio Hara³, Yasuhiro Hara³, and Manabu Hamagaki⁴

¹Department of Electrical and Electronic Engineering, Daido University, Nagoya 457-8530, Japan

²Surface Science Laboratory, Toyota Technological Institute, Nagoya 468-8511, Japan

³Plasma R&D Laboratory Co., Ltd., Nagoya 468-8511, Japan

⁴RIKEN, Wako, Saitama 351-0198, Japan

*E-mail: hashi-y@daido-it.ac.jp

Received July 3, 2018; accepted October 1, 2018; published online November 1, 2018

We investigated the contribution of kinetic energy of ions on nitrogen plasma treatment of high ordered pyrolytic graphite (HOPG) film for electro-catalyst material. The treatment was carried out to modify the HOPG surface by nitrogen ion irradiation between 10 and 100 eV using electron-beam-excited plasma (EBEP). In the case of treatment by nitrogen ions with kinetic energy of 60 eV, the oxygen reduction reaction (ORR) activity was markedly improved and the ORR current increased by about 15 times as compared with untreated specimen. The enhancement of ORR activity was explained in terms of an increase of graphitic-N and pyridinic-N components, which act as reaction sites of ORR, from the results of Raman spectroscopy, X-ray photoelectron spectroscopy, low-energy photoelectron counter in air, and atomic force microscopy.

© 2018 The Japan Society of Applied Physics

1. Introduction

It has been expected that the carbon-based materials are used as new types of catalyst in the electrodes of fuel cell and various batteries. For the improvement of the electro-catalyst properties, theoretical and experimental studies have revealed that nitrogen ion-doping into carbon-based materials can significantly alter its electronic properties.^{1–22} The typical irradiation energy was between several tens and several kilo eV for the nitrogen ion treatment by the conventional ion beam technique.^{11–22} Kondo et al. observed two types of nitrogen species, that is, graphite-N and pyridinic-N, by irradiation of nitrogen ion beam of several hundreds eV to highly ordered pyrolytic graphite (HOPG) surface.¹² It has currently been reported that the active sites of oxygen reduction reaction (ORR) are created by the graphite-N and pyridinic-N components, and the mixing of the nitrogen species in the carbon materials.^{1,7–10,13,16,19,22,23} However, the high energy bombardment in the doping process may cause a significantly damage on the surface morphology of carbon material. In spite of such efforts, the relationship between the nitrogen ion energy and the resultant electronic properties of carbon-based materials, remains far from being completely understood. It is therefore expected that the contribution of treatment energy to carbon-based materials is elucidated for providing advances of electro-catalyst technologies.

In a previous paper, we have reported that the ORR activity of HOPG film is improved when its surface is modified by a short time treatment with low-energy nitrogen ions of 20 eV.²³ The nitrogen doping into HOPG film was carried out using the electron beam excited plasma (EBEP).^{23–29} Nitrogen plasma using the EBEP system can generate the higher density nitrogen atoms and ions when compared to the conventional plasma system. The HOPG films at the treatment time of 60 s using the nitrogen ion of 20 eV, indicated that the ORR current increased by about 2 times as compared with the untreated specimen. In the treated HOPG films, the component of graphite-N increased

by about 3 times compared to that of pyridinic-N, though it is difficult to obtain by nitrogen ion irradiation of higher energies more than several hundred eV.^{11–22}

In this study, we have investigated the contribution of nitrogen ion energy on the ORR activity and nitrogen component configuration in the HOPG film. The treatment was carried out to modify the HOPG surface by nitrogen ion irradiation between 10 and 100 eV for a short time of 60 s. From the experimental results, it was clarified that the treatment by nitrogen ions with the kinetic energy of 60 eV was an effective way to modify the HOPG surface for markedly improving the ORR activity. The proportion of the graphite-N and pyridinic-N components in the total of nitrogen species of HOPG surface treated with nitrogen ion of 60 eV increased by 2.5 times compared to that of HOPG surface treated with nitrogen ion of 20 eV. The high ORR performance by treatment of 60 eV is concluded to be due to the increases in the graphite-N and pyridinic-N components, because the two types of nitrogen species are much effective concerning the ORR activity. We will discuss that the graphite-N and pyridinic-N components are closely related with the ORR activity of HOPG film, based on the surface properties of HOPG film after the treatment by different nitrogen ion energy.

2. Experimental methods

Highly ordered pyrolytic graphite (HOPG) films ($12 \times 12 \text{ mm}^2$) of about $20 \mu\text{m}$ thickness were prepared by mechanical exfoliation of HOPG sheet ($12 \times 12 \times 1 \text{ mm}^3$, Panasonic PGCX04) using the adhesive tape method under atmospheric condition.²³

After the exfoliated HOPG specimens without thermal annealing were mounted on an aluminum (Al) plate ($20 \times 60 \times 1 \text{ mm}^3$), the specimens were electrically connected to the Al plate by conductive carbon adhesive sheets (Nisshin EM). The specimens on Al plate were placed parallel to the electron beam in the chamber as shown in Fig. 1. It was reported in Ref. 23 for detailed information on optimized nitrogen plasma condition using the EBEP system.

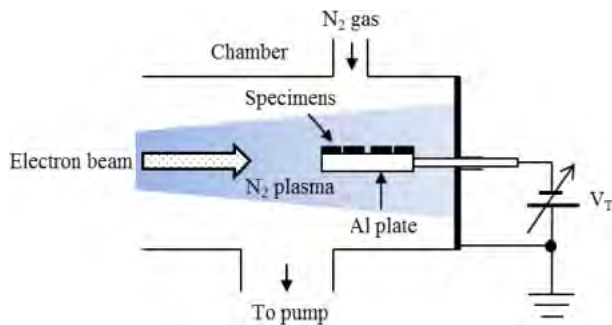


Fig. 1. (Color online) Schematic diagram of nitrogen plasma treatment using EBEP system.

For the nitrogen plasma treatment, the specimens were exposed to nitrogen plasma for 60 s under the application of DC voltage from -10 to -100 V to the Al plate (V_t). In the system, the value of the treated voltage (V_t) applied to the specimens corresponds to that of the incidence kinetic energy of nitrogen ions. In the case of an application of DC voltage of -10 V, it should be noted that the specimens are treated by nitrogen ions with a kinetic energy of 10 eV, as the space potential of the plasma was almost zero volt. The incident current density into the specimen during the treatment was several $\mu\text{A}/\text{cm}^2$.

To estimate the morphology of the specimen, the HOPG surface at the different treatment voltage was observed using an atomic force microscope (AFM) in tapping mode (Hitachi-Technologies 5100N). The structure and quality of the specimen were determined using a Raman spectroscopy system (Renishaw inVia Reflex). The binding energy analysis for the specimen was carried out using an X-ray photoelectron spectroscope (XPS; Ulvac Phi PHI 5000 Versa Probe II) with a source of Al $K\alpha$ 1486.6 eV. To evaluate the electronic properties of the HOPG surface after the treatments, the work function of the HOPG film was measured by a low-energy photoelectron counter in air (Rikenkeiki AC-2).^{30–32}

The electrochemical measurements were performed on an electrochemical workstation (Hokuto Denko HZ-5000) in a standard three-electrode electrochemical cell at room temperature. The measurement carried out in aqueous solution of 0.16 mol/L perchloric acid. A platinum electrode was used as the counter electrode, and a reversible hydrogen electrode (RHE) was used as the reference electrode. Fabrication of the working electrode was done by putting the specimen onto a glassy-like carbon disk electrode ($\phi 4$ mm, BAS) with a conductive carbon paste (Fujikura Kasei XC-32). The electrochemical activities of electrocatalysts were evaluated by cyclic voltammetry (CV) in nitrogen saturated aqueous solution and linear sweep voltammetry techniques on rotating disk electrode (RDE) in oxygen saturated aqueous solution.

3. Results and discussion

The HOPG surface was investigated to clarify the influence of the treatment voltage on the variation of electronic and chemical properties of the HOPG surface. The AFM images in Fig. 2 clearly show surface structure changes due to the treatment, where nanometer-scale irregularities are present at the HOPG surface. The surfaces have been transformed into a network of carbon filaments (light color) separated by cavities (dark color). Figure 3 shows resultant values of the roughness

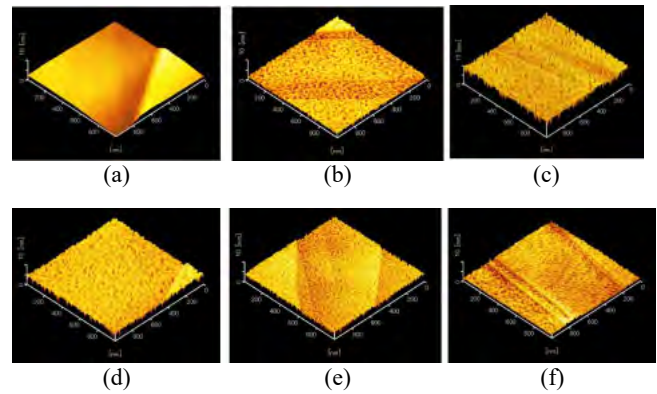


Fig. 2. (Color online) AFM images of HOPG films at different treatment voltage: (a) untreated, (b) 10 V, (c) 20 V, (d) 40 V, (e) 60 V, and (f) 100 V.

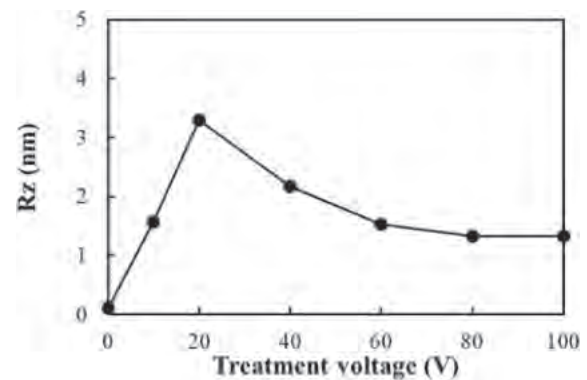


Fig. 3. Effect of treatment voltage on roughness (R_z) of HOPG surface.

(R_z : mean value of 30 data) of the HOPG specimens at different treatment voltages. The roughness changed markedly with an increase of the treatment voltage. The observed roughness of these treated specimens suggests an increase of active sites on the HOPG surface, where it relates to the electrolytic double layer. The roughness increased up to 3.3 nm at the treatment voltage of 20 V and gradually decreased to 1.3 nm at the treatment voltage of 100 V. In addition, width of the cavities decreased with an increase of treatment voltage. The values of the width of cavities for the 10-, 20-, 40-, 60-, and 100-V-treated specimens were 34, 33, 27, 25, and 22 nm, respectively. Next the effect of ion energy on the surface structure of HOPG specimens will be discussed to be caused by variations in physical, chemical and electronic properties, that is, the disorder in carbon structure, the content of various C–N bonds and the work function.

To determine the effect of treatment voltage on the structure of HOPG specimens, the specimens were examined by Raman spectroscopy. Figure 4 shows Raman spectra for the specimens treated at different voltages. The spectra obtained for the treated specimens have two different composite structures, i.e., crystalline graphite or amorphous carbon at around 1580 cm^{-1} (G-band) and another band at around 1360 cm^{-1} referred to as the disorder peak (D-band).^{33–35}

Figure 5 shows the I_D/I_G ratio of specimens on treatment voltage. The I_D/I_G ratio of specimen increased monotonously with increasing treatment voltage. Thus increasing of I_D/I_G suggests that the specimens at larger treatment voltage had greater concentration of imperfection. The roughness (R_z) of treatment voltage between 40 and 100 V, however, gradually

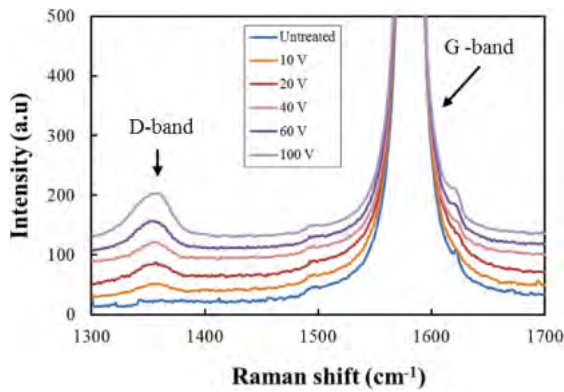


Fig. 4. (Color online) Raman spectra of HOPG films at different treatment voltage.

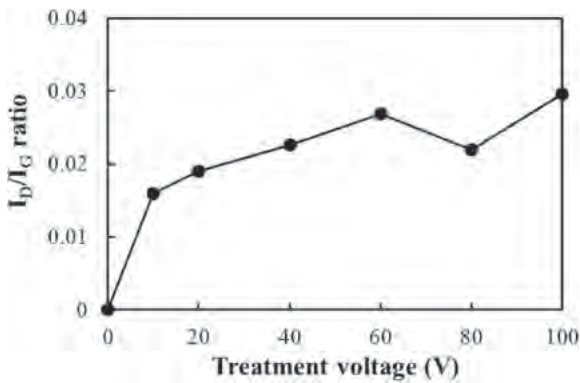


Fig. 5. I_D/I_G ratio of HOPG films at different treatment voltage.

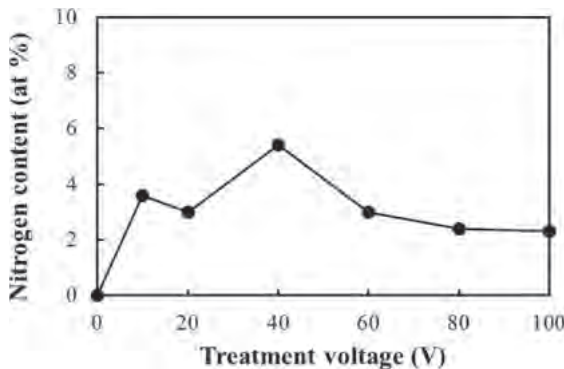


Fig. 6. Nitrogen content of the HOPG films at different treatment voltage.

decreased as shown in Fig. 3. It is supposed that the increase of I_D/I_G ratio is caused by increases of fine cavities, that is, an increase of surface area.

XPS is used mainly to analyze the relative content of various C–N bonds in the nitrogen doped HOPG films.^{11–23} Figure 6 shows the typical values of nitrogen atomic concentrations of the HOPG specimens at different treatment voltages. The 40-V-treated specimen showed the highest nitrogen concentration (5.4 at.%) as compared to the other treated specimens (2.3–3.6 at.%). In Fig. 7(a), the three deconvoluted peaks for N element at 398.5, 399.9, and 401.5 eV belong to pyrolic-N, pyridinic-N, and graphitic-N/oxidized-N species. Figure 7(b) shows the chemical composition of each component for the HOPG specimens treated at different voltages. Most importantly, up to 60 V, the graph-

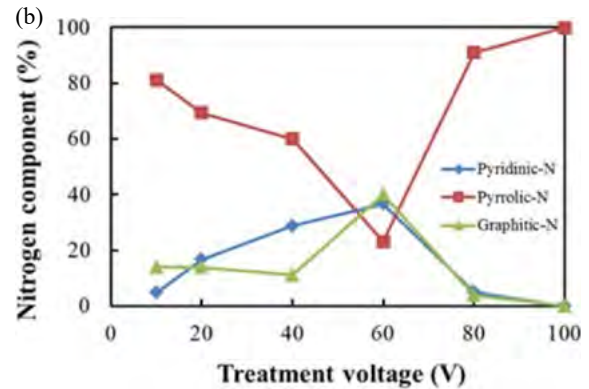
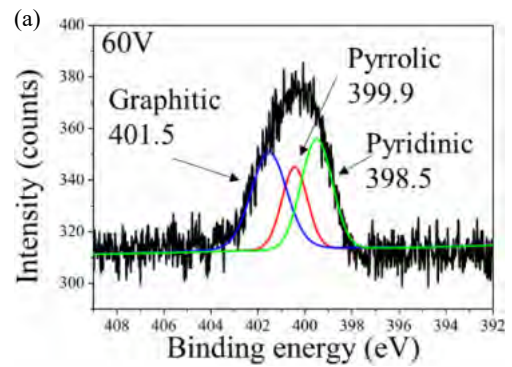


Fig. 7. (Color online) (a) Nitrogen peak of 60-V-treated specimen and (b) Nitrogen components of the graphitic-N, pyridinic-N, and pyrolic-N for the HOPG films at different treatment voltage.

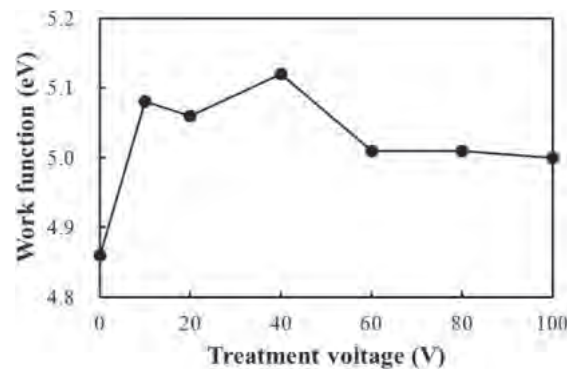


Fig. 8. Effect of treatment voltage on work function of HOPG film.

itic-N and pyridinic-N components were increased to 40.1% and 36.7%, respectively. In contrast, the pyrolic-N component was decreased to 23.2%. The total percentage of the graphitic-N and pyridinic-N components of 60-V-treated specimen increased by 2.5 times compared to that of 20-V-treated specimen as previously reported.²³ That is, it suggested that the treatment energy of nitrogen ions for the doping process of HOPG surface has an optimum value for the formation of pyridinic-N and graphitic-N components.

Next, the work functions of the HOPG specimens were investigated to clarify the surface electronic properties. The work functions of the HOPG specimens were markedly increased by the treatment, as shown in Fig. 8. Even though the relationship between the work function and nitrogen doping has been reported,^{36,37} the study of the effect of treating conditions such as voltage on the work function is limited. It was found that the work function markedly

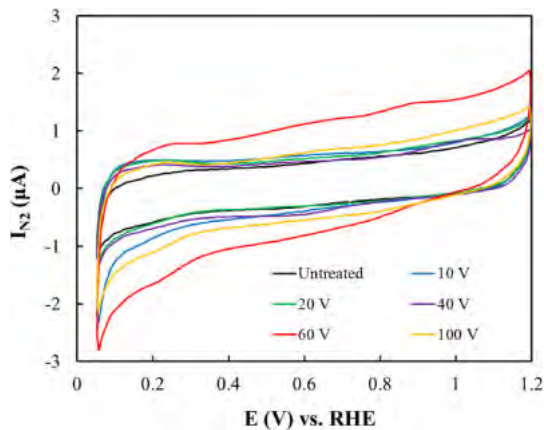


Fig. 9. (Color online) CV of HOPG films treated at different voltage.

increased from 4.86 eV (untreated specimen) to 5.12 eV (40-V-treated specimen) and gradually decreased to 5.0 eV at treatment voltages between 60 and 100 V. Akada et al. have reported that the work function of graphene correlates strongly with the site and amount of doped nitrogen.³⁶⁾ As compared with the results in Figs. 6 and 8, the two diagrams showed a similar tendency towards the treatment voltage. Therefore, the large value (5.12 eV) of work function for the 40-V-treated specimen is concluded to be due to the increases in the amount of doped nitrogen (5.4 at. %).

The variations in CV of specimens treated at different voltage are shown in Fig. 9. In particular, the 60-V-treated specimen had the greatest reduction current at 0.05 V versus RHE and double layer capacitance of CV curve under a nitrogen atmosphere. The CV curves in the potential range around 0.05 V represent the reduction current corresponding to hydrogen evolution reaction on the HOPG surface. The broad peaks around 0.6 V, especially the 40- and 60-V-treated specimens, is due to redox reaction of oxide containing functional groups such as quinone derivative induced defect site on the HOPG surface. The CV curves suggest that the HOPG surfaces treated by nitrogen ions have higher surface area than untreated surface, consisting with the AFM observation.

Figure 10 shows the ORR voltammograms at a rotation of 2500 rpm and a scan rate of 10 mV/s for the 10-, 20-, 40-, 60-, and 100-V-treated specimens. On the ORR voltammograms in Fig. 10, the background current, which was calculated from the CV obtained under oxygen-free (N_2) condition with the different scan rate, 50 mV/s, as shown in Fig. 9, could be estimated 0.2 μ A or less. The value of the estimated background current consists with current at onset potential, ca. 1.0 V, of ORR. Therefore, it is considered that the obtained ORR voltammograms are not influenced by the current taken under oxygen-free conditions. In Fig. 10, the 40- and 60-V-treated specimens display high activity at the voltage between 0.8 and 0.9 V compared to the low ORR activities of the 10-, 20-, and 100-V-treated specimens.

We also evaluated the ORR activities of the treated specimens by the Koutecky–Levich plot.^{38–40)} Electron transfer number (n) and kinetic current density during oxygen reduction of the specimens treated at different voltages were estimated from the current density with various rotation rate of the disk electrode at 0.85 V versus RHE. In

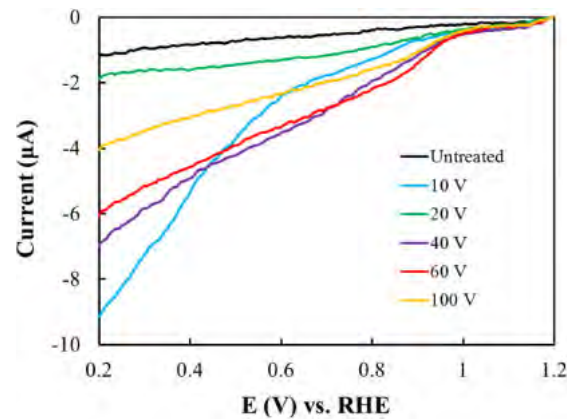


Fig. 10. (Color online) Potential versus ORR current curves measured under an oxygen-saturated 0.16 mol/L perchloric acid at rotation speed of 2500 rpm and a scan rate of 10 mV/s for HOPG films at different treatment voltage.

general, the kinetic control region is determined by potential between 0.8 and 0.95 V, and the diffusion control region is the potential lower than 0.65 V, though it is depended on an electrode. Therefore, the reaction at 0.85 V versus RHE is under kinetic control and the effect of diffusion limitation of oxygen is negligible. In addition, the ORR activity is evaluated by two factors, i.e., electron transfer number and kinetic current density, which are estimated from a slope and y -intercept of Koutecky–Levich plot, respectively. It is noteworthy that the electron transfer number was increased with same tendency of the ORR activity at 0.85 V. The values of electron transfer number (n) of 10-, 20-, 40-, 60-, and 100-V-treated specimens were 3.4, 3.3, 3.5, 3.8, and 3.2, respectively. In aqueous solutions, there are primarily two reaction pathways in the ORR: (a) a four-electron process in which oxygen is reduced to H_2O ($n = 4$), (b) a two-electron process in which oxygen is reduced to H_2O_2 ($n = 2$). The RDE measurement suggests two-electron ORR pathway partially shifts to four electron pathway by the nitrogen doping process of HOPG using the EBEP. In particular, the treatment using the nitrogen ion of 60 eV has greatly enhanced the four-electron reaction process ($n = 3.8$). In addition, the kinetic current density, which means reaction rate of ORR, has also shown the same trend. The values of kinetic current density of 10-, 20-, 40-, 60-, and 100-V-treated specimens were 1.1, 1.0, 1.6, 2.1, and 1.5 μ A/cm², respectively. It was clarified that the 60-V-treated specimen had a higher ORR activity by a synergistic effect of the four-electron reaction process and higher reaction rate for ORR.

Figure 11 shows the resultant ORR current at 0.85 V (I_{ORR}). The I_{ORR} increased with an increase of the treatment voltage to the HOPG surface. Most importantly, the treatment by nitrogen ions with kinetic energy of 60 eV, that is, treatment voltage of 60 V, the I_{ORR} increased up to 15.2 μ A/cm². It is noted here that the 60-V-treated specimen is much more active than the 40-V-treated specimen, whereas nitrogen concentration of the 60-V-treated specimen (3.0 at. %) is lower than that of the 40-V-treated specimen (5.4 at. %). In the case of 40-V-treated specimen, the graphitic-N component (11.2%) is lower than the pyridinic-N component (28.8%), while the graphitic-N component of 60-V-treated one shows a marked increase to 40.1%. The

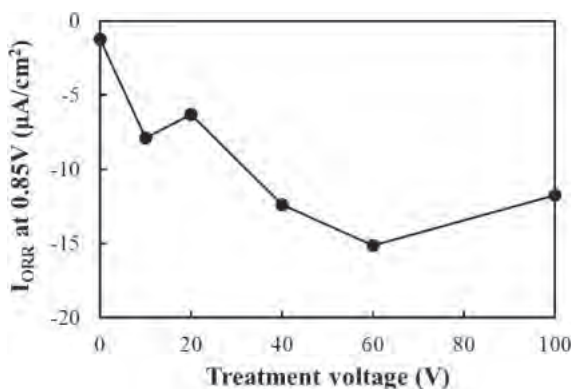


Fig. 11. Relationship between the treatment voltage and the ORR current at 0.85 V (I_{ORR}) of HOPG films. Potential sweep rate was 50 mV/s.

distinct increase in graphitic-N component could well be related the ORR activity altered by the 60 V treatment which modified the surface structure of HOPG specimen.

Ikeda et al. have reported that the graphitic-N component of N-doped graphite plays an important role in ORR as a fuel cell catalyst.¹⁾ On the other hand, the experimental study by Guo et al. has indicated that the pyridinic-N component creates the active sites for the ORR performance.¹⁹⁾ The nitrogen components obtained in our experiments, that is, the graphitic-N and pyridinic-N components at 60-V-treated specimen were 40.1% and 36.7%, respectively, inducing a marked decrease of the pyrrolic-N component. The relationship between the ORR activity and the two components (the graphitic-N and pyridinic-N components) of HOPG surface therefore are considered to be due to the mixing of different types of nitrogen species in the HOPG film. However, further studies are needed to clarify the selective formation mechanism of the two components in the HOPG film treated by nitrogen ion of 60 eV.

4. Conclusions

The highest ORR current of HOPG film was obtained when the treatment energy of nitrogen ions was 60 eV. In the case of treatment by nitrogen ions with kinetic energy of 60 eV, the ORR current increased by about 15 times as compared with the untreated specimen.

The enhancement of ORR current was explained in terms of an increase of graphitic-N and pyridinic-N components, which act as reaction sites of ORR. The experimental findings have suggested that the ORR performance of HOPG film can improve by the selection of an optimum ion energy using the nitrogen plasma treatment.

Acknowledgment

The authors would like to thank Ms. Mieko Kondo for her beneficial assistance in carrying out the electrochemical experiments.

- 1) T. Ikeda, M. Boero, S.-F. Huang, K. Terakura, M. Oshima, and J. Ozaki, *J. Phys. Chem. C* **112**, 14706 (2008).
- 2) Y. Li, W. Zhou, H. Wang, L. Xie, Y. Liang, F. Wei, J.-C. Idrobo, S. J. Pennycook, and H. Dai, *Nat. Nanotechnol.* **7**, 394 (2012).

- 3) J. Ozaki, N. Kimura, T. Anahara, and A. Oya, *Carbon* **45**, 1847 (2007).
- 4) Y. Gong, H. Fei, X. Zou, W. Zhou, S. Yang, G. Ye, Z. Liu, Z. Peng, J. Lou, R. Vajtai, B. I. Yakobson, J. M. Tour, and P. M. Ajayan, *Chem. Mater.* **27**, 1181 (2015).
- 5) X. Guo, P. Liu, J. Han, Y. Ito, A. Hirata, T. Fujita, and M. Chen, *Adv. Mater.* **27**, 6137 (2015).
- 6) R. Lv, Q. Li, A. R. Botello-Méndez, T. Hayashi, B. Wang, A. Berkdemir, Q. Hao, A. L. Elías, R. Cruz-Silva, H. R. Gutiérrez, Y. A. Kim, H. Muramatsu, J. Zhu, M. Endo, H. Terrones, J.-C. Charlier, M. Pan, and M. Terrones, *Sci. Rep.* **2**, 586 (2012).
- 7) K. Gong, F. Du, Z. Xia, M. Durstock, and L. Dai, *Science* **323**, 760 (2009).
- 8) L. Qu, Y. Liu, J.-B. Baek, and L. Dai, *ACS Nano* **4**, 1321 (2010).
- 9) M. Wang, Z. Wu, and L. Dai, *J. Electroanal. Chem.* **753**, 16 (2015).
- 10) Y. Ito, H.-J. Qiu, T. Fujita, Y. Tanabe, K. Tanigaki, and M. Chen, *Adv. Mater.* **26**, 4145 (2014).
- 11) B. Guo, Q. Liu, E. Chen, H. Zhu, L. Fang, and J. R. Gong, *Nano Lett.* **10**, 4975 (2010).
- 12) T. Kondo, S. Casolo, T. Suzuki, T. Shikano, M. Sakurai, Y. Harada, M. Saito, M. Oshima, M. I. Trioni, and G. F. Tantardini, *Phys. Rev. B* **86**, 035436 (2012).
- 13) F. Xu, M. Minniti, P. Barone, A. Sindona, A. Bonnano, and A. Oliva, *Carbon* **46**, 1489 (2008).
- 14) K. J. Kim, H. Lee, J. Choi, H. Lee, M. C. Jung, H. J. Shin, T. H. Kang, B. Kim, and S. Kim, *J. Phys.: Condens. Matter* **22**, 045005 (2010).
- 15) W. Zhao, O. Hofert, K. Gotterbarm, J. F. Zhu, C. Papp, and H.-P. Steinruck, *J. Phys. Chem. C* **116**, 5062 (2012).
- 16) S. Pylypenko, A. Queen, T. S. Olson, A. Dameron, K. O'Neill, K. C. Neyerlin, B. Pivovar, H. N. Dinh, D. S. Ginley, T. Gennett, and R. O'Hayre, *J. Phys. Chem. C* **115**, 13667 (2011).
- 17) M. Favaro, L. Perini, S. Agnoli, C. Durante, G. Granozzi, and A. Gennaro, *Electrochim. Acta* **88**, 477 (2013).
- 18) D.-Q. Yang and E. Sacher, *Surf. Sci.* **531**, 185 (2003).
- 19) D. Guo, R. Shibuya, C. Akiba, S. Saji, and T. Kondo, *Science* **351**, 361 (2016).
- 20) I. Kusunoki, M. Sakai, Y. Igari, S. Ishidzuka, T. Takami, T. Takaoka, M. Nishitani-Gamo, and T. Ando, *Surf. Sci.* **492**, 315 (2001).
- 21) I. Gouzman, R. Brenner, and A. Hoffman, *J. Vac. Sci. Technol. A* **17**, 411 (1999).
- 22) H. Kiuchi, T. Kondo, M. Sakurai, D. Guo, J. Nakamura, H. Niwa, J. Miyawaki, M. Kawai, M. Oshima, and Y. Harada, *Phys. Chem. Chem. Phys.* **18**, 458 (2016).
- 23) Y. Hashimoto, S. Katafuchi, M. Yoshimura, T. Hara, Y. Hara, and M. Hamagaki, *Nanomater. Nanotechnol.* **7**, 1 (2017).
- 24) S. Tada, S. Takashima, M. Ito, M. Hamagaki, M. Hori, and T. Goto, *Jpn. J. Appl. Phys.* **41**, 4691 (2002).
- 25) H. Shoyama, T. Hishida, T. Hara, Y. Dake, T. Mori, H. Nagi, M. Hori, and T. Goto, *J. Vac. Sci. Technol. A* **24**, 1999 (2006).
- 26) L. Liu, A. Yamamoto, T. Hishida, T. Hara, and H. Tsubakino, *Mater. Trans.* **46**, 687 (2005).
- 27) Y. Hara, Y. Yoshikawa, T. Hara, and P. Abraha, *Jpn. J. Appl. Phys.* **46**, L1077 (2007).
- 28) P. Abraha, Y. Yoshikawa, and Y. Katayama, *Vacuum* **83**, 497 (2008).
- 29) R. Ichiki, Y. Kubota, M. Yoshida, Y. Fukuda, Y. Mizukamo, and T. Hara, *J. Plasma Fusion Res. Ser.* **8**, 1408 (2009).
- 30) H. Kirihaata and M. Uda, *Rev. Sci. Instrum.* **52**, 68 (1981).
- 31) A. Koyama, M. Kawai, H. Zenba, Y. Nakajima, A. Yoneda, and M. Uda, *Nucl. Instrum. Methods Phys. Res., Sect. A* **422**, 309 (1999).
- 32) Y. Nakajima, M. Hoshino, D. Yamashita, and M. Uda, *Adv. Quantum Chem.* **42**, 399 (2003).
- 33) A. C. Ferrari and J. Robertson, *Phys. Rev. B* **61**, 14095 (2000).
- 34) Y. W. Li, C. F. Chen, and Y. J. Tseng, *Jpn. J. Appl. Phys.* **40**, 777 (2001).
- 35) N. Apakina, A. L. Karuzskii, M. S. Kogan, A. V. Kvit, N. N. Melnik, Y. A. Mityagin, V. N. Murzin, A. A. Orlikovsky, A. V. Perestoronia, S. D. Tkachenko, and N. A. Volchkov, *Diamond Relat. Mater.* **6**, 564 (1997).
- 36) K. Akada, T. Terasawa, G. Imamura, S. Obata, and K. Saiki, *Appl. Phys. Lett.* **104**, 131602 (2014).
- 37) J.-J. Zeng and Y.-J. Lin, *Appl. Phys. Lett.* **104**, 233103 (2014).
- 38) A. J. Bard and L. R. Faulkner, *Electrochemical Methods: Fundamentals and Application* (Wiley, New York, 2001).
- 39) G. He, Y. Song, K. Liu, A. Walter, S. Chen, and S. Chen, *ACS Catal.* **3**, 831 (2013).
- 40) S. Kundu, T. C. Nagaiah, W. Xia, Y. Wang, S. V. Dommele, J. H. Bitter, M. Santa, G. Grundmeier, M. Bron, W. Schunmann, and M. Muhler, *J. Phys. Chem. C* **113**, 14302 (2009).



Formation of preferentially oriented $Y_3Al_5O_{12}$ film on a reactive sapphire substrate: Phase and texture transitions from Y_2O_3



Shuichi Arakawa^{a,*}, Hiroaki Kadoura^b, Takeshi Uyama^b, Kazumasa Takatori^b, Yasuhiko Takeda^b, Toshihiko Tani^{a,b}

^a Graduate School of Engineering, Toyota Technological Institute, 2-12-1 Hisakata, Tempaku, Nagoya 468-8511, Japan

^b Toyota Central Research and Development Laboratories, Inc., Yokomichi, Nagakute, 480-1192, Japan

ARTICLE INFO

Article history:

Received 31 August 2015

Received in revised form 15 October 2015

Accepted 16 October 2015

Available online 29 October 2015

Keywords:

Yttrium aluminum garnet (YAG)

Preferential orientation

Reactive substrate

Epitaxial growth

Thin film

ABSTRACT

Yttrium aluminum garnet ($Y_3Al_5O_{12}$, YAG) thin films were synthesized by reacting sol–gel derived Y_2O_3 $\langle 111 \rangle$ -oriented films with sapphire substrates. Phase development and inheritance of crystallographic orientation during the formation of YAG was investigated. The major sequence of the phase development from Y_2O_3 to YAG with increasing temperature was $Y_2O_3 \rightarrow$ hexagonal yttrium aluminate ($YAlO_3$, YAH) \rightarrow YAG, showing that the diffusion of Al^{3+} into Y_2O_3 films occurred. The highly $\{10\bar{1}1\}$ -textured YAH phase, which was first synthesized in the present study, would inherit the preferred $\{111\}$ plane of self-textured Y_2O_3 with structural similarity. The YAG phase also showed highly preferred $\langle 211 \rangle$ orientation (Lotgering's factor, $F=0.57$) only when the films were prepared on the sapphire (0001) substrate. X-ray pole figure and electron backscatter diffraction results suggested an epitaxial growth of $\{211\}$ -textured YAG, which was supported by the consideration of lattice matching between the planes of YAG (211) and sapphire (0001).

© 2015 Elsevier Ltd. All rights reserved.

1. Introduction

Rare-earth-doped yttrium aluminum garnets ($Y_3Al_5O_{12}$, YAG) are well known as important solid-state laser media because of their superior thermo-mechanical and optical properties with excellent chemical stability. Among them, one of the most common laser gain medium is a neodymium-doped YAG (Nd:YAG) single crystal fabricated by the Czochralski method. This method offers single crystals with high performance; however, there remain some issues in manufacturing to be resolved such as limited dimensions, high production cost, defects caused at the melt-crystal interfaces, and contamination from Ir crucibles hard to avoid. On the other hand, much work on a sintered Nd:YAG ceramic as an alternative to the single crystal has been performed since the first success in the laser oscillation by Ikesue et al. [1–5] because the ceramic fabrication process enables not only overcoming the above described disadvantages but also doping or co-doping a variety of functional dopants with high concentrations. High laser efficiency and transparency comparable to those of Nd:YAG single crystals have been

achieved on Nd:YAG ceramics with high dopant concentration ($>1\%$).

Although a YAG single crystal has a cubic symmetry and is optically isotropic, thermally induced birefringence originated in the photoelastic effect causes under high-power operation, which is a serious problem in developing the high performance laser. Shoji et al. [6] have reported the thermal-birefringence-induced depolarization effect in also the Nd:YAG ceramics consisting of a huge number of single-crystal grains whose respective crystallographic axes are randomly oriented. Furthermore, Shoji and Taira [7] reported that the depolarization of YAG single crystals depends on their crystallographic planes and especially the depolarization of (110)-cut crystal is small by one order of magnitude as compared with that of (111)-cut one. The depolarization of (111) cut crystal is comparable to that of YAG ceramics; therefore, providing a texture to the YAG ceramics is expected to improve the laser performance. However, the isotropic crystal structure of garnet makes the fabrication of textured ceramics difficult *via* normal field-induced processing methods such as magnetic-field alignment and hot-forging.

The reactive-templated grain growth (RTGG) method has been applied to fabricating highly textured polycrystals such as simple perovskite-type piezoelectric materials and layer-structured materials including bismuth layer-structured ferroelectric and both p-

* Corresponding author. Fax: +81 52 809 1721.

E-mail address: arakawa@toyota-ti.ac.jp (S. Arakawa).

and n-type oxidethermoelectrics [8–11], which is considered to be one of the key technologies for fabricating electronic ceramics with high performances comparable to those of single crystals. In the RTGG method, anisometric single-crystal reactive-template particles are mixed with complementary reactants and aligned, followed by heat-treatment. The product formed *in-situ* during the heat-treatment preserves the crystallographic orientation of the template; therefore, the fabrication of textured ceramics by the RTGG method has been confined to material systems in which topochemical orientation relationship is obvious between a template and a product. A garnet has a complicated crystal structure and no topochemical orientation relationships between YAG and α - Al_2O_3 or any yttrium aluminate compounds have been known. However, YAG has been known to form eutectic composite with α - Al_2O_3 through directional solidification, and some crystallographic relationships between these crystals have been observed although the mechanism has not been clear yet [12–14]. In this sense, α - Al_2O_3 with an anisotropic corundum structure can be a candidate for the template crystal when considering the fabrication of textured YAG ceramics *via* the RTGG method.

This study is intended to apply the RTGG method to fabricating the textured YAG ceramics for the first time. For this ultimate goal, a fundamental investigation on the phase transitions and crystallographic orientation inheritance from α - Al_2O_3 single crystal to YAG crystal is essential. In the present study, we selected α - Al_2O_3 single crystal, sapphire, as a “reactive substrate” and deposited Y_2O_3 precursor on the substrate to be heat-treated as a simple model for the RTGG processing. Through this study, in addition to the phase transitions, the texture development mechanism is clarified from viewpoints of self-texture and lattice matching. Indeed, no precedent work has discussed the preferred orientation of YAG films on the sapphire substrates from a viewpoint of the lattice matching, even for the YAG-based films synthesized “directly” on the sapphire substrates, *i.e.*, without any reactions between the films and the substrates [15–18].

2. Experimental

2.1. Materials and methods

Commercially available reagent of yttrium isopropoxide ($\text{Y}(\text{O}^i\text{C}_3\text{H}_7)_3$, 3N, Ko-jundo Chemical Lab.) was selected as a starting material. Yttrium isopropoxide was dissolved in absolute 2-methoxyethanol(ethylene glycol monomethyl ether, EGMME), and then the solution was refluxed at 125 °C for 20 h. This solution was partially hydrolyzed by adding deionized water (mole ratio of $\text{H}_2\text{O}/\text{Y}_2\text{O}_3 = 0.5$), which was diluted with the absolute 2-methoxyethanol, and was again refluxed at 125 °C for 12 h. The yttrium concentration of the precursor solution was 0.25 M. All reactions were run in a dry nitrogen atmosphere.

Y–O gel films were deposited on (0001) and (11 $\bar{2}$ 0) sapphire substrates by spin coating of the precursor at a spinning rate of 3000 rpm for 20 s, followed by heat-treatment at 400 °C on a hot plate in air. The spin-coating/heat-treatment process was repeated 10 times. These films were heat-treated at various temperatures between 400 °C and 1000 °C for 10 min in flowing oxygen gas and between 1100 °C and 1600 °C for 10 min in air.

2.2. Characterization

X-ray diffraction (XRD) analysis was performed to identify the transitions of crystalline phases and texture development of the films with an X-ray diffractometer (Rigaku Corp.; 18 kW, graphite monochromator, $\text{CuK}\alpha$ radiation ($\lambda = 0.154$ nm), operated at 40 kV and 200 mA) at room temperature. Samples were scanned in fixed

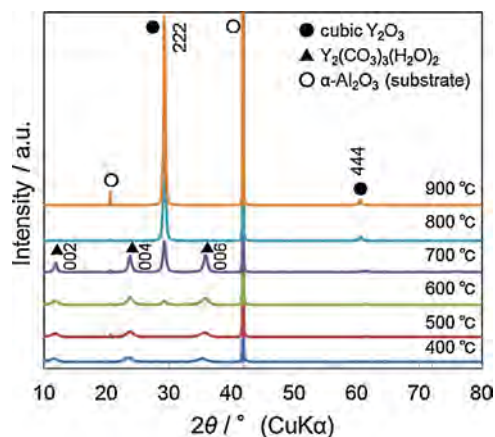


Fig. 1. XRD profiles of the Y–O thin films prepared on the sapphire (0001) substrates at various heating temperatures.

time mode with counting time of 0.2 s under diffraction angle 2θ in the range of 10–80°. XRD pole-figure measurement was conducted for the determination of in-plane texture of the films over $\chi = 0$ –70° by the Schultz reflection technique (RINT-TTR II, Rigaku Corp.) with step angles of 2° in χ and 1° in β . The morphological features of the films were observed by field emission scanning electron microscopy (FE-SEM) (JSM-7000F, JEOL Ltd.) equipped with energy dispersive X-ray spectroscopy (EDS) and electron backscatter diffraction (EBSD) (TSL, Orientation imaging microscopy (OIM) system) after the samples were sputter-coated with carbon. EBSD patterns were collected from a hexagonal grid with a step size of 0.2 μm over a total area of $20 \times 30 \mu\text{m}^2$ at an acceleration voltage of 15 kV.

3. Results and discussion

3.1. Crystallization of Y_2O_3

Fig. 1 shows the XRD patterns of the films prepared on the sapphire (0001) substrates, which were heat-treated at 900 °C or below. The XRD profile of the fired film showed peaks at $2\theta = 11.84^\circ$, 23.76° , and 35.76° , which were assigned to reflections from (002), (004), and (006) planes of $\text{Y}_2(\text{CO}_3)_3(\text{H}_2\text{O})_2$, respectively (JCPDS card number: 01-81-1538 [19]). The intermediate phase of $\text{Y}_2(\text{CO}_3)_3(\text{H}_2\text{O})_2$ disappeared at 800 °C. On the other hand, Y_2O_3 phase appeared at 600 °C which indicates that $\text{Y}_2(\text{CO}_3)_3(\text{H}_2\text{O})_2$ phase started to turn into Y_2O_3 phase at 600 °C. The intensity of the peaks located at 29.26° and 60.60° which correspond to 222 and 444 peaks, respectively, increased with increasing heating temperature. No other peaks were present, so that the Y_2O_3 phase has highly preferential orientation along the $\langle 111 \rangle$ direction, which is distinguished from the previous reports that the sol–gel derived Y_2O_3 films showed no or weak preferred orientation [20,21].

Fig. 2 shows the (400) and (440) XRD pole figures for the Y_2O_3 film synthesized at 900 °C on the sapphire substrates. Ring patterns were observed at $\chi = 55^\circ$ for 400 reflection and at $\chi = 35^\circ$ for 440 reflection on both the sapphire (0001) and (11 $\bar{2}$ 0) substrates. These results indicate that the $\langle 111 \rangle$ axis of the Y_2O_3 film stands perpendicular to the sample surface and the orientation distribution around the axis is random. In other words, the Y_2O_3 film has a fiber texture. The film texture independent of the cut-plane of the sapphire substrates suggests that Y_2O_3 films were preferentially $\langle 111 \rangle$ -oriented by self-texture. Y_2O_3 has a cubic structure and can be described as a fluorite-type oxide with disordered oxygen vacancies. The observed $\{111\}$ texture is supported by the fact that the

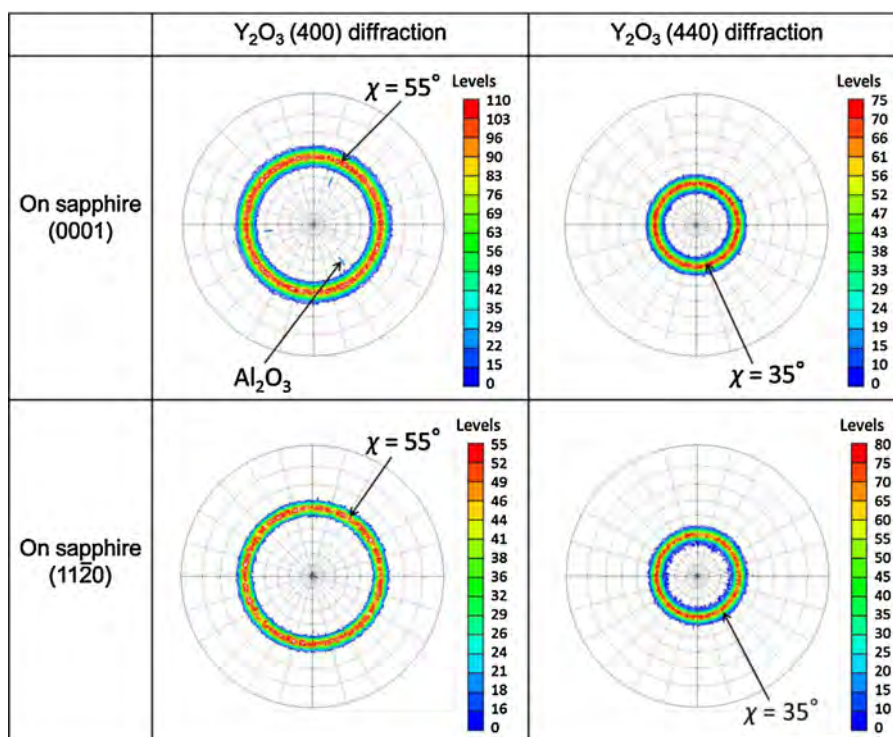


Fig. 2. X-ray pole figures of Y_2O_3 (400) and (440), for Y–O thin films on the sapphire (0001) and (11 $\bar{2}$ 0) substrates heat-treated at 900 °C for 10 min.

{111} plane has the lowest surface energy in fluorite-derivative oxides [22,23].

3.2. Phase development

Three stable compounds including monoclinic yttrium aluminate ($Y_4Al_2O_9$, YAM), yttrium aluminum perovskite ($YAlO_3$, YAP), and yttrium aluminum garnet ($Y_3Al_5O_{12}$, YAG) are known to be present in the pseudo-binary Al_2O_3 – Y_2O_3 system. Reactions between the Y_2O_3 films and the sapphire substrates were investigated by XRD analysis. The crystalline phases of YAM, YAP, and YAG were identified in reference to JCPDS cards of number 01-083-0934, 33-0041, and 33-0040, respectively. Fig. 3a shows the XRD profiles of the Y–Al–O films on sapphire (0001) substrate heat-treated at various temperatures between 1000 °C and 1600 °C. The single-phase YAG appeared via formation of the various crystalline phases. The crystalline phases which appeared at each temperature are summarized in Table 1. Fig. 4 also shows the change in the XRD peak intensities of the respective product phases on the sapphire (0001) with the heating temperature. It can be seen that YAM phase appeared at 1000 °C, and YAP and YAG at 1300 °C, and also the temperatures at which most intense XRD reflections appeared in each phase were 1100 °C for YAM, 1400 °C for YAP, and 1600 °C for YAG. One of the most peculiar results is that the oriented Y_2O_3 222 peak disappeared and two peaks, one of which is comparable to the extremely intense 222 peak, appeared at $2\theta = 28.76^\circ$ and 29.50° for the film heat-treated at 1300 °C, as is shown in Fig. 3b. Because the crystal system of Y_2O_3 is cubic up to near its melting temperature, occurrence of a splitting of the 222 peak due to lowering of the crystal symmetry of Y_2O_3 itself is excluded [24]. The metastable hexagonal yttrium aluminate ($YAlO_3$, YAH) with a space group of $P6_3/mmc$ with $a = 0.368$ nm and $b = 1.052$ nm has often been observed mainly in soft-chemical processes for YAG powders and films [25–30]. These two peaks observed were assigned to reflections from (10 $\bar{1}$ 0) and (10 $\bar{1}$ 1) planes of YAH phase, respectively, although the peak positions were somewhat higher than the JCPDS

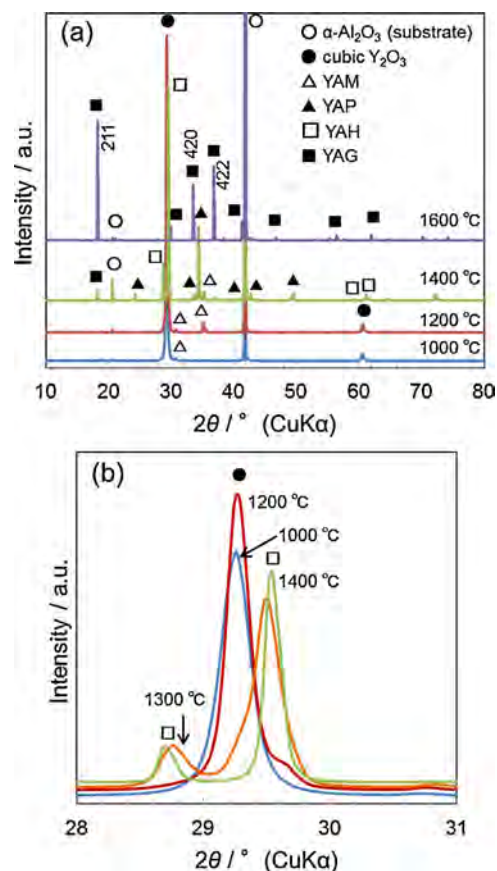


Fig. 3. XRD profiles of the Y–Al–O thin films on the sapphire (0001) substrates heat-treated at various temperatures, (a) and enlarged figure for the 2θ range between 28° to 31° in (a), (b).

Table 1

Summary of the phase development of the Y_2O_3 films crystallized on the sapphire (0001) and (11 $\bar{2}$ 0) substrates. Samples were heat-treated for 10 min at each temperature.

Substrate	Temperature (°C)	Phases
Sapphire (0001)	900	Y_2O_3
	1000	Y_2O_3 + YAM
	1100	Y_2O_3 + YAM
	1200	Y_2O_3 + YAH + YAM
	1300	YAH + YAM + YAP + YAG
	1400	YAH + YAM + YAP + YAG
	1500	YAH + YAG
Sapphire (11 $\bar{2}$ 0)	900	Y_2O_3
	1000	Y_2O_3 + YAM
	1100	Y_2O_3 + YAM
	1200	Y_2O_3 + YAH + YAM + YAP
	1300	Y_2O_3 + YAH + YAM + YAP + YAG
	1400	YAH + YAM + YAP + YAG
	1600	YAG

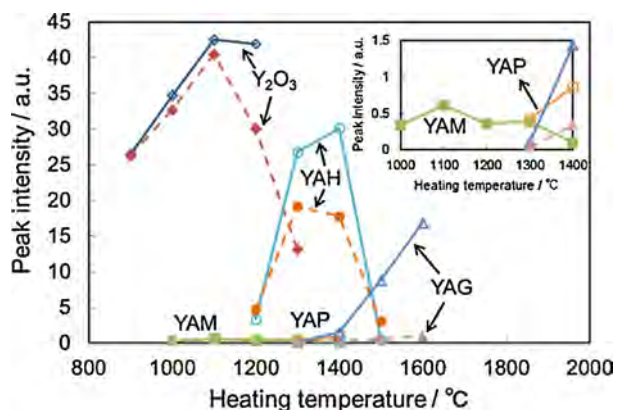


Fig. 4. XRD peak intensities of the product phases appeared on the sapphire (0001) substrates at each heating temperature. The intensities are plotted for 222 peak of Y_2O_3 , 023 of YAM, 200 of YAP, 10 $\bar{1}$ 1 of YAH, and 211 of YAG. The inset is an enlarged figure for YAM, YAP and YAG. Data for the Y_2O_3 , YAH and YAG phases on the sapphire (11 $\bar{2}$ 0) are also shown in the figure as broken lines for comparison.

data of YAH (card number 16-0219): $2\theta = 28.13^\circ$ for 10 $\bar{1}$ 0 and 29.36° for 10 $\bar{1}$ 1. Yamaguchi et al. have reported that solid solutions of YAH crystallize between 50 and 62.5 mol% Al_2O_3 [26]. Higher Al concentration than the stoichiometric composition might shift the XRD peak positions of YAH to the higher angles. A new hexagonal phase which has a structure similar to YAH but has $Y_3Al_5O_{12}$ composition has also been reported by Laine et al. [31]; however, the XRD data of the present study revealed no peak at $2\theta = 8.3\text{--}8.5^\circ$ which is one of the characteristics of this new hexagonal $Y_3Al_5O_{12}$ phase. Fig. 3a shows that no other peaks excepting for 10 $\bar{1}$ 0 and 10 $\bar{1}$ 1 peaks can be assigned to YAH phase. This result is the first case for obtaining the textured YAH phase. The YAH phase is inferred to be the main phase in the films heat-treated at 1300 and 1400 °C, by the rough estimation from their XRD peak intensities in Fig. 4. The film turned into YAG with a trace amount of YAH after heat-treatment at 1500 °C, and single-phase YAG after heat-treatment at 1600 °C; therefore, the YAH phase must be converted to the YAG phase, which is consistent with literatures [25,27,28]. The YAG phase showed {211} texture when formed on sapphire (0001) substrate. The crystallographic orientation of YAG is described in the next section.

As a result, there must be two routes to yield single YAG phase in our system; one is the $Y_2O_3 \rightarrow YAH \rightarrow YAG$ route yielding the majority of YAG and another is the $Y_2O_3 \rightarrow YAM \rightarrow YAP \rightarrow YAG$ yielding the minor amount of YAG in the film. This result implies

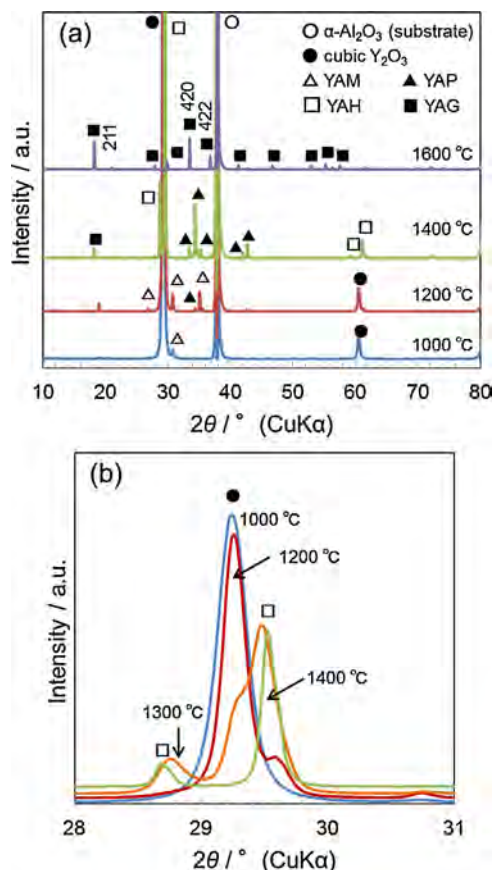


Fig. 5. XRD profiles of the Y–Al–O thin films on the sapphire (11 $\bar{2}$ 0) substrates heat-treated at various temperatures. (a) and enlarged figure for the 2θ range between 28° to 31° in (a), (b).

that the Al content in the resultant compounds increased with increasing heat-treatment temperature. Both the sequences of the phase change, $Y_2O_3 \rightarrow YAH \rightarrow YAG$ and $Y_2O_3 \rightarrow YAM \rightarrow YAP \rightarrow YAG$, without direct formation of Al-rich phases suggest that the phase development proceeded by the predominant diffusion of Al^{3+} in the substrate into the Y_2O_3 film. This result is supported by the fact that the ionic mobility of Al^{3+} is generally accepted to be higher than that of Y^{3+} in the oxide structure, and, the sequence of $YAM \rightarrow YAP \rightarrow YAG$ has been observed in most $Y_2O_3\text{--}Al_2O_3$ reaction systems [25].

Fig. 5 shows the XRD profiles of the films synthesized on the sapphire (11 $\bar{2}$ 0) substrates heat-treated at various temperatures between 1000 °C and 1400 °C. The {10 $\bar{1}$ 1} texture of the YAH phase and the presence of the two routes for obtaining the YAG phase were also confirmed regardless of the cut-plane of the sapphire substrate. The appearance of the intense 10 $\bar{1}$ 1 peak of YAH was coincident with the disappearance of the intense 222 peak of Y_2O_3 on both the sapphire (0001) and (11 $\bar{2}$ 0) substrates, suggesting that highly {10 $\bar{1}$ 1}-textured YAH can have a structural similarity with {111}-textured Y_2O_3 films rather than the sapphire substrates. Fig. 6 shows superposition of component atoms of YAH (10 $\bar{1}$ 1) and Y_2O_3 (111). Their lattice matching looks good, especially in the directions of Y_2O_3 [10 $\bar{1}$] and YAH [12 $\bar{1}$ 0]. Fig. 4 shows that the rate of phase change between the films on the sapphire (0001) and (11 $\bar{2}$ 0) slightly differed from one another, which may result from a non-identical Al concentration in the surfaces of both the sapphire planes.

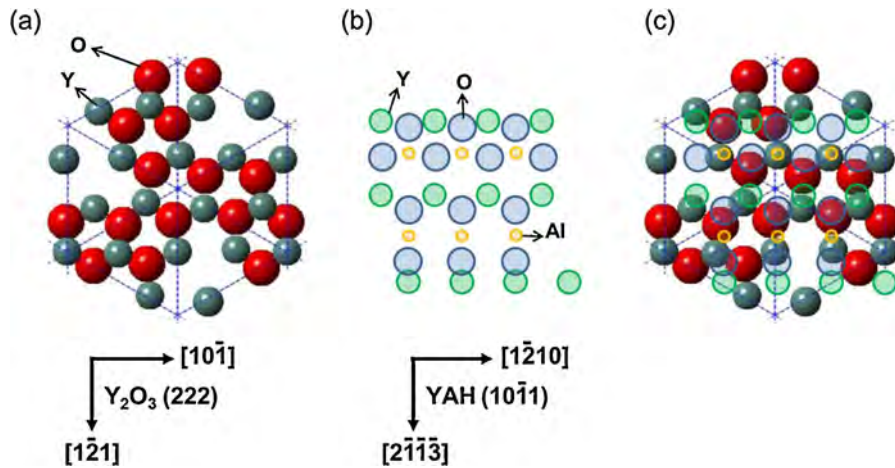


Fig. 6. Atomic arrangements of (a) Y_2O_3 (222) and (b) YAH (1011), and (c) their superposition.

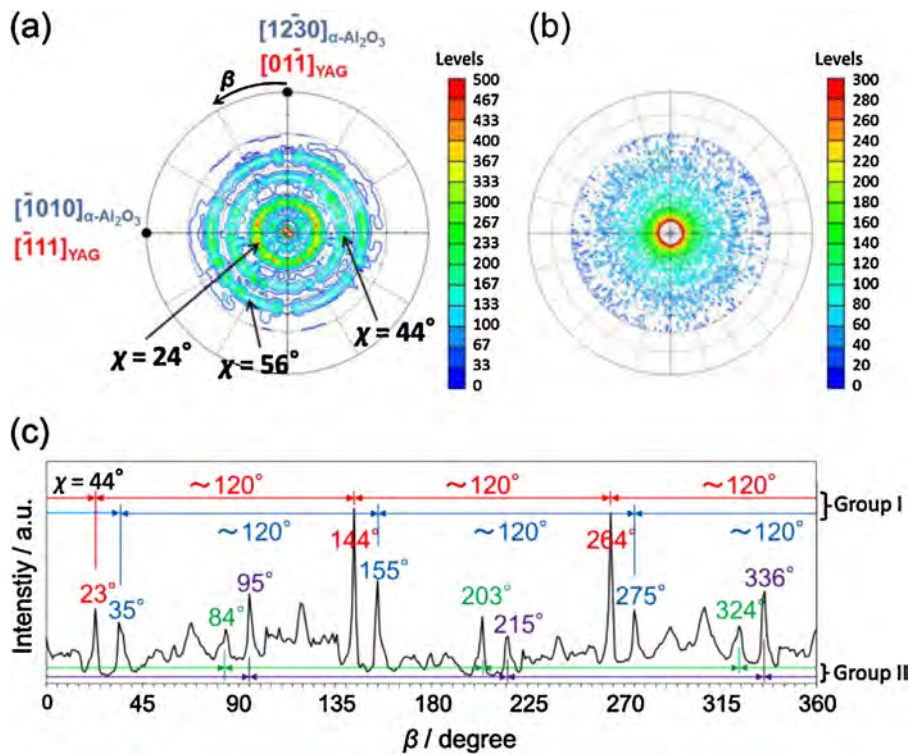


Fig. 7. X-ray pole figures of $\text{Y}_3\text{Al}_5\text{O}_{12}$ (420) on the (a) sapphire (0001) and (b) (1120) substrates, and (c) β -scanned diffraction intensity at $\chi = 44^\circ$ of (a), for YAG thin films heat-treated at 1600°C for 10 min. The sample of (a) and (c) was set as $[12\bar{3}0]$ of the sapphire directed to β of 0.

3.3. Crystallographic orientation of YAG

As previously stated, the film heat-treated at 1600°C on the sapphire (0001) substrate showed highly $\langle 211 \rangle$ orientation, which is shown in Fig. 3a. The degree of orientation can be expressed by Lotgering's factor, F [32]. For the $\langle 211 \rangle$ orientation, F is determined by the equation,

$$F = \frac{P - P_0}{1 - P_0} \quad (1)$$

where $P = \sum I(2kkk) / \sum I(hkl)$, $P_0 = \sum I_0(2kkk) / \sum I_0(hkl)$, $\sum I$ is the sum of the peak intensities of the XRD profile of the film, and $\sum I_0$ is that of randomly oriented reference powder [8,9]. The F value estimated within a 2θ range of $10\text{--}80^\circ$ was as high as 0.57 for

the film heat-treated at 1600°C on the sapphire (0001) substrate, whereas that on (1120) was as low as 0.23.

Fig. 7a shows the (420) XRD pole figure for the YAG film synthesized at 1600°C on the sapphire (0001) substrate, where the sample was set as $[12\bar{3}0]$ of the sapphire substrate directed to β of 0. The 420 poles seem to be regularly clustered on each ring at $\chi = 24^\circ, 44^\circ$, and 56° ; the position of the rings shows that the $\langle 211 \rangle$ axis of the YAG crystals stands perpendicular to the film surface. This result relates to the high F value of 0.57. The diffraction rings show some regular patterns in the rotational β direction, suggesting an in-plane texture in the YAG film on the sapphire (0001) substrate. Fig. 7c shows the β -scanned 420 diffraction intensity at $\chi = 44^\circ$, extracted from Fig. 7a. Strong diffraction spots in a set of two appeared at every 60° along β direction although two 210-family diffraction spots of (120) and (102) should appear apart

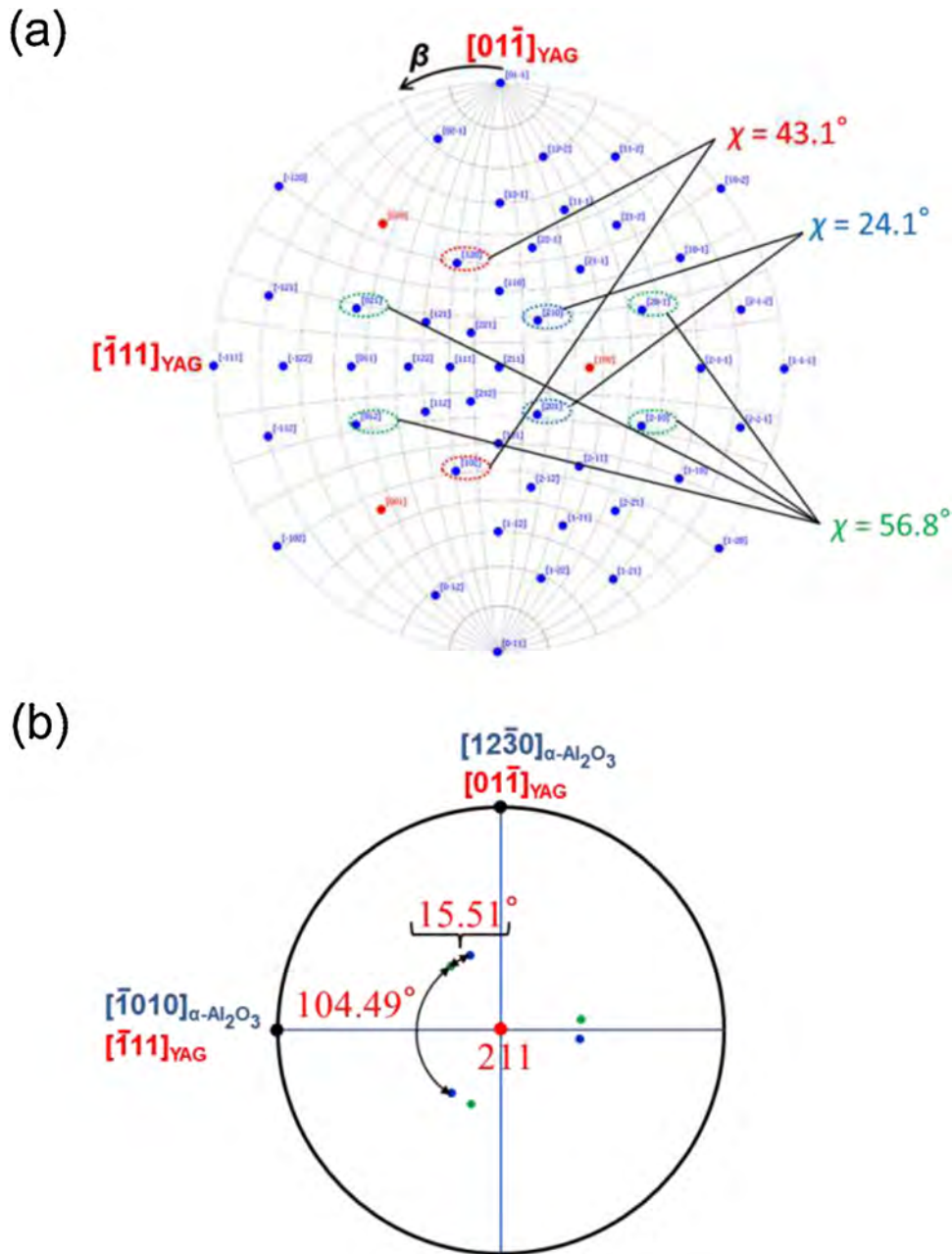


Fig. 8. (420) stereographic projection of a single-crystal YAG around $\langle 211 \rangle$, (a), and schematic diagram showing the positions of the diffraction spots of YAG crystals epitaxially grown on the sapphire (0001), (b). $[01\bar{1}]_{\text{YAG}}$ and $[12\bar{3}0]_{\alpha\text{-Al}_2\text{O}_3}$ are made the same direction.

$\Delta\beta = 135.51^\circ$ from one another at $\chi = 43.1^\circ$ in the pole figure for a single-crystal YAG around $\langle 211 \rangle$ axis (Fig. 8a). Assuming that an epitaxial growth of YAG (211) with one-fold symmetry on the sapphire $\{0001\}$ with three-fold symmetry, the pole figure is expected to show three-fold in-plane symmetry around $\langle 211 \rangle$. Making $[01\bar{1}]_{\text{YAG}}$ and $[12\bar{3}0]_{\alpha\text{-Al}_2\text{O}_3}$ the same direction well reproduced the positions of half the diffraction spot pairs (Group I) in the β -scan: $23^\circ, 35^\circ; 144^\circ, 155^\circ; 264^\circ, 275^\circ$ (Fig. 8b). The β -scanned 420 diffraction intensity shown in Fig. 7c includes also other half of the spot pairs (Group II), *i.e.*, $84^\circ, 95^\circ; 203^\circ, 215^\circ; 324^\circ, 336^\circ$ whose positions are shifted by 60° to the higher β angle, respectively. As a result, Fig. 7a suggests two sets of three-fold in-plane symmetry around $\langle 211 \rangle$ whose β -positions are shifted by 60° one another, and therefore, substantial six-fold one. In contrast to the results on the sapphire (0001) substrate, no systematic spots or rings can be observed in the (420) pole figure of the film heat-treated at 1600°C

on the sapphire $(11\bar{2}0)$ substrate as is shown in Fig. 7b. This indicates that the YAG crystals are randomly distributed throughout the film.

Geographical information of the orientation of the YAG phase crystallized on the sapphire (0001) substrate was also obtained from the EBSD measurement. Fig. 9 shows SEM image and the inverse pole figures and their maps of a surface of the YAG film on the sapphire (0001) substrate. The orientation of the YAG grains in the inverse pole figure with respect to the normal direction (ND) to the film surface undoubtedly concentrates near the $\langle 211 \rangle$ orientation. It should be noted that the larger grains exhibited purple-colored $\langle 211 \rangle$ orientation normal to the film surface. On the other hand, the crystallographic orientations of YAG grains with respect to the transverse and rolling directions (TD and RD, respectively) show clusters rather than uniform distribution along the orientations perpendicular to the $\langle 211 \rangle$. There are, especially, sev-

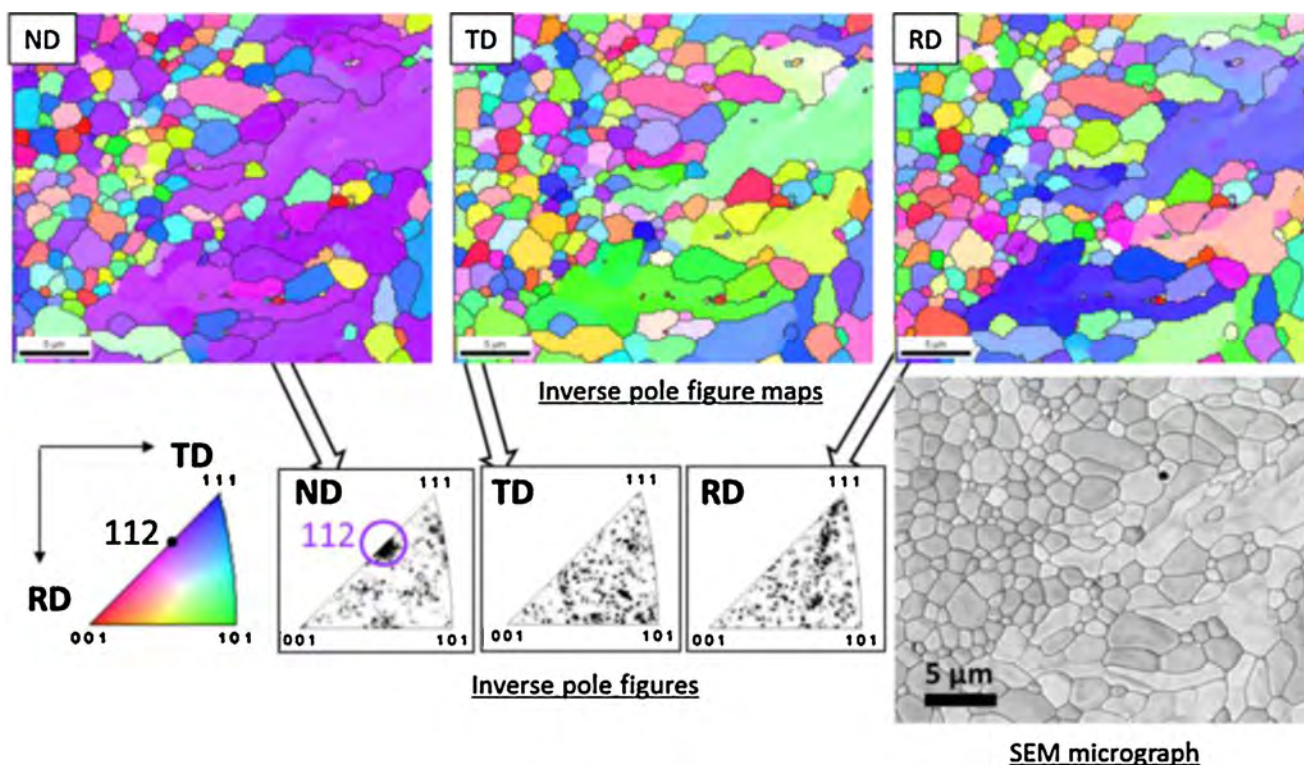


Fig. 9. Inverse pole figures and their maps of the surface of YAG films heat-treated at 1600 °C on the (0001) sapphire substrate.

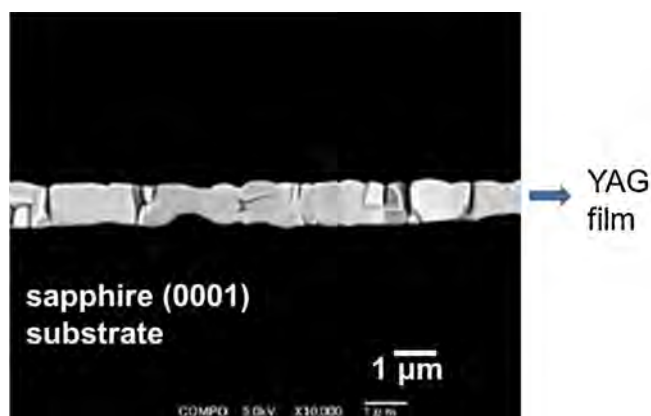


Fig. 10. SEM micrograph of the fractured surface of the YAG thin film on the sapphire (0001) substrate heat-treated at 1600 °C for 10 min.

eral large grains with similar orientations both in TD and RD. These results suggest that $[2\ 1\ 1]$ axis of substantial YAG crystals stands perpendicular to the film surface and the distribution around the axis is not random; therefore, the YAG crystals grew epitaxially on the sapphire (0001) substrate. Fig. 10 shows a SEM micrograph of a cross section of the film synthesized on the sapphire (0001) substrate where no intermediate phase at the interface between the film and the substrate was observed. It was also confirmed from Fig. 10 that the film thickness was about 1 μm and the film was composed of single domains in the thickness direction. EDS analysis confirmed the composition of the film was equal to that of YAG.

Few papers have reported on preferentially oriented YAG thin films on the sapphire substrates. Mizoguchi et al. [16] have reported the $\langle 2\ 1\ 1 \rangle$ oriented-YAG thin film synthesized on the sapphire (11 $\bar{2}$ 0) substrate by a spray-inductively coupled plasma technique, where the origin of the preferential orientation was attributed

to the highest reticular density of YAG $\{2\ 1\ 1\}$. However, for the YAG phase which we grew on the sapphire (11 $\bar{2}$ 0) substrate, the XRD profile showed the low preferential $\langle 2\ 1\ 1 \rangle$ orientation with $F=0.23$, and the X-ray pole figure no apparent one. On the other hand, as mentioned above, the $\langle 2\ 1\ 1 \rangle$ -oriented YAG film which we grew on the sapphire (0001) substrate was epitaxially formed. Therefore, we confirmed the lattice matching between YAG (211) and sapphire (0001), which is shown in Fig. 11. A directional relationship, $[01\bar{1}]_{\text{YAG}} \parallel [12\bar{3}0]_{\alpha\text{-Al}_2\text{O}_3}$, with the good lattice matching was revealed, which supports the experimentally obtained epitaxial formation of YAG on the “reactive” sapphire (0001) substrate. On the other hand, similarly good lattice matching was not obtained for the YAG thin film on the sapphire (11 $\bar{2}$ 0) substrate, which would account for the absence of the $\{2\ 1\ 1\}$ texture on the sapphire (11 $\bar{2}$ 0) substrate.

4. Conclusions

Using *c*-plane sapphire as a reactive substrate, we prepared the single-phase YAG thin film with highly preferred $\langle 2\ 1\ 1 \rangle$ orientation from the sol-gel derived Y_2O_3 thin film after heat-treatment at 1600 °C. We elucidated that the YAG film formed on the sapphire (0001) substrate showed six domains composed of two sets of three-fold in-plane symmetry around $\langle 2\ 1\ 1 \rangle$, and therefore, was epitaxially grown on the sapphire (0001) substrate. The crystallographic orientation relationship of $[01\bar{1}]_{\text{YAG}} \parallel [12\bar{3}0]_{\alpha\text{-Al}_2\text{O}_3}$ was also suggested. This finding was supported by the consideration of the lattice arrangement between YAG (211) and sapphire (0001). The major route for the YAG formation was $\text{Y}_2\text{O}_3 \rightarrow \text{YAH} \rightarrow \text{YAG}$ through the Al diffusion to the film. We also found for the first time that the metastable YAH phase with $\{10\bar{1}1\}$ self-texture can be formed through the inheritance of the preferential $\{1\ 1\ 1\}$ self-texture of Y_2O_3 . Our findings obtained by using the “reactive” substrate may afford a novel method for fabricating the textured

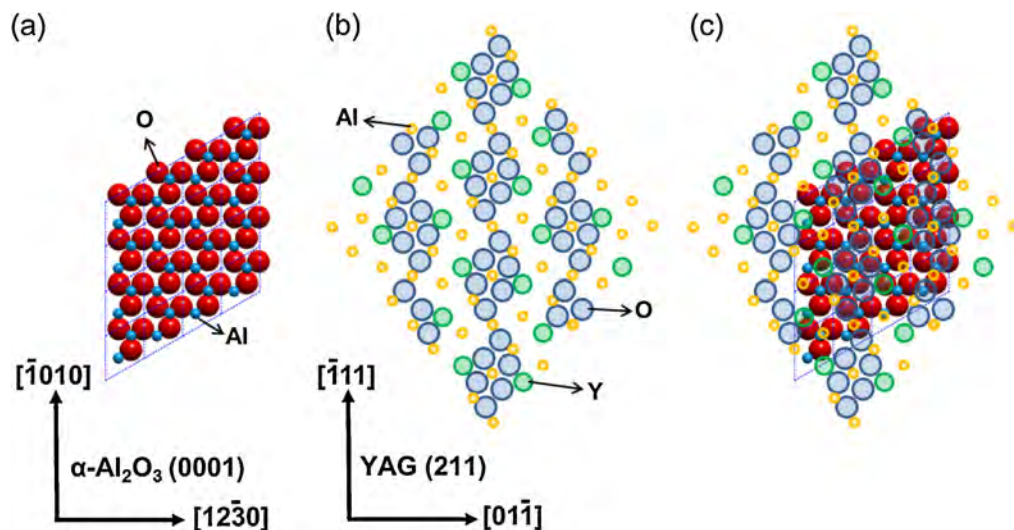


Fig. 11. Atomic arrangements of (a) α - Al_2O_3 (0001) and (b) YAG (211), and (c) their superposition.

thin films and further lead the way for realizing the oriented YAG ceramics by the evolved RTGG method.

Acknowledgements

The authors would like to thank Messrs. Satoshi Yamaguchi and Yoshihiro Kishida for their valuable discussion on the pole figure measurement results. This work was partially supported by MEXT-Supported Program for the Strategic Research Foundation at Private Universities, 2015–2019 (Grant No. S1411027).

References

- [1] A. Ikesue, T. Kinoshita, K. Kamata, K. Yoshida, Fabrication and optical properties of high-performance polycrystalline Nd:YAG ceramics for solid-state lasers, *J. Am. Ceram. Soc.* 78 (4) (1995) 1033–1040.
- [2] A. Ikesue, K. Kamata, K. Yoshida, Synthesis of Nd^{3+} , Cr^{3+} -codoped YAG ceramics for high-efficiency solid-state lasers, *J. Am. Ceram. Soc.* 78 (9) (1995) 2545–2547.
- [3] J. Lu, M. Prabhu, J. Song, C. Li, J. Xu, K. Ueda, A. Kaminskii, H. Yagi, T. Yanagitani, Optical properties and highly efficient laser oscillation of Nd:YAG ceramics, *Appl. Phys. B* 71 (2000) 469–473.
- [4] J. Lu, M. Prabhu, J. Xu, K. Ueda, H. Yagi, T. Yanagitani, A. Kaminskii, Highly efficient 2% Nd:yttrium aluminum garnet ceramic laser, *Appl. Phys. Lett.* 77 (23) (2000) 3707–3709.
- [5] J. Lu, K. Ueda, H. Yagi, T. Yanagitani, Y. Akiyama, Neodymium doped yttrium aluminum garnet ($\text{Y}_3\text{Al}_5\text{O}_{12}$) nanocrystalline ceramics—a new generation of solid state laser and optical materials, *J. Alloy Compd.* 341 (2002) 220–225.
- [6] I. Shoji, Y. Sato, S. Kurimura, V. Lupei, T. Taira, A. Ikesue, K. Yoshida, Thermal-birefringence-induced depolarization in Nd:YAG ceramics, *Opt. Lett.* 27 (4) (2002) 234–236.
- [7] I. Shoji, T. Taira, Intrinsic reduction of the depolarization loss in solid-state lasers by use of a (110)-cut $\text{Y}_3\text{Al}_5\text{O}_{12}$ crystal, *Appl. Phys. Lett.* 80 (17) (2002) 3048–3050.
- [8] T. Takeuchi, T. Tani, Texture development of SrTiO_3 ceramics during reactive templated grain growth processing, *J. Ceram. Soc. Jpn.* 110 (4) (2002) 232–236.
- [9] H. Itahara, K. Fujita, J. Sugiyama, K. Nakamura, T. Tani, Highly textured $\text{Na}_x\text{CoO}_{2-x}$ ceramics fabricated by both templated grain growth and reactive templated grain growth methods using single-crystalline particles as templates, *J. Ceram. Soc. Jpn.* 111 (4) (2003) 227–231.
- [10] T. Kimura, E. Fukuchi, T. Tani, Fabrication of textured bismuth sodium titanate using excess bismuth oxide, *Jpn. J. Appl. Phys.* 44 (11) (2005) 8055–8061.
- [11] T. Tani, Texture engineering of electronic ceramics by the reactive-templated grain growth method, *J. Ceram. Soc. Jpn.* 114 (5) (2006) 363–370.
- [12] C.S. Frazer, E.C. Dickey, A. Sayir, Crystallographic texture and orientation variants in Al_2O_3 - $\text{Y}_3\text{Al}_5\text{O}_{12}$ directionally solidified eutectic crystals, *J. Cryst. Growth* 233 (2001) 187–195.
- [13] Y. Murayama, S. Hanada, Y. Waku, Microstructure and high-temperature strength of directionally solidified Al_2O_3 /YAG eutectic composite, *Mater. Trans.* 44 (9) (2003) 1690–1693.
- [14] S. Sakata, A. Mitani, K. Shimizu, Y. Waku, Crystallographic orientation analysis and high temperature strength of melt growth composite, *J. Eur. Ceram. Soc.* 25 (2005) 1441–1445.
- [15] G.A. Hirata, O.A. Lopez, L.E. Shea, J.Y. Yi, T. Cheeks, J. McKittrick, J. Siqueiros, M. Avalos-Borja, A. Esparza, C. Falcony, Pulsed laser deposition of $\text{Y}_3\text{Al}_5\text{O}_{12}:\text{Tb}$ photoluminescent thin films, *J. Vac. Sci. Technol. A* 14 (3) (1996) 1694–1696.
- [16] Y. Mizoguchi, M. Kagawa, Y. Syono, T. Hirai, Film synthesis of $\text{Y}_3\text{Al}_5\text{O}_{12}$ and $\text{Y}_3\text{Fe}_5\text{O}_{12}$ by the spray-inductively coupled plasma technique, *J. Am. Ceram. Soc.* 84 (3) (2001) 651–653.
- [17] J.Y. Choe, D. Ravichandran, S.M. Blomquist, D.C. Morton, K.W. Kirchner, M.H. Ervin, U. Lee, Alkoxy sol-gel derived $\text{Y}_{3-x}\text{Al}_5\text{O}_{12}:\text{Tb}_x$ thin films as efficient cathodoluminescent phosphors, *Appl. Phys. Lett.* 78 (24) (2001) 3800–3802.
- [18] J.W. Kim, Y.J. Kim, The effects of substrates and deposition parameters on the growing and luminescent properties of $\text{Y}_3\text{Al}_5\text{O}_{12}:\text{Ce}$ thin films, *Opt. Mater.* 28 (2006) 698–702.
- [19] B.Y. Kokuoz, K. Seivalsatit, B. Kokuoz, O. Geiculescu, E. McCormick, J. Ballato, Er-doped Y_2O_3 nanoparticles: a comparison of different synthesis methods, *J. Am. Ceram. Soc.* 92 (10) (2009) 2247–2253.
- [20] Y.-C. Wu, S. Parola, O. Marty, J. Mugnier, Elaboration, structural characterization and optical properties of the yttrium alkoxy derived Y_2O_3 planar optical waveguides, *Opt. Mater.* 27 (2004) 21–27.
- [21] J.Y. Cho, K.Y. Ko, Y.R. Do, Optical properties of sol-gel derived $\text{Y}_2\text{O}_3:\text{Eu}^{3+}$ thin-film phosphors for display applications, *Thin Solid Films* 515 (2007) 3373–3379.
- [22] S.-J. Park, D.P. Norton, Ion beam assisted texturing of polycrystalline Y_2O_3 films deposited via electron-beam evaporation, *Thin Solid Films* 510 (2006) 143–147.
- [23] M. Tsuchiya, N.A. Bojarczuk, S. Guha, S. Ramanathan, Transmission electron microscopy studies on structure and defects in crystalline yttria and lanthanum oxide thin films grown on single crystal sapphire by molecular beam synthesis, *Philos. Mag.* 90 (9) (2010) 1123–1139.
- [24] V. Swamy, N.A. Dubrovinskaya, L.S. Dubrovinsky, High-temperature powder X-ray diffraction of yttria to melting point, *J. Mater. Res.* 14 (2) (1999) 456–459.
- [25] M.J. Li, Y.C. Wu, F.S. Yen, C.Y. Huang, Influence of ionic mobility on the phase transformation route in $\text{Y}_3\text{Al}_5\text{O}_{12}$ (YAG) stoichiometry, *J. Eur. Ceram. Soc.* 31 (2011) 2099–2106.
- [26] O. Yamaguchi, K. Takeoka, K. Hirota, H. Takano, A. Hayashida, Formation of alkoxy-derived yttrium aluminum oxides, *J. Mater. Sci.* 27 (1992) 1261–1264.
- [27] S.M. Sim, K.A. Keller, T.I. Mah, Phase formation in yttrium aluminum garnet powders synthesized by chemical methods, *J. Mater. Sci.* 35 (2000) 713–717.
- [28] S.D. Parukuttyamma, J. Margolis, H. Liu, C.P. Grey, S. Sampath, H. Herman, J.B. Parise, Yttrium aluminum garnet (YAG) films through a precursor plasma spraying technique, *J. Am. Ceram. Soc.* 84 (8) (2001) 1906–1908.
- [29] X. Li, J.G. Li, Z. Xiu, D. Huo, X. Sun, Transparent Nd:YAG ceramics fabricated using nanosized γ -alumina and yttria powders, *J. Am. Ceram. Soc.* 92 (1) (2009) 241–244.
- [30] A. Gandhi, C.G. Levi, Phase selection in precursor-derived yttrium aluminum garnet and related Al_2O_3 - Y_2O_3 compositions, *J. Mater. Res.* 20 (4) (2005) 1017–1025.
- [31] R.M. Laine, J. Marchal, H. Sun, X.Q. Pan, A new $\text{Y}_3\text{Al}_5\text{O}_{12}$ phase produced by liquid-feed flame spray pyrolysis (LF-FSP), *Adv. Mater.* 17 (7) (2005) 830–833.
- [32] K. Lotgering, Topotactical reactions with ferrimagnetic oxides having hexagonal crystal structures—I, *J. Inorg. Nucl. Chem.* 9 (1959) 113–123.

[doi:10.2109/jcersj2.15261](https://doi.org/10.2109/jcersj2.15261)

Microstructural evolution of high purity alumina ceramics prepared by a templated grain growth method

**Kazumasa TAKATORI,* Hiroaki KADOURA,* Hidehito MATSUO,*
Shuichi ARAKAWA** and Toshihiko TANI*,****

*Toyota Central Research and Development Laboratories, Inc., Nagakute, Aichi 480-1192, Japan

**Toyota Technological Institute, Nagoya 468-8511, Japan

Microstructural evolution of high purity alumina ceramics prepared by a templated grain growth method

Kazumasa TAKATORI,^{*,†} Hiroaki KADOURA,^{*} Hidehito MATSUO,^{*}
Shuichi ARAKAWA^{**} and Toshihiko TANI^{*,**}

^{*}Toyota Central Research and Development Laboratories, Inc., Nagakute, Aichi 480-1192, Japan

^{**}Toyota Technological Institute, Nagoya 468-8511, Japan

Textured α -alumina ceramics were prepared by mixing different ratios of three-sized plate-like α -alumina particles and fine equiaxed particles without the use of sintering aids. The plate-like particles have developed a - b planes and were incorporated as an aligned template. Mixed powders were formed into a green sheet using a doctor blade technique and sintered under various conditions (temperature, duration and atmosphere). The development of microstructure and texture in the sintered bodies was examined and correlated with the preparation conditions. The addition of plate-like particles to the fine equiaxed powder suppressed densification and grain growth during sintering. The plate-like particles tend to grow with a lower aspect ratio at high temperatures, especially under vacuum sintering conditions. The addition of 30% plate-like particles produced sintered bodies with the highest uniaxial (001) orientation, but with residual porosity. The addition of 5% plate-like particles resulted in sintered bodies with almost full density but texture development was inferior to that of 30%. The vacuum-sintered specimens with larger amounts of platelets exhibited pseudo-isotropic grain growth and high-to-medium uniaxial (001) orientation, which suggests that anisotropic grain growth is not essential to achieve a high degree of orientation.

©2016 The Ceramic Society of Japan. All rights reserved.

Key-words : Alumina, Templated grain growth, Microstructure, Platelet, Aspect ratio

[Received October 30, 2015; Accepted December 27, 2015]

1. Introduction

Single crystal α -alumina is colorless and transparent; however, sintered bodies of α -alumina are typically white in color due to the presence of residual porosity and intergranular phases. The real in-line transmission (RIT) of single crystal α -alumina in the visible light region at a wavelength of 640 nm is 86% at best.¹⁾ Light scattering at grain boundaries further reduces the transmission for polycrystalline α -alumina because of its anisotropic refractive index. Therefore, sintered alumina, even without the presence of secondary phases, has no advantage with regard to transparency over optically isotropic materials such as yttrium aluminum garnet (YAG).²⁾ However, translucent polycrystalline alumina, which has high mechanical strength and thermal conductivity, is chemically and thermally stable, and is naturally abundant, is considered to be an industrially important material.³⁾

Since Coble reported the translucency of alumina ceramics prepared with a high-purity raw material in around 1960,⁴⁾ translucent alumina sintered bodies have been utilized in light-emitting tubes for high-pressure sodium lamps by taking advantage of their mechanical strength and chemical stability. Much effort has been devoted to the development of high-purity and easily sinterable particulate materials, in addition to the development of novel densification processes, such as hot isostatic pressing (HIP)⁵⁾ and spark plasma sintering (SPS),⁶⁾ which can reduce residual pores and inhibit grain growth in a sintered body. As a result, the RIT of translucent alumina has been reported to be approximately 70%.⁷⁾ In recent years,

colloidal processing under a strong magnetic field prior to sintering was reported to produce dense alumina ceramics with not only high RIT greater than 50%, but also uniaxial crystal orientation.^{8),9)} Another approach to achieve crystal-oriented ceramics has been the use of anisometric particles.

The fabrication of textured alumina ceramics using flake-like alumina particles as a template was studied by Brandon et al.^{10),11)} and Messing et al.^{12),13)} in the 1990s. Brandon et al. reported grains with uniformly aligned crystal axes, improved flexural strength, and 10% anisotropy of the thermal expansion coefficients by the addition of 5–10% flaky alumina particles with sizes less than 10 μm to granular α -alumina powder.¹¹⁾ Messing et al. examined the addition of approximately 5% CaO and SiO₂ along with flaky alumina particles, and concluded that the calcium silicate-based liquid phase acts as a sintering aid at high temperature and is effective for achieving crystal orientation of the sintered body.¹²⁾ They evaluated the evolution of the grain orientation using X-ray diffraction (XRD) and scanning electron microscopy (SEM) observations and determined that the templates predominantly grow to develop grain orientation, which they expressed as templated grain growth (TGG). Snel et al. then examined the detailed parameters in the doctor blade molding of an aqueous slurry containing a mixture of granular alumina and ca. 10% flaky alumina particles (ca. 3 μm diameter and ca. 0.1 μm thick).¹⁴⁾ The shearing force during molding was determined as an important parameter for developing orientation, and the Lotgering factor, which is an index of crystal orientation, was increased to as high as 0.67.

However, systematic experimental studies have not been conducted to observe the development of microstructure and texture in high-purity alumina. The present study is intended to examine the feasibility of the production of dense alumina

[†] Corresponding author: K. Takatori; E-mail: g.nanasino@gmail.com

[‡] Preface for this article: DOI <http://dx.doi.org/10.2109/jcersj2.124.P4-1>

ceramics with uniaxially oriented grains by an industrially realizable process. We have selected a sheet forming process using commercially available plate-like alumina particles as templates without the use of sintering aids, which would be applicable to large-sized alumina ceramics for thermal, mechanical and optical applications. In the present study, the effects of the template (size and amount) and the sintering conditions (temperature, duration and atmosphere) on the development of microstructure and texture were examined systematically.

2. Experimental

2.1 Raw materials

Three types of plate-like alumina particles with different sizes (Serath YFA00610, YFA02025, YFA05025, Kinsei Matec Co., Ltd.) and high-purity equiaxed-grain α -alumina (Taimicron TM-DAR, Taimei Chemicals Co., Ltd.; BET specific surface area = $13.2 \text{ m}^2 \cdot \text{g}^{-1}$, average particle size = $0.17 \mu\text{m}$) were used respectively as template powders and matrix powder for the raw material. The average particle diameters and aspect ratios reported by the manufacturer for Serath YFA00610, YFA02025, and YFA05025 are 0.51, 2.11, and $4.62 \mu\text{m}$, and 10, 25, 25, respectively. TM-DAR is reported to be sintered up to a density of $3.96 \text{ g} \cdot \text{cm}^{-3}$ by firing at 1350°C for 1 h in air.¹⁵⁾ All the raw materials were subjected to SEM (SU3500, Hitachi High-Technologies) observations and XRD (Ultima IV, Rigaku Corporation, Cu-K α) measurements to identify the morphology and crystal phases, respectively. Oriented particle monolayer XRD (OPML-XRD) was also conducted for the platelets to determine the developed plane.¹⁶⁾ The specimen names and compositions are listed in **Table 1**. The names represent the size of plate-like particles and the weight fractions in the specimens, and S, M, and L correspond to YFA00610, YFA02025, and YFA05025, respectively. Control sample was described as Tref which contained only equiaxed-grain α -alumina.

2.2 Forming

The powders were weighed in the ratio in Table 1 for total 20.4 g in each batch and mixed together with 2.2 g of polyvinyl butyral (PVB) and 36.5 ml of organic solvents (ethanol: toluene = 2:3) in a polyethylene pot with alumina balls. After ball-milling for 20 h, the slurry was formed into a sheet with a thickness of ca. $100 \mu\text{m}$ using a doctor blade with a slit spacing of 0.5 mm. The sheet was cut at regular intervals and laminated to prepare a plate specimen with a thickness of ca. 5 mm using a heater press (80°C , 10 MPa). The plate was heated to remove organic binder at a heating rate of $10^\circ\text{C} \cdot \text{h}^{-1}$ in an electric furnace of air circulation and soaked at 600°C for 2 h.

The dewaxed plate specimens ($10 \times 10 \times 5 \text{ mm}^3$) were sintered in an electrical furnace at 1400, 1600 and 1700°C for 4 h and 1700°C for 20 h in air. Heating and cooling were conducted at a heating rate of $300^\circ\text{C} \cdot \text{h}^{-1}$ and with furnace cooling, respectively.

Table 1. Specimen names and compositions

Specimen name	YFA (platelike particle)			TM-DAR (equiaxed particulate)
	05025	02025	00610	
M100	—	100%	—	0%
M60	—	60%	—	40%
M30	—	30%	—	70%
M5	—	5%	—	95%
L5	5%	—	—	95%
S5	—	—	5%	95%
Tref	—	—	—	100%

Plate specimens were also sintered in a vacuum sintering furnace with graphite heating elements. The plate specimen was embedded in a high purity alumina granulated powder in a silicon carbide (SiC) cylindrical container and sintered at 1700°C for 4 h. The heating and cooling conditions were the same as those used for sintering in air.

2.3 Characterization

The bulk densities of the sintered bodies were measured using the water displacement method. The degree of crystal orientation (F value) for each specimen was evaluated according to the Lotgering method¹⁷⁾ from the XRD diffraction peak intensities for a sintered body that was surface-polished parallel to the original sheet-formed surface. The F values for α -alumina for the (0 0 6) and (1 0 10) crystal planes were calculated using the following equations:

$$F = (\rho - \rho_0)/(1 - \rho_0), \text{ where}$$

$$\rho = I/\Sigma I(h k l),$$

$$\rho_0 = I_0/\Sigma I_0(h k l).$$

Here, the subscript in ρ_0 represents the data for the reference specimen. In the case of (0 0 6), I_0 is the (0 0 6) peak intensity and $\Sigma I_0(h k l)$ is the sum of the XRD peak intensities for the reference specimen. Specimen Tref sintered at 1400°C was used as the reference because the XRD pattern had a high intensity and resembled the powder diffraction pattern (PDF01-089-7717). Thirteen main diffraction peaks in the range of $2\theta = 10\text{--}80^\circ$ were subject to calculation. Similarly, ρ , I , and $\Sigma I(h k l)$ represent the values for the test specimens used for evaluation of the degree of orientation.

SEM observations of the plate specimen microstructures were conducted for the fracture surface perpendicular to the original sheet surface. Selected specimens were also mirror-polished and carbon-coated on the section perpendicular to the original sheet surface for evaluation of the crystallographic orientation of individual grains by electron backscatter diffraction (EBSD) analysis.

3. Results

3.1 Characteristics of the raw materials

Figures 1 and **2** show SEM images and XRD patterns for the raw materials, respectively. The hexagonal platelets observed in Figs. 1(b)–1(d) suggest the developed plane corresponds to a -

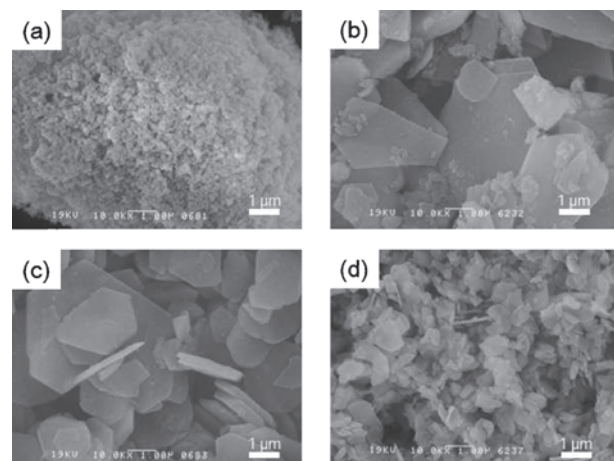


Fig. 1. SEM images of starting powders; (a) TM-DAR, (b) YFA05025, (c) YFA02025, and (d) YFA00610.

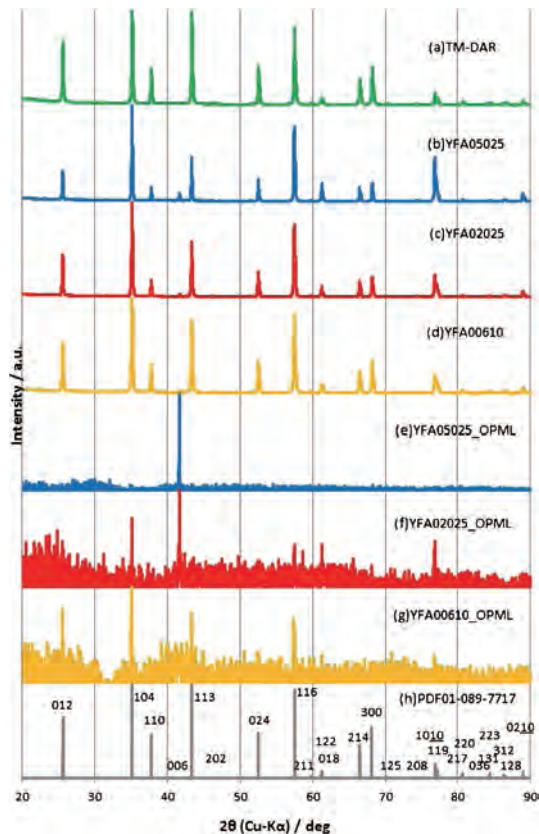


Fig. 2. Powder XRD patterns for (a) TM-DAR, (b) YFA05025, (c) YFA02025, and (d) YFA00610. OPML-XRD patterns for (e) YFA05025, (f) YFA02025, and (g) YFA00610. (h) Diffraction intensity chart from PDF01-089-7717.

plane of the corundum crystal structure. Although the intensities for the (0 0 6) diffraction peak at $2\theta \approx 41.7^\circ$ are in the order of (d) < (c) < (b), the intensity level was quite low, which suggests the difficulty in aligning these platelets by dry processing. On the other hand, the OPML-XRD pattern for the largest platelets (YFA05025) shows a strong (0 0 6) peak while the other peaks are suppressed in Fig. 2(e), which confirms the developed plane of the platelets is the *a-b* plane, (0 0 *l*). However, this tendency for the aligned platelets in the OPML-XRD specimens becomes weaker as the particle size decreases. Except for suppression of the (*h k* 0) diffractions, the OPML-XRD pattern for the smallest platelets [YFA00610; Fig. 2(g)] is similar to its powder XRD pattern [Fig. 2(d)]. This demonstrates the difficulty in the alignment of small platelets, even by wet processing with a high shear stress.

3.2 Density of sintered bodies

Figure 3 shows the relationship between the sintering conditions and the bulk density of the plate specimens sintered in air and under vacuum. The rightmost data of Fig. 3 corresponds to those for the specimens sintered at 1700°C for 20 h in air. Specimen M100 with only medium-sized plate-like particles was difficult to consolidate and contained over 1% open pores, even after sintering at 1700°C for 20 h in air. For the other specimens sintered in air for 4 h, the densities of specimens M60 and M30 reached over $3.9 \text{ g}\cdot\text{cm}^{-3}$ at 1700°C for 4 h and open pores were absent. In contrast, the specimens prepared with plate-like particles were low in density when sintered under vacuum, and this tendency was the same for the specimens with a high plate-

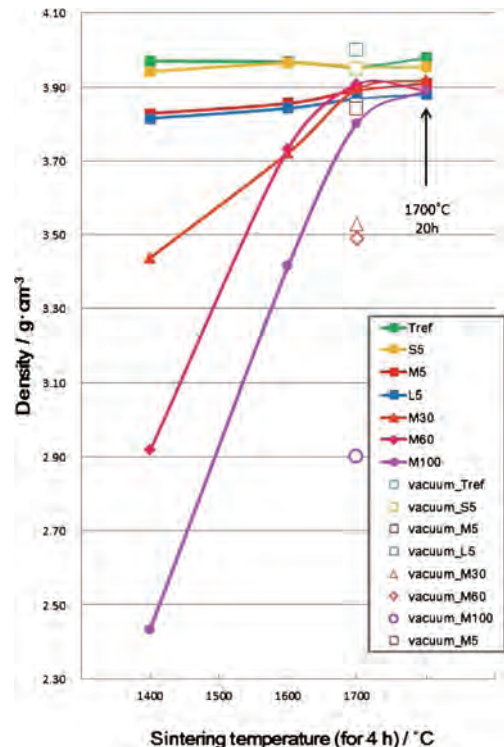


Fig. 3. Relationship between bulk density of sintered body and sintering conditions. Right side data are for sintering at 1700°C for 20 h. The sintering time for the other specimens was 4 h. Filled and open marks represent normal and vacuum sintering, respectively.

like particle loading.

The size of the plate-like particles influences the density of the specimen, although there was no significant temperature dependence of the density when sintering above 1400°C in air for the specimens prepared with 5% plate-like particles, which is evident from the results for L5, M5 and S5 shown in Fig. 3. Although the vacuum-sintered L5 and M5 specimens had lower density than the normal-sintered specimens, at 1700°C, S5 reached the same density as Tref by either normal- or vacuum-sintering.

3.3 XRD of sintered bodies

Figure 4 shows XRD patterns for the specimens prepared with various amounts of medium-sized plate-like particles by normal sintering. The peak intensity is normalized by the strongest peak. Figures 4(a)–4(d) correspond to the four sintering regimes at 1400–1700°C. Tref showed almost the same XRD profile in any of the firing conditions and it was similar to the reported powder XRD pattern (ICDD: PDF01-089-7717). For the specimens sintered at 1400°C, M30 exhibited the most noticeable change from Tref; the (1 0 10), (0 0 6) and (0 1 8) diffraction peaks became stronger and the other peaks became weaker. This trend became more pronounced for the M30 specimens for higher sintering temperatures and longer times. In the XRD pattern for M5 sintered at 1600°C or above, (1 0 10) was the strongest peak. For the specimens prepared with 5% of plate-like particles, there was no clear relationship between the platelet size and the XRD pattern.

Figure 5 shows XRD patterns for the vacuum-sintered specimens prepared with 5% of different-sized plate-like particles. The peak strength is normalized by the strongest peak. The intensities of the (0 0 6) and (1 0 10) peaks became stronger than that of

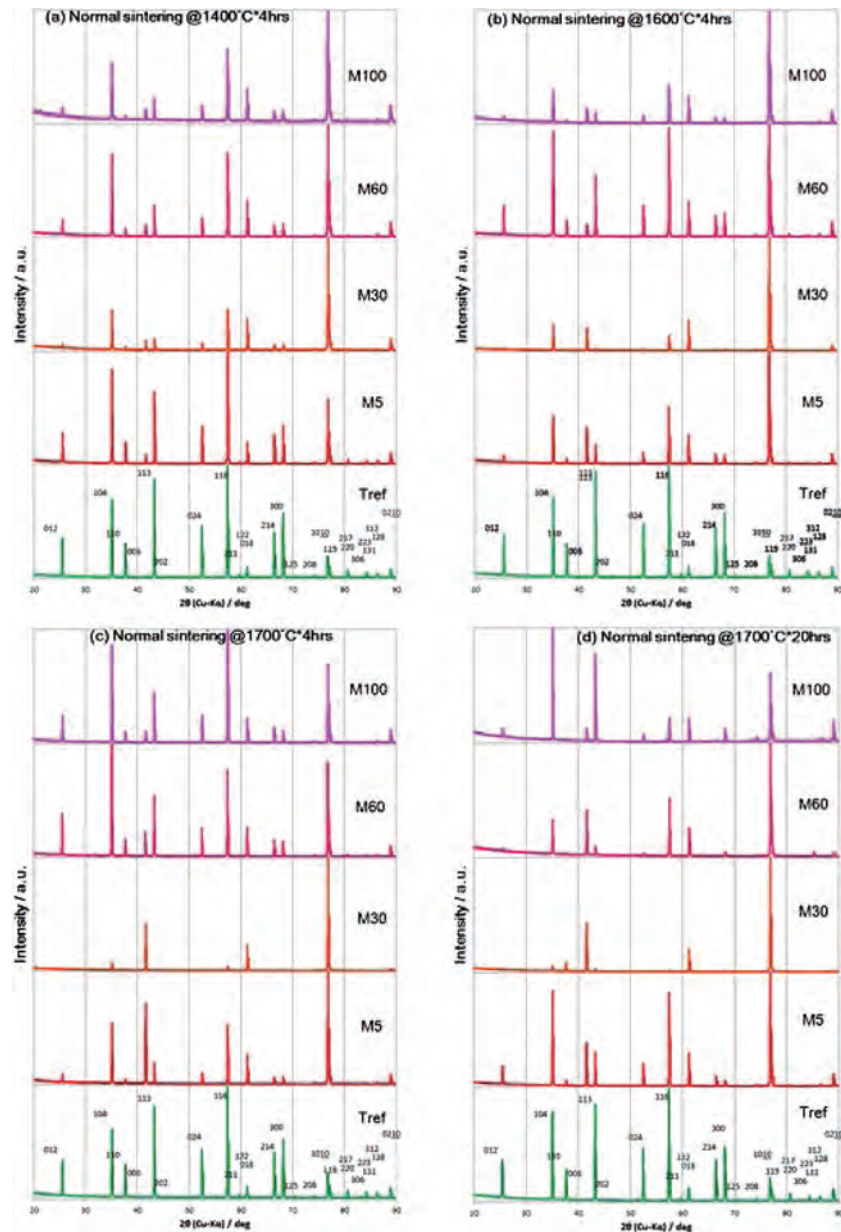


Fig. 4. XRD patterns for normal-sintered M100–M5 and Tref specimens. The patterns were normalized by the strongest peak. (a) 1400°C for 4 h, (b) 1600°C for 4 h, (c) 1700°C for 4 h, and (d) 1700°C for 20 h. Plate-like particles were loaded at 100, 60, 30, 5, and 0% (Tref) accompanied by the Miller indices reported in ICDD-PDF01-089-7717.

Tref, and the (0 0 6) peak intensity was in the order of $L5 > M5 > S5$, which may reflect the order of ease of platelet alignment.

3.4 Microstructure of sintered body fracture surface

Figures 6 and 7 show SEM images of the fracture surfaces of specimens sintered at 1700°C for 20 h, and four S5 specimens normal-sintered under different conditions, together with Tref, respectively. The vertical direction in each micrograph corresponds to the stacking direction of the formed sheets, so that the length direction of the plate-like particles was expected to align in the horizontal direction and perpendicular to the plane of the sheets.

Figure 6(a) shows the originally 100% plate-like particles coalesced to form large grains with many closed pores trapped

inside and no trace of the original plate-like particles. The constituent grains shown in Fig. 6(b) are much smaller than those in Fig. 6(a) and a tendency for long thin grains to align in the horizontal direction is observed. The fracture surfaces shown in Figs. 6(c) and 6(d) are dominated by a transgranular fracture mode, and elongated grains are observed due to the shape of the original plate-like particles. Considering that the medium-sized YFA02025 platelets have an average diameter of ca. 2 μm and an average thickness of ca. 0.08 μm , the grain size in Fig. 6(c) was estimated to be ca. 30 and 5 μm in the horizontal and vertical directions, respectively, which indicates dominant grain growth in the thickness direction. Figures 6(e) and 6(f) comprise five weight percent large and small size plate-like particles. Comparing these photos with Fig. 6(d), the average grain sizes of the sintered bodies were observed to be almost the same but in the order of $S5 \geq M5 \geq L5$ in these normal sintering conditions,

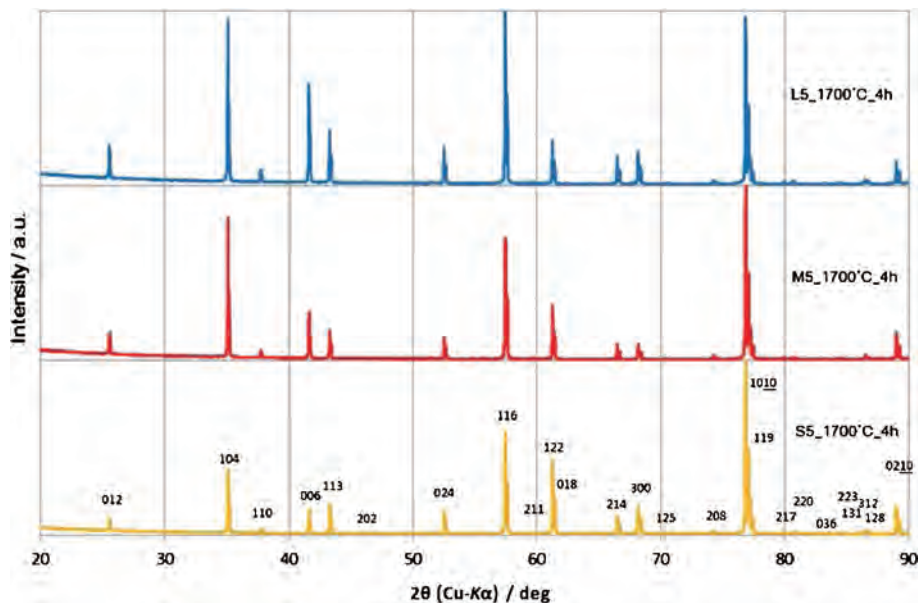


Fig. 5. XRD profiles for vacuum-sintered specimens (1700°C for 4 h) for (a) L5, (b) M5 and (c) S5.

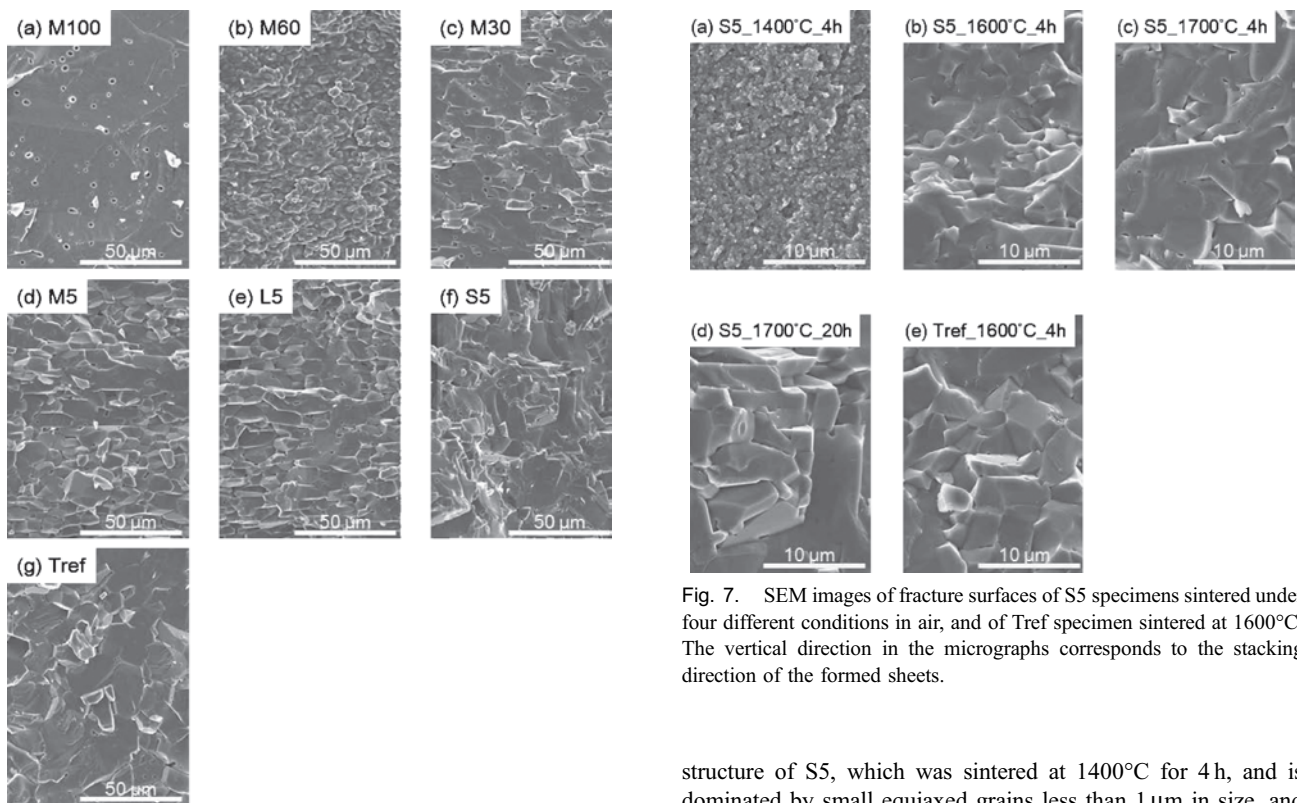


Fig. 6. SEM images of fracture surfaces for specimens normal-sintered at 1700°C for 20 h. The vertical direction in the micrographs corresponds to the stacking direction of the formed sheets.

which means drastic grain growth for S5 specimen. Figure 6(g) shows the fracture surface of Tref, which is typical of that observed for a pure alumina sintered body. The size of the equiaxed grains after sintering was over 10 μm, which is approximately 100 times larger than the original TM-DAR particles.

Figures 7(a)–7(d) show the fracture surfaces of S5 sintered under several conditions in air. Figure 7(a) shows the micro-

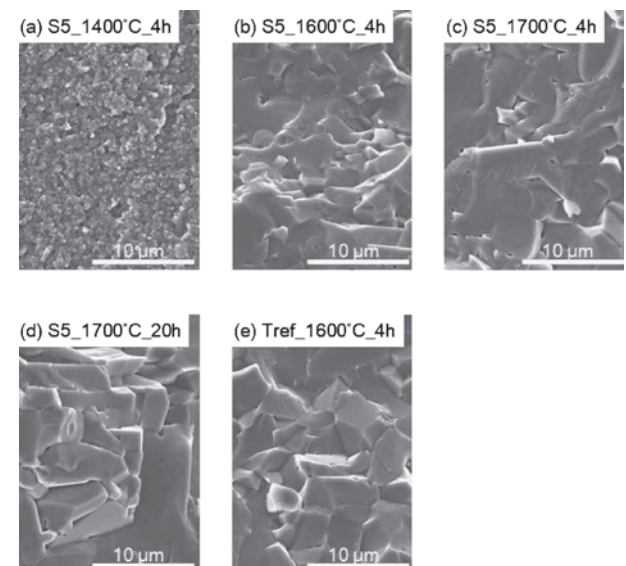


Fig. 7. SEM images of fracture surfaces of S5 specimens sintered under four different conditions in air, and of Tref specimen sintered at 1600°C. The vertical direction in the micrographs corresponds to the stacking direction of the formed sheets.

structure of S5, which was sintered at 1400°C for 4 h, and is dominated by small equiaxed grains less than 1 μm in size, and no plate-like particles are observed. Figure 7(b) shows significant grain growth up to 10 μm, and grains that are elongated in the horizontal direction are observed. Further elongated grain growth to over 20 μm in length in the horizontal direction and to 5 μm in thickness is observed for the specimen sintered at 1700°C for 4 h [Fig. 7(c)]. Longer heat treatment caused further grain growth [Fig. 7(d)]; however, a quantitative discussion of grain growth is not possible based on the fracture surface. Figure 7(e) shows the microstructure of Tref sintered under the same conditions as S5 in Fig. 7(b), where the same density of 3.96 g·cm⁻³ was obtained. However, the average grain size in Tref was larger than that in S5, which suggests that the incorporation of a small amount of

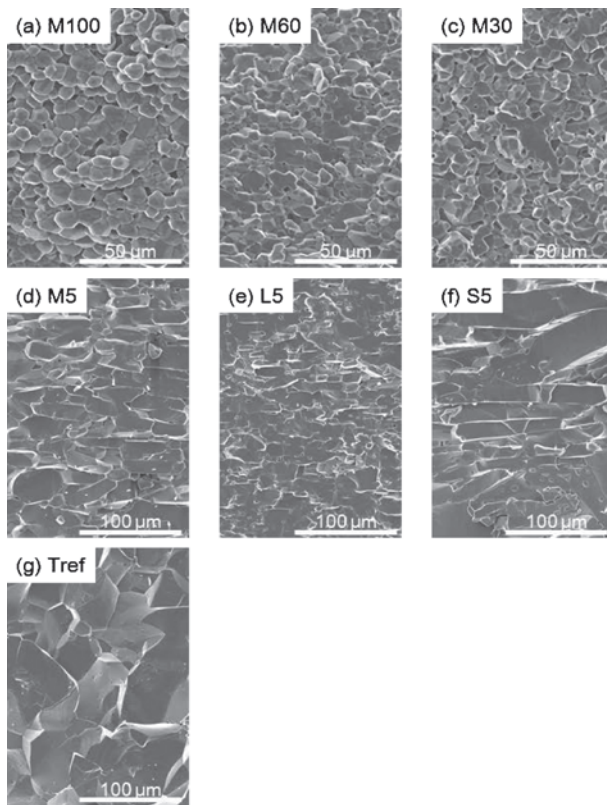


Fig. 8. SEM images for fracture surfaces of specimens vacuum-sintered at 1700°C for 4h. The vertical direction in the micrographs corresponds to the stacking direction of the formed sheets.

plate-like particles retards the grain growth of alumina. This effect was already observed in a comparison of Tref in Fig. 6(g) with Figs. 6(d)–6(f), where a higher sintering temperature was considered to have promoted not only the exaggerated grain growth of both plate-like particles and fine equiaxed particles but also the retardation of grain growth introduced by the incorporated plate-like particles into the fine equiaxed particles.

Figure 8 shows the fracture surfaces of specimens vacuum-sintered at 1700°C for 4h, where the vertical direction in the photograph corresponds to the stacking direction of the formed sheets. Figure 8(a) shows a homogeneous porous structure without a trace of the original plate-like particles, with grain growth to more than 5 μm. Figures 8(b) and 8(c) also show equiaxed grain microstructures with similar sized grains as in Fig. 8(a). Necking between the equiaxed grains is more obvious as the amount of plate-like particles is reduced from 100 to 30%. These equiaxed-grain-structured specimens have lower densities of less than 90% with open pores. Figure 8(d) shows a dominantly transgranular fracture mode surface, where in contrast to Figs. 8(a)–8(c), grains elongated in the horizontal direction are observed without open pores. Figure 8(e) shows the elongated grain structure of the vacuum-sintered L5 specimen, where the grain size appears smaller than that in Fig. 8(d), indicating an inverse relationship with the incorporated plate-like particle size. The growth of elongated grains is most remarkable in the S5 specimen [Fig. 8(f)], which originally contained 5% of small-sized plate-like particles, and the grain size was estimated to be ca. 100 μm in length in the horizontal direction and ca. 10 μm thick in the vertical direction. Therefore, the order of the grain size in the sintered specimens prepared with 5% plate-like particles is S5 > M5 > L5, indicating an inverse relationship

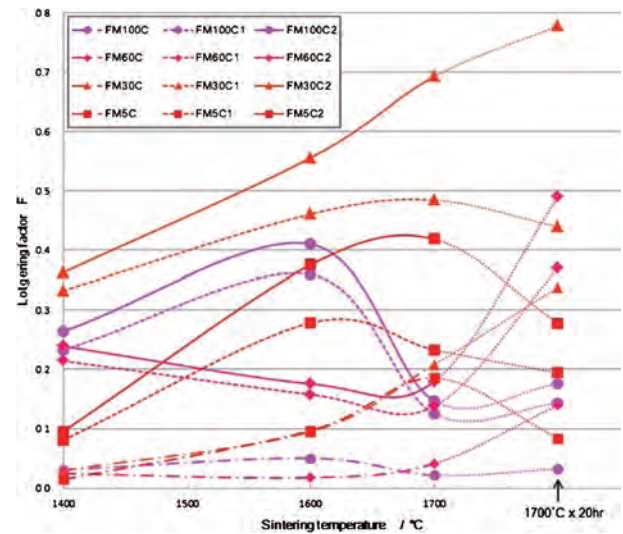


Fig. 9. Relationship between F value and sintering conditions for normal-sintered bodies prepared with medium-sized plate-like particles. The key legend shows the specimen name and corresponding Miller indices from which the Lotgering factors were calculated. C, C1 and C2 correspond to $F_{(0\ 0\ 6)}$, $F_{(1\ 0\ 10)}$ and $F_{(0\ 0\ 6)+(1\ 0\ 10)}$, respectively.

with the incorporated plate-like particle size. Figure 8(g) shows that the grains in the Tref specimen sintered at 1700°C for 4h grew to over 30 μm in diameter, which is approximately 200 times larger than the TM-DAR particles.

3.5 Crystal orientation of sintered bodies

Figure 9 shows the relationship between the Lotgering factor F , and the sintering conditions for normal-sintered bodies that contain medium-sized plate-like particles. Two Lotgering factors of $F_{(0\ 0\ 6)}$ and $F_{(1\ 0\ 10)}$ and their summation ($F_{(0\ 0\ 6)+(1\ 0\ 10)}$) are shown as dashed-dotted, dashed and solid lines with the notations C, C1 and C2, respectively. The angle between the (0 0 6) and (1 0 10) crystal planes is 17.5°. Therefore, $F_{(0\ 0\ 6)+(1\ 0\ 10)}$ can be used as an index of the amount of roughly aligned grains with the {001} planes parallel to the original sheet surface. The maximum F value was attained for M30, and $F_{(0\ 0\ 6)+(1\ 0\ 10)}$ reached 0.78 for the specimen sintered at 1700°C for 20h.

The relationship between F and the sintering conditions for the specimens prepared with 5% of different-sized plate-like particles is shown in Fig. 10. M5 exhibited higher $F_{(0\ 0\ 6)+(1\ 0\ 10)}$ than both L5 and S5. Figure 10 shows the general tendency that higher sintering temperatures result in higher F . In contrast, increased sintering time at 1700°C reduced the F values for the M5 and S5 specimens.

The Lotgering factors for the vacuum-sintered specimens are listed in Table 2. The maximum F value was obtained for M30, and $F_{(0\ 0\ 6)+(1\ 0\ 10)}$ reached 0.30 or above for most of the other specimens. Although three specimens prepared with 5% of plate-like particles had similar $F_{(0\ 0\ 6)+(1\ 0\ 10)}$, the values of $F_{(0\ 0\ 6)}$ divided by $F_{(1\ 0\ 10)}$ were smaller for smaller plate-like particles, which reflects the difficulty in alignment of small plate-like particles as noted in 3.3.

3.6 Observation of microstructure using EBSD

Figures 11 and 12 show crystal direction maps obtained from EBSD for specimens sintered in air and vacuum, respectively, at 1700°C for 4h. The vertical direction in the pattern corresponds to the stacking direction of the formed sheets. Red grains in the

figures indicate that the (001) crystal axis of each grain is oriented within 20° from the vertical direction. These results indicate several features: non-uniformity in terms of both grain shape and crystallographic orientation is present in many of the specimens, the grain size in a vacuum-sintered body is larger than that in the normal -sintered body prepared from the same batch, and the crystal axis orientation of each grain does not necessarily correlate with its shape.

4. Discussion

4.1 Microstructure of normal-sintered ceramics

As shown in Fig. 3, the addition of plate-like particles retards the densification of alumina by normal sintering. Therefore, the use of a small amount of small plate-like particles is desirable to

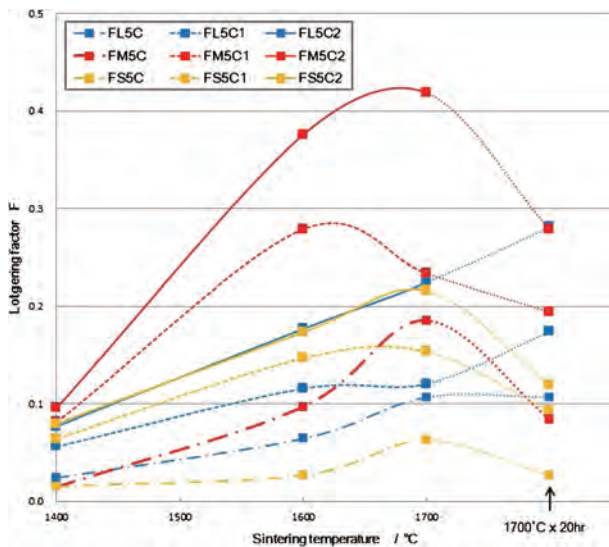


Fig. 10. Relationship between *F* value and normal-sintering conditions for specimens prepared with different platelet size particles. The key legend shows the specimen names and Miller indices from which the Lotgering factors were calculated. C, C1 and C2 correspond to $F_{(0\ 0\ 6)}$, $F_{(1\ 0\ 10)}$ and $F_{(0\ 0\ 6)+(1\ 0\ 10)}$, respectively.

obtain dense sintered bodies of high-purity alumina by the TGG method in the present study. On the other hand, the addition of sintering aids promotes densification, often accompanied by the spontaneous development of plate-like alumina grains in the sintered body.¹⁸⁾

4.2 Texture of normal-sintered ceramics

No evidence of plate-like particles was observed for M100 in Fig. 6(a), which originally consisted of only plate-like particles before sintering. The $F_{(0\ 0\ 6)+(1\ 0\ 10)}$ value evaluated from XRD measurements for M100 was ca. 0.2, while that for the same specimen was 0.4 when sintered at 1600°C for 4 h. This indicates that the crystal orientation of the sheet compact remained, even though there was no clear evidence in the microstructure from SEM observations. For M30, which originally contained 30% plate-like particles, the microstructure shown in Fig. 6(c) reveals anisotropic grains that are longer in the horizontal direction, which corresponds well with $F_{(0\ 0\ 6)+(1\ 0\ 10)} = 0.78$ shown in Fig. 9. Thus, the fracture surfaces of the M100 and M30 specimens are compared for each sintering temperature in Fig. 13 to discuss the evolution of the grains during sintering.

The grains shown in Fig. 13(a) are ca. 2 μm in length and have an aspect ratio of around 10, corresponding to approximately the same length and half the aspect ratio as those for the original plate-like particles, indicating dominant growth in the thickness direction when sintering at 1400°C. This specimen was not almost densified, i.e., a bulk density was 2.43 g·cm⁻³ and an open

Table 2. Lotgering factors for specimens vacuum sintered at 1700°C for 4 h

Specimen name	$F_{(0\ 0\ 6)}$	$F_{(1\ 0\ 10)}$	$F_{(0\ 0\ 6) + F_{(1\ 0\ 10)}}$	$F_{(0\ 0\ 6)}/F_{(1\ 0\ 10)}$
M100	0.08	0.34	0.43	0.24
M60	0.08	0.42	0.50	0.19
M30	0.12	0.49	0.61	0.24
M5	0.07	0.23	0.30	0.30
L5	0.11	0.17	0.28	0.65
S5	0.04	0.27	0.31	0.15

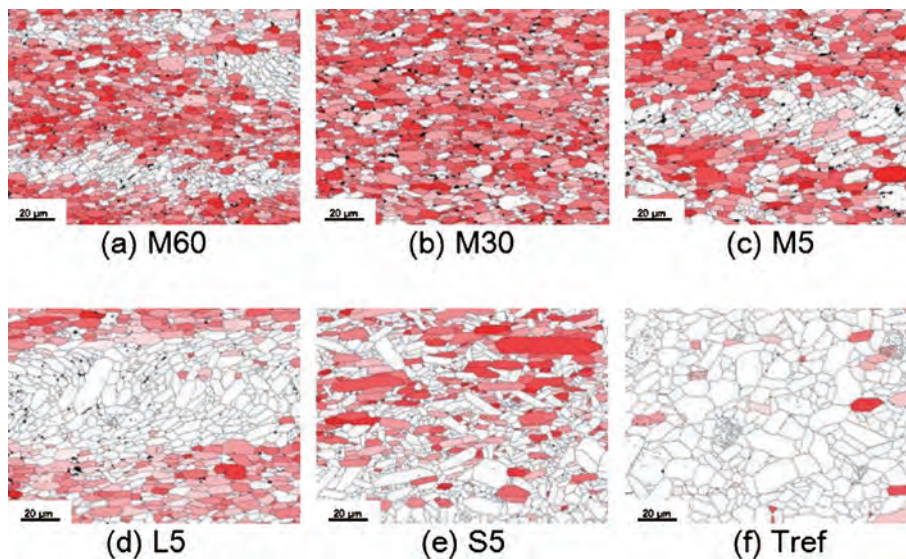


Fig. 11. Crystal direction maps obtained using EBSD for specimens sintered in air at 1700°C for 4 h. The vertical direction in the micrographs corresponds to the stacking direction of the formed sheets. Red-colored grains indicate that the (001) crystal axis of each grain is oriented within 20° from the vertical direction in each map.

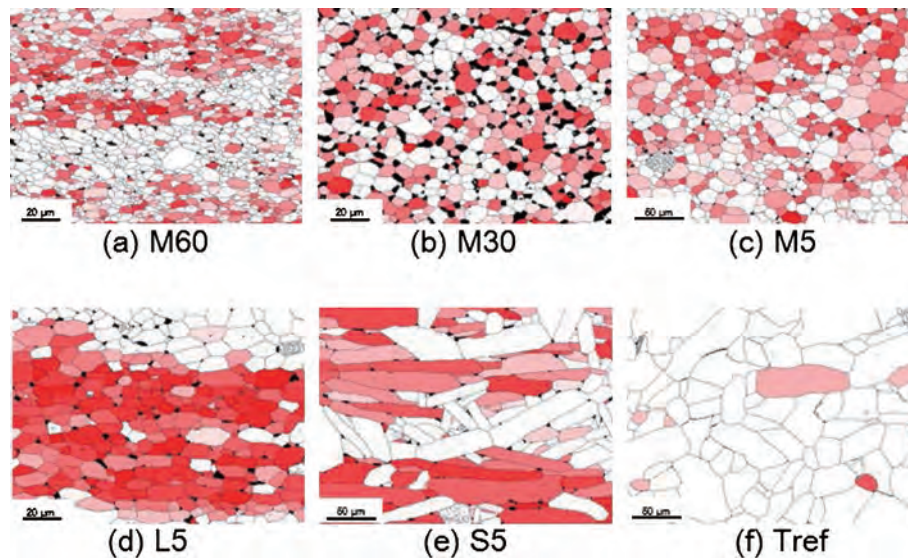


Fig. 12. Crystal direction maps obtained using EBSD for specimens sintered under vacuum at 1700°C for 4 h. The vertical direction in the micrographs corresponds to the stacking direction of the formed sheets. Red-colored grains indicate that the (001) crystal axis of each grain is oriented within 20° from the vertical direction in each map.

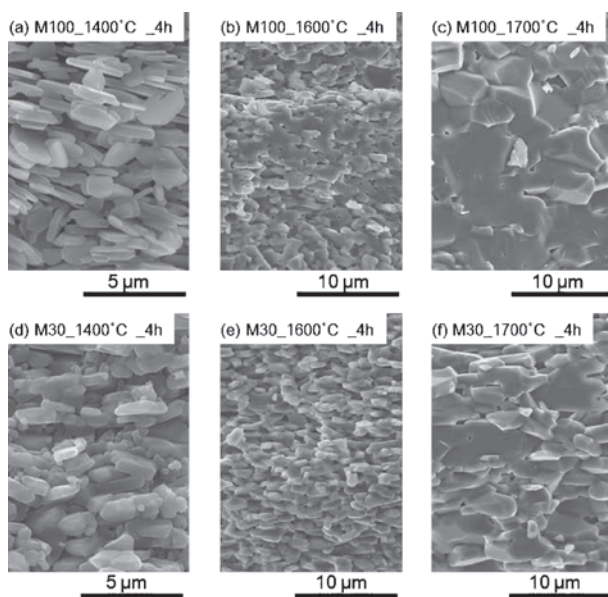


Fig. 13. SEM images of fracture surfaces of M100 and M30 sintered at three different temperatures for 4 h in air. The vertical direction in the micrographs corresponds to the stacking direction of the formed sheets.

porosity was 38.5%. The M100 specimen shown in Fig. 13(b) was sintered at 1600°C and has a bulk density of 3.41 g·cm⁻³ and an open porosity of 14.2%, which indicates significant growth in thickness accompanied by growth in the length direction, and tight bonding between grains. This stage is the so-called intermediate stage in sintering theory. The specimen in Fig. 13(c) was sintered at 1700°C and shows further grain growth to form a granular structure with no evidence of the original plate-like particles. The corresponding $F_{(006)+(1010)}$ values vary from 0.26 for Fig. 13(a), 0.41 for (b) to 0.14 for (c). The sintering mechanism for the pure plate-like particle compact was considered to involve growth in the thickness direction, followed by coalescence of grains to form granular shapes, and further grain growth. The mechanism for the degradation of crystal orientation

above 1600°C may be the rearrangement of grains; however, further investigation is required to understand the intermediate stage of sintering.

M30 sintered at 1400°C [Fig. 13(d)] reached a bulk density of 3.44 g·cm⁻³ and an open porosity of 14.3%, which are almost the same as those for M100 sintered at 1600°C [Fig. 13(b)], which indicates the effective role of equiaxed fine particles for densification at relatively low temperatures. Equiaxed particles blended at 70% in the raw material are not distinguishable in Fig. 13(d) and a significant increase in thickness was evident compared with that observed in Fig. 13(a). The specimen in Fig. 13(e), which reached a bulk density of 3.72 g·cm⁻³ and an open porosity of 3.6%, has uniform small elongated grains in the horizontal direction of the micrograph. The specimen shown in Fig. 13(f) was sintered at 1700°C and shows both further anisotropic grain growth and densification. The specimen with an extended sintering time is shown in Fig. 6(c), where a continuous development of the microstructure is observed; however, it is necessary to examine the relationship between the increased orientation and the developed microstructure in more detail.

4.3 Microstructure of vacuum-sintered ceramics

As shown in Fig. 3, specimens M100, M60 and M30, which originally contained large amounts of plate-like particles, remained at low density after vacuum sintering compared with the specimens that were sintered at the same temperature in air. However, both the vacuum-sintered specimens with and without the addition of 5% plate-like particles reached densities as high as the normal-sintered specimens. Considering the final stage of sintering, heating in vacuum is advantageous to eliminate closed pores in the sintered body because there is no residual air in the pores. Therefore, densification of the vacuum-sintered specimens with larger amounts of plate-like particles was retarded before the formation of closed pores. The occurrence of neck formation in the vacuum-sintered specimens with ≥30% plate-like particles [Figs. 8(a)–8(c)] suggests that surface diffusion rather than volume diffusion may be dominant under vacuum conditions at 1700°C.

Figures 11 and 12 enable a comparison of the specimen

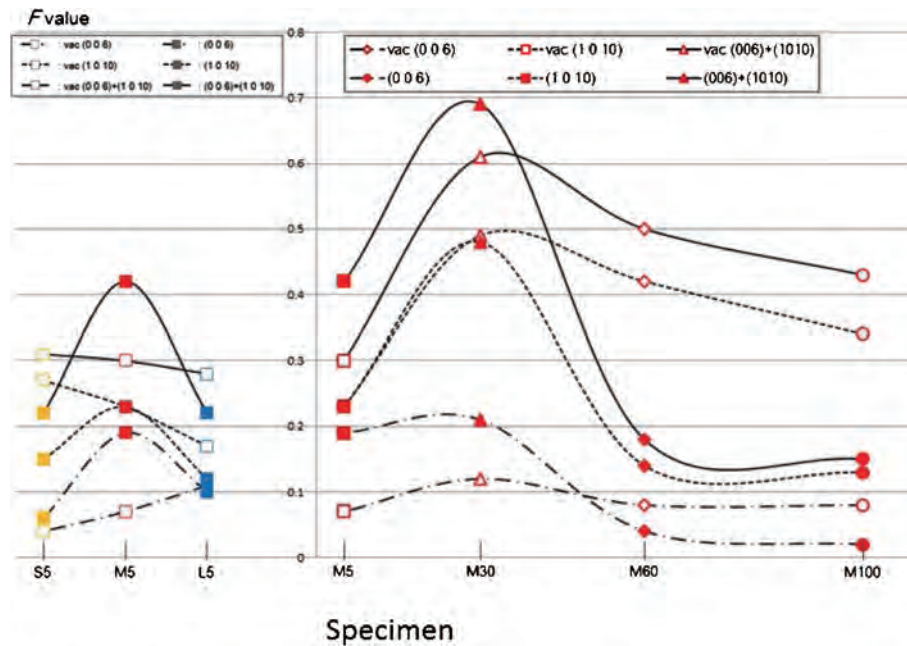


Fig. 14. F values for specimens sintered at 1700°C for 4h. Filled and open marks represent normal and vacuum sintering, respectively.

microstructures produced by sintering in air and under vacuum, respectively. Whereas the vacuum-sintered M30 in Fig. 12(b) has a porous structure composed of equiaxed grains, the normal-sintered M30 in Fig. 11(b) is dense and composed of small elongated grains. The vacuum-sintered S5 in Fig. 12(e) has a dense structure and significantly large elongated grains are observed, while the normal-sintered S5 in Fig. 11(e) is dense and composed of small anisotropic grains. From this evidence, the vacuum sintering of α -alumina is considered to result in significant grain growth compared with normal sintering, which is probably facilitated by the promotion of grain boundary diffusion by the introduction of oxygen defects followed by densification. When significant grain growth occurs before densification, a porous structure with low density would result, as if a coarse powder compact had been used as a starter. For dense specimens such as those shown in Figs. 12(e) and 12(f), significant grain growth may occur by enhanced diffusion.

4.4 Texture of vacuum-sintered ceramics

Figure 14 shows the F values for specimens sintered at 1700°C for 4h by both normal- and vacuum-sintering. It should be noted that the vacuum-sintered M100, M60, and M30 specimens exhibited relatively high F values, even though their microstructures (Figs. 8 and 12) are dominated by equiaxed grains. This result indicates that anisotropic grain growth is not necessarily an essential condition for macroscopic texture in alumina ceramics.

4.5 Non-uniformity of sintered body microstructure

The layered microstructures shown in Figs. 11 and 12 indicate that there is significant non-uniformity in the original tape-cast sheet, in terms of both the amount and alignment of plate-like particles. For the large and medium-sized platelets (YFA05025 and YFA02025), the weights of the platelets were estimated to be 1000 and 100 times higher than the matrix TM-DAR particles, respectively. Therefore, the sedimentation of heavy platelets may have easily occurred during the sheet forming process.

5. Conclusion

Tailoring techniques for the formation of alumina polycrystalline sintered bodies without the use of sintering aids was investigated. Plate-like corundum particles with a high aspect ratio and developed a - b planes were blended with readily sinterable fine equiaxed particles in several ratios, formed into a green sheet by a doctor blade technique, and sintered in air or under vacuum to examine whether and how the sintered body inherits the crystal orientation of the template. Unlike a system with a liquid phase former, plate-like particles tend to grow with a lower aspect ratio at high temperatures. Such pseudo-isotropic grain growth was more notable for the vacuum-sintered specimens with larger amounts of plate-like particles. The addition of plate-like particles to fine equiaxed powder suppresses grain growth and densification during sintering compared to a system with pure equiaxed powder. The degradation of crystal orientation was considered to be attributed to the rearrangement of grains during the intermediate stage of sintering. The addition of 30% plate-like particles produced sintered bodies with the highest texture ($F_{(006)+(1010)}$ ca. 0.7–0.8), although some pores still remained. The addition of 5% plate-like particles resulted in sintered bodies with full density and medium texture. The texture in ceramics could be improved by optimization of the sheet forming process to achieve uniformly-dispersed and well-aligned plate-like particles in a green sheet.

Acknowledgement The authors would like to thank Professor M. A. Gulgun of Sabanci University and Dr. Y. Takeda of Toyota CRDL for fruitful discussions on the microstructural development and the light transmission of alumina, respectively.

References

- 1) R. Apetz and M. P. B. van Bruggen, *J. Am. Ceram. Soc.*, **86**, 480–486 (2003).
- 2) A. Ikesue, I. Furusato and K. Kamata, *J. Am. Ceram. Soc.*, **78**, 225–228 (1995).

- 3) A. Krell, P. Blank, H. W. Ma, T. Hutzler, M. P. B. van Bruggen and R. Apetz, *J. Am. Ceram. Soc.*, **86**, 12–18 (2003).
- 4) R. L. Coble, US 3,026,210 (1962).
- 5) J. Petit, P. Dethare, A. Sergent, R. Marino, M.-H. Ritti, S. Landais, J.-L. Lunel and S. Trombert, *J. Eur. Ceram. Soc.*, **31**, 1957–1963 (2011).
- 6) X. Jin, L. Gao and J. Sun, *J. Am. Ceram. Soc.*, **93**, 1232–1236 (2010).
- 7) A. Krell, T. Hutzler and J. Klimke, *J. Eur. Ceram. Soc.*, **29**, 207–221 (2009).
- 8) T. Suzuki, Y. Sakka and K. Kitazawa, *Adv. Eng. Mater.*, **3**, 490–492 (2001).
- 9) X. Mao, S. Wang, S. Shimai and J. Guo, *J. Am. Ceram. Soc.*, **91**, 3431–3433 (2008).
- 10) D. Brandon, D. Z. Chen and H. L. Chan, *Mater. Sci. Eng. A-Struct.*, **195**, 189–196 (1995).
- 11) T. Carisey, I. Levin and D. G. Brandon, *J. Eur. Ceram. Soc.*, **15**, 283–289 (1995).
- 12) M. M. Seabaugh, I. H. Kerscht and G. L. Messing, *J. Am. Ceram. Soc.*, **80**, 1181–1188 (1997).
- 13) E. Suvaci, M. M. Seabaugh and G. L. Messing, *J. Eur. Ceram. Soc.*, **19**, 2465–2474 (1999).
- 14) M. D. Snel, J. van Hoolst, A. M. de Wilde, M. Mertens, F. Snijkers and J. Luyten, *J. Eur. Ceram. Soc.*, **29**, 2757–2763 (2009).
- 15) Taimei Chemicals Co., <http://www.taimei-chem.co.jp/product/english/01.html>.
- 16) T. Sugimoto, A. Muramatsu, K. Sakata and D. Shindo, *J. Colloid Interface Sci.*, **158**, 420–428 (1993).
- 17) K. Lotgering, *J. Inorg. Nucl. Chem.*, **9**, 113–123 (1959).
- 18) K. Yokota and Y. Kondo, *J. Ceram. Soc. Japan*, **106**, 855–859 (1998).